

# 12th Heavy Ion Accelerator Technology Conference (HIAT2012)

June 18-21, 2012  
Chicago, Illinois





## WELCOME

Dear Attendee,

On behalf of the Local Organizing Committee, we would like to welcome you to Chicago for the 12<sup>th</sup> Heavy Ion Accelerator Technology Conference (HIAT2012) hosted by Argonne National Laboratory, June 18-21, 2012. We hope many of you will be able to participate in the High-Mass RIB Workshop on June 22<sup>nd</sup> at Argonne.

HIAT is an international conference dedicated to the design, construction, development and operation of heavy-ion accelerators and their components. It focuses on the operational experience of existing facilities, achievements in heavy-ion accelerator physics and technology, progress on the implementation of new projects and infrastructure upgrades, and trends in the proposal and design of heavy ion accelerators as well as their main systems and components.

Sincerely,



Richard Pardo, Co-Chair



Richard Vondrasek, Co-Chair



# Contents

|  |          |
|--|----------|
| <b>Preface</b>   | <b>i</b> |
| Foreword . . . . .   | iii      |
| Contents . . . . .   | v        |
| Committees . . . . .   | vii      |
| <br>   |          |
| <b>Papers</b>  | <b>1</b> |
| MOA01 – Frontier Technologies and Future Directions in High Intensity ISOL RIB Production . . . . .  | 1        |
| MOB01 – The FRIB Project – Accelerator Challenges and Progress . . . . .   | 8        |
| MOB02 – Design Study of In-flight Fragment Separator for Rare Isotope Science Project in Korea . . . . .   | 20       |
| MOB03 – Design and Status of the Super Separator Spectrometer for the GANIL SPIRAL2 Project . . . . .  | 23       |
| MOB04 – Argonne In-flight Radioactive Ion Separator . . . . .  | 24       |
| MOB05 – Rare-Isotope Beam Facilities in Asia . . . . .   | 28       |
| MOC01 – Progress and Plans for High Mass Beam Delivery at TRIUMF . . . . .   | 33       |
| MOC02 – Progress of the SPIRAL2 Project . . . . .  | 40       |
| MOC03 – Operational Considerations for Future Multi-user RIB Facilities . . . . .  | 41       |
| MOC04 – Commissioning Experience with CARIBU . . . . .   | 45       |
| PO02 – GANIL Operation Status and Upgrade of SPIRAL1 . . . . .   | 51       |
| PO03 – The RIB Dynamics of the SPIRAL 2 Transfer Line . . . . .  | 54       |
| PO04 – The Darmstadt Multi-Frequency Digital Low Level RF System in Pulsed Application . . . . .   | 58       |
| PO05 – Control and Information System for BARC – TIFR Superconducting LINAC Booster . . . . .  | 62       |
| PO06 – Extension of Superconducting LINAC Operation to Lighter Beams . . . . .   | 65       |
| PO09 – Progress on the RFQ Beam Cooler Design for SPES Project . . . . .   | 68       |
| PO10 – Performance of ALPI New Medium Beta Resonators . . . . .  | 73       |
| PO12 – Damage Situation of the 12UD Pelletron Tandem Accelerator at the University of Tsukuba by the Great East Japan Earthquake . . . . .                     | 80       |
| PO13 – Longitudinal Beam Motion in the KEK Digital Accelerator: Tracking Simulation and Experimental Results . . . . .   | 83       |
| PO14 – Feedback of Slow Extraction in CSRm . . . . .   | 89       |
| PO16 – MULTIPHYSICS AND PRESSURE CODE ANALYSIS FOR QUARTER WAVE $\beta=0.085$ AND HALF WAVE $\beta=0.29$ RESONATORS . . . . .                                  | 92       |
| PO17 – Simulation of Electron and Ion Dynamics in an EBIS . . . . .  | 97       |
| PO18 – Tandem EBIS . . . . .   | 101      |
| TUA01 – Heavy Ion Accelerator Development at IUAC Delhi . . . . .  | 105      |
| TUA02 – A Cost-Effective Energy Upgrade of the ALPI Linac at INFN-Legnaro . . . . .  | 106      |
| TUA03 – The Compact Pulsed Hadron Source Status* . . . . .   | 112      |
| TUB01 – Development of NRA System for a 1.7MV Tandem Accelerator-Human Resource Development Program for Nuclear Engineering, The University of Tokyo . . . . . | 115      |
| TUB02 – New Developments at the Tandem Accelerators Laboratory at IFIN-HH . . . . .  | 118      |
| TUB03 – Terminal Voltage Stabilization of Pelletron Tandem Accelerator . . . . .   | 124      |
| TUB04 – LINAC Experience In The First Two Years of Operation @ CNAO (Centro Nazionale Adroterapia Oncologica) . . . . .  | 129      |
| TUC01 – Physical Design of the SPES Facility . . . . .   | 136      |
| TUC02 – KEK Digital Accelerator and Recent Beam Commissioning Result . . . . .   | 143      |
| TUC03 – Laser Ablation of Solids into an Electron Cyclotron Resonance Ion Sources for Accelerator Mass Spectroscopy . . . . .                                  | 149      |
| TUC04 – Experiences and Lessons Learned at CARIBU with an Open 252Cf Source . . . . .  | 155      |
| WEA01 – Advanced Accelerator Technology Aspects for Hadron Therapy . . . . .   | 156      |
| WEA02 – Focusing of Intense Heavy Ion Beams with Plasma Lenses . . . . .   | 163      |
| WEB01 – Electron Beam Ion Sources, Traps, and Strings: Versatile Devices to Meet the High Charge State Ion Needs of Modern Facilities . . . . .                | 164      |
| WEB02 – Commissioning of CARIBU EBIS Charge Breeder Sub-systems . . . . .  | 165      |
| WEB03 – DREEBIT EBIS/T for Applications in Accelerator Physics . . . . .   | 170      |
| WEB04 – Electron and Ion Beam Dynamics in the CARIBU EBIS Charge Breeder . . . . .   | 172      |
| WEB05 – ECRIS Latest Developments . . . . .  | 173      |

|  |            |
|--|------------|
| WEC01 – Production 72 MHz $\beta=0.077$ Superconducting Quarter-wave Cavities for ATLAS . . . . .                  | 174        |
| WEC02 – Status of the HIE-ISOLDE Project at CERN . . . . .   | 175        |
| WEC03 – The SC CW LINAC Demonstrator – 1st Test of an SC CH-cavity with Heavy Ions . . . . .                       | 182        |
| WEC04 – Operation of Superconducting Linac and Commissioning of the Last Linac at IUAC Delhi . . . . .             | 185        |
| WEC05 – Design Studies for a New Heavy Ion Injector Linac for FAIR . . . . .                                       | 191        |
| THA01 – Heavy Ion Superconducting Linacs: Status and Upgrade Projects . . . . .                                    | 196        |
| THA02 – Overview of the RISP Superconducting Linac . . . . .   | 197        |
| THA03 – Status and Upgrade Project of HIRFL . . . . .  | 198        |
| THB01 – New Developments in Low-Z Gas Stripper Sstem at RIKEN Radioactive Isotope Beam Factory<br>(RIBF) . . . . . | 199        |
| THB02 – New Design for the SARAF Phase II Linac . . . . .  | 206        |
| THB03 – Design Sudy for Front-End System at Rare Isotope Science Project (RISP) . . . . .                          | 207        |
| THB04 – Development of the Intensity and Quality of the Heavy Ion Beams at GSI . . . . .                           | 211        |
| THB05 – The HITRAP Decelerator and Beam Instrumentation . . . . .  | 217        |
| <b>Appendices</b>  | <b>223</b> |
| List of Authors . . . . .  | 223        |
| Institutes List . . . . .  | 227        |
| Participants List . . . . .  | 232        |

### **Conference Co-Chairs**

Richard Pardo, pardo@phy.anl.gov  
Richard Vondrasek, vondrasek@anl.gov

Janet Bergman, Conference Secretary  
HIAT2012@phy.anl.gov

Maria Power, Proceedings Editor  
mpower@anl.gov

Argonne National Laboratory  
9700 South Cass Avenue  
Argonne, IL 60439

Phone: (630) 252-4085  
Fax: (630) 252-9647

### **International Advisory Committee**

Giovanni Bisoffi, INFN-LNL, Legnaro, Italy  
Osamu Kamigaito, RIKEN, Japan  
Oliver Kester, GSI, Germany  
Bernard Laune, Orsay, France  
Robert Laxdal, TRIUMF, Canada  
Daniela Leitner, MSU, USA  
Nikolai Lobanov, Australian National Univ., Australia  
Francis Osswald, IPHC and SPIRAL2, France  
Richard Pardo, ANL, USA  
Zhaohua Peng, China Institute of Atomic Energy, China  
Roland Repnhow, Max-Planck-Inst., Germany  
Danilo Rifuggiato, INFN, Catania, Italy  
Amit Roy, Inter-University Accelerator Centre, India  
Kimikazu Sasa, University of Tsukuba, Japan

### **Local Organizing Committee**

Richard Pardo, Co-Chairman  
Richard Vondrasek, Co-Chairman  
Judy Benigno  
Janet Bergman  
Jacque LeBreck  
Tala Palchan-Hazan  
Kim Miller  
Maria Power  
Robert Scott

# FRONTIER TECHNOLOGIES AND FUTURE DIRECTIONS IN HIGH INTENSITY ISOL RIB PRODUCTION\*

P. G. Bricault<sup>#</sup>, F. Ames, N. Bernier, M. Dombbsky, F. Labrecque, J. Lassen, P. Kunz, A. Mjøs, M. Nozar, J. Wong, TRIUMF, Vancouver, Canada

## Abstract

The future frontier of the ISOL technique is to increase the intensity of the RIB beams. In the ISOL technique several ways to increase substantially the production of rare isotope beam. The most expedient one is to increase the incident beam. Increasing the overall release efficiency and ionization efficiency are the other two easiest ways to increase the overall RIB intensity.

Now with the TRIUMF/ISAC facility the ISOL RIB facility can operate routinely up to 50 kW, this is 100  $\mu$ A on target. But, the driver beam intensity cannot increase without considering the radiation damage issues and the challenge to the ion source itself where ionization efficiency is dramatically affected by target out-gazing.

The other technology challenge for the ISOL technique is the target material itself. The main concern is the capability of the target material to sustain high power density deposited by the driver beam. Refractory metals foil target are suitable but nevertheless very limited in the available species we can produce with those targets. We have developed composite target at ISAC that increases the overall target thermal conductivity in order to be able to operate carbide and oxide at full beam intensity for the carbide and at 30 kW for the oxide targets, respectively. The other solution is to use two-step target where the driver beam impinges a converter, which is decoupled from the ISOL target.

## INTRODUCTION

The production of Rare Isotope Beam (RIB) is quite a challenge mainly due to fact that the most interesting rare isotopes are the one that lied close to the limit of stability both on the neutron rich and deficient side and most of the time very have short half-life. Making it difficult to make them using techniques such as chemical or mass separation off-line. In the On-Line Isotope Separation (ISOL) method, the isotopes are produced by nuclear reactions in a thick target that is closely coupled to the ion source, allowing them to be quickly turned into an ion beam that can be mass analyzed and transport efficiently to experiments.

The main challenge comes from the fact that the reaction products stop in the bulk of the target and the atoms have to be released efficiently out of the target container before we can make an ion beam. The steps for producing RIB from the ISOL method are:

- A high energy beam impinging onto a thick target material enclosed in a target container, which is directly coupled to an ion source,

- The isotopes are produced in nuclear reactions and come to rest embedded in the target material,
- The rare atoms have to diffuse through the target material grain or foil lattice to the surface, diffusion process,
- The rare atoms have to effuse, meaning bounce around until it reaches the exit hole of the target container leading to the ion source. Each time the rare atom has to desorb from the surface, effusion process,
- The rare atoms has to be ionized and extracted to form an ion beam, ionization process,
- The beam is mass analyzed and transported to the experiment.

The challenge is to optimize each step if to produce an intense, pure ISOL RIB.

The frontier technologies in ISOL RIB production are to achieve higher RIB intensity of nearly all isotopes, especially in the extreme neutron rich area of the nuclear chart. There are several paths to achieve higher RIB intensity,

- Increase of the driver beam intensity on target,
- Improve the release efficiencies out of the ISOL target, especially for the refractory species,
- Improve the ionization efficiency and
- Efficient high charge state breeding.

Increasing the driver intensity will lead directly to higher ISOL RIB intensity, but to do so we need to improve the target material and the target container for higher power deposition, section 1 and 2 describes the advance in target material fabrication and target container at ISAC. Section 3 describes the attempt to improve the release of radioactive isotope from thick target and section 4 describes the advance in the ion source technology to improve the beam purity from Resonant Ionization Laser Ion Source and plasma ion sources, electron impact and cyclotron resonances ion sources. Finally, section 5 describes the future project under construction and the next generation of ISOL target station.

## ISOL RIB PRODUCTION

To reach higher ISOL RIB one can increase the incident driver beam on target. This can only be achieved at the condition that the target material and the target container are capable of sustaining reliably the power deposition by the driver beam. Firstly, the target material has to have a thermal conductivity high enough to release the power deposited inside the target material to the target container. Secondly, the target container has to be capable of dissipating the heat from the target material to the

\*Work supported by TRIUMF who receives funds from the federal government through the Canadian NRC.  
# bricault@triumf.ca

surrounding while keeping the target material at its optimum temperature.

### Target Material for High Power Beam

In the ISOL method the radioactive atoms produced during the interaction of the driver beam onto the target material nucleus come to rest and are embedded into the target material lattice. In order to have a high release efficiency the target material has to be operating at its temperature limit which keeps the vapor pressure acceptable for the ion source. It is important to select the target material for:

- Its ability to produce the RIB species desired by the experimentalist,
- High thermal conductivity,
- Low vapor pressure.

Usually, refractory foils made of tantalum and niobium and carbides discs are among the best candidates.

Table 1 gives the list of the target material and the type in used at ISAC and the power on target of the incident beam. To achieve high power density on target the target material has to have large thermal conductivity. For the refractory foils it is possible to go up to 50 kW, while it is more difficult for other target material such as carbide or oxide. In those cases we have developed the composite foil target allowing an increase of the power on target by more than an order of magnitude for the oxide and by a factor 5 for the carbide target material.

Table 1: Target Material in Used at ISAC

| Material                       | Type      | Backing Support | Beam Power kW |
|--------------------------------|-----------|-----------------|---------------|
| Ta                             | Foil      | -               | 50            |
| Nb                             | Foil      | -               | 50            |
| CaO                            | Pellet    | -               | 0.5 to 1      |
| Al <sub>2</sub> O <sub>3</sub> | Composite | Nb foil         | 12.5          |
| UO <sub>2</sub>                | Pellet    | -               | 1             |
| SiC                            | Pellet    | -               | 5             |
| SiC                            | Composite | Graphite foil   | 35            |
| TiC                            | Composite | Graphite foil   | 35            |
| ZrC                            | Composite | Graphite foil   | 40            |
| TaC                            | Composite | Graphite foil   | 35            |
| UCx                            | Composite | Graphite foil   | 5             |

### ISOL Target Container for High Intensity RIB

Challenging experiments forced us to increase the incident driver beam on target with the goal of producing higher RIB intensity. To do so the ISOL target oven has to

be capable of dissipating the power deposited by the incident beam very efficiently.

The ISAC high power target[1] (IHPT) was developed to accommodate the TRIUMF 50 kW proton beam. The conventional target at ISOL facilities such as ISOLDE, SPIRAL and HRIBF can only accommodate for less than 1 kW dissipated power inside the target. There were several attempts in developing the ISOL target for higher power dissipation, by Ravn[2], Talbert[3], Nitschke[4] and RIST collaboration[5]. The most promising being the RIST because of the simple cooling design. But, the target fabrication is quite limiting because it required diffusion bonding and can only be applied to a few target materials, Mo, Nb, Ta and W. The ISAC High Power Target, IHPT, utilizes the thermal radiation cooling and is made of a 20 cm long and 2 cm in diameter tantalum tube onto which radial fins are installed. The fins are diffusion bonded to the target container by heating the tube in vacuum at 1500 °C for a period of approximately 20 hours. The overall emissivity measured is 0.92 which allows operating the target at nominal 2200 °C up to 20 kW of deposited power by the proton beam.

The challenge with increasing proton beam on target comes in several forms: 1) the radiation damage of the tantalum tube, 2) the thermal shock when the proton beam goes off and 3) chemical reactions between the tantalum container and the target material or the radiological impurities created.

All these processes create cracks in the tantalum container allowing the rare isotope atoms of interest to escape the container reducing the output yield.

### ARIEL TARGET STATION TECHNOLOGY

The goal of the ARIEL project is to be able to deliver more RIB to experiments. The project is based on a 50 MeV: 10 mA electron LINAC and on another 100 μA proton beam for producing the ISOL RIB. This means that we will have two new target stations, one for the electron beam and one for the proton beam. The target stations will be based on the ISAC technologies developed over the past 10 years.

The target stations are located in a sealed building serviced by an overhead crane. The target maintenance facility includes a hot cell, warm cell, decontamination facilities and a radioactive storage area. The target area is sufficiently shielded so that the building is accessible during operation at the maximum proton beam current.

Beam-line elements near the target are installed inside a large T-shaped vacuum chamber surrounded by close-packed iron shield. This general design eliminates the air activation problem associated with high current target areas by removing all the air from the surrounding area. The design breaks naturally into modules; an entrance module containing the primary beam diagnostics, an entrance collimator and a pump port; a beam dump module containing a water cooled copper beam dump; a target module containing the target/ion source, extraction electrodes and first guiding component and heavy ion diagnostics; and two exit modules containing the optics

and the associated diagnostics for the transport of heavy ion beams.

The vacuum design seeks to eliminate the need for radiation-hard vacuum connections at beam level by using a single vessel approach. The front-end components, with their integral shields, are inserted vertically into the T shaped single large vacuum vessel. Most vacuum connections are situated where elastomer seals may be used. Only two beam-level connections exist; one at the proton beam entrance and one at the heavy ion beam exit.

The target stations are shielded by approximately 2 m of steel placed above the target. Outside this steel shielding the operating radiation fields will be sufficiently low so that radiation damage to equipment is not a concern. The steel shielding is surrounded by an additional 2-4 m of concrete, which provides the required personnel protection during operation. To service the targets, shielding above the target station is removed giving access to the services at the top of the steel shielding plugs. Residual radiation fields at this level will be low enough to allow hands-on servicing.

With ARIEL new target stations we have an opportunity to improve the current target station design and bring it to the next level. We have learn so much from the past ten years of operation at ISAC and this is why the next generation of ISOL target station will not be an exact copy of the ISAC target station. At the time we had to invent most of the technologies without very much experience. Before designing the design of the new target stations we must evaluate the existing ISAC target technologies we used a type of analysis used in product manufacturing, it is called design failure mode effect analysis, DFMEA. Each item or function of the system is analyzed. A list of potential or experienced failure, potential or experienced effect of the failure mode, the causes of the failure are described. Then the severity (S) of the failure is given a number from 1 to 10, 1 being benign and 10 severe. The occurrence (O) of the failure is also given a number from 1 to 10, 1 being 1 in  $10^3$  cycle and 10 is a failure that arise 1 every running period. The ease of detection (D) to prevent the failure is given a number from 1 to 10, 1 being easy to detect the failure and 10 being very difficult. The product of  $S \cdot O \cdot D$  represent the risk priority given for that failure mode. From there we decide of the criticality of that failure mode and recommend action and record the Engineering Change Order associated with the action. The person responsible for the action and the date of completion is also recorded in the DFMEA documents. This document follows the product in its life cycle. The following findings were made during a design failure mode effect analysis, DFMEA, of the target station and target module.

On the pros side:

- 1) The modular approach allows us to operate at the design proton beam intensity, 100  $\mu$ A. The non radiation resistant components, such as o-rings, turbo pumps, actuators, cable, ... are well

protected by the module and target station steel shielding.

- 2) The two stage mass separator composed of a low and a high-resolution separator in cascade. The first set of selection slit located at the focal plane of the first separator inside the heavily shielded target hall allow the elimination of most of the unwanted radioactive beam isotopes in a well defined manner, limiting the contamination.
- 3) We never had to change the optics in the two modules for the heavy ions beam transport from the ion source to the pre-separator and the entrance and beam dump modules.

On the cons side:

- Vacuum system is very complex. There two different pressure volumes, the primary and the secondary vacuum envelopes. Pillow seals are used to seal the target box volume to the exit module vacuum for the heavy ions beam line.
- The target box housing the target/ion source assembly is not hermetically sealed. This makes the target module transfer of the spent target from the target station to the hot cell is done at atmospheric pressure. There is a risk of spreading contamination during the transfer of volatile species. Or more importantly, target materials that are sensitive to moisture in air may reacts strongly and become flammable. In that case the fumes may exit the target box and contaminate the target hall.
  - In the new design the target box will be an hermetically sealable vessel preventing the contamination during the transfer of the irradiated target from the target station to the hot-cell.
  - The fact that the target box is hermetically sealable will allow the elimination of the two vacuum zones. Only one single zone is necessary.
  - This will allow us to condition fully the high voltage of the target module equipped with the new target and keep the target module under vacuum during the transfer limiting the risk of spreading contamination and delay in the start up of a new target.
- The mechanical and electrical service connections necessary to operate the target/ion source assembly have to be disconnected manually. In order to permit a person to disconnect the services we have to allow for a cool down period. A complete cycle for the target exchange takes about 3 to 4 weeks.
  - A built in remote service connection and disconnection has to be incorporated into the design at the beginning. T
- Since the target exchange take so long we are forced to operate the target / ion source much longer than desired. We have notices that after two weeks of continuous operation at 70  $\mu$ A and above the production yield drop significantly. Radiation damages are clearly visible on the target container

and it reduces the overall target performances. We can see cracks on the target container, which can lead to radioactive atoms to leave the target container before reaching the ion source.

- The servicing of the selection slits is made using human intervention in the present design. This limits greatly the maintenance to the minimum until it breaks creating reliability issues.
  - In the new design the selection slits as well as all the target station beam diagnostics will be accessible with the overhead crane, allowing maintenance and repair in the hot-cell.

The new target station design addresses the mentioned findings by implementing new vacuum joint technology and remote services connection.

The remote vacuum seal requirements specification are:

- Provide vacuum seal with a leak rate lower than  $5 \times 10^{-9}$  mbar liter/s,
- Remote actuation, connection and disconnection,
- Robust and reliable, since the area will be highly active due to the high neutron flux, maintenance shall be minimum around these vacuum seals.

In the next generation the steel plug module will be replaced by beam pipe section. Each section will have its own vacuum pumping station composed of two turbo pumps connected to the main beam pipe by a large tube. The rationale is to keep the turbo pumps as far as possible from high radiation field. The beam dump and the entrance module are also replaced by standalone diagnostics box, and beam water-cooled copper plug, respectively. Again the rationale is that we never had to replace any of these devices since starting ISAC operation 12 years ago. These decisions make the vacuum envelope of the target station much simpler than it is for the ISAC case. It also makes the target station much cheaper since 4 module steel plugs are replaced by less expansive shielding, like cast steel plug and concrete block.

The vacuum envelope will comprise the target module containment box, heavy ion beam line and pre-separator to the mass separator. The heavy ion beam line will be built in section that can fit into the hot-cell for maintenance and repair of the sections. The vacuum envelope will be sealed using all metal vacuum joints.

Figure 1 shows a 3-D view of the next generation of target station proposed for the ARIEL project. The new target station will be made of a target module, heavy ion beam line, pre-separator and beam dump. Contrary to the actual ISAC target station there will be only one module, which is the target module. The entrance diagnostics and beam dump will be stand alone device which will not share the same vacuum envelope as the target station.

### *Vacuum Joint Options*

There two vacuum joint technologies envisaged for the ARIEL target stations. The pillow seal, which was

originally developed at Paul Scherrer Institute (PSI) in Switzerland[6] uses a single thin foil to make the vacuum seal. The pillow seal is made using a thin metal foil electron beam welded on a flange. The pillow is inserted between two flanges. High pressure He is pump to inflate the thin foil, also called pillow. The seal joint is made than of two flanges equipped with pillows and two concentric bellow welded on each side to the flanges. The helium gas used to inflate the pillow is also injected into the concentric bellows pushing the flanges outward toward the fixed flanges on each side. A newer design developed for T2K beam window[7] uses a double pillows setup allowing a pump down in between the pillows. They reported in reference 2 a leak rate of  $10^{-8}$  Pa m<sup>3</sup>/s. Unfortunately, this is larger than desirable for constructing the whole heavy ion beam line with this technology. There will be fours of these vacuum joints in the heavy ion beam line, making the total leak rate much larger than acceptable.

Another option is to use HELICOFLEX<sup>®</sup>, C-FLEX<sup>™</sup> seals. This seal technology relies on elastic deformation of the metal “C” shape metal. During compression we obtain a contact point of each sealing surface. The key of success of this joint is to provide the proper, compression force and surface finish.

## **NEUTRON RICH ISOTOPES**

At TRIUMF we are fortunate to have a high energy and high intensity proton driver with the H<sup>-</sup> 500 MeV Cyclotron and a high intensity, 50 MeV: 10 mA, electron driver under construction[8]. We can produce neutron rich isotopes using three different techniques, 5 kW direct proton onto the UCx target, 500 kW two-stage photo-fission using the electron driver and a 50 kW two-stage neutron induced fission using the proton beam on a converter and UCx target. Figure 2 shows all the possible options available at TRIUMF to produce neutron rich rare isotope beams.

### *5 kW Proton on UCx*

This is the actual situation, where the high energetic proton beam impinges onto the UCx target discs. There is several reaction processes as mentioned earlier. This setup is less suitable since the spallation reaction produces isobars that contaminate the desired neutron rich species. Further more, the high energetic proton beam induces fission that yield to less neutron rich isotopes than pure low energy neutron induced fission. The limitation to 5 kW is only due to regulatory consideration not due to the capability of power dissipation of the UCx target, which can go up to 20 kW.

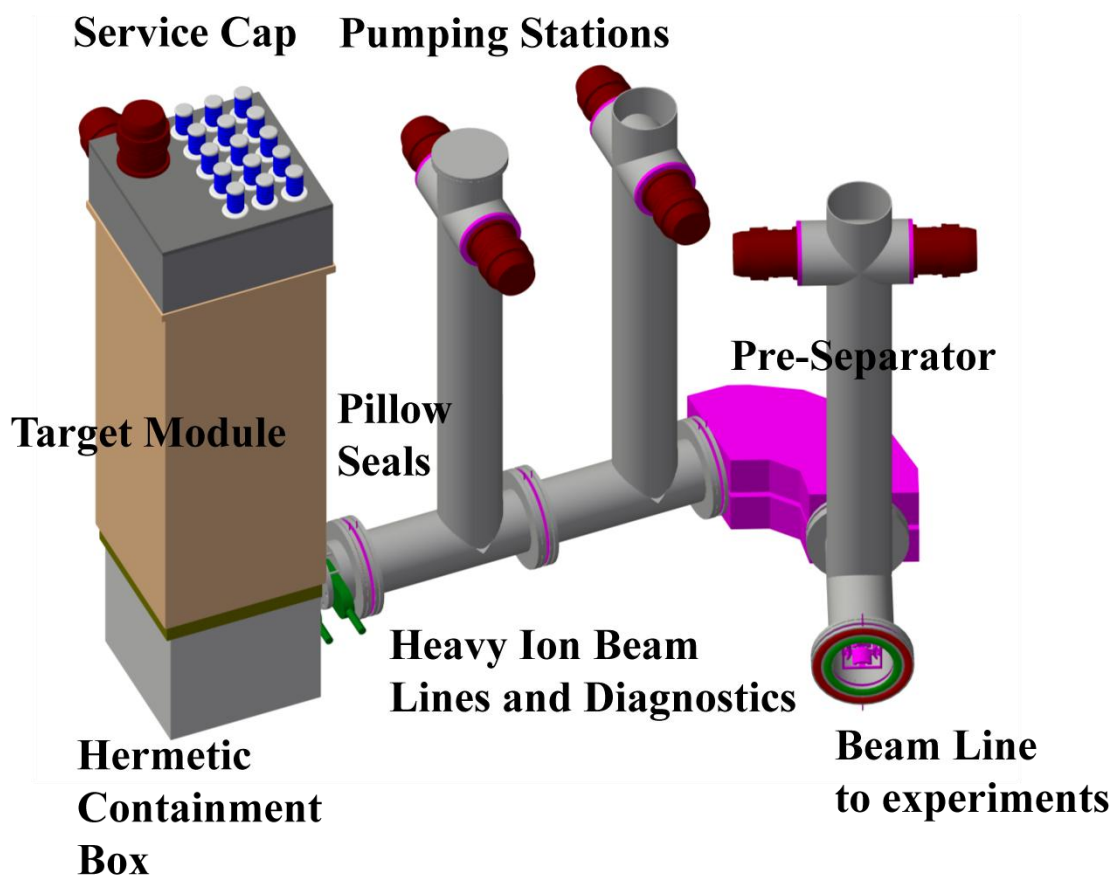


Figure 1: 3-D view of the next generation of target station proposed for the ARIEL project.

*500 kW Electron, Two-stage Photo-fission of  $^{238}\text{U}$*

ARIEL as mention aims to accelerate electron beam up to 50 MeV and 500 kW total beam power. The converter for such power can only be made using liquid lead. Simulation shows that 375 kW is deposited into the converter and 75 kW in the target itself. This is 7 times larger than the power we can handle in one single target. To handle the power deposition in the UCx we will use the composite target technique as described earlier, the uranium carbide will be deposited onto an exfoliated graphite foil. Furthermore, we will divide the target into seven smaller target containers and we will use helium gas to cool the whole target assembly. The minimum flow rate is estimated at 18 He mole/s.

*50 kW Proton on Two-stage U Target*

In this option the proton beam impinges onto a converter material, for example W, Nb, Mo or Ta. The U target is made as an annulus into which the proton beam goes without interacting with the U target. This target is placed in the backward position in such a way that only low energy neutrons can reach the U target. In this case the power deposited in the U target is small since its mainly coming from the fission products stopping in the target material. It is estimated to be only 400 Watts.

*Comparison*

It is interesting to compare the production of some key nuclei with the actual ISAC 5kW proton beam on UCx target, the ARIEL 500 kW electron beam producing photo-fission and the 50 kW proton beam, two-stage target using a W converter and U target. Table 2 gives the production yield in target for the three different setups. As we can see from the table 2 there is not very much difference in the production of the key isotopes between the three options. While option 2 with the photo converter is not readily feasible, option 1 and 3 using 5 and 50 kW, respectively, are readily possible using the actual technologies developed at ISAC.

The main concern for the option 2 is the feasibility of the converter itself. The power density at the entrance window is quite large and we are far from being sure that such window will work. One option is to operate the liquid lead converter without the entrance window.

**ARIEL FIRST BEAM**

A ½ MW electron LINAC accelerator, e-linac , will be built in phases[9,10]. The main components of the eLinac are, an injector cryomodule composed of two capture cavities, and a 5 cell cavity capable of accelerating the electron beam up to 10 MeV and two cryomodules composed of two 9 cell cavities capable of 20 MV each.

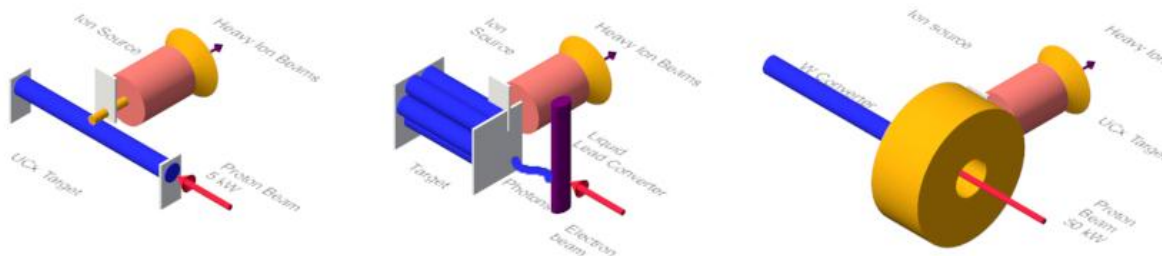


Figure 2: Schematic of the three options available at TRIUMF for producing neutron rich isotopes. From the far left, this represents the actual 5 kW proton beam on UCx target, the middle one is the 500 kW electron beam on a liquid lead converter producing gammas inducing photo-fission and the last one on the right is the two stage target concept. The 50 kW proton beam impinges onto a converter and the UCx target is placed in the backward direction in such way that only slow neutron that are emitted can reach the UCx target.

Table 2- In target production of key nuclei using a 5 kW proton, 500 kW electron and two stage using 50 kW proton on W converter, beam on UCx target.

| Nuclei | 5 kW proton | 500 kW electron | 50 kW proton two-stage |
|--------|-------------|-----------------|------------------------|
| Ni-72  | 3.8E+08     | 2.0E+08         | 8.0E+07                |
| Zn-78  | 1.4E+09     | 3.4E+09         | 8.9E+08                |
| Kr-91  | 5.3E+10     | 2.3E+11         | 2.7E+11                |
| Kr-94  | 1.3E+10     | 1.3E+11         | 6.7E+10                |
| Rb-97  | 7.4E+09     | 1.1E+11         | 1.9E+10                |
| Sn-132 | 1.1E+10     | 2.5E+10         | 1.5E+11                |
| Sn-134 | 1.0E+09     | 2.4E+09         | 1.3E+10                |
| Xe-142 | 1.1E+10     | 5.2E+10         | 1.2E+11                |
| Xe-144 | 1.0E+09     | 7.9E+09         | 9.5E+09                |
| Cs-144 | 6.8E+09     | 6.0E+10         | 7.7E+10                |
| Cs-146 | 5.0E+07     | 9.2E+08         | 9.8E+09                |

Table 3 gives the main specifications for each of the phases.

The electron linear accelerator is due to be fully commissioned by end of 2013 but the target hall will not be ready for uranium target for the photo-fission before the fall of 2017. In the mean time we can produce low activity rare isotope, namely, 8-Li from a beryllium oxide target using the 9-Be( $\gamma$ , p)8-Li.

Figure 3 shows the results of FLUKA[11] simulations showing the 8-Li production as a function of electron energy for a fixed beam intensity of 4 mA.

Table 3: ARIEL eLinac construction phases

| Final Energy (MeV) | Current (mA) | Configuration           | Status/ expected date for completion |
|--------------------|--------------|-------------------------|--------------------------------------|
| 25                 | 1            | Injector + 1 cryomodule | Funded/ 2013 commissioning           |
| 25                 | 4            | Injector + 1 cryomodule | Funded/ 2014 operational for 8-Li    |
| 50                 | 10           | Injector + 2 cryomodule | Proposed /2017 photo-fission         |

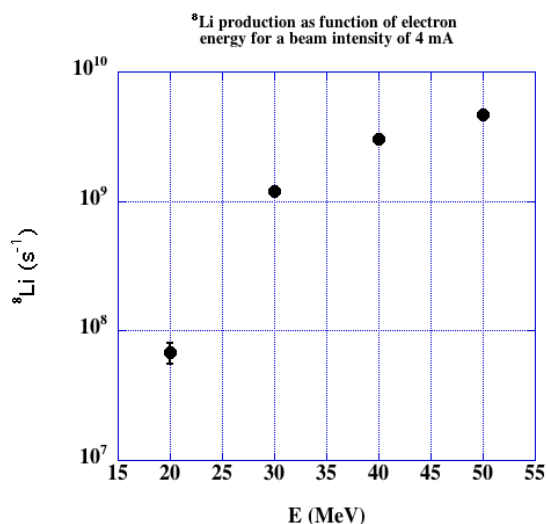


Figure 3: Results of FLUKA simulations of the 8-Li production in target as a function of electron energy for a fixed intensity of 4 mA on a BeO target.

The advantages of using 8-Li from a BeO target are:

- The level of radiation is not extremely large and the 8-Li has a very short half-life of 840 ms only.
- The longest half-life nuclei produced in the target is 7-Be,  $T_{1/2}$  is 53 days.
- We can start an early experimental program with the ARIEL facility.

This mean that the whole target station operation commissioning can be accomplished without risking to contaminate the beam lines as it will be the case for an uranium target.

The 8-Li beam is used by the beta-NMR material science community. High nuclear spin polarization is achieved using a collinear optical pumping method in which polarized light from a laser is directed along the beam axis. The method is well established for the case of alkalis such as 8Li where the neutral atom can be excited with visible laser light. The first step in the procedure is to

neutralize the ion beam by passing it through a Na vapor cell. The neutral beam then drifts 1.9 m in the optical pumping region in the presence of a small longitudinal magnetic holding field of 1 mT. Then the beam goes through a helium gas where the neutral 8-Li is ionized and then it is sent to the beta-NMR experimental setup[12].

### CONCLUDING REMARKS

To satisfy the demand for higher RIB intensity we raise the incident proton beam intensity on target. This was only possible by pushing the technologies for material target and target container to sustain the high power deposition in the ISOL RIB production.

We have developed a technique to make composite target material capable of dissipating larger power deposition. This technique increases the overall thermal conductivity of the target material. The target material is deposited onto a highly conductive substrate, exfoliated graphite foil for the carbide target material and metal foil for oxide target material. Now we are routinely operating the proton beam at 35 to 50 kW.

The target container has to take the heat coming from the target material and dissipate that heat to the target cooling system. We use radiative cooling to get the heat out of the target. A fin target container has been developed for this purpose and it is capable of dissipating up to 20 kW of beam power deposited in the target[13].

With the ARIEL project we have an opportunity to build the next generation of high power target station for producing high intensity ISOL RIB. An analysis of the actual ISAC target station has been performed and the findings will be applied to the design of the next generation of target station.

The ARIEL first beam will be made using a BeO target to produce 8-Li for the material science community. We used FLUKA to obtain the production rate of 8-Li in target, the estimated intensity is well above the need for performing beta-NMR studies.

There are several new projects around the world with the aim of producing intense RIB using fission reaction. The power density inside the U target in all of these projects are exciting the actual capability of carbide material thermal conductivity. A high thermal conductivity target material is mandatory for the success of these projects final goals.

The development of composite target material at TRIUMF/ISAC is a good way to achieve such high thermal conductivity allowing high power RIB production ISOL facility.

Furthermore, the dissipation of the power to the cooling system must use a target oven capable of dissipating the power release from the target material to the cooling environment. The IHPT has proven its capability to dissipate up to 20 kW. To go beyond that we need to use other means like helium gas cooling as anticipated at ARIEL photo-fission target.

Finally, one of the frontiers in physics is the capability of producing intense and pure neutron rich RIB. These

beams can be produced using fission reaction. At TRIUMF we will have access to the fission products by using the photo-fission and a two-stage target system using 50 kW proton beam on a converter.

### ACKNOWLEDGMENT

The authors wish to acknowledge the excellent work of the target/ ion sources and remote handling staff for their excellent work for the ISAC operation and target development.

### REFERENCES

- [1] P. Bricault, M. Dombbsky, A. Dowling and M. Lane, Nucl. Instr. and Meth. B 204 (2003) 319.
- [2] T.W. Eaton, H.L. Ravn and the ISOLDE Collaboration, Nucl. Instr. and Meth. B26 (1987) 190.
- [3] W.L. Talbert, H.H. Hsu and F.C. Prenger, Nucl. Instr. and Meth. B70 (1992) 175.
- [4] J.A. Maddi, M.A. Stoyer, L.F. Archambault, J.J. Ayers and J.M. Nitschke, Nucl. Instr. and Meth. A 397 (1997) 209.
- [5] J.R.J. Bennett, Nucl. Instr. and Meth. B 126 (1997) 105.
- [6] SIN report, Jahresberitch (1984) JB11-18.
- [7] M. Rooney, C. Densham, M. Filton, V. Francis, Y. Yamada, C. Mark and M. Gallop, 3<sup>rd</sup> High-Power Targetry Workshop, Paul Scherrer Institute, Sept. 10-14, 2007, Bad Zurzach, Switzerland.
- [8] L. Merminga, F. Ames, R. Baartman, P. Bricault, Y. Bylinski, Y-C. Chao, R. Dawson, D. Kaltchev, S. Koscielniak, R. Laxdal, F. Mammarella, M. Marchetto, G. Minor, A. Mitra, Y.-N. Rao, M. Trinczek, A. Trudel, V. Verzilov, V. Zvyagintsev, Proceeding of the International Particle Accelerator Conference 2011, San Sebastian, Spain. WEOBA01.
- [9] I. Bylinskii, F. Ames, R. Baartman, P. G. Bricault, Y. Chao, K. Fong, S.R. Koscielniak, R.E. Laxdal, M. Marchetto, L. Merminga, A.K. Mitra, I. Sekachev, V.A. Verzilov, Proceeding of the Particle Accelerator Conference 2009, Vancouver, Canada, WE4PBC04.
- [10] S. Koscielniak, P. Bricault, B. Davids, J. Dilling, M. Dombbsky, D. Karlen, W.A. MacFarlane, Proceedings of EPAC08, Genoa, Italy TUOCG03.
- [11] "FLUKA: a multi-particle transport code" A. Ferrari, P.R. Sala, A. Fassio, and J. Ranft, CERN-2005-10 (2005), INFN/TC\_05/11, SLAC-R-773.
- [12] K.H. Chow, Z. Salman, R.F. Kiefl, W.A. MacFarlane, C.D.P. Levy, P. Amaudruz, R. Baartman, J. Chakhalian, S. Daviel, Y. Hirayama, A. Hatakeyama, D.J. Arseneau, B. Hitti, S.R. Kreitzman, G.D. Morris, R. Poutissou, E. Reynard, Physica B 340 (2003) 1151-1154.
- [13] P. G. Bricault, M. Dombbsky, P. W. Schmor, A. Dowling, Proceeding of the 2003 Particle Accelerator Conference, Portland, Oregon, USA, p. 439-443.

## THE FRIB PROJECT – ACCELERATOR CHALLENGES AND PROGRESS\*

J. Wei<sup>#1</sup>, D. Arenius<sup>2</sup>, E. Bernard<sup>1</sup>, N. Bultman<sup>1</sup>, F. Casagrande<sup>1</sup>, S. Chouhan<sup>1</sup>, C. Compton<sup>1</sup>, K. Davidson<sup>1</sup>, A. Facco<sup>1,4</sup>, V. Ganni<sup>2</sup>, P. Gibson<sup>1</sup>, T. Glasmacher<sup>1</sup>, L. Harle<sup>1</sup>, K. Holland<sup>1</sup>, M. Johnson<sup>1</sup>, S. Jones<sup>1</sup>, D. Leitner<sup>1</sup>, M. Leitner<sup>1</sup>, G. Machicoane<sup>1</sup>, F. Marti<sup>1</sup>, D. Morris<sup>1</sup>, J. Nolen<sup>1,3</sup>, J. Ozelis<sup>1</sup>, S. Peng<sup>1</sup>, J. Popielarski<sup>1</sup>, L. Popielarski<sup>1</sup>, E. Pozdeyev<sup>1</sup>, T. Russo<sup>1</sup>, K. Saito<sup>1</sup>, R. Webber<sup>1</sup>, J. Weisend<sup>1</sup>, M. Williams<sup>1</sup>, Y. Yamazaki<sup>1</sup>, A. Zeller<sup>1</sup>, Y. Zhang<sup>1</sup>, Q. Zhao<sup>1</sup>

<sup>1</sup> Facility for Rare Isotope Beams, Michigan State University, East Lansing, MI 48824 USA

<sup>2</sup> Thomas Jefferson National Laboratory, Newport News, VA 23606, USA

<sup>3</sup> Physics Division, Argonne National Laboratory, Argonne, IL 60439, USA

<sup>4</sup> Istituto Nazionale di Fisica Nucleare Laboratori Nazionali di Legnaro, Legnaro, Italy

### Abstract

The Facility for Rare Isotope Beams, a new national user facility funded by the U.S. Department of Energy Office of Science to be constructed and operated by MSU, is currently being designed to provide intense beams of rare isotopes to better understand the nuclear physics, nuclear astrophysics, fundamental interactions, and industrial and medical applications. The FRIB driver linac can accelerate all stable isotopes to energies beyond 200 MeV/u at beam powers up to 400 kW. Key technical R&D programs include low- $\beta$  CW SRF cryomodules and highly efficient charge stripping using a liquid lithium film. Accelerator-physics challenges include acceleration of multiple charge states of beams to meet beam-on-target requirements, efficient production and acceleration of intense heavy-ion beams from low energies, accommodation of multiple charge stripping scenarios and ion species, designs for both baseline in-flight fragmentation and ISOL upgrade options, and design considerations of machine availability, tunability, reliability, maintainability, and upgradability.

### INTRODUCTION

The Facility for Rare Isotope Beams (FRIB), baselined as a 7-year, US\$680 million construction project, is to be built at the Michigan State University under a corporate agreement with the US DOE [1]. FRIB driver accelerator is designed to accelerate all stable ions to energies above 200 MeV/u with beam power on the target up to 400 kW (Table 1). After production and fragment separation, the rare isotope beams can also be stopped, or stopped and then reaccelerated. The fast, stopped, and reaccelerated rare isotope beams serve a vast range of scientific users in the fields of nuclear physics and applications.

As shown in Figure 1, the driver accelerator consists of Electron Cyclotron Resonance (ECR) ion sources, a low energy beam transport containing a pre-buncher and

electrostatic deflectors for machine protection, a Radiofrequency Quadrupole (RFQ) linac, linac segment 1 (with Quarter-wave Resonators (QWR) of  $\beta=0.041$  and 0.085) accelerating the beam up to 20 MeV/u where the beam is stripped to higher charge states, linac segments 2 and 3 (with Half-wave Resonators (HWR) of  $\beta=0.29$  and 0.53) accelerating the beam above 200 MeV/u, folding segments to confine the footprint and facilitate beam collimation, and a beam delivery system to transport to the target a tightly focused beam. The reaccelerator (ReA) consists of similar  $\beta=0.041$  and 0.085 accelerating structures [2].

Table 1: FRIB driver accelerator primary parameters.

| Parameter                                   | Value                 | Unit  |
|---|-----------------------|-------|
| Primary beam ion species                    | H to $^{238}\text{U}$ |       |
| Beam kinetic energy on target               | > 200                 | MeV/u |
| Maximum beam power on target                | 400                   | kW    |
| Macropulse duty factor                      | 100                   | %     |
| Beam current on target ( $^{238}\text{U}$ ) | 0.7                   | emA   |
| Beam radius on target (90%)                 | 0.5                   | mm    |
| Driver linac beam-path length               | 517                   | m     |
| Average uncontrolled beam loss              | < 1                   | W/m   |

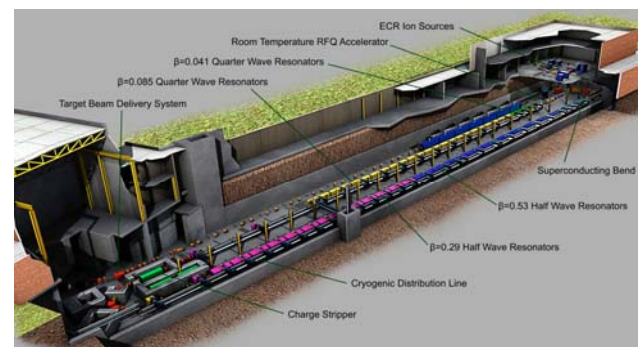


Figure 1: Layout of the FRIB driver accelerator.

\*Work supported by the U.S. Department of Energy Office of Science under Cooperative Agreement DE-SC0000661  
#wei@frib.msu.edu

## DESIGN PHILOSOPHY

Full-energy linac technology is chosen to deliver primary beam that can meet the FRIB requirements of rare-isotope productivity and separation accuracy. Up to 400 kW of beams are focused to a diameter of 1 mm (90%), energy spread of 1% (95% peak-to-peak), and bunch length of  $< 3$  ns (95%) on the target.

In contrast to high-intensity spallation neutron sources and neutrino sources that require pulsed beams, most of FRIB experiments prefer high-duty or continuous-wave (CW) beams. By choosing CW acceleration, a low beam current ( $< 2$  mA) can generate the required beam power of 400 kW. Except for the ion source, effects of space charge are mostly negligible.

Superconducting (SC) technology is the energy-efficient choice for the CW linac. SC acceleration of heavy-ion beams is feasible from very low energy (500 keV/u) with practically sized cavity bores by housing both the cavities and solenoids in a cryomodule. A two-cell scheme is chosen throughout the entire linac providing both efficient acceleration and focusing. Developments of digital low-level RF control and solid-state RF amplifier technologies have made individual cavity powering and control reliable and cost efficient.

Furthermore, high availability, maintainability, reliability, tunability, and upgradability are especially required for the FRIB accelerator to operate as a national scientific user facility.

- **Availability:** The accelerator is designed with high beam-on-target availability accommodating normal, alternative, and fault scenarios. In the normal scenario, a liquid lithium stripper is used to raise the average charge state of  $^{238}\text{U}$  beam to 78+ for efficient acceleration. Alternatively, helium gas confined by plasma windows with differential pumping can be used to strip the  $^{238}\text{U}$  beam to a lower average charge state of 71+. Fault scenarios include the situation when superconducting (SC) cavities underperform by up to 20% of the design gradients. Furthermore, key components (e.g., QWR cryomodules) and subsystems (e.g., machine protection) are implemented with spares and design redundancies.
- **Maintainability:** The average uncontrolled beam loss is limited to below 1 W/m level for all ion species from proton to uranium, to facilitate hands-on maintenance. For a proton beam at high energy, this level corresponds to an average activation of about 1 mSv/h measured at a distance of 30 cm from the beam chamber surface, 4 hours after operations shutdown [3]. For heavy ions like uranium at low energies, activation and radiation shielding is of less concern; the 1 W/m limit addresses concerns in damage on superconducting cavity surfaces and in cryogenic heat load. To facilitate maintenance of individual cryomodules, warm interconnect sections are used between cryomodules, and U-tubes with bayonet connections are used for cryogenic distribution (Figure 2).

- **Reliability:** A Machine Protection System (MPS) minimizes component damage and operational interruption (e.g. magnet quench and cryogenic load increase) caused by both acute (fast) and chronic (slow) beam losses. Upon acute beam loss, the MPS response time is 35 $\mu\text{s}$  (including diagnostics, signal processing, and residual beam dumping). MPS responding to slow beam loss is complicated by low sensitivity of conventional ion chamber loss detection to low-energy heavy ions and beam-loss signal background from adjacent linac segments with which beam energies are significantly different. Beam-halo- scraping rings in the warm interconnect sections and possible thermal sensors at cold regions are planned for more sensitive loss detection [4].
- **Tunability:** The accelerator is designed to be easily tunable during both beam commissioning and operations [5]. In linac segment 1, where beam transverse-phase advance is large, cold beam-position monitors (BPM) are implemented in the cryomodules. Efforts are made in establishing beam-tuning strategies based on virtual accelerators and on-line models under normal and fault conditions.
- **Upgradeability:** Space is reserved in linac segment 3 to house another 12 cryomodules to readily increase the energy of  $^{238}\text{U}$  beam above 300 MeV/u. If cavities with 35% higher accelerating gradient are used in linac segments 2 and 3, the beam-on-target energy can be raised above 400 MeV/u for  $^{238}\text{U}$ . The linac tunnel allows future expansion so that a dedicated light-ion injector can be added supporting rare isotope production using the isotope separation on-line (ISOL) method [1]. Using an RF deflector cavity and a Lambertson septum magnet,  $^3\text{He}^+$  beam supplying protons to the ISOL target can share cycle with the  $^{238}\text{U}$  beam feeding the fragmentation target; thus simultaneous users are supported. Furthermore, space is reserved to house instrumentations including non-destructive diagnostics and sub-harmonic (e.g. 20.125 MHz) buncher that are compatible with future user demands of experiments.

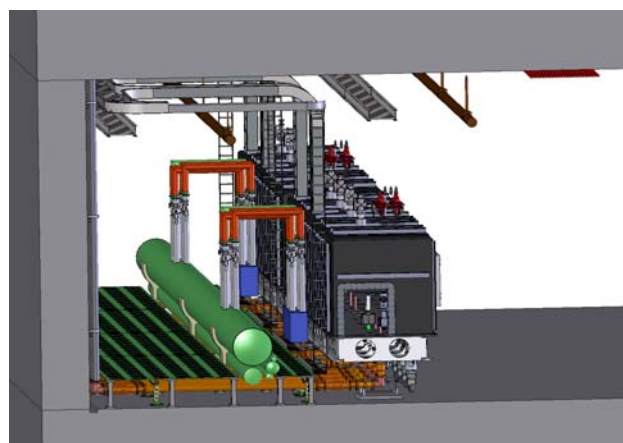


Figure 2: Layout of cryomodule inside FRIB driver accelerator tunnel showing U-tube cryogenic connections.

## ACCELERATOR PHYSICS CHALLENGES

The FRIB accelerator design combines the complexity of heavy ion accelerators with the engineering challenges of high-power accelerators [3]. Due to the low charge-to-mass ratio, heavy ion acceleration is often not efficient. Uncontrolled beam loss, which usually is not an issue for low-power heavy ion machines, is of primary concern for the FRIB accelerator. Comparing with high-power proton machines like the Spallation Neutron Source (SNS) linac where apertures of the elliptical SC cavities [6] are large and beam amplitude reaches maxima in the warm locations of the focusing quadrupole magnets, the apertures of the FRIB QWR and HWR accelerating structures are small and beam amplitude reaches maxima in the cold solenoid locations inside cryomodules. Requirements on beam halo prevention, detection and mitigation are stringent.

To maximize beam intensity on the target, beams of multiple charge states are accelerated simultaneously (2 charge states of 33+ and 34+ before stripping, and 5 charge states of 76+ to 80+ after stripping for  $^{238}\text{U}$ ). Bends of second-order achromatic optics are used to fold the beams, and cavity phases are adjusted so that beams are longitudinally overlapping at the charge stripper [7].

Conventional charge strippers like solid carbon foils are not sustainable at the power of a  $^{238}\text{U}$  beam at 17 MeV/u during normal operations [8]. FRIB accelerator lattice needs to accommodate beam acceleration of different charge states resulting from various stripping methods including liquid lithium and helium gas (average charge state from 63+ to 78+ for  $^{238}\text{U}$ ). Buncher cavities of fundamental (80.5 MHz and 322 MHz) and double (161 MHz) linac RF frequencies are strategically placed in the folding segments to preserve beam quality.

Due to the short stopping distance in surrounding materials, uncontrolled beam loss of the low-energy heavy ions can cause damage to the surface of accelerating structures much more easily than a proton beam. On the other hand, due to the low level of radio-activation [9], losses of low-energy heavy-ion beams are difficult to detect [4]. Beam-loss detection and machine protection often rely on beam scraping. On the other hand, scraping of partially stripped ions may lead to higher ionization further complicating beam collimation and machine protection [10].

Due to requirements of frequent longitudinal and transverse focusing in the superconducting acceleration structure, focusing solenoids are placed inside cryomodules adjacent to cavities. Alignment tolerance of these solenoids is  $\pm 1$  mm under cryogenic conditions. Horizontal and vertical steerers are needed to thread the beam and correct the beam orbit.

Stringent beam-on-target requirements demand tight optical control, error control, and advanced beam diagnostics. The primary beam of 400 kW needs to be focused into a diameter of 1 mm with below  $\pm 5$  mrad transverse angular spread. The desired range of beam power variation on target is 8 orders of magnitude. Orbit stability needs to be controlled at 0.1 mm level.

## TECHNOLOGY CHALLENGES

Major R&D topics of FRIB accelerator systems include high-efficiency charge stripping and superconducting RF technologies for low- $\beta$  acceleration.

### *Charge Stripper*

The FRIB baseline design of charge stripping [11] was based on the ANL work on a liquid-lithium high-power thick target where it was demonstrated power deposition of 20 kW (from an electron beam) with the liquid lithium operating well in an accelerator environment. During the last couple of years the stability of a thin liquid film with the correct thickness for the FRIB stripper ( $\sim 600 \mu\text{g}/\text{cm}^2$ ) was achieved (Figure 3). The next step is to show that the power deposited by the primary beam on the moving film ( $\sim 1$  kW) will not destroy or perturb it. With this purpose we borrowed the LEDA ion source and LEPT from LANL and plan to modify the optics to obtain a 1 to 3 mm diameter beam spot on the liquid-lithium film. As the protons will stop on the film the power will be comparable to the power deposited by the heavy ions during operation. The source reconfiguration is taking place at MSU. Once the new optics is checked on a new platform that is matched to the ANL lithium loop, the device will be moved to ANL for the integrated test.

A second option for the stripper consisting of a helium gas cell enclosed by plasma windows was considered. The RIKEN group has shown [12] that helium gas produces a higher average charge state than a nitrogen gas stripper. The purpose of the plasma windows is to limit the helium gas leaking out of the gas cell [8].



Figure 3: Liquid lithium film established at ANL.

### *Superconducting RF*

FRIB driver linac is the first full-size SC linac using a large quantity (340) of low- $\beta$  cavities. Cavity design is optimized not only for optimum performance but also for low production cost [13]. This requirement guided the choice of the cavity geometries, materials and mechanical solutions, avoiding complicated shapes, minimizing the amount of electron beam welds, eliminating bellows, optimizing construction and surface treatment procedures. FRIB cavities work with superfluid helium at 2 K. The increase in cavity Q more than compensates the loss of efficiency of the 2 K cryogenic system. This innovative

choice in a low- $\beta$  linac allows operation of cavities in stable pressure conditions with high safety margin on the maximum surface fields.

**Cavity Development.** After a 10-year development, the 2<sup>nd</sup> generation QWR prototypes are used in the ReA3 linac (7 with  $\beta_0=0.041$  in operation and 8 with  $\beta_0=0.085$  under installation). This cavity type underwent modifications including the displacement of the RF coupler from the bottom plate to the resonator side and an increased distance between the tuning plate and the inner conductor tip, in order to remove a critical thermal problem in the design. The new tuning plate includes slots and undulations to increase its maximum elastic displacement and thus its tuning range, and a “puck” whose length can be adjusted for cavity tuning before final welding. Concerning the  $\beta_0=0.53$  HWR prototype, which is similar in design to the  $\beta_0=0.29$  cavity, 4 units of the 2<sup>nd</sup> generation have been built by 2 different vendors in addition to the one built in house. After positive test results, the  $\beta_0=0.085$  QWR and the HWRs designs have been further refined in a 3<sup>rd</sup> generation, upgraded design with increased diameter that takes maximum advantage of the space available in FRIB cryomodules (Figure 4 and Table 2) [14].

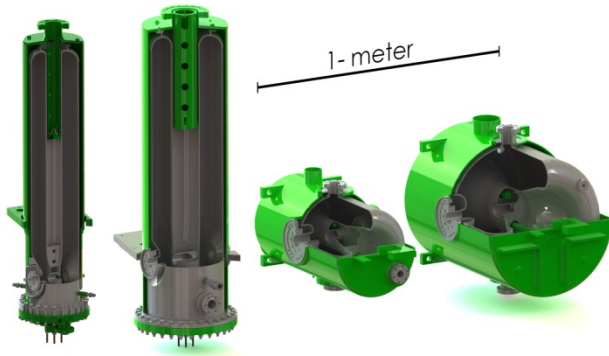


Figure 4: FRIB SC cavities. From left:  $\beta_0=0.041$  and  $0.085$  QWRs,  $\beta_0=0.29$  and  $0.53$  HWRs.

Table 2: Upgraded FRIB cavity parameters

| Resonator                                 | QWR1  | QWR2  | HWR1 | HWR2 |
|---|-------|-------|------|------|
| $\beta_0$                                 | 0.041 | 0.085 | 0.29 | 0.53 |
| $f$ (MHz)                                 | 80.5  | 80.5  | 322  | 322  |
| $V_a$ (MV)                                | 0.81  | 1.8   | 2.1  | 3.7  |
| $E_p$ (MV/m)                              | 31    | 33    | 33   | 26   |
| $B_p$ (mT)                                | 55    | 70    | 60   | 63   |
| $Q_0$ ( $10^9$ )                          | 1.2   | 1.8   | 5.5  | 7.6  |
| R/Q ( $\Omega$ )                          | 402   | 452   | 224  | 230  |
| G ( $\Omega$ )                            | 15    | 22    | 78   | 107  |
| Aperture (mm)                             | 34    | 34    | 40   | 40   |
| $L_{\text{eff}} \equiv \beta\lambda$ (mm) | 160   | 320   | 270  | 503  |
| Number of cavities                        | 12    | 94    | 76   | 148  |

**Surface Treatments.** Test results and production cost considerations led to the choice of buffered chemical polishing (BCP) for FRIB cavity’s surface treatment. The effort was concentrated in the development of a reliable procedure [15] able to produce field-emission free, high gradient cavities. The treatment includes the following BCP steps: 1) bulk etch ( $\sim 150\mu\text{m}$  removal), 2) differential etching in QWRs for final cavity tuning if required, 3) light etch ( $\sim 30\mu\text{m}$  removal). Thermal treatment in high vacuum at  $600\text{ }^\circ\text{C}$  is applied before step 3) for Hydrogen removal to prevent Q disease. High pressure water rinsing (HPR) is applied before cavity final installation. To assure surface cleanliness, dust particle count is performed on resonator surfaces during cavity assembly in the clean room and the water purity is continuously monitored during HPR. During BCP both the cavity and acid temperatures are stabilized to control the removal rate and to avoid excess of hydrogen absorption in Nb. The acid flow path in the  $\beta_0=0.53$  HWR was studied by means of simulations and experiments to obtain homogeneous removal over the entire inner resonator surface. Final thermal treatment at  $120^\circ\text{C}$  was also implemented, showing significant reduction of the Q-slope at 4.2 K, but negligible improvement at 2 K.

**Test Results in Prototypes.** The 2<sup>nd</sup> generation prototypes of  $\beta_0=0.085$  QWR and  $0.53$  HWR have been tested in vertical dewars at 2 K exceeding FRIB design specifications (Figures 5 and 6) [14].

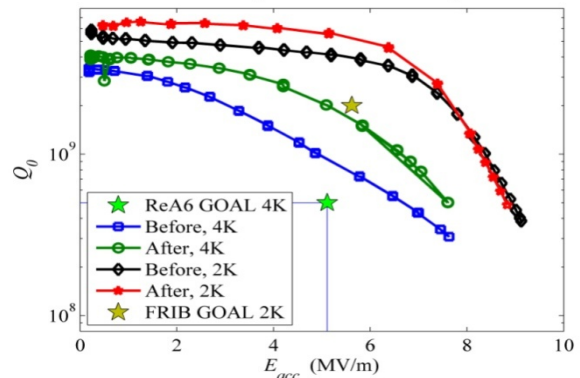


Figure 5: ReA3,  $\beta_0=0.085$  QWR prototype  $Q_0$  vs.  $E_{\text{acc}}$  at 2 K and 4.2 K, before and after  $120^\circ\text{C}$  baking.

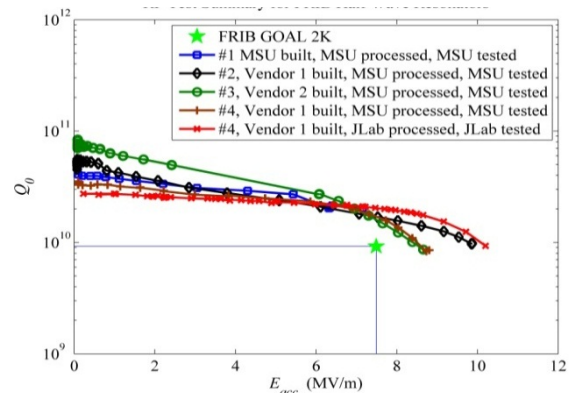


Figure 6: Performance of the  $\beta_0=0.53$  HWR prototypes  $Q_0$  vs.  $E_{\text{acc}}$  processed and tested at MSU and JLAB.

The residual resistance measured in the prototype families was below 5 nΩ up to about 100 mT in QWRs, and about 80 mT in HWRs. Considering that the FRIB specified limits are 11 nΩ and 70 mT, a large safety margin exists for future upgrades (Figure 7).

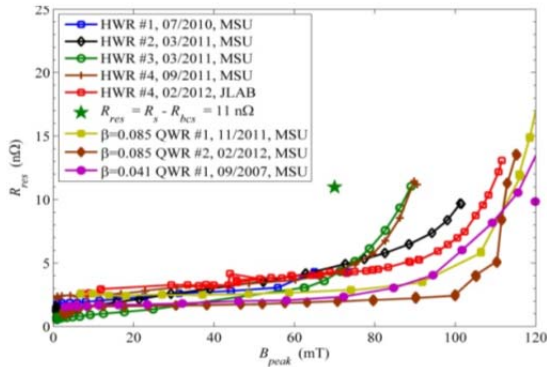


Figure 7: Residual surface resistance at 2 K of  $\beta_0=0.041$  and  $0.085$  QWR and  $\beta_0=0.53$  HWR prototypes.

**Design Upgrade.** The 3<sup>rd</sup>-generation cavity design optimization resulted in significant improvement of peak fields  $E_p/E_{acc}$ ,  $B_p/E_{acc}$  and shunt impedance  $R_{sh}$ , with consequent reduction of the overall linac cost and operational risk.  $E_p$  and  $B_p$  in operation could be moved below the safe values of 35 MV/m and 70 mT in all cavities. The design gradients of the  $\beta_0=0.085$  QWR and  $\beta_0=0.29$  HWR are raised by 10% without increasing the total cryogenic load, allowing a reduction of two cryomodules. The apertures of all QWRs were enlarged from 30 to 34 mm, and their bottom rings were modified for efficient tuning-plate cooling using a low-cost design [14]. The HWR designs were optimized to facilitate the mechanical construction and tuning procedure. In all cavities, the helium vessel is made of titanium to avoid brazed Nb-to-stainless-steel interface.



Figure 8: TDCM containing two  $\beta_0=0.53$  prototype HWR and a solenoid during installation in the test bunker.

**$\beta_0=0.53$  Prototype Cryomodule (TDCM).** The Technology Demonstration Cryomodule (TDCM) consists of two  $\beta_0=0.53$  HWRs operating at 2 K and a 9 T solenoid operating at 4.5 K arranged in a “top-down” configuration (Figure 8). The cryomodule was tested at the design cryogenic temperatures demonstrating excellent cryogenic and LLRF control stabilities.

Multipacting was found to impede the performance of the cavities and the coupler. Future tests are planned starting August 2012 on magnetic field and shielding studies, mechanical-type and pneumatic-type tuner evaluations, multipacting mitigation, and integrated tests with both  $\beta_0=0.29$  and  $\beta_0=0.53$  HWRs.

## ACCELERATOR DESIGN

The FRIB facility is designed adjacent to the ReA facility [2] to benefit fully from the existing experimental infrastructure at the National Superconducting Cyclotron Laboratory (NSCL) (Figure 9). The driver linac is folded twice to minimize the footprint impact on campus, and the tunnel layout allows “open cutting” to save on civil construction costs. Design of the penetrations between the tunnel and the service buildings is compatible with the planned energy upgrade. Space is reserved to house kickers, septums, and target of a future ISOL facility and “stubs” are built to the tunnel walls to allow connection to a future light-ion injector for the planned upgrades.

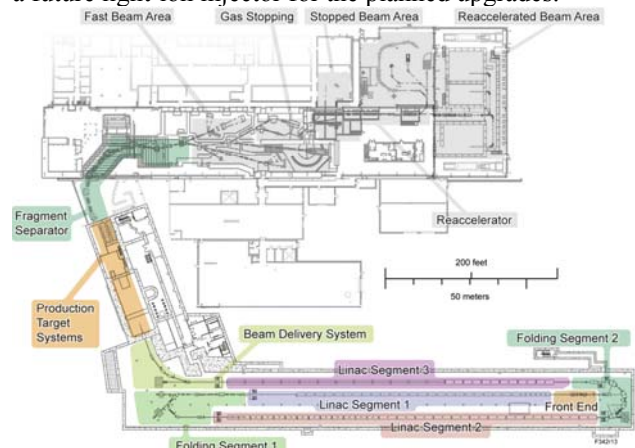


Figure 9: Layout of the FRIB facility (colored) at MSU.

### Front End

The FRIB Front End includes two ECR sources (ECRIS), two charge selection systems, a LEBT, a RFQ, and a MEBT (Figure 10). To enhance availability and maintainability, placed at the ground level in the support building about 10 m above the tunnel level are two ECR sources: a SC high-power source based on the SC ECRIS VENUS developed at LBNL [16] and, initially, a room-temperature ECRIS ARTEMIS available at NSCL.

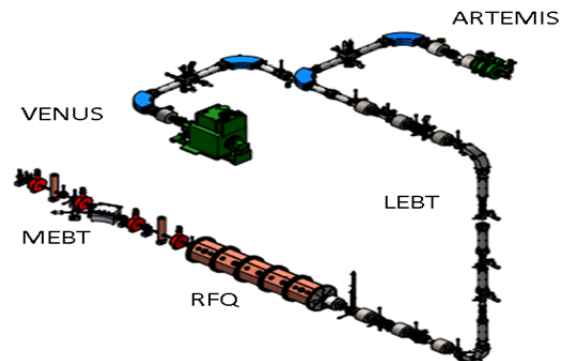


Figure 10: FRIB Front End with its major subsystems.

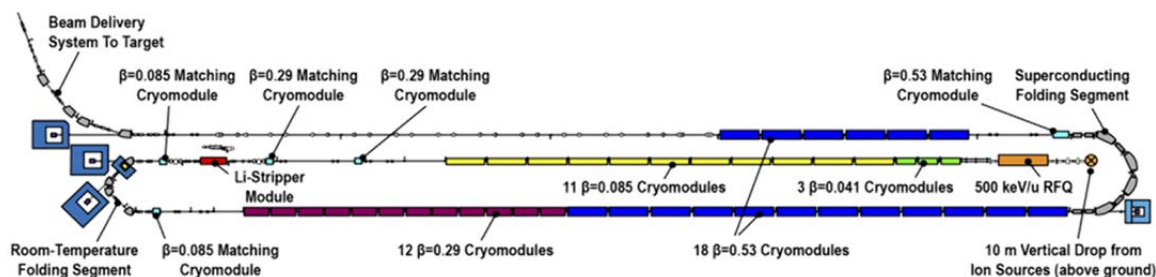


Figure 11: Layout of the FRIB driver accelerator at the tunnel level.

The beams extracted from the sources are filtered in the charge selection systems. The LEBT design is achromatic allowing transporting two charge states simultaneously to double the accelerated beam intensity. To facilitate transport of the two-charge state beams the LEBT uses electrostatic quadrupoles and two  $90^\circ$  dipole deflectors in the vertical transport line. To reduce losses in the superconducting linac, the beam is collimated by several apertures in the LEBT. Then, the CW beam is bunched by a multi-harmonic buncher operating at 40.25, 80.5, and 120.75 MHz before injection into the RFQ. A second RF cavity operating at 40.25 MHz upstream of the RFQ is required for two-charge-state beam injection acting as a velocity equalizer and reducing the longitudinal beam emittance. A chopper is used to vary the duty cycle controlling the pulse length from several hundreds of ns to CW and the pulse frequency from 0 to 30 kHz. Several mesh screens allow reduction of the beam intensity by several orders of magnitude while keeping the nominal bunch frequency. The two  $90^\circ$  electrostatic deflectors in the vertical transport line are incorporated into the machine protection system. The voltage on the deflector plates with shut-off time below  $1 \mu\text{s}$  are controlled by fast switches that receive the inhibit signal from the MPS.

The RFQ accelerates the beam from 12 to 500 keV/u. Downstream of the RFQ, the MEBT consists of two room-temperature QWR bunchers, four SC solenoids, an energy analyzing dipole, and diagnostics. It matches the beam to the SC linac and removes un-accelerated beam that is not longitudinally captured in the RFQ.

### Linac Segments

Three sequential linac segments (LS1, LS2, and LS3), each over 100-m long, accelerate the beam from 500 keV/u to above 200 MeV/u (Figure 11). There are 44 acceleration cryomodules and 5 rebuncher cryomodules in the linac containing a total of 330 QWR and HWR cavities. 9-T SC solenoids provide beam transverse focusing in all the acceleration cryomodules. In order not to quench adjacent SC cavities, buckling coils are equipped with each solenoid to limit the stray fields. Meanwhile, residual magnetic fields are limited to no more than 15 mG to ensure SRF performance of the cavities. Along with cryomodule magnetic shielding, an automatic degaussing process is designed for the SC solenoid.

Several potential “hot spots” are likely to compromise SRF performance: ion source, charge stripper, charge selector, and fragment target. Fast acting valves of ms response time are designed at both ends of each linac segment to protect cryomodules against vacuum failures.

Since energy gains in the cavity are different for beams of different charge states, a multi-reference-particle model is established to handle various charge states of respective beam trajectory, beam energy, synchronous phase, focal length and phase advance. Transverse coupling in a lattice containing solenoids presents another challenge to beam matching even though the beam is nominally round. Particle tracking simulation with 3D fields indicates that even if a round beam is injected into the linac, it will become tilted in the linac presumably due to the quadrupole components of the QWR cavities. Transverse matching of a coupled beam requires fitting of 10 variables comparing with 6 of a decoupled beam.

### Folding Segments and Beam Delivery System

Two folding segments split the linac in three segments. The stripper is located just upstream of the first  $180^\circ$  bend. Four  $45^\circ$  room-temperature dipoles and several combined function (quadrupole/sextupole) magnets control the chromatic effects. Five charge states of  $^{238}\text{U}$  are transported with different rigidities ( $\Delta Q/Q \sim 3\%$ ). SRF rebunchers are located before and after the bend to match the longitudinal phase space to the acceptance of the second linac segment. This first bend effectively facilitates charge selection and beam halo scraping.

The second bend was introduced to reduce the tunnel footprint, as shown in Figure 11. Four superconducting dipoles of 2 T maximum field adopt similar design to the dipoles used at NSCL in the A1900 fragment separator. Afterwards, the beam is further accelerated in the third segment and then bent  $70^\circ$  toward the production target where the objective is to achieve 90% of the beam in a 1 mm diameter beam spot with all five charge states superimposed. The final component of the transport line is the final focus triplet where special care is taken to reduce the chromatic aberrations.

### Reaccelerator

The re-accelerator facility (ReA) is a heavy ion linac consisting of an Electron Beam Ion Trap (EBIT) charge breeder, an off-line stable ion beam injector, a multi-

harmonic buncher, an RFQ, and 8 cryomodules (one  $\beta_0=0.041$  cryomodule, four  $\beta_0=0.085$  cryomodules, and three bunchers) with a total of 41 SC cavities. ReA reaccelerates the rare isotope ion beam after it was mass-separated in the fragment separator and decelerated to thermal energies. The  $1+$  rare isotope beam is injected into an EBIT charge breeder, stripped to a Q/A between 0.2 and 0.5 and accelerated in the linac. ReA is designed to provide beams with energies from 0.3 to 12 MeV/u for heavier ions and from 0.3 up to 20 MeV/u for light ions.

The first stage of ReA (ReA3) is partly under beam commissioning. The first two  $\beta_0=0.041$  cryomodules were installed in 2010 and commissioned in 2011. The third cryomodule ( $\beta_0=0.085$ ) is planned to be installed by the end of 2012 completing the ReA3 project. In 2014 an additional  $\beta_0=0.085$  cryomodule will be added which will enable acceleration of all ions above the Coulomb barriers. A limited user program utilizing rare isotopes produced by the Coupled Cyclotron Facility (CCF) is scheduled to start in 2013.

During the commissioning of the cryomodules, the stabilities of SRF cavities and LLRF control were successfully demonstrated to FRIB requirements [2]. Figure 12 shows the first beam energy spectrum observed in ReA3 during commissioning with a  $\text{He}^+$  beam. Each peak corresponds to a beam energy shift after the RFQ when each cavity is sequentially turned on and phased for acceleration at nominal ReA3 gradients ( $V_a=0.432\text{MV}$ ). In addition, the first  $1+$  to  $n+$  acceleration using the EBIT charge breeder was recently demonstrated. For this test, a single charged  $^{39}\text{K}$  beam was injected into the EBIT source from the off-line test source, charge bred to  $16+$  and accelerated through the linac.

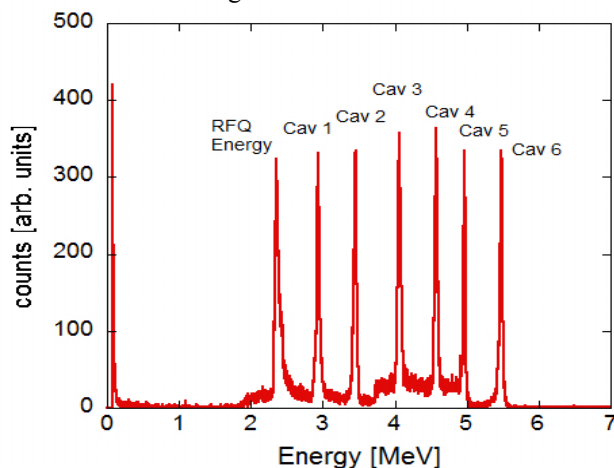


Figure 12: Energy spectra measured with a silicon detector. By turning on one cavity at a time the nominal final energy of 5.486 MeV (1.38MeV/u) was reached.

## SUBSYSTEM DESIGN & ACQUISITION

### Design & Acquisition Strategy

After the project baseline, the FRIB project entered into its final design phase when detail engineering designs are performed at MSU. While critical processing and

assembly are planned to be performed in house, fabrication of a large quantity of repetitive components are planned through mass production and out-sourcing by industrial providers. Based on quoting and purchasing experiences, a cost reduction of 2 to 3 times is expected between prototypes and mass-produced items.

The FRIB project plans to place approximately 450 procurements valued at more than \$50k each. The sum of all technical equipment procurements amounts to \$217M excluding conventional facility construction. We have implemented a procurement strategy that strives to reduce vendor risks for the best value to the FRIB project:

- We work directly with the vendors understanding their individual risk concerns and proposing mitigations:
  - Perform certain tasks in-house if the vendor lacks capability;
  - Adjust engineering designs to allow vendor to implement familiar fabrication approaches;
  - Identify key-personnel bottlenecks at the vendor, and provide technical support where necessary;
  - Work closely with the vendor in mass-production planning and subsequent quality monitoring;
  - Accept components on mechanical (dimensional) properties instead of functional (e.g. electromagnetic, RF) performance;
  - FRIB to purchase high-cost materials that expose to market fluctuations (e.g., Nb).
- We evaluate how the project fits into the supplier's total capabilities and long-term business plans to gauge supplier management's commitment to solve production challenges and risks.
- We develop long-term supplier relationships for mass production. Phasing of procurements from prototypes to production sensitizes vendors to be able to successfully produce the unique components.

So far we have implemented this strategy to negotiated favorable prices for all the SRF material purchases and the production of 174  $\beta=0.53$  HRWs [17].

### Cryogenics

The cryogenics system is designed to support the operation of both SC cavities at a sub-atmospheric pressure (2 K) and SC magnets at a pressure slightly over atmospheric. The system must also provide a 4.5 K liquefaction load to support the magnet's power leads and a non-isothermal refrigeration-shield load between 38 and 55 K. Table 3 summarizes the interface heat load requirements for each load temperature.

The distribution system consists of three separate linac-segment lines and a separator-area distribution line. It uses cryogenic disconnects consisting of vacuum insulated "U-tubes" and bayonets integrated with non-cryogenic isolation valves that are similar to JLab and SNS designs. Each segment, as well as individual cryomodules, may be cooled down and warmed up independently.

The options to support various cryomodule loads are described and evaluated in [18]. The number and location

of valves and interface locations between distribution system and cryomodules are considered to accomplish cool down, warm up, and isolation, as well as for efficient and steady operations.

Since the dominant refrigeration load is at 2 K, the refrigeration process is based on the process options study presented in [19] and incorporates the cumulative experience from both JLab and SNS cryogenic systems. Since the load estimates are approximate, margins are included in these load estimates for the refrigerator. The recent experience gained from the JLab 12 GeV cryogenic system design is utilized for both the refrigerator cold box and the compression system designs. The Floating Pressure Process – Ganni Cycle [20] is to be implemented to provide efficient adaptation to the actual loads.

Table 3: Interface Load Requirements. In addition, the total magnet lead flow is 3.2 g/s, representing 3% of the total load exergy.

| Source               | Heat load [W] |       |           |
|----------------------|---------------|-------|-----------|
|                      | 2 K           | 4.5 K | 38 – 55 K |
| Cryomodule           | 2490          | 1470  | 7690      |
| Magnets              | 0             | 670   | 1000      |
| Cryodistribution     | 0             | 950   | 5000      |
| Beam loss            | 0             | 25    | 0         |
| Total load           | 2490          | 3115  | 13690     |
| Load exergy fraction | 54%           | 30%   | 13%       |

**Cryomodule**

After the conceptual design, the FRIB cryomodule design has evolved significantly from the “top-down” ReA3 style to a “bottom-up” design. Key features including rail system, support system, heat and magnetic shields are simplified along with improvements in assembly and alignment. Figure 13 shows the current design incorporating a torque-resistant structural frame made of stainless steel. We incorporate machined fiberglass compression posts supporting the coldmass in the cryomodule vacuum vessel. Three posts on linear roller bearings oriented towards the center of thermal contraction serve as 6-degree-of-freedom kinematic supports. This design controls the alignment of the coldmass while allowing thermal contraction. Cavity and solenoid attachment points to the rails are all machined after welding to ensure assembly consistency [21].

The FRIB cryomodules contain separate cryogenic circuits at 4 K for the solenoids and at 2 K for the cavities with the 2 K heat exchanger residing inside. We are currently evaluating cavity operation at 2.1 K. The slight reduction in cavity Q would be offset by substantial savings in cryoplant costs. However, care must be taken for quiescent cavity operation close to the helium  $\lambda$ -point.

The project schedule calls for a production rate of 2 cryomodules per month. Cavity processing, vertical tests

and coldmass assembly are planned to be performed in-house. The cryomodule thermal shield, magnetic shield, cryogenic plumbing, and vacuum vessel will be procured from industry as complete “plug-in” units ready for assembly in the cryomodules.

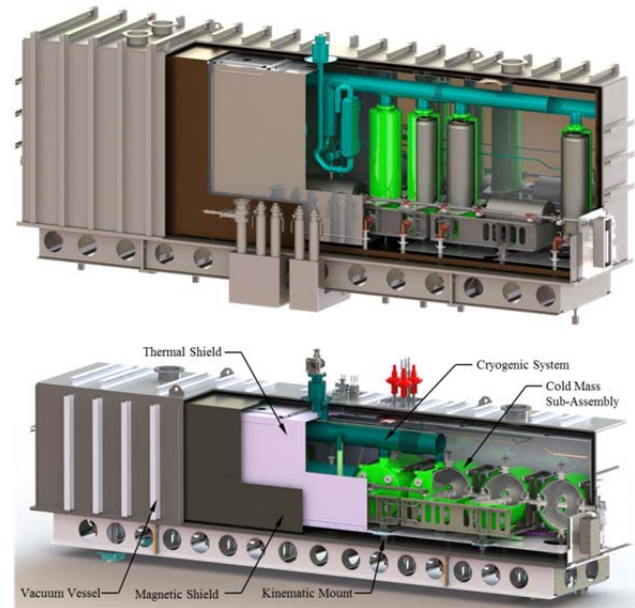


Figure 13: FRIB “bottom-up” cryomodule designs. The top cryomodule incorporates 8  $\beta=0.085$  QWRs, 3 solenoids, and 3 cold beam position monitors; the bottom cryomodule incorporates 8  $\beta=0.53$  HWRs and a solenoid.

**RF**

The RF System monitors and controls the amplitude and phase of the voltage in the cavities. The RF System consists of the reference clock generation and distribution line, LLRF controllers, RF amplifiers, RF transmission lines including couplers and pickup cables, cavity spark detectors, and cavity tuner controls (Figure 14).

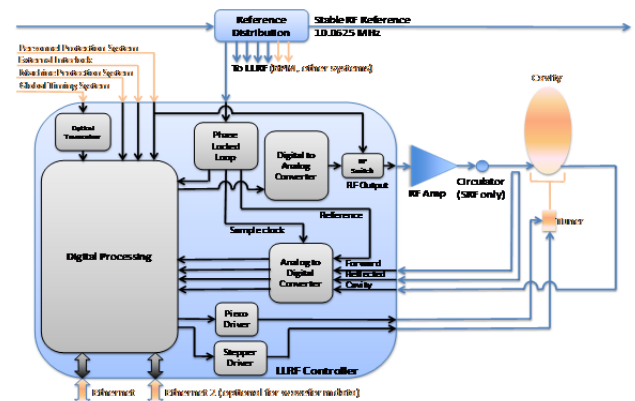


Figure 14: RF system interface block diagram.

The RF Reference clock is generated by a 10.0625 MHz oven-controlled crystal oscillator and distributed along the linac via phase-stabilized RF cable with temperature variation below  $\pm 5\text{ppm}/^\circ\text{C}$ . The reference line has directional couplers near each cryomodule. The

reference signal cable from the directional coupler to the LLRF module in the service building is routed as close as possible to the forward, reflected, and cavity feedback signals to minimize the effects of temperature drift.

The LLRF controller directly samples the cavity feedback signals and the reference signal. The sample clock is locked to and derived from the reference clock. The sample clock frequency is chosen to minimize the aliasing effects of harmonics that may be present in the incoming signals. The raw samples are filtered and converted to phase and amplitude in the field-programmable gate array (FPGA) and control logic directly produces the output frequencies using a high-speed digital-to-analog converter (DAC). The tuner control signals are also generated in the FPGA using information from the RF feedback signals.

A new control method - active disturbance rejection control (ADRC), is applied to solve the problem of microphonics detuning in the SC cavities. ADRC provides 200% improvement over the proportional-integral-derivative (PID) method in simulations and 400% improvement in hardware tests. A digital self-excited loop mode was also implemented in the LLRF controllers.

With the exception of the RFQ amplifier (200 kW tetrode), the FRIB RF amplifiers use solid-state technology. Multiple amplifiers can be combined to generate the required power (up to 8 kW for  $\beta=0.53$  HWRs). The isolation provided by the circulators allows the use of N-way power combiners which saves space and cost. The high-power RF cables, connectors, circulators, power combiners and transmission lines for the SRF amplifiers are rated to handle the standing waves produced by the reflected power due to over-coupling.

### Ion Source

The ARTEMIS ECR source built at MSU based on the AECR-U design at LBNL operates at 14.5 GHz with room-temperature coils.

The VENUS-style ECR source will be a SC high-performance ECR source operating at 28 GHz. In 2007, VENUS demonstrated the FRIB current [16] for a  $^{238}\text{U}$  beam when combining the two charge states of 33+ and 34+. Recent beam measurements demonstrated that better performances from VENUS can be obtained by coupling additional microwave power (up to 8 kW) to the ion source. A new intensity record of 450 eμA of  $^{238}\text{U}^{33+}$  was obtained with VENUS at LBNL. The measured emittance for this charge state showed that 95% of the beam was within the FRIB acceptance. FRIB modifications to the original design of the VENUS cryostat include the cooling capacity at 4.2K been extended from 6 W to 12 W to include the dynamic heat load generated by the plasma Bremsstrahlung electrons.

Both sources are installed on a high-voltage platform to provide an initial beam acceleration of 12 keV/u at FRIB.

### RFQ

The FRIB RFQ accelerates the multi-charge state beam from 12 to 500 keV/u over a 5-m distance with estimated

transmission efficiency above 80%. It operates at 80.5 MHz and requires about 100 kW of CW RF power. A 4-vane resonator is utilized with a liner ramped accelerating voltage profile (Figure 15).

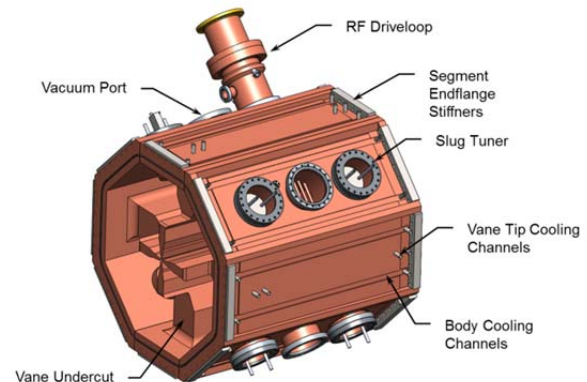


Figure 15: RFQ assembly view of segment 1 with endplate removed.

Mechanical construction of the RFQ will be performed as an integral brazed structure with dual-circuit cooling water resonance control. Overall mechanical fabrication is performed in 5 longitudinal sections to minimize machining and handling weight. The quadrupole and dipole mode frequencies are fine-tuned during construction using fixed mechanical slug tuners in all 4 quadrants distributed along the length of the machine. Dipole mode suppression rods attached to the structure endplates are utilized to separate and move dipole mode frequencies away from the accelerating mode frequency, thus stabilizing the desired quadrupole accelerating mode at 80.5 MHz. The field ramp in the accelerating mode is accomplished through proper sizing of the magnetic return vane undercuts at the ends of the structure and power is fed using a magnetic-field loop-coupler drive.

Thermal management of CW RFQ's is challenging but given the modest drive power of below 100 kW, no significant cooling issues exist. All components are made of high-conductivity copper and actively water cooled: resonator vanes, endplates, slug tuners, vacuum pumping port grills and the 15.6-cm diameter coaxial drive coupler power feed. Additional care is taken in the vane-undercut regions where the local RF heating is increased due to magnetic-field compression in these zones.

### Magnet and Power Supply

Most of the magnets in the driver linac are resistive due to the relatively low beam rigidity. Superconducting dipoles are used when fields of 2 T are required (folding segment 2). The fragment separator uses SC technology to allow the high pole-tip fields and large apertures required to maximize the acceptance. Re-configuration of the existing A1900 fragment separator allows connection to the existing NSCL experimental equipment.

Power supplies are largely in three categories, room-temperature magnet power supplies, SC magnet power

supplies, and high-voltage power supplies. Programmable power supplies provide regulated DC current to the magnets, or regulated high voltage to electrostatic elements and ion source components.

### Diagnostics

The driver linac is planned to be commissioned with single-shot or low repetition rate, 50  $\mu\text{A}$  and 50  $\mu\text{s}$  beam pulses. This sets the fundamental operating specification for most diagnostics systems. In full operation, the diagnostics must accommodate low-to-moderate energy, low instantaneous current, CW, high-power beams of differing ion species with high charge states.

Use of intercepting diagnostic devices is acceptable only under tightly controlled, low-beam-power conditions and only at locations not adjacent to SC cavities. Also, FRIB low-energy, heavy-ion beams do not avail themselves to many optical diagnostics techniques used for highly-relativistic beams. Beam position and beam current monitoring system design is challenged by the continuous, low-current (500  $\mu\text{A}$  maximum) nature of the FRIB beam. The present specification for the operational “CW” beam includes a 50  $\mu\text{s}$  beam gap at 100 Hz primarily for diagnostics purposes.

The FRIB beams present particular challenges for beam loss monitoring, which is traditionally expected to provide important signals for machine protection and for beam tuning and optimization. Full loss of the CW heavy ion beam, even at relatively low energies, can cause component damage in tens of microseconds. At low energies, e.g. all of LS1, the radiation signature outside the beam line elements can be vanishingly small. Distributed, chronic, fractionally small losses of the CW beam can adversely load the cryogenic system. Radiation cross-talk between adjacent segments of the folded FRIB linac configuration is large [4]. Finally, there is expected to be a competing radiation field due to X-rays from SRF cavities, which is yet to be quantified.

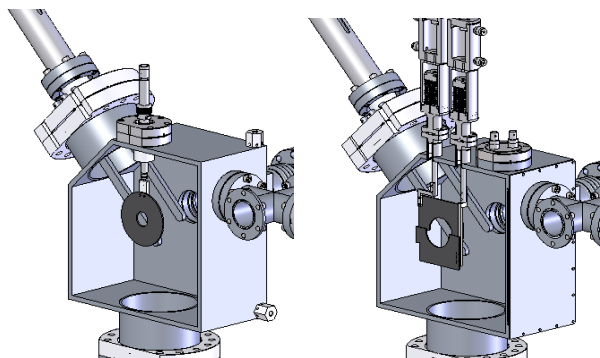


Figure 16: Standardized accelerator vacuum chambers with diagnostics ports. Also shown are fixed (left) and variable (right) diameter halo scrapers for interceptive beam-loss monitoring.

Aperture-limiting “halo rings”, instrumented to sense the deposited charge, are being considered for monitoring chronic, small beam losses [4]. The halo rings would be located in the warm, inter-cryomodule regions.

Conceptual designs for fixed- and adjustable-aperture halo rings are shown in Figure 16.

### Vacuum and Alignment

Beam-boxes as shown in Figure 16 of two standardized lengths and identical diagnostics ports will be installed across the entire driver accelerator. Over 100 ion pumps are used to generate vacuum ranging from  $10^{-6}$  Torr (charge-stripping section) to  $5 \times 10^{-9}$  Torr (warm region between cryomodules). Vacuum requirements are primarily determined by the need to minimize stripping of the highly-charged heavy ions. Effects of electron cloud are expected to be negligible. The Molflow+ codes [22] are used to guide the pump sizing and placements.

Planning for the alignment of the facility is underway. In the near-term we focus on designing the alignment network including characterization of the existing network in the NSCL facility matching the FRIB global-coordinate system. The alignment network encompasses the front end beam lines at ground level, a 10-m vertical drop to the over 3,066  $\text{m}^2$  linac tunnel, heavily shielded target system chambers, and a vertical rise back to and including the entire existing NSCL facility.

Weight and structural analysis and differential-settlement monitoring is included as part of conventional-facility design.

### Controls

As the interface for operators and physicists to commission and operate the FRIB accelerator, the control system provides supervisory and model-driven control (Table 4).

Table 4: FRIB distributed control system.

|                       |  |
|-----------------------|--|
| Physical Distribution | ~200 m * 200 m   |
| IOCs                  | ~150 Computers/EPICS<br>Input/Output Controllers (IOC) |
| PLCs                  | ~100 Programmable Logic<br>Controllers (PLC)           |
| Network               | ~ 3000 GbE ports                                       |
| Global Timing         | >500 timing drop points                                |
| Machine Protection    | ~2000 MPS fast protection inputs                       |
| Conventional Facility | ~760 racks and more than 100<br>with controls devices  |

The low-level control system consists of programmable-logic-controllers (PLC), input-output-controllers (IOC) and signal-conditioning modules to provide process control and remote operation to the field devices including vacuum devices, power supplies, RF controllers and cryogenic sensors/controllers.

The global system provides site-wide timing (event and data), network connectivity and integration of machine protection to allow all subsystems to work together with synchronized real-time information, Ethernet-based communication and consistent fault handling. The machine mode, beam mode and particle type are first set in global system and then distributed throughout the facility to ensure that every related subsystem has consistent information.

The high-level applications provide both web- and console-based operation toolkits, relational-database services and model-based physics applications to support installation, commissioning and operations. The service-oriented architecture is selected, the key technologies such as Eclipse/CSS, J2EE, XAL and MySQL are decided and a set of tools are developed.

### *Utilities*

A robust infrastructure is designed to support FRIB accelerator operations including facility power, cooling water, air, cable trays and conduits, facility layout and grounding.

The FRIB facility will be served by two 25 MW, 13.8 kV primary feeders from the MSU T.B. Simon Power Plant using an automatic transfer arrangement to transfer load in the event of a circuit failure. The feeders are installed in an underground duct bank providing protection from foreseeable hazardous weather. An additional 4 MW, 13.8 kV primary feeder is also routed to the site to serve as investment protection in the unlikely scenario that both primary feeders are lost. This 4-MW feeder requires manual operation to energize and serve loads associated with cryogenics operations. These three circuits serve a line-up of medium-voltage 15 kV switches in a loop configuration with multiple tie-switches offering flexibility in transporting power to various substations throughout the facility. Critical loads that cannot tolerate a power failure such as control equipment for cryogenics, communications, oxygen-deficiency-hazard (ODH) monitoring, personnel and safety protection systems are served by three 200 kW (N+1) uninterruptible power supplies (UPS). The UPS's will maintain power to the critical loads while two 800-kW diesel generators operating in parallel come on-line to provide power to the critical, emergency, legally required standby, and optional standby loads and the fire pump. A facility grounding plan was developed that minimizes conducted and radiated electromagnetic interferences. Ground mesh and mechanical bonding are strategically located to optimize effectiveness [23].

FRIB driver accelerator's electrical components will be housed in 768 racks in the service building. The racks are organized in 120 groups that follow the contour of the accelerator. Conduit banks are located near each rack group to keep cable lengths as short as possible. There are 1200 conduits in these banks that carry electrical signals from RF, power supplies, diagnostics, and controls in the accelerator tunnel. The conduits are 6-m long, and nominal cable lengths are about 30-m long. Thermal modelling is being performed for cable heating in the conduits. The conduits are organized for each rack grouping by RF, DC power supply leads, high voltage, controls, personnel-protection system (PPS), and AC power distribution for cryogenic heaters.

Three primary water cooling loops are specified for the accelerator systems' technical equipment. An activated low-conductivity-water (LCW) system supplies the equipment in the accelerator tunnel while a non-activated

LCW system supplies the Front End systems. These are nominally 3-M $\Omega$  systems at 32°C supply temperature incorporating oxygen reducing system and ultra-violet (UV) control of biological growth. Service building rack cooling is accomplished using filtered, treated water since LCW is not required.

Instrument-grade compressed air is routed throughout the facility for the operation of control valves and solenoids, as well as for blowing out water lines and magnets during maintenance.

Heating, ventilation, and air-condition (HVAC) system loads and type are specified for all areas of the facility. Fan-coil units which are supplied by hot and cold water systems are located throughout the accelerator tunnel. These units provide the primary air temperature management during operation. A negative (5 mbar sub-atmospheric) tunnel pressure during operation is provided via a 142 m<sup>3</sup>/min exhaust system venting through an exhaust gas management system with make-up air being pre-conditioned through a conventional HVAC unit. Service building rack area cooling is via a raised floor "server room" style cooling system. Air will be supplied at 13°C through the floor and ducted to racks as needed.

Ground vibration may induce movement in the SC cavities, disrupting the beam and demanding increased RF power. The warm-gas compressors of the helium refrigeration system are a major concern, especially since the system is planned to be housed adjacent to the service building above the tunnel to save conventional-construction costs. Studies concluded that the compressor vibration can be adequately mitigated by mechanically isolating compressors using commercially-available foundation pads [24]. The effects from other equipment like cooling-water pumps and chillers also are assessed and comparable vibration-reduction measures implemented.

## **FUTURE PERSPECTIVES**

The FRIB accelerator design is advanced towards beginning construction in 2014. Early procurements before 2014 is strategically planned to establish the front end test stand to demonstrate critical components of the ECR ion source and the fully powered RFQ, to contract on long lead-time cryogenic refrigeration subcomponents, to acquire cryogenic distribution equipment that needs to be installed before accelerator tunnel completion, and to acquire SRF components to be assembled in the pre-production cryomodules. Upon fabrication, installation, and integrated tests, early beam commissioning is expected to be staged from 2017 to 2019. The facility is scheduled to meet key performance parameters supporting routine user operations before 2021. Full design capability is expected to be reached within 4 years after the beginning of routine operations. Science driven upgrade options may be pursued at any stage of the project.

## ACKNOWLEDGMENTS

FRIB accelerator systems design has been assisted under work-for-others agreements by many national laboratories including ANL, BNL, FNAL, JLAB, LANL, LBNL, ORNL, and SLAC, and in collaboration with many institutes including BINP, KEK, IMP, INFN, INR, RIKEN, TRIUMF, and Tsinghua University. We thank the Accelerator Systems Advisory Committee chaired by S. Ozaki for their valuable advice and guidance, B. Laxdal, P. Kneisel, and A.C. Crawford for their participation in the FRIB weekly teleconference, colleagues who participated in FRIB accelerator peer reviews including A. Aleksandrov, G. Ambrosio, W. Barletta, G. Bauer, G. Biallas, J. Bisognano, S. Bousson, M. Champion, M. Crofford, R. Cutler, B. Dalesio, G. Decker, J. Delayen, H. Edwards, J. Error, J. Fuerst, K. Kurukawa, J. Galambos, J. Galayda, J. Gilpatrick, S. Gourlay, S. Henderson, L. Hoff, G. Hoffstaetter, J. Hogan, N. Holtkamp, H. Horiike, C. Hovater, H. Imao, R. Janssens, R. Keller, J. Kelley, P. Kelley, M. Kelly, J. Kerby, A. Klebaner, J. Knobloch, J. Mammosser, T. Mann, N. Mokhov, G. Murdoch, H. Okuno, P. Ostroumov, R. Pardo, S. Peggs, T. Peterson, C. Piller, J. Power, T. Powers, J. Preble, D. Raparia, T. Roser, R. Ruland, W.J. Schneider, D. Schrage, J. Sondericker, W. Soyars, C. Spencer, R. Stanek, M. Stettler, J. Stovall, V. Verzilov, P. Wanderer, M. Wiseman, L. Young, and A. Zaltsman, and colleagues who advised and collaborated with the FRIB team including A. Burrill, K. Davis, W. Hartung, A. Hutton, R. Kersevan, S.H. Kim, K. Macha, G. Maler, E.A. McEwen, W. Meng, T. Reilly, J. Sandberg, J. Tuozzolo, and J. Vincent. At Michigan State University, the FRIB accelerator design is executed by a dedicated team of the FRIB Accelerator Systems Division with close collaboration with the Experimental Systems Division headed by G. Bollen, the Conventional Facility Division headed by B. Bull, the Chief Engineer's team headed by D. Stout, and supported by the project controls, procurements, ES&H of the FRIB Project, by the NSCL, and by the MSU.

## REFERENCES

- [1] Web site <http://www.frib.msu.edu/>
- [2] D. Leitner et al, "Status of the ReAccelerator Facility ReA for Rare Isotopes beam research", SRF'2011, Chicago (2011, in press).
- [3] J. Wei, *Rev. Mod. Phys.*, 75, (2003) 1383.
- [4] Z. Liu, Y. Zhang et al, "Ion Chambers and Halo Rings for Loss Detection at FRIB", IPAC'12, New Orleans (2012, in press).
- [5] Y. Zhang, "Beam Tuning Strategy of the FRIB Linac Driver"; P. Chu et al, "Online Physics Model Platform", IPAC'12, New Orleans (2012, in press).
- [6] N. Holtkamp, "The SNS Linac and Storage Ring: Challenges and Progress Towards Meeting Them", EPAC'02, Paris, p. 164.
- [7] X. Wu et al, "The Overview of the Accelerator System for the Facility for Rare Isotope Beams at Michigan State University, LINAC'10, Tsukuba, p. 163; Q. Zhao et al, "Beam Dynamics in the FRIB Linac", HB'12, Beijing (2012, to be published).
- [8] F. Marti et al., "Development of Stripper Options for FRIB", LINAC'10, Tsukuba, p. 662.
- [9] R. Ronningen et al, *Nucl. Tech.*, 168 (2009) 670.
- [10] T. Roser, private communications.
- [11] Y. Momozaki et al., *JINST* 4 (2009) P04005.
- [12] H. Okuno et al., *Phys. Rev. ST Accel. Beams*, 14, (2011) 033503.
- [13] C. Compton et al., "Superconducting Resonators Production for Ion Linacs at Michigan State University", SRF'11, Chicago (2012, in press).
- [14] A. Facco et al, "Superconducting Resonators Development for the FRIB and ReA Linacs at MSU: Recent Achievements and Future Goals", IPAC'12; J. Popielarski et al., "Dewar Testing of Coaxial Resonators at Michigan State University", IPAC'12, New Orleans (2012, in press).
- [15] L. Popielarski et al., "Cleanroom Techniques to Improve Surface Cleanliness and Repeatability for SRF Coldmass Production", IPAC'12, New Orleans (2012, in press).
- [16] D. Leitner et al, *Rev. Sci. Instru.* 79 (2008) 02C710.
- [17] M. Leitner, "Design Status of the SRF Linac Systems for the Facility for Rare Isotope Beams", SRF'11, Chicago (2011, in press).
- [18] V. Ganni, "Helium Refrigeration Considerations for Cryomodule Design," *Proc. ADS Conf.*, Mumbai (2011, in press).
- [19] P. Knudsen, V. Ganni, "Process Options for Nominal 2-K Helium Refrigeration System Designs", *Adv. Cryo. Eng.* 57, AIP, New York (2012, in press).
- [20] V. Ganni, P. Knudsen, "Optimal Design and Operation of Helium Refrigeration Systems Using the Ganni Cycle," *Adv. Cryo. Eng.* 55, AIP, New York (2010) p. 1057.
- [21] M. Johnson et al, "Design of the FRIB Cryomodule", IPAC'12, New Orleans (2012, in press).
- [22] Codes Molflow+, R. Kersevan, CERN.
- [23] M. Thuot, "Using the FRIB Facility Grounding Mesh Effectively", FRIB Internal Document T10503-VS-000001 (2012); D. Stout et al, "201105 Grounding Workshop Report", FRIB Internal Document T20100-RA-000043 (2011).
- [24] H. Amick, "Review of Ground-Borne Vibration Issues", FRIB Internal Document T20201-TD-000082 (2011); J.A. Moore, E. E. Ungar, FRIB Internal Document T20201-TD-000083 (2011); D. Stout et al, "FRIB Ground-Born Vibration Studies", FRIB Internal Document T31200-TD-000084 (2011).

# DESIGN STUDY OF IN-FLIGHT FRAGMENT SEPARATOR FOR RARE ISOTOPE SCIENCE PROJECT IN KOREA

J. Kim, D. Kim, M. Kim, J. Song, C. Yun, S. Kim, Institute for Basic Science, Daejeon, Korea  
W. Wan, Lawrence Berkeley Laboratory, Berkeley, USA

## Abstract

A heavy-ion accelerator complex has been designed for rare isotope beam production utilizing both in-flight fragmentation and ISOL methods in Korea. The project had been planned with conceptual design efforts, and was officially launched in January this year. The driver accelerator is a superconducting linac with a beam power of 400 kW. The uranium beam for projectile fragmentation is to be accelerated to 200 MeV/u. The in-flight fragment separator can be divided into pre and main separators. The target system and beam dump to handle the full beam power are located in the front part of the pre-separator. Radiation transport and shielding have been studied using PHITS and MCNPX. Beam optics design performed in the previous conceptual study is being further optimized. The separator will be composed of superconducting quadrupole magnets and conventional dipole magnets. Prototyping of the superconducting magnets is planned.

## INTRODUCTION

The rare isotope science project (RISP) was initiated in Korea this year to establish a radioisotope beam facility. The facility will use both in-flight fragmentation (IF) and ISOL methods to produce rare isotope beams. A superconducting linear accelerator with the maximum beam power of 400 kW will drive the IF system, and an H<sup>-</sup> cyclotron of 70 kW will be used for ISOL. The uranium beam of 200 MeV/u is a main beam for IF.

A schematic configuration of the facility is shown in Fig. 1 [1]. The separator is divided into pre and main stages. The shape of pre-separator is close to S as the two dipole magnets bend the beam in the opposite direction while the shape of main separator is C using four dipole magnets. Beam optics of different configurations of pre-separator has been studied in the aspect of removing unwanted beams. The basic beam optics design of main separator is currently thought to be kept the same as the one previously designed [1], and we are trying to refine the pre-separator design.

The pre-separator includes a target and beam dump system to separate the isotope beam of interest so that the primary and unwanted isotope beams are dumped into water-cooled shielding structure in a localized area, where remote handling devices are employed. The pre-separator should be well isolated from downstream components. The radiation shielding, damage and heat deposit have been calculated using PHITS [2] and MCNPX [3]. The entire separator is located at the same vertical level in the current design.

The separator consists of large-aperture superconducting quadrupole magnets for large angular and momentum acceptance, which operate at 4 K, and conventional dipole magnets with the maximum magnetic rigidity of 8 T·m. In the front end of pre-separator, superconducting magnets utilizing high-T<sub>c</sub> superconductor are considered to avoid large cryogenic loads at 4 K. We will prototype both low-temperature and high-T<sub>c</sub> superconducting magnets, and will be tested in a cryostat with cryo-coolers installed.

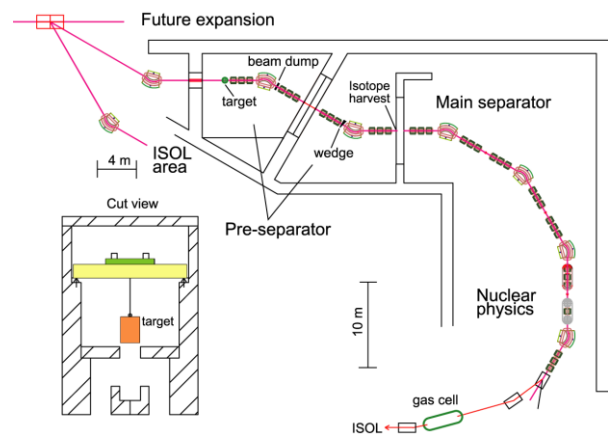


Figure 1: Conceptual layout of the in-flight fragment separator facility.

## BEAM OPTICS DESIGN OF PRE-SEPARATOR

An array of magnetic elements of the pre-separator, which employs four dipoles in C-shape, is shown in Fig. 2 together with beam trajectories in the transverse planes. The calculations were performed using COSY Infinity [4]. The locations of beam dump, radiation shielding wall and a wedge are indicated. Momentum dispersion at the beam dump is enlarged compared to the S-shape pre-separator case using two dipole magnets. However, beam is vertically not focused at the wedge, which can cause additional momentum spread.

A result of beam optics calculation using TURTLE [5] is shown in Fig. 3 for the case of four dipole magnets in C-shape. Beam emittance is  $4 \pi \cdot \text{mm} \cdot \text{mrad}$  assuming a Gaussian beam distribution, and momentum dispersion of the beam is  $\pm 5\%$ . The beam distributions at the locations of beam dump and wedge show the beam spreads by momentum dispersion.

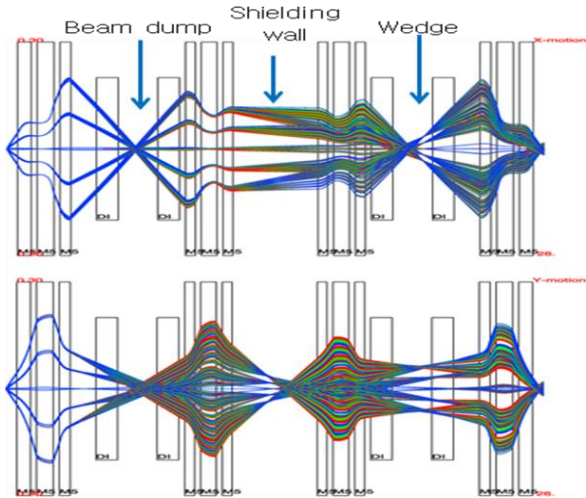


Figure 2: (Upper) Horizontal and (Lower) vertical beam trajectories for the pre-separator in C-shape. The locations of the major components are indicated.

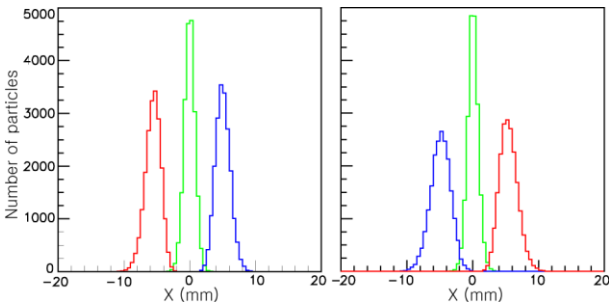


Figure 3: (Left) Beam distribution at the location of beam dump, (Right) at the location of the wedge.

To accomplish an enhanced separation of primary and unwanted beams, we have considered the feasibility of using more magnetic elements as shown in Fig. 4. A better separation of primary beam can be achieved at the cost of larger number of magnetic elements, which is applicable to both C and S shapes.

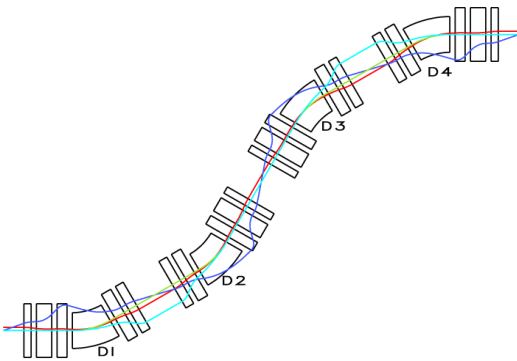


Figure 4: S-shape pre-separator with four dipole magnets and a larger number of quadrupole magnets.

## RADIATION SHIELDING AND TRANSPORT CALCULATION

The pre-separator is designed to remove unwanted beams including the primary beam. The shielding for the beam dump area is a critical consideration in the design. The radiation shielding and transport have been calculated using MCNPX and PHITS. Heat deposits in the elements of the front end of pre-separator have been calculated using the geometry as shown in Fig. 5 [6].

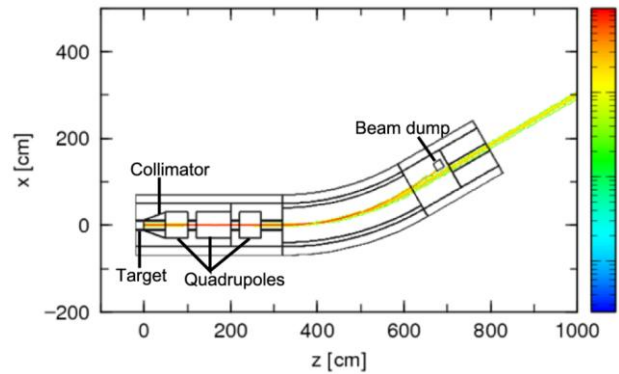


Figure 5: Geometry of the front end of the pre-separator used for calculations on radiation heat deposit.

The maximal heat influx is calculated to be about  $0.3 \text{ W/cm}^3$  for a U beam at 400 kW in the front-end quadrupole magnet. This high heat deposit makes the use of low-temperature superconductor difficult. Feasibility of using high-Tc superconducting magnet has been explored for the FRIB project [7].

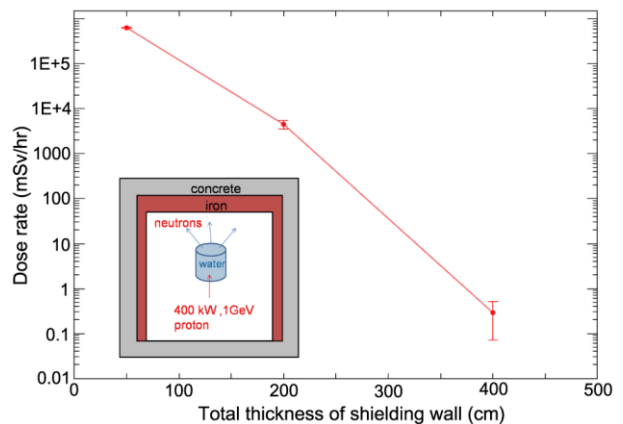


Figure 6: Estimation of shielding wall thickness in the beam direction at the beam dump assuming a proton beam of 1 GeV irradiates a water target. Also shown is the geometry for the MCNPX calculation.

A result of radiation shielding in the beam dump area calculated using MCNPX is shown in Fig. 6. The dose rate in the beam direction becomes below 1 mSv/h when the total shielding wall is roughly thicker than 4 m. The

thickness of concrete is assumed to be the same as that of iron wall in the beam direction as shown in Fig.6. A proton beam of 1 GeV at 400 kW is used as neutron generation in the forward direction is highest when compared to the bombardment of other kinds of primary beams.

A thin target is used to induce fragmentation of the projectile beam. Thickness of the target has been first optimized using LISE++ [8]. Heat generation by neutron and gamma radiations, and radiation dose deposit were calculated using PHITS. Radioactivity on the target was then calculated using DCHAIN-SP [9].

The heat deposit up to 30 % of the primary beam power on fragmentation target makes a usual single-slice target unsustainable. Use of multi-slice target has been proposed and will be tested.

### SC-MAGNET PROTOTYPING

We plan to prototype both the superferric and high-Tc superconductor magnets, which are the major components of the separator. For the superferric quadrupole magnet, multipole coils will be wound on the bore tube. The beam optics tells that efficient correction of multiple field components can be performed by placing them at the locations of quadrupole magnets. The test cryostat will house two or three quadrupole magnets to test interference among adjacent quadrupole magnets and with multipole coils. Also, measurement results will be compared with 3D calculations. The heat leak to 4 K in the cryostat is estimated to be roughly 3 W.

### RF DEFLECTOR

In-flight fragmentation method has advantage in producing neutron-rich rare isotopes as the wedge at the location of dispersive focusing is effective in separating them. The IF separator also produces proton-rich radioisotopes, but the long-tails of neighbouring unwanted beams make the separation of isotope beam of interest difficult by magnetic dispersion and energy loss mechanism.

Contamination can be severe for highly proton rich isotope beams. A method to increase the beam purity is to utilize velocity difference in the isotope beams after the IF separator. The beam contaminant can be largely deflected away by the rf reflector located downstream of the separator, which requires well defined longitudinal emittance of the primary beam at the target.

### CONCLUSION

The design of a fragment separator is underway for the rare isotope science project in Korea. Feasible design schemes have been studied in beam optics to optimize the configuration of the separator especially for the pre-separator. The other main design considerations include radiation transport, shielding, heat deposit and radioactivity calculations. Different codes have been used to evaluate differing design aspects.

### REFERENCES

- [1] W. Wan, Y. Park and J. Kim, Proc. of 2010 Cyclotron Conf., Lanzhou, China 123 (2010).
- [2] K. Niita et al., PHITS: Particle and Heavy Ion Transport code System, Version 2.23, JAEA-Data/Code 2010-022 (2010).
- [3] MCNPX User's Manual Version 2.4.0. Report LACP-02-408 (2002).
- [4] K. Makino and M. Berz, Nucl. Instr. and Meth. A 558, 346 (2006).
- [5] K.L. Brown, Ch. Iselin, D.C. Carey: Decay Turtle, CERN 74-2 (1974).
- [6] I. Baek et al., Proc. of PAC07, New Mexico, USA 1763 (2007).
- [7] J. Cozzolino et al., Proc. of PAC11, New York, USA 1124 (2011).
- [8] O.Tarasov and D.Bazin, Nucl. Instr. and Meth. B 266 4657 (2008)
- [9] T. Kai, F. Maekawa, et al., "DCHAIN-SP2001: High Energy Particle Induced Radioactivity Calculation Code," JAERI-Data/Code 2001-016 (2001).

## DESIGN AND STATUS OF THE SUPER SEPARATOR SPECTROMETER FOR THE GANIL SPIRAL2 PROJECT

J.A. Nolen, S.L. Manikonda [ANL, Argonne, USA]  
M. Authier, A. Drouart, J. Payet [CEA/DSM/IRFU, France]  
O. Delferriere (O. Delferrière) [CEA/IRFU, Gif-sur-Yvette, France]  
J. Laune [IPN, Orsay, France]  
F. Lutton, H. Savajols, M. Souli, M.-H. Stodel [GANIL, Caen, France]

### *Abstract*

The Super Separator Spectrometer (S3) is a device designed for experiments with the very high intensity stable heavy ion beams of the superconducting linear accelerator of the SPIRAL2 Project at GANIL. S3 is designed to combine high acceptance, a high degree of primary beam rejection, and high mass resolving power to enable new opportunities in several physics domains, e.g. super-heavy and very-heavy nuclei, spectroscopy at and beyond the drip-line, isomers and ground state properties, multi-nucleon transfer and deep-inelastic reactions. The spectrometer comprises 8 large aperture multipole triplets (7 superconducting and 1 open-sided room temperature), 3 magnetic dipoles, and 1 electrostatic dipole arranged as a momentum achromat followed by a mass separator. A summary of the beam-optical simulations and the status of the main spectrometer components will be presented with special emphasis on the design of the superconducting multipole triplets.

**CONTRIBUTION NOT  
RECEIVED**

# ARGONNE IN-FLIGHT RADIOACTIVE ION SEPARATOR\*

S. Manikonda<sup>†</sup>, J. Nolen, B. Back, K.-E. Rehm, M. Alcorta, R. Pardo  
G. Savard, D. Seweryniak, B. Erdelyi, C.R. Hoffman  
ANL, Argonne, IL 60439, USA

## Abstract

The Argonne In-flight Radioactive Ion Separator (AIRIS) is a new device that is being designed as a part of proposed future upgrade of the ATLAS facility at Argonne. AIRIS is a large recoil separator for the in-flight radioactive beam that will provide at least 10 times more collection efficiency than the existing system. In combination with other proposed ATLAS upgrades it will provide a 2 orders of magnitude gain in the intensity for the in-flight produced secondary beams compared to the existing facility. The resulting unprecedented intensities for the recoil beam open new opportunities in several physics domains, e.g.: gamma ray spectroscopy after secondary reactions, reactions for  $rp$ -,  $\gamma p$ -,  $\alpha p$ - processes and CNO cycle. The proposed design for the AIRIS device is based on four multipole magnets and four dipole magnets arranged in a so called broadband spectrometer configuration. This arrangement will be followed by two RF cavities to provide further selection. The advantages of such a design as well as key device parameters will be discussed in detail. We will also demonstrate the performance of the device for few representative reaction cases that can be studied using AIRIS.

## INTRODUCTION

ATLAS at Argonne is undergoing an efficiency and intensity upgrade. The proposed upgrade is being done in two stages, details are presented in [1, 2, 3]. One of the upgrades being proposed in the second stage of the upgrade is the installation of a large recoil separator for the in-flight radioactive beam program resulting in a better separation of the desired rare isotope beam from the primary production beam. The schematic layout of the proposed device, the Argonne In-flight Radioactive Ion Separator (AIRIS), is shown in Fig. 1. AIRIS, along with other intensity and efficiency upgrades, will result in two orders of magnitude increase in the intensity of the in-flight rare isotope beams, and the availability of higher energies also augments the range of rare ions that can be produced with this technique. The physics that is proposed to be studied includes nuclear structure studies and study of nuclear astrophysics processes. This paper summarizes the current status of design studies for AIRIS.

## AIRIS DESIGN

AIRIS design is comprised of a magnetic chicane that is preceded by a target station and followed by a RF sweeper

and a superconducting debuncher section, as shown in Fig. 1. The selection of recoil beams of interest will be done by appropriately placing slits and beam blockers at the central image of the magnetic chicane. Further selection will happen along the second half of the chicane and at the end slit placed at the final image. Further purification of the recoil beam will be done in the RF sweeper where the tail of the primary beam whose rigidity overlaps with the recoil beam are separated in time and can easily be separated. Finally the recoil beam will go through the debuncher section that will reduce the energy spread and will allow efficient beam transport to experimental stations.

It is a design goal for AIRIS to work for recoil beams of up to 1Tm. It is envisioned that up to 1 pμA stable beams will be used and will require development of new suitable production targets based on rotating target wheels or liquid oil films. The recoil beam will have angular spread of  $\pm 50$  mrad in X and Y, momentum spread of  $\pm 5\%$  and have beam spots of  $\pm 5$  mm x  $\pm 5$  mm.

Table 1 summarizes key parameters for the AIRIS device.

Table 1: AIRIS parameters

| Parameter   | Units | Value |
|---|-------|-------|
| Magnetic chicane length   | m     | 5.87  |
| Dispersion at the central image per percent of kinetic energy deviation | mm    | 1.2   |
| Angular acceptance  | mrad  | 50    |
| Minimum drift space   | cm    | 15    |
| <b>Multipole parameters</b>   |       |       |
| Number of multipole magnets   |       | 4     |
| Half aperture   | cm    | 10    |
| Multipole magnet length   | cm    | 20    |
| Maximum quadrupole poletip field  | T     | 1.5   |
| Maximum sextupole poletip field   | T     | 0.05  |
| <b>Dipole parameters</b>  |       |       |
| Number of dipoles   |       | 4     |
| Maximum dipole field  | T     | 1     |
| Dipole bend angle   | deg   | 22.5  |
| Dipole radius of curvature  | m     | 1     |
| Dipole half gap   | cm    | 5     |
| <b>Debuncher parameters</b>   |       |       |
| Maximum Debuncher cavity field  | MV/m  | 4     |
| Debuncher frequency   | MHz   | 72    |
| Debuncher length  | cm    | 10    |
| Debuncher half aperture   | cm    | 2     |

\* This work was supported by the U.S. Department of Energy, Office of Nuclear Physics, under Contract No. DE-AC02-06CH11357

<sup>†</sup> manikonda@anl.gov

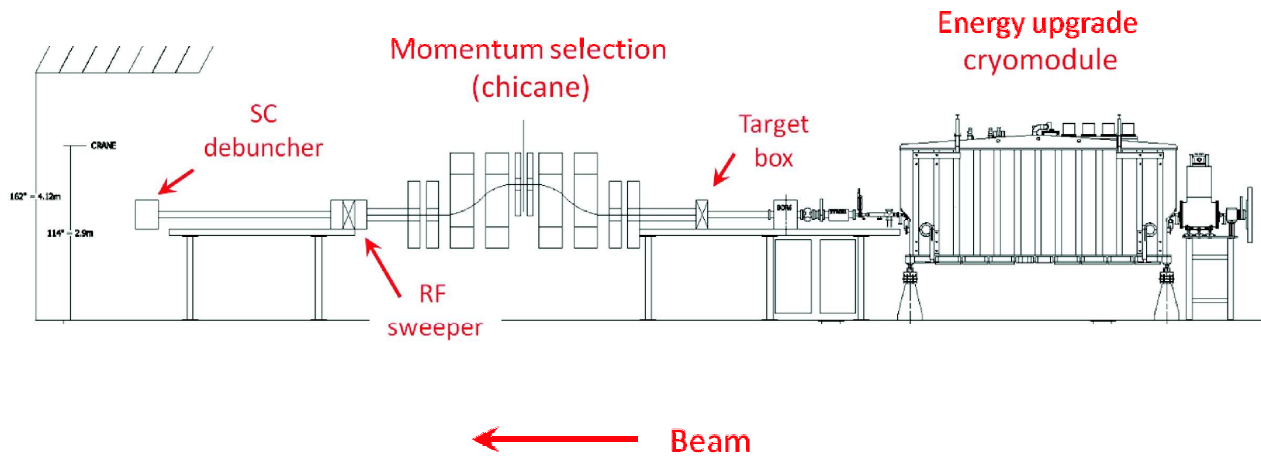


Figure 1: The schematic view of the AIRIS layout in ATLAS.

### The First Order Layout Of Magnetic Chicane

The proposed design for the magnetic chicane is based on four multipole magnets and four dipole magnets arranged in a so-called broadband spectrometer configuration. First order design studies have been performed for the proposed design using COSY Infinity [4, 5]. Fig. 2 shows the first order optics for the device. The center of magnetic chicane is a dispersive image where most of the primary beam can be separated. Magnetic chicane is tuned to the desired recoil beam rigidity and provides a separation of 1.2 mm per percent of kinetic energy deviation at the central image. At the final image the system is dispersion-less, but not achromatic.

**Fringe fields** for multipole magnets and the dipole magnets have been included for realistic simulations of optics. The COSY Infinity's fringe field model that uses symplectically scaled fields of real magnets has been used for the purpose [6].

**Aberration corrections** are important due to the large angular and energy acceptance of the momentum chicane. Only second order aberration correction at the central image has been performed using the four available multipole magnets and by introducing sextupole component in the four dipole magnets. This assumes a mirror symmetric layout for the sextupoles about the center of chicane. It also possible to consider layout where first and second half of the chicane are independently tuned to reduce aberration at the central image and the final image. But in practice it did not yield better results than the mirror symmetric layout. For this paper we will consider mirror symmetric layout for studying transmission efficiency of the device in the following section.

### TRANSMISSION EFFICIENCY OF AIRIS

Simulation of transmission efficiency requires the detailed reaction kinematics of the specific reaction being studied. As test cases for the calculations, beams such as

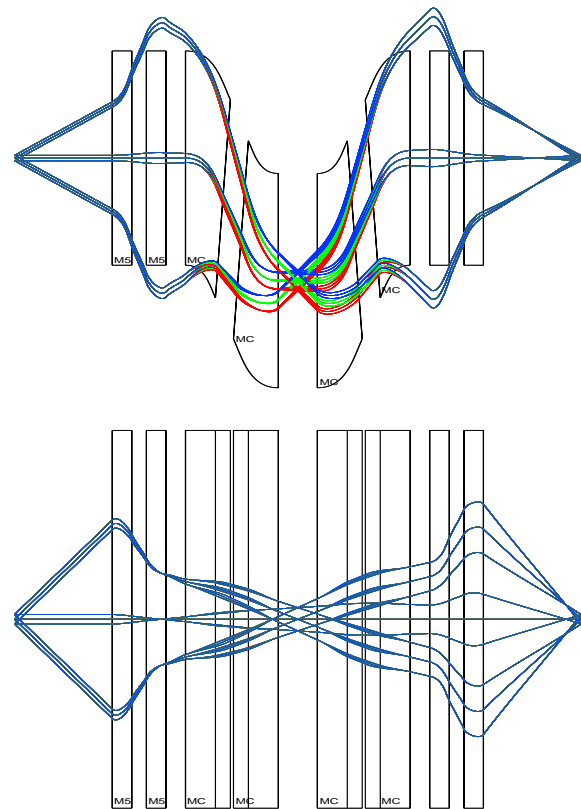


Figure 2: The schematic view of the layout showing the X-projection (left), Y-projection (right) of first order layout.

$^{14}\text{O}$ ,  $^{19}\text{O}$ ,  $^{33}\text{Cl}$  that have been produced in the existing In-Flight facility [7] were chosen. In this contribution we will concentrate on  $^{14}\text{O}$  beams, which were generated via inverse (p,n) reactions. The physics cases for these proton-rich beams cover the study of the ( $\alpha$ ,p) process occurring during on the surface of neutron stars during X-ray bursts [8].

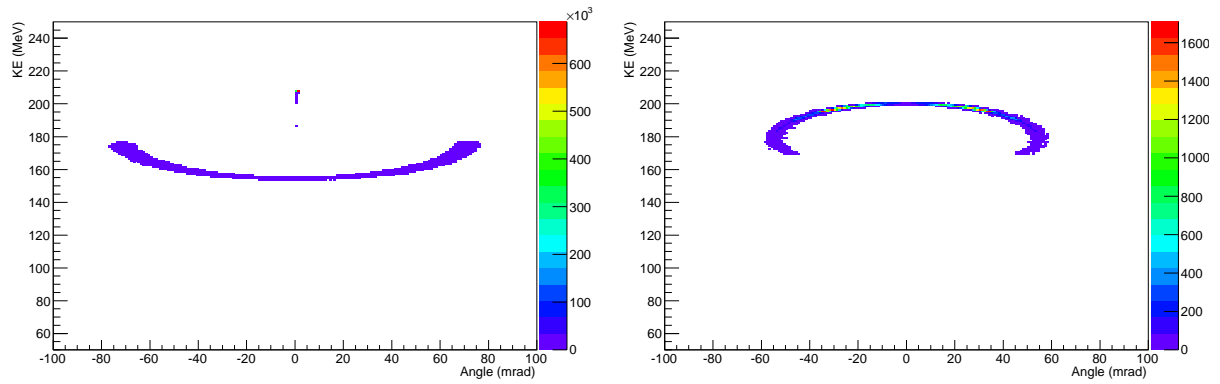


Figure 3: Angle energy distribution for primary beam  $^{14}\text{N}$  (left) and recoil beam  $^{14}\text{O}$  (right). Beam center and beam tail have been simulated separately. The intense beam center is several orders of magnitude greater than the beam tail.

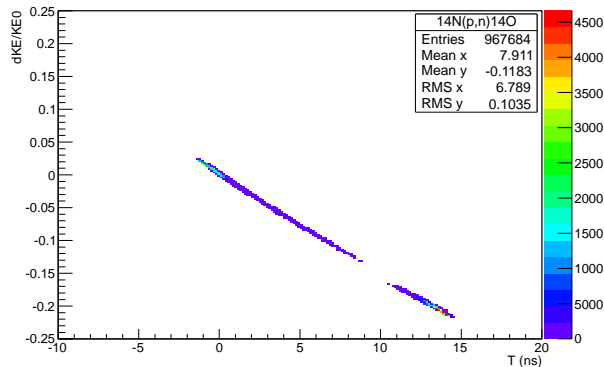


Figure 4: Longitudinal phase space plot of the recoil and remaining beam tail that is now well separated in time.

The angle-energy correlated distribution of the recoils and primary beams were simulated using LISE++ [9] and SRIM codes [10]. LISE++ was used to simulate angle-energy correlation for the recoil beams and the low energy tail of the primary beam that overlaps in rigidity with the recoil beam. The SRIM code provides the angle-energy correlated distribution for the intense beam center that is several orders of magnitude larger than the beam tail.

$^{14}\text{O}$  beams are produced via the (p,n) mechanism using  $^{14}\text{N}$  primary beams on a  $1.5\text{mg}/\text{cm}^2$   $\text{CH}_2$  target. The 10 MeV/nucleon and 15 MeV/nucleon  $^{14}\text{N}$  beam were considered for simulations. The angle-energy distributions are simulated using experimental differential cross sections taken from the literature. For the intense beam center realistic profile for angle-energy distribution was considered but the number of particles was only limited to  $10^6$  due to limited computing resources. For the case of 15 MeV/nucleon  $^{14}\text{O}$  beams the angle energy distribution of the  $^{14}\text{N}$  and the  $^{14}\text{O}$  are shown in Fig. 3. To select recoils of interest, 5 mm slits are placed at the center and end of magnetic chicane. The central rigidity of the magnetic chicane is tuned such that it allows maximum transmission

for the recoils while rejecting a large portion of the beam tail. Transmission calculations were performed using 5th order Taylor transfer maps with fringe fields. The results are summarized in Table 2 for 10 MeV/nucleon case and Table 3 for 15 MeV/nucleon case.

Table 2: Transmissions for the case of 10 MeV/nucleon  $^{14}\text{O}$  beam

|                            | Ions              | Transmission (%) |
|----------------------------|-------------------|------------------|
| Recoil, $^{14}\text{O}$    | $1 \times 10^6$   | 64               |
| Beam tail, $^{14}\text{N}$ | $2.5 \times 10^6$ | 7.6              |

Table 3: Transmission for the case 15 MeV/nucleon  $^{14}\text{O}$  beam

|                            | Ions            | Transmission (%) |
|----------------------------|-----------------|------------------|
| Recoil, $^{14}\text{O}$    | $5 \times 10^5$ | 78.4             |
| Beam tail, $^{14}\text{N}$ | $5 \times 10^6$ | 11.5             |

**RF sweeper** is used to further separate the beam tail from recoils of interest. Longitudinal phase space at the end of chicane is shown in Fig. 4, where the beam tail ( $^{14}\text{N}$ ) and the recoil of interest ( $^{14}\text{O}$ ) are separated in time and can be easily be separated using a RF sweeper whose frequency is harmonic of beam bunch frequency, 12.125 MHz.

**Debunching** of the transmitted beams is essential to efficiently transport the beams after AIRIS. Debuncher parameters are summarized in Table 1. Fig. 5 show the longitudinal phase space and spread in kinetic energy deviation of the recoil beam ( $^{14}\text{O}$ ) at the entrance and exit of the debuncher. For this specific case the spread in kinetic energy deviation is reduced by factor of 10.

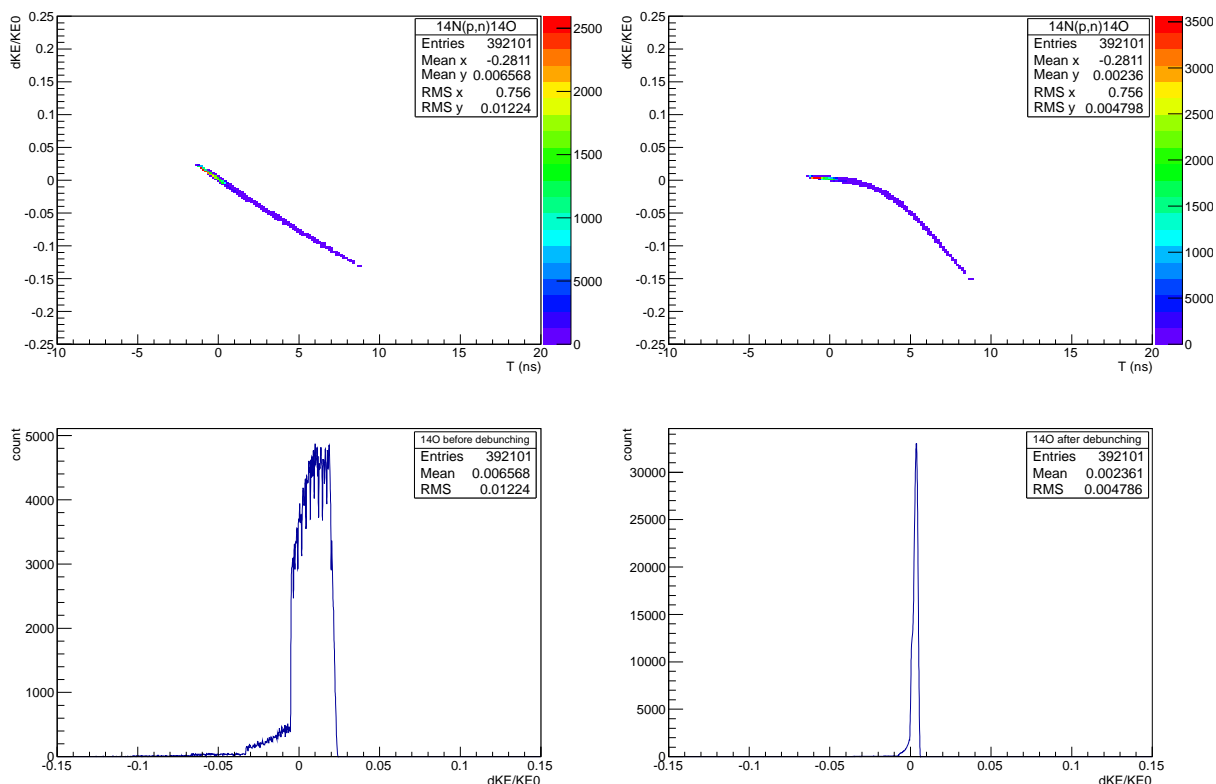


Figure 5: Plot on top left and top right show the longitudinal phase space of the recoil beam ( $^{14}\text{O}$ ) at the entrance and exit of the debuncher. Plots on bottom left and bottom right show the spread in kinetic energy deviation at the entrance and exit of debuncher.

## CONCLUSIONS

A new design for AIRIS has been presented. For the example case of  $^{14}\text{O}$  beams, produced via the (p,n) reaction mechanism, a detailed simulation studies have been performed to shown that  $^{14}\text{O}$  beams can be well separated and transmitted with high efficiency using the present design. Simulation studies to determine the separation and transmission for other radioactive beams of interest are on going.

## REFERENCES

- [1] A Strategic Plan for the Argonne Tandem Linac Accelerator System. [http://www.phy.anl.gov/atlas/workshop09/ATLAS\\_Strategic\\_Plan\\_09.pdf](http://www.phy.anl.gov/atlas/workshop09/ATLAS_Strategic_Plan_09.pdf), November 2009.
- [2] P. N. Ostroumov, J. D. Fuerst, M. P. Kelly, B. Mustapha, K. W. Shepard, and J. Xu. A new ATLAS efficiency and intensity upgrade project. In *Proceedings of SRF-2009*, September 20-25, 2009.
- [3] M.P. Kelly S.A. Kondrashev B. Mustapha R.C. Pardo P.N. Ostroumov, R.V.F. Janssens and G. Savard. Efficiency and intensity upgrade of the atlas facility. In *Proceedings of LINAC-2010*, September 12-17, 2010.
- [4] M. Berz and K. Makino. COSY INFINITY programmer's manual. Technical Report MSUHEP-60803, Department of Physics and Astronomy, Michigan State University, East Lansing, MI 48824, 2006. see also <http://cosy.pa.msu.edu>.
- [5] M. Berz and K. Makino. COSY INFINITY beam physics manual. Technical Report MSUHEP-60804, Department of Physics and Astronomy, Michigan State University, East Lansing, MI 48824, 2006. see also <http://cosy.pa.msu.edu>.
- [6] G. Hoffstätter and M. Berz. Symplectic scaling of transfer maps including fringe fields. *Physical Review E*, 54,4, 1996.
- [7] B Harss, RC Pardo, KE Rehm, F Borasi, JP Greene, RVF Janssens, CL Jiang, J Nolen, M Paul, JP Schiffer, RE Segel, J Specht, TF Wang, P Wilt, and B Zabransky. Production of radioactive ion beams using the in-flight technique. *REVIEW OF SCIENTIFIC INSTRUMENTS*, 71(2, Part 1):380–387, FEB 2000. 8th International Conference on Ion Sources (ICIS 99), KYOTO, JAPAN, SEP 06-10, 1999.
- [8] C. M. Deibel, K. E. Rehm, J. M. Figueira, J. P. Greene, C. L. Jiang, B. P. Kay, H. Y. Lee, J. C. Lighthall, S. T. Marley, R. C. Pardo, N. Patel, M. Paul, C. Ugalde, A. Woodard, A. H. Wuosmaa, and G. Zinkann. First measurement of the  $^{33}\text{Cl}(p,\alpha)^{30}\text{S}$  reaction. , 84(4):045802, October 2011.
- [9] O.B. Tarasov and D. Bazin. LISE++: Radioactive beam production with in-flight separators. *Nuclear Instruments and Methods in Physics Research Section B: Beam Interactions with Materials and Atoms*, 266(19-20):4657 – 4664, 2008.
- [10] James F. Ziegler, M.D. Ziegler, and J.P. Biersack. SRIM - the stopping and range of ions in matter (2010). *Nuclear Instruments and Methods in Physics Research Section B: Beam Interactions with Materials and Atoms*, 268(11-12):1818 – 1823, 2010. 19th International Conference on Ion Beam Analysis.

# RARE-ISOTOPE BEAM FACILITIES IN ASIA

O. Kamigaito\*

RIKEN Nishina Center for Accelerator-Based Science  
Wako-shi, Saitama 351-0198 Japan

## Abstract

Growing activities in the rare-isotope beam (RIB) facilities in Asian countries are reviewed herein. The status of and planned developments are presented for several RIB facilities in Japan, China, India, and Korea.

## INTRODUCTION

Recent research fields of the nuclear physics are widely spread on the nuclear chart. Studies in these fields require the use of a wide variety of rare-isotope beams (RIBs); the ion species, intensity, and quality of the RIBs strongly depend on the scientific objectives of the study. In other words, the accelerator technologies required for rare-isotope studies need to fulfill diverse requirements. These requirements cannot be fulfilled by a single RIB facility. Therefore, a number of facilities that are complementary to each other have either been constructed or are being planned worldwide[1, 2].

In Asian countries, the number of activities at RIB facilities is rapidly growing. This paper presents a brief review of the present status and future plans of several RIB facilities that are located in Japan, China, India, and Korea.

## JAPAN

### RIKEN RIBF

The RIKEN Radioactive-Isotope Beam Factory (RIBF)[3], which was started in 2006, is based on the in-flight fragmentation scheme. Figure 1 shows a schematic layout of RIBF. The main accelerator of RIBF is the superconducting ring cyclotron (SRC)[4]. In 2010, a new injector known as RILAC2 was commissioned, which is dedicatedly used for the acceleration of very heavy ions such as xenon and uranium[5]. While this acceleration mode is being used at RIBF, the original linac injector can be used independently, for the production of super-heavy elements, for instance.

Figure 2 shows a schematic drawing of the RILAC2 injector. It accelerates heavy ions with  $M/q < 7$ , that are produced by a 28-GHz superconducting ECR ion source, up to 680 keV/u with an RFQ and three DTLs. The accelerated beams are injected into the RIKEN Ring Cyclotron (RRC:  $K = 540$  MeV) without charge-stripping. A major portion of the rf system of RILAC2 operates at a fixed frequency of 36.5 MHz, where the maximum power consumption of each rf resonator is designed to be below 20 kW. It has been operating very stably since the beam commissioning.

\* kamigait@riken.jp

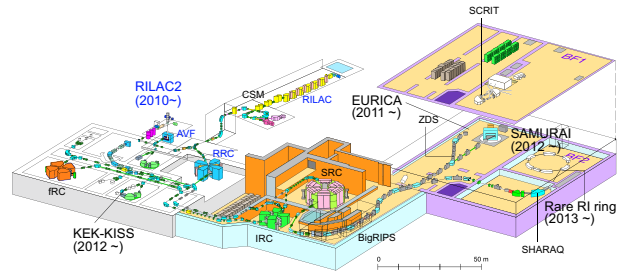


Figure 1: Layout of the RIKEN RIBF.

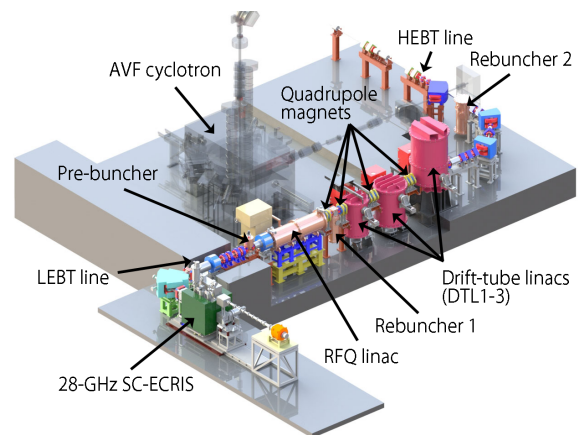


Figure 2: Schematic drawing of RILAC2 injector.

The evolution of maximum beam intensities for beams accelerated at RIBF is summarized in Fig. 3. Owing to the continuous efforts, the intensities are gradually becoming improved[6, 7]. It should be noted that the intensities of light ions such as deuterons and  $^{18}\text{O}$  have already reached  $1 \text{ p}\mu\text{A}$ . On the other hand, the maximum currents in the RILAC2 injection mode are  $3.5 \text{ p}\mu\text{A}$  for  $^{238}\text{U}$ ,  $15 \text{ p}\mu\text{A}$  for  $^{124}\text{Xe}$ ; the heavy-ion intensities remain to be improved.

One of the major obstacles in increasing the intensity of uranium and xenon beams is the limited lifetime of the carbon-foil strippers currently used. In order to overcome this difficulty, a gas-stripper system employing helium is being developed[8, 9]. An actual structure of the stripper has already been constructed based on several test results, and the beam commissioning has recently been started. A drawback of the gas stripper is that the available charge state becomes smaller compared to that obtained in the carbon-foil stripper. Therefore, the magnet power supplies of the fRC cyclotron have been upgraded in order to accommodate the lower charge states. Acceleration tests with the

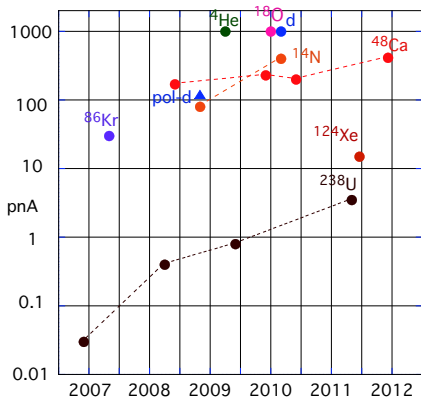


Figure 3: Evolution of maximum beam intensities at RIKEN RIBF.

upgraded fRC will be carried out in the near future.

At RIBF, the operation of a variety of experimental equipments has recently been commenced. For example, the Euroball-RIKEN Cluster Array (EURICA) collaboration for gamma ray spectroscopy was started last year[10]. A new superconducting analyzer with a large acceptance, which is known as SAMURAI, has been commissioned[11]. Moreover, the construction budget of the Rare-RI Ring[12] has been approved, and this ring will be used for performing precise mass measurements of rare isotopes. The number of papers published in scientific journals is also steadily increasing[13].

### KEK KISS at RIBF

After the recent shutdown of the TRIAC facility[14] in Tokai, the RNB group members of KEK started the construction of the new apparatus which is named KEK Isotope Separation System (KISS) at RIKEN RIBF[15]. The layout of this system is shown in Fig. 4.

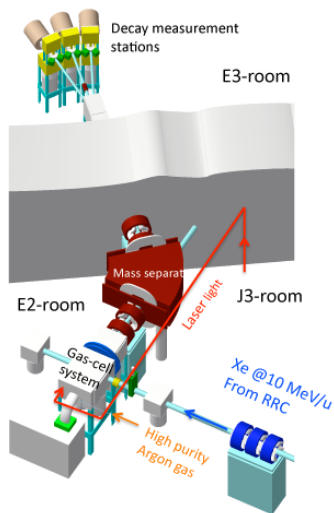


Figure 4: KEK KISS project at RIBF (Courtesy Prof. Miyatake).

KISS has been designed to investigate the origin of the third peak in the element distribution through measurements of the  $\beta$ -decay properties of neutron-rich isotopes having  $N \approx 126$ . These unstable nuclei can be produced by multi-nucleon transfer reactions induced by the  $^{136}\text{Xe}$  beam accelerated by RRC. Among the reaction products collected in the gas cell, the unstable nuclei used for the investigation, such as tungsten isotopes, are ionized by the laser resonance ionization technique. The ions are mass-analyzed by an electromagnetic separator and transported to the next room for the decay measurements performed with a low background. The system construction is nearing completion and beam commissioning will be carried out this year.

## CHINA

### IMP HIRFL

The accelerator complex of the Heavy Ion Research Facility in Lanzhou (HIRFL)[16] is shown in Fig. 5. The injector is a coupled cyclotron system consisting of a sector focusing cyclotron (SFC:  $K = 69 \text{ MeV}$ ) and separated-sector cyclotron (SSC:  $K = 450 \text{ MeV}$ ). Rare isotope research was started here in the 1990s using the heavy ion beams from the SSC and based on the in-flight fragmentation scheme. In 2006, two cooler-storage rings, CSR-m and CSR-e, were constructed in order to expand the scientific opportunities provided by the RIBs; the high energy heavy-ion beams accelerated by the CSR-m produce more intense RIBs in a larger fragment separator placed after the ring. These RIBs are used for fixed-target experiments as well as mass measurements in CSR-e. The heavy-ion beams from CSR-m are used also for cancer therapy with a dedicated beam line.

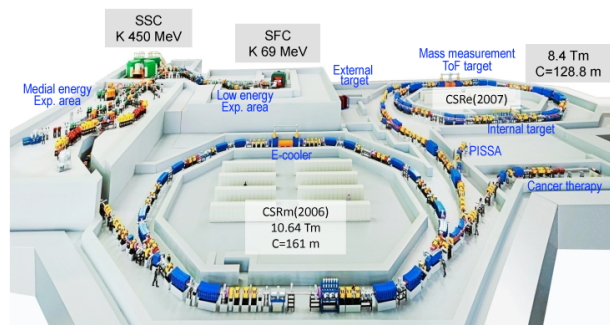


Figure 5: Layout of HIRFL (Courtesy Prof. Zhao).

Since 2011, three new beams, including those of uranium and hydrogen, have been successfully accelerated and accumulated in the CSR-m, and this will provide new scientific opportunities. In addition, very slow extraction from CSR-m that lasted almost three hours was achieved by improving the control system[17]. The mass-measurement program using CSR-e is rapidly progressing; measured masses of astrophysical interest, for four nuclei around the proton drip line, were recently published[18]. The mass

resolution in the isochronous mass spectrometry for CSR-e is as high as  $10^{-6}$ .

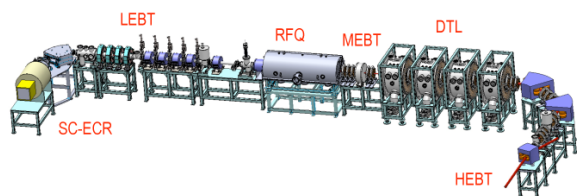


Figure 6: Layout of linac injector for SSC under construction at IMP (Courtesy Prof. Zhao).

In order to increase the beam intensities of the heavy-ion beams, a new linac injector is being constructed for the SSC[19]. As shown in Fig. 6, it consists of a superconducting ECR ion source, an RFQ, and four DTLs operated at 54 MHz. The SSC will be operated in two modes with this injector. One mode is for the injection to CSR-m and the other is for stand-alone use for the synthesis of super-heavy elements. The accelerator components of the injector are under fabrication in the indigenous companies, and they will become operational within three years. Another plan in the short term is constructing a pulsed-mode linac for direct injection into the CSR-m. The uranium beam intensity will be greatly improved by this injector, and parallel operation of the cyclotron facility and synchrotron facility will become possible. The construction is expected to be completed in five years.

More details of the recent achievements and future plans of HIRFL are reviewed in the proceedings[20].

### CIAE BRIF

There is a second RIB project being run in China by CIAE. The project is referred to as the Beijing Rare Ion beam Facility (BRIF)[21], which is intended to accelerate rare-isotope beams based on the ISOL scheme, as shown Fig. 7. The driver accelerator is a 100 MeV, 200  $\mu$ A  $H^-$  cyclotron[22]. A superconducting linac will be added as a Tandem booster. This project was proposed in 1997, and the upgraded scheme currently under operation was approved in 2009.

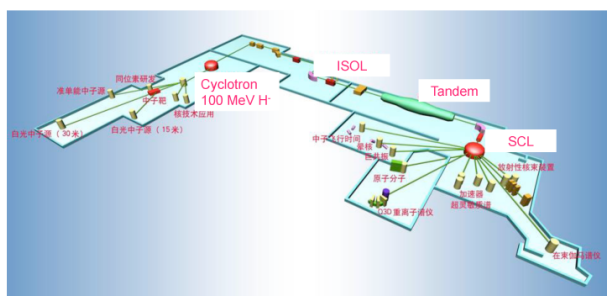


Figure 7: Layout of BRIF (Courtesy Prof. Liu).

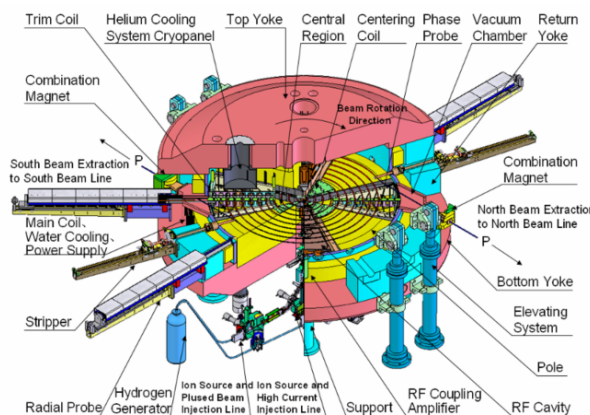


Figure 8: Schematic drawing of BRIF cyclotron (Courtesy Prof. Liu).

Figure 8 shows a schematic layout of the driver cyclotron. It is based on a four-sector AVF cyclotron, equipped with two double-gap resonators and two extraction ports with stripper foils. The construction of the cyclotron has almost been completed[23]. The superconducting cavities are also under fabrication at CIAE, by employing the sputtering technique. The BRIF project will be commissioned in 2014.

CIAE has planned a large future project for the RIB facility known as the China Advanced Rare Ion beam Facility (CARIF)[21]. This project aims to achieve the production of rare isotopes that are very far from the stability line with in-flight fragmentation of unstable nuclei accelerated by a post-accelerator with an ISOL. An interesting fact about this project is that the driver is not an accelerator, but the research reactor known as the China Advanced Research Reactor (CARR) of 60 MW, which recently entered a critical stage. The estimated fission rate in the  $^{235}\text{U}$  target is as high as  $10^{15}$  per second when using the powerful neutron flux from the reactor. Rare isotope beams such as  $^{132}\text{Sn}$  are accelerated up to 150 MeV/u with an intensity of  $5 \times 10^{10}$ , and the secondary fragmentation reaction is expected to produce  $^{78}\text{Ni}$  at 250 pps. The construction is slated for completion by around 2020.

## INDIA

### VECC

VECC, Kolkata, is executing their RIB project based on the ISOL scheme[24]. Figure 9 shows a schematic drawing of their post accelerator consisting of an RFQ (RFQ2) and six DTLs (LINAC1–6). The final energy of the post acceleration is set at 1.3 MeV/u. In 2011, they commissioned LINAC3, and the LINAC4 cavity is almost ready for operation. The low-energy beams from the smaller RFQ (RFQ1) are also used for the material science programs.

This year they succeeded in the production and transfer of radioactive isotopes that were produced in the He-jet multiple target system irradiated by alpha-particle beams

Table 1: RI-beam facilities that are in operation or under construction in Asian countries.

| In-flight facilities | Driver            | Mass  | MeV/u     | I (pps)            | Separator              | Exp.     |
|----------------------|-------------------|-------|-----------|--------------------|------------------------|----------|
| RIBF (RIKEN, Japan)  | SRC               | - 238 | 440–345   | $6 \times 10^{12}$ | BigRIPS (PF)           | ZDS etc. |
| HIRFL (IMP, China)   | CSRm              | - 238 | 2800–500  | $10^9$             | RIBLL2 (PF)            | CSRc     |
| IUAC (India)         | SC-Linac          | - 238 | $\sim 5$  | $\sim 10^{12}$     | HIRA, HYRA (p,n),(d,n) | (PSSD)   |
| ISOL facilities      | Driver            | Mass  | MeV/u     | kW                 | Post Acc.              | MeV/u    |
| RIB (VECC, India)    | Cyclotron/e-Linac | 4/(e) | 16 / (10) | 1.2 / 20           | Linac                  | 1.3      |
| BRIF (CIAE, China)   | Cyclotron         | 1     | 100       | 20                 | SC-Linac               | 2        |

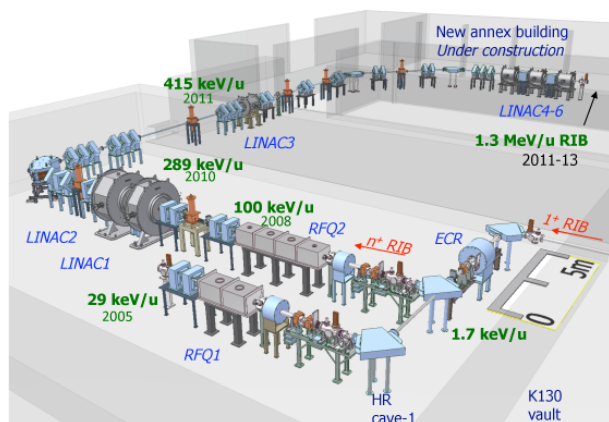


Figure 9: Layout of VECC-RIB (Courtesy Prof. Chakrabarti).

from the K-130 cyclotron. Gamma-ray spectra from the transported isotopes such as  $^{14}\text{O}$  and  $^{41}\text{Ar}$  were clearly measured in front of RFQ2[25].

On the other hand, the production efficiency of rare isotopes is expected to be enhanced by the photo-fission of the uranium target. For achieving this goal, VECC and TRIUMF are collaborating to develop a superconducting electron linac operating at 1.3 GHz for use as a new ISOL driver[26]. The first module, 10MeV-2mA linac, is expected to be ready in 2013.

VECC has recently proposed their future project known as ANURIB, which is an acronym for A National Facility for Unstable and Rare Isotope Beams[27]. This project is divided into two phases. The first phase, which will be completed in 2017, consists of the ISOL-post accelerator combination. The second phase is aimed at achieving the secondary fragmentation of unstable nuclei. In order to further accelerate the rare isotope beams from the first-phase accelerators, the construction of a superconducting ring cyclotron is planned. The second phase is expected to start in 2017.

## IUAC

IUAC, New Delhi, has developed a low-energy beam of  $^7\text{Be}$  using their Heavy-Ion Reaction Analyzer (HIRA)[28],

through (p,n) or (d,n) reactions with inverse kinematics. A beam energy of about 20 MeV has been produced with very high purity by operating the analyzer in a new beam optics.

Recently, they constructed the HYbrid Recoil mass Analyzer (HYRA)[29], as shown in Fig. 10, to fully exploit the heavy-ion beams provided by the ECR ion source and the superconducting linac. The primary purpose of this device is to efficiently collect the fusion evaporation residues with its gas-filled mode operation. However, it is also possible to operate it in the achromatic mode in order to produce radioactive beams. Ion species such as  $^7\text{Be}$  and  $^{18}\text{F}$  will be available at 20–50 MeV with a  $10^3$ – $10^4$  pps.

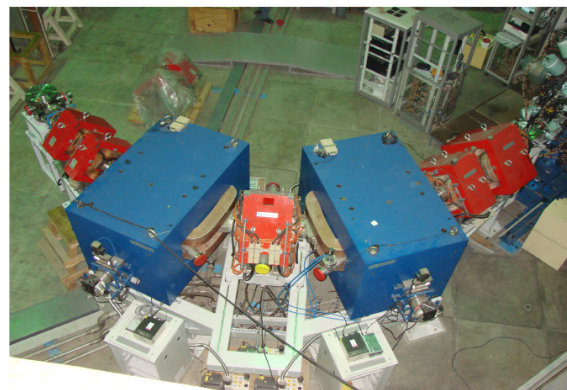


Figure 10: Photograph of the first stage of the HYbrid Recoil mass Analyzer (HYRA) at IUAC (Courtesy Prof. Roy).

## KOREA

### RISP

A large RIB project is known to have been proposed in Korea several years ago. Recently, the project was reopened with the name Rare Isotope Science Project (RISP) under the newly established Institute of Basic Science (IBS) in Daejeong[30].

Figure 11 shows the redesigned accelerator complex of RISP[31]. The main accelerator is a superconducting heavy-ion linac, which accelerates high-power uranium beam up to 200 MeV/u for a fragment separator. This linac can be also used as a driver accelerator for light ions

## Concept of the Accelerator Complex

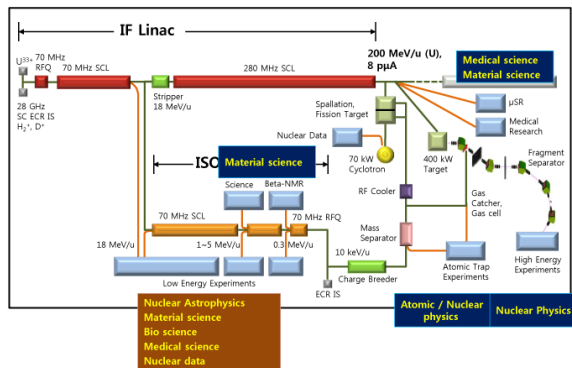


Figure 11: Conceptual drawing of accelerator complex of RISP (Courtesy Prof. Kim).

impinging on the spallation and fission target. The construction of a post-accelerator is planned for this ISOL scheme. Moreover, according to the plans, a 70-kW proton cyclotron will be added as an alternative driver for the fission target. The rare-isotope beam in the third mode can be finally accelerated through the main linac up to 200 MeV/u to produce secondary fragmentation with the RIBs. Beam commissioning of the initial part of the project is expected to start in 2017.

## SUMMARY

A list of the facilities that are in operation and under construction in Asian countries is given in Table 1. Facilities that are still in the design stage have been omitted. International collaborations will gain increased importance for further progress.

## ACKNOWLEDGMENTS

The author is grateful to the following people for helping him prepare the paper: Alok Chakrabarti, Eun-San Kim, Sun Kee Kim, Weiping Liu, Hiroari Miyatake, Shunji Nishimura, Amit Roy, Hiroyoshi Sakurai, Masanori Wakasugi, and Hongwei Zhao. He sincerely thanks all the members of the Accelerator Group at the RIKEN Nishina Center.

## REFERENCES

- [1] OECD Megascience Forum, Report on Working Group on Nuclear Physics, January 1999.
- [2] J. Nolen, "Complementarity of New RNB Facilities and Their Technological Challenges," HIAT09, Venezia, June 2009, MO-02 (2009).
- [3] Y. Yano, Nucl. Instr. & Meth. **B261**, 1007 (2007).
- [4] H. Okuno et al., IEEE Trans. Appl. Supercond. **17**, 1063 (2007).

- [5] K. Yamada et al., "Beam Commissioning and Operation of New Linac Injector for RIKEN RI Beam Factory," IPAC12, New Orleans, May 2012, TUOBA02 (2012).
- [6] N. Fukunishi et al., "Operating Experience with the RIKEN Radioactive Isotope Beam Factory," Proceedings of PAC'09, Vancouver, May 2009, MO3GRI01 (2009).
- [7] H. Okuno et al., "Recent Achievements and Upgrade Programs at RIKEN Radioactive Isotope Beam Factory," IPAC12, New Orleans, May 2012, MOPPD029 (2012).
- [8] H. Imao et al., "Charge Stripping of Uranium-238 Ion Beam with Helium Gas Stripper," IPAC12, New Orleans, May 2012, THPP084 (2012).
- [9] H. Okuno et al., HIAT12, Chicago, May 2012, THB02 (2012).
- [10] <http://ribf.riken.jp/EURICA/>
- [11] K. Yoneda et al., to appear in RIKEN Accel. Prog. Rep. **45** (2012).
- [12] Y. Yamaguchi et al., Nucl. Instr. & Meth. **B266**, 4575 (2008).
- [13] For example, S. Nishimiura et al., Phys. Rev. Lett. **106**, 052502 (2011).
- [14] H. Miyatake, et al., Nucl. Instr. & Meth. **B204**, 746 (2003).
- [15] Y. Hirayama et al., "Beta-Decay Spectroscopy of r-Process Nuclei using KEK Isotope Separation System," ARIS2011, Leuven, May 2011 (2011).
- [16] J. W. Xia et al., Nucl. Instr. & Meth. **A488**, 11 (2002).
- [17] H. W. Zhao, private communications.
- [18] X. L. Tu et al., Phys. Rev. Lett. **106**, 112501 (2011).
- [19] Y. He et al., "Progress of Linac Injector for SSC at HIRFL," Proceedings of IPAC2011, San Sebastián, September 2011, WEPS052 (2011).
- [20] Y. He, HIAT12, Chicago, May 2012, THA03 (2012).
- [21] W. P. Liu et al., Science China Physics, Mechanics and Astronomy, **54**, 14 (2011).
- [22] T. Zhang et al., Nucl. Instr. & Meth. **B269**, 2863 (2011).
- [23] X. Guan, HIAT12, Chicago, May 2012, TUA03 (2012).
- [24] A. Chakrabarti et al.: Nucl. Instr. & Meth. **B261**, 1018 (2007).
- [25] A. Chakrabarti, private communications.
- [26] V. Naik et al., "VECC/TRIUMF Injector for the e-Linac Project," Proceedings of LINAC2010, Tsukuba, September 2010, TH202 (2010).
- [27] R. K. Bhandari et al., "Rare Ion Beam Facility at VECC: Present and Future," Proceedings of IPAC2011, San Sebastián, September 2011, THPS016 (2011).
- [28] A. K. Sinha et al., Nucl. Instr. & Meth. **A339**, 543 (1994).
- [29] N. Madhavan et al., PRAMANA J. Phys. **75**, 317 (2010).
- [30] <http://www.ibs.re.kr/en/>
- [31] D. Jeon, HIAT12, Chicago, May 2012, THA02 (2012).

# PROGRESS AND PLANS FOR HIGH MASS BEAM DELIVERY AT TRIUMF\*

M. Marchetto<sup>†</sup>, TRIUMF, Vancouver, Canada

## Abstract

ISAC is a TRIUMF facility for the production and post-acceleration of radioactive ion beams (RIB). The RIBs are produced in two target stations using a 500 MeV proton beam up to 100  $\mu\text{A}$  of beam current. The produced radioactive species are then ionized and extracted up to 60 kV. The ions of interest are mass selected and transported to either the low energy experimental area or to the post-accelerators. The first stage of acceleration is accomplished via an RFQ followed by a DTL; at this medium stage the energy ranges between 0.15 MeV/u and 1.8 MeV/u for a mass to charge ratio range between  $3 \leq A/q \leq 7$ . The second stage of the acceleration is achieved with a 40 MV superconducting linac for a final energy up to 18 MeV/u. High mass (greater than 30) beams need multiple charges to be accepted by the RFQ. The single charge ions out of the target source are charge bred using an ECR charge state booster. The breeding process generates a significant amount of background contamination that masks the desired ions inside a mixed 'cocktail beam'. Such a cocktail needs to be cleaned of contaminants to be useful for the experiments. An unprecedented effort is going on at TRIUMF trying to clean the high mass cocktail beams using the accelerator chain as filter. The progress and future plans of the project will be presented in this paper.

## INTRODUCTION

The ISAC facility at TRIUMF, represented in Fig. 1, produces, post-accelerates and delivers radioactive ion beams (RIB) using the isotope separation on line (ISOL) method.

A general scheme for this type of facility sees an accelerator, the driver, accelerates light projectiles, the primary beam, toward a thick target. The light projectiles, protons or light ions, break the target nuclei producing neutral radioactive isotopes. These neutral atoms diffuse into a source where they are ionized and extracted at source potential. In general the ISOL method produces high quality emittances but the complicated and relatively slow process reduces the possibility of extracting isotopes with few ms half-lives. The radioactive ions are magnetically separated and if necessary post accelerated to reach the final energy requested.

The singly charged RIB produced in the ISAC target ion source can be either used by the low energy experimental station with an energy up to 60 keV (extraction voltage) or post accelerated to the medium and high energy experiments. In order to inject ion beams with mass greater

than 30 in the post accelerators we have to further strip the singly charged to reduce the mass to charge ratio to value  $\leq 7$ . The charge state is boosted by means of an electron cyclotron resonance (ECR) source located downstream of the mass separator that select the RIB coming from the target.

The charge state booster ionized non only the RIB but also any other element present in its ionization chamber and immediate surrounding. Such elements belong either to the background residual gas or to the materials that constitute the vacuum chamber itself. These undesired element ionization generates a background current of orders of magnitude higher with respect to the radioactive species. This background makes extremely challenging identifying and selecting the RIB.

TRIUMF Accelerator division in collaboration with Science division (high mass task force) is engaged in an effort to develop a toolkit for such challenging charge bred beams. This toolkit includes separation and filtration techniques as well as software and diagnostic aids to plan and streamline the beam tuning and delivery.

ISAC-I and ISAC-II Facility

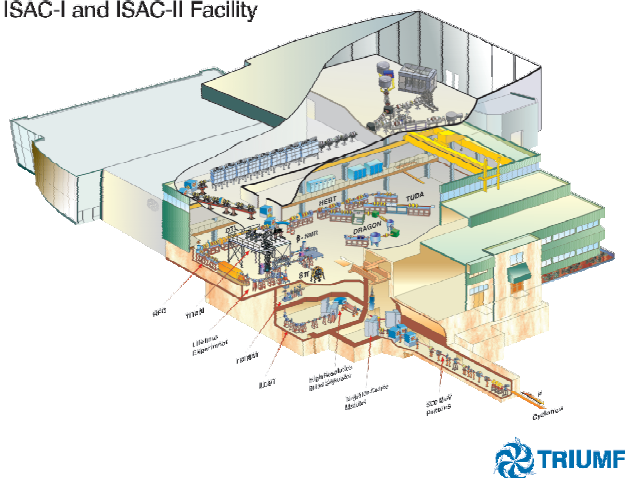


Figure 1: Overview of the ISAC facility at TRIUMF.

## THE ISAC FACILITY

The ISAC facility has the highest power (50 kW) driver proton beam. The plain overview of the facility is represented in Fig. 2. The target stations, mass separator and charge breeder are located in the well shielded ISAC basement (see shaded area in Fig. 2). The target stations are inside a vault to contain radiation in a confined area. Different target materials are available for the production target including silicon carbide, tantalum, uranium carbide and niobium. Two target configurations are available: low and

\* TRIUMF receives federal funding via a contribution agreement through the National Research Council of Canada

<sup>†</sup> marco@triumf.ca

high power respectively for proton beam powers up to 20 kW and 50 kW respectively.

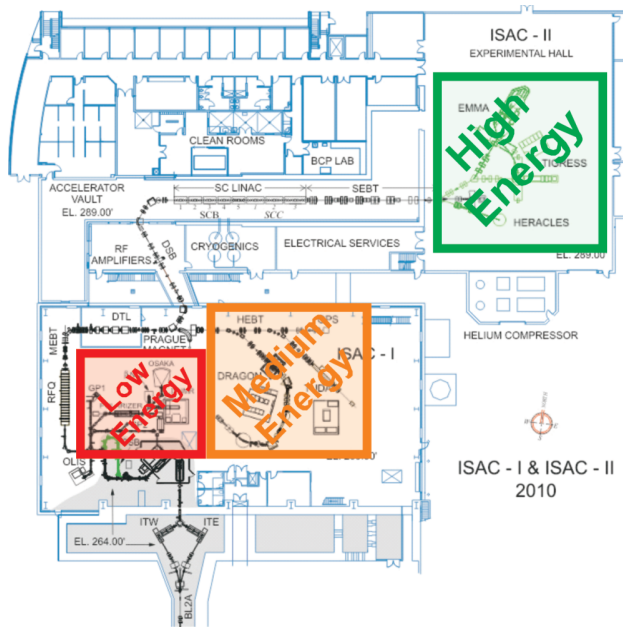


Figure 2: Overview of the ISAC facility at TRIUMF. The ISAC II linac is superconducting while in ISAC I the RFQ and the DTL are room temperature machines.

At ground level the facility has three different experimental areas characterized by the delivered energy range (see Fig. 2). The low energy experimental stations receive beam with energy up to 60 keV (source potential). The medium energy area in ISAC-I and the high energy area in ISAC-II receive post-accelerated beam with energy range respectively of  $0.150 \text{ MeV/u} \leq E \leq 1.8 \text{ MeV/u}$  ( $\beta=1.8\% \rightarrow 6\%$ ) and  $1.5 \text{ MeV/u} \leq E \leq 18 \text{ MeV/u}$  area ( $\beta=6\% \rightarrow 15\%$ ).

### Driver

The TRIUMF  $H^-$  cyclotron [1] accelerates  $H^-$  ions up to an intensity of  $250 \mu\text{A}$  to a maximum energy of 500 MeV. The  $H^-$  are then stripped and protons are extracted in three different beam lines at different energies the maximum being 500 MeV. One of these beam lines is dedicated for the ISAC radioactive beam production. In this case the beam is extracted at 500 MeV and up to  $100 \mu\text{A}$ .

### Target Station and Mass Separator

The two independent target stations [2] allow some services on one target station while producing and delivering radioactive beams with the other.

Each target station is composed of five modules. The entrance module houses the diagnostic and protection monitors for the proton beam. The target module contains the target and the source; this module is routinely removed to change both target and source. Four target modules are available. Different types of on-line ion sources are also

available (surface, LASER, FEBIAD) while others are under development (ECR). The beam dump module is located downstream of the target module. The last two are the extraction modules housing the optics elements. They are oriented perpendicular to the proton beam direction.

Downstream of the targets there is a common pre-separator. The target modules and pre-separator are inside a concrete shielded area. The pre-separator reduces the radioactivity transported outside the shielded area in the downstream beam line.

After the pre-separator the RIBs are selected using the mass separator. The typical operational resolution of the separator magnet is  $\Delta M/M=3000$ . The magnet is installed on a biased platform as an option to increase the resolution.

### The Charge Breeder

After selection it is possible to divert the beam through an electron cyclotron resonance ion source (ECRIS) before sending it to ground level. The source is a 14.5 GHz PHOENIX by Pantechnik [6].

This source is a charge state booster (CSB) that further strips electrons from the singly charged beam. The selected charge state at the exit of the booster is such that the mass to charge ratio is  $\leq 7$  for  $A > 30$ . This upper limit is dictated from the installed linacs.

A NIER type spectrometer with a resolution of  $\Delta M/M=100$  is located downstream of the ECR to select the desired charge state.

A small source face Cs ion source is placed upstream of the CSB to allow tuning it independently from the target station status.

### Post Accelerators

The injector of the post-accelerator chain is a radio frequency quadrupole (RFQ) [3]. The RFQ boosts the energy from  $2 \text{ keV/u}$  to  $150 \text{ keV/u}$ . It can accelerate mass to charge ratio of  $3 \leq A/Q \leq 30$ . The RFQ is a room temperature CW machine operating at 35.36 MHz. The eight meter long resonant structure is composed of nineteen split rings supporting the electrodes. The RFQ doesn't have a bunching section; the beam is pre-bunched at the entrance with a three harmonics (quasi sawtooth) RF buncher, the fundamental being 11.78 MHz. This configuration produces a high quality longitudinal emittance after the RFQ ( $0.22 \pi \text{ keV/u}\cdot\text{ns}$ ). Part of the beam transmitted but not accelerated is stopped into a fixed collimator downstream of the RFQ. The beam inside the longitudinal emittance after the slit is around 80% of the injected.

After the RFQ the charge state of ions with  $7 < A/Q \leq 30$  is increased by stripping them through a thin carbon foil ( $4 \mu\text{g}/\text{cm}^2$ ). As a general rule the most populated charge state is selected using magnetic benders as long as the mass to charge ratio is within  $2 \leq A/Q \leq 7$  set by the following drift tube linac (DTL). The efficiency of the stripping foil depends on the mass of the stripped ions; in most of the cases it ranges between 30% to 50% for  $A \leq 30$ .

The DTL [4] is a variable energy machine covering the entire range of energies  $150 \text{ keV/u} \leq E \leq 1.8 \text{ MeV/u}$ . The beam is matched longitudinally into the DTL by means of a 35.36 MHz spiral buncher (MEBT buncher) located 1.5 m upstream in the medium energy beam transport (MEBT) line. The DTL is a separated function machine composed of five IH interdigital structure accelerating tanks and three split ring bunchers located between the first four tanks. This layout produces good beam quality for each energy. After the fourth tank the beam quality is already sufficient that no buncher is required. The resonance frequency of the tanks and bunchers is 106.08 MHz and they operate at room temperature in CW mode. Transverse focus through the linac is provided by quadrupoles triplets between each tank. The transmission of this linac is greater than 95%. The DTL is also used as an injector for the ISAC II superconducting (SC) linac.

The SCLinac [5] is composed of eight cryomodules. The beam is matched longitudinally into the SC linac by means of a 35.36 MHz spiral buncher (DSB buncher) located 13.3 m upstream in the DTL to SC linac beam (DSB) transport line. This buncher differs from the MEBT one only for the design velocity  $\beta$ . Each of the first five cryomodules (identified as SCB) houses four superconducting cavities and one superconducting solenoid in the center position between cavity two and three. The last three cryomodule (identified as SCC) houses respectively 6-6-8 cavities. Each SCC module has also a superconducting solenoid in the center position similarly to the SCB's. The superconducting cavities are bulk niobium quarter wave resonators at 4K. The SCB cavities resonate at 106.08 MHz while the SCC resonant frequency is 141.36 MHz. The total accelerating voltage of the SC linac is 40 MV. Each cavity is independently phased at  $-25^\circ$  synchronous phase. The transmission through the SC linac is 100%.

### The Off-line Ion Sources

The post accelerator sections are tuned by means of the pilot beam technique. This technique consists in setting the beam lines and accelerators with a beam of stable ions with the same mass to charge ratio as the RIB. This is necessary because the intensity of the radioactive beam typically ranges between  $10^3$  and  $10^6$  particle per second. The pilot beam is produced by an off line ion source (OLIS) system that has multiple sources. A microwave cusp source is generally used to produce singly charged beam matching the production target. A surface source is also available for mono-charge beam. In order to match the radioactive beam coming from the CSB instead, an electron cyclotron resonance (ECR) source that can produce stable ions with higher charge states is installed. This source is a 14.5 GHz Supernanogan by Pantechnik [7].

## HIGH MASS BEAM DELIVERY

The ISAC-II project characterized by the installation of the SC-linac has two goals with respect to ISAC-I: reaching higher energies (above the Coulomb barrier) and deliv-

ering high masses (beyond 30, ISAC-I limit). The Charge Breeder is instrumental to reach the second goal by reducing the  $M/q$  of high mass beams within the ISAC-I accelerators acceptance.

The fact is that the ECR type breeder produces a background of stable species (by ionizing residual gasses and vacuum chamber material) that can hide the RIB. Even few electrical pico-ampere of stable beam can overwhelm the radioactive beam that usually range between  $10^3$ - $10^6$  particle/s in intensity.

The issue is that the RIB need to be delivered relatively pure (free of contaminants).

## THE TOOLKIT

The ongoing effort has the main goal of producing an ensemble of filtering techniques (we call it the toolkit) to choose from when planning the delivery of an RIB. This is of particular interest when the beam is composed of charge bred high mass ( $A > 30$ ) ions and the background level is significantly higher than the desired species.

The toolkit includes new diagnostic instrumentation, stripping and energy degrading carbon foils, software applications as well as it takes advantage of existing beam line and accelerator characteristics to filter out the beam.

### Pre-buncher and RFQ Filter

It is possible to achieve a longitudinal selection of  $(M/q)/\Delta(M/q) \sim 1000$  by exploiting the time of flight separation between the pre-buncher and the RFQ.

The pre-buncher is 5 m upstream of the RFQ as represented in Fig. 3. The source extraction voltage is fixed; this means that different  $M/q$ 's are extracted with different velocities  $v = (2 \cdot q \cdot V_{ext} / M)^{1/2}$ . Different velocities generated different time of flights between the pre-buncher and the RFQ. The RFQ phase acceptance is 40 or  $\delta t = 3 \cdot 10^{-9}$  s. So  $M/q$ s that are spaced in time more than  $\delta t = 3 \cdot 10^{-9}$  s at the RFQ injection can be filtered by adjusting the pre-buncher phase (namely synchronizing the desired  $M/q$  with the RFQ accelerating bucket).

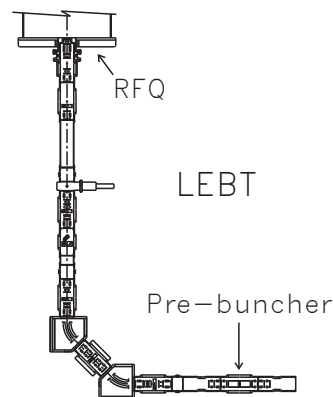


Figure 3: The three harmonics pre-buncher is located in the low energy beam transport (LEBT) line 5 meters upstream of the RFQ.

In numbers we have the following. At 2 keV/u (the injection energy for the RFQ) the beam velocity is  $v=6 \cdot 10^5$  m/s ( $\beta=0.002$ ). This produces a time of flight  $t=8.3 \cdot 10^{-6}$  s. The RFQ relative phase acceptance is then  $\delta t/t=3.6 \cdot 10^{-4}$ .

The velocity  $\delta v$  due to the source fixed extraction voltage is such that  $\delta(M/q)/(M/q)=-2 \cdot \delta v/v$ . We also have that the relative velocity  $\delta v/v$  is equal to  $\delta t/t$ . The relative phase acceptance at the entrance of the RFQ becomes then a relative  $M/q$  acceptance equal (in absolute value) to  $\delta(M/q)/(M/q)=7.2 \cdot 10^{-4}$  or  $(M/q)/\Delta(M/q)=1389$ .

Such a resolution is demonstrated using stable beam with multiple components (cocktail beam) from the OLIS ECR source. A first cocktail beam have  $^{116}\text{Sn}^{18+}$  with  $M/q=6.439$  and  $^{84}\text{Kr}^{13+}$  with  $M/q=6.455$  with a resolution of  $(M/q)/\Delta(M/q)=408$ . By changing the relative phase of the pre-buncher with respect to the RFQ we preferentially select either Sn or Kr namely we synchronized the RFQ bucket with either one of the two elements that arrive at the RFQ at different time (as explained above). By preferentially selecting the Kr we increase its purity with respect to Sn of two order of magnitude.

A second cocktail beam used is composed by  $^{19}\text{F}^{3+}$  with  $M/q=6.333$  and  $^{38}\text{Ar}^{6+}$  with  $M/q=6.327$ . The two has a resolution of  $(M/q)/\Delta(M/q)=1115$ . The calculated separation is between F and Ar at the RFQ entrance is 49 degree. By changing the relative phase of 30 degree the  $^{38}\text{Ar}$  purity increases of one order of magnitude (see Fig. 4).

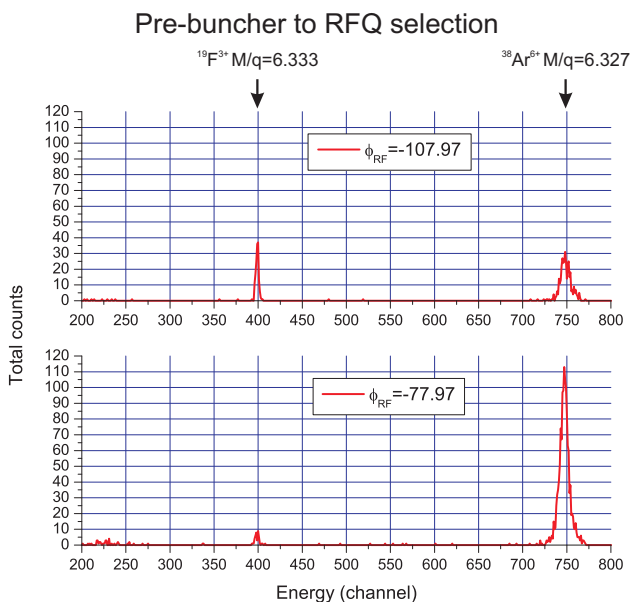


Figure 4: The pre-buncher to RFQ time of flight difference is used increase the purity of  $^{38}\text{Ar}^{6+}$  with respect to  $^{19}\text{F}^{3+}$  of one order of magnitude.

Beam dynamics simulation are underway to support the experimental results.

### Carbon Foil Stripper-degraders

Beam with different mass but same  $M/q$  ratio are accelerated at the same final velocity by the DTL corresponding

to 1.5 MeV/u. A stripper-degrader is installed between the DTL and the SC linac. This is a relatively thick carbon foil with two functions: stripping the beam and creating velocity difference depending on the particle  $Z$  by mean of energy loss (according to the non-relativistic Bethe formula). A mechanism drives the foil in and out by means of a stepper motor (by default we run with the foil in the out position); it can hold up to four foils. The standard foil thickness is  $44 \mu\text{g}/\text{cm}^2$  in order to reach charge state equilibrium. It is possible to load different thickness according the need.

The stripping aim to shifting the  $M/q$  of the contaminant further enough to be resolved downstream.

The velocity difference allows magnetic selection around the bending section of the beam line (DSB) that connects the two linacs (see next paragraph). It also induces transverse beam loss since the optics is optimized for a reference beam with certain  $M/q$  and velocity.

There are two identified locations for the degrader along the DSB beam line as represented in Fig. 5.

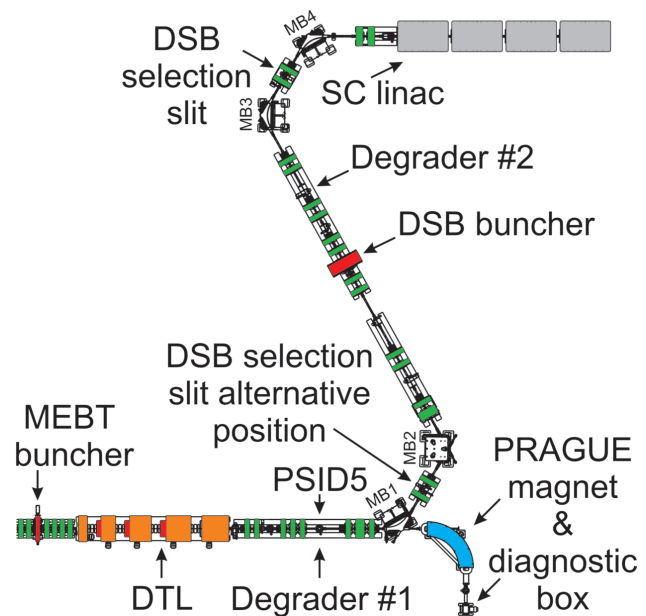


Figure 5: The DTL to SC linac beam (DSB) transport line has an S-shape with two achromatic bending section. The DSB buncher is needed to match the beam into the SC linac. A stripper-degrader (thick carbon foil) is used to generate velocity difference and therefore selection along the beam line.

The first one is 3.6 m downstream of the DTL. In this case the degraded beam travels 14.6 m before entering the DSB buncher (that match the beam into the SCLinac) and 13.3 m from the buncher to the SC linac. Considering the distance from the foil to the SC linac equal to 27.9 m and that the beam velocity after the DTL is  $v=1.71 \cdot 10^7$  m/s ( $\beta=0.057$ ), the time of flight is  $t=1.63 \cdot 10^{-6}$  s. Assuming again a 40 degree phase acceptance for the 106.08 MHz SCB cavities we then have a selection  $\delta v/v=6.4 \cdot 10^{-4}$ . The

velocity difference at this location though is going to be partially compensated by the function of the DSB buncher.

The second location is 3.2 m downstream of the DSB buncher (or 10.1 m upstream of the SC linac). The reduced distance from the degrading point to the SC linac reduce the velocity selection to  $\delta v/v=1.8 \cdot 10^{-3}$  but in this case there is no compensation by the buncher.

The effectiveness of the longitudinal selection after the degrader depends on the species entering the carbon foil (Z dependence) and their final  $\delta v/v$ .

Presently the stripper-degrader is installed in the second location.

### The DSB Selection

It is possible to exploit the dispersion of the DSB bending magnets by installing a downstream selection slit.

The first dipole of the first achromatic bending section (MB1 see Fig. 5) of the DSB line creates a dispersion of  $\sim 1.5$  m in the center of the same section. The beam spot at this location is  $\sim 4$  mm wide including 90% of the beam. This makes possible to achieve a resolution of  $(M/q)/\Delta(M/q)=375$  where peaks are fully separated.

The first dipole of the second achromatic bending section (MB3 see Fig. 5) of the DSB line creates a dispersion of  $\sim 1.6$  m in the center of the same section. The beam spot at this location is  $\sim 5$  mm wide including 90% of the beam. This makes possible to achieve a resolution of  $(M/q)/\Delta(M/q)=320$  where peaks are fully separated. Such a resolution is confirmed by simulation.

resented in Fig. 6. The two elements are separated by  $(M/q)/\Delta(M/q)=309$  therefore they can be fully separated. The measurement show that by setting the bending magnet for  $M/q=5.709$  the Kr peak after the slit disappear and vice-versa.

The same measurement show also that we can change the aspect ratio of  $^{40}\text{Ar}^{7+}$  with respect to  $^{63}\text{Cu}^{11+}$  that has  $M/q=5.722$ . These two has a resolution of  $(M/q)/\Delta(M/q)=477$  therefore they can not be fully separated.

### Software Tools and Diagnostics

There are two software applications in support of the high mass beam delivery.

The first is a web based application [8] (called CSBassistant) that predicts all the possible contaminants for a given accelerated species. This application can be used as a general tool but it has some specific characteristics based on the ISAC beam lines. It includes possible contaminants coming from the ISAC CSB based on the measured background. It also include filtration based on the ISAC accelerator chain and the above reported resolution in the different sections. It uses real atomic mass. In general we use this tool to decide the  $M/q$  that provide the best compromise between transport efficiency and beam purity.

The second application is the scaling routine. This as an EPICS application that is custom built around ISAC beam lines. It scales all the optics element (both electrostatic and magnetic): quadrupole, bender, correction steerers and dipole.

The voltage is the quantity scaled in the electrostatic elements. The current is scaled in the magnetic quadrupole and steerers.

It is not possible to hysteresis cycle the magnetic quadrupole since we don't have the possibility to reverse the polarity. Studies show that cycling the quadrupole current to a set point give a field reproducibility of 2.26 G over 1240.26 G. The same studies also show that only approaching the field from the same side of the hysteresis curve give a field reproducibility of  $<0.05$  G over 1240.8. In order to provide the best reproducibility, the scaling routine as the option to drive each quadrupole to the maximum current, back down to zero and finally back up to the final set-point.

Each magnetic dipole has a an hall probe. The magnetic field read by the probe is scaled.

The routine also scaled the amplitudes of all the RF cavities (RFQ, DTL, SC linac, etc.).

The scaling factors are calculated in each section defined in term of  $M/q$  ratio (either from the source or after a stripper-degrader foil) and energy (form the ion source or after a linac). It is demonstrated that the scaling routine can precisely step to the desired  $M/q$  starting from a reference one. It is crucial to know exactly the species we tune the accelerator with and their  $M/q$  to select a reference starting point for the scaling.

It's also fundamental to have a dedicated diagnostic in order to identify the RIB.

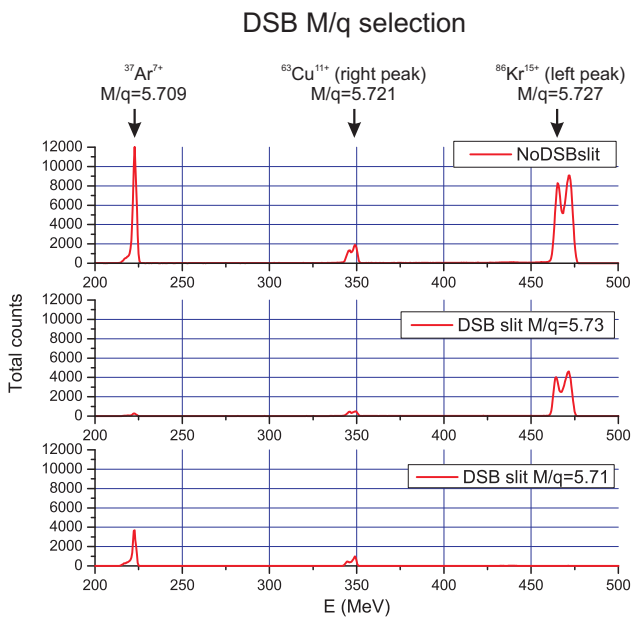


Figure 6: The three different spectra show the effectiveness of the DSB selection.

A selection slit 2 mm wide is installed in the center of the second bending section downstream of MB3. The calculated resolution is demonstrated by selecting  $^{40}\text{Ar}^{7+}$  with  $M/q=5.709$  over  $^{86}\text{Kr}^{15+}$  with  $M/q=5.727$ , as rep-

The available diagnostic (beyond the standard ISAC diagnostic [9]) is a purity monitor (PSID5) downstream of the DTL (see Fig. 5). This is silicon detector positioned at  $30^\circ$  with respect to the beam direction that intercepts the beam scattered from a gold foil. The beam components are identified in terms of total energy; this means that two species with the same mass but different  $Z$  can not be distinguished.

Two new detectors located downstream of the SC linac serve the same purpose, they are used to determine the beam composition before delivering to the high energy experimental area (see Fig. 2). The new diagnostic already in place is a  $\Delta E$ - $E$  silicon detector telescope that provides information and it's capable of identifying beam with same  $M/q$  but different mass and  $Z$ . This detector is extremely valuable but we are limited in the amount of current we can send through it. A second  $\Delta E$ - $E$  detector capable of handling much higher current (gas Bragg detector) is in the final assembly stage.

## RIB BEAM DEVELOPMENT RUN

The main goal of the high mass task force is to prove that is possible to deliver a relatively pure charge bred high mass radioactive beam to an ISAC-II experiment.

Results from a recent dedicated development run show that it's possible but extremely challenging. The RIB chosen for the run is  $^{76}\text{Rb}^{1+}$  from the ISAC target charge bred to  $^{76}\text{Rb}^{15+}$ . The choice of  $^{76}\text{Rb}^{15+}$  is based on the ISAC-I accelerator acceptance and the purity calculated by the CSBassistant.

Since a exact match for the  $^{76}\text{Rb}^{15+}$  was not available, the accelerator was set up with  $^{12}\text{C}^{2+}$  from the off line ion source. The C was further stripped to  $^{12}\text{C}^{5+}$  in the DSB stripper degrader.

The measurements consist in stepping through the  $M/q$  from 2.581 to 2.896 using the scaling routine and characterizing the charge state distribution of each component of the cocktail beam. Each  $M/q$  is associated with an accelerator and beam lines scaled tune. The abundance of each component is measured downstream of the SCLinac at the silicon detector telescope. The silicon telescope is calibrated based on known beam components and their energies. Once a single element (ideally the RIB of interest, in this case  $^{76}\text{Rb}$ ) and its charge state are identified, we select them as reference  $M/q$  to scale the linac.

In Fig. 7 it is represented the charge state distribution of the cocktail beam downstream of the DSB stripper-degrader. Two components are preliminary identified with  $^{61}\text{Ni}$  and  $^{56}\text{Fe}$ . A third component  $^A\text{X}$  is not clearly identified. The  $^{76}\text{Rb}$  is not one of the component since it was blocked at the source during the charge state distribution measurements. The higher peak of the  $^{61}\text{Ni}$  distribution that shows at  $M/q=2.821$  is identified as charge state  $21+$ . The real  $M/q$  of  $^{61}\text{Ni}^{21+}$  is 2.902.

This  $^{61}\text{Ni}^{21+}$  scaled tune is the reference point to re-scale the linac for  $^{76}\text{Rb}^{26+}$ . This last choice take into consideration purity and relative abundance of the  $^{76}\text{Rb}$  charge

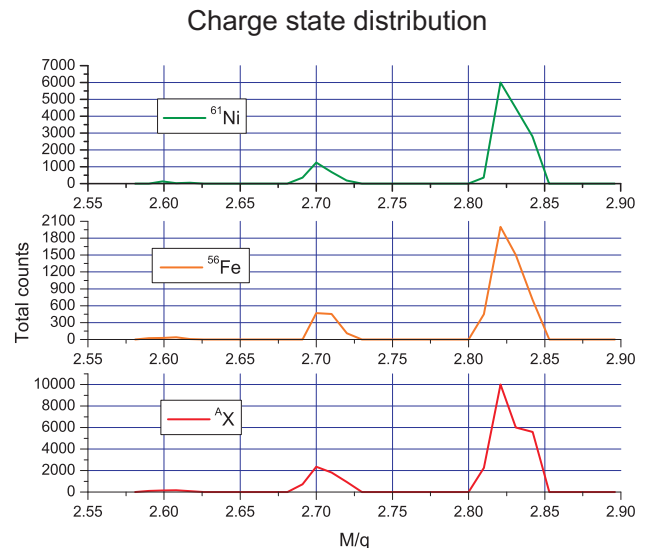


Figure 7: Charge state distribution of the cocktail beam downstream of the DSB stripper-degrader. Two components are preliminary identified with  $^{61}\text{Ni}$  and  $^{56}\text{Fe}$ . A third component  $^A\text{X}$  is not clearly identified. The  $^{76}\text{Rb}$  is not one of the component since it was blocked at the source during the charge state distribution measurements.

state distribution. With the linac scaled on the right  $M/q$  the  $^{76}\text{Rb}$  was released from the source. Fig. 8 shows the different spectra at the telescope with and without the Rb injected into the system. The Rb is expected to grow in the red square marked on the graph. As expected the Rb counts are extremely low but identifiable.

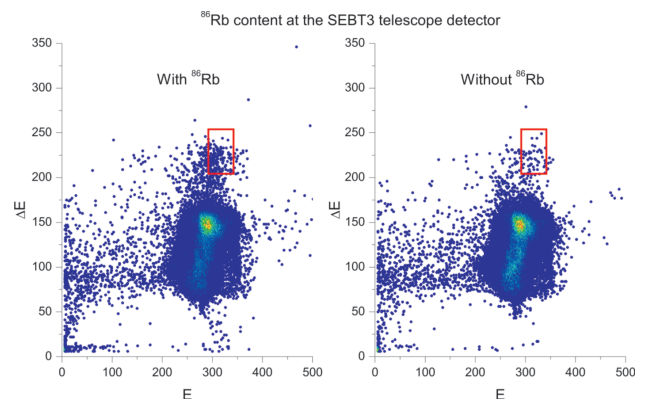


Figure 8:  $^{76}\text{Rb}$  trace at the silicon telescope installed downstream of the SCLinac. The total counts in the red square are three time higher when the  $^{76}\text{Rb}$  is injected into the CSB.

## FUTURE DEVELOPMENT

The stripper-degrader second location is not ideal. The DSB buncher is used to compensate the energy loss through the carbon foil moving the RF phase beyond the linear region and as consequence we lose the proper match into the SCLinac.

The stripper-degrader is going to be moved in the first location (see Fig. 5). The energy loss for the desired  $M/q$  through the carbon foil can be properly compensated by increasing the output energy of the DTL (and so restoring the nominal 1.5 MeV/u after the foil). In this case the DSB buncher has only to match the beam into the SC linac. Also the time of flight between these two is not changed so there is no need to re-phase the buncher with respect to the linac. The time of flight from the DTL to the carbon foil (covering the 3.6 m distance) is instead going to change by increasing the final energy of the DTL. This change the beam time of arrival at the DSB buncher location. Such a time shift can be easily compensated with an already present phase shifter that moves the DSB buncher and SC linac cavity phases with respect to the DTL.

The carbon foil in this first location allow also to use the DTL analyzing (PRAGUE) magnet as a spectrometer. The PRAGUE diagnostic box (see Fig. 5) has an harp profile monitor that gives information about total energy, energy spread. The diagnostic box has also a Faraday cup (FC) that provide the intensity of the beam so it's possible to reconstruct the charge distribution of the different beams. As an upgrade we are going to instrument the box with a beta counter in order to detect radioactivity from the weak RIB.

## CONCLUSION

We demonstrated that phase selection in the accelerator chain can be use as  $M/q$  resolution. Dedicated diagnostics is fundamental to tune RIB above all when stable background is present. The scaling routine is crucial to set the beam lines on the right  $M/q$ . A CSBassistant type of calculator is important to predict the purity of the beam and therefore tune on the most favourable  $M/q$  region.

An unprecedented effort to the issue of delivering high mass charge bred beam at ISAC is showing the first encouraging result. It remains clear that the delivery of such beam is not going to be effortless. Every new RIB delivery has to be planned in advance and required development time.

TRIUMF is gaining valuable knowledge to understand and exploit the full potential of ISAC as well as to design future facilities.

## ACKNOWLEDGMENT

The High Mass Task Force (HMTF) is a collaboration between TRIUMF Accelerator and Science division. Friedhelm Ames, Bob Laxdal, Marco Marchetto and Colin Morton are the representative of the accelerator division. Barry Davids, Adam Garnsworthy and Greg Hackman are the representative of the science division. What reported in this paper is the result of the collaborative effort of all the people mentioned above. Of course nothing would be possible without the strong support of TRIUMF Accelerator and Science divisions.

## REFERENCES

- [1] I. Bylinskii et al., "TRIUMF 500 MeV Cyclotron Refurbishment", Cyclotrons and Their Application, Giardini Naxos, ITALY, September 2007, p. 143.
- [2] P. Bricault et Al. "Progress Towards New RIB and Higher Intensities at TRIUMF", CYCLOTRONS 2010, Lanzhou, China, September 2010, p. 365.
- [3] R.L. Poirier et al., "CW Performance of the TRIUMF 8 Meter Long RFQ for Exotic Ions", LINAC2000, Monterey, California, USA, August 2000, p. 1023.
- [4] R.E. Laxdal et al., "Beam Commissioning and First Operation of the ISAC DTL at TRIUMF", PAC2001, Chicago, Illinois, USA, June 2001, p. 3942.
- [5] R.E. Laxdal, "Commissioning and Early Experiments with ISACII", PAC07, Albuquerque, New Mexico, USA, June 2007, p. 2593.
- [6] F. Ames et Al., "Commissioning of the ECRIS Charge State Breeder at TRIUMF", ECRIS2010, Grenoble, France, August 2010, p. 178.
- [7] K. Jayamanna et al., "A Multicharge Ion Source (SUPER-NANOGAN) for the OLIS Facility at ISAC/TRIUMF", Review of Scientific Instruments 81, 02A331 (2010).
- [8] A. Garnsworthy, <http://trshare.triumf.ca/garns/CSBExperts/>.
- [9] M. Marchetto et al., "Beam Dynamics Studies on the ISAC II Superconducting LINAC", LINAC2006, Knoxville, Tennessee, USA, August 2006, p. 312.

## PROGRESS OF THE SPIRAL2 PROJECT

E. Petit [GANIL, Caen, France]

### *Abstract*

The SPIRAL2 facility will extend the possibilities offered at GANIL to heavier radioactive beams, with much higher intensities : it will provide intense beams of neutron-rich exotic nuclei created by the ISOL production method. The extracted exotic beam will be used either in a new low energy experimental area called DESIR, or accelerated by the existing SPIRAL 1 cyclotron (CIME. The intense primary stable beams (deuterons, protons, light and heavy ions) will also be used at various energies for nuclear physics, as well as for neutron-based research and multi-disciplinary research, in dedicated caves called S3 and NFS. During year 2008, the decision has been taken to build the SPIRAL2 machine in two phases: - first phase including the driver accelerator and its associated new experimental areas (S3 and NFS caves), - second phase including the RIB production part, with the low energy RIB experimental hall called DESIR, and the connection to the GANIL existing facility for post-acceleration by the existing CIME cyclotron. The SPIRAL2 facility is now in its construction phase, with the objective of obtaining the first beams for physics during year 2014 with the first phase.

**CONTRIBUTION NOT  
RECEIVED**

# OPERATIONAL CONSIDERATIONS FOR FUTURE MULTI-USER RIB FACILITIES\*

Colin Morton<sup>#</sup>, TRIUMF, Vancouver, BC, Canada

## Abstract

Like other radioactive ion beam facilities, the ISAC facility at TRIUMF is capable of serving only a single RIB user at a time. With the construction of ARIEL, the Advanced Rare-Isotope Laboratory, ISAC will gain a second RIB production front end and the ability to serve multiple users simultaneously. This will introduce significant new complexity to operations and beam delivery at ISAC and place additional constraints on experimental scheduling and personnel requirements. These constraints will have to be taken into consideration when planning the operation of the combined ARIEL and ISAC facilities in order to maximize the benefits associated with having multiple RIB production facilities.

## INTRODUCTION

ISAC, the Isotope Separator and Accelerator facility at TRIUMF, is a high-power ISOL-type rare-isotope beam (RIB) facility [1,2]. RIB production is driven by 480–520 MeV protons from TRIUMF’s main cyclotron at currents of up to 100  $\mu$ A. An artist’s rendering of the facility is shown in Fig. 1 with the proton beamline visible at lower right. As ISAC has only a single driver and mass separator, only one RIB can be produced at any one time. This limits the amount of RIB that can be delivered to experiments to ~2500–3000 hours/year.

To increase the amount of RIB available to experiments, a new facility, the Advanced Rare Isotope Laboratory (ARIEL) [3], is currently under construction. In its initial phase, ARIEL will comprise a 10-mA, 50-MeV superconducting electron linac, target station(s), mass separators and low-energy beam transport to the existing ISAC experimental beamlines (Fig. 2). The e-linac will serve as a driver for RIB production by photofission and other photon-induced reactions. With ISAC, this will allow the simultaneous delivery of two RIB, doubling the number of hours of RIB available to experiments. Plans for the future expansion of ARIEL include a second high-current proton beamline to complement that already driving RIB production at ISAC and the ability to deliver three RIB simultaneously.

The move from single-user to multi-user operation brings with it a number of challenges. Many of these are technical in nature and beyond the scope of this paper. From an operations and beam delivery standpoint, however, there are still significant challenges to be addressed, in particular because of the impact that multi-user operation will have on both experiment scheduling and personnel requirements.

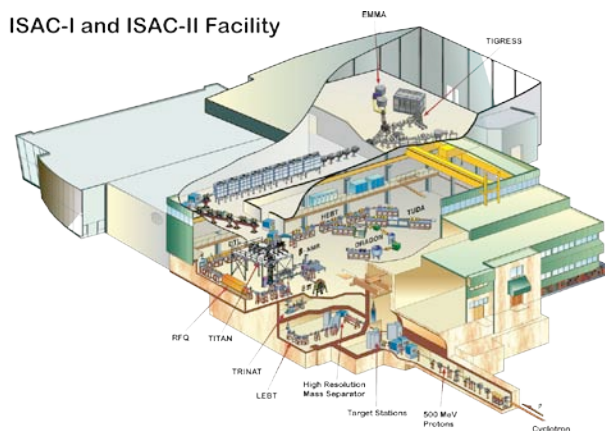


Figure 1: The ISAC facility at TRIUMF.

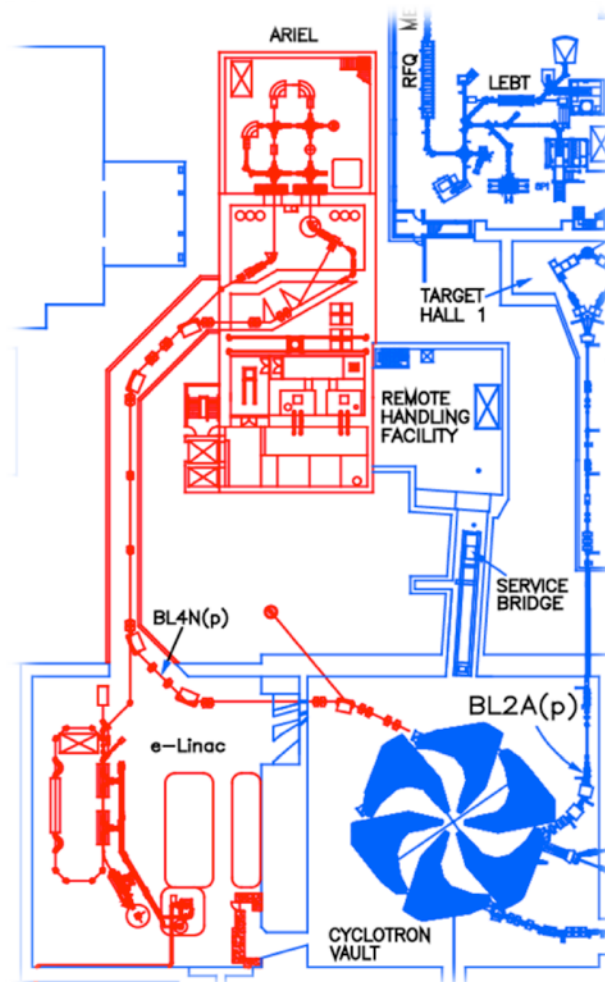


Figure 2: Beamline layout of the Advanced Rare Isotope Laboratory, showing its location relative to existing TRIUMF facilities. ISAC is at top right.

\*TRIUMF receives federal funding via a contribution agreement through the National Research Council of Canada  
<sup>#</sup>morton@triumf.ca

### EXPERIMENT SCHEDULING

As shown in Fig. 3, low-energy RIB transport from ARIEL will be coupled into the existing ISAC LEBT so as to allow simultaneous delivery to two low-energy experimental beamlines or to the combined ISAC-I and ISAC-II high energy areas. (Simultaneous delivery to both ISAC-I and ISAC-II will not be possible without the addition of a second low-beta acceleration section parallel to the existing ISAC-I RFQ and DTL.) Additional destinations, such as the TRINAT neutral atom trap, the ISAC yield station and a future ARIEL yield station, will only be accessible from either ISAC or ARIEL; however, they represent special cases that have only a limited impact on the overall beam schedule. For typical operation, the combined ARIEL and ISAC facilities can be thought of as sharing three distinct experimental areas that can be served independently.

The existing ISAC beamline layout dictates where beam can or cannot be delivered simultaneously. Because the two production facilities will share a single set of experimental destinations they will have to be scheduled in concert taking into consideration the fact that changing the destination of RIB being delivered from one of ARIEL or ISAC will have knock-on effects on delivery from the other. Delivering RIB from multiple sources simultaneously will introduce both greater complexity and additional constraints on the experimental schedule.

Figure 4 illustrates four options for scheduling a typical week of operation. In options a) and b), the week begins with ISAC RIB being delivered to one of two low-energy areas (ILE1) and ARIEL RIB being delivered to the combined high-energy area (HEBT). The goal in both cases is to end the week with ISAC beam being delivered to HEBT and ARIEL beam to the other low-energy area (ILE2). The cyclotron maintenance scheduled mid-week serves as an incentive to switch ISAC operation from ILE1 to HEBT at that time. The need for setup time using stable beam from the ISAC offline ion source (OLIS) dictates that ARIEL delivery to HEBT end early on the Tuesday. In option a), ARIEL delivery to HEBT is

maintained to that time then switched immediately to ILE2. This creates a “pinch point” in the schedule as beam tuning and RIB setup are then required for both ILE2 and HEBT at the same time, increasing the need for personnel and/or time to complete the setup of both successfully. In option b), ARIEL delivery to HEBT is suspended a day earlier. This eliminates the conflict with the start of OLIS tuning to the HEBT area but represents a loss of high-energy beam time.

In options c) and d) delivery from one of ARIEL or ISAC is maintained to a single experimental area while delivery from the other is changed between areas. In these cases it is sufficient to stagger experiments and setup times in order to eliminate scheduling conflicts. In studying numerous options for scheduling beam delivery it becomes apparent that the most straightforward way to avoid conflicts is to maintain delivery from one RIB

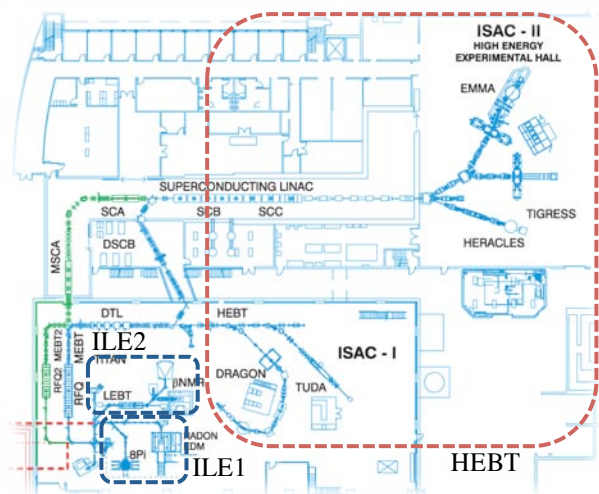


Figure 3: Experimental areas at ISAC.

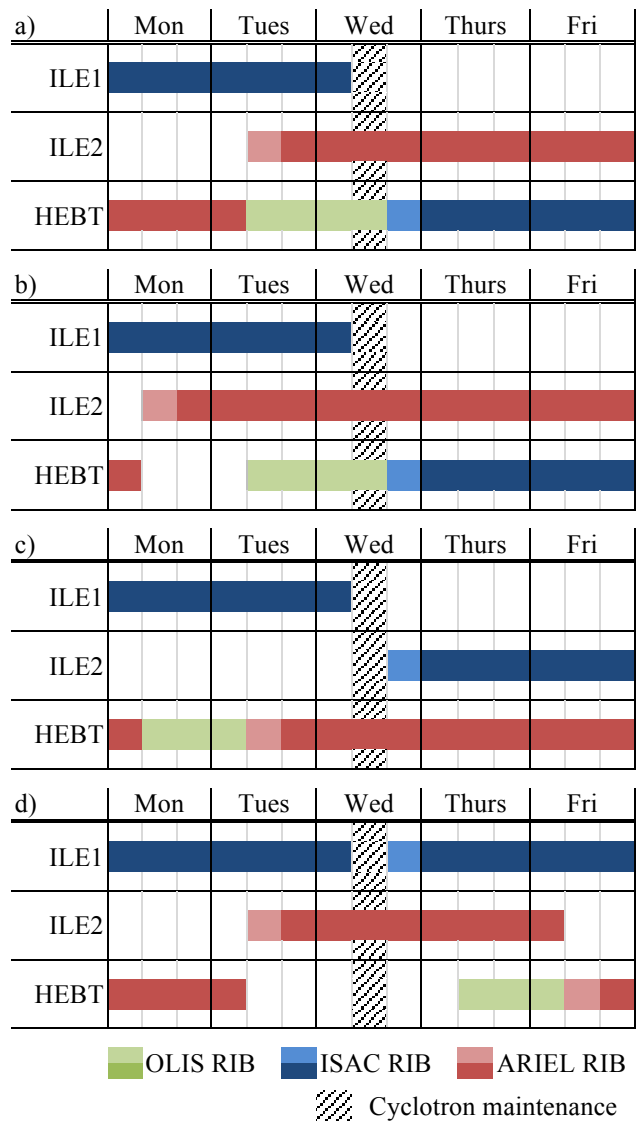


Figure 4: Representative options for scheduling RIB setup and delivery for the combined ARIEL and ISAC facilities. Lighter shades denote tuning and setup time; darker, delivery to experiment. Note the conflicting ILE2 and HEBT setup time (Tuesday, mid-day) in option a).

source to a single area for extended periods of time. This is not unusual at present; as an example, ISAC RIB were scheduled to be delivered solely to high-energy locations from June 1, 2012 to July 14, 2012, a period spanning the operation of two ISAC production targets. The ideal situation would be to deliver beam to a single experimental location with only minimal intervention for several weeks at a time. The specific need for  $^8\text{Li}$  to serve the materials science program is a good candidate for such a mode of operation; this could be produced via the  $^9\text{Be}(\gamma,p)$  reaction using a beryllium target at ARIEL and delivered exclusively to the  $\beta\text{NMR}$  location in the ILE2 area while RIB from ISAC are delivered to either ILE1 or HEBT.

Accepting constraints on beam scheduling can help to limit the need for additional personnel or tuning time when setting up RIB delivery to experiments. This does, however, come at the cost of scheduling flexibility and, ultimately, the amount of RIB delivered to experiments. There is a trade-off between personnel requirements and flexibility. With even the most stringent constraints on scheduling, there is some minimal level of staffing needed to maintain operations. Increasing the number of available personnel allows greater freedom to plan beam delivery, accounting for technical or experimental constraints, but only to the point at which scheduling can be carried out without regard to personnel availability; beyond that, additional personnel provide little further benefit. Assuming too much scheduling flexibility for the personnel available will result in an inefficient use of beam time as conflicts arise in beam tuning and setup. Conversely, assuming too little flexibility will introduce unnecessary constraints on the scheduling process and result in an inefficient use of the available personnel. Figure 5 shows in schematic form the relationship between the two quantities; the ideal operating regime will lie in the shaded region near the top of the curve, before it flattens out as the gains from additional hires diminish.

## PERSONNEL REQUIREMENTS

TRIUMF presently has a single Operations group comprising both ISAC and Main Control Room (MCR) operators located in separate control rooms. The MCR has a full complement of 15 operators, with three on shift at any given time. There are ten ISAC operators, scheduled two to a shift 24 hours/day when running; during shutdown periods, operators are only on shift 12 hours/day Monday through Friday and pursue other tasks when not on shift. Both e-linac operation and ARIEL RIB delivery will have to be incorporated into TRIUMF Operations once ARIEL comes online.

While ISAC operators are responsible for the safe, efficient delivery of RIB to experiments, they are also responsible for aspects of things such as maintenance coordination, work permits, and site services. From past beam delivery experience, having two fully trained and experienced operators on shift is sufficient to *e.g.* establish RIB delivery to one experimental location while

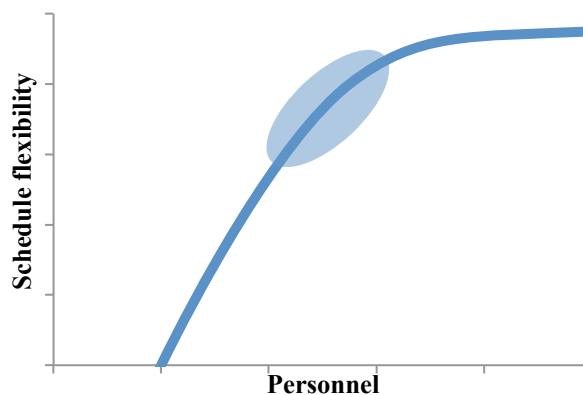


Figure 5: Schematic representation of the relationship between flexibility in beam scheduling and personnel availability. The shaded region represents an operating regime in which a high degree of scheduling flexibility is achieved with a minimum of personnel.

delivering stable beam (from OLIS) to another, though even this assumes some measure of coordination and support from TRIUMF's Beam Delivery group. With fewer experienced operators on shift, or setting up both RIB and stable beam delivery at the same time, additional personnel are generally required.

There are several options for addressing the personnel requirements associated with multi-user delivery. It is planned to move both the MCR and ISAC operators into a common control facility. This would allow operators from one group, when not actively tuning beam or otherwise managing delivery at their own facility, to assist with the operation of the other given appropriate cross-training. Furthermore, it may be possible to move things like maintenance coordination, work permits and site services out of the control room, allowing the operators on shift to focus on their core responsibilities of safety, machine protection and beam delivery. (There may be additional efficiencies to be gained with the development and increased use of high-level applications within the ISAC and cyclotron control systems, but that is also beyond the scope of this paper.) Combining control facilities and reducing operators' responsibilities may be sufficient to allow e-linac operation with the existing complement of operators as the machine is not expected to require significant intervention when running and it is not possible to tune drivers and RIB at the same time (as RIB delivery requires stable driver operation), but it is unlikely that this will be sufficient for both e-linac operation and the simultaneous delivery of multiple RIB.

Simply achieving the full desired shift coverage of three operators per shift in the MCR and two per shift at ISAC requires the hiring of additional operators to account for the fact that, with 25 operators, an average of two will be on vacation in any given week. Managing ARIEL RIB delivery on top of existing commitments will likely require an additional person to be available for beam tuning and setup. There are two options for addressing this need: hiring additional operators, or hiring Ph.D.-level physicists (or similar) to provide expert

support on an as-needed basis. The main difficulty with hiring additional operators lies in shift scheduling. Adding a single operator position requires hiring five operators in order to maintain that position throughout an entire shift rotation. While that would provide significant flexibility from a beam scheduling standpoint, the cost is large.

Hiring physicists to provide support as needed requires fewer new hires, but their availability will be limited outside of normal working hours. This is an acceptable compromise as setting up RIB for delivery during daylight hours is desirable for other reasons, in particular the lack of availability of technical staff after hours in the event of equipment or controls problems that might arise during setup. Physicists offer the additional advantage of having advanced knowledge of beam delivery systems and procedures and can provide research and development effort when not actively supporting operations. Key to this approach, however, is ensuring that those hired to support beam delivery and operations have a well-defined service role. It should be noted that this role could change with time: a physicist could be hired before ARIEL comes online to pursue his or her own research interests on a part-time basis while working on a particular aspect of the ARIEL project as a service to the lab, then take over an operations support role as the project phase of ARIEL comes to a close. Using this model an additional 40 hours/week of operations support could be provided with one full-time equivalent, or two highly-qualified personnel working half-time in a service role and half-time in research and development.

## CONCLUSIONS

With the combined ARIEL and ISAC facilities, TRIUMF will be able to support multiple RIB users simultaneously. The move to multi-user operation will bring additional challenges and introduce a number of operational considerations:

- beam scheduling to avoid tuning conflicts;
- long-term scheduling to limit the number of changes between experimental destinations;
- personnel requirements; and
- the nature of additional personnel that may be needed.

Some lack of scheduling flexibility will have to be accepted as a trade-off against personnel requirements. Even then, it is likely that additional personnel will be needed, including additional operators to ensure full shift coverage. Beyond that, hiring Ph.D.-level physicists (or similar) to provide expert-level support when necessary may provide the greatest benefit to the lab.

## ACKNOWLEDGMENT

The author gratefully acknowledges the help and support of TRIUMF's Beam Delivery and Operations groups and thanks Pierre Bricault for providing the beamline layout in Figure 2.

## REFERENCES

- [1] M. Trinczek et al., "Beam delivery and future initiatives at the ISAC radioactive ion beam facility," PAC09, Vancouver, May 2009, FR5REP124, p. 5074 (2009); <http://www.JACoW.org>.
- [2] M. Marchetto, "Progress and plans for high mass beam delivery at TRIUMF," HIAT2012, Chicago, June 2012 (in press); <http://www.JACoW.org>.
- [3] L. Meringa et al., "ARIEL: TRIUMF's Advanced Rare Isotope Laboratory," IPAC2011, San Sebastián, September 2011, WEOBA01, p. 1917 (2011); <http://www.JACoW.org>.

## COMMISSIONING EXPERIENCE WITH CARIBU

Richard Vondrasek, Sam Baker, Peter Bertone, Shane Caldwell, Jason Clark, Cary Davids, Daniel Lascar, Anthony Levand, Kim Lister, Richard Pardo, Donald Peterson, Don Phillips, Guy Savard, Matthew Sternberg, Tao Sun, Jon Van Schelt, Bruce Zabransky, Argonne National Laboratory, Argonne, IL 60439, USA

### Abstract

The Californium Rare Ion Breeder Upgrade (CARIBU) of the ATLAS superconducting linac facility aims at providing low-energy and reaccelerated neutron-rich radioactive beams to address key nuclear physics and astrophysics questions. These beams are obtained from fission fragments of a Cf-252 source, thermalized and collected into a low-energy particle beam by a helium gas catcher, mass analyzed by an isobar separator, and charge bred with an ECR ion source to higher charge states for acceleration in ATLAS. The facility has ramped up operation from an initial 2.5 mCi source to the present 55 mCi source. A 500 mCi source has been produced at Oak Ridge National Laboratory and is expected to be ready for installation in mid-2012. Low-energy mass separated radioactive beams have been extracted, charge bred with a 10% efficiency, reaccelerated to 6 MeV/u, and delivered to GAMMASPHERE for beta decay studies. The Canadian Penning Trap (CPT) mass spectrometer has been relocated to the CARIBU low-energy beam line. Mass measurements on over 60 neutron-rich nuclei have already been performed and additional measurements are underway. In addition, a new tape station for beta decay studies has just been commissioned.

### THE CARIBU FACILITY

Science is driving the development of ever more capable radioactive beam facilities. While present day facilities (REX-ISOLDE, TRIUMF, TRIAC, ANL) can deliver particle intensities in the  $10^4$  to  $10^8$  pps range, future facilities (FRIB, HIE ISOLDE, SPES, SPIRAL2, EURISOL) will deliver beams in the  $10^{10}$  to  $10^{13}$  pps regime. However, these are large costly projects which have a long timeline from conception to full operation. In the United States, the Facility for Rare Ion Beams (FRIB) [1] will be the flagship radioactive beam facility producing a wide array of beams via in flight fragmentation, but the facility is not expected to be fully functional until 2021. In the interim, the CARIBU facility [2] (Fig. 1) will provide beams of radioactive nuclei albeit with a more limited reach and intensity but also at a substantially reduced cost and project footprint. CARIBU will utilize fission fragments from  $^{252}\text{Cf}$  to provide nuclei which will be thermalized in a helium gas-catcher, mass separated and injected into an ECR charge breeder (ECRCB) to raise their charge state for subsequent acceleration in the ATLAS superconducting linear accelerator. The facility also encompasses a low-energy experimental area for mass measurements and decay studies.

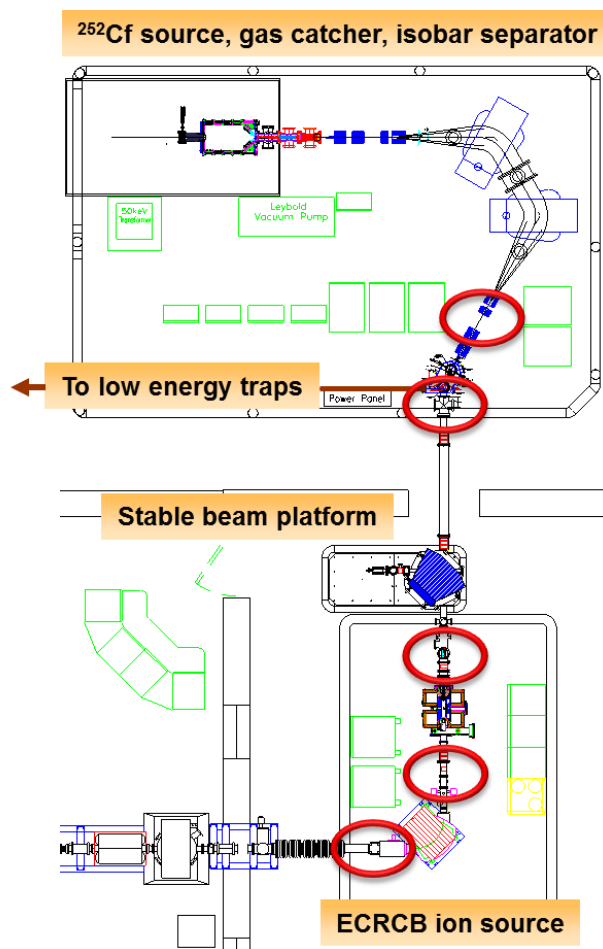


Figure 1: Overview of CARIBU facility and ECR charge breeder. The locations of surface barrier detectors used for radioactive beam tuning are marked with red ovals.

### Californium Source

A  $^{252}\text{Cf}$  fission source is used to produce the neutron-rich nuclei with a fission fragment distribution peaked in regions of interest that are not well populated by uranium fission. With a 2.6 year half-life and a 3.1% fission branch,  $^{252}\text{Cf}$  has a relatively long source lifetime and thus minimizes the need for source replacement. The source is stored in a heavily shielded cask assembly which attaches to the helium gas catcher/RFQ ion guide system. In its final configuration, CARIBU will utilize a 1Ci  $^{252}\text{Cf}$  source, but facility commissioning took place with a 55 mCi source. This served as a test of the shielding integrity and allowed for safe equipment modifications.

## Gas Catcher

The gas catcher is a large-volume high-intensity device measuring 50 cm in diameter and 1 m in length. The UHV construction, utilizing all stainless steel and ceramic components, allows for a clean system that can be baked after source installation. The fission fragments lose the majority of their energy in a degrader foil placed over the Cf source. The fragments are then thermalized in the ultra-pure helium gas operating at a pressure of 150 mbar. A combination of RF and DC fields keep the ions off of the wall and move them towards extraction at which point the helium gas flow in the RF cone section serves to transport the ions to two differentially pumped RFQ sections. The extraction RFQ leads to a 50 kV acceleration section forming a beam containing all off the  $^{252}\text{Cf}$  fission products but of very good quality – 1 eV energy spread and  $3\pi$  mm mrad emittance. The typical extraction time is 10 msec with an overall efficiency of 20%. Some of the expected yields for a 1 Ci source both at low energy and after acceleration are shown in Table 1.

## Isobar Separator

The fission fragments are delivered to a compact isobar separator with a design mass resolution of 1:20,000. Matching sections at the entrance and exit form a vertical ribbon beam for mass selection, and all optics are electrostatic so that the beamline tune is mass independent. To date, the best achieved resolution has been 1:10,000 in part due to difficulties with the field control of the magnets. There are several surface barrier detectors installed in the beam transport line for diagnostics. These are used to monitor the radioactive isotope intensity via beta decay. For beam identification, the magnets are ramped in the traditional manner while observing the beta activity as shown in Fig. 2. The spectrum is divided into several regions representing the heavy  $2+$  fission products, the light and heavy  $1+$  products, and the molecular components with an underlying decay tail from the long-lived activity. Higher resolution scans are performed on regions of interest allowing definitive beam identification as shown in the lower panel of Fig. 2.

Table 1: Isotope yields at low energy and after acceleration in the ATLAS linac assuming a 1 Ci source.

| Isotope           | Half-life (s) | Low-energy Beam Yield ( $\text{s}^{-1}$ ) | High-energy Beam Yield ( $\text{s}^{-1}$ ) |
|-------------------|---------------|---|--|
| $^{104}\text{Zr}$ | 1.2           | $6.0 \times 10^5$                         | $2.1 \times 10^4$                          |
| $^{143}\text{Ba}$ | 14.3          | $1.2 \times 10^7$                         | $4.3 \times 10^5$                          |
| $^{145}\text{Ba}$ | 4.0           | $5.5 \times 10^6$                         | $2.0 \times 10^5$                          |
| $^{130}\text{Sn}$ | 222           | $9.8 \times 10^5$                         | $3.6 \times 10^4$                          |
| $^{132}\text{Sn}$ | 40            | $3.7 \times 10^5$                         | $1.4 \times 10^4$                          |
| $^{110}\text{Mo}$ | 2.8           | $6.2 \times 10^4$                         | $2.3 \times 10^3$                          |
| $^{111}\text{Mo}$ | 0.5           | $3.3 \times 10^3$                         | $1.2 \times 10^2$                          |

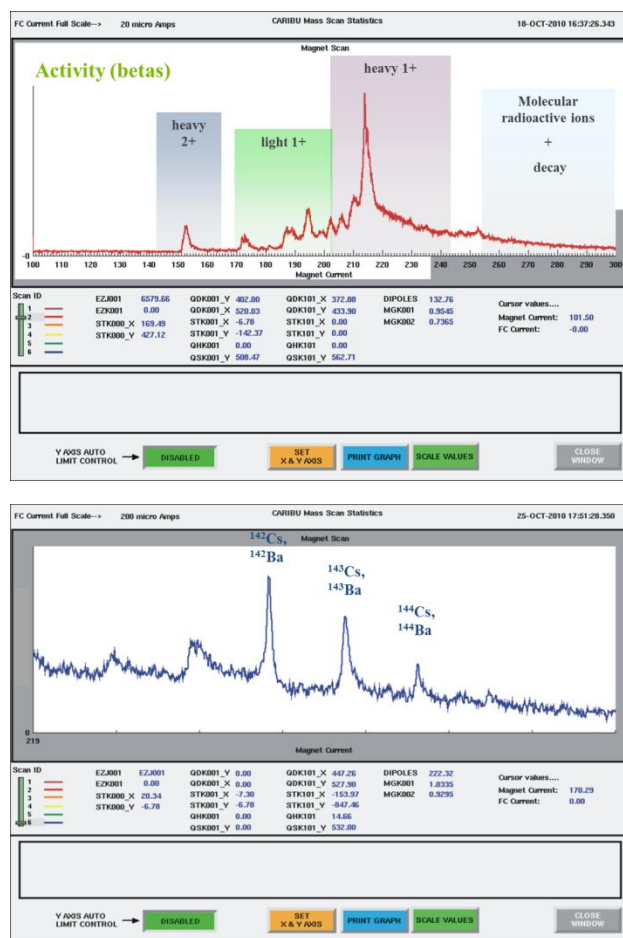


Figure 2: Scans of the isobar separator magnets showing the beta activity of the radioactive fission products. The coarse upper scan delineates the various regions of interest, while the fine lower scan displays positive beam separation and identification.

## LOW-ENERGY EXPERIMENTS

CARIBU provides a wealth of neutron-rich nuclei available for study. For many of these nuclei, not even their fundamental properties, such as mass and half-life, are known. To measure these properties, it is not necessary to accelerate the neutron-rich nuclei produced by CARIBU. Instead, the beams from CARIBU are delivered to a low-energy experimental area after they are further cooled and bunched with an RFQ along a low-energy beamline, ejected at rates of  $\sim 10$  Hz, and transformed by an ‘elevator’ from the  $\sim 50$  kV beam extracted from the gas catcher to a  $\sim 2$ -10 kV beam.

The first experiments using low-energy beams from CARIBU have begun. A program to measure the masses of neutron-rich nuclei has been initiated with the Canadian Penning Trap (CPT) mass spectrometer. Masses of neutron-rich nuclei not only help to disentangle the underlying nature of nuclei, but they are also essential ingredients for understanding the astrophysical r-process thought to produce more than half of the heavy elements

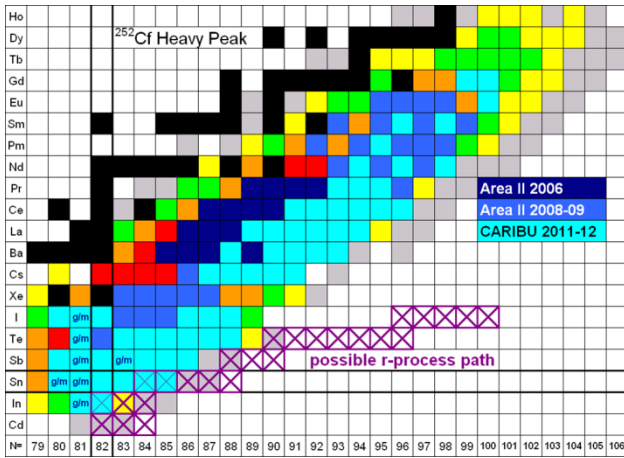


Figure 3: Masses measured during the various campaigns with the Canadian Penning Trap.

in the universe. To date, masses have been measured with the CPT for 62 nuclei along the In, Sn, Sb, Te, I, Cs, Ba, La, Ce, Pr, Nd, Pm, Sm, Eu, and Gd isotopic chains (Fig. 3) to a precision of typically 10 keV/c<sup>2</sup>. Of these, 17 masses were obtained for the very first time, and the mass precision of the other masses was vastly improved. After the 500 mCi source is installed, it is expected that more than 100 additional mass measurements of neutron-rich nuclei will be made.

A moving tape collector system, or "tape station", has been constructed and installed in the low energy experimental area of CARIBU. The system consists of an implantation chamber and tape transport/storage mechanism. Fission fragments from CARIBU are implanted on 35 mm aluminized tape and beta/gamma activity is detected using plastic scintillators and high purity germanium detectors. Once a counting cycle is completed, the activity can be transported on the tape away from the detectors to a shielded location within a storage unit capable of holding ~350 ft of tape. The system has been commissioned by using it to measure half-lives for <sup>142</sup>Cs and <sup>144</sup>Cs. Preliminary values of 1.68(2) s and 0.99(5) s, respectively, were obtained on the first attempt with 7 hours of beam time. The quoted uncertainties are purely statistical. The system is capable of operating with a sufficiently short duty cycle to study nuclei with half-lives as short as 300 ms and has been observed to operate reliably in this mode for 16 hours.

### CHARGE BREEDER

The charge breeder is a room temperature ECR ion source operating at 10-14 GHz with a design extraction voltage of 50 kV, matching that of the gas catcher. The ECRIS has an open-structure NdFeB hexapole with six radial ports. The radial ports which are each 17 x 41 mm in size act as pumping channels resulting in a plasma chamber pressure of 5 x 10<sup>-8</sup> Torr. They also serve to introduce the RF and support gas into the plasma chamber. This eliminates the need for cut-outs in the injection side iron plug and results in a large peak and

highly symmetric axial magnetic field where the ions enter the plasma. This scheme differs from other ECR charge breeders in existence which are closed hexapole devices with axial RF injection. For the ANL ECRCB, the low charge-state ions are introduced into the plasma through a grounded stainless steel tube mounted on a linear motion stage. The stage has a 30 mm range of travel, and thus the deceleration point of the low-charge state ions can be adjusted on-line without disturbing the source conditions [3, 4].

### Breeding Efficiency

A summary of achieved charge breeding efficiencies of the ANL ECRCB compared to that of other breeders operating in the world is given in Fig. 4. The ANL charge breeding development system consists of a source for the production of stable ions (either a surface ionization source or an RF discharge source), a transport system, and the ECR charge breeder (see Fig. 1). A diagnostics region includes a fully shielded Faraday cup for measuring the 1+ beam and a silicon surface barrier detector (SBD) for measuring radioactive beams via beta decay. After charge breeding, the intensity of the mass analyzed n+ ions is observed on either a Faraday cup for the stable beams or a SBD (which has an identical configuration to the 1+ SBD) near the Faraday cup for the radioactive beams. The breeding efficiency and time are determined by pulsing the incoming 1+ beam, using an electrostatic steerer voltage, and measuring the n+ response on the Faraday cup or SBD. The breeder typically operates at 36 kV potential with two RF frequencies (11.44 + 11.7 GHz) exciting the plasma. While the breeding efficiencies of the stable and radioactive species have been similar, the beamline tunes used to achieve these results are different. There is some evidence that the beam extracted from the ECRCB differs in its trajectory depending upon the source of the feed material – neutral gas injection versus 1+ injection. This is quite unexpected for a plasma driven device given the long ion confinement time, and this phenomenon is being investigated.

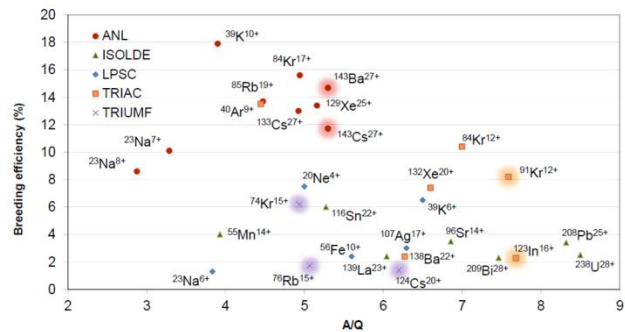


Figure 4: Summary of charge breeding results for the CARIBU program as well as other charge breeding programs. Radioactive isotopes are denoted with shading.

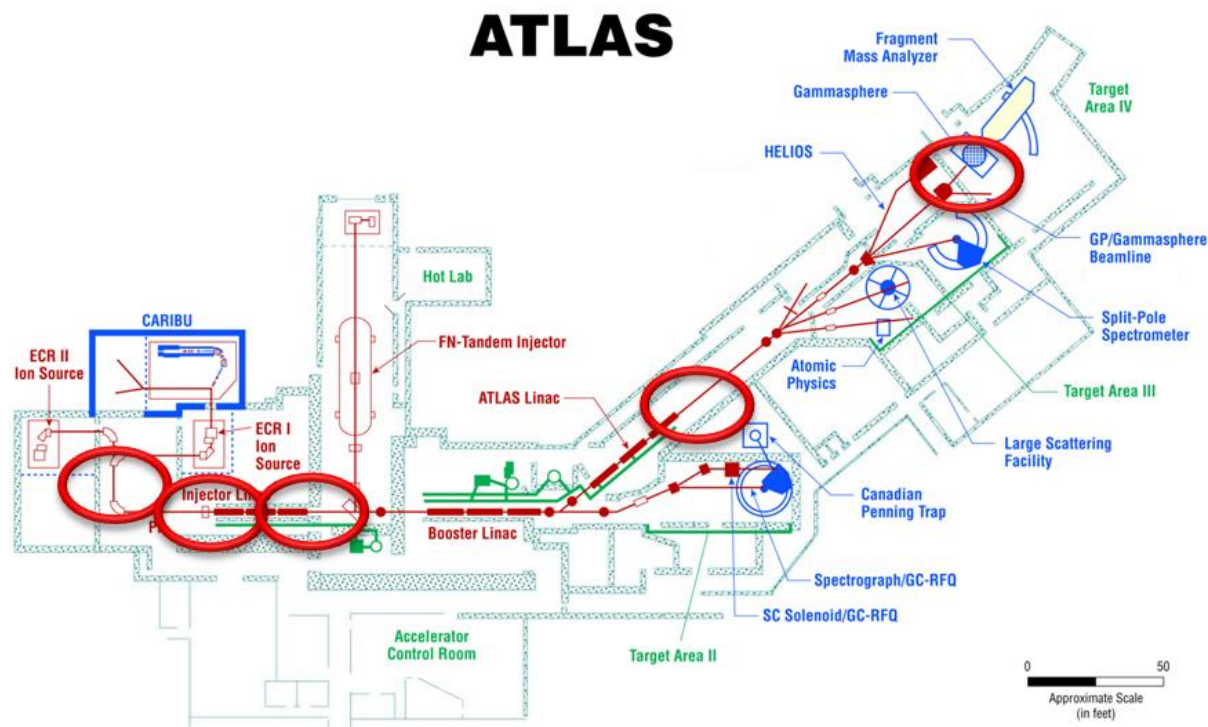


Figure 5: The ATLAS facility with CARIBU addition marked in blue. The locations of the silicon surface barrier detectors for beam tuning are marked with red ovals.

## BEAM TUNING

The ATLAS facility has had a robust Accelerator Mass Spectrometry (AMS) program for several decades, and the experience gained in that time has been adapted for use with the CARIBU radioactive beams. First a stable beam with very similar  $A/Q$  to the radioactive beam of interest is identified. Typically an isotope of krypton or xenon fulfills this role, and that beam is produced via neutral gas injection into the ECRCB. The accelerator is tuned with this beam, optimizing transmission to target. The tune is stored in a database which is then scaled to the charge-bred beam of interest. This allows rapid cycling between machine tune configurations as the entire machine can be shifted from one tune to another via computer control. After all elements have been optimized with the guide beam, all machine elements are scaled to the  $A/Q$  of interest with no tuning of the machine elements after scaling. The SBDs arrayed throughout the machine (Fig. 5) are then used for beam detection and optimization. It has been observed that the set value for the steerer immediately after extraction changes based upon the origin of the ion source feed material - neutral gas versus a  $1+$  injected beam - and has a direct impact on overall beam transmission. With the steerer set for optimum transmission of the stable guide beam, the radioactive beam transmission is greatly diminished. Once the steerer value has been optimized utilizing the SBDs, the radioactive beam transmission approaches that of the stable beam. As stated earlier, this effect is still being investigated.

## Beam Contaminants

The negative of an ECRCB is the stable background produced by the ion source which can be in the enA range ( $10^{10}$  pps). The background originates from the constituents of the plasma chamber wall material as well as those of the source neutral gas load and can obscure any low-flux radioactive beams and complicate the experimental set up. Methods are being investigated to minimize the background, but there are also many  $A/Q$  combinations which can yield a relatively clean energy spectrum with the current level of background. First, a program is used to identify potential conflicts based upon  $A/Q$  ratio as well as the likelihood of particular contaminants being present in the ion source. Once a potential  $A/Q$  combination has been identified, it is investigated with the beam energy acquisition system. Two energy spectra for Cs are shown in Fig. 6. The upper spectrum is the energy spectrum of the beam taken at  $0^\circ$  with x1000 attenuation. Large contaminants of  $^{53}\text{Cr}$ ,  $^{90}\text{Zr}$ , and  $^{126}\text{Sn}$  can be clearly seen as well as lower level contaminants. For this case, a beam of  $^{143}\text{Cs}^{27+}$ , the background rate was 330 kHz, but moving to  $^{143}\text{Cs}^{25+}$  produced a background level of 66 kHz. The lower spectrum is that of  $^{144}\text{Cs}^{25+}$  taken at  $0^\circ$  with no attenuation with a background rate of 900 Hz as opposed to  $^{144}\text{Cs}^{26+}$  which had a background rate of 10 kHz. With this system, it is possible to find  $A/Q$  combinations which make beam contaminants less troublesome.

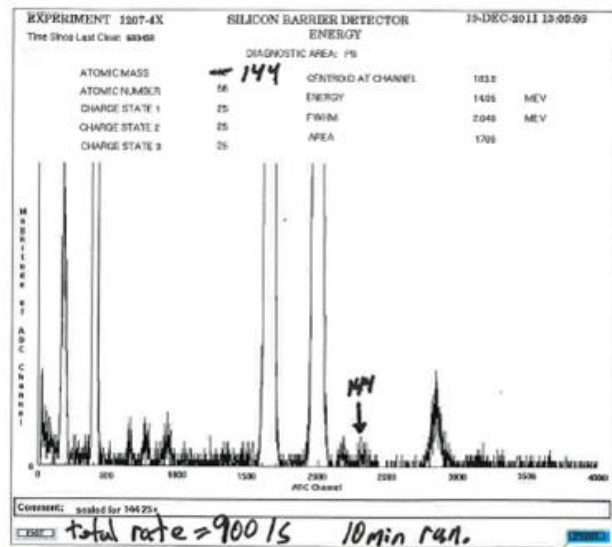
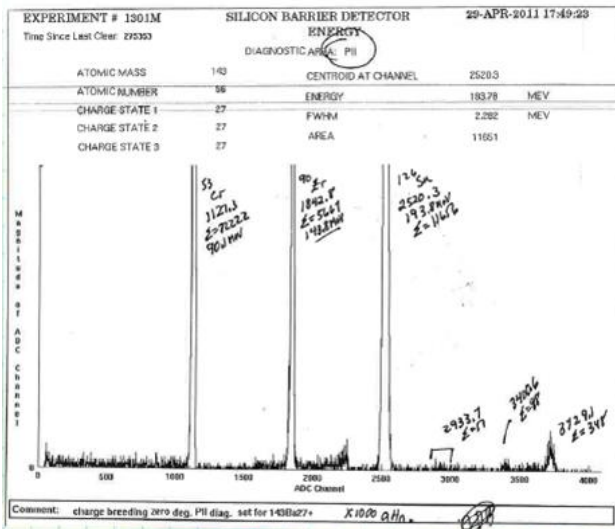


Figure 6: Energy spectra of  $^{143}\text{Cs}^{27+}$  (top panel) and  $^{144}\text{Cs}^{25+}$  (bottom panel) taken at 1.5 MeV/u at  $0^\circ$  on a silicon surface barrier detector.

### COMMISSIONING

The CARIBU project commissioning goal was a beam of  $^{143}\text{Ba}^{18+}$  accelerated to 6.0 MeV/u with a rate of 700 Hz. Commissioning was achieved with a beam of  $^{143}\text{Ba}^{27+}$  accelerated to 6.1 MeV/u with a rate at the high energy end of 900 Hz. The ECRCB breeding efficiency was 12% with a total machine transmission from ECRCB to target of 12%.

### CURRENT ACTIVITIES

The facility has ramped up operation from an initial 2.5 mCi source to the present 55 mCi source. This was done to verify the efficacy of the shielding as well as the gas catcher system operation. Recently, a 500 mCi source has been produced at Oak Ridge National Laboratory and is expected to be ready for installation in mid-2012. This

will result in a factor of 10 increase in available beam intensities to the experimental program.

The isobar separator resolution continues to improve as a better understanding of the system optics is gained. The field instability of the magnets due to the power supplies not maintaining field lock is an issue which is being addressed.

In an effort to reduce the source background, the ANL ECRCB has been fitted with a high purity quartz liner. This shields the plasma chamber wall and should allow us to determine what percentage of background is due to the wall. The extraction electrode and the grounded tube have been replaced with identical components fabricated from high purity aluminum also allowing us to determine their contribution to the source background.

But even these modifications will not approach the cleanliness level possible with an electron beam ion source (EBIS). A typical EBIS will have regions with background levels  $<10^6$  pps, breeding times in the 20-200 msec range, and A/Q of 2.5-4.5. These attributes are well suited to the CARIBU program, and with this in mind, an EBIS is being constructed which will replace the ECRCB. Charge breeding tests have been carried out on the BNL TestEBIS, the device which served as the model for the ANL EBIS breeder. The BNL TestEBIS has a peak electron beam current of 10 A and a current density of 575 A/cm<sup>2</sup>. The ANL EBIS will operate with a 2 A electron gun and 500 A/cm<sup>2</sup>. For the test, the BNL TestEBIS electron beam parameters were adjusted down to 1.5 A and 76 A/cm<sup>2</sup> with a 5.3 msec breeding time resulting in a calculated transverse acceptance of 80  $\pi$  mm mrad. It should also be noted that while the beam was injected with a 70  $\mu$ sec bunch length through pulsing the voltage on the ion source, it did not undergo any cooling via a Penning trap. A charge breeding efficiency of 17% into  $\text{Cs}^{8+}$  was achieved with a breeding time of 5.3 msec [5]. The low charge state was chosen in order to not interfere with the residual gas background. Shifting to a higher charge state would introduce interferences, but in almost all cases a charge state can be chosen which exhibits very low residual contamination. Since the CARIBU program will not provide primary beams above  $10^7$  ions/s, the charge capacity of the EBIS is also not an issue.

### ACKNOWLEDGMENT

This work was supported by the U.S. Department of Energy, Office of Nuclear Physics, under contract number DE-AC02-06CH11357.

**REFERENCES**

- [1] G. Machicoane, M. Doleans, O. Kester, E. Pozdeyev, T. Ropponen, L. Sun, E. Tanke, and X. Wu, Proceedings of the 19th International Workshop on ECR Ion Sources (ECRIS'10), Grenoble, August 2010, p. 14, <http://www.jacow.org>.
- [2] R. Pardo, Guy Savard, Sam Baker, Cary Davids, E. Frank Moore, Rick Vondrasek, Gary Zinkann, NIM-B 261, Issues 1-2, 965 (2007).
- [3] R. C. Vondrasek, R. Scott, J. Carr, R. C. Pardo, Rev. Sci. Instrum. 79, 02A901 (2008)
- [4] R. Vondrasek, A. Kolomiets, A. Levand, R. Pardo, G. Savard, R. Scott, Rev. Sci. Instrum. 82, 053301 (2011).
- [5] S. Kondrashev, J.G. Alessi, E.N. Beebe, C. Dickerson, P.N. Ostroumov, A. Pikin, G. Savard, Nuc. Instrum. And Methods in Physics Research A, 642 (2011).

# GANIL OPERATION STATUS AND UPGRADE OF SPIRAL1

F. Chautard, O. Bajeat, P. Delahaye, M. Dubois, P. Jardin, O. Kamalou,  
L. Maunoury, G. Sénécal

GANIL, Grand Accélérateur National d'Ions Lourds, CEA-DSM/CNRS-IN2P3, Bvd H. Becquerel, BP  
55027 14076 Caen cedex 5, France

## Abstract

The GANIL facility (Caen, France) is dedicated to the acceleration of heavy ion beams for nuclear physics, atomic physics, radiobiology and material irradiation. The production of stable and radioactive ion beams for nuclear physics studies represents the main part of the activity. The exotic beams are produced by the Isotope Separation On-Line method with SPIRAL1 facility. It is running since 2001, producing and post-accelerating radioactive ion beams. The review of the operation from 2001 to 2011 is presented. Because of the physicist demands, the facility is about to be improved with the project Upgrade SPIRAL1. The goal of the project is to extend the range of post-accelerated exotic beams available. The upgrade of the “Système de Production d'Ions Radioactifs en Ligne” phase I (SPIRAL1) is in progress and should be ready by 2015.

- A high-energy beam out of CSS2 is transported to experimental areas (<95MeV/u).
- An auxiliary experiments shares the previous CSS2 beam (10% of the pilot experiment time)
- Finally, stable beams from SPIRAL1 source can be sent to LIRAT (<34keV/A) or post-accelerated by CIME and given to detector tests for example.

During radioactive beam production with SPIRAL1, the combination are reduced to the four first and with radioactive beam sent to the 2 last experimental areas mentioned.

## 2001-2009 GANIL OPERATION STATUS

Since 2001 (Figure 2), more than 38280 hours of beam time has been delivered by GANIL to physics. A third of this time is given to SPIRAL1. The total beam time for physics (tuning and maintenance excluded) is on the average around 3400 hours a year.

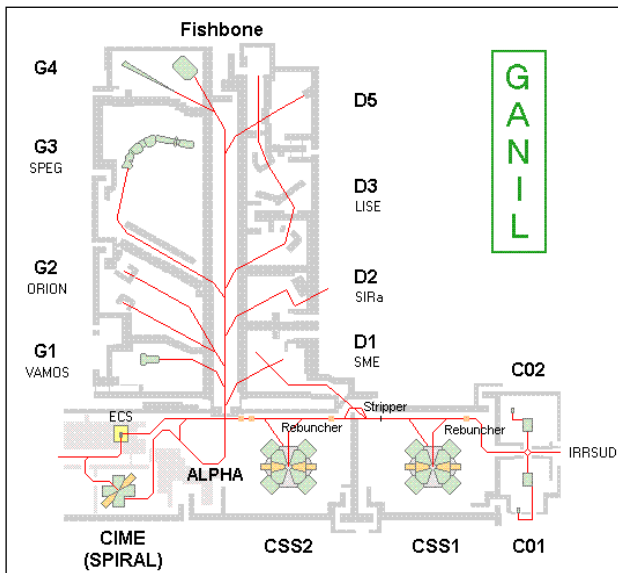


Figure 1: GANIL layout.

## OPERATION REVIEW

Multi-beam delivery is routinely done at GANIL using its 5 existing cyclotrons. Up to five experiments can be ran simultaneously in different rooms with stable beams (Figure 1):

- Beams from C01 or C02 are sent to an irradiation beam line IRRSUD (<1MeV/u).
- A charge state of the ion distribution after the ion stripping downstream CSS1 is sent to atomic physics, biology and solid states physics line D1 (4-13MeV/u).

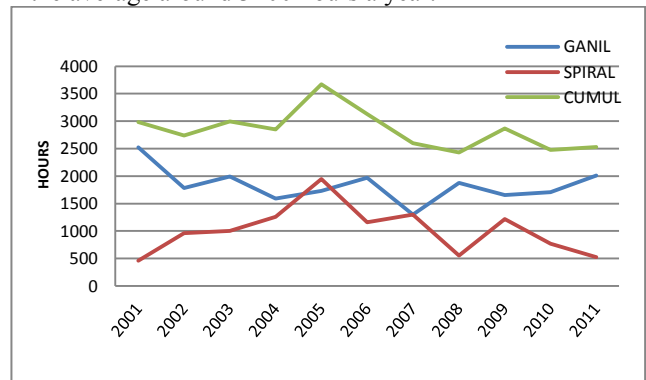


Figure 2: Beam time repartition between SPIRAL and GANIL beams over 11 years.

The number of beam delivered per year (Figure 3) has increased until 2010. Owing to the arrival of SPIRAL2, the running time has been reduced to devote more ressources to the project.

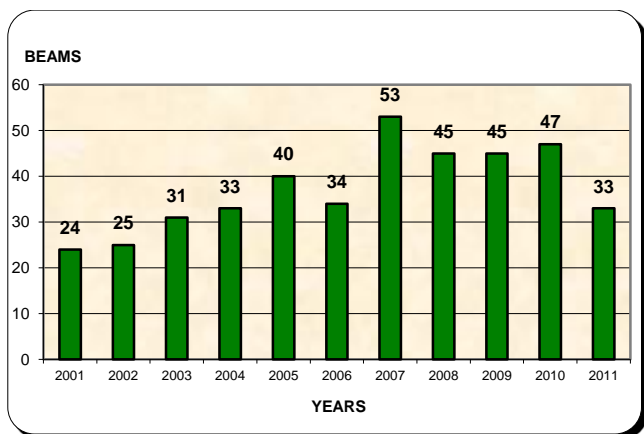


Figure 3: Number of beams tuned between 2001 and 2011.

Figure 4 shows such maintenance actions have given rise to higher time availability.

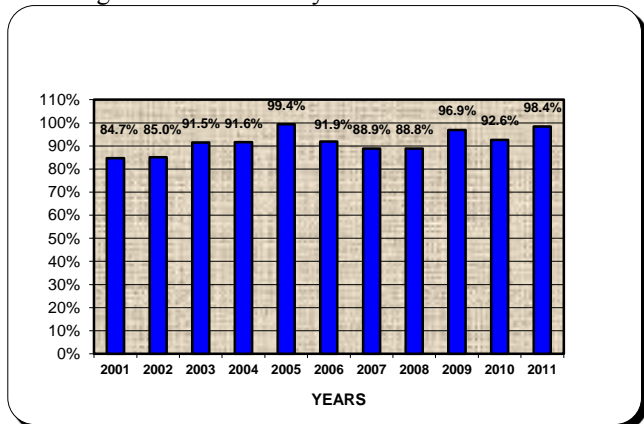


Figure 4: Ratio of beam time available for physics to scheduled beam time online.

### UPGRADE SPIRAL1

The first Isotope Separator On Line System installed at GANIL, named SPIRAL1, has delivered radioactive ions for 10 years. Radioactive atoms produced by fragmentation of swift heavy ions (up to 95 MeV/u) on a carbon target are ionized in a multi-charged ECR ion source before being post-accelerated in a cyclotron. Owing to the design of the target ion source system (TISS), mainly gaseous ions are produced. To satisfy the request of physics community in extending the choice of ions to those made from condensable elements, with masses up to Xe an upgrade of SPIRAL1 has been undertaken. Beams and technical options considered during the prospective phase have been sorted out. A schematic of the ongoing upgrade is presented Figure 5. Surface ionization, FEBIAD or ECR ion sources will be installed in the production cave after its modification to provide 1+ beams of condensable elements. Out of the cave and after mass separation, a Phoenix type charge booster will be installed on the present low energy beam line to

increase the charge of the radioactive ions from 1+ to N+ for post-acceleration.

The upgrade of SPIRAL1 and its technical environment need to conform to stringent regulation requirements as explained below.

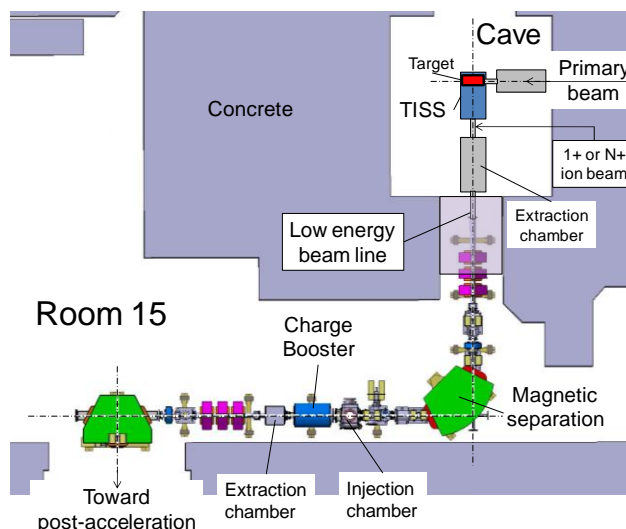


Figure 5: Schematic of the SPIRAL1 upgrade.

### NEW BEAMS VERSUS NEW TISS

New elements will be mainly produced by fragmentation of primary beam ions on a graphite target. Thus most of the masses and atomic numbers will generally not be higher than those of the primary beams available at GANIL. The elements to be produced can be divided in three groups:

1- alkali elements and rare earth elements (Li, Na, K, Rb and Sr). The elements will be ionized in an existing TISS already tested on line at GANIL on a test bench.

2- metallic ions (Mg, Al, Ca, Sc, Cr, Mn, Co, Ni, Cu, Zn, Ga, Ge, As and Se). They will be produced by association of a carbon target with a FEBIAD of VADIS type developed at CERN (Figure 6). This association has been recently tested on line with primary beams of  $^{58}\text{Ni}$  (intensity up to 270 nA) and of  $^{36}\text{Ar}$  (intensity up to 77 nA).  $^{23}\text{Mg}^+$ ,  $^{25}\text{Al}^+$ ,  $^{33}\text{Cl}^+$ ,  $^{38}\text{K}^+$ ,  $^{58}\text{Mn}^+$ ,  $^{58-60}\text{Cu}^+$  and  $^{53-53m}\text{Fe}^+$  ions have been produced. Preliminary estimates give intensities of  $6.6 \times 10^4$  and  $1.4 \times 10^4$  pps for  $^{53}\text{Fe}$  and  $^{53m}\text{Fe}$  respectively for  $^{58}\text{Ni}$  at 72 MeV/u. They indicate good performances for the TISS as Fe beams were only recently observed at ISOLDE. A forthcoming article should describe these tests in detail. The technical design is being pursued, mainly for improving the setup reliability. The final version should be ready in 2013.

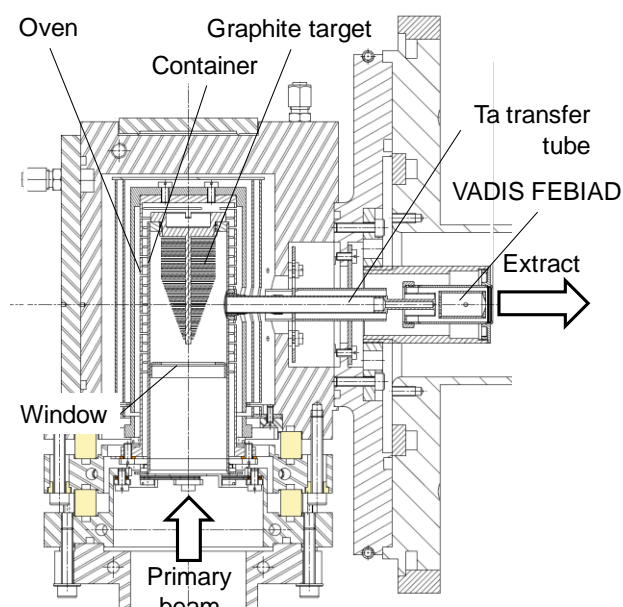


Figure 6: TISS made by association of a graphite target with a VADIS FEBIAD ion source.

3- non-metallic ions, halogen and rare gas ions (He, Ne, Ar, Kr, O, C, P, Cl and Br). Multi-charged ions from rare gases, C and O are currently produced using the ECR ion source of SPIRAL1.

Because the singly-charged ion sources are shorter than the present NANOGAN III ECRIS along the low energy beam line axis, a chamber containing optical elements will be installed in place of it to adapt the 1+ beams to the present low energy beam line.

Some elements heavier than the projectiles will be produced by fusion-evaporation reactions, at lower beam energies. Using heavier target material than graphite will also be possible and beneficial in a 2<sup>nd</sup> step. As an example, to produce  $^{62,63}\text{Ga}$  isotopes, the reaction  $3.6 \text{ kW } ^{12}\text{C} (95 \text{ MeV/u}) + \text{Nb}$  leads to gain a factor of six on the yields compared to  $1.2 \text{ kW } ^{78}\text{Kr} (70 \text{ MeV/u}) + \text{C}$  reaction.

### CAVE UPGRADE

Ten years after delivering its first radioactive ion beam, the cave of SPIRAL1 must be modified to accommodate the new TISSs. Up to now, multi-charged radioactive ions could be directly produced in the cave for post acceleration. After the modification, it will also be possible to produce singly charged ions in the cave, which will be charge bred in a booster after mass separation. The main advantages are a higher purity of the beam of interest owing to a pre-separation of the singly charged ions in the first magnetic dipole and production of higher charge states which will allow heavier elements to be injected in the post accelerator (cyclotron) and thus higher final energy.

The upgrade of the cave attempts to fulfill simultaneously the two following conditions: minimizing the transformation of the cave and of its

environment (building, handling systems, safety protections and process, cooling system, nuclear ventilation system etc...) while increasing its flexibility in terms of useable TISS. The modification of the cave will start during the second semester of 2012. In the course of 2013, the cave should be able to accept both the former and new TISSs.

### CHARGE BOOSTER

An important part of the upgrade consists in the installation of the charge booster on the low energy beam line (room 15), after the mass separator. The booster that will be used at SPIRAL1 is a commercial version of the Phoenix booster designed by LPSC, GRENOBLE, and constructed by Pantechnik. It has been tested at CERN and then at TRIUMF. Moreover, the same principle has been successfully tested at ANL. The possibility to make the 1+ and existing N+ beams going through the booster when it is off has been taken into account. This function is essential when the beam delivered by the TISS is directly used, *i.e.* without charge breeding, either for post-acceleration or in the experimental beam line LIRAT (Ligne d'Ions Radioactifs A Très basse énergie).

The singly charged ions coming from the cave will cover the range from  $\text{He}^+$  to  $\text{Xe}^+$ , with post-accelerated energies ranging from  $\sim 25 \text{ MeV/u}$  to  $\sim 7 \text{ MeV/u}$  respectively, depending on the isotopes considered. The breeding efficiency is generally better for ion masses higher than  $\sim 30$ . Beyond mass higher than  $\sim 100$ , the transport between the TISS and the booster must be made at lower extraction voltage, due to the limit of the magnetic rigidity of the mass separator, which limits the transport efficiency. Thus the preferential mass range of SPIRAL1 upgrade goes from  $\sim 30$  to  $\sim 100$ .

The booster has been recently shipped from CERN to GANIL. The optical study is done. The design of the booster has been consolidated in particular with UHV components, double RF injection, and a position - tunable injection tube. The design of mechanical supports and injection/extraction chambers is underway, as is the supplying of services (power supplies, RF emitter). The installation of the booster will be achieved by end of 2014.

New singly-charged radioactive ion beams are expected by 2013, and multi-charged ion beams by 2015.

## THE RIB DYNAMICS OF THE SPIRAL 2 TRANSFER LINE

D. Boutin<sup>1</sup>, N. Kazarinov<sup>2</sup>, F. Osswald<sup>#1</sup>, C. Peaucelle<sup>3</sup>, T. Thuillier<sup>4</sup>

<sup>1</sup> CNRS/IN2P3/IPHC, Université de Strasbourg, 67037 Strasbourg, France

<sup>2</sup> JINR/FLNR, 141980 Dubna, Russia

<sup>3</sup> IPNL, Université de Lyon, Université Lyon 1, CNRS/IN2P3, 69622 Villeurbanne, France

<sup>4</sup> LPSC, UJF-CNRS/IN2P3-INPG, 38026 Grenoble, France

### Abstract

The design of the SPIRAL 2 RIB extraction and mass analysis is the result of previous experiences at GANIL (SIRa) and SPIRAL and concerns the ISOL process [1]. The layout presents different beam sections of optical interest starting after the target ion source (TIS) with a conventional Einzel lens, a 1 T solenoid, a triplet of magnetic quadrupoles and a magnetic dipole for the mass analysis. The down-stream 1+ ions transfer line to the users is designed following a conservative solution composed of emittance limitation, homothetic betatron matching, passive and symmetrical optical lattices (point to point and unitary transport) as well as beam instrumentation enabling the control of the losses (pepperpots, slits, beam profilers, Faraday cup, etc.). This contribution will mainly focus on the description of the beam line, its characteristics and on some side effects which have to be taken into account in order to match the beam properly during the operations.

## INTRODUCTION

### The SPIRAL 2 Project

The SPIRAL2 project is based on a multi-beam driver for both ISOL and low-energy in-flight RIB production. A superconducting light/heavy-ion linear accelerator capable of accelerating 5 mA deuterons up to 40 MeV and 1 mA heavy ions up to 14.5 MeV/u is used to feed both thick and thin targets. The intense RIBs are produced by several reaction mechanisms (fusion, fission, transfer, etc.) and technical methods (ISOL, recoil spectrometers, etc.). The production of high intensity RIBs of neutron-rich nuclei will be based on fission of a uranium target induced by neutrons, obtained from a deuteron beam impinging on a graphite converter (up to  $10^{14}$  fissions/s) or by direct irradiation with a deuteron,  $^3\text{He}$  or  $^4\text{He}$  beam. The post acceleration of RIBs in the SPIRAL2 project is provided by the existing CIME cyclotron, which is well adapted for separation and acceleration of ions in the energy range from about 3 to 10 MeV/u for masses  $A \sim 100-150$ . SPIRAL2 beams, both before and after acceleration, can be used in the present experimental area of GANIL [2].

### The RIB Lines

The RIBs have a relatively large beam emittance,

#francis.osswald@iphc.cnrs.fr

therefore a dedicated beam transport system is built to extract, separate and transport the desired single-charged ion 1+ beam. The beam lines are designed to accept a transverse geometric emittance of  $80 \pi$  mm.mrad, in horizontal and vertical planes. Most of the contaminants must be suppressed by means of slits, collimators and magnetic analysis. This is the role of the Beam Production Zone (ZPF), see top part of Figure 1. The beam lines must connect different areas of the SPIRAL 2 project (identification station IBE, low energy experiments area DESIR, N+ multi-charged ion beam line leading to the existing GANIL facility). This is the role of the Beam Transport Zone, see bottom part of Figure 1. In order to achieve all the requirements a structure divided into “stages” or “sections” has been developed. The different sections are described in the following. All the ion-optical simulations except for the high current beam calculations have been performed with the TraceWin code [3].

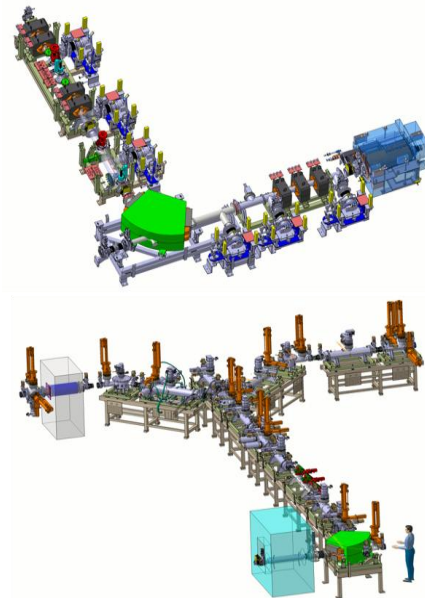


Figure 1: 3D view of the Beam Production Zone (top) and Beam Transport Zone (bottom) of the SPIRAL2 1+ lines.

## LATTICE DESCRIPTION AND BEAM SETTINGS

### Beam Extraction

The beam is extracted from the source and sent to the first optical section (“optical section 0”), which is composed of an Einzel lens (LR1-EIN01), a solenoid (LR1-SOL01) and a magnetic quadrupole triplet (LR1-Q01 to LR1-Q03). The Einzel lens (and the solenoid to a lesser extent) allows different tunings of the optical section for different beam sizes at the extraction, without having to change the tuning of the quadrupole triplet. Slits and collimators positioned at the beam image point ensure that the most intense beam contaminants, mainly the support gases used for the beam extraction, are suppressed. The structure of this optical section is shown in the top part of Figure 2. An example of beam envelope for a 122 u reference mass and a 50  $\mu$ A beam current is shown in the bottom part of Figure 2.

### Mass Analysis

After the beam image point, the beam propagates through a mass analyser designed to separate the ions of interest from the isotopic contaminants. The mass resolving power at the first dipole image point (D1 on Figure 3) has been evaluated as about 300 (with  $\pm 3$  standard deviations) for a reference beam of mass 122.

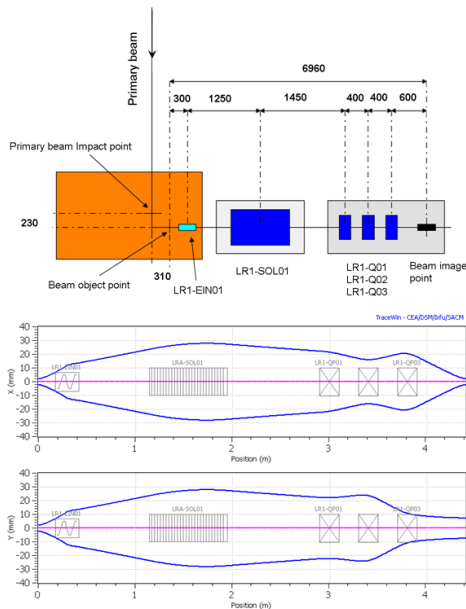


Figure 2: (top) Structure of the “optical section 0”. All distances indicated are in mm. (bottom) Horizontal and vertical beam envelopes at first order of a mass 122 u beam with 60 keV energy, 1+ charge and 50  $\mu$ A current going through the optical section.

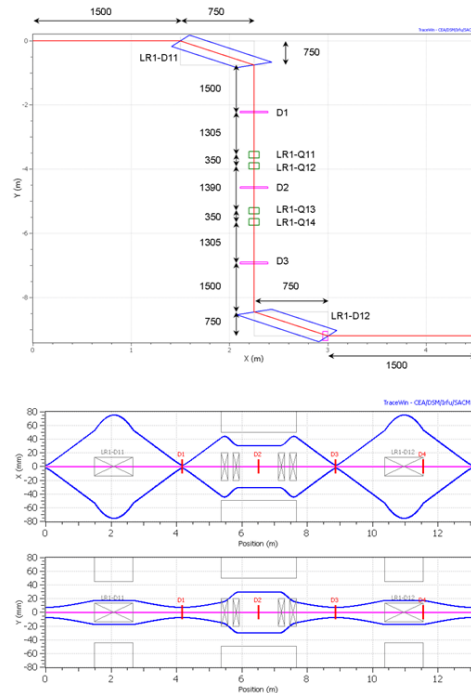


Figure 3: (top) Structure of the “optical section 1”. All distances indicated are in mm. (bottom) Horizontal and vertical beam envelopes at first order, of a mass 122 u beam with 60 keV energy, and 1+ charge going through the optical section.

### Achromatic Deviation

The “optical section 1” consists of two opposite signs dipoles (LR1-D11 and LR1-D12), the first being the mass analyzer described above. Two magnetic quadrupole doublets (LR1-Q11 to LR1-Q14) are located around the intermediate image point of the optical section. The quadrupoles control the achromatism provided by the two dipoles and the symmetry of the beam envelope. The structure and the first order beam envelope of the optical section are seen in Figure 3.

### Betatron Matching

Once the contaminants have been rejected, the beam goes through an adaptation section composed of four electrostatic quadrupoles, where the beam size is modified and adjusted to the following sections.

### Beam Switching Yard

A switching electrostatic deflector (LR1-D51) is used to send the beam of interest to three different branches (IBE identification station, charge breeder or DESIR). When the beam is deviated from  $\pm 45^\circ$  it is sent to the IBE station or to the charge breeder. Then, the beam goes through an electrostatic quadrupole triplet, and a second deflector (LR1-D61 or LR1-D71) which makes the complete section achromatic and deflects the beam by an additional  $45^\circ$ . When the upstream electrostatic deflector (LR1-D51) is switched off, the beam is transferred to the DESIR area. In order to send the beam to the IBE and

charge breeder beam lines, a 2° kicker is placed in front of the deflector in order to reach the 45° total deviation. The overview of the “optical section 7”, with the beam being sent to the charge breeder, and the corresponding optics are shown in Figure 4. The “optical section 6” going to the IBE identification station is identical by symmetry around the first electrostatic deflector.

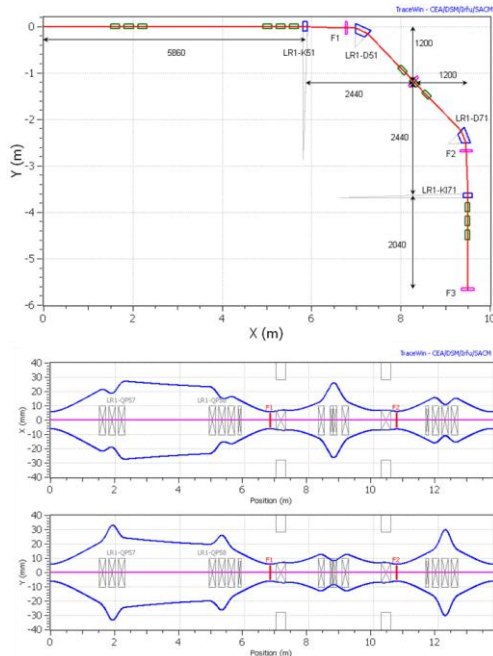


Figure 4: (top) Structure of the “optical section 7”. All distances indicated are in mm. (bottom) Horizontal and vertical beam envelopes in first order, of a mass 122 u beam with 60 keV energy, and 1+ charge going through the optical section.

**BEAM DIAGNOSTICS**

*MIPPS*

In both beam production and beam transport areas, a MIPPS (Measurement of Intensity in Particles Per Second) system has been implemented to allow the beam current measurement even for very low intensities. A small electrostatic deflector is placed in front of a Faraday cup, which is itself shifted from the beam axis to be able to stop the deflected beam. The deflector will be switchable with appropriate time structure so that around 10 % of the beam is deviated to the Faraday cup.

*Conventional Diagnostics*

The conventional (diagnostics FC, BPM, etc.) are mainly used in the Beam Production Zone (BPZ) as radiation, mechanical integration and maintenance constraints are too severe to enable some equipment in the BPZ.

**SIDE EFFECTS**

*High Current Multi-Species Beam Extraction*

The beam extraction section down to the analysing magnet has been investigated with a numerical model and the MCIB04 beam dynamics code [4]. As seen in other facilities [5, 6], perturbations of the beam transport happen with demanding conditions, i.e. with high current supporting gas used in Electron Cyclotron Resonance Ion Source (ECRIS) and high current contaminants. The formation of a hollow in the beam distribution of interest is related to the solenoid focusing placed between the ion source and the analysing magnet. The focusing length of the solenoid for the lighter ions (with a smaller mass-to-charge ratio) is less than for the beam of interest. For this reason in the region between the solenoid and the analysing magnet the lighter ion beams have significantly smaller transverse dimensions compared to the reference beam. In the region out of the lighter ion beam boundary, the defocusing field decreases as inverse distance of the ions from the axis of the beam. For larger intensities of the lighter ion beam, the space charge effect leads to the hollow structure formation of the beam of interest just after the analysing magnet and increases the emittance of the injected ion beam, see Figure 5 [7].

An experiment with a stable beam and comparable conditions has been performed on the SPIRAL 2 low energy beam line LBE1 at LPSC during last winter. A 40Ar+ beam extracted from an ECRIS source with nitrogen as supporting gas has been analyzed and observed with a BPM in order to reproduce the hollow effect. Despite the fact that a perturbation has been clearly observed, see Figure 6, an unequivocal answer was not possible due to some experimental artefacts. A further experiment with direct beam observation (quartz) is in preparation.

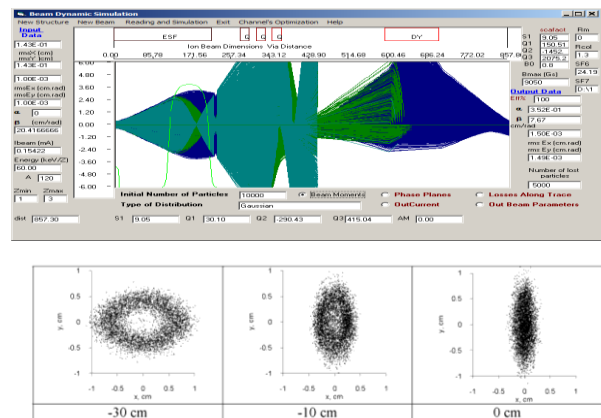


Figure 5: (top) Simulation of the behaviour of 1µA=120 u ion beam at 60 keV mixed with a co-extracted Nitrogen beam (800 µA) used as supporting gas in the ECRIS. One can see a strong focusing inside the solenoid (left) and the beam separation (right) inside the analysing magnet. (bottom) Hollow beam at different distances prior to the analysing magnet focal plane, depending on the beam matching conditions.

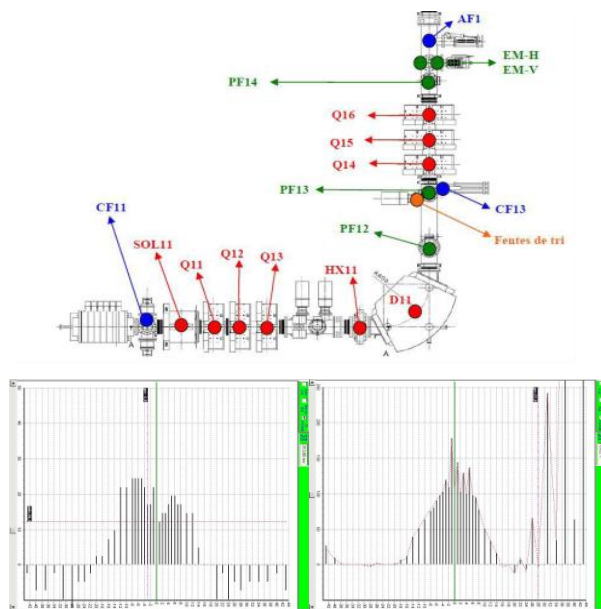


Figure 6: (top) LBE1 test beam line. (bottom) Beam profile with and without hollow effect observed with BPM on focal plane.

**Beam Losses**

The supporting gases used in the ECRIS help ionizing efficiently the radioactive atom of interest but on the other hand generate parasitic low charged beams. Those beam contaminants have a very different behaviour compared with the reference beam due to their different magnetic rigidity. This means that a large fraction, if not all, of these contaminants will be lost in the upstream part of the beam line, in the “optical section 0”. For all beams produced by fission, the losses will mostly occur before the quadrupole triplet of optical section 0. Figure 7 shows the example of nitrogen mixed with the mass 122 setting.

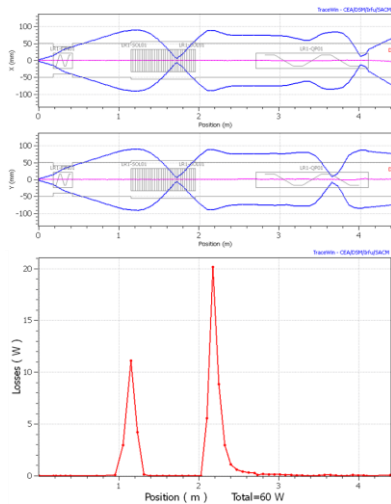


Figure 7: (top) Horizontal and vertical beam envelopes at first order, of a 1 mA  $^{14}\text{N}^+$  beam and 60 keV energy, with the setting on mass 122 u as described before. (bottom) Power losses of the same  $^{14}\text{N}^+$  beam along the beam line.

**CONCLUSION**

A complex beam line system, being able to extract, separate and transport the RIBs from the ion source to the different branches of the SPIRAL2 project has been described. It achieves the specifications goals for the transport of large emittance beams up to 80 pi.mm.mrad, and for the separation of the beam of interest from the neighbouring isotopes. Several side effects have been identified. The hollow effect has been identified as a potential perturbation of the beam of interest dynamics at the beginning of the beam line. The loss effect of large amount of parasitic co-extracted beams induced by the use of a supporting gas in the ECRIS has to be further investigated to avoid heating and activation problems.

**ACKNOWLEDGMENT**

We would like to thank D. Uriot (IRFU) and F. Varenne (GANIL) for their contribution.

**REFERENCES**

- [1] On Line Isotopic Separator Test Benches at GANIL, R. Anne et al., PAC proceed. ed. IEEE, 1993
- [2] Progress of the SPIRAL 2 project, E. Petit, this conference (RIB Facilities session)
- [3] TraceWin code, can be downloaded at: <http://irfu.cea.fr/Sacm/logiciels/index3.php>
- [4] Multicomponent ion beam code-MCIB04, V. Aleksandrov, N. Kazarinov, V. Shevtsov, Proc. of RuPAC XIX, Dubna 2004
- [5] Non-linear distortion of multi component heavy ion beam emittance caused by space charge fields, N.Y. Kazarinov RSI, 75, n° 5, May 2004
- [6] Hollow beam formation in the intense multi-component heavy ion beam caused by beam self-fields, N. Kazarinov, PEPAN letters, v.7, n 3(159), Dubna, 2010
- [7] Simulation of hollow beam formation at the initial part of the RIB transport channel of SPIRAL2, N.Kazarinov, F.Osswald, IPAC, San Sebastian, 2011

# THE DARMSTADT MULTI-FREQUENCY DIGITAL LOW LEVEL RF SYSTEM IN PULSED APPLICATION\*

R. Eichhorn<sup>#</sup>, U. Bonnes, C. Burandt, M. Konrad, P. Nonn,  
IKP, TU Darmstadt, Darmstadt, Germany  
G. Schreiber, W. Vinzenz, GSI Darmstadt, Germany

## Abstract

Triggered by the need to control the superconducting cavities of the S-DALINAC, the development of a digital low level RF control system was started several years ago. The chosen design proved to be very flexible since other frequencies than the original 3 GHz may be adapted easily: The system converts the RF signal coming from the cavity (e. g. 3 GHz) down to the base band using a hardware I/Q demodulator. The base band signals are digitized by ADCs and fed into a FPGA where the control algorithm is implemented. The resulting signals are I/Q modulated before they are sent back to the cavity. Meanwhile, this system has been successfully operated on 3 GHz, 6 GHz and 325 MHz cavities, on normal and superconducting cavities as well as in cw or pulsed mode. This contribution will focus on the 325 MHz version built to control a pulsed prototype test stand for the p-LINAC at FAIR and possible extensions to even lower frequencies. We will present the architecture of the RF control system as well as results obtained during operation.

## INTRODUCTION

The S-DALINAC is an 130MeV recirculating electron linac that is operated in CW mode [1]. It uses superconducting niobium cavities at 2K with a loaded Q of  $3 \cdot 10^7$  for acceleration. Their 20 cell design and the

high operating frequency of 3GHz make them very susceptible for microphonics. Designing and improving the Low-Level RF System therefore was and is one major research activity [2,3].

In addition to the superconducting cavities, room-temperature chopper and buncher cavities are operated. As the new polarized electron injector has been assembled in the accelerator hall [4] the need for a harmonic system arose: Its bunching system consists of a chopper cavity and a 3 GHz as well as a 6 GHz harmonic buncher. Currently, our RF control system has to deal with different loaded quality factors ( $Q_L$ ) ranging from some 5000 to  $3 \cdot 10^7$  as well as with different operating frequencies. Due to its modular design, reflected in the hardware design as well as in the control algorithm (being programmed into an FPGA) the system was adapted to the needs of proton Linac currently under design at GSI/FAIR [5]. This normal conducting drift tube linac comprises 12 crossed-bar H-mode cavities (CH cavities) that are operated at 325.224MHz in pulsed mode, requiring some major changes in the RF control, described lateron. The cavities are fed with RF pulses of 200  $\mu$ s length at a maximum repetition rate of 4 Hz [6]. The beam pulse length is 36  $\mu$ s, representing a significant beam load of approx. 80 %. Based on beam dynamics calculations, the field stability requirements were set to 0.1 % and .5°.

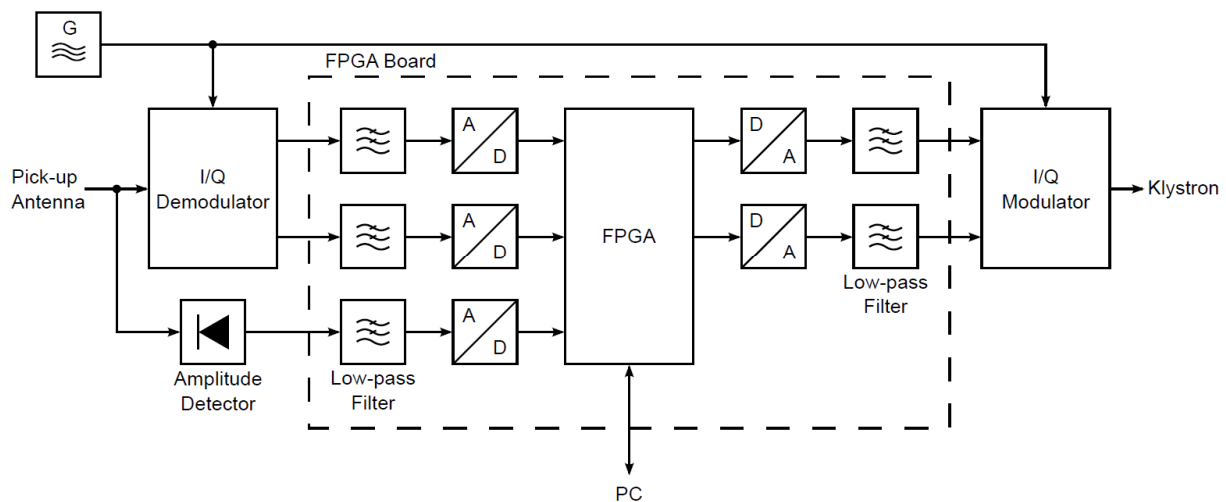


Figure 1: Overview of the hardware components of the rf control system. The (frequency dependant) modulator and demodulator are located on the rf board whereas the FPGA board only contains the signal processing hardware. The control algorithm itself is programmed into the FPGA, allowing SEL and GDS operation.

\*Work supported by DFG through CRC 634 and by the BMBF under 06 DA 9024 I

<sup>#</sup> eichhorn@ikp.tu-darmstadt.de, affiliation starting July 2012: Cornell University, Ithaca, NY, USA

## SYSTEM ARCHITECTURE

The approach to control the RF chosen in Darmstadt was the base-band solution: All RF signals are down converted to the base band by mixing with the operation frequency, processed in the remaining low frequency domain and up converted later on by modulation, again using the master oscillator running at the operation frequency. This allows splitting the hardware into two parts: A frequency dependent RF board containing the I/Q (de)modulator and a frequency independent FPGA board processing the signals (see Fig. 1). All hardware components have been developed in-house. A separate power detector located on the RF board improves the accuracy of the magnitude measurement.

### RF BOARD

The photo of the RF board, given in fig. 2, displays the principle of the layout: The incoming signal (right connector) is split and fed to the I/Q demodulator and the power detector. The low frequency signals then leave to the FPGA board (shown later on in fig. 4) via the multipole connector. After the signal processing, the signals are I/Q modulated and leave by the left RF connector.

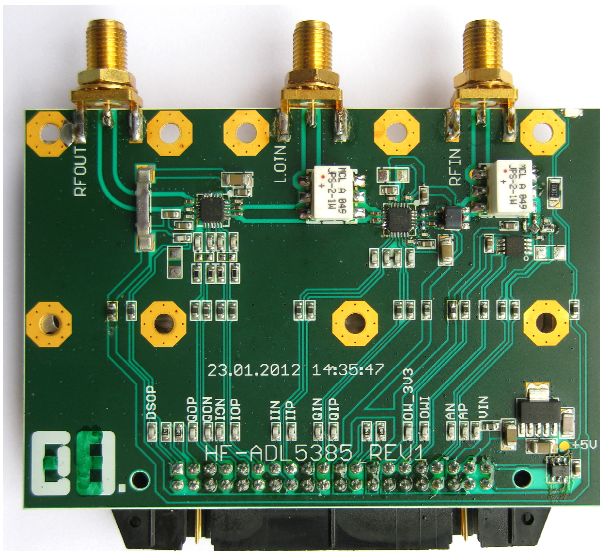


Figure 2: Photo of the (frequency dependent) RF control board. The signal from the cavity is connected to the right SMA connector; the left connector delivers the signal to the cavity while the Local Oscillator (LO) connects to the middle.

Depending on the operation frequency of the cavity, the splitters, modulator and demodulator as well as the power detector have to be chosen accordingly, being a minor modification. So far, we developed a 3 GHz, a 6 GHz, one 1.3 GHz, a 325 MHz and a 160 MHz version of the RF board, all of them were operating successfully. It should be noted that the low frequency versions (325 & 160 MHz) require a doubled LO frequency (650 and 320 MHz) for accuracy reasons.

Every board requires a careful calibration, the details of which have been described before [3]. However, not all errors of the (de)modulator can be compensated by calibration. An important figure of merit of the demodulator is the deviation of the measured input phase from the actual input phase, as shown in fig. 3. This has been measured by applying an rf input signal to the rf board with a frequency that is slightly shifted to the LO frequency (1 kHz away). The result is a rotating vector in the I/Q plane that is recorded over many periods. Figure 3 shows the deviation (for the 325 MHz board) of the phase calculated from I and Q and the input phase. The phase error is dominated by noise, produced by the two rf generators. With the result of  $0.2^\circ$  rms gained after some major design changes[7], the deviation is smaller than the phase error of the 3 GHz boards now, currently used at the S-DALINAC. All together the described hardware errors are negligible, showing the substantial improvements compared to the boards used before.

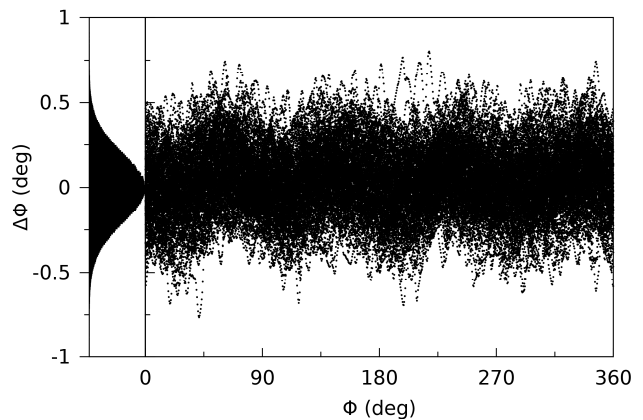


Figure 3: Characterization of the 325 MHz demodulator showing the typical deviation of the measured input phase from the actual input phase. The histogram on the left shows a projection to the y axis representing the phase deviation, being  $0.2^\circ$  rms.

### FPGA BOARD

The FPGA board digitizes the analogue signals coming from the RF board and feeds them into its FPGA where the control algorithm is carried out. The resulting I and Q output signals are converted back to analogue before they are sent back.

The hardware of the FPGA board, shown in fig.3 is identical with the boards used at the S-DALINAC except for the filters: Low-pass filters in front of the ADCs ensure that frequencies above the Nyquist frequency are damped to avoid aliasing effects. Identical reconstruction filters at the output remove harmonics created by the DACs.

The filters have been designed for the S-DALINAC's RF control system which has to deal mainly with microphonics at frequencies below 10 kHz. High requirements with respect to accuracy together with

an adjacent mode of the cavity that is only 700 kHz away from the operating frequency led to third order filters with an cut off-frequency of 100 kHz. On the other hand the phase shift introduced by the filters decreases the gain margin of the controller. That is why the filters have been reduced to first order filters with the same cut off-frequency for the p-Linac RF control system. These filters still provide enough attenuation for the neighbouring modes.



Figure 4: Photo of the FPGA control board, housing the filters, the ADCs/ DACs, the FPGA itself and some interfacing circuits. The signals from the RF board connect to the multi-pole connector in the middle of the board.

## CONTROL ALGORITHM

Two different control algorithms have been implemented for the S-DALINAC: A generator-driven resonator control algorithm for normal-conducting cavities and a self-excited loop algorithm for superconducting cavities. Both algorithms are optimized for cw operation and cannot be used in pulsed mode with the p-Linac as they completely rely on static settings.

For pulsed operation, the programming of the FPGA had to undergo a major extension to allow time-dependant settings. In addition, a pulse shape generator has been implemented in the FPGA code. It consists of a memory storing 2048 set values that constitute a pulse shape of up to 2 ms in length. Up to now, the trigger signal for the pulse generator is generated periodically inside the FPGA. At the p-Linac test stand an external trigger signal will be used.

The control algorithm for the p-Linac is an enhanced version of the generator-driven algorithm for the S-DALINAC. A first revision of the p-Linac control algorithm is shown in fig. 5 with separated phase and amplitude controllers. The input phase is calculated from I and Q (provided by the RF board) using the CORDIC [8] algorithm, while the amplitude is measured directly with the power detector on the RF board. The amplitude as well as the phase controller use integral controllers in addition to the proportional controllers to eliminate steady-state offsets that remain after applying proportional control. A differential controller has been foreseen, but is finally used with zero gain as it turned out to amplify the noise solely without contributing to the control accuracy.

Between pulses the input signal vanishes, and thus the input phase has no meaningful value. To ensure that this does not affect the integral phase controller, its accumulator is set to hold between pulses.

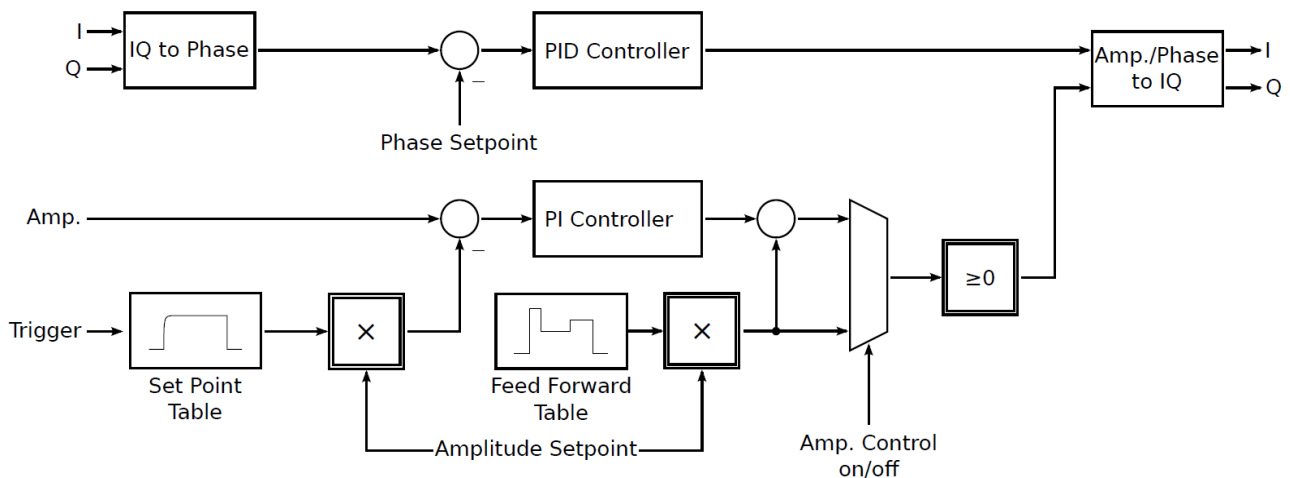


Figure 5: Algorithm flow chart: The I/Q signals from the RF board are converted to a phase signal which is controlled via a PID controller. The amplitude controller uses the signal from the power detector being compared to the time dependant set point table value. In a recent modification, an additional feed forward table was implemented to allow fast beam load compensation.

## RESULTS

The performance of this control algorithm has been tested by measuring the amplitude and phase errors using a dummy cavity with a loaded quality factor around 1000. Figure 6 shows the step response of the closed loop whereas fig. 7 shows the rms errors over the time relative to the beginning of the pulse. The rms errors have been calculated from the corresponding errors at the same relative time over a set of 1000 pulses. It takes about 50  $\mu\text{s}$  to stabilize amplitude and phase to the target specification.

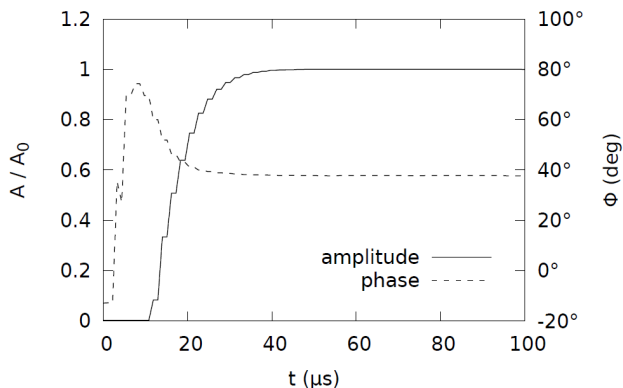


Figure 6: Step response of the the closed control loop measured using a test cavity with  $Q_L \sim 1000$ .

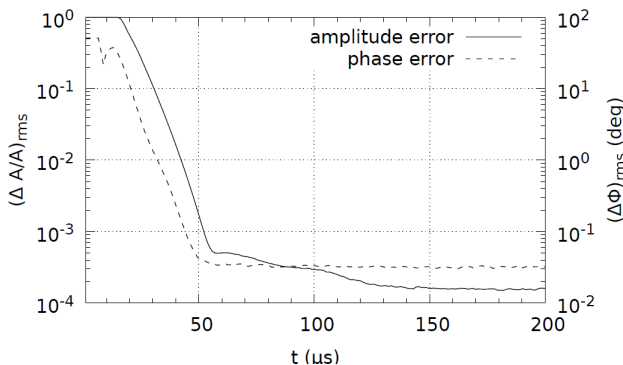


Figure 7: Amplitude and phase error during a 200  $\mu\text{s}$  pulse. The pulse starts at 0  $\mu\text{s}$  when the set value jumps from 0 to the set value.

To achieve a faster response the control algorithm has to provide a feed forward signal which was implemented recently, the need of which can clearly be seen in fig. 7: As the beam pulse planned for the pLinac has a length of 36  $\mu\text{s}$ , a close loop time constant of 50  $\mu\text{s}$  to reach a control accuracy better  $10^{-3}$  is not acceptable. First optimization steps using this feed forward system have been performed and will continue by making use of a cavity simulator developed in house that allows implementation of different beam loading scenarios.

## CONCLUSION

The rf control hardware initially designed for the S-DALINAC has been successfully adapted for the FAIR p-Linac. A newly designed RF board allows operation at 325 MHz, whereas redesigned filters provide a much faster response of the controller. Until the first cavity arrives at the test stand at GSI, tests of the RF control system are done with an FPGA-based cavity simulator that is currently under development [9].

During the course of this project, the potential of the base band approach was clearly visible: Within minor redesign steps, the adaption of other frequencies than the original 3 GHz is possible. Currently, first tests with a 160 MHz version to control a quarter wave resonator at ALPI, Legnaro are performed, results of which will be presented soon.

The extension of the operation mode of the system from cw to pulsed was realized within the project. This opens up the perspective for further improvements: Multi-pulse operations with different pulse shapes as well as ramped operation are now easy to realize. Together with the freedom of the algorithm programming this finally let us conclude that the Low Level RF system developed at TU Darmstadt has a great flexibility which seems to be unique.

## REFERENCES

- [1] A. Richter, "Operational experience at the S-DALINAC", EPAC'96, Sitges (1996) 110.
- [2] J. Auerhammer et. al., "Progress and Status of the S-DALINAC" Proc. 1993 RF Superc. Workshop, Newport News, pp. 1203.
- [3] M. Konrad, et. al., "Digital base-band rf control system for the superconducting Darmstadt electron linear accelerator", Phys. Rev. ST Accel. Beams 15 (2012) 052802.
- [4] C. Eckardt et al., "The S-DALINAC Polarized Injector SPIN – Performance and Results", Proceedings of PAC 2011, New York, USA.
- [5] L. Groening et. al., "The 70 MeV proton linac for the Facility for Antiproton and Ion Research FAIR". Proceedings of LINAC 2006, Knoxville, USA, pp. 186–188.
- [6] W. Vinzenz et. al., "High power rf supplies for the FAIR injector linacs", Proceedings of LINAC 2008, Victoria, Canada, pp. 975–977.
- [7] A. Araz et al., "A Digital Baseband Low Level RF Control for the p-LINAC Test Stand at GSI", Proceedings of IPAC, 2010, Kyoto, Japan, p. 1413.
- [8] Xilinx Inc., "LogiCORE IP CORDIC v4.0—product specification", [http://www.xilinx.com/support/documentation/ip\\_documentation/cordic\\_ds249.pdf](http://www.xilinx.com/support/documentation/ip_documentation/cordic_ds249.pdf).
- [9] T. Bahlo et. al., Proceedings of ICAP, 2012, Rostock, Germany, in preparation.

# CONTROL AND INFORMATION SYSTEM FOR BARC-TIFR SUPERCONDUCTING LINAC BOOSTER

Sudheer Kumar Singh, Pitamber Singh, IADD, BARC, Mumbai, India  
 J.N. Karande, Vandana Nanal, RG Pillay, TIFR, Mumbai, India

## Abstract

Superconducting LINAC booster is modular machine which consists of 7 cryomodules each consisting four quarter wave resonators and one superbuncher module. The control system is a mixed distributed control system. Geometrical distributed system architecture has been followed for RF control. RF control has four local nodes( RF LCS) each nodes catering to two cryostat. Two additional nodes are made for beam line system and cryogenics distribution system, making it a systematic distribution system. The system is developed on Linux operating system but the software is portable on Linux and Microsoft windows. The software is developed in two layers namely scanner and operator interface. Scanners interacts with the interface hardware. All scanners are developed in JAVA , which is very challenging job looking towards the feature of JAVA. Various issues regarding this were closely investigated and solved to overcome the deficiency of JAVA .A micro-controller based board has been developed for cryogenics line distribution system. Different subsystems of the control system has been developed independently. A complete integration of the system will be completed before December 2012.

## CONTROL SYSTEM ARCHITECTURE

LINAC is a booster to existing 14 MV Pelletron accelerator and built as moduler structure[1]. LINAC Booster's layout is given in fig 1.

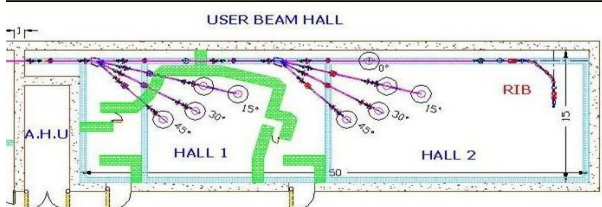
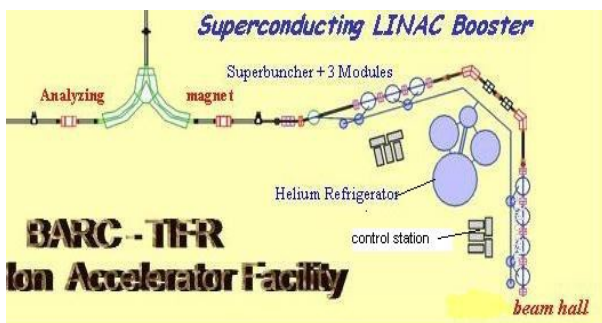


Figure 1: LINAC booster Layout.

LINAC can be divide in two half LIN1 and LIN2 . LIN1 consisting of three cryomodules for accelerating cavities , one cryomodule with single Superbuncher cavity and achromatic bending section. LIN2 consisting of four cryomodules with accelerating cavity.

LINAC control system follows the LINAC modular structure and gemetric distributed control system has been selected for RF control with four nodes for RF control each node (RF LCS) is connected to each two nearby cryomodules. One node has been put for Beam line devices which include focussing magnets , bending magnets and Beam diagnostics devices . One node has been dedicated for Cryogenics distribution system. Each nodes are totally independent to each other which makes it possible to operate the system even when pelletron beam without further acceleration from LINAC have to be transported to beam hall. All nodes are interconnected to each other using Ethernet Link as filed bus. All control nodes LCS ( Local Control stations) are located in accelerator hall. In main control room two PCs known as MCS ( Main Control Station) are connected via Ethernet for interaction with the control system(fig 2) .

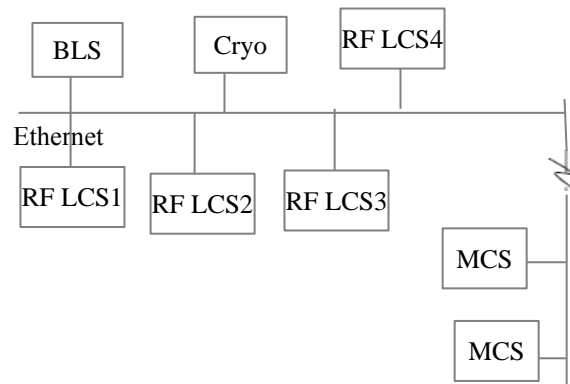


Figure 2: LINAC booster Layout.

A multilayer Hardware architecture has been followed each RF node consists of a CAMAC crate at Front Equipment Interface unit. CAMAC crates (fig3). CAMAC crates have an in house developed Ethernet based crate controller though the crates can be accessed from any PC connected in the network , its accesses has been limited to a single PC at Device interface unit . Device interface unit PC is connected. Communication between different LCSs and MCS is through Device Interface unit PC.

CAMAC crate is connected to RF Electronics bin using Digital Electronics modules ( ADC, DAC , DI, DO, Pulser modules). Electronics bins consists of Signal Distribution module ,RF controllers[2] and RF amplifiers. Each RF LCS controls eight QWR Cavities, Except LCS1 which controls only five QWR s ( 1 super buncher + 4 Accelerating cavities ) LCS1 consists one two channel phase shifter one at the entry of LIN1 and other on eat the entry of LIN2. These phase shifter are helpful to tune the beam through the LINAC in case of slight energy variation from pelletron.

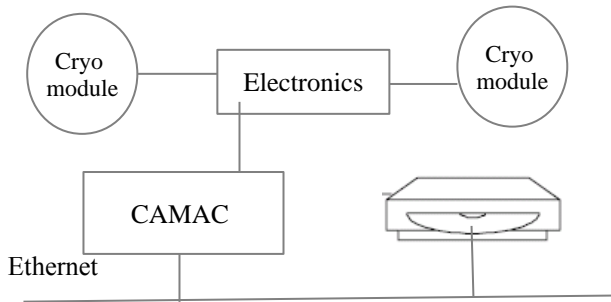


Figure 3: RF LCS Architecture.

Beam Line control node ( BLS) [fig.4], consists of magnet power supplies , steerers , Faraday cups and Beam Profile monitors. Magnet power supplies are having RS232 serial interface. Faraday cup control unit and BPM control units are developed on 8085 microcontroller boards based on Silabs microcontroller boards with rs232 serial interface for remote control and monitoring. Steerers are using power supplies procured from Delta with Rs232 remote interface units . In addition to these devices there are several hall probes connected to the system .All serial devices are connected to Serial to Ethernet converter switch unit from Moxa[3] .

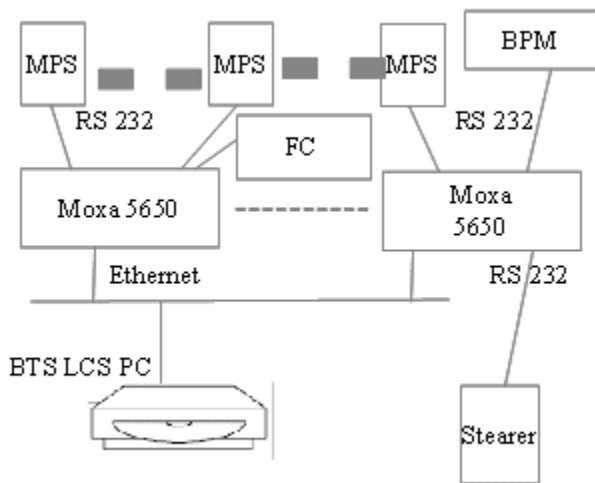


Figure 4: Beam Line LCS Architecture.

Each Moxa unit can be connected to 16 serial Device and can be operated in Rs232 mode or TCP/IP mode. TCP/IP server mode has been selected for LINAC control system.

Presently there are 30 MPS s , 2 Faraday cup controller units , 2 BPM controller units in the system. The system is extensible new system can be easily added on spare MOXA rs232 ports or by adding additional MOXA boards.

Cryo LCS is made up of Silabs based microcontroller board with associated electronics , two such boards have been made and are connected to MOXA serial to ethernet converter . A dedicated PC has been setup as Cryogenics Distribution system ( CDS) node . Cryogenics Distribution system

### CONTROL SYSTEM SOFTWARE

Control system software is developed as a portable system which can be ported on either MS windows and Linux. The control system software is written in JAVA except Cryogenics system which is implemented in Trolltech 's QT[4]. Software is written as client server architecture. Servers are running at LCS and client is running at Main control station PC. MCS software is a graphicle user interface. Its a multilayer software. Each node has GUI less software acting as TCP server and called as scanner . Scanner is responsible for interaction with hardware and message passing from graphicle user interface and in between different scanners. The system is configurable by using a database known as system configuration database. System configuration data base is stored at scanner. LCS architecture is given in fig 5. which has been used for all LCSs. It is a layered architecture . Device scan scans all device and system status periodically, scan time is passed as a commend line parameter. Communication Server interface listen for the new connection requests and open communication thread for each client.

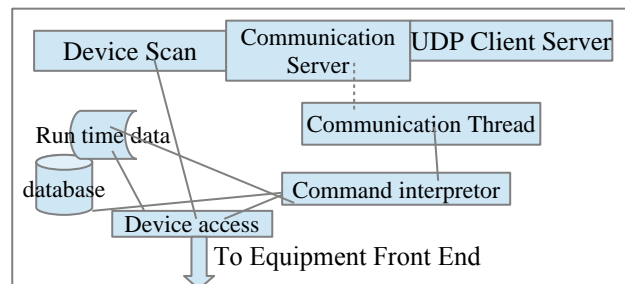


Figure 5: LCS Architecture.

MCS software connects to all LCS nodes and presents the overall system information to the operator. Different colour notations and audio alarm provides the important information to the operator. MCS screen is given in fig 6.

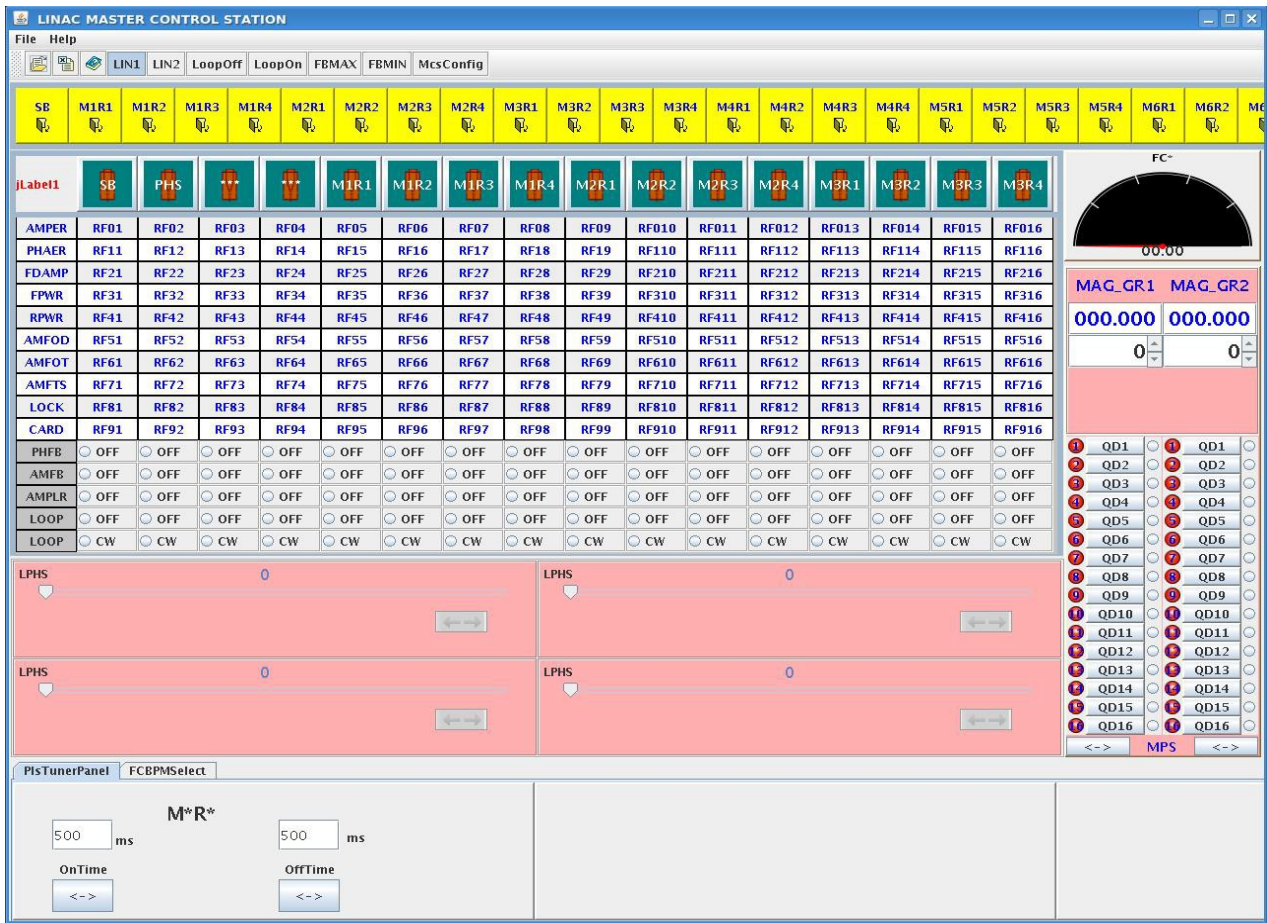


Figure 6: Main control Station ( MCS ) operator interface.

### ACKNOWLEDGMENT

We would like to thank the pelletron LINAC facility members for there support in installation and Electronics division BARC for the excellent electronics hardware and devices.

### REFERENCES

- [1] Bsrinivasan, S K Singh et al.,”Superconducting LINAC Booster for Mumbai Pelletron” Pramana journal of physics, Indian Academy of Science Vol 57, No. 2 & 3 Aug -Sept 2001 p 651-658.
- [2] Gopal Joshi et al. “RF Control Electronics for Linear Accelerator” DAE Symposium on Peaceful Atom 2009”.
- [3] MOXA 5650 Manuals [www.moxa.com](http://www.moxa.com)
- [4] QT API [qt.nokia.com/products](http://qt.nokia.com/products)

## EXTENSION OF SUPERCONDUCTING LINAC OPERATION TO LIGHTER BEAMS

Vandana Nanal<sup>#</sup>, R.G. Pillay, R. Palit, J. N. Karande, P. Dhumal, M.S. Pose, C. Rozario, S.K. Sarkar, M.E. Sawant, A.N. Takke, S.M. Powale, A.A. Shinde, R.D. Deshpande and S.R. Sinha,

Pelletron Linac Facility, Department of Nuclear and Atomic Physics, TIFR, Mumbai – 400005  
S.K. Singh, Ion Accelerator Development Division, BARC, Mumbai – 400085

### Abstract

The Pelletron LINAC Facility, Mumbai is a major centre for heavy ion accelerator based research in India. The superconducting linear accelerator, indigenously developed to boost the energy of heavy ion beams delivered by the Pelletron accelerator, has been operational since July, 2007. The Liquid Helium Refrigeration plant for the LINAC has been upgraded to enhance the refrigeration capacity to ~450 Watts at 4.5K without LN<sub>2</sub> pre-cool, from the earlier capacity of ~300 Watts. All beam lines in new user halls have been commissioned and new experimental setups have been added. Several experiments have been carried out using beams of <sup>12</sup>C, <sup>16</sup>O, <sup>19</sup>F, <sup>28</sup>Si, <sup>31</sup>P. The superconducting lead on Copper QWR cavity used in the LINAC is designed for  $\beta=0.1$  and hence it is difficult to accelerate lighter beams. Due to growing interest in studying Li induced reactions on fissile targets at energies higher than 55 MeV, we have recently accelerated <sup>7</sup>Li beam using four cryostat modules. Starting with 40 MeV <sup>7</sup>Li beam from the Pelletron, 56 MeV beam was successfully delivered at target station for a test experiment.

### INTRODUCTION

The Pelletron LINAC Facility at TIFR, Mumbai, comprising the 14 MV Pelletron (commissioned in 1989) and the superconducting LINAC booster (operational since 2007) [1,2] caters to a variety of experiments in Nuclear Physics, Atomic Physics, Condensed Matter Physics, Material Science, Radiochemistry, Accelerator Mass Spectroscopy, etc. The Pelletron serves both as a standalone accelerator and as an injector to the superconducting LINAC booster. Several modifications have been made to improve the performance of accelerator.

The Liquid Helium Refrigeration plant for the LINAC has been upgraded to enhance the refrigeration capacity to ~450 Watts at 4.5K without LN<sub>2</sub> pre-cool, from the earlier capacity of ~300 Watts. A vacuum jacketed liquid nitrogen transport line from the Low Temperature Facility (LTF) to LINAC accelerator and user halls (~200 m long) has been installed to provide continuous supply of liquid nitrogen.

New micro-controller based instrumentation and interface has been developed for control and monitor of

<sup>#</sup>vnanal@gmail.com

the cryogenic parameters, beam diagnostics and beam transport devices. The operator Graphical User Interface (GUI) in the control room has been suitably enhanced, which communicates with the remote devices via individually addressable 16-port Ethernet to RS232 serial switch [3]. A digital implementation of the Low-Level RF controller based on a self-excited loop (SEL) with phase and amplitude feedback has been developed and successfully tested on a single superconducting cavity [4]. This paper describes some of the recent developments.

### CRYOGENICS

The Linac utilizes a custom-built liquid helium refrigerator Linde TCF50S, installed in 1999. It was originally rated for a refrigeration power of 300 Watts at 4.5 K, which could be further enhanced by a maximum of 150 W with LN<sub>2</sub> pre-cool. The two-phase helium at 4.5 K produced at the JT stage in the refrigerator is delivered to the LINAC through a cryogenic distribution system at a supply pressure of 1.6 bara. The phase separation is achieved in the individual cryostat, typically at a pressure of 1.35 bara. The cold helium gas (4.5 K) is returned to the helium refrigerator at a pressure of 1.20 bara. The observed pressure drops in the distribution network and the mass flows have been modelled to estimate the overall thermodynamic efficiency of the system. Due to the elevated delivery pressure of the cryogen to the LINAC, the effective total available cooling power reduces to ~260 Watts. For the whole system without RF power, the estimated heat load is ~140 W. Therefore, the net available cooling power for RF load is only ~120 W, which is not adequate to power up all the accelerating cavities. Hence, during the accelerator operation, the refrigerator was used with partial liquid nitrogen pre-cooling. In order to eliminate the use of liquid Nitrogen pre-cooling, the plant has been upgraded to deliver ~450 W at 4.5 K. This has been done by replacing the original compressor having a flow rate of 62g/s by a new one having a capacity of 79g/s. Also, two turbines in the cold box have been replaced by more efficient versions and all the valve seats in the plant were changed to adapt to the higher mass flow rate. The upgraded plant has been fully tested and commissioned. The cryogenic system was found to be very stable during the accelerator operation with full RF load. The helium gas recovery system has been augmented with an additional recovery compressor and a 30 m<sup>3</sup> gas bag, to provide to total capacity of 60 m<sup>3</sup>. This is expected to significantly reduce the helium gas

losses in case of sudden power failures during LINAC operation.

The liquid Nitrogen required for shield cooling in the LINAC distribution and module cryostats as well as user requirements are fully met by the LTF, TIFR. To facilitate ease of operations, a vacuum jacketed liquid nitrogen transport line from the LTF to the LINAC accelerator and user halls (~200m long) has been installed to provide a continuous supply of liquid nitrogen.

## INSTRUMENTATION & CONTROL SYSTEM

As a part of an ongoing effort, the interface and control electronics have been upgraded for various accelerator subsystems. In particular, new micro-controller based instrumentation has been developed for cryogenic parameters, beam diagnostics and beam transport devices.

A CAMAC based accelerator control system based on a master-slave configuration has been developed using JAVA operating on Linux OS [3]. The operator GUI deployed on the Master Control Station (MCS) in the accelerator control room is designed to communicate with individual devices. All power supplies for the beam transport elements like magnetic steerers, quadrupoles and dipoles are controlled from the MCS via individually addressable 16-port Ethernet to RS232 serial switch. Several other devices like Faraday Cups, BPMs, Cryogenic controls etc. are also connected via serial to Ethernet switches in a similar manner.

On selection of a particular Faraday Cup, the measured beam current is displayed on an on-screen panel meter with suitable auto-scaling. Similarly, up to two BPMs can be simultaneously selected on the GUI and displayed on a multi-channel oscilloscope. The updated control system allows simultaneous setting up and monitoring of parameters for the different LINAC subsystems. The system is operator friendly, stable and very reliable.

We have developed a digital implementation of the Low-Level RF controller based on a self-excited loop (SEL) with phase and amplitude feedback. The digital LLRF controller is expected to be inherently free of certain limitations like: DC off-sets, drifts, gain imbalance, impedance mismatch, etc besides having the flexibility and ability to execute complex algorithms. Figure 1 shows a schematic view of digital RF control architecture. The digital control card has been successfully tested on a single superconducting cavity [1,4].

In addition, a two channel BPM digitizer and FPGA based CAMAC ADC, DAC cards have been developed. These cards have been designed in a modular fashion to

enable ease of trouble shooting and maintenance. These cards are installed in the Pelletron control system.

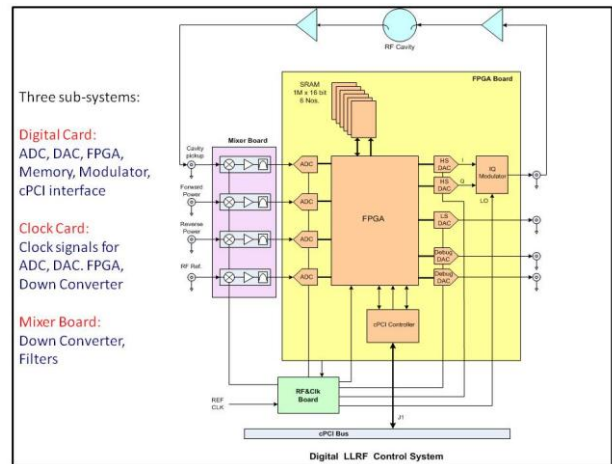


Figure 1: A Schematic of digital RF control architecture

## ACCELERATOR OPERATION

All beam lines in new user halls have been commissioned and several new experimental setups have been added. Figure 2 shows a schematic layout of the LINAC and user halls. Table 1 gives a summary of various beams and energies delivered for user experiments. Typical beam transmission from LINAC entry to exit is found to be 80-85%. The available beam current on target after collimators is 1-5 pA with very good timing,  $\sigma \sim 0.3$  ns.

Table 1: Beams accelerated through LINAC

| Beam             | $E_{\text{pell}}$ (MeV) | $E_{\text{LINAC}}$ (MeV) | $E_{\text{total}}$ (MeV) |
|------------------|-------------------------|--------------------------|--------------------------|
| $^{12}\text{C}$  | 70-82                   | 28-38                    | 100-120                  |
| $^{16}\text{O}$  | 80-94                   | 22-55                    | 110-135                  |
| $^{19}\text{F}$  | 80-94                   | 45-55                    | 135-145                  |
| $^{28}\text{Si}$ | 90-100                  | 45-109                   | 135-209                  |
| $^{31}\text{P}$  | 95-111                  | 30-94                    | 125-207                  |

The superconducting lead on Copper QWR cavity is designed for  $\beta=0.1$  and hence it is difficult to accelerate lighter beams. Due to growing interest in studying Li induced reactions on fissile targets at energies higher than 55 MeV, we have recently accelerated  $^7\text{Li}$  beam using four cryostat modules. The  $^7\text{Li}^{3+}$  beam of 42 MeV from the Pelletron was accelerated to 56.8 MeV using 16 resonators. Time spectra measured with  $1''$  BaF2 at LINAC I entry (top panel) and after the mid-bend at LINAC II entry (bottom panel) are shown in Figure 3. Nearly same time structure of beam at lin4 diagnostic station ensured good acceptance in LINAC II. The measured time spread " $\sigma$ " is inclusive of detector resolution.

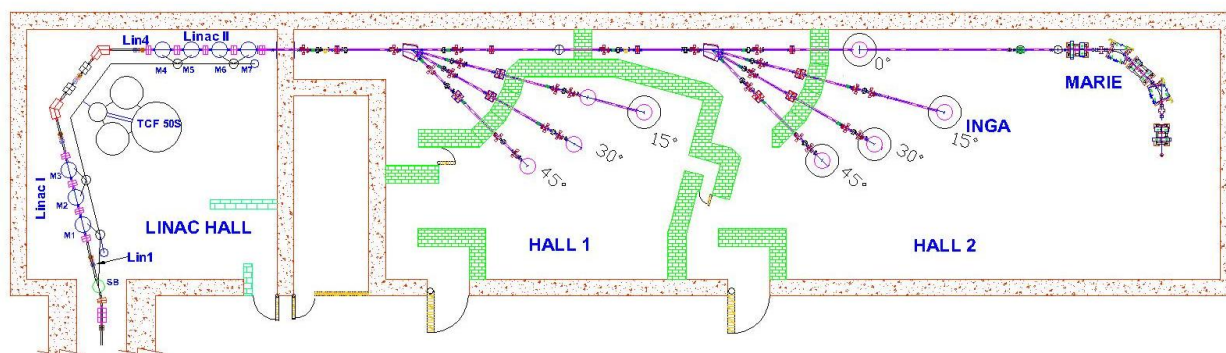


Figure 2: A Schematic layout of Linac and user halls

A test experiment with this accelerated beam, namely,  ${}^7\text{Li}$  ( $E \sim 45$  to  $55.6$  MeV) +  ${}^{232}\text{Th}$  ( $\sim 3$  mg/cm<sup>2</sup>) was carried out to study the yields of fusion evaporation residues and fission fragments using Indian National Gamma Array (INGA). A total of 18 Compton suppressed Clover detectors were used to measure the prompt gamma rays from the excited nuclei produced in the reaction and detailed analysis is in progress [5].

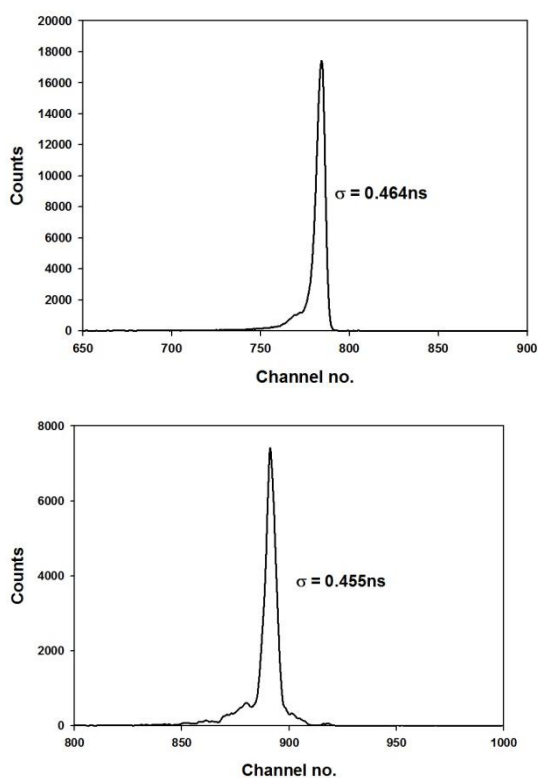


Figure 3: Beam Timing spectra for  ${}^7\text{Li}$  measured at the entrance of LINAC I (top panel) and LINAC II (bottom panel). The measured  $\sigma$  is inclusive of detector resolution.

## SUMMARY

The Pelletron LINAC facility is regularly operated for a variety of experiments. The cryogenics system of the LINAC has been upgraded for the enhanced capacity, such that the full LINAC can be operated without LN<sub>2</sub> precool. Starting with 40 MeV  ${}^7\text{Li}$  beam from the Pelletron, 56 MeV beam was successfully delivered at target station for a test experiment. We also plan to upgrade the Pelletron and associated subsystems, in order to extend operations of LINAC to heavier beams. Design of low beta, high performance niobium superconducting half wave resonator (HWR) with  $\beta_0 = 0.05$  is in progress. The development of digital RF controller cards is being planned for better performance. Instrumentation and interface for control and monitor of various accelerator subsystems is continuously being upgraded for ease of operations and performance.

## ACKNOWLEDGEMENT

We would like to thank the Pelletron-LINAC staff, DNAP, Low Temperature Facility, Central Workshop and Electronics Division (BARC) for their support.

## REFERENCES

- [1] R.G. Pillay, "Overview of the Pelletron Linac Facility", InPAC2011 proceedings.
- [2] V. Nanal *et al.*, "Operational experience of superconducting Linac booster at Mumbai", <http://accelconf.web.cern.ch/AccelConf/HIAT2009/papers/th-07.pdf>; HIAT09, Venice (Italy) 2009.
- [3] S.K. Singh *et al.*, InPAC2011 proceedings.
- [4] G. Joshi *et al.* "Development of the Model of a Self-Excited Loop", <http://accelconf.web.cern.ch/AccelConf/PAC2009/papers/we3rac06.pdf>; PAC09, Vancouver (Canada), 2009.
- [5] R. Palit *et al.*, to be published.

## PROGRESS ON THE RFQ BEAM COOLER DESIGN FOR SPES PROJECT

M. Maggiore, A.M. Porcellato, S. Stark, F. Chiurlotto, M. Comunian, A. Dainelli, M. De Lazzari,  
A. Galatà, A. Minarello, INFN - Laboratori Nazionali di Legnaro, Legnaro (Padova), Italy

### Abstract

The SPES project is the new Radioactive Ion Beam facility under construction at Laboratori Nazionali di Legnaro, Italy. In this framework, a study of a new RFQ beam cooler device is in progress in order to improve the beam quality in terms of transverse emittance and energy spread. The electromagnetic design of the RFQ section and the electrostatic layout of the injection and extraction regions have been done. The beam dynamics study is going on by means of dedicated codes which allow to take into account the interaction of the ions with the buffer gas needed to cool the beams. The preliminary design of the device started in 2011 by V Committee of INFN in the framework of the REGATA experiment. Both beam dynamics study and the electromagnetic design are presented in this work together with the experimental set up to investigate the sustainability of high voltages at low He pressure.

### INTRODUCTION

The experiments with radioactive beams require beams of high purity while the methodology ISOL (Isotope Separator On Line), used to produce them is isotopically unselective. Actually the output beam from the first mass selection (resolution 1/200) is constituted by all the radioisotopes with charge +1 and with almost the same mass number. In order to separate the radioisotope of interest from the contaminants, which may have intensities orders of magnitude higher a further mass selection, is required. This mass selection is carried out by High Resolution Mass Spectrometers (HRMS) whose capacity of selection (1/20000), without loss of transmission, depends on the emittance of the incoming beam. A lower emittance has the further advantage of reducing the beam transport losses and, moreover, makes easier the detection of radioisotopes and increases the accuracy of the measurement of their properties.

The devices used to reduce the emittance of low energy (a few tens of keV) radioactive beams are called buffer gas-filled Radio Frequency Quadrupoles (RFQ) cooler [1]. Many devices of this type have been successfully used up to now to reduce the beam emittance of low current (a few pA) ion beams. However, the increased beam current intensity (up to 1 μA) of the new generation ISOL facilities such as for example SPIRAL2, asks for new technological challenges for their fulfilment [2,3].

### BEAM COOLER CONCEPT

In a RFQ cooler, a quadrupolar electric field, generated by two pairs of electrodes placed at distance  $2r_0$ , oscillating in phase opposition at frequency  $\omega/2\pi$  and at

amplitude voltage  $V_{rf}$ , provides a potential well which can confine the motion of a particle of charge  $e$  and mass  $m$ . It can be shown that the particle motion is stable when the Mathieu parameter  $q$ , given by:

$$q = \frac{4eV_{rf}}{m\omega^2 r_0^2} \quad (1)$$

satisfies the conditions  $0 < q < 1$ .

For  $q$  values within this range, the particle motion in the quadrupole is, in first approximation, the sum of two predominant motions, the micromotion, which is the particle oscillation at the frequency of applied electric field, and the macromotion, which is due to the effect of the potential well created by the quadrupolar RF field configuration. The micromotion amplitude is attenuated approaching the axis of the quadrupole, according to the decrease of the electric field. It is then amplified when the ion moves away from the axis. This type of motion is always revitalized by the electric field applied to the electrodes.

As a first approximation (for values of  $q$  less than 0.5), the frequency of the macromotion is related to that of the micromotion by the relation

$$\omega_M = \frac{q}{2\sqrt{2}} \omega \quad (2)$$

It may likewise be shown that, the amplitude of the macromotion oscillation exceeds of a factor  $2/q$  the maximum micromotion amplitude. The ion then performs a wide oscillations at macromotion frequency, that are perturbed by micromotion. The amplitude of the macromotion movement is reduced in presence of dissipative processes, as collision with gas molecules present in the RFQ structure. The ion exchanges part of its energy with the gas molecule in the impact. It can be shown that, in average, the ion loses energy only if the gas molecule has an atomic weight lower than the ion ones [4]. It is also important that the buffer gas is neutral and inert in order to not remove beam ions by chemical reactions or charge exchange processes. The energy loss increases with the number of collisions, which is proportional to gas pressure. A gas inlet in the structure makes the process more efficient. The overall effect of the collisions is to introduce a viscous force which slows the ion until it reaches a constant drift speed. The introduction of this force in the equation of motion reduces the amplitude and lowers the frequency of the macromotion oscillation. The effect of the gas is therefore to reduce both transverse size and speed of the beam so to decrease its transverse emittance.

The component of the viscous force along the axis of the structure also produces a decrease in the longitudinal component of the ion speed and then lowers, together with it, also the energy spread.

To guide the beam to the exit and, if required, to allow beam bunching, a longitudinal electric field is created. The beam cooling can be carried out only when the incoming beam energy is sufficiently low to allow both the beam trapping in the potential well created by the RF field and a sufficient number of interactions between the beam ions and the buffer gas. For this reason an RFQ cooler for an ISOL facility foresees an entrance section for beam deceleration down to energy of about 100-200eV, limit given by the necessity to penetrate the potential well. An exit section makes the beam to recover the original energy.

High buffer gas pressure (up to few Pa) in the quadrupole makes the beam dumping faster but, in order not to lose beam intensity, high vacuum conditions have instead to be assured at quadrupole injection and extraction sections. Therefore, it is mandatory to maintain high differential vacuum conditions between the three cooler sections. At high beam intensities, high RF voltage amplitude (up to some kV) and, related by the  $q$  formula, also high frequencies (tens of MHz), are required in order to compensate for the space charge effects.

An R&D program is going on in parallel with the preliminary RFQ cooler electromagnetic and electrodynamic design in the frame of the INFN-CNV experiment REGATA.

## REQUIREMENTS FOR THE SPES BEAM COOLER

SPES is an ISOL radioactive beam facility under construction at LNL [5]. The radioactive beam produced by the target station [6] can be re-accelerated by ALPI, the superconducting linac for heavy ions in operation at LNL, to reach an energy exceeding 10 MeV/A. SPES production facility foresees a cyclotron accelerating a primary beam consisting of 700  $\mu$ A of protons up to 70 MeV.

The impingement of the primary beam on the original production UCx target, developed at LNL, provides radioactive ions with a current intensity up to 2  $\mu$ A in the mass range of 9-160 AMU. The target station is placed on a 40 kV platform.

A Wien Filter located downstream the source makes a first stage mass selection and reduces the beam intensity to about 50 nA. The ion beam is then delivered through the transport line with a geometric emittance of  $30 \pi$  mm mrad at 40 kV. To achieve the resolving power higher than 1/20000 for the HRMS, the Cooler device, placed upstream the mass selection, has to reduce the transverse beam emittance of about a factor 8. Once the beam is selected in mass, it is injected into the Charge Breeder

(CB) [7] based on a ECRIS design, in order to lower the mass to charge ratio down to  $A/Q \leq 7$ . To get the maximum injection efficiency of the CB, it is crucial to keep below some eV the energy spread of the ion beam.

The main goal of a Beam Cooler is therefore both to reduce the transverse emittance of the radioactive ion beam by a factor 8 and to maintain low the longitudinal emittance providing an energy spread of the cooled beams to about 1eV.

## PRELIMINARY COOLER DESIGN

The RFQ beam cooler device is composed by 3 main sections: the deceleration system, which lowers the energy of the incoming beam from 40 keV down to some hundreds of eV; the confinement and cooling section which consists of the RFQ device and the main vacuum vessel placed on a 40 kV high voltage platform; finally the acceleration section where the cooled beam is extracted and achieves the initial energy of 40 keV. The buffer gas is injected in the cooling section in order to reach a pressure within  $0.5 \div 3$  Pa

The energy of the reference beam was decreased in respect of the previous calculation [8] in order to make easy the RFQ accelerator design expected for SPES [9].

The electromagnetic field configuration was studied by the use of 3D FEM code OPERA, whereas the beam dynamic was analyzed by the dedicated code SIMION ver 8 in order to take into account the collisional effects with the buffer gas molecules for simulating the cooling process. In this preliminary design phase, we neglected the space charge effects on the beam transport since the current of the Radioactive Ion Beams is lower than 100 nA.

Table 1 sums up the main parameters of the device.

Table 1: Design parameters of a beam cooler for SPES

| Parameter                          | Value                            |
|------------------------------------|----------------------------------|
| Mass Range                         | 9-200 AMU                        |
| Buffer Gas                         | He @ 293 K                       |
| Transverse Emittance injected beam | $30 \pi$ mm mrad @ 40 keV (Q=1+) |
| Beam current                       | 50-100 nA ( $10^{11}$ pps)       |
| Emittance reduction factor         | 10 (max)                         |
| Energy Spread                      | < 5 eV                           |
| RF frequency range                 | 1-30 MHz                         |
| RF Voltage range                   | 0.5-2.5 kV                       |
| RFQ gap radius ( $r_0$ )           | 4 mm                             |
| RFQ total length                   | 700 mm                           |
| Pressure Buffer Gas                | 0.1 – 2.5 Pa                     |
| Ion energy at cooling              | 100 – 200 eV                     |

### Injection and Extraction Sections

SPES target station delivers radioactive beams with charge  $Q=1+$  and energy of 40 keV at the entrance of the RFQ Beam Cooler device. A system of four electrostatic lens decelerates the beam to 200 eV before the RFQ cooling section. The lens array gradually decelerates the ion beams to low energy, thus avoiding strong ion-optical effect that leads to harmful beam losses during the injection into the collisional ion guide.

The conical shape of the two mid stage electrodes allows beam focusing and compensates the natural diverging effect due to the deceleration process. We chose such electrode configuration in order to achieve the 100% transmission efficiency between the injection and the RFQ sections.

Figure 1 shows a sample plot of the trajectories of Cs  $1+$  ion through the electrode system. As shown, all of the ions are focused into the RFQ through the 6 mm diameter entrance aperture.

Following the cooling process through the RFQ, the ion beams exit through a 6 mm diameter aperture and then they recovered the initial energy by a two electrode stages.

### Confinement and Cooling Section

The RF quadrupole consists of four cylindrical rods of 9 mm of diameter. The distance between the opposite pair of rods is  $2r_o=8$  mm. The rods are 700 mm length and they are divided into 10 segments of 69.5 mm each.

The segmentation allows to produce an axial field which provides the drag force needed to bring out the cooled beam. The total voltage applied along the segmentation is 100 V.

The applied RF voltage and the operating frequency depends on the ion mass delivered which varies within 9-200 AMU and on the current intensity of the incoming beam. Table 1 shows the ranges of the different parameters.

He at 293 K was chosen as buffer gas for ion cooling. The operational gas pressure varies from 0.5 to 3 Pa, depending on the ion mass of the beam and on the RF voltage applied to the quadrupole.

By the preliminary results given by the SIMION code using the hard sphere model to calculate the interaction gas-ion, we simulated the cooling process and we achieved a transverse emittance reduction of a factor 8-10.

The differential pumping system is very crucial for obtaining optimal cooling and transmission efficiency.

The gas leakage through the entrance apertures causes the energy degradation of the beam and the related beam losses due to the scattering with molecules of the residual gas. These harmful effect can be reduced by both the careful design of the differential pumping system and the optimization of the design of the injection and extraction electrodes and their placing with respect to the entrance and exit of the vacuum chamber where the RFQ is placed.

This design is under study in collaboration with the CERN team.

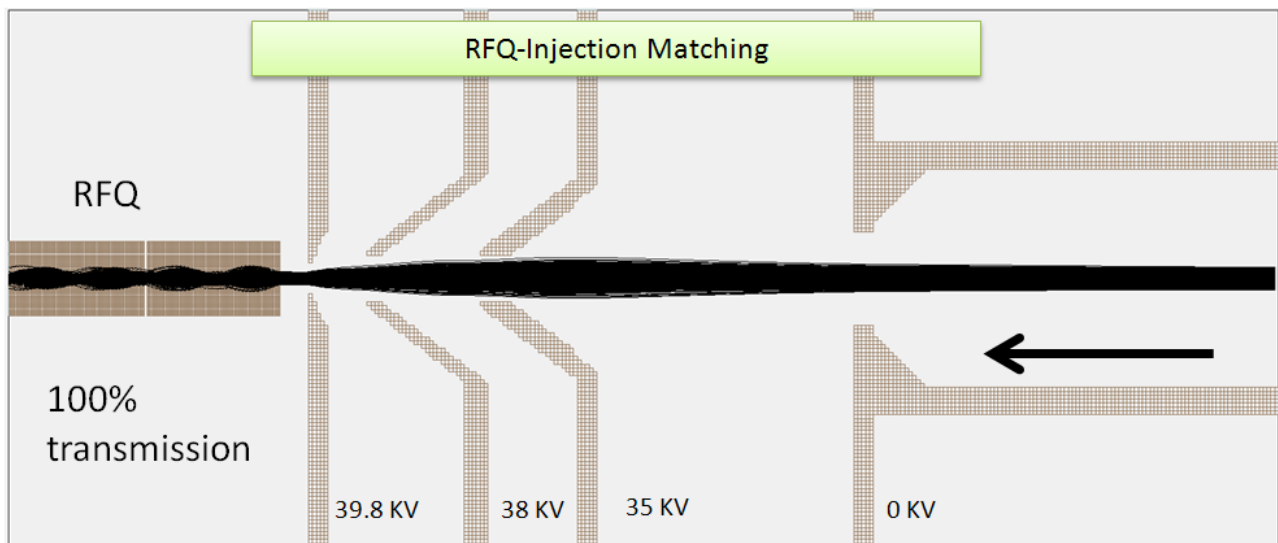


Figure 1: The SIMION beam transport simulation for the  $^{133}\text{Cs}^{1+}$  beam along the deceleration system. This is composed by 4 stage of electrodes at different voltage. As shown the waist is placed as close as possible to the RFQ entrance in order to fully match the related acceptance.

## APPARATUS FOR DISCHARGE DETECTING

Despite the expected radioactive ion beam intensity for SPES (50 nA) is lower than ones reachable in the facility SPIRAL 2, however it is anyway much higher than other coolers in operation.

As described in the previous paragraph, a high current cooler requires to apply an RF voltage of some kV to the electrodes in presence of a buffer gas at pressure of some Pa.

This pressure range is near to the minimum of the Paschen curve [10], showing the discharge voltage as a function of the product between pressure and electrode distance, as a consequence electrical discharge can be an issue for the beam cooler operation. For this reason we foresaw, in the frame of the experiment REGATA, the construction of an experimental set up aimed at studying experimentally study the conditions at which the discharges between the electrodes may occur. In such apparatus we can assemble electrodes of different shape and automatically vary their distance without the necessity of opening the vacuum chamber. In addition we can easily change the applied (DC) voltage or Helium pressure level. In such way we can evaluate the dependence of the discharge offset from such parameters and, moreover, the influence of shape and surface preparation of electrodes.

The test apparatus includes a CF150 flange (fig 2) which holds the two electrodes.

One of the electrode, supported by PEEK made insulators is connected by an high voltage feed-through to a high voltage power supply.

A linear actuator allows to change the position of the second electrode, maintained at ground potential. The assembling system is designed in order to make an easy exchange and alignment of the electrodes.

The CF flange has apertures for the pressure gauge and gas inlet and will be integrated in an existing high vacuum apparatus. Figure 3 presents the working scheme of the test discharge apparatus and of its control system.

A 10 kV programmable power supply creates the voltage ramps. Both a four channel oscilloscope and an universal USB Card allow the acquisition of possible current spikes and of their dynamic behavior.

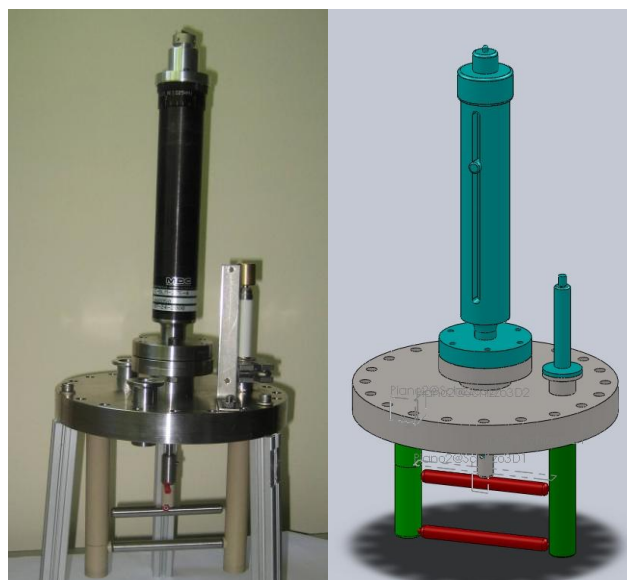


Figure 2: Drawing of the pressure test system and top flange of the apparatus under construction for testing conditions of discharges at low He pressures.

The USB card also controls the HV power supply and gas flow equipment. A computer controlled stepping motor moves the electrodes by a linear feed-trough.

All the data are gathered and visualized by a PC controlling both electrode movement and test operation sequence.

## CONCLUSION

The design of the RFQ beam cooler for SPES project started in 2011

This report presents the results of the electromagnetic layout and the first analysis of the beam dynamics

We chose the operational parameters of the device and we are now carrying on the process of optimization of the structure. Once this first phase of study is accomplished out, we will complete the beam dynamics analysis by the introduction of the space charge effects.

An experimental set up for testing the sustainability of the high voltage necessary to the cooler operation is now ready for measurements.

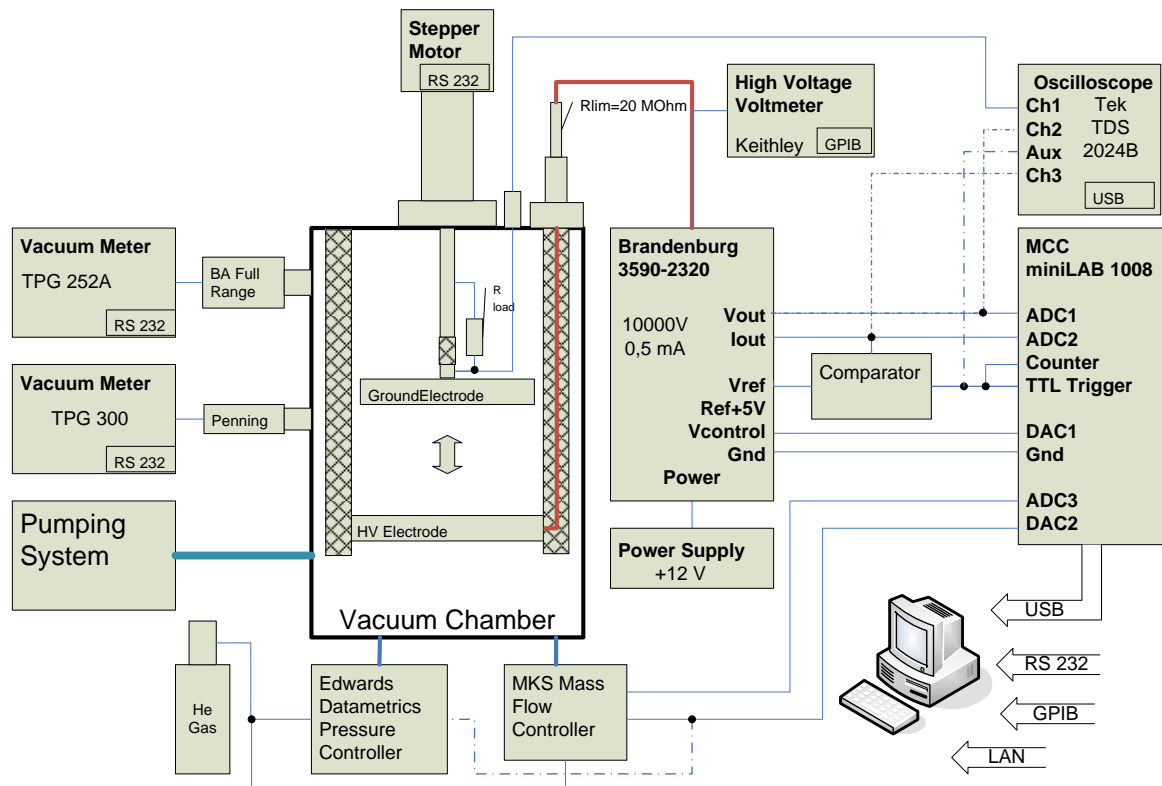


Figure 3: Working scheme of the test set up for detecting discharges at low gas pressure.

## REFERENCES

- [1] R.B. Moore et al., Nucl. Instr. and Meth. B 204 (2003) 557.
- [2] R.B. Moore et al. Int. J. Mass Spectrometry 251 (2006) 190.
- [3] O. Gianfrancesco, et al., Nucl. Instr. and Meth. B 266 (2008) 4483.
- [4] F.G. Major and H.G. Dehmelt, Phys. Rev. 170, 91 (1968).
- [5] A. Andrighetto et al. "The SPES project at LNL" AIP Conf. Proc. 1099 pp. 728-732.
- [6] A. Andrighetto et al., Eur.Phys. J. A 42, 517-521 (2009)
- [7] A. Galatà INFN-LNL Annual Report 2011, 249.
- [8] M. Comunian et al., Proceeding of this Conference (HIAT2012), Chicago, USA.
- [9] G. Bisoffi et al. Proceedings of this Conference, (HIAT2012), Chicago, USA.
- [10] P. Hartmann et al., Plasma Source Sci. Technol. 9 (2000) 183.

## PERFORMANCE OF ALPI NEW MEDIUM BETA RESONATORS

A.M. Porcellato, S. Stark, F. Chiurlotto, M. De Lazzari, A. Palmieri, V. Palmieri, F. Stivanello, Istituto di Fisica Nucleare - Laboratori Nazionali di Legnaro, Legnaro, Padova, Italy

### Abstract

All the Nb sputtered medium  $\beta$  cavities installed up to 2011 in ALPI were produced by upgrading of old previously Pb plated substrates. For the first time this year we had the opportunity to test on line four 160 MHz,  $\beta=0.11$  QWRs which were designed and built in order to be Nb sputtered. These resonators were built in between 2007 and 2008 and they were tested at low fields (up to 3 MV/m) just after their production, when they showed  $Q_0$  values exceeding  $1 \times 10^9$ . They were then stored for about three years in plastic bags and they were installed in ALPI only this year. The on line tests showed  $Q_0$  values reduced of about a factor five with respect to the ones measured in laboratory. It is the first time we could pick out a Q deterioration caused by storage in air, probably because we previously had the possibility to install the cavities in the on line cryostats within some weeks from the time of cavity production.

So far we have not recognized any Q-degradation, both when the sputtered cavities were maintained in vacuum for many years and also when they were open to air for a few weeks for cryostat maintenance. This time, as it had happened in the maintenance of cryostat CR19 housing high  $\beta$  resonators, we could instead improve the Q-curves by high pressure rinsing the resonators and by making a better rf contact between the cavity and its bottom plate.

### INTRODUCTION

A large number of Nb on Cu sputtered cavities are in operation in ALPI since many years [1]. They are Quarter Wave Resonators (QWRs) operating at 160 MHz. Eight high  $\beta$  ( $\beta=0.13$ ) and 44 medium  $\beta$  ( $\beta=0.11$ ) units are used for beam acceleration. In ALPI there are also further 16, 80 MHz, low  $\beta$ , bulk Nb accelerating QWRs [2]. All these resonators are housed in cryostats containing four cavities each. Further 4Nb/Cu+2Pb/Cu QWRs, two per cryostat, are used for beam bunching.

The four high  $\beta$  cavities presently installed in cryostat CR20 are on line since 1998. Their substrates were designed and built in order to be sputtered and their on line performance exceeds 6 MV/m @ 7 W in average [3]. The remaining four high  $\beta$  resonators, have the same inner shape, but they have a different construction technology [4]. They had been housed in the cryostat CR20 in between 1995 and 1997; in 2001, after being re-sputtered, they were moved into the cryostat CR19. Their maintenance, in 2010, produced a substantial improvement in performance, as described later in this paper. Up to the last year all the installed accelerating medium  $\beta$  resonators were obtained by sputtering old

substrates previously lead plated [5]. The cavity renewing process started at the end of 1998 and was completed by 2004 [6]. The cavity upgrading practically doubled their averaged operational accelerating field (4.8 MV/m @ 7 W), but the drawbacks of old substrates did not allow to reach the results obtained in high  $\beta$  resonators [6].

Between 2007 and 2009 we built and tested in laboratory four new medium  $\beta$  cavities properly designed to be sputtered, but only this year we had the possibility to test them on line [7].

### THE NEW MEDIUM BETA CAVITY

The new medium  $\beta$  cavity has a shape similar to the ALPI high  $\beta$  resonators: a rounded shorting plate links the inner and the outer conductors. The first, 60 mm in diameter, ends in an hemisphere, the latter, which has an inner radius of 90 mm, extends about 70 mm beyond the inner conductor.

The necessary reduction of optimum  $\beta$  with respect to the high  $\beta$  cavity, is achieved by the plastic deformation of the outer conductor which, around the beam axis, is protruded toward the inner cavity side. The beam ports are external to the cavity body and are screwed to the outer conductor without any gasket. Both the original beam port design and the rounded shorting plate allow smooth connection surfaces where a better sputtered film can be obtained. The cavity shares the cryostat vacuum. Figures 1 and 2 show the new medium  $\beta$  substrate before chemical treatment.

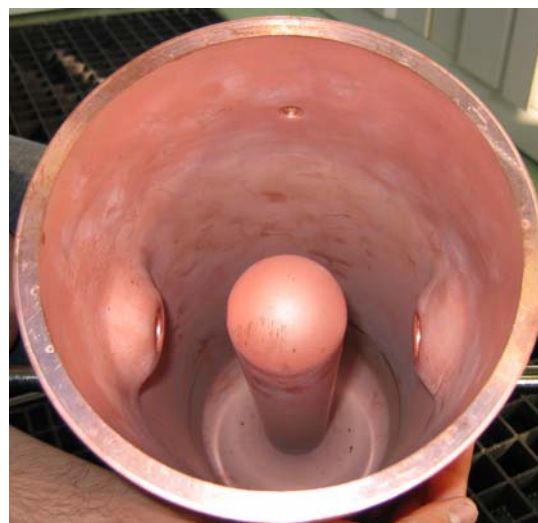


Figure 1: The inside of new medium  $\beta$  substrate before chemical treatment.

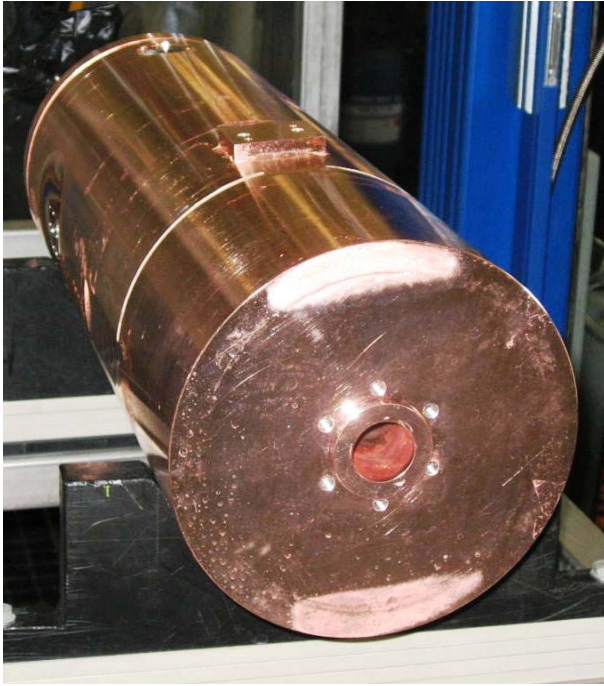


Figure 2: outer part of the new medium  $\beta$  cavity. In the foreground the seating for the cavity collar for connection to the liquid He piping. On top there are the cavity holder and the coupler hole.

It adopts a capacitive coupler, whose antenna penetrates in to the cavity at  $90^\circ$  with respect to the beam axis, shifted of 70 mm towards the cavity bottom. The pick-up antenna is located symmetrically with respect to the coupler. In this way the cavity does not have holes in high current region. The cavity tuning is performed pushing/pulling the bottom plate.

### Electromagnetic Parameters

The resonator electromagnetic parameters, computed by HFSS, are listed in Table 1.

Table 1: Electromagnetic parameters of the new medium  $\beta$  cavity.

|                              |             |                        |
|------------------------------|-------------|------------------------|
| Frequency                    | 160         | MHz                    |
| Stored Energy/ $(E_a)^2$     | 65          | mJ/(MV/m) <sup>2</sup> |
| $\beta_{opt}$                | 0.11        |                        |
| Peak magnetic field/ $E_a$   | $\cong 110$ | Gauss/(MV/m)           |
| Peak electrical field/ $E_a$ | $\cong 4.5$ |                        |
| T.T.F. ( $\beta_{op}$ )      | 0.899       |                        |
| Active length                | 180         | mm                     |
| $\Gamma$                     | 29          | $\Omega$               |

The cavity, set at 1 MV/m, provides an energy gain of 0.18 MeV/(MVm)/q to the synchronous  $\beta_{opt}$  particle with state of charge q. The wide TTF curve allows efficient acceleration for beams having  $0.07 < \beta < 0.2$ .

### Substrate Construction

We produced four cavities starting from OFHC Cu parts left unused since the first ALPI cavity production [5] and named MD1, MBD2, MBD3, MBD4.

Each substrate was obtained from a preformed mushroom shape and a cylinder jointed together by vacuum brazing (fig.3). In order to make the cavities compatible with the standard ALPI cryostat, two cavity supports were connected to the cavity body by a subsequent brazing cycle.

The beam port shaping was developed and performed in house at room temperature and in a single step, after the brazing cycles.

Later on, we drilled the holes for the beam line, coupler and pick up. We had then to mill the cavity for preparing the seats both for coupler and external beam ports. The latter are screwed to the cavity body before the sputtering process in order to be covered with the Nb film together with the cavity inner surface (figure 4). The final substrate machining includes turning of the groove for fixing the tuning system, preparation, always by lathe machining, of the surface where the stainless steel cavity collar is fixed and, at the end, drilling and threading of the holes used for joining the ancillary equipment to the cavity.

A detailed description of the substrate construction technology is reported in reference 8.

The inner cavity surfaces needed to be grinded both to eliminate the signs left by the dies used during the plastic deformation and to smooth the surface interested by the mechanical deformation.

The cavity target frequency was reached by decreasing the inner conductor length, purposely left slightly longer than necessary.



Figure 3: OFHC Cu cavity parts before vacuum brazing.

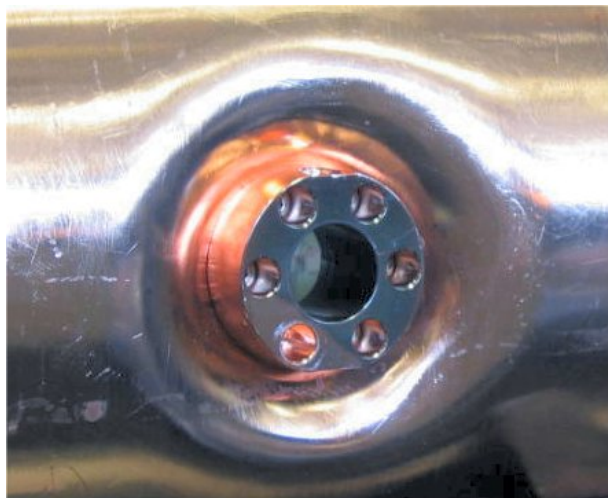


Figure 4: Particular of the external beam port. It is screwed to the cavity body before the cavity sputtering process.

This process was performed by removing material from the inner conductor tip by electro-polishing. If the electro-polishing solution was suitably mixed during the process, a few hundred microns were easily subtracted leading to a smooth surface.

In these cavities we eliminated the indium wire traditionally used to ensure rf contact between the cavity and its bottom plate to have the possibility to rinse the resonator by high pressure water just before its assembling into the line cryostat. This asked for minor changes both in the standard cavity bottom plate and in its fixing ring in order both to increase the tightening torque and to shift the contact line between the plate and the cavity border towards the inner cavity side, where the sputtered film has still a sufficiently good quality. Small adjustments on the standard tuning system allowed maintaining a smooth tuning movement in all its range.

### Surface Preparation

The inner cavity surface treatment included a few days of tumbling followed by the electro-polishing and chemical polishing cycles and by a final high water pressure rinsing according to a well established procedure [8].

The chemical solution is renewed only after treating two/three cavities, one after the other in following days. Usually the first polished cavity was immediately put in vacuum in the sputtering chamber, the others were instead stored in plastic bags in air and rinsed again just before their assembling in the sputtering chamber.

Fresh chemical solution was used for all the new medium  $\beta$  cavities, but MBD2, which then had its sputtering postponed of about one month with respect to the chemical treatment. As usual, few days of resonator baking in the sputtering chamber, up to 700° C, preceded the superconducting layer deposition.

By the D.C. biased Nb sputtering technology developed at LNL [3], we deposited a Nb layer, about 2 microns thick, in 14 sputtering steps of about 15 minutes each with three hours of pause in between to maintain the cavity below the baking temperature. Figure 5 shows the first sputtered new medium  $\beta$  cavity.

Regarding to the sputtering process, we used the standard sputtering parameters which were adopted for the production of ALPI cavities and initially we tried the cathodes which were already available.

For MBD3, the first cavity produced, we adopted the cathode used for the old medium  $\beta$  cavities and we obtained an inner resonator surface having some shadows in the beam port area; in spite of that the cavity presented quite good performances, though lower than those obtained in high  $\beta$  cavities.

The use of the cathode for high  $\beta$  substrates in the sputtering of the cavity MBD2 led instead to bad results ( $Q_0 = 2 \times 10^8$ ) so the cavity had to be stripped.

We were consequently forced to build a new cathode more appropriate for the new resonator shape. It was adopted for the production of MBD1, MBD4 and also for the new sputtering of the cavity MBD2. Being the obtained cavities performance better than the old medium  $\beta$  resonators, we did not look for further improvements of the sputtering process, but we installed the cavities in ALPI as soon as possible in order to take advantage of their performance.

We, as usual, prepared the cavity bottom plates in a different sputtering chamber where it is possible to produce up to 9 units in the same time by D.C biased sputtering.



Figure 5: New medium  $\beta$  cavity after being sputtered and before being closed by its bottom plate.

## PERFORMANCE OF THE NEW MEDIUM BETA RESONATORS

### Laboratory Tests

As soon as dismantled from the sputtering chamber, we tested the cavities one by one up to an accelerating field of 3MV/m (maximum allowed field by radioprotection rules in the test laboratory). As usual, we rinsed the cavities by high pressure water before closing them by their bottom plate without any gasket.

We mounted the cavities in the test cryostat equipped with their coupler, pick-up, tuner, resistors and temperature sensors. We pumped down the cryostat very slowly (a few hours before opening the turbo pump gate) in order to reduce cavity contaminations, that are possible because we did not have the possibility to assemble cryostat and cavities in clean room. We baked the cavities in vacuum for about 24 hours at 350 K. We started to perform multipactoring conditioning at room temperature and we completed it in few hours during the cooling of the cryostat thermal shield. As usual, we cooled the resonators at 77 K by liquid nitrogen and then to 4.2 K by liquid He. The cooling time is not critical for these resonators because they are not affected by Q-disease.

At liquid He temperature we performed only low power conditioning to get rid both of the multipactoring level which usually appears at about 1.2 MV/m and of any other residual low field multipactoring.

Fig. 6 presents the Q-curves obtained after 1-2 hours of conditioning. As it is possible to notice, MBD4 presented a  $Q_0$  value of  $2 \times 10^9$  and its Q-curve at low field was comparable to the best ones obtained in high  $\beta$  resonators [3]. The Q-curve slope above 2 MV/m was due to the short conditioning. As we mentioned before, MBD3 was sputtered using the old, not optimized, medium  $\beta$  cathode. The resulting cavity inner surface presented shadows in the beam ports area and this is a possible reason of the lower Q curve.

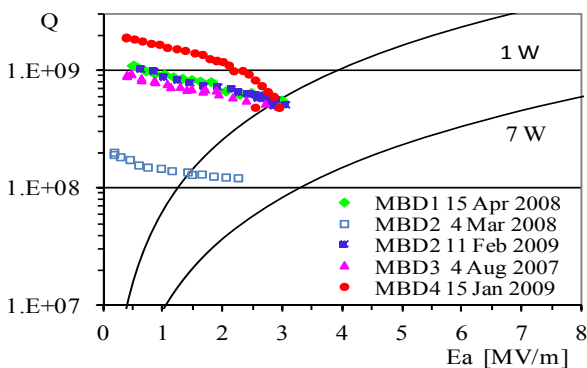


Figure 6: Q-Curves of the new medium  $\beta$  resonators as measured in laboratory after low power conditioning. Radioprotection rules do not allow to exceed 3 MV/m. After the first sputtering cycle the Cavity MBD2 was stripped and sputtered again.

A further contribution to the lower performance could be due to the cryostat venting we had to perform before the cavity test to adjust the coupling range of the cavity.

The replacement of the sputtering cathode in the second sputtering cycle significantly increased the performance of the cavity MBD2, which remains however lower than MBD4 cavity. MBD2 was chemically treated using the same solutions previously used for cavity MBD4 and it was sputtered a few weeks after the chemical process. Both these conditions may be a possible reason for the reduction in performance.

The first circumferential brazing of the MBD1 substrate was not performed correctly and had to be repeated without having the possibility to follow the standard assembling procedure [5]. As a consequence, some unusual shadows of brazing material appeared around the brazed joint. We tried to scratch out all the visible material, but it is probable that some contamination remained still included in the copper surface thus affecting the surface quality and consequently the cavity performance.

Certainly it would have been interesting to repeat the sputtering process in the less performing cavities, but we preferred to take advantage immediately of the new cavities better performance.

### On-line Performance

Once dismantled from the test cryostat, the cavities were stored in plastic (PE-LD) bags waiting to be installed in ALPI. We had all the cavities ready by the beginning of 2009, but, unfortunately, the cryostat installation was postponed up to end of 2011, when we had the possibility to open the cryostat CR15, the first medium  $\beta$  cryostat uninstalled.

The absence of the indium gasket gave the possibility to open the cavity bottom plate and to rinse each cavity by high pressure water before installation into the line cryostat. This does not prevent possible contamination during cryostat assembling and alignment procedures, the latter performed with cavities opened to the unclean laboratory air, but it can remove dust entering into the cavity during the test cryostat venting.

After the assembling procedure, we slowly pumped the cryostat down to  $1 \times 10^{-6}$  mbar and we installed it on line without breaking the vacuum.

The cavities were again baked on line in vacuum at 350 K for 24 hours and then conditioned before being cooled to 4 K. As expected by the not clean assembling, the cavities were heavily affected by field emission. They were conditioned for a few hours using the line amplifiers and then in pulsed mode (1 kW peak; about 20 W average power) by an auxiliary amplifier for about 3 hours each. Later the cavity were warmed up to 20 K before being cooled down again at 4 K for the final Q measurements.

Figure 7 presents laboratory and on line Q-curves of the four new medium  $\beta$  resonators while table 2 shows  $Q_0$  and Q-curve slope values obtained fitting the  $\log_{10} Q$  data of the new medium  $\beta$  resonators (fig.7).

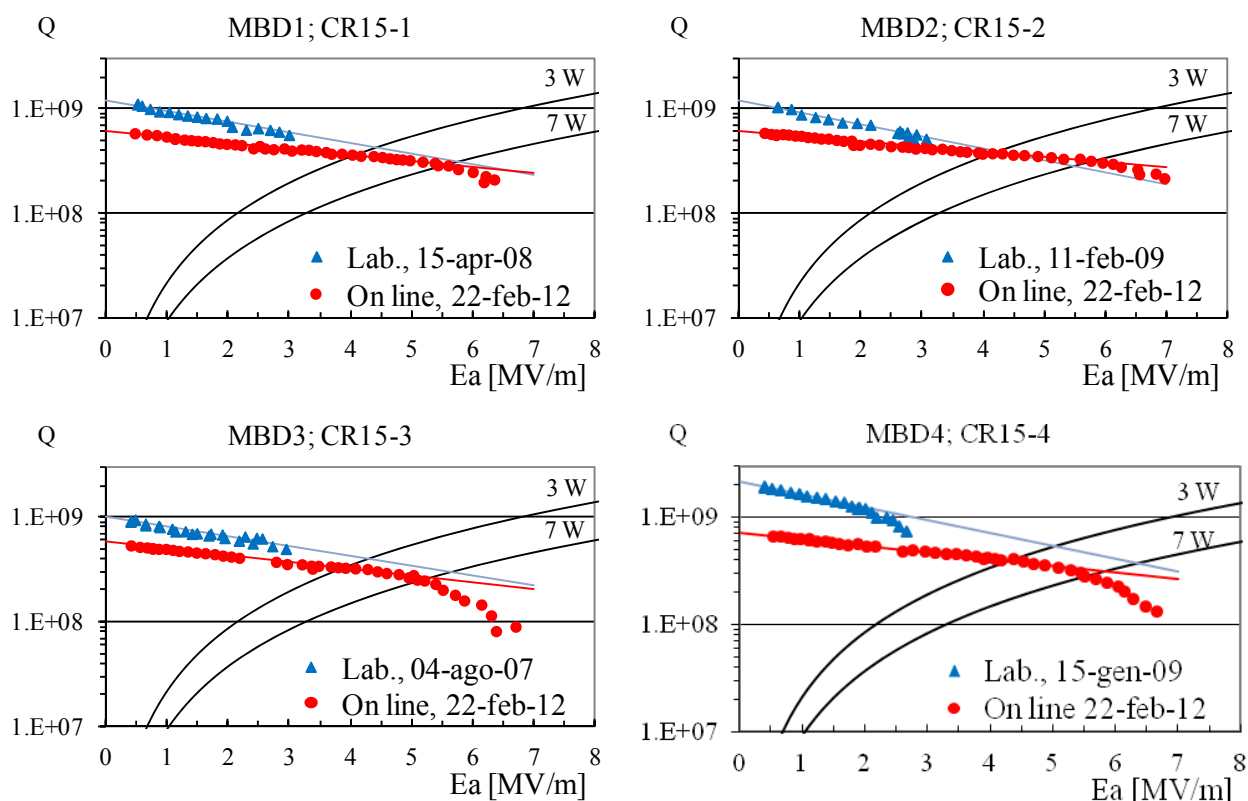


Figure 7: Laboratory (blue) and on line (red) measurements of the four new medium  $\beta$  resonators installed in cryostat CR15 after they had been stored in air for at least 3 years. The straight lines represents the linear best fit of the  $\log_{10}$  of the Q-data as a function of the accelerating field in the linear range of the Q-curve. The fit parameters are summed up in Table 3. The  $Q_0$  values are lower in the on line measurements for all resonators, but the reduced slope in the on line measurement mitigates the accelerating field losses at 7W.

As it is possible to notice in fig. 7, the  $Q_0$  values measured on line are all lower by at least a factor 5 with respect to those measured in laboratory. The on line Q-curves are straight up to an accelerating field exceeding 5 MV/m; their slope is lower than the one obtained in laboratory for all the cavities. This is compatible with an increase in the surface resistance which depends on the accelerating field. It can be due to surface degradation during the long storage in air. It is the first time we put in evidence such effects, probably, not only because it is the first time we store high Q cavities in air for such a long time, but also because, the more reliable cavity closing method and the rinsing procedure we adopted, made the cavity performance less depending from events difficult to control.

The resonator Q measured on line in these cavities can be obtained by the parallel contribution of the Q measured in laboratory and of a constant Q value ( $Q_{//}$ ). That means that the Q decrease of resonators can be thought as to the contribution of a surface resistance, depending quadratically by the accelerating field, in series to the cavity initial surface resistances.

Table 1 sums up both the values of  $Q_{//}$  we found for the four new medium  $\beta$  resonators and their accelerating

fields at 7W, as deduced by the Q-curve fitting. In spite of the losses of performance with respect to the laboratory tests, the new cavities can operate at accelerating fields exceeding 5.6 MV/m at 7W in average, after a full conditioning process.

A reduced storage time and the use of the optimized cathode for all the resonators would have certainly increased the average accelerating field value of 6 MV/m.

If properly built substrates were available it would be then possible increase substantially the ALPI accelerating voltage

Table 2: Values of  $Q_0$  and Q-curve slope obtained fitting the  $\log_{10}$  Q data of the new medium  $\beta$  resonators (fig.7).

| Cavity | Laboratory |                            | On line test |                            |
|--------|------------|----------------------------|--------------|----------------------------|
|        | $Q_0$      | Slope [MV/m] <sup>-1</sup> | $Q_0$        | Slope [MV/m] <sup>-1</sup> |
| MBD1   | 1.19E+09   | -0.100                     | 6.02E+08     | -0.056                     |
| MBD2   | 1.17E+09   | -0.112                     | 6.00E+08     | -0.049                     |
| MBD3   | 9.93E+08   | -0.093                     | 5.71E+08     | -0.065                     |
| MBD4   | 2.14E+09   | -0.120                     | 7.20E+08     | -0.061                     |

Table 3:  $Q_{//}$ : constant Q-value that, added in parallel to the laboratory measured Q-curve data, reproduces the on line Q curve;  $E_a$  is the accelerating field at 7W as it results by the fitting process.

| Cavity      | $Q_{//}$ due to storage | $E_a$ at 7W |
|-------------|-------------------------|-------------|
| <b>MBD1</b> | 1.22E+09                | 5.64        |
| <b>MBD2</b> | 1.24E+09                | 5.81        |
| <b>MBD3</b> | 1.34E+09                | 5.31        |
| <b>MBD4</b> | 1.08E+09                | 5.86        |

## IMPROVEMENT IN HIGH BETA RESONATOR PERFORMANCE

The benefit of the better cavity closing system that we systematically stated to adopt in 2007 for the new medium  $\beta$  resonators, appears evident also in the increment of performance we obtained in CR19 cavities after the cryostat maintenance we performed in 2010. This cryostat houses the high  $\beta$  resonators hb1, hb2, hb3, hb4. They were sputtered a first time in 1995 and they were installed in ALPI in the cryostat CR20 up to 1998, when they were substituted by new more performing cavities that are still in operation at an average accelerating field approaching 6 MV/m @ 7 W cryogenic dissipated power.

In 2001 the uninstalled hb cavity substrates were stripped and Nb sputtered again. All the resonators reached in laboratory  $Q_0$  values in between 5 and  $7 \times 10^8$ . We have to mention that the cavity hb2 obtained such result only after a third sputtering process, once that a small pit, located on the cavity shorting plate, was detected and smoothed. At the end of 2001 we installed the renewed cavities in the cryostat CR19 where they reached on line accelerating field in between 4 and 5 MV/m, limited by field emission. However the hb1 resonator became unusable just after the first high power conditioning (1kW, pulsed); due to a short in the rf input line. Moreover, a couple of years ago, the use of the second cavity, hb2, became impossible because its tuner stuck.

When we uninstalled the cryostat CR19 in 2009 for maintenance, we decided to re-sputter only hb2, which was both the worst performing resonator and the only one which needed frequency readjustment. Before to re-sputter the resonator, we took the opportunity to open and rub up a new pit which showed up in the cavity shorting plate during the stripping of the old Nb film. We also smoothed more deeply the pit we had already discovered before the previous sputtering. The cavity was then chemically treated and sputtered again in the standard

way before being tested in laboratory. The only difference of this resonator with respect to the cavities produced in 2001 was the higher number of sputtering cycles, which results in a film thickness about 50% higher.

All the other cavities maintained their previous sputtered film, but had their bottom plate changed. We removed accurately the indium gasket that was previously used to join the old plate to the cavity body. All the cavities were then High-Pressure Water Rinsed and closed by bottom plates, which were previously modified on the lathe to improve their rf contact with the cavity body. We also modified the connection flanges in order to increase further the strength on the junction.

Once the cryostat CR19 was again on line, we tested again the cavities. Figures 8 shows their Q- curve, after a few hours of He conditioning using the 100 W installed amplifiers.

As it is possible to notice in the picture, all the cavities raised their  $Q_0$  values to about  $1 \times 10^9$ . This is a clear evidence of the benefit of the newly adopted plate assembling procedure, which allows avoiding the indium gasket.

The Q-curve slopes of the cavities, that were only rinsed and closed by the new plate closure system, remained practically unchanged, only the curves were shifted towards higher Q-values. This suggested that, by the new assembling system, we could eliminate a power dissipation process depending quadratically by the accelerating field or, in other words, that we eliminate the contribution of a constant resistance to the cavity power losses.

The cavity hb2 was tested, just after its new sputtering, without indium gasket also in laboratory and, consequently, there was no reason to have better performance. It presents instead an increased Q slope, however lower than the ones of CR15 cavities.

Table 4 sums up the fitting parameters of Q-curves both for laboratory and on line measurements.

Table 4: Values of  $Q_0$  and Q-curve slope obtained fitting the  $\log_{10}$  Q data (fig. 8) of the high  $\beta$  resonators installed in cryostat CR19. Only hb2 had its superconducting layer renewed before being tested in laboratory, all the others, produced in 2001, were only rinsed

| Cavity     | Laboratory test |                            | On line test |                            |
|------------|-----------------|----------------------------|--------------|----------------------------|
|            | $Q_0$           | Slope [MV/m] <sup>-1</sup> | $Q_0$        | Slope [MV/m] <sup>-1</sup> |
| <b>hb1</b> | 1.19E+09        | -0.100                     | 9.28E+08     | -0.061                     |
| <b>hb2</b> | 1.17E+09        | -0.112                     | 1.14E+09     | -0.064                     |
| <b>hb3</b> | 9.93E+08        | -0.093                     | 1.16E+09     | -0.070                     |
| <b>hb4</b> | 2.14E+09        | -0.120                     | 1.16E+09     | -0.070                     |

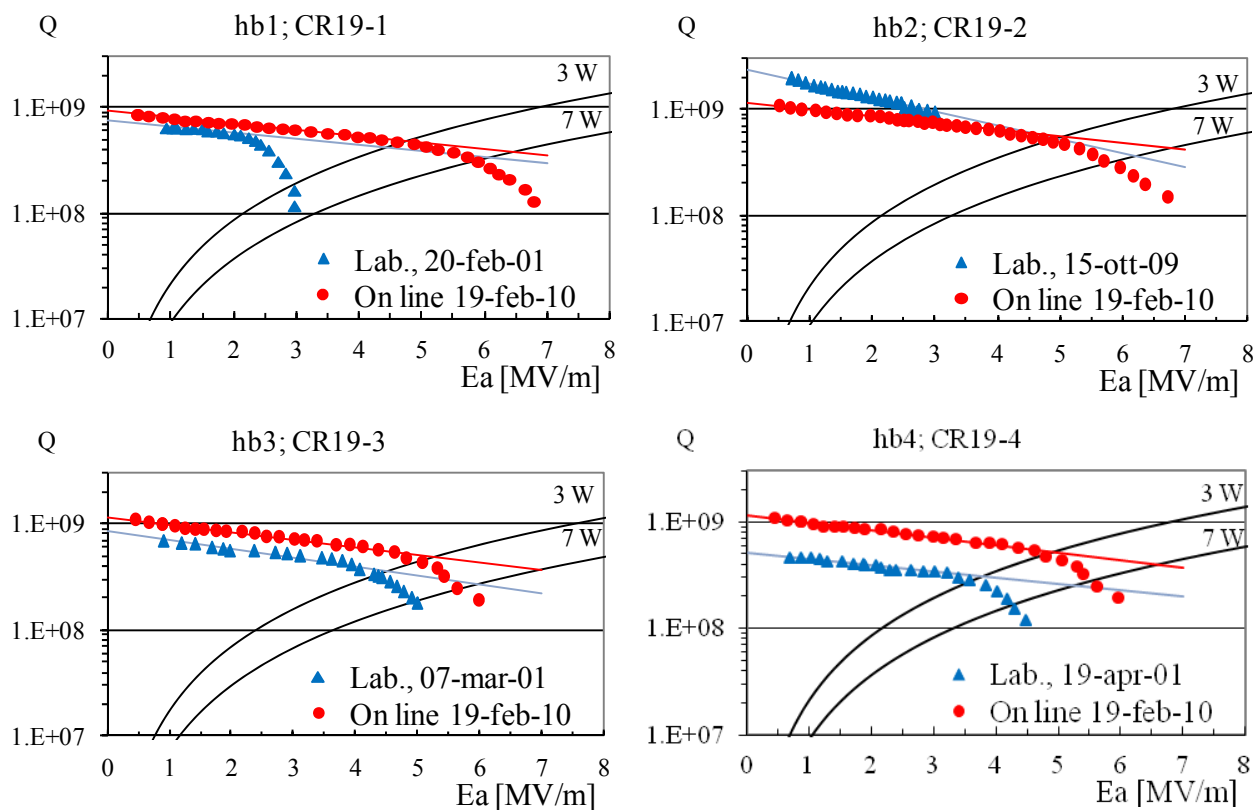


Figure 8: Laboratory (blue) and on line (red) Q curves of the high  $\beta$  resonators installed in ALPI cryostat CR19. Only hb2 had its superconducting layer renewed before being tested in laboratory, all the others were only rinsed. The straight lines represents the liner best fit of the  $\log_{10}$  of the Q-data as a function of the accelerating field.

### CONCLUSIONS

Four new Nb sputtered medium  $\beta$  cavities have been developed and built at Legnaro. The performance obtained in these cavities demonstrate that it would be possible to obtain accelerating fields exceeding 6 MV/m at 7W also in medium  $\beta$  cavities if properly built substrates were available, thus increasing substantially ALPI accelerating voltage. We obtained an increase of performance also in three high  $\beta$  Nb/Cu cavities, which were produced more than nine years ago, by changing the closure system of their bottom plate and performing high pressure water rinsing on them. We also were able to re-sputter a cavity and maintain the same level of performance we used to have in the production stage of the high  $\beta$  section.

### ACKNOWLEDGMENT

We thank Enzo Bissiato, Diego Giora, Alessandro Minarello for resonator construction and maintenance and the LNL cryogenic and operation staff for cryostat assembling and help in resonator conditioning.

### REFERENCES

- [1] A. M. Porcellato, S. Stark, V. Palmieri, F. Stivanello, Niobium Sputtered QWR, Proceeding of the 12th International Workshop on RF Superconductivity, Cornell University, Ithaca, NY 10-15 July 2005
- [2] G. Bisoffi et al. ALPI QWR and S.RFQ operating experience, proceeding of the 13th International Workshop on RF Superconductivity, Beijing October 2007
- [3] Stark et al., "Niobium sputter-coated QWRs", Particle Accelerators, Vol.61 (1998) p. 383
- [4] Palmieri et al., Nucl. Instr. and Meth., Installation in LNL ALPI linac of the first cryostat with four niobium quarter wave resonators, A382 (1996), p. 112
- [5] A. M. Porcellato, "Experience with the ALPI Linac resonators", Nucl. Instr. and Meth. A382 (1996) p. 121
- [6] A.M. Porcellato et al., Proceedings of the 11th H.I.A.T. Conference, Venice 7-12 June 2009
- [7] S. Stark et al., A Novel sputtered medium beta cavity for ALPI, Proceeding of the 13th International Workshop on RF Superconductivity, Beijing October 2007
- [8] A.M. Porcellato et al., "Production Installation and test of Nb sputtered QWRs for ALPI", Pramana J. Phys. Vol. 59 p. 871 (2002)

# DAMAGE SITUATION OF THE 12UD PELLETRON TANDEM ACCELERATOR AT THE UNIVERSITY OF TSUKUBA BY THE GREAT EAST JAPAN EARTHQUAKE

Kimikazu Sasa<sup>#</sup>, UTTAC, University of Tsukuba, Tsukuba, Japan

## Abstract

The 12UD Pelletron tandem accelerator at the University of Tsukuba suffered serious damage from the Great East Japan Earthquake on 11 March 2011. On the day, the 12UD Pelletron tandem accelerator was in operation at 8 MV. A main tank of the 12 UD Pelletron tandem accelerator located from downstairs 4th floor to 7th floor was strongly shaken by the shock of the earthquake. All high voltage accelerating columns fell down in the accelerator tank. A situation of the damage and a post-quake reconstruction project of the Tandem Accelerator Facility at the University of Tsukuba are reported.

## INTRODUCTION

The 12 UD Pelletron tandem accelerator was manufactured by National Electrostatic Corp. (NEC), USA and was installed at the University of Tsukuba, Tandem Accelerator Complex (UTTAC) in 1975 [1]. A maximum terminal voltage of 12 MV is available for various ion beam applications [2]. By the Great East Japan Earthquake on 11 March 2011, the 12UD Pelletron tandem accelerator suffered serious damages. The 9.0-magnitude earthquake hit the east Japan area. Many accelerator facilities were damaged by this earthquake [3]. A maximum acceleration was  $371.7 \text{ cm/s}^2$  (gal) with the duration time of 300 s that registered by the Kyoshin-Net (NIED) [4] at the site of the University of Tsukuba. On the day, 12UD Pelletron tandem accelerator was in operation at 8 MV for  $^{41}\text{Ca}$  trial measurements by AMS. The electricity supply went out during the earthquake. The blackout lasted for 4 days, and we had to continuously stop the electric power for 2 days for hazard avoidance. We could not access our facility for the first week because of many aftershocks. Fortunately, there were no casualties by this earthquake in the facility. The 1 MV Tandetron accelerator at the facility did not have any serious damage because of its T type hard structure and it has worked properly after the earthquake.

## DAMAGE OF THE 12UD PELLETRON TANDEM ACCELERATOR

Fig.1 shows a cross-section drawing of the 12UD Pelletron tandem accelerator facility which is a vertical type. A main tank of the 12 UD Pelletron tandem accelerator is located from downstairs 4th floor to 7th floor in the accelerator tower. Fig. 2 shows a plane view of the 1st floor with two experimental rooms.

## Accelerator Tank

The accelerator tank was strongly shaken by the shock of the earthquake. Three shock prevention devices for the accelerator tank at the 7th floor were pushed out with breaking anchor bolts of 1 inch in diameter as shown in Fig. 3. Weight supports and jacks at the 4th floor were moved as nearly taken off as shown in Fig. 4. All high voltage accelerating columns fell down in the accelerator tank. Fig. 5 shows the downed accelerating column in the tank at the bottom. Structures of the terminal shell and columns inside the tank were completely collapsed.

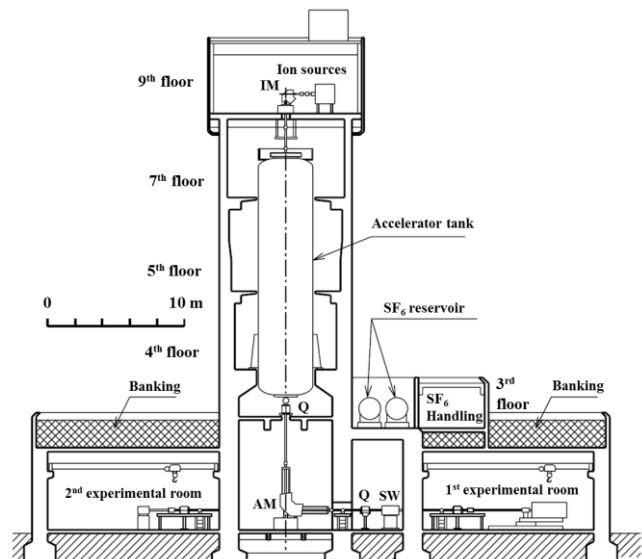


Figure 1: Layout of the 12UD Pelletron tandem accelerator facility at the University of Tsukuba.

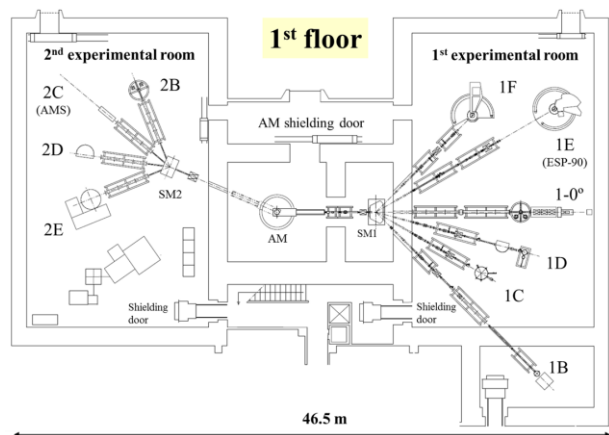


Figure 2: A plane view of the 1st floor at the facility

<sup>#</sup> ksasa@tac.tsukuba.ac.jp



Figure 3: Broken shock prevention device for the accelerator tank at the 7th floor. Anchor bolts of 1 inch in diameter for the shock prevention device were severed by the shock of the earthquake.

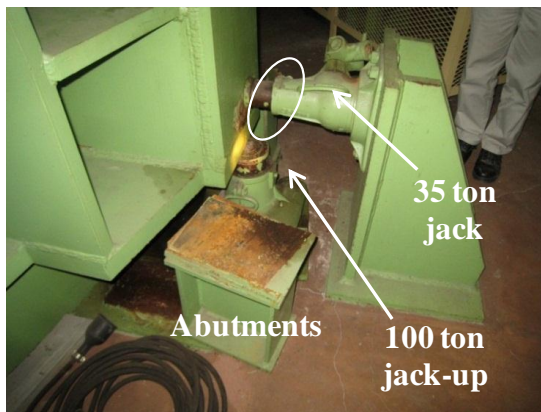


Figure 4: Moved weight supports and jacks at the 4th floor by the shock of the earthquake.



Figure 5: Collapsed accelerating column and terminal (the view from the 7th floor).

### *Ion Sources at the 9th Floor*

Two of three ion sources at the 9th floor were also seriously damaged by the earthquake. The anchor bolts of the Wien filter for the polarized ion source were destroyed by the earthquake. Finally, the Wien filter was moved 1 m

from the beam line by the earthquake and aftershocks for a month as shown in Fig. 6. Almost piping bellows between connected heavy loads were broken by shaking at the 9th floor. Ceramic columns of the AMS ion source were also broken. Water pressure gauges of the cooling water system were shaken and broken off by its root on the plumbing. A water spurt came out the polarized ion source. The inflection magnet weight of 4 tons at the 9th floor was moved 5 cm on the mount by the earthquake as shown in Fig. 7.

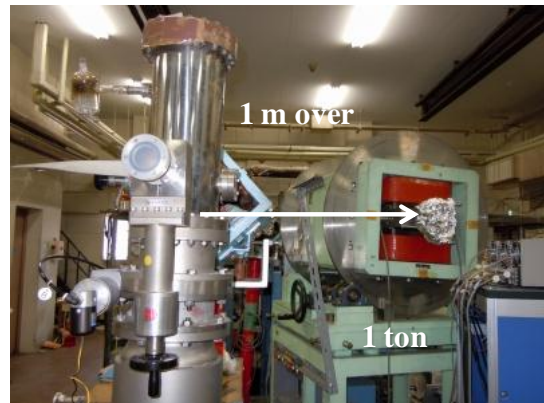


Figure 6: Broken Wien filter for the polarized ion source. The Wien filter was moved 1 m from the beam line after the earthquake and aftershocks.

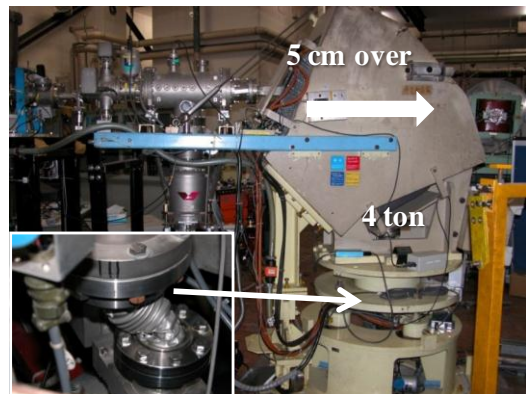


Figure 7: Moved inflection magnet at the 9th floor.

### *Experimental Rooms at the First Floor*

At the 1st floor, a  $\beta$ -NMR experimental magnet weight of 800 kg at the 1-F beam course was dropped from heights of 1.75 m with breaking a stepladder as shown in Fig. 8. Several tool racks also fell down in the facility (Fig. 9). Many magnets were moved and a number of joint bellows were broken as shown in Fig. 10. Many vacuum apparatuses such as turbo-molecular pumps and ion pumps were damaged at points around broken joint bellows. A shielding door motor was broken by the shock of the earthquake at the analyzer magnet room. Therefore, we could not access immediately in the analyzer magnet

room after the earthquake. Shielding concrete blocks at the analyzer magnet room came down to the floor.



Figure 8: Dropped  $\beta$ -NMR experimental magnet at the 1-F beam course of the 1st floor.



Figure 9: Fallen shelf at the 1-0° beam course.

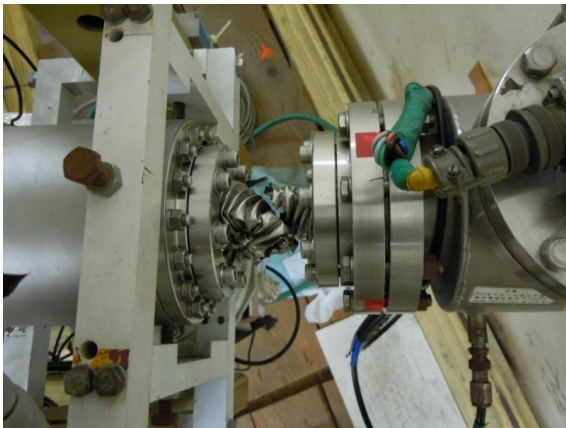


Figure 10: Broken joint bellows after the analyzer magnet of the 1st floor.

## EARTHQUAKE DISASTER RECONSTRUCTION PROJECT

We decided to shut down the 12UD Pelletron tandem accelerator in 2011. At present, we are planning to install a new middle-sized tandem accelerator at the 2nd experimental room instead of the broken 12UD Pelletron tandem accelerator since it is difficult to repair the previous one due to some boundaries in the building construction. A new accelerator system will consist of a horizontal type 6 MV Pelletron tandem accelerator, new 3 ion sources and the polarized ion source which will be moved from the 9th floor to a new experimental booth at the ground, an accelerator mass spectrometry system and an ion beam analysis system. High energy beam transport line will be connected from the 2nd experimental room to the present experimental facilities at the 1st experimental room. The new AMS system will be capable of measuring environmental levels of long-lived radioisotopes of  $^{10}\text{Be}$ ,  $^{14}\text{C}$ ,  $^{26}\text{Al}$ ,  $^{36}\text{Cl}$ ,  $^{41}\text{Ca}$  and  $^{129}\text{I}$ . The new IBA system will be equipped with a high-precision five-axis goniometer. The construction of the new accelerator system is scheduled in the spring of 2014.

### SUMMARY

The 12UD Pelletron tandem accelerator with a history of over 35 years at the University of Tsukuba was destroyed by the Great East Japan Earthquake in 2011. We decided to update the 12UD Pelletron tandem accelerator to the new 6 MV tandem accelerator. We have mapped out a strategy for reconstruction project. The 6 MV tandem accelerator will mainly be applied for AMS, IBA, beam irradiation research and nuclear physics. The beam delivery will start on September 2014.

### ACKNOWLEDGMENT

I would like to thank all my colleagues for their excessive hard work in post-quake recovery. I also acknowledge related businesses and other accelerator facilities for all their help, especially Hakuto Co., Ltd. Japan, National Electrostatics Corp. USA, MALT the University of Tokyo, RIBF Riken, RCNP Osaka University and Tokai tandem accelerator facility JAEA.

### REFERENCES

- [1] S. Seki, K. Furuno, T. Ishihara, Y. Nagashima, M. Yamanouchi, T. Aoki, T. Mikumo, J. Sanada, *Nucl. Instr. and Meth.* 184 (1981) 113.
- [2] K. Sasa et al., JACoW, HIAT09, TU-06, 2009, p. 49.
- [3] *Science*, Vol. 333, 8 July 2011, 154.
- [4] K-NET, the National Research Institute for Earth Science and Disaster Prevention (NIED), Japan. <http://www.kyoshin.bosai.go.jp/>.

# LONGITUDINAL BEAM MOTION IN THE KEK DIGITAL ACCELERATOR: TRACKING SIMULATION AND EXPERIMENTAL RESULTS

X.Liu<sup>1\*</sup>, T.Adachi<sup>2,3</sup>, S.Harada<sup>3</sup>, T.Iwashita<sup>4</sup>, K.Takayama<sup>1,2,4</sup>, T.Yoshimoto<sup>1</sup>

<sup>1</sup>*Tokyo Institute of Technology, Nagatsuta, Kanagawa, Japan*

<sup>2</sup>*Graduate University for Advanced Studies, Tsukuba, Ibaraki, Japan*

<sup>3</sup>*Tokyo City University, Todoroki, Tokyo, Japan*

<sup>4</sup>*High Energy Accelerator Research Organization (KEK), Tsukuba, Ibaraki, Japan*

## Abstract

Beam commissioning in the KEK Digital Accelerator, which is a small scale induction synchrotron (IS), has been conducted since the middle of 2011. Longitudinal beam motion in the induction synchrotron, utilizing induction cells (IC) for acceleration and confinement, is characterized as barrier bucket acceleration. A tracking code has been developed to understand the longitudinal motion affected by longitudinal space charge forces, considering programmed settings of confinement and acceleration voltage. This code, in which the trigger control scenario is fully implemented, calculates temporal evolution of momentum and phase of macro-particles. Beam commissioning results without acceleration and confinement are compared with simulation results.

## INTRODUCTION

The induction synchrotron concept for accelerating charged particles, was introduced by K.Takayama and his colleagues in 2000[1] and demonstrated using the KEK 12 GeV synchrotron[2] at High Energy Research Organization (KEK). Later this idea had been adapted to the booster ring, which is a rapid cycle synchrotron. For this purpose, necessary modifications and upgrades had been conducted over 3 years. Now it is officially called the KEK Digital Accelerator(KEK-DA). Its details are described in reference [3]. In addition, the ideas and basics behind the KEK-DA are well explained in K.Takayama’s text book [4], and the latest status will be presented in this conference.

In this paper, after a short introduction of the KEK-DA system with its layout, the model used to describe the longitudinal motion including longitudinal space charge forces will be discussed. Then the commissioning results and simulation results are shown to be well consistent with each other. Through extensive studies, it turns out that the momentum distribution in the longitudinal phase space is mainly determined by electric fields of the Einzel lens chopper [5] where several  $\mu s$ -long beam is chopped out of a 5 ms-long beam pulse extracted from the ECRIS. The simulations shows that this initial momentum distribution evolves through the low energy beam transport line from the ECRIS to the ring and the beam arrives at the ring with bump profiles both on the beam bunch head and tail. This property in the pulse profile have been observed in the ex-

periment. Further more experiments and simulation works have pursued how the profile evolves in the ring. The simulation will manifest what role space charge forces take in the temporal evolution of the phase space distribution, comparing with experimental data.

## OUTLINE OF KEK-DA

The KEK-DA complex consists of many subsystems just as other accelerator facilities. Fig.1 shows an overview of KEK-DA.

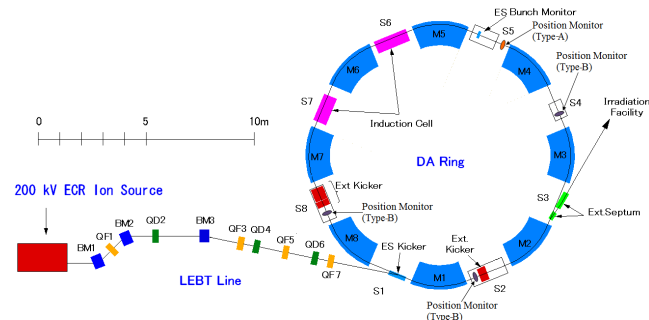


Figure 1: Layout of KEK-DA.

For the present beam commissioning, He<sup>1+</sup> beam is extracted from an Electron Cyclotron Resonance Ion Source(ECRIS)[6] and chopped by the Einzel lens chopper to be several  $\mu s$  beam bunch. The beam bunch is then accelerated to 200 keV by a post-acceleration column installed right after the chopper and guided through Low Energy Transport Line(LEBT). Electrostatic Kicker, installed at one of the drift section (S1 in Fig.1) of the ring, is used to kick the beam bunch on the ring orbit. 8 combined function magnets are installed in the ring to bend the beam and confine it transversely. Induction cells are installed at S6 and S7 section to provide longitudinal confinement and acceleration for the beam bunch. These induction cells are driven by switching power supply [3] powered by DC power supply. Trigger of pulse voltages for acceleration and confinement are fully controlled by the digital control system consisting of the FPGA and DSP[7] A combination of several extraction kickers and septum magnets is used for beam extraction.

\* liuxg@post.kek.jp

## LONGITUDINAL MOTION

### Acceleration Model

The longitudinal equation of motion in the KEK-DA is similar to but different from that of the traditional RF synchrotron. The equations used for a turn-by-turn track in simulations are[4],

$$(\Delta E)_{n+1}^j = (\Delta E)_n^j + Ze[V(\Delta t)_n^j - V_n^s] \quad (1)$$

$$(\Delta t)_{n+1}^j = (\Delta t)_n^j + (T_c)_{n+1}^s \eta_{n+1}^s \left(\frac{\Delta p}{p}\right)_{n+1}^j \quad (2)$$

Eq.1 describes the energy difference  $\Delta E$  for the specific particle with ID “j” to the synchronous particle which is supposed to always stay on the ideal orbit under the ramping magnetic field. In this equation, “n” is the turn number. Z is the charge state (here is positive 1 for He<sup>1+</sup>). e is the unit charge.  $V(\Delta t)$  is the voltage felt by the particle which has a time difference  $\Delta t$  from the synchronous particle.  $V_n^s$  is the required acceleration voltage for the synchronous particle at n-th turn. Eq.2 describes the time difference at n-th turn between a particle with ID j and synchronous particle.  $T_c^s$ ,  $\eta^s$  are revolution time and so-called slippage factor ( $\eta = \frac{1}{\gamma^2} - \frac{1}{\gamma_t^2}$ , where  $\gamma$  is relativistic factor and  $\gamma_t$  is transition gamma), respectively.

As seen in Fig.1, the induction cells with a finite physical size are located at different places. However, the acceleration gap size of each cell is so small that the transit time is negligible. In the model described by the above equation of motion, the acceleration or confinement voltage is assumed to be applied instantly as a  $\delta$ -function like kick. The observation points are chosen to be just in front of the induction cells. As a result, as in the above equations, the energy difference (Eq.1) should be calculated first then this information could be used for calculating new parameters  $T_c$ ,  $\eta$  and  $\frac{\Delta p}{p}$  for Eq.2.

### Longitudinal Space Charge Forces

Injection energy of the KEK-DA is quite low, for example, for He<sup>1+</sup> with the injection energy of 200 keV,  $\beta \approx 0.01$ . Therefore, space charge effects should be significant. The longitudinal space charge forces are evaluated assuming a round beam in a cylindrical chamber model. This model is commonly used, for instance in[8]. The electrical field along the orbit coordinate  $s$  is written by,

$$E_s = \frac{Z_0 g}{4\pi(\beta\gamma)^2 c} \frac{\partial I}{\partial t} + E_W \quad (3)$$

where  $Z_0 = 377\Omega$ , and  $g$  is geometric factor,  $I$  is the beam current,  $c$  is the speed of light.  $E_W$  is the electric field on the chamber wall which is simply ignored in the simulation. In the simulation, an FFT method[8] is used to calculate the electric field instead of directly calculating from Eq.3.

The equation of motion describes the beam motion in a discrete form. This is an exact form without approximation because the induction acceleration devices are localized

at specific positions. Meanwhile the longitudinal space charge forces continuously affect the longitudinal motion of particle. Strictly speaking, the differential equation of motion for the system perturbed with space charge forces must be integrated. Instead of the integration, the differential equation is approximated in the discrete form, where the path length is divided into multiple segments with a small distance and the particle distribution is updated after each segment. Its extreme case corresponds to Eq.1 with a single kick resulting from the space charge forces,  $E_s C_0$ , where the number of segment is just 1; in the other extreme case, the circumference is divided into infinite number of segments. The latter case is unrealistic and we have to choose a finite number of segments.

### Simulation Model

**Justification** Here by justification two things are expected: first, the electric field for a chosen profile should provide the same result as calculated from Eq.3; second, some optimization of the parameters is needed to prevent from producing wrong results. Some common parameters required in Eq.3 and in simulation are assumed as in Table 1. Note that the number of macro-particle and number of bin in Table 1 are parameters used in the FFT method and have been optimized by choosing different combinations of the two so that the electric field in the regions of interest becomes the mathematically calculated value.

Table 1: Parameters Used for Justification

| Inj V     | g                   | I          |
|-----------|---------------------|------------|
| 200 keV   | 6.4161              | 90 $\mu$ A |
| beta      | N of macro-particle | N of bin   |
| 0.0103197 | 10000               | 500        |

Here a trapezoidal profile with 80 ns rise and fall time for beam current is assumed as shown in Fig.2. The longitudinal electric field is plotted together(red line). With these parameters, the calculation result from Eq.3 is  $E_s = 6.78$  V/m. Thus, within the rise region and fall region of this trapezoidal profile, the electric field is 6.78 V/m. In the FFT method, time length of 12  $\mu$ s is chosen and divided into 500 bins, and filled with 10k macro-particles that produce the same trapezoidal profile. Fig.2 shows that the peak electric field is almost the same as that calculated by Eq.3. In order to obtain more accurate electric fields in these regions, a larger bin number and accordingly, a larger macro-particle number seem to be required. However, that would increase the computation time; therefore a compromise must be made between the computation time and resolution.

**Initial distribution** As mentioned,the pulse length of the beam from the ECRIS before being chopped is about 5 ms. For He<sup>1+</sup> at 200 keV, the revolution time just after injection is about 12  $\mu$ s(given that KEK-DA’s main ring has

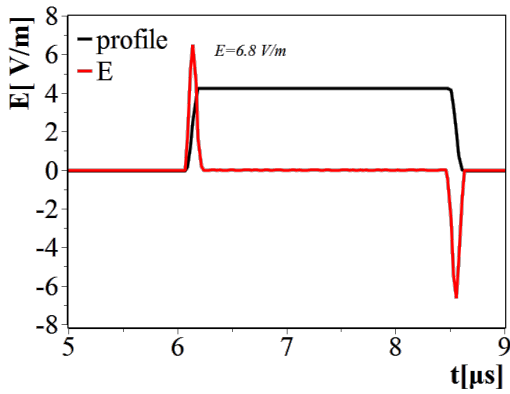


Figure 2: Justification of the FFT method.

a circumference of 37.7 m). Usually a 3 μs beam bunch is used in beam commissioning. The initial distribution includes a pulse profile of the bunch and a momentum distribution associated with this pulse profile. It has been realized that momentum modulation is induced at the head and tail of the beam bunch when the beam is chopped by the Einzel lens chopper[9]. A momentum distribution similar to the simulation results in Ref.[9] is assumed here.

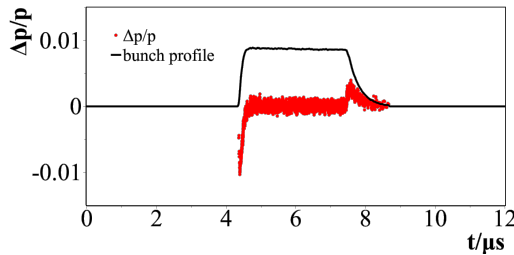


Figure 3: Initial distribution for simulation.

The black line is assumed pulse profile, which corresponds to the bunch signal captured by the wall current bunch monitor in experiments. Note that the l.h.s is bunch head and r.h.s is bunch tail. The red scattering dots are macro-particles in the phase space, where the bunch head part has a negative momentum deviation with a maximum of -1% while the tail part 0.5%. In addition, an “intrinsic” momentum deviation of  $\sigma = 0.05\%$  and  $2\sigma$  cut-off is assumed.

The distribution is assumed just after the post-acceleration column after which the bunch has a kinetic energy of 200 keV. Though at this momentum, there’s no good method to confirm the momentum distribution directly by measurement, the beam current and profile can be measured at the test stand with a Faraday cup which is 2.5 meters down from the post-acceleration column.

Fig.4 is the measurement result by Faraday cup.

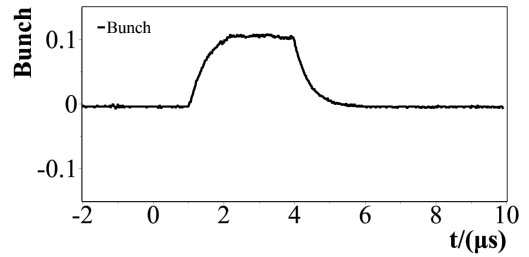


Figure 4: Bunch signal by Faraday cup.

## COMPARISON BETWEEN EXPERIMENTAL RESULTS AND SIMULATION

### Bunch Profile Evolution

Fig.5 shows turn-by-turn plots by plotting all the bunch signals one after another for a 3 μs He<sup>1+</sup> under the constant magnetic field without confinement or acceleration.

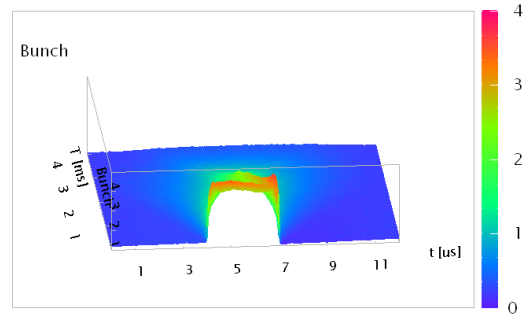


Figure 5: Mountain view of the observed bunch profile.

The horizontal axis,  $t[\mu s]$  is time position within one revolution(single bunch signal). The second axis,  $T[ms]$ , denotes the time from the injection for each bunch signal, corresponding to different turn number. The third axis is the beam current intensity. Fig.5 shows that the bunch structure gradually decays to fill the ring within 4 ms as the intensity drops.

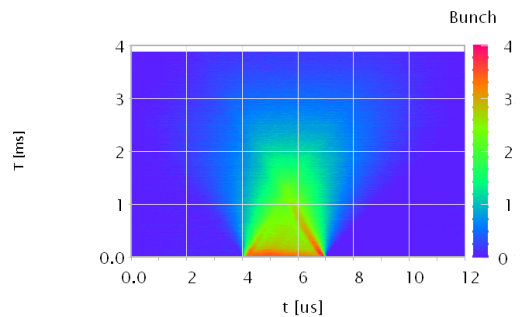


Figure 6: Projection of Mountain view.

Fig.6 shows the projected view of Fig.5 to the plane of the first and second axis(hereafter called time-turn plane).

The projection view is much easier to show the result thus will be frequently used later.

As seen in both Fig.5 and Fig.6, there's a peak at bunch head (l.h.s) and another one at the bunch tail(r.h.s). Moreover, the peak at the bunch tail survives for a longer time period and sharper than that at the bunch head. Besides, in fact for this result, those signals from the bunch monitor at the beginning are saturated. So peaks on bunch head and tail are much higher. However, the Faraday Cup measurement shows no such peaks.

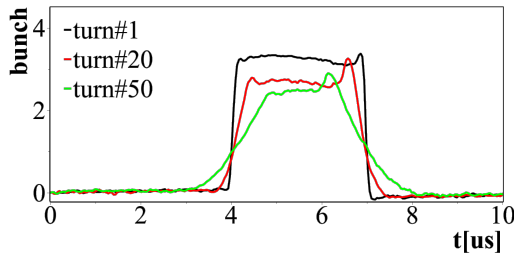


Figure 7: turn#1, #20,#50 of the experiment for  $3\mu\text{s He}^{1+}$  bunch,  $I = 50\mu\text{A}$ .

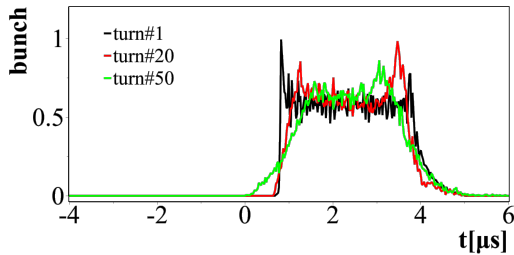


Figure 8: simulation with longitudinal space charge forces.

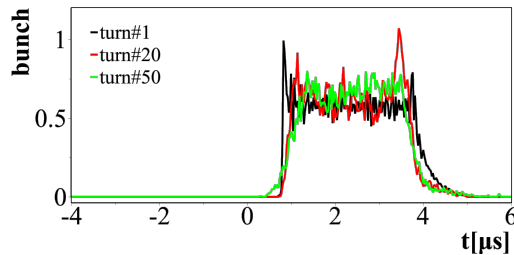


Figure 9: simulation without longitudinal space charge forces.

Fig.7 shows pulse signals of turn#1, #20 and #50 for the same experiment in Fig.5 and Fig.6. The beam current for this experiment was about  $50\mu\text{A}$ . This figure shows how the bunch profile evolves. Fig.8 shows the simulation result assuming a beam current of  $I = 50\mu\text{A}$ , taking into account of longitudinal space charge forces. Except for the first turn (which is supposed to be like the first signal on oscilloscope in experiment), the typical temporal evolution of the bunch profile, where the bunch tends to diffuse in the time axis and two peaks emerge at both ends of the bunch, is well

reproduced. The difference, if noticed, should come from the difference between initial distribution assumed in Fig.3 and that of the real beam bunch. For comparison, the simulation result without longitudinal space charge forces is shown in Fig.9. Compared with Fig.9, Fig.8 shows clearer peak formation and that the beam diffuse faster. The results on time-turn plane suggest the same observations as shown in Fig.10 and Fig.11.

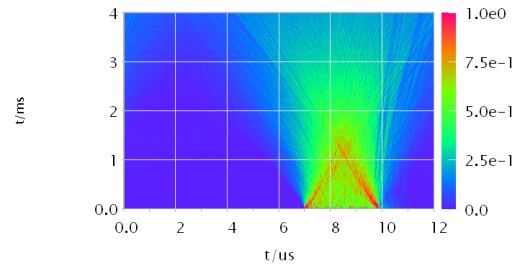


Figure 10: simulation with longitudinal space charge force.

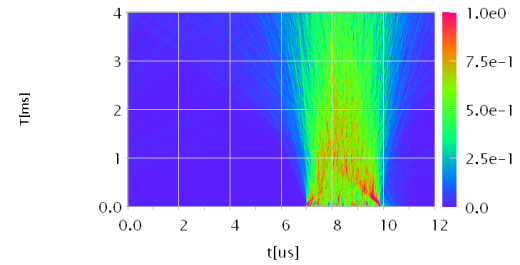


Figure 11: simulation without longitudinal space charge force.

The simulation without longitudinal space charge forces fails to reproduce the experimental result. On the contrary, the longitudinal space charge forces not only succeed in reconstructing the overall profile but also give the same cross point where two peaks finally meet, as seen from Fig.6 and Fig.10. The peak on the bunch head meet the bunch tail's at around  $1\text{ ms}$  after injection, or  $70 \sim 80$  turns after injection.

All these results suggest that longitudinal space charge forces are essential to understand how the bunch profile evolves like this.

When considering about longitudinal space charge forces, as indicated by Eq.3, higher beam current will have higher electric field. Comparisons between the experimental and simulation results including the longitudinal space charge forces for two beam currents of  $22\mu\text{A}$  and  $49\mu\text{A}$  are given in Figs.12, 13, 14, and 15.

In Fig.12 to Fig.15, they're different runs from that shown in Fig.10. However, the result of  $49\mu\text{A}$  is close to that of  $50\mu\text{A}$ . In present simulation, same intrinsic momentum deviation is assumed through all cases. In addition, the initial momentum deviation may depend on the beam current. These may explain why there exists slight difference between the experimental result and simulation

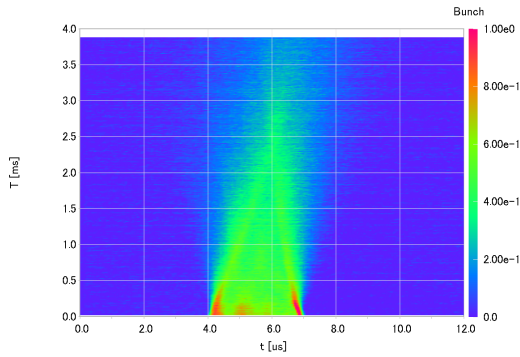


Figure 12: He<sup>1+</sup>, 22 $\mu$ A, experiment.

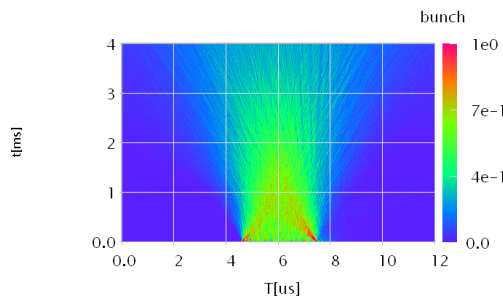


Figure 13: He<sup>1+</sup>, 22 $\mu$ A, simulation.

for 22  $\mu$ A. But as in all, both of the experimental results and simulation strongly support the fact that for higher beam current the bunch head peak and tail peak will meet earlier.

### The Role of Longitudinal Space Charge Force

It is understandable that the peak formation results partly from the initial momentum distribution as shown in Fig.3. Particles with negative momentum deviation in the bunch head move towards the positive direction in time, that is, the bunch tail. Because of the negative slippage factor,  $\eta$  (as  $\gamma < \gamma_t$ ). Particles with positive momentum deviation in the tail region will move towards the bunch head. Eventually, they will meet somewhere in the middle to form the cross point seen on Fig.6 and Fig.10. However, the simulation re-

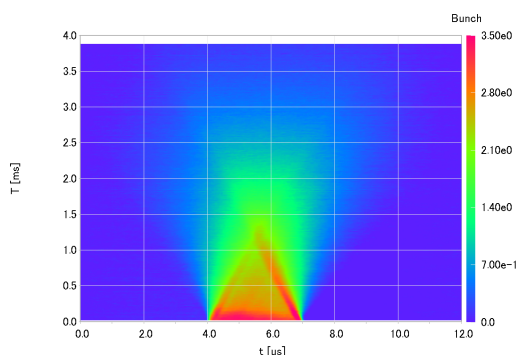


Figure 14: He<sup>1+</sup>, 49 $\mu$ A, experiment.

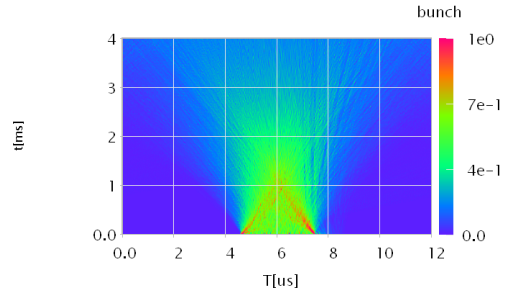


Figure 15: He<sup>1+</sup>, 49 $\mu$ A, simulation.

sult in Fig.11 shows that, without longitudinal space charge forces, these peaks dissipate quickly thus no apparent cross point.

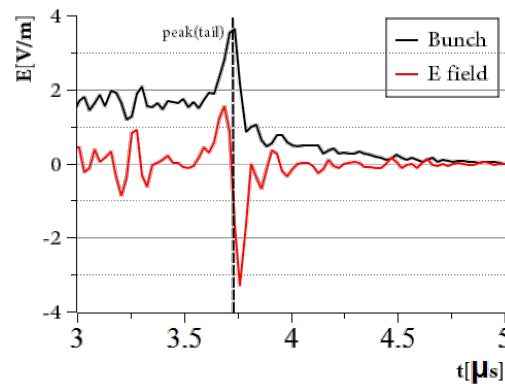


Figure 16: He<sup>1+</sup>, 49 $\mu$ A, tail part and associated electric field in simulation.

In order to explain the role of longitudinal space charge forces, Fig.16 shows the tail part of the bunch with electric field. At beginning, the peak comes into exist due to positive momentum deviation as just discussed. The dash line in Fig.16 marks the position of the peak. On the right side of the peak, the electric field is negative so that particles in this region will be kick down by the longitudinal charge forces in the phase space. If this field is large enough then these particles will have a negative momentum deviation and move to the right, making the bunch become longer, or bunch is spreading in the longitudinal direction. Because at the beginning the momentum deviation in this region is positive, so space charge forces make these particles slow down as they move to the left side. After that, once particles fall into negative momentum deviation region, they will move to the right and make the bunch spread. Without longitudinal space charge forces, bunch will only spread according to the momentum spread, which is much slower as seen in Fig.9. If only the electric field on the right side of the peak the beam is considered, the bunch will spread as discussed and the peak will disappear quickly. However, as noted in Fig.16, the electric field due to longitudinal space charge forces is positive, that is, this field will kick particles in that region upward. Because these particles have a

larger momentum deviation than the intrinsic momentum deviation, new peak will emerge just as the peak formation happens at the very beginning. The total effect of the electric field on both sides of the peak is that the peak lasts for a longer time. Because the electric field on the left side of the peak is smaller than the right, the peak will become smaller and appear not so obvious, as seen in Fig.12 and Fig.13. For higher beam current, the peak will last for such a longer time that two peaks on the bunch head and tail will merge when they meet each other, forming a cross point, as seen in Fig.14 and Fig.15. How fast a particle will move in phase space depends on its momentum deviation. As a result, in case of higher beam current, due to the role of the electric field on the left side of the peak shown in Fig.16, affected particles will have a larger momentum deviation and move faster towards the beam center. That's why bunch with higher beam current has an earlier cross point when comparing Fig.12 and Fig.14.

## CONCLUSION AND FUTURE WORK

As in short, the Einzel lens chopper induces a momentum modulation on the bunch head and tail while chopping the beam. Then longitudinal space charge forces affect a great deal of the bunch profile evolution and peak formation. Because KEK-DA is an induction synchrotron capable of accelerating ion beam from a very low energy to relatively high energy, the space charge force is one of the most important topics in the beam physics related to it. More studies and results where space charge force plays an essential role could be anticipated.

The beam commissioning will go on and some application studies by using KEK-DA would follow. As for the simulation, which is now short of motion of transverse direction, will include it to be a more useful tool for beam commissioning and analysis.

## ACKNOWLEDGEMENT

This work is supported by a Grant-In-Aid for Scientific Research (A) (KAKENHI NO.23240082).

## REFERENCES

- [1] K.Takayama, and J.Kishiro, Induction Synchrotron, Nucl. Inst. Meth. Phys. Res. A 451, 304 (2000).
- [2] Takayama, K., Arakida, Y., Dixit, T., Iwashita, T., Kono, T., Nakamura, E., Otsuka, K., et al. (2007). Experimental Demonstration of the Induction Synchrotron. Physical Review Letters, 98(5), 8-11.
- [3] T. Iwashita et al., KEK Digital Accelerator, Phys. Rev. ST-AB 14, 071301 (2011). And K.Takayama et al., in this conference.
- [4] K.Takayama and R.J.Briggs (Eds), Induction Accelerators, (Springer, 2010).
- [5] T. Adachi, T. Arai, K. W. Leo, K. Takayama, and A. Tokuchi, A Solid-State Marx Generator Driven Einzel Lens Chopper, Rev. Sci. Instrum. 82, 083305 (2011).
- [6] Leo Kwee Wah, K.Takayama, T.Arai, et al., Permanent Magnet ECRIS for the KEK Digital Accelerator, Proceedings of 19th International workshop on ECR Ion Sources, August 23rd -26th, 2010 Grenoble, France, Pg. 150 (2010).
- [7] S.Harada, Ms. Thesis (Tokyo City University) (2011).
- [8] MacLachlan, J. A., Longitudinal Phase Space Tracking With Space Charge and Wall Coupling Impedance, FermiLab Note, FN-446, (1987).
- [9] K.W.Leo, Doctor Thesis(The Graduate University For Advanced Studies)(2012).

# FEEDBACK OF SLOW EXTRACTION IN CSRm\*

J. Shi<sup>1,2</sup>, J. C. Yang<sup>1</sup>, J. W. Xia<sup>1</sup>, Y. J. Yuan<sup>1</sup>, J. Li<sup>1,2</sup>, W. P. Chai<sup>1,2</sup>

1 Institution of Modern Physics, Chinese Academy of Sciences, Lanzhou 730000, China

2 Graduate University of Chinese Academy of Sciences, Beijing 100049, China

## Abstract

The transverse tune of the beam in the synchrotron will fluctuate due to the quadrupole current ripple, which lead the spill ripple through the variation of the separatrices area. In order to reduce the ripple of the spill, a pair of fast response quadrupole (FQ) is adopted to compensate the tune ripple caused by other quadrupoles. After using the FQ feedback, the amplitude of the spill ripple within 800Hz has been reduced to 1/10 times from the normal mode. This method will be used in the HITFiL (Heavy Ion Therapy Facility in Lanzhou).

## INTRODUCTION

The CSRm [1] is the main cooler storage ring in the national laboratory of heavy ion accelerators in China. The slow extraction [2] has been realized in CSRm in June 2008. In order to suppress the spill ripple which modulated by the quadrupole power ripple, a group of fast response quadrupole has been adopted in the synchrotron. The spill structure is improved greatly compare with the normal mode.

## THE MECHANISM OF SLOW EXTRACTION

The RF-Knock Out [3] slow extraction method is adopted in CSRm. The work point of the synchrotron has be set to near the 1/3 resonant line, then the phase space is divided into 2 parts by resonant sextupoles. The particle is stable until it reaches the unstable area by transverse RF. The emittance of the stable area is described as [4]:

$$E_{stable} = 48\sqrt{3}\pi \frac{q^2}{S^2} \quad (1)$$

Where,  $q = Q_x - Q_{res}$  is the difference between the particle tune and the resonant tune. In ideal situation the q keep constant during the extraction process, actually, the current of the quadrupoles will fluctuated with the external power grid. The tune of the particle which lies on the strength of the quadrupoles in the synchrotron will fluctuated, i.e., the q will fluctuated with the external power grid, which cause the stable area fluctuating. Since the emittance of the beam increased smoothly, the stable area fluctuation will bring the spill ripple. If the emittance growth rate is less than the fluctuation of the stable area, the spill will appear discontinuity [4].

## THE NORMAL MODE OF SLOW EXTRACTION IN CSRm

### Status of Normal Mode

Figure 1 shows the experiment result of normal mode in CSRm. The duration of the extraction time is set as 5 seconds. As one can seen in the figure,

- the spill ripple is large, and there is no beam extraction in the later part; The spill is not continuous but a series linear peak;
- The spill ripple in 50Hz and its harmonic under 250Hz is visible;

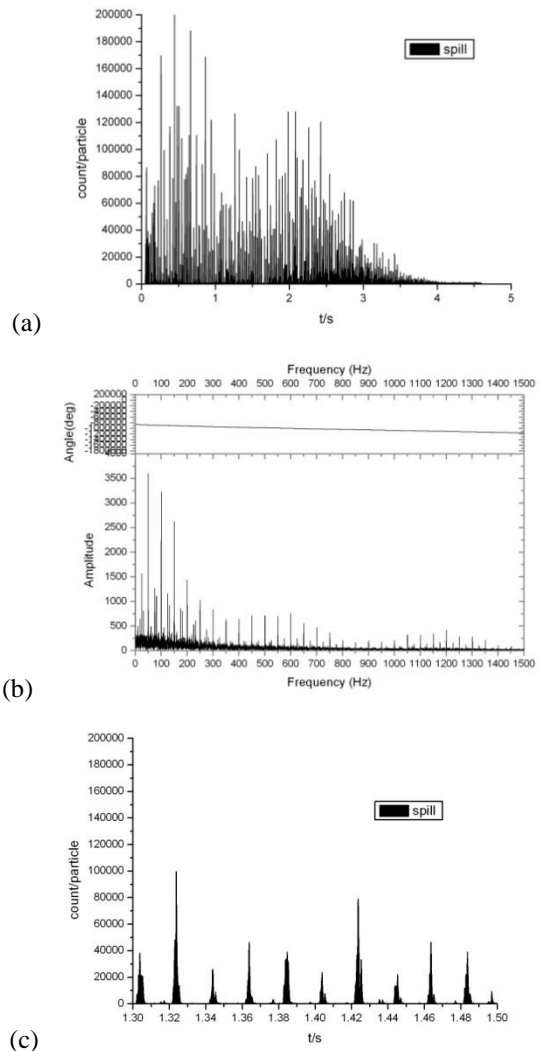


Figure 1: Spill in normal mode (sample rate is 10 kHz). (a) Structure of one spill, (b) The FFT of one spill, (c) Detailed spill structure in 1.3s-1.5s.

\*Work supported by State Key Development Program of Basic Research of China (2010CB834204)  
shijian@impcas.ac.cn

Analysis

The emittance of the particle growth with the transverse RF voltage until it reaches  $E_{stable}$ , but for the actual cases, the stable area changes its size with the quadrupole magnet power ripple, so maybe the particles reach the unstable area with the emittance larger than  $E_{stable}$ , and the stable area will be reduced in the rest power ripple cycle, then the spill ripple generated. Since the particle density in the phase space get smaller and smaller in a extraction cycle, the spill intensity will be reduced with time (as shown in Fig. 2(a)). The amplitude modulation method can be used to overcome this problem [5] [6].

The main ripple of the spill is 50 Hz and its harmonics, which is consistent with the quadrupole power ripple in the actual machine commissioning.

**THE SLOW EXTRACTION WITH FEEDBACK**

*The Mechanism of Feedback*

In order to compensate the affection of the quadrupole power ripple, many works have been done in HIMAC, such as using the AM modulation feedback [7], keep the tune of the beam away from the resonant line [8], and so on. Fig.3 is the schematic diagram of the feedback control loop in CSRm. A pair of fast quadrupole (FQ1, FQ2 in Fig.2) has been adopted to compensate the fluctuation of the work point in CSRm. The ionization chamber will monitor the intensity of the spill real time. When the intensity deviate from the theoretical intensity (reference value), the FQ will change the work point of the synchrotron through the current strength to keep the spill intensity unchanged. In other words, the work point fluctuation will be compensated by FQ to make the spill uniform. Table.1 shows the parameters of the FQ. The ceramics vacuum chamber is adopted for the FQ to meet the fast response.

Table 1: parameters of the FQ and transverse RF

| Element | Number | Strength | Rise Time             |
|---------|--------|----------|-----------------------|
| FQ      | 2      | 0.23T/m  | 170T/ms <sup>-1</sup> |
| RF      | 1      | 15V/cm   | -                     |

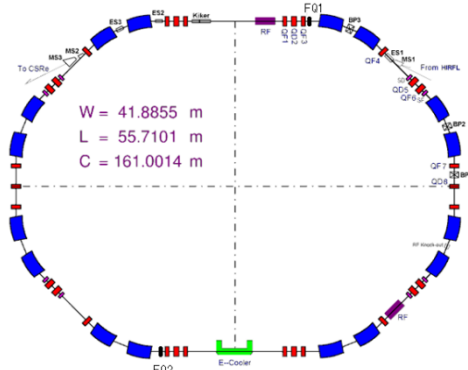


Figure 2: Layout of FQ, RF-KO.

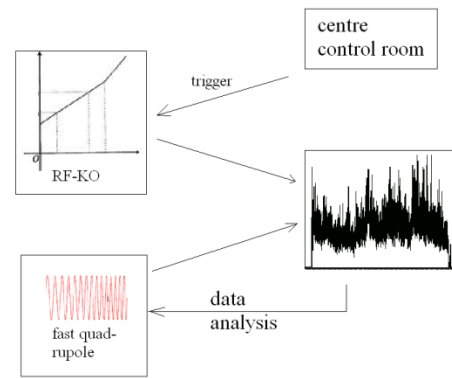


Figure 3: Schematic diagram of feedback.

*Result and Analysis*

Figure 4 is the spill structure and corresponding analysis. As seeing from the figure,

- The time structure of the spill has been improved a lot compared to the normal mode, though obviously there are still many spikes. Because the reference intensity is too larger, the spill time is less than the set time (5 seconds).
- As one can seen from the Table.1, the 370 Hz and below ripple will be suppressed, but actually the spill ripple below 800 Hz has successfully been suppressed to the 1/10 of the normal mode (as shown in Fig.4b). That is because the fast quadrupole does not need to reach the extreme value, so the response frequency can exceed 370 Hz. The time needed from the spill intensity signal be measured and the spill structure been changed by the FQ is nearly 1 ms, so the spill ripple near 1 kHz is larger than normal mode.
- The blank gap between the spikes has been disappeared, but there are still many spike in the spill.

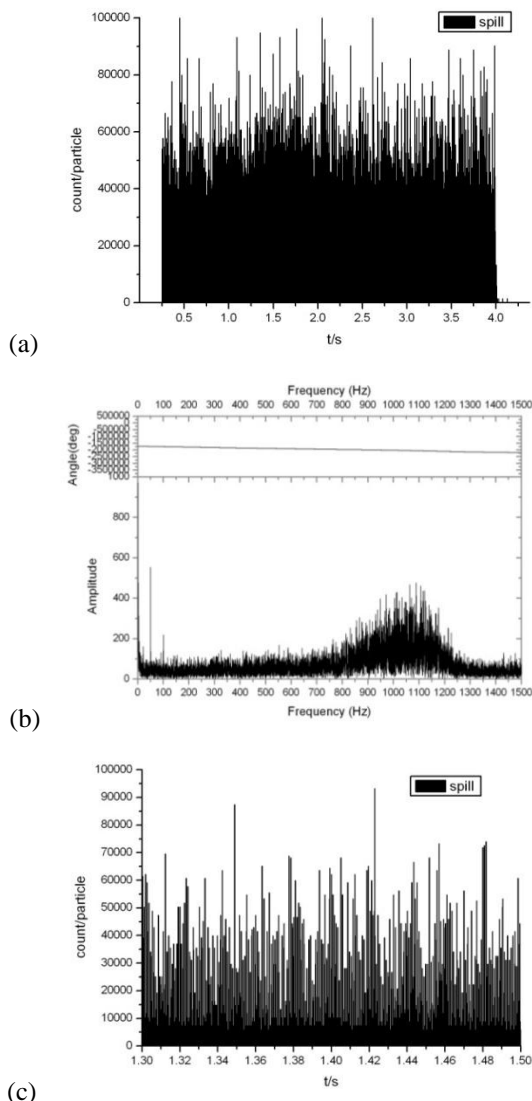


Figure 4: Spill in feedback mode(sample rate is 10 kHz). (a) Structure of one spill, (b)FFT of one spill, (c) Detailed spill structure in 1.3s-1.5s.

### CONCLUSION

After the FQ has been adopted in the CSRm, the spill ripple has been suppressed greatly. Because of the delay of the FQ action, the spill is not smooth enough. The thickness of the lamination steel is 0.5 mm, to reduce the delay time of the fast quadrupole, a new pair of FQ with the lamination steel thickness of 0.2 mm is under consideration. All in all, the quadrupole power supply ripple is too large, the fundamental method is to reduce the power ripple of the quadrupoles.

### REFERENCES

- [1] Xia J W, Zhan W L, Wei B W, et al. Nuclear Instruments and Methods in Physics Research A, 2002, 11–25.
- [2] YUAN You-jin, SONG Min-tao, DONG Jin-me, et al. HIGH POWER LASER AND PARTICLE BEAMS, 2005, 17(2)275-278.
- [3] Noda K, Furukawa T, Shibuya S, et al. Nuclear Instruments and Methods in Physics Research A 492 (2002) 241–252.
- [4] Bryant P, Benedikt M, Badano L. CERN/PS 99-010 (DI), 1999.
- [5] T. Furukawa, K. Noda, M. Muramatsu, Global spill control in RF-knockout slow-extraction, Nuclear Instruments and Methods in Physics Research A 522 (2004) 196–204.
- [6] T. Furukawa, K. Noda, T.H. Uesugi, Intensity control in RF-knockout extraction for scanning irradiation, Nuclear Instruments and Methods in Physics Research B 240 (2005) 32–35.
- [7] Sato Shinji, Furukawa Takuji, Noda Koji, Dynamic intensity control system with RF-knockout slow-extraction in the HIMAC synchrotron, Nuclear Instruments and Methods in Physics Research A574 (2007) 226–231.
- [8] K. Mizushima, T. Shirai, T. Furukawa, Proceedings of IPAC'10, THPEB008.

# MULTIPHYSICS AND PRESSURE CODE ANALYSIS FOR QUARTER WAVE $\beta=0.085$ AND HALF WAVE $\beta=0.29$ RESONATORS\*

S. Miller<sup>#</sup>, M. Johnson, A Facco, Y. Xu, J. Binkowski,  
Facility For Rare Isotope Beams, Michigan State University, MI 48824, USA

## Abstract

The driver linac design for the Facility for Rare Isotope Beams (FRIB) at Michigan State University (MSU) makes use of four optimized superconducting radio frequency (RF) resonators to accelerate exotic ions to 200 MeV/ $\mu$ . The RF resonators were optimized using computer simulations for all expected physical encounters and corresponding electrical resonant frequency changes. Principal guidance from the ASME boiler and pressure vessel code (BPVC) were applied.

## INTRODUCTION

The FRIB, a new national user facility funded by the U.S. Department of Energy Office of Science to be constructed and operated by MSU, is currently being designed to provide intense beams of rare isotopes to better understand the physics of nuclei, nuclear astrophysics, fundamental interactions, and applications for society. The FRIB driver accelerator can accelerate all stable isotopes to energies beyond 200 MeV/u at beam powers up to 400 kW [1]. FRIB uses two 80.5 MHz  $\lambda/4$  quarter wavelength resonators (QWR) operate at  $\beta_{opt} = v/c = 0.041$  and  $0.085$  and two 322 MHz  $\lambda/2$  half wavelength resonators (HWR) operate at  $\beta_{opt} = 0.29$  and  $0.53$ ; Figure 1.

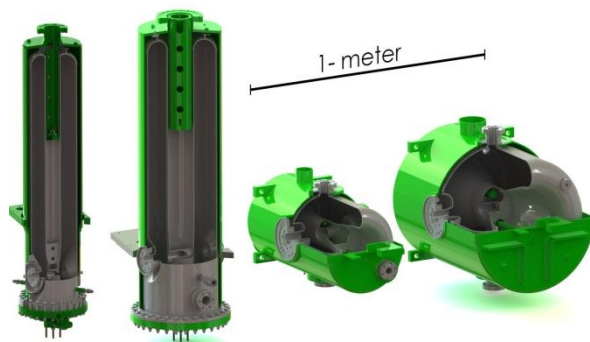


Figure 1: The FRIB Resonators. From left to right: 80.5 MHz  $\beta = 0.041$ , 80.5 MHz  $\beta = 0.085$ , 322 MHz,  $\beta = 0.29$ , 322 MHz  $\beta = 0.53$ .

## INTEGRATED ANALYSIS APPROACH

Project requirements state resonator designs must satisfy BPVC. The analysis for the 80.5 MHz  $\beta = 0.041$  has been completed and was presented at SRF2009 [2]. For the remaining 3 resonators, the first step of the

analysis was to validate the design using equivalence of the ASME Section VIII, Division 2. This analysis[3] yields pressure capability for 300K and 2K. Table 1 displays the material allowable stresses as established by ASME code, and the Table 2 displays the stress states that exist during the pressurization of the helium vessel.  $P_m$  is the general membrane stress allowable,  $P_l$  is the local membrane stress allowable, and  $P_l + P_b$  is the local plus the bending stress allowable.

Table 1: Resonator Material Properties [4], [5], [6]

| Material            | Temp (K) | Elastic Modulus (GPa) | Yield Strength (MPa) |
|---------------------|----------|-----------------------|----------------------|
| Niobium RRR250      | 295      | 103.0                 | 38                   |
| Niobium RRR250      | 4        | 104.0                 | 372                  |
| Niobium-45 Titanium | 295      | 62.1                  | 475                  |
| Niobium-45 Titanium | 4        | 68.2                  | 680                  |
| Grade 2 Titanium    | 295      | 106.9                 | 275                  |
| Grade 2 Titanium    | 4        | 118.8                 | 560                  |

Table 2: Resonator Stress Allowable [4], [5], [6]

| Material            | Temp (K) | $P_m$ (MPa) | $P_l$ (MPa) | $P_l + P_b$ (MPa) |
|---------------------|----------|-------------|-------------|-------------------|
| Niobium RRR250      | 295      | 25          | 38          | 38                |
| Niobium RRR250      | 4        | 248         | 372         | 372               |
| Niobium-45 Titanium | 295      | 226         | 340         | 340               |
| Niobium-45 Titanium | 4        | 450         | 680         | 680               |
| Grade 2 Titanium    | 295      | 143         | 214         | 214               |
| Grade 2 Titanium    | 4        | 375         | 560         | 560               |

The second step verified the resonator tuning sensitivity, tuning range, and tuning force. The simulation was also used to determine maximum stresses in the resonator and stiffen the resonator as needed to achieve the required tuning range.

The next step of the integrated approach was to determine the resonators helium pressure sensitivity. If the pressure sensitivity was found to be too high, stiffeners were added accordingly.

The final step of the integrated analysis was to compute the Lorentz Force Detuning (LFD). The LFD value was compared to the target goal and if too high design changes were necessary.

\*Work supported by US DOE Cooperative Agreement DE-SC000061  
#millers@frib.msu.edu

**Requirements**

The four resonator types share a common set of mechanical requirements:

- Satisfy Elastic Stress Analysis Method at 2.0 ATM for 300K
- Capable of sustaining tuning stresses generated at maximum tuning range and pressure
- Pressure sensitivity between +/-4Hz/torr
- LFD >-4Hz/(MV-m)<sup>2</sup>

**Quarter Wave Resonator**

The  $\beta=0.085$  resonator (shown in Figure 2 with labels) underwent pressure simulation. The first step of the process was to apply stress classification lines (SCLs) to the expected high stress areas of the resonator. Figure 3 display the stress line locations on the  $\beta=0.085$  resonator. High stress regions on this resonator are predominantly interface points. These include the short plate to inner conductor interface, short plate to outer conductor interface. Other areas include port interface to the outer conductor and the helium vessel.

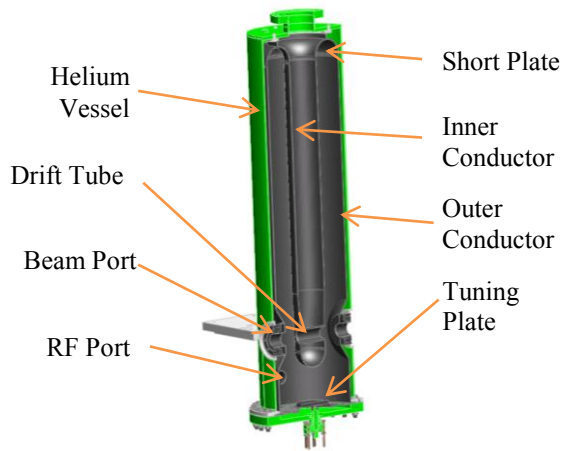


Figure 2: Labeled  $\beta=0.085$  Resonator.

The next step in the pressure simulation was to apply pressure to the interior surface on the helium vessel and the exterior surfaces of the cavity. Figure 3 displays the pressure areas of the  $\beta=0.085$  resonator.

After the pressure has been applied, the stress at each of the SCLs is evaluated. The pressure is increased until one of the SCLs exceeds the limits established by the Elastic Stress Analysis Method for 300K and 2K material properties. The last point where the SCL satisfies the Elastic Stress Analysis Method establishes the pressure capability at the material properties temperature. The  $\beta=0.085$  resonator design achieved a 300K pressure capability of 2.2 ATM and a 2K pressure capability of 15 ATM. Figure 4 displays the equivalent stress plot at a high stress location near the beam port at 300K. Figure 5 shows its corresponding SCL plot through the wall thickness.

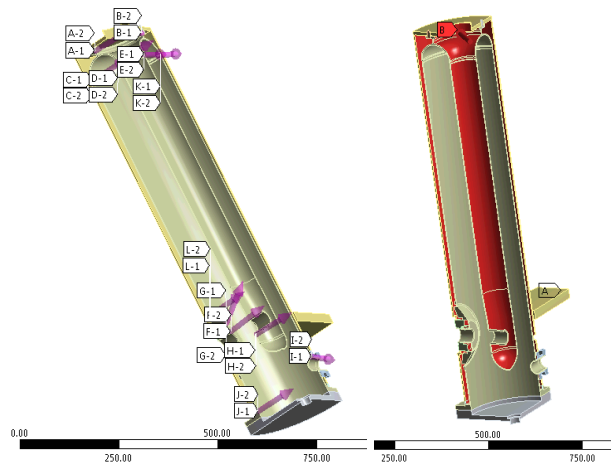


Figure 3:  $\beta=0.085$  Resonator Stress Line Locations and Resonator Boundary Conditions (Pressure Area in Red).

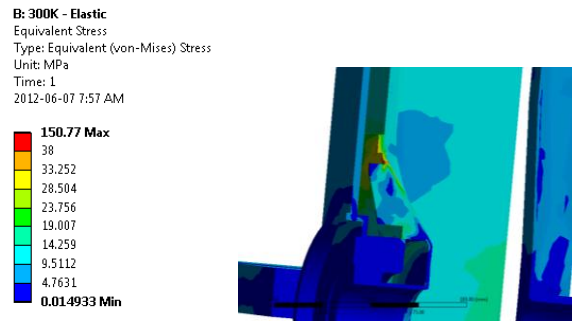


Figure 4:  $\beta=0.085$  Resonator High Stress Location.

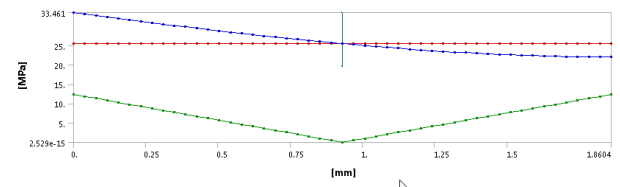


Figure 5:  $\beta=0.085$  Resonator SCL Result (Pm=Red, Pb=Green, Pl+Pb=Blue).

The next phase of integrated testing was to find the tuning parameters for the  $\beta=0.085$  resonator. The first step of this process was to find the tuning sensitivity. On the  $\beta=0.085$  resonator, a tuning plate is present on the bottom of the resonator (See Figure 2) and is actuated inwards and outwards to adjust the frequency. This adjustment results in 3.2 kHz/mm shift on the resonator. With a tuning range of +/- 10 kHz required for this resonator, this requires 3.125 mm of adjustment, inward and outward. Figure 6 displays the stress generated on tuning plate at 4 mm upward adjustment at 2K, the temperature at which tuning would takes place. The tuning plate is capable of the required tuning range without yield through its thickness.

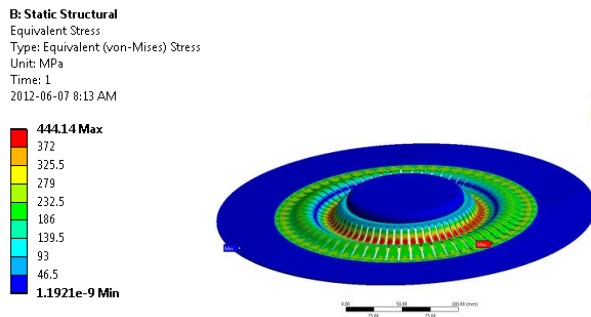


Figure 6:  $\beta=0.085$  Resonator Tuning Plate Stress.

The third step of integrated analysis was to find the pressure sensitivity. This was performed by applying pressure (1 ATM) to the same surfaces shown in Figure 3, and simulating the frequency shift due to this pressure. Figure 7 displays the deformation due to the pressure application, this deformation results in a -1.4 Hz/torr frequency shift. This falls within the requirement for pressure sensitivity.

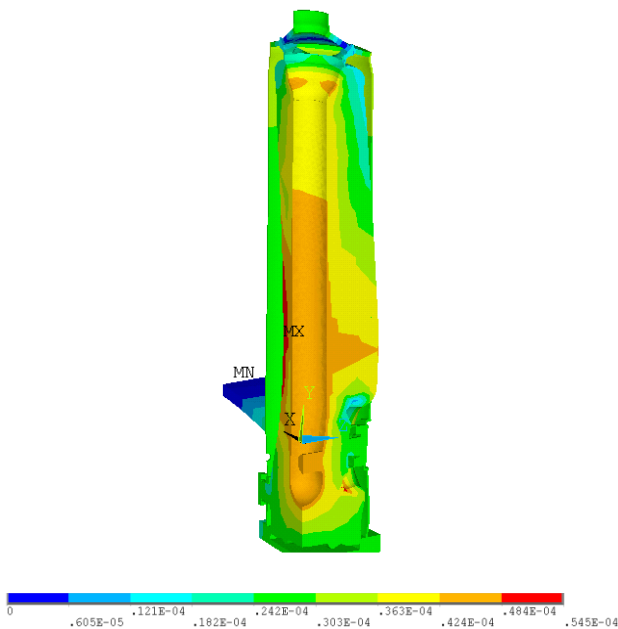


Figure 7:  $\beta=0.085$  Resonator Helium Pressure Response.

The last step of the integrated analysis for the  $\beta=0.085$  was to compute the LFD value. This simulation used the same model as the pressure sensitivity; however, instead of pressure loads being added, Lorentz Forces are computed and applied to the model. In the same fashion as the pressure sensitivity, the frequency shift is determined due to this force. Figure 8 depicts the deformed shape of the  $\beta=0.085$  resonator due the Lorentz Force. This plots displays the high electric field regions pulling towards each other, predominantly on the beam port and drift tube areas. Conversely, the magnetic field regions are pushing outward. From this plot it was found the LFD value for this resonator was  $-0.7 \text{ Hz}/(\text{MV}\cdot\text{m})^2$ . This meets the goal of being greater than  $-4 \text{ Hz}/(\text{MV}\cdot\text{m})^2$ .

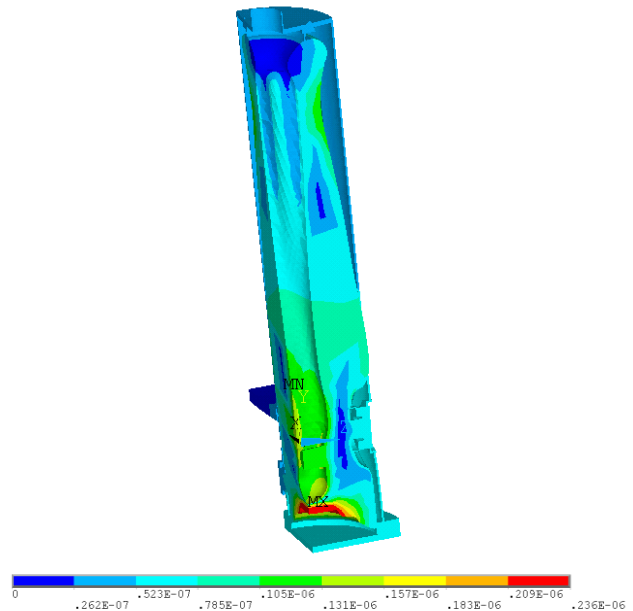


Figure 8:  $\beta=0.085$  Resonator LFD Response.

### Half Wave Resonator

The  $\beta=0.29$  resonator (shown in Figure 9 with labels) underwent pressure simulation. The first step of the process was to apply stress classification lines (SCLs) to the expected high stress areas of the resonator. Figure 10 displays the stress line locations on the  $\beta=0.29$  resonator. High stress regions on this resonator are predominantly interface points. These include the short plate to inner conductor interface, short plate to outer conductor interface. Other areas include port interface to the outer conductor and the helium vessel.

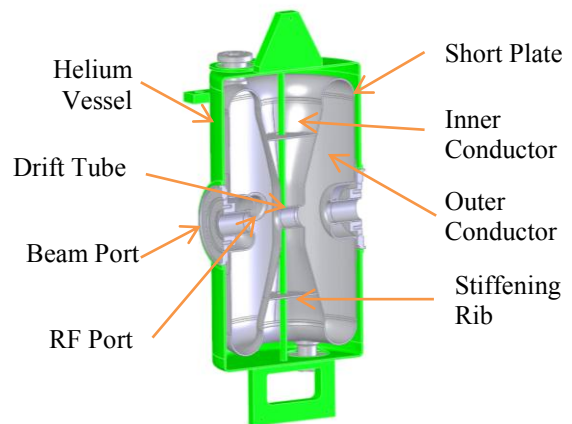


Figure 9:  $\beta=0.29$  Labeled Resonator.

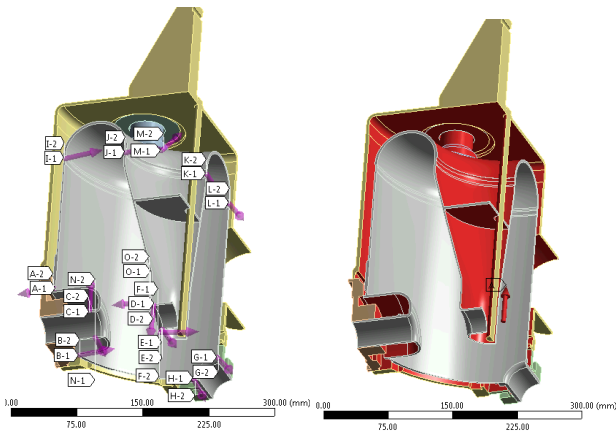


Figure 10:  $\beta=0.29$  Resonator Stress Line Locations and Resonator Boundary Conditions (Pressure Area in Red).

The next step in the pressure simulation was to apply pressure to the interior surface on the helium vessel and the exterior surfaces of the cavity. Figure 10 displays the pressure areas of the  $\beta=0.29$  resonator.

After the pressure has been applied, the stress at each of the stress lines is evaluated. The pressure is increased until one of the SCLs exceeds the limits established by the Elastic Stress Analysis Method for 300K and 2K material properties. The last point where the SCL satisfies the Elastic Stress Analysis Method establishes the pressure capability at the material properties temperature. The  $\beta=0.29$  resonator design achieved a 300K pressure capability of 2.2 ATM and 2K pressure capability of 20 ATM. Figure 11 display the equivalent stress plot at a high stress location for 300K and Figure 12 shows its corresponding SCL plot through the wall thickness.

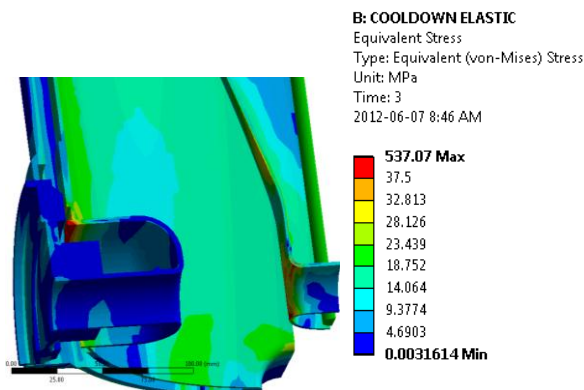


Figure 11:  $\beta=0.29$  Resonator High Stress Location.

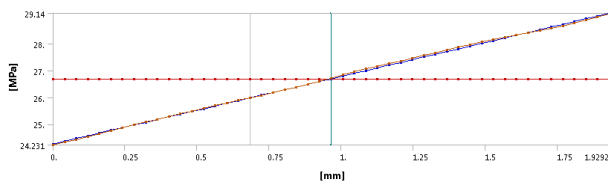


Figure 12:  $\beta=0.29$  Resonator SCL Result (Pm=Red, Pb=Green, Pl+Pb=Blue).

The next phase of integrated testing was to find the tuning parameters for the  $\beta=0.29$  resonator. The first step of this process was to find the tuning sensitivity. On the  $\beta=0.29$  resonator, the beam port flanges on the resonator are actuated inwards to adjust the frequency. This adjustment results in 216.5 kHz/mm shift on the resonator. With a tuning range of  $\pm 120$  kHz required for this resonator, this necessitates .554 mm of flange to flange adjustment inward. Figure 13 display the stress generated on the resonator at .554 mm of adjustment at 2K. This figure displays that the resonator is capable of the required tuning range, since there is not yielding present due to the tuning deflection and pressure.

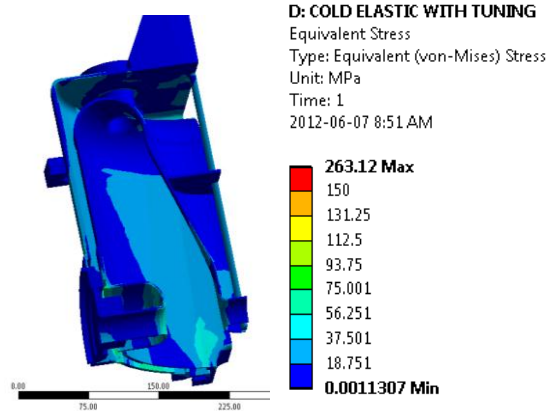


Figure 13:  $\beta=0.29$  Resonator stresses during maximum tuning.

The third step of integrated analysis is to find the pressure sensitivity. This was performed by applying pressure (1 ATM) to the same surfaces shown in Figure 10, and simulating the frequency shift due to this pressure. Two scenarios were simulated, one where the beam port flanges are fixed (representing an ideal tuner) and the other where the beam port flanges are free. The two scenarios help define the resonator's overall pressure sensitivity due to the tuner. The tuner will have a finite rigidity that is somewhere between the fixed and free condition. Figure 14 displays the deformation due to the pressure application at the fixed condition, this deformation results in a 0.55 Hz/torr frequency shift. At the free condition, the pressure sensitivity is 1.42 Hz/torr. Both of these conditions fall within the requirement for pressure sensitivity, which demonstrates that the resonator's pressure sensitivity can meet its requirement independent of the tuner.

A study was performed on the  $\beta=0.29$  Resonator, to find the ideal location of the stiffening ribs (Figure 9). By moving the rib up and down on the inner conductor, the pressure sensitivity could be altered. The rib was finally placed at the location (185.75 mm above and below the drift tube) that results in the 0.55 Hz/torr frequency shift at the fixed condition. Figure 15 displays the results of this study.

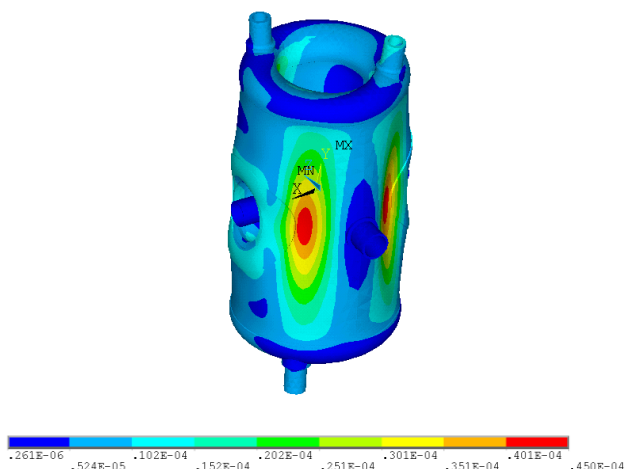


Figure 14:  $\beta=0.29$  Resonator Helium Pressure Response.

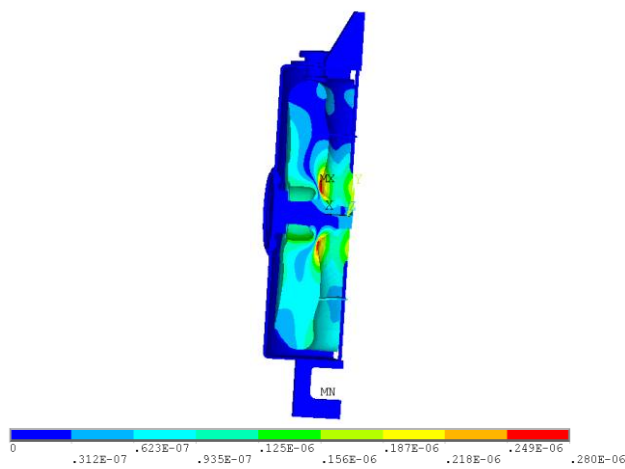


Figure 16:  $\beta=0.29$  Resonator LFD Response.

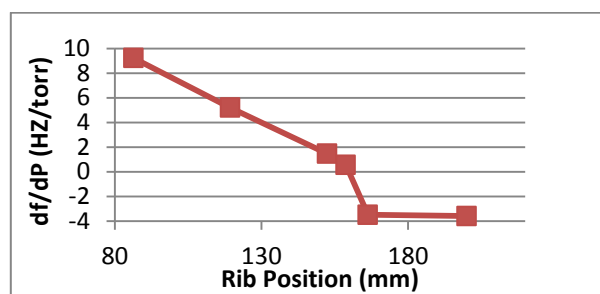


Figure 15:  $\beta=0.29$  Resonator Stiffening Rib Study.

The last step of the integrated analysis for the  $\beta=0.29$  was to compute the LFD value. This simulation used the same model as the pressure sensitivity; however, instead of pressure loads being added, Lorentz Forces are computed and applied to the model. In the same fashion as the pressure sensitivity, the frequency shift is determined due to this force. Like the pressure sensitivity, two scenarios were simulated; one with beam ports fixed and the other with beam ports free (representing an ideal tuner and no tuner respectively). Figure 16 depicts the deformed shape of the  $\beta=0.29$  resonator due the Lorentz Force at the fixed condition. This plots displays the high electric field regions pulling towards each other, predominantly on the beam port and drift tube areas. Conversely the magnetic field regions are pushing outward. From this figure, it was found the LFD value for the resonator at the fixed condition was  $-2.71 \text{ Hz}/(\text{MV}\cdot\text{m})^2$ . At the free condition, the value is  $-3.72 \text{ Hz}/(\text{MV}\cdot\text{m})^2$ . Both conditions meet the requirement for LFD, demonstrating that the resonator can achieve its requirement independent of the tuner.

### CONCLUSION

| Property   | $\beta=0.085$ | $\beta=0.29$ |
|--|---------------|--------------|
| Pressure Capability 300K (ATM)                       | 2.2           | 2.2          |
| Pressure Capability 2K (ATM)                         | 15            | 20           |
| Tuning Sensitivity (kHz/mm)                          | 3.2           | 216.5        |
| Pressure Sensitivity (Hz/torr) Fixed Tuner           | N/A           | 0.55         |
| Pressure Sensitivity (Hz/torr) Free Tuner            | -1.4          | 1.42         |
| LFD $(\text{Hz}/(\text{MV}/\text{m})^2)$ Fixed Tuner | N/A           | -2.71        |
| LFD $(\text{Hz}/(\text{MV}/\text{m})^2)$ Free Tuner  | -0.7          | -3.72        |

Table 3 summarizes the resonators mechanical attributes. The integrated mechanical analysis of the  $\beta=0.29$  and  $\beta=0.085$  resonator types at FRIB is complete. The  $\beta=0.29$  half wave resonator has completed the analysis and has been shown to exceed the mechanical requirements. This resonator type has already undergone the request for quote process and two development resonators are expected by the end of 2012. The  $\beta=0.085$  resonator has also completed its integrated mechanical analysis and exceeds the mechanical requirements. This resonator has also completed a request for quote process and two development resonators of this type are expected by the end of 2012.

### REFERENCES

- [1] J.Weil et al., "The FRIB Project – Accelerator Challenges and Progress", these proceedings.
- [2] E. Zaplatin et al., "Structural Analyses of MSU Quarter-Wave Resonators". SRF 2009: Berlin, Germany.
- [3] ANSYS, Inc., Cannonsburg, Pennsylvania, USA.
- [4] T.J. Peterson et al., "Pure Niobium as a Pressure Vessel Material," Fermi National Accelerator Laboratory, Batavia, IL, USA.
- [5] ASME Boiler and Pressure Vessel Code, 2010 edition.
- [6] ATI Wah Chang, Technical Data for Niobium-Titanium, 2011.

## SIMULATION OF ELECTRON AND ION DYNAMICS IN AN EBIS\*

L. Zhao<sup>#</sup>, J. S. Kim<sup>+</sup>, E. G. Evstatiev, FAR-TECH, Inc., San Diego, CA 92121, USA  
 E. Beebe, A. Pikin, BNL, Upton, NY 11973, USA

### Abstract

To model the dynamics and charge state distribution (CSD) of the ions in an Electron Beam Ion Source (EBIS), a time-dependent, self-consistent particle-in-cell Monte Carlo code (EBIS-PIC) has been developed by FAR-TECH, Inc. The energetic background electron beam is modelled by PBGUNS by dividing the long beam path into several segments to resolve the big length-to-radius spatial scaling problem. The injected primary ions and ionized neutral gas ions are tracked using Monte Carlo method which includes the ionization, charge-exchange and Coulomb collisions with the electron beam. The potential well is calculated by solving the Poisson equation each time step. EBIS-PIC calculates the spatial and velocity space distributions and the evolution of the charge state distribution of trapped ions in EBIS devices operating in fast or slow trapping mode. The physical model of EBIS-PIC and the simulations of the experiments on the Test EBIS at BNL are described. The results are in good agreement with the experimental measurements.

### INTRODUCTION

In an EBIS, a high current electron beam created by an electron gun is compressed to high density as it enters a strong solenoidal magnetic field (Figure 1). The beam is stopped by an electron collector after passing through a series of drift tubes and exiting the solenoid. The injected primary ions are confined in the radial direction by the potential well created by the space charge of the electrons, and in the axial direction by positive potential barriers on the drift tubes at the two ends of the device. Ions are then ionized to high charge states by electron impact and extracted as the output beam. EBIS are one of the best candidates for producing highly charged radioactive ions.

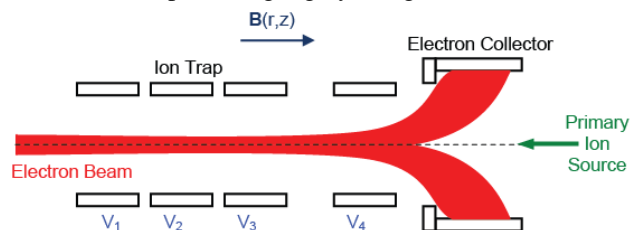


Figure 1: Diagram of EBIS device. The electron beam travels to the right until stopped by the electron collector. The primary ion source is to the right of the collector.

FAR-TECH has developed a numerical tool, EBIS-PIC, to simulate ion dynamics and charge breeding in an EBIS. The tool has modules to model various physics in the

EBIS. The initial electron beam is simulated by PBGUNS [1] by dividing the beam path into several segments. The injected primary ions and ions from neutral gas are tracked using a time dependent Monte Carlo method which includes Coulomb collisions and ionizations with background electron beam and charge exchange with neutrals. The electrostatic potential is updated by solving Poisson's equation. The EBIS-PIC has been used to simulate Cs 1+ charge breeding experiments on Test EBIS [2, 3] at BNL. The basic parameters of Test EBIS are listed in Table 1. We use the Test EBIS as an example device to illustrate the simulation of electron beam and ions.

Table 1: Operation Parameters of Test EBIS

| Parameter           | Value                    |
|---------------------|--------------------------|
| Trap length         | 0.7 m                    |
| Drift tube radius   | 1.5 cm                   |
| Max magnetic field  | 5 T                      |
| Drift tube voltages | 12, 6, 9 kV              |
| Ion Specie          | Cs                       |
| Ion Current         | 15 $\mu$ A               |
| Ion Energy          | 9kV                      |
| Pressure            | $5 \times 10^{-10}$ Torr |

### ELECTRON BEAM MODELING

In EBIS operation, the electron beam propagates several meters from the cathode to collector through drift tubes. The length to radius ratio could be from 200 to 1000. To resolve such big spatial scaling issue, the electron beam is simulated by PBGUNS in several regions to increase accuracy. The PBGUNS code uses relaxation techniques to solve the Poisson's Equation for the potentials on a large, rectangular array of squares, alternately computing potentials and trajectories. It is modified to be able to perform the simulation of the long electron beam path in sections with different grid settings to achieve required accuracy. The sectional simulations were linked continually from the gun to the collector by passing the beam conditions, including the radial distribution of beam energy, angle and spin velocities, and ensuring a steady state in all the sections.

A full electron beam simulation for Test EBIS was performed in 4 regions with their boundaries shown in Figure 2b as vertical dashed lines. The steady state electron beam (shown in Figure 2b) travels  $\sim 3$  meters from the gun to the electron collector in the magnetic field shown in Figure 2a. The electrostatic potential along

\*Grant supported by DOE Office of Nuclear Physics  
 #zhao@far-tech.com  
 +kim@far-tech.com

the axis is shown in Figure 2c. Here the cathode voltage was set as zero. The trap region is from around 1m to 2m along the z axis where the magnetic field is 5 T. The simulated electron beam current is about 2A and the beam radius is about 0.75mm in the trap region.

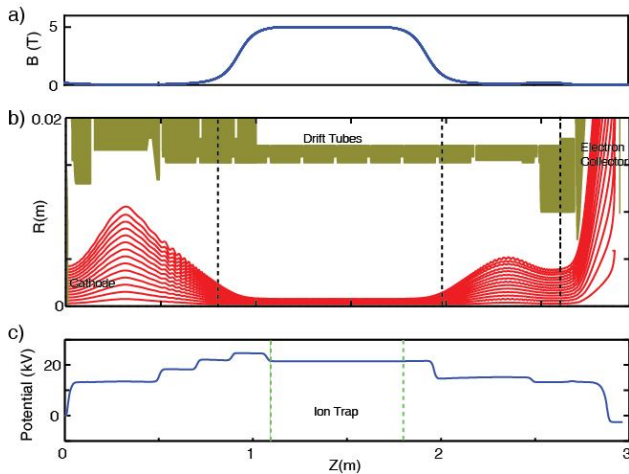


Figure 2: PBGUNS simulation. a) Axial magnetic field; b) electron beam simulated by PBGUNS in 4 sections indicated by the dashed lines; c) the simulated electric potential along the axis. The ion trap region is indicated by the dashed lines.

The 3D view of the electrostatic potential obtained from the PBGUNS simulation is shown in Figure 3. The potential well shown is from the trap region to the electron collector. Due to the negative space charge of the electron beam, the potential well is  $\sim 1700$  V in the trap region.

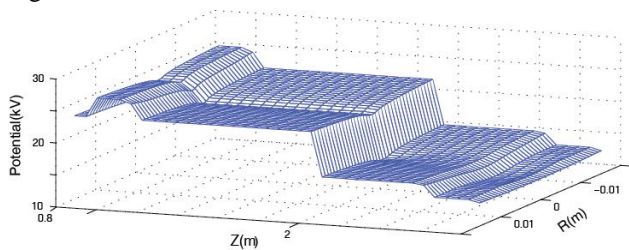


Figure 3: 3D plot of electrostatic potential, for  $R < 2$  cm, from trap to electron collector.

The axial profiles of the electron beam in the trap region are shown in the left column in Figure 4. From top to bottom shown are the axial profiles of axial-magnetic field (without the beam), the electron density, axial kinetic energy of the electron beam, and the electrostatic potential. The radial profiles of the electrostatic potential up to 1.5 cm and electron density up to 1.5 mm are shown in the right column. The radial beam profile is convex near the axis, showing increased density in radius with a sharp drop at the beam edge. When ions are injected and trapped in the electron beam, the space charge potential will be modified according to Poisson's equation and the

electron density will also be updated while keeping the total electron current constant.

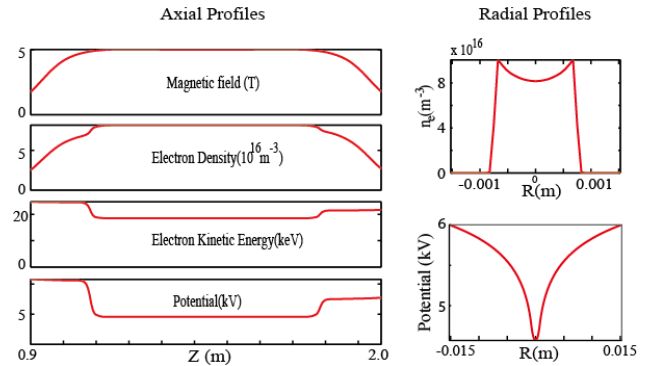


Figure 4: Left column: from top to bottom shown are axial profiles of the magnetic field (T), electron density  $n_e$  ( $m^{-3}$ ), electron kinetic energy (keV), and electrostatic potential (kV). Right column: electron density,  $r$  only up to  $\sim 1.5$  mm and radial profile of electrostatic potential up to  $r \sim 1.5$  cm.

## ION DYNAMICS

In EBIS, the ion dynamics is governed by both the electrostatic potential (shown in Figure 3) and the magnetic fields (in Figure 2a). The orbit of an ion is the combination of gyro-motion and the oscillation motion in radial direction. Experimentally, ions are injected meters away from the trap region (Figure 1). It is important to understand the ion dynamics from beam injection plane, where the initial beam emittance is measured, to the trap.

The orbit of an ion injected from outside of electron collector is shown in Figure 5. From the projections of the orbit (Figure 5a and 5b), one can see that the ion is oscillating mostly in the y-plane due to the electric field generated by the electron beam, and slowly rotates as the ion enters the trap as the magnetic field increases and starts acting on the ion, as seen in Figure 5c. In the trap, where magnetic field is strong, ions rotate fast around the axis, and at the same time they oscillate radially close to simple harmonic oscillation due to the almost linearly increasing radial electric field. Once being trapped, ions will bounce back and forth between the voltage barriers until they are extracted or lost to the wall due to electron heating.

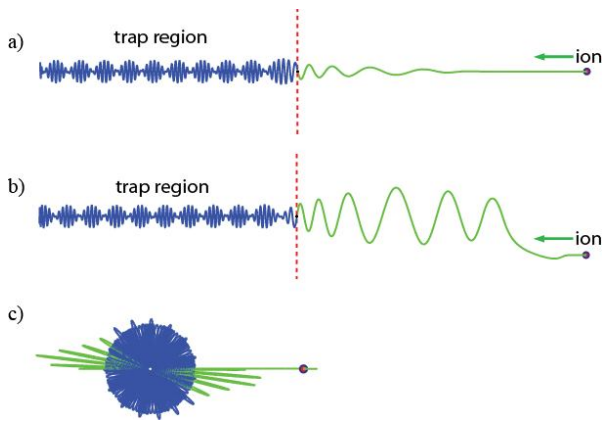


Figure 5: An orbit of a primary ion that is injected from outside of the electron collector into the trap. Shown are the projections of the orbit onto x-z plane (a), y-z plane (b), and x-y plane (c). The dot is the initial point of the orbit.

The acceptance of the ion beam is an important factor to determine the efficiency of EBIS operation. The acceptance is estimated when the ion trajectory is completely within the electron beam in the trap region. To study the acceptance of the ion beam with respect to the electron beam in the trap region, ions with different pitch angles and radial positions are launched from the plane at the same initial position as shown in figure 5. Figure 6 shows an X-X' phase space acceptance plot for the ions that are launched from the electron beam dump. Ions with initial conditions inside the outer dashed ellipse overlap with the electron beam over 50% (the inner solid ellipse is for ions with 100% overlapping) in the trap. The estimated acceptance is about  $100\pi$  mm mrad which is about the same as other predictions [3].

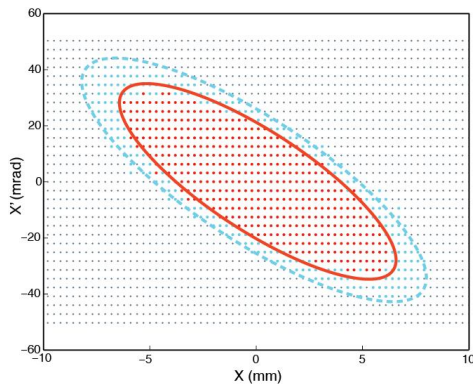


Figure 6: Estimated acceptance of the ion beam in Test EBIS. Ions with initial conditions within the solid ellipse have 100% overlap of the ion trajectories with the electron beam, and more than 50% if inside the dashed ellipse.

In the trap region, the ions were tracked by time-dependent PIC Monte Carlo method, utilizing the electron current density obtained by the PBGUNS simulations (Figures 2 and 3). The electric fields are solved self-consistently with the ion and electron space charge

evolving as ions being ionized to higher charge states. The ionization of the ions by electron impact, charge exchange of the ions with the background neutral gas, and heating of the ions by Coulomb collisions with the electrons are included in the Monte-Carlo model. The ion density was calculated on the grid based on the ion locations and the charge states. Detailed description of the setup and physical model can also be found in [4]. EBIS-PIC is able to predict the evolution of ion charge states, the distribution of ions and the CSD of trapped ions.

### EBIS-PIC SIMULATION RESULTS

We have performed a full EBIS-PIC simulation for an EBIS experiment [2] of the Test EBTS at BNL using the experimental parameters listed in Table 1. The primary ions were Cs 1+ and injected for 0.2 ms, after which the trap voltage was ramped down to 6 kV in 10 microseconds. The ions were then confined for an additional 2 ms before being extracted.

The details of the EBIS-PIC simulation results are shown in Figure 7. Time evolution of ion charge states in the trap is shown in Figure 7a, and the charge breeding times for different charge states are shown in Figure 7c. The charge breeding time is defined as the time that an ion charge state reaches its peak. The charge state distribution (CSD) of trapped ions is shown in Figure 7d. Figure 7b shows the radial distribution of captured ions in the trap in the fast trapping test. The profiles are all peaked near the center of the electron beam. The radial distribution of each ion charge state keeps rising until the number of the ions with that charge state reaches its peak and starts to drop. In general, the higher the charge states, the ion distribution are more concentrated at the center if the number of that charge state has reached its peak.

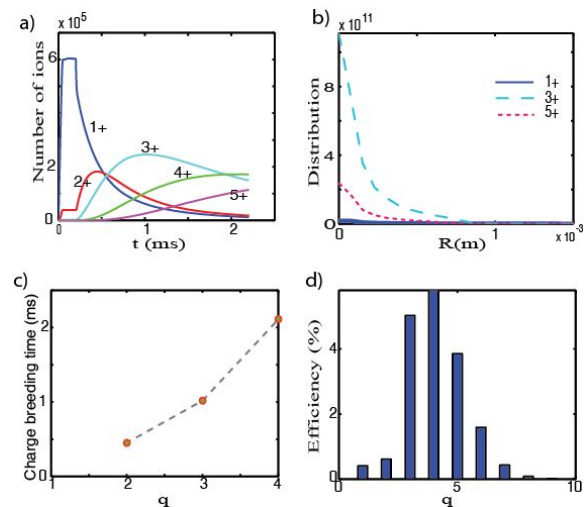


Figure 7: EBIS-PIC simulation results: a) time evolution of ion charge states in the trap; b) Radial distribution of different ion charge states; c) Charge breeding time for different charge states; and d) CSD of trapped ion charge states.

The result was compared with experiments and summarized in Table 2. Here, the trapping efficiency for a

charge state is defined as the ratio between the number of ions in that charge state and the total injected ions. Including ion space charge and background gas ionization, our simulations show both agreement and disagreement. Our simulations gave the trapping efficiency 17.4%, lower than experimental value of 19%, while Cs ions was 95% of the trapped charge, the same as the experimental value. The average cesium charge state in the simulations was about +4, while +6 was observed in the experiments.

Table 2: Comparison of simulation and experimental results

| Results                      | Simulation | Experiment |
|------------------------------|------------|------------|
| Primary ion trap efficiency  | 17.4%      | 19%        |
| Gas ion trap efficiency      | 83.8%      |            |
| Total primary ion charge(pC) | 2178       | 3400       |
| Total gas ion charge(pC)     | 119        | 170        |
| Average primary ion charge   | 4.1        | 6.0        |
| Average gas ion charge       | 2.0        |            |

## CONCLUSIONS

EBIS-PIC has been developed and tested for ion capture and breeding simulations in EBIS. The energetic background electron beam is modelled by PBGUNS by dividing the long beam path into several segments to resolve the big length-to-radius spatial scaling problem. The ion dynamics has been studied using time-dependent PIC Monte Carlo method. The simulation results of EBIS-PIC show qualitative agreement with the experiment. Future improvements of the code will be focused on improving the physical model by adding ion-ion collision and recombination and speeding the code by using non-uniform grid.

## REFERENCES

- [1] PBGUNS code page: <http://www.far-tech.com/pbguns/>
- [2] A. Pikin, J. Alessi, E. Beebe, A. Kponou, K. Prelec, G. Kuznetsov, and M. Tiunov, AIP Conf. Proc. . Vo. 572, pp. 3-19.
- [3] S. Kondrashev, J.G. Alessi, E.N.Beebe, C. Dickerson, P.N.Ostroumov, A. Pikin, G. Savard, Measurement of Charge State Breeding Efficiency at BNL Test EBIS, Nuclear Instruments and Methods in Physics Research A, 642 (2011), 18-24.
- [4] L. Zhao, B. Cluggish, J. S. Kim, and E. G. Evstatiev, "A particle-in-cell Monte Carlo code for electron beam ion source simulation ", Rev. Sci. Instrum. **83**, 02A508 (2012).

## TANDEM EBIS\*

A. Pikin<sup>#</sup>, J. G. Alessi, E. N. Beebe, M. Okamura, D. Raparia, J. Ritter, L. Snyderstrup  
Brookhaven National Laboratory, Upton, 11973, USA

### Abstract

A method to increase the ion beam intensity of RHIC EBIS by extending its ion trap into magnetic field of an additional superconducting solenoid is described. The strong axial support of the cold masses in these solenoids is required to place them on a common axis close to each other. Such configuration of solenoids allows to produce a long EBIS with a single electron gun, electron collector and injection system. Preliminary calculations of magnetic forces, magnetic field and potential distributions are presented along with proposed structure of the ion traps.

### INTRODUCTION

RHIC EBIS supplies the RHIC accelerating facility with highly charged ions from He<sup>2+</sup> to U<sup>39+</sup>. The design of this ion source and its main components can be found in [1-9] and the results of its experimental study and commissioning on RHIC accelerating facility can be found in [10-13]. The total ion charge, which can be accumulated in the ion trap of the Electron Beam Ion Source (EBIS) is limited by the charge of the electrons within the axial ion trap. Usually some factors like an insufficient ion injection, not full axial trapping, and contamination of the trap with the residual gas ions result in a reduction of the accumulated charge of working ions below this maximum value. For electron current 10.0 A, electron energy 20 keV, and the trap length 1.5 m the project value of the RHIC EBIS ion capacity is 177 nC or  $1.1 \cdot 10^{12}$  el. ch. with the charge of working ions constituting 50% of the electron charge. It has been experimentally proven that the extension of the ion trap beyond the limits of the uniform magnetic field results in an increased accumulated ion charge at a cost of some

reduction of the effective electron beam density [14]. No disruption of the EBIS operation has been observed. The reduction of the effective current density of the ion trap extended into a low magnetic field area requires some longer confinement time to produce the required charge state of the working ion specie compare to a trap with uniform magnetic field.

### THE CONCEPT OF TANDEM EBIS

One way to increase the intensity of the extracted ion beam from EBIS is an axial extension of the ion trap, making it longer. The capacity of the ion trap is proportional to the length of the trap if the radial depth of the potential well remains the same in any axial position of the trap. The extension of the ion trap requires an additional area with an acceptable value of the magnetic field, which is concentric with the existing one. Extending the magnetic field by building a longer superconducting solenoid or placing two solenoids in the same cryostat seem not practical. It is proposed to use an additional superconducting solenoid of the same length and a "warm" inner diameter (ID) as the existing one to extend the magnetic structure and the ion trap of the existing RHIC EBIS creating a longer Tandem EBIS (Fig. 1) with a single electron gun, a single electron collector and a common vacuum system. For the presented geometry the preliminary PerMag simulations give the value of the minimum magnetic field in a gap between two solenoids of 2.1 kGs for magnetic field in the center of each of two superconducting solenoids 4.8 T. This value of minimum magnetic field is quite sufficient for the electron beam transmission in the transition region between both magnets.

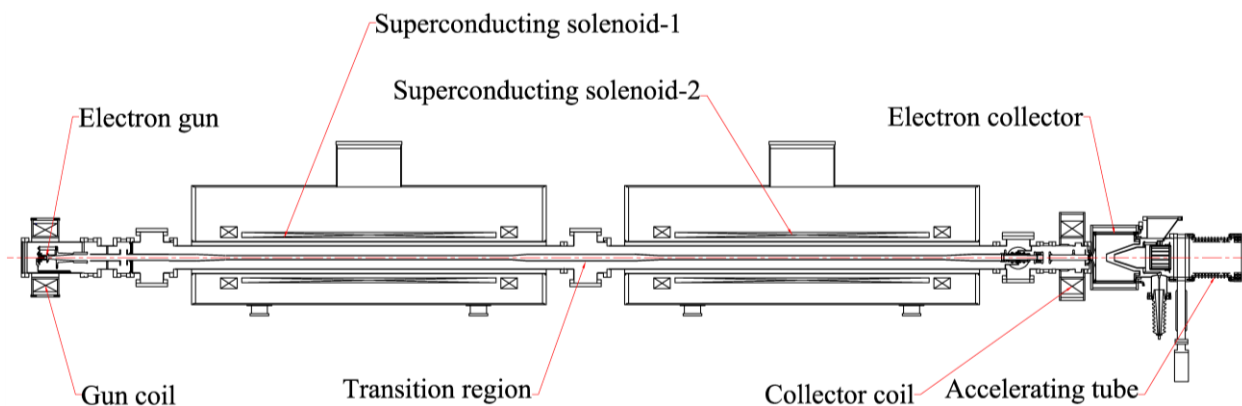


Fig. 1. Schematic of the Tandem EBIS.

\*Work supported under the auspices of the US Department of Energy and the National Aeronautics and Space Administration.  
<sup>#</sup> pikin@bnl.gov

According to the PerMag simulations, the axial force acting on each of the cold masses is approximately 1200 kg if both magnets have the magnetic structure of our ACCEL solenoid.

A possible sequence of axial potential distributions for one ionization cycle in a Tandem EBIS with one injection trap and two pre-extraction traps is presented in Fig. 2.

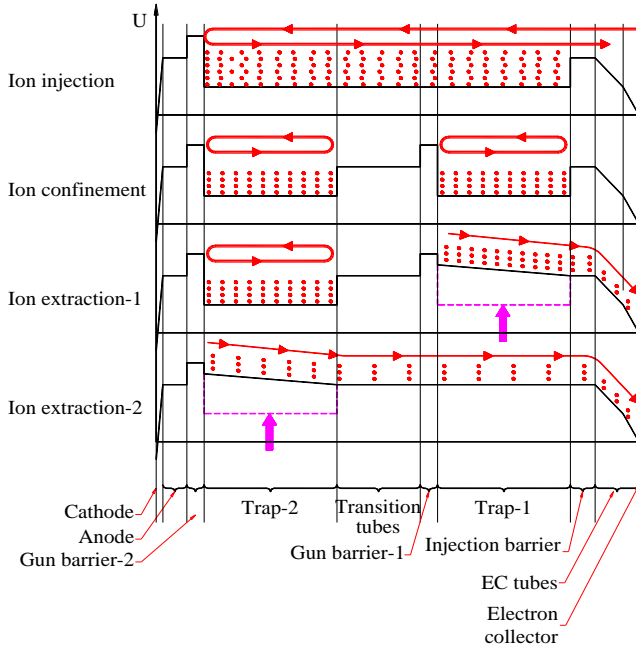


Fig. 2. Ionization cycle diagram for Tandem EBIS with two pre-extraction traps.

### DRIFT TUBE STRUCTURE OF TANDEM EBIS

To provide access for ions to all parts of the trap during the ion injection one needs to keep uniform the potential on the axis. In a “conventional” EBIS the magnetic field distribution within the ion trap is usually uniform and so is the ID of the drift tubes. The idea of extending the ion trap into the regions with lower values of the magnetic field seems attractive because it promises increase of capacity of the ion trap and therefore the intensity of the extracted ion beam. However, the variations of the magnetic field within the ion trap have several consequences, which need to be taken into account on a design stage of such EBIS. If all the drift tubes have uniform ID the extending of the ion trap into regions with lower magnetic field would result in a radial potential well having different depth within the drift tubes located in a gradient of magnetic field. These drift tubes would have radial potential wells varying according to the magnetic field values. The potential well is deeper in a high magnetic field region and more shallow in a low magnetic field region.

The potential difference between the axis of the electron beam and the drift tube  $\Delta U$  can be expressed as:

$$\Delta U = \frac{q/l}{4\pi\epsilon_0} \cdot \left[ 1 + 2Ln\left(\frac{r_t}{r_b}\right) \right] \quad (1)$$

$q/l$  – total linear electric charge density (includes electrons and ions),

$\epsilon_0$  – vacuum permittivity,

$r_t$  – drift tube radius,

$r_b$  – electron beam radius,

For an electro-optical system with an immersed electron gun the average radius of the electron beam changes with magnetic field as:

$$r_b(z) = r_c \cdot \sqrt{\frac{B_c}{B(z)}} \quad (2)$$

$r_b(z)$  – electron beam radius in a point with axial coordinate  $z$ ,

$B_c$  – magnetic field on the cathode,

$B(z)$  – magnetic field in a point with axial coordinate  $z$ .

One can maintain the value of  $r_t/r_b$  the same within the drift tube if the inner radius of this tube changes with magnetic field according to (3).

$$r_t(z) = r_{t,0} \cdot \sqrt{\frac{B_0}{B(z)}} \quad (3)$$

$r_t(z)$  – drift tube inner radius in a point with axial coordinate  $z$  and magnetic field  $B(z)$ ,

$r_{t,0}$  – inner radius of the drift tube in the point with magnetic field  $B_0$

In an ideal case with uniform value of  $r_t/r_b$  in all drift tubes in the trap one can maintain a uniform potential distribution in the trap with the same potential on all drift tubes involved because the value of the radial potential well remains the same. In this case the “flat” potential distribution on the axis does not change with the degree of the electron beam neutralization. For practical reason a complicated shape of the drift tubes inner surface defined by (3) can be substituted with simple conical shapes, which will cause small variations of axial potential within one drift tube, which are much smaller than the radial potential well and therefore can be acceptable.

If the magnetic field variations within the extended ion trap are too large, maintaining the same value of  $r_t/r_b$  becomes impractical because of space limitations and one has to change the value of  $r_t/r_b$  for some tubes. The different values of this ratio would require different potentials to be applied to the drift tubes to maintain the axial potential distribution for a not-neutralized electron beam “flat”. Keeping the axial potential distribution without bumps in the middle is important for distributing ions over the whole trap during the ion injection, especially for breeders with small number of ions and small final neutralization. Ion charge build-up during the confinement reduces the radial potential well and with full neutralization a uniform potential distribution on the drift tubes within the trap is needed. One consequence of having different values of  $r_t/r_b$  within the ion trap is

different rate of ion losses in such drift tube structure with higher losses in the drift tubes with lower value of  $r_i/r_b$ , which have the minimum depth of the radial potential well.

The Tandem EBIS layout presented in Fig. 1 has a crude drift tube structure with two values of inner diameter and only one drift tube in a transition region between the superconducting magnets. Such structure can provide a relatively uniform potential distribution on the axis for over 5 m long ion trap with a not neutralized electron beam, it is presented in Fig. 3.

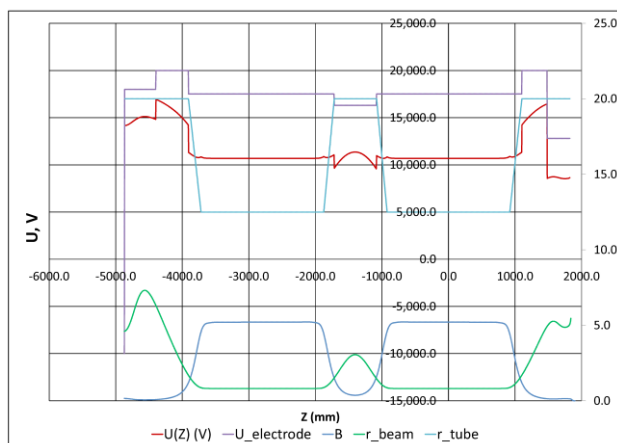


Fig. 3. Axial distributions of magnetic field, electron beam radius, drift tube radii and potential distributions on the drift tubes and on the axis with “flat” bottom in the Tandem EBIS for electron beam with current 10.0 A and energy 20 keV for a single injection trap.

The presented axial potential distribution includes the electron space charge but it does not take into account a mutual penetration of potentials in the adjacent drift tubes gaps, which makes the actual potential distribution smoother.

The long drift structure of the Tandem EBIS is flexible and allows different configurations of ion traps at different periods of the ionization cycle. There can be one or two ion traps with the required time structure of the extracted ion pulses. For the RHIC EBIS application the ion injection can be done into a single ion trap for the entire length. After the injection is completed, the potential on the transition section, which is located in a low magnetic field area, can be raised and two axial potential traps can be created. This transition should be done adiabatically for ions with respect to their axial oscillations, so the ions from an initial single trap are distributed between the two new traps with minimal losses. At the end of the ionization cycle the highly charged ions can be extracted with the time pattern optimized for the best RHIC performance.

It may be possible to extend the ion traps into areas with magnetic field much lower than in the centers of solenoids (around 5T), probably to as low as 1.5 kGs. The electron beam current density in these areas is much

lower than in the center, so the main contributors to the ionization process remain the central areas of the both solenoids, and the peripheral regions can be used for increased trap capacity. Such trap extension will result in some increase of the confinement time compare to the “conventional” trap with uniform magnetic field, but it will have increased total accumulated ion charge. For a trap with length 5.2 m and electron current 10.0 A the average current density is  $j_{aver} = 385 \text{ A/cm}^2$ , as compare to  $487 \text{ A/cm}^2$  for a trap with uniform magnetic field and the length of 1.5 m in a central region of each solenoids.

A gap between two solenoids is used for high voltage feedthroughs and vacuum pumping. It is preferred not to have in-line gate valves between the two central chambers inside the both solenoids to avoid detrimental axial potential well due to penetrating of a ground potential in a valve’s gap.

## CONCLUSION

The Tandem EBIS concept is a relatively low-cost modification of the existing RHIC EBIS if two superconducting magnets with sufficient axial supports are available. It has potential to double the EBIS intensity using the existing units: electron gun, electron collector, extraction/injection ion optics, and ion injection system. One of problems, which require addressing in Tandem EBIS for RHIC application, is a fast ion extraction from a long trap. The longitudinal energy spread and a possible transverse emittance growth resulting from a fast ion extraction need to be minimized for effective injection into RFQ.

The increased ion trap capacity is not the only possible benefit of EBIS structure with two solenoids and a single electron beam. For the radioactive ion beam (RIB) breeder with continuous ion injection one of two traps can be used as an accumulator with low current density and a large acceptance. The accumulated ions can be transferred in a short bunch into the second trap for the final ionization. At the end of the ionization cycle the highly charged ions can be extracted over the operating accumulating trap. An efficient vacuum separation between two regions allows use of gas in one trap either for injection of the working gas or for ion cooling.

## REFERENCES

- [1] J. G. Alessi, D. Barton, E. Beebe, S. Bellavia, O. Gould, A. Kponou, R. Lambiase, R. Lockey, McNerney, M. Mapes, Y. Marneris, M. Okamura, D. Phillips, A. I. Pikin, D. Raparia, J. Ritter, L. Snydstrup, C. Theisen, and M. Wilinski, *The Brookhaven National Laboratory electron beam ion source for RHIC*, Rev. of Sci. Instrum, 81, 02A509 (2010).
- [2] A. Kponou, E. Beebe, A. Pikin, G. Kuznetsov, M. Batazova, and M. Tiunov, *Simulation of 10 A electron-beam formation and collection for electron-beam ion source*, Rev. Sci. Instrum., V. 69, #2, 1120-1122, (1998).

- [3] A. Pikin, J. G. Alessi, E. N. Beebe, A. Kponou, R. Lambiase, R. Lockey, D. Raparia, J. Ritter, L. Snyderstrup, Y. Tan, *RHIC EBIS: basics of design and status of commissioning*, Journal of Instrumentation, 5, C09003, (2010).
- [4] A. Pikin, *Electron gun for RHIC EBIS*, BNL Tech note C-A/AP #245, (2006).
- [5] A. Pikin, A. Kponou, L. Snyderstrup, *Optical, Thermal and Stress Simulations of a 300-kwatt Electron Collector*, BNL Tech note C-A/AP #246, (2006).
- [6] Alexander Pikin, James G. Alessi, Edward N. Beebe, Ahovi Kponou, Krsto Prelec, John Ritter, Louis Snyderstrup, *Analysis of a possible 20 A electron gun and collector design for the RHIC EBIS*, Journal of Physics: Conference series, 2, pp. 28-34, (2004).
- [7] E. Beebe, J. G. Alessi, O. Gould, D. Graham, A. Kponou, A. Pikin, K. Prelec, J. Ritter and V. Zajic, *Control and diagnostics for the high current electron beam ion source at BNL*, Proceedings of EPAC-2002, pp. 1688-1690, (2002).
- [8] Edward N. Beebe, James G. Alessi, David Graham, Ahovi Kponou, Alexander Pikin, Krsto Prelec, John Ritter, Vladimir Zajic, *Test EBIS operation and component development for the RHIC EBIS*, Journal of Physics: Conference series, 2, pp.164-173, (2004).
- [9] E. Beebe, J. Alessi, A. Kponou, A. Pikin, K. Prelec, G. Kuznetsov, M. Tiunov, *Design Issues for the RHIC EBIS*, AIP Conference Proceedings, 572, pp. 43-47, (2001).
- [10] A. Pikin, J. Alessi, E. Beebe, A. Kponou, K. Prelec, G. Kuznetsov, M. Tiunov, *EBTS: Design and experimental study*, AIP Conf. Proc., V. 572, pp. 3-19, (2001).
- [11] A. Pikin, J. Alessi, E. Beebe, A. Kponou, M. Okamura, D. Raparia, J. Ritter, Y. Tan, G. Kuznetsov, *Ion optics of RHIC electron beam ion source*, Rev. Sci. Instrum., 83, 02A504 (2012).
- [12] E. Beebe, J. Alessi, A. Kponou, A. Pikin, K. Prelec, *Heavy ion extraction from the BNL high current EBIS Test Stand*, Proceedings of EPAC-2000, pp. 1589-1591, (2000).
- [13] J. G. Alessi, E. Beebe, S. Binello, L. Hoff, K. Kondo, R. Lambiase, V. LoDestro, M. Mapes, A. McNerney, J. Morris, M. Okamura, A. I. Pikin, D. Raparia, J. Ritter, L. Snyderstrup, M. Wilinski, A. Zaltsman, *Commissioning of the EBIS-based heavy ion preinjector at Brookhaven*, BNL-95272-2011-CP, Proceedings of LINAC-2010, FR103 (2010).
- [14] A. Pikin, J. Alessi, E. Beebe, A. Kponou, and K. Prelec, *Experimental study of ion injection into an extended trap of the Brookhaven National Laboratory EBIS*, Rev. Sci. Instrum., V. 73, 2, pp. 670-672, (2002).

## HEAVY ION ACCELERATOR DEVELOPMENT AT IUAC DELHI

D. Kanjilal [IUAC, New Delhi, India]

### *Abstract*

Inter University Accelerator Centre has been involved in the development of heavy ion accelerators, ion sources, beam lines and experimental facilities for providing various heavy ion beams in a wide energy range varying from a few tens of keV to hundreds of MeV for experiments by more than four hundred research groups from all over India and abroad. A large vertical Pelletron electrostatic tandem accelerator capable of achieving terminal voltage up to 16MV has been in operational for more than a couple of decades. Superconducting niobium linac booster accelerating modules having eight niobium quarter wave resonators each have been developed and used. A high temperature superconducting electron cyclotron resonance ion source (HTS-ECRIS) was designed, fabricated and installed. It is in regular operation for production of highly charged ion beams for alternate high current injector (HCI) system consisting of radio frequency quadrupole and drift tube Linacs. Details of developments of various heavy ion beam facilities and experimental systems at IUAC will be presented.

**CONTRIBUTION NOT  
RECEIVED**

# A COST-EFFECTIVE ENERGY UPGRADE OF THE ALPI LINAC AT INFN-LEGNARO\*

G. Bisoffi, M. Comunian, A. Facco, A. Galatà, P. Modanese, A. Pisent, A. M. Porcellato, R. Pengo, S. Stark (INFN/LNL, Legnaro (PD)), B. B. Chalykh (ITEP, Moscow)

## Abstract

The ALPI SC linac at INFN-LNL is being constantly upgraded in terms of maximum beam energy ( $E_f$ ) and current, made available for experiments. Presently, a liquid-N cooling scheme is being applied to the RF power couplers of the 16 full Nb resonators, to keep them locked at 5 MV/m, vs. present 3 MV/m. A further upgrade of the 44 “medium beta section” cavities, changing the cavity Cu substrates, was prototyped and is reported at this conference: however it is not fully funded yet and is extremely time-consuming. A cost-effective  $E_f$  upgrade is proposed here: to move 2 SC buncher cryostats, which house a single working SC QWR but were designed for 4, at the end of ALPI, equipping them with 4 Nb/Cu QWRs each (new bunchers would either be NC QWRs or a single SC cavity cryostat). The contribution of these cryostats to  $E_f$  would be extremely effective: e.g. a  $E_f \sim 10$  MeV/A ( $I_{\text{beam}} \geq 1$  pnA) Pb beam, a very attractive tool for the nuclear physics community, is achievable. A being performed upgrade of ALPI cryoplant, expected to increase the refrigeration capability by  $\sim 25\%$ , makes this change possible today. Details of this solution, as well as its limits, will be presented and discussed

## INTRODUCTION

The heavy ion accelerator complex at INFN-LNL is based on the superconducting (SC) linac ALPI, which may be alternatively fed by the 15 MV XTU Tandem or by the SC injector PIAVE ( $V_{\text{eq}} = 8$  MV), based on superconducting RFQs. For masses heavier than  $A \sim 100$  the use of the Tandem tends to become unpractical due to the limited life-time of the terminal stripper foils and PIAVE is left as the only option.

At present, for masses beyond  $A \sim 150$ , the maximum available energy with PIAVE-ALPI ranges between 7,5 and 8,5 MeV/A. In addition, the development of new heavy mass ions with the ECR ion source is not always straightforward nor particularly swift, having to be carried out only in those periods when the accelerators are not delivering beams to users (30% of the year time, without considering the time necessary for periodic maintenance), since an ECR test bench is not available.

The quest for the heaviest masses is indeed increasing: a large fraction of the proposed experiments at INFN-LNL aims at populating neutron-rich nuclei via multinucleon transfer or deep inelastic reactions with stable beams, as an alternative tool to fragmentation or the use of exotic beams. With very heavy stable projectiles (e.g. Pb), one could populate, in particular, nuclei in the regions of shell closures  $N=82$  or  $N=126$ ,

which are beyond reach, incidentally, with fission or fragmentation.

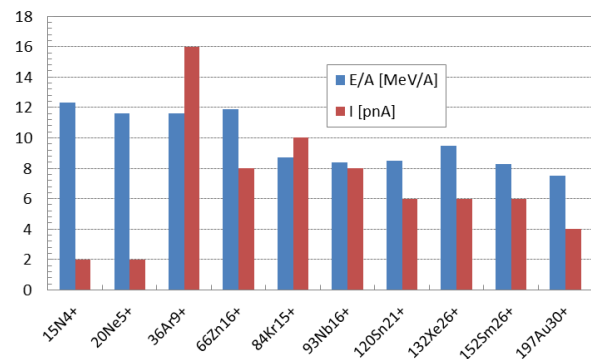
This quest determines the need to increase the final energy of PIAVE-ALPI, so as to go beyond the Coulomb barrier for nuclear reactions involving heavy projectiles and targets. For the Pb-onto-Pb case, for instance, the requested energy is  $9,5 \div 10$  MeV/A.

The paper deals with the status of beam developments with the PIAVE-ALPI linac; covers the recent and present upgrades in the SC QWR performance; describes the being performed upgrade of the cryoplant which, for the first time, gives that minimum redundancy in refrigeration power which makes it possible to add two cryostats with accelerating cavities at the end of ALPI. The reuse of the two “bunching” cryostats CRB2 and CRB4 as “accelerating” ones is finally discussed, together with proposal for new bunching units in their place.

## BEAM DEVELOPMENTS WITH THE ECR ION SOURCE

Albeit affected by the limited time left available by nuclear physics experiments, the development of new beam species with the ECR ion source made some progress lately. The original Alice ion source was replaced in 2008 by a Supernanogan type ECRIS (Pantechnik), a source which – though not being top rated in terms of performance - was particularly suitable for use on the PIAVE HV platform thanks to its whole-permanent-magnet structure. Beams of noble gases were tested and made available pretty soon (Ar, Kr, Xe), together with a number of species which had already been developed by the company itself (Ag, Ta, Au).

Table 1: Present Performance of PIAVE-ALPI Beams, in Terms of Final Energy (MeV/A) and Current (pnA)



Nuclear physics experiments required additional ion species, for each one of which a dedicated development effort was necessary, up to the level where both performance (beam current and charge state distribution) and stability over a time of a few days at least had to be verified.

Table 1 represents the achievement, in terms of final beam energy and currents, of typical ion species available at present on the PIAVE injector ECR ion source, where only the most abundant charge state is reported for each case.

In Spring 2012, we proved that the maximum current which can be transported through PIAVE SRFQs could exceed 2 euA, as the consequence of dedicated beam tests with a  $^{16}\text{O}^{3+}$  beam. Such current limit could be easily pushed at least to 5 euA, since temperature diagnostics on all SC resonators did not show any deviations from their normal behavior and no locking problems were observed. However, beam diagnostics instrumentation in ALPI must be upgraded in order to safely withstand such current, therefore we set 2 euA as a practical limit for the moment.

At the request of the INFN-LNL nuclear physics community, the next elements in the development list are (more or less in chronological order of development): Ca, Mo, Pb, Dy and Pd.

As reported in the introduction, beams of the heavier masses bear a special interest. A Pb beam, though not formally developed yet, seems to be feasible looking at the performances obtained with Au (the element of closest mass produced up to now): by using the frequency tuning technique as a first step and then the double frequency heating one can reasonably expect to obtain a final current with a  $^{208}\text{Pb}^{30+}$  beam (and perhaps  $^{208}\text{Pb}^{31+}$ ), useful for experiments.

### RUNNING PROGRESS IN THE FINAL BEAM ENERGY ACHIEVABLE WITH ALPI

The ALPI linac has seen a continuous upgrade in the number and performance of its accelerating cavities, and consequently of the maximum achievable beam energy. In the early nineties, the 160 MHz QWR resonators (medium  $\beta_{\text{opt}}$  section) originally featured a superconducting Pb layer, electrodeposited onto a bulk Cu substrate, with the rather modest average accelerating field  $E_{a,av} \sim 2,4$  MV/m at 7W. Once the Nb sputtering technology was mature, it was successfully applied to the higher  $\beta_{\text{opt}}$  section resonators (also at 160 MHz), the Cu substrate of which had been optimized for the sputtering deposition, achieving  $E_{a,av} \sim 6$  MV/m. Later on all resonators were stripped of the Pb layer and equipped with a Nb one, onto the same Cu substrates (not optimized for sputtering): the average accelerating field of the medium  $\beta_{\text{opt}}$  section thus increased from 2,4 to 4,8 MV/m at 7W. The increase of ALPI equivalent voltage in the period 2000-2006 is shown in fig.1, where the contribution of full Nb lower beta resonators (see relevant paragraph below) is also shown.

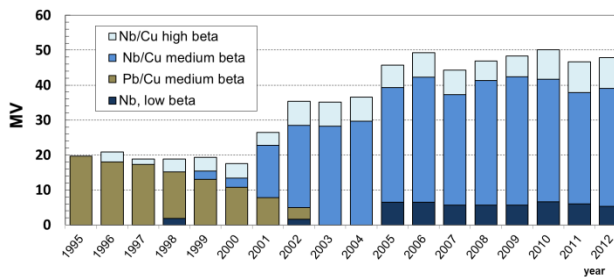


Fig. 1: Previous upgrades of the accelerating field of ALPI resonators ended up in more than doubling the linac overall equivalent voltage.

### Further Upgrade of the Medium Beta Resonators

As anticipated above, a further optimization of the accelerating field of the medium beta resonators can be achieved, if the geometry of their Cu substrate is modified, and made more appropriate for the deposition of a Nb layer per sputtering. A specific paper is presented in these proceedings on this topic, which is just briefly recalled hereinafter [1,2].

Similarly to higher beta resonators, the high-H field region in the medium  $\beta_{\text{opt}}$  QWR resonator (connecting the central stem to the outer conductor) of a prototype ALPI cryostat (CR15) was much better rounded off mechanically, allowing for an improved quality of the SC layer there. Moreover, while higher beta resonators require large accelerating gaps and therefore their beam ports are simple rounded off holes in the outer conductor, the smaller accelerating gap of medium beta resonators asks for a new shape of the beam port, which is no longer brazed (with a sharp corner) but rather extruded from the Cu outer conductor itself (with a rounded-off corner), as shown in fig.2.

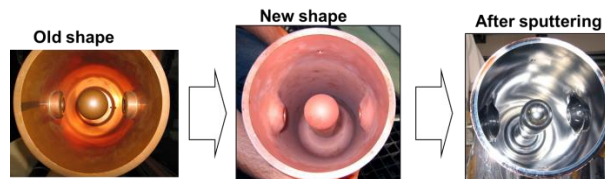


Fig. 2: The change in shape of the interior of medium beta resonators, tested on cryostat CR15 on ALPI linac in 2012, is shown. See a detailed report in ref. 1.

As shown in [1], the results obtained on the prototype cryostat CR15 are promising ( $E_{a,av} = 5,5$  MV/m at 7W), and susceptible of significant improvement, due to the long storage time that these cavities had to suffer since they were sputtered, before being assembled on ALPI.

Such upgrade, which is certainly cost-effective, is however significantly time consuming since it requires dismantling operational cryostats – one by one – while keeping all others operational for the scheduled experimental campaigns. It will be applied, in the future, for any cryostats requiring special maintenance, but for a

swifter energy upgrade of ALPI the preferred option is different (described in the following).

### *Upgrade of the Full Nb Lower Beta Resonators*

Last not least, four additional cryostats were added at the beginning of the linac, housing 80 MHz full Nb QWR resonators. The performance of these cavities, exceeding 6,5 MV/m at 7W in the laboratory tests, could hardly exceed 3 MV/m in operation: in fact they are 100 times more sensitive to He pressure variations than Cu-based cavities are (1 Hz/mbar vs. 0,01 Hz/mbar); in addition, they are less stiff and hence more susceptible to mechanical vibrations. The use of mechanical dampers, originally developed at INFN-LNL and then successfully employed in other labs [3,4], turned out to be a very effective cure but not sufficient to exceed  $E_{a,av} \sim 3,5$  MV/m values in operation. A factor 10 higher RF power (from 150 to 1000 W) proved necessary to exceed 5 MV/m, but this required substantial changes in the design of the input power coupler which had to be cooled with liquid nitrogen. This upgrade is being presently carried out and is expected to be completed in the first half of 2013.

Out of the four cryostats with lower beta full Nb resonators (CR03-CR06): one (CR03) has been fully upgraded and is now operational since 2010; another one has been upgraded but not tested yet (CR05); a third cryostat is being maintained in 2012 (CR04), while the intervention on CR06 is foreseen to take place in Spring 2013.

Fig. 3 shows a photo of the liquid nitrogen refrigeration system of the resonators in the CR03 cryostat. Extended tests carried out in 2010 on cryostat CR03 [5] showed that an accelerating field of 5 MV/m (at a forward power of  $P_f = 200$  W) could be sustained (phase-amplitude locked conditions) during 5 days. Cavities were locked even at 6 MV/m for shorter periods.



Fig. 3: Photo of the N-cooling scheme of full Nb 80 MHz QWRs of ALPI.

It needs to be emphasized that all changes on these cryostats too proceed at the low pace dictated by the

priority use of the facility to deliver beams to the experimental stations for a large fraction of the time.

### **ALPI REFRIGERATOR UPGRADE**

The helium refrigerator of the superconducting ALPI accelerator was commissioned in 1991. It is manufactured by Air Liquide, it uses a Claude cycle processing up to 150 g/s of helium. It consisted of a Brayton cycle with two gas bearing turbines, also used to cool the thermal shields of the cryostats, and Joule-Thomson (JT) expansion valve or, as an alternative, a reciprocating wet expander (WE) for the liquid helium production. In 1991 the refrigerator was accepted, with the WE in operation, giving a refrigeration power of 3900 W at 60-70 K plus 1180 W at 4.5 K. The use of the wet expander was abandoned soon due to its discontinuous stability of operation. The subsequent continuous operation with only the JT valve was just enough, in terms of refrigeration capacity to comply both for the shields and at 4.5K with the number of cavities and cryostats installed ( $\sim 700$  W).

In 2008 it was proposed by LNL to install on the JT circuit, in order to increase the refrigeration capacity at 4.5 K with respect to the use of only the JT expansion valve, a third helium turbine as an alternative to the WE. The design of the supercritical turbine was assigned to Air Liquide. According to the calculation carried out the third turbine, processing up to 70 g/s of helium, between 300 and 400 W at 4.5 K can be added to the existing refrigeration capacity.



Fig. 4: Photo of ALPI Cold Box, recently upgraded with a 3<sup>rd</sup> turbine.

Due to impossibility to stop the ALPI accelerator and as a consequence the refrigerator in the past years, the upgrade was postponed to March 2012 and has just been completed. Fig. 4 shows ALPI cold box after the installation of the third turbine. In Fig. 5 the results in terms of refrigeration capacity at 4.5 K after the upgrade are shown. A measured increase of 360 W, with respect to the previous JT configuration, can be observed. Furthermore the refrigerator can process more helium gas, thus exceeding the 1100 W refrigeration capacity at 4.5K as shown.

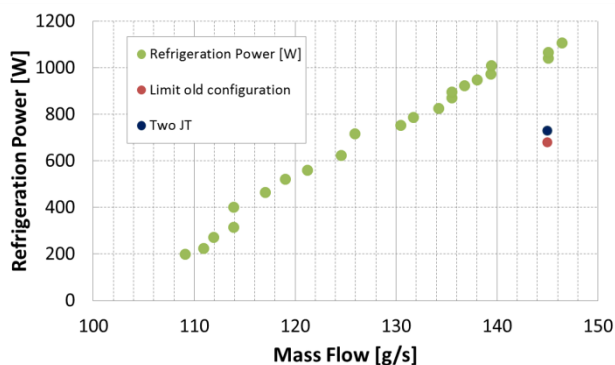


Fig. 5: Refrigeration capacity available at 4.5 K after the installation of the supercritical turbine (green dots). The gain at 145 g/s, with respect to the previous configuration (red dot) is  $(1040-680) = 360$  W. In the actual configuration, without T3, an additional capacity is available, due the by-pass valve of T3 action as an additional isenthalpic expansion in series with the JT valve (blue dot).

The achieved result, in terms of refrigeration capacity, makes it possible to add 100W power dissipation, from the cryostat reshuffling proposed in the next paragraph, while leaving some margin in refrigeration power redundancy.

## THE NEXT FRONTIER ON STABLE BEAMS AT LNL: LEAD AT 10 MEV/A

The recent and on-going progress on the on-line performance of SC cavities made it possible to increase the final available energy of medium-A ( $^{120}\text{Sn}$ ,  $^{132}\text{Xe}$ ,  $^{152}\text{Sm}$ ) nuclei to 8,5÷9,5 MeV/A and of heavier nuclei ( $^{197}\text{Au}$ ) to 7,5 MeV/A. Further upgrade is necessary to reach 9,5 MeV/A for heavier species and more than 11 MeV/A for medium-A ones.

It is easy to calculate with an Excel spread-sheet that approximately the same improvement in final energy, which is achievable by the further upgrade of medium beta resonators described above, can be obtained adding two additional cryostats (CR21 and CR22) with high beta resonators at the end of ALPI. The final beam energy for the reference  $^{208}\text{Pb}$  beam would be 9,5 MeV/m with a charge state  $q=30+$ , and 10 MeV/A with charge state  $q=31+$  (see next paragraph).

It is proposed to promote cryostats CRB2 and CRB4 to positions CR21 and CR22. CRB2 and CRB4 are identical to all other cryostats and perfectly suited to house four accelerating cavities each but, as a matter of fact, they presently house only two SC cavities each, which are used as beam bunchers. Beams injected from PIAVE (housing 80 MHz SC cavities) already by-pass CRB2 (kept off) and are re-bunched by the NC bunchers HEB1 and HEB2, the latter one being placed right after CRB2 on ALPI beam line.

Cryostat CRB2 (housing 2 160 MHz SC QWRs, only one of which is needed, and with the marginal maximum accelerating field of 0,3 MV/m), is used nowadays only with beams injected from the Tandem, when the 80 MHz section is off and the beam is sent directly into the 160 MHz medium  $\beta_{\text{opt}}$  section (cryostat CR07 onwards). If possible, the role of CRB2 would be simply taken in the future by HEB2: only simulations can indicate (see next paragraph), whether the smaller longitudinal acceptance of the 80 MHz HEB2 buncher is adequate to this purpose, or whether it would be a bottleneck, causing a drop in beam transmission.

In place of CRB4, at present requiring one cavity working at the maximum field of 0.36 MV/m, either two normal conducting resonators or a SC one will be needed, depending on the maximum field required.

A complete simulation of the beam transport in ALPI, with the addition of the two high  $\beta_{\text{opt}}$  cryostats, is described in the next paragraph. The case studied is a  $^{208}\text{Pb}^{30+}$  beam from PIAVE.

## BEAM DYNAMICS STUDY ON THE MODIFIED LINAC

Multiparticle beam simulations were performed with the code TRACEWIN [6], starting from the exit of the second SC RFQ in the PIAVE injector, down to the linac end where two additional cryostats with accelerating resonators, derived from bunching cryostats CRB2 and CRB4, are added on the beam line. The main purpose was to optimize acceleration efficiency together with overall ion transmission and determine the required field of the rebunching resonator at the end of ALPI.

The maximum value of  $E_a$  available in the simulations is consistent with state-of-the-art values on ALPI, per each family of resonators: 5 MV/m for lower  $\beta_{\text{opt}}$  cavities, 4,5 MV/m for intermediate  $\beta_{\text{opt}}$  and 6,5 MV/m for higher  $\beta_{\text{opt}}$  ones, including the newly added resonators. Maximum gradient of the magnetic triplets is the presently available value of 20 T/m.

As anticipated, the studied case is  $^{208}\text{Pb}^{30+}$ , i.e. an  $A/q \sim 7$  beam, which – as explained in the introduction – has a vast application interest for the nuclear physics niche at INFN-LNL.

The final energy of the  $^{208}\text{Pb}^{30+}$  beam increases up to 9,8 MeV/A, from the 8.5 MeV/A which would be available till cryostat CR20, the last one on ALPI beam line today. Fig. 6 shows the final result, in terms of transverse envelopes and corresponding beam losses along ALPI.

As can be observed, losses are concentrated along the accelerating sections of the accelerator, the so called low-energy and high-energy branches, which are separated by the achromatic isochronous U-bend. Marginal losses (0.5%) are estimated, as a consequence of the addition of cryostats CR21 and CR22.

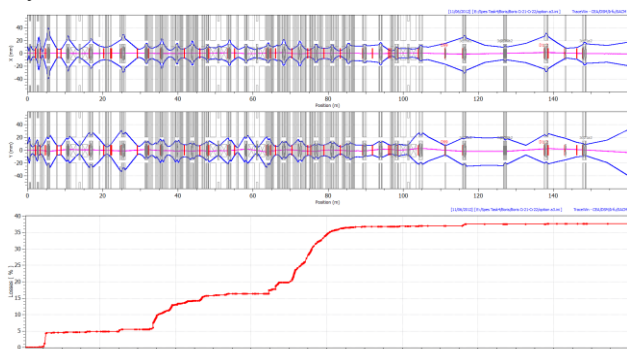


Fig.6: Horizontal and vertical envelopes of the  $^{208}\text{Pb}^{30+}$  beam along ALPI (above) and the corresponding beam losses (below). Most losses are concentrated along the lower and higher energy branches of ALPI, where the accelerating elements are located

As can be seen in the zoom of fig.7, ions are lost mostly on the entrance cavity of the triplet-cryostat-triplet period, both in the low and high energy branches of the linac.

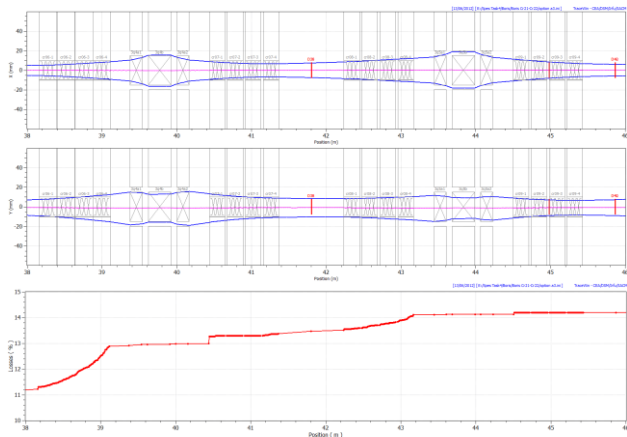


Fig. 7: A zoom of fig.5 is shown, where the detailed location of losses along the linac can be observed.

Those losses which are due to the asymmetry of the magnetic field along the accelerating path in a QWR [8,9] is mitigated by a proper choice of either a  $+20^\circ$  or  $-20^\circ$  accelerating phase in the resonators.

The simulation result shows an overall beam loss of  $\sim 37\%$ , due to the above explained effects. It should be recalled that, in practice, losses are in the order of  $50\div 60\%$  [10]. This is probably to be imputed both to the rather rough present alignment status and to the residual uncertainty in the definition of the amplitude and phase of the accelerating fields on our QWRs, which should be improved thanks to the evolution to more stable digital cavity controllers.

A beneficial effect on the overall beam transmission is expected in Fall 2012, when an overall laser-tracking realignment of the accelerator, in progress on ALPI at present, shall have been completed and, in particular, appropriate displacement of the accelerating cavity axis with respect to the beam axis [9] shall have been applied.

In ref.7 a denser lattice is considered as a possible future upgrade option, in the SPES project framework, with one doublet lens every single cryostat instead of the present triplet lenses every two cryostats. It remains to be seen if such layout change is worth the non-negligible investment, i.e. if the resulting enhancement in the longitudinal acceptance is likely to substantially reduce the gap between the theoretically predicted beam losses and the actual ones.

For the case considered herein, where a  $^{208}\text{Pb}^{30+}$  beam is injected from PIAVE into the 80 MHz full Nb cavities of cryostat CR03, the existing 80 MHz NC bunchers HEB1 and HEB2 are fully appropriate ( $E_a \leq 0.54$  MV/m).

The addition of CR21 and CR22, on the other hand, will increase the final beam energy and, moreover, significantly reduce the distance to the rebunching resonator, which will be still conveniently located in the same place as today, i.e. upstreams of the final L-bend leading to the experimental halls. Both these factors make the required field of this resonator to increase, from the present 1,8 to 3,8 MV/m. This means that a single, but superconducting, cavity must undertake the bunching function when cryostats CR21 and CR22 shall have been added.

It is to be noted, incidentally, that 9,8 MeV/A of an  $A/q=7$  ( $^{208}\text{Pb}^{30+}$ ) beam corresponds to a 1,64 T field in the final dipoles, which is 2,5% more than the dipole rated values: however, both the power supply and the magnets should be able to achieve such value reliably, provided that appropriate refrigeration flux is guaranteed.

The remaining issue is to check whether, for lighter beams injected by the Tandem directly into the 160 MHz medium- $\beta_{\text{opt}}$  Nb accelerating cavities, the use of the PIAVE ALPI 80 MHz buncher HEB2, in place of the 160 MHz SC buncher housed in the to-be-removed cryostat CRB2, would contribute to any additional beam loss downstreams, i.e. if it would act as a bottleneck for the longitudinal acceptance of the machine. Simulations with  $^{65}\text{Cu}^{11+}$ , i.e. one of the most critical – in terms of  $A/q$  ( $\sim 7$ ) – injected into ALPI from the tandem ion source (worst case) are on-going at the present date. This beam – because of its initial relatively high values of  $\beta=v/c$  (7,7%) and  $\text{TTF}_n$  (0,8) – would be conveniently accelerated only by ALPI medium-and-high  $\beta_{\text{opt}}$  sections, i.e. from cryostat CR07 onwards.

## NEW ACCELERATING CAVITIES

The 8 new accelerating cavities, to be installed in refurbished cryostats CR21 and CR22, shall be of the high- $\beta_{\text{opt}}$  Nb-Sputtered type, as well as the new one which must be dedicated to beam bunching.

It is proposed that this resonator be housed in a single-QWR rebunching cryostat. For homogeneity with the rest of the plant, this cryostat shall have a gaseous He thermal shield and common vacuum for thermal insulation and the beam transport.

## CONCLUSIONS

The just accomplished upgrade of ALPI cryogenic plant has provided an increase in the refrigeration power by more than 300 W (from 800 to more than 1100 W), thus providing adequate redundancy and leaving ~ 100W available for new cryogenic installations.

In this framework, it has been proposed to promote the presently “bunching” cryostats CRB2 and CRB4 (at the beginning and end of ALPI) to the role of “accelerating” cryostats CR21 and CR22, equipping them with 8 additional Nb-sputtered QWRs.

As a consequence, with no further cost in beam transmission, the final energy of a very heavy stable beam as  $^{208}\text{Pb}$  would increase from 8,8 to 9,8 MV/m, thus exceeding the Coulomb barrier for Pb-Pb reactions by a large enough amount to make it appealing for the nuclear physics experimental campaign at INFN-LNL.

The role of the 160 MHz buncher CRB2 can be probably taken by the already existing 80 MHz NC buncher HEB2 for relatively light beams injected by the Tandem directly into the 160 MHz medium  $\beta_{\text{opt}}$  section, with negligible beam loss: dedicated simulations are in progress.

The whole project requires modest investment, since it exploits most of the existing equipment, conveniently reshuffled: a limited readjustment of the cryogenic lines and the addition of a single-QWR rebunching cryostat would be the higher cost components required.

## REFERENCES

- [1] A.M. Porcellato et al., Performance of ALPI New Medium Beta Resonators, these proceedings.
- [2] S. Stark et al., Proc. of of SRF2007, Peking Univ., Beijing, China, 216.
- [3] A. Facco et al., Proc of the 1999 Workshop on RF Superconductivity, Santa Fe, NM, USA, 309.
- [4] W. Hartung, [http://accelconf.web.cern.ch/AccelConf/LINAC08/talks/thp033\\_talk.pdf](http://accelconf.web.cern.ch/AccelConf/LINAC08/talks/thp033_talk.pdf).
- [5] A. Facco et al., Proc. of LINAC2010, 181.
- [6] TraceWin CEA, <http://irfu.cea.fr/Sacm/logiciels/index.php>.
- [7] M. Comunian, Physical Design of the SPES Facility, these proceedings.
- [8] P.N. Ostroumov and K.W. Shepard, Phys. Rev. ST Accel. Beams 4, 110101 (2001).
- [9] A. Facco and V. Zviagintsev, Phys. Rev. ST Accel. Beams 14, 070101 (2011).
- [10] M. Comunian et al., Proceedings of IPAC2011, San Sebastian (E), 2034.

## THE COMPACT PULSED HADRON SOURCE STATUS\*

Guan Xialing#, Wang Xuewu, Loong Chunkeung, Cheng Cheng, Du Qiang, Du Taibin, Jiang Chong,  
Wang Dong, Xing Qingzi, Zhang Huayi, Zheng Shuxin,  
Department of Engineering Physics, Tsinghua University, Beijing 100084, China

### Abstract

The Compact Pulsed Hadron Source (CPHS) at the Tsinghua University in Beijing, China has been reported in this paper. CPHS consists of a proton linac, a neutron target station, and a small-angle neutron scattering instrument, a neutron imaging/radiology station, and a proton irradiation station. The proton linac accelerator part is composed of a ECR ion source, LEBT section, a RFQ accelerator, a DTL linac and a HEBT. Up to now, the IS/LEBT and the RFQ have ready. The first phase of the CPHS construction is scheduled to complete 3MeV proton beam on the target in the end of 2012.

### INTRODUCTION

In 2010 June, Tsinghua University, in order to respond the increasing demand in China of accelerator-based neutron and proton experimental platforms for basic researches and technological developments, startup a project of building a Hadron Application and Technology Complex (HATC) which begins with a relatively small and moderate-power facility but later expandable. The initial phase of the HATC is called the Compact Pulsed Hadron Source (CPHS)[1]. The missions of CPHS are education student & staff training; instrumentation and R&D; neutron instrumentation tests; limited-scale science discovery & applications with neutron imaging & scattering instruments. It will be completed as soon as possible in 3 years.

CPHS consists of a proton linac (13 MeV, 16 kW, peak current 50 mA, 0.5 ms pulse width at 50 Hz), a neutron target station, a small-angle neutron scattering instrument, a neutron imaging/radiology station, and a proton irradiation station. The initial phase of the CPHS construction is scheduled to complete in the end of 2012.

The accelerator consists of a ECR ion source, LEBT section, a RFQ accelerator, a DTL linac and a HEBT. ECR ion source will give up to 60mA at 50keV proton beam with proton ration large than 85%, and 0.02  $\pi$ cm mrad normalized rms-emittance. A very short length of LEBT(less than 1.3m) will be used to matching the beam from ion source to the RFQ entrance. A 3 meters long of RFQ accelerate the proton to 3MeV. No MEBT will be requirement in this project. The Drift Tube Linac with permanent magnets focusing lens will accept the proton beam direct from RFQ. A 4.3 meters length of DTL with 43 cells will accelerate the beam up to 13MeV and the HEBT section will transport the proton beam from output of DTL to the Be target inside with 3.5cmX3.5cm

uniform distribution. The main parameters of CPHS are listed in Table 1. Figure 1 shows the CPHS facility layout.

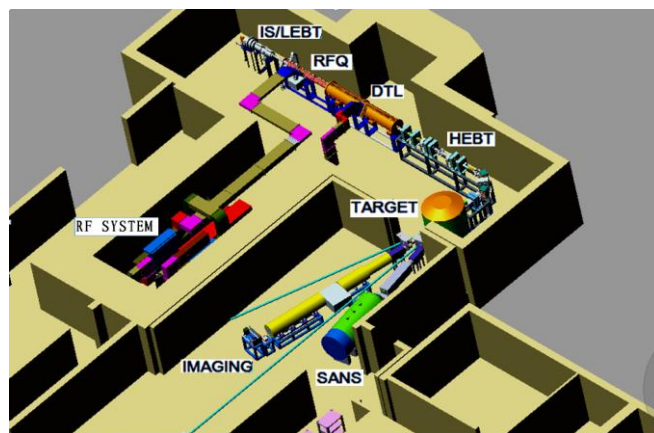


Figure 1: CPHS main facility layout.

Table 1: CPHS primary design parameters.

|                               |   |
|-------------------------------|---|
| Species                       | proton  |
| Proton power on target ( kW ) | 16  |
| Proton energy ( MeV )         | 13  |
| Average beam current ( mA )   | 1.25  |
| Pulse repetition rate ( Hz )  | 50  |
| Protons per pulse             | $1.56 \times 10^{14}$                             |
| Pulse length ( ms )           | 0.5   |
| Peak beam current ( mA )      | 50  |
| Target material               | Be  |
| Moderator type                | H <sub>2</sub> O (300K),<br>CH <sub>4</sub> (20K) |

### IS & LEBT

The proton beam is produced from the electron cyclotron resonance (ECR) proton source (2.45 GHz, 1.5 kW) and transported through the LEBT. The H<sub>2</sub> plasma is restricted by an axial magnetic field shaped by the source body of an all-permanent-magnet (NdFeB rings) design. The 50 keV pulsed beam of 0.5 ms length is extracted by a four-electrode system. The 1.3 m long LEBT consists

\*Work supported by the "985 Project" of the Ministry of Education of China, & Tsinghua University Independent Science and research Plan 20091081263

#guanxialing7911@vip.sina.com

of two solenoid lens, two steering magnets, and a cone configuration optically matches to the RFQ with the Courant-Snyder parameters of  $\alpha=1.354$  and  $\beta=7.731$  cm/rad [2]. The design was assisted by Trace-3D and PBGUN simulations for a beam of 97% space-charge neutralization rate reaching the RFQ with 60 mA peak current and 0.2  $\mu\text{m}$  rms normalized emittance. Figure 2 has shown CPHS ECR ion source and the LEBT.



Figure 2: CPHS ECR ion source and the LEBT.

### RFQ & DTL

The RFQ cavity cross-section is the “conventional” triangular shape with a significant longitudinal variation in the width of the vane skirt [3].

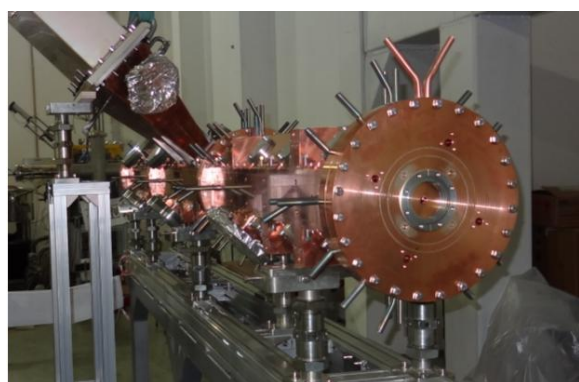


Figure 3: The RFQ photo in site.

The transmission rate given by the PARMTEQM codes is 97.2%. The transverse emittance increases by ~20% when the beam reaches the RFQ exit. Mechanically, the 3-m long RFQ of the 3 MeV, 50 mA peak-current RFQ is separated into three sections of 1 m each to facilitate machining and brazing. Three sections fabrication has finished at the Kelin Co. Ltd. in Shanghai (Fig. 3). No middle energy beam transport will be adopted. The beam focusing in exit of RFQ and the entrance of DTL have a matching design for the transverse and longitudinal. Figure 4 shows the quadrupole and dipole components after tuning which shows that the resulting fields are in excellent agreement with the design (<1% and  $\pm 1\%$ ).

Figure 5 shows the frequency spectrum of the RFQ after tuning.

The physical design of the 13 MeV, 50 mA peak-current DTL was revised in late 2009[4]. The 4.4-m long DTL cavity in a FD lattice consists of two sections of totally 40 cells. Permanent-magnet quadrupoles (PMQs) are used for the transverse focusing at the constant gradient (84.6 T/m). The average accelerating field varies from 2.2 to 3.8 MV/m with the maximum surface field up to 1.6 Kilpatrick. Presently, the full cross-section prototype is under development at Tsinghua university. The parameters of the DTL linac as shown in table 2.

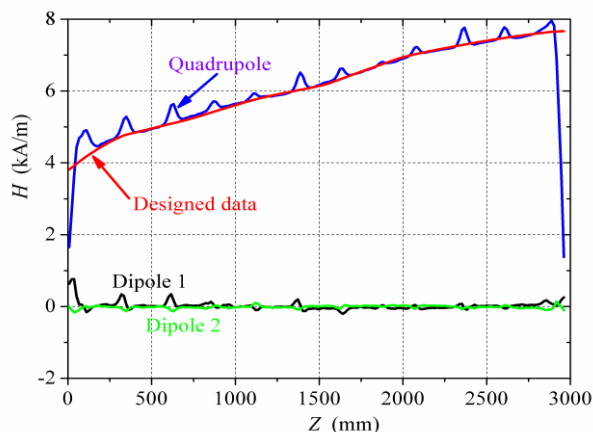


Figure 4: Quadrupole and dipole components after tuning.

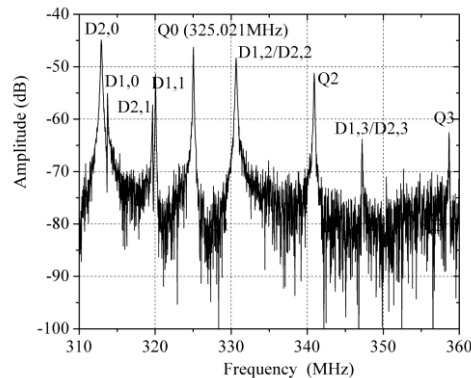


Figure 5: The frequency spectrum of the RFQ after tuning.

Table 2: The parameters of DTL

|                                       |            |
|---------------------------------------|------------|
| Extraction energy (MeV)               | 13         |
| Peak current (mA)                     | 50         |
| RF frequency (MHz)                    | 325        |
| RF peak power (MW)                    | 1.2        |
| Emittance norm. rms ( $\mu\text{m}$ ) | 0.2        |
| Average current (mA)                  | 1.25       |
| RF duty factor (%)                    | 3          |
| Synchronous phase (degree)            | -30 to -24 |

|                           |            |
|---------------------------|------------|
| Accelerating field (MV/m) | 2.2 to 3.8 |
| Focusing magnet type      | PMQ        |
| Quad gradient (kG/cm)     | 8.46       |
| Cell number               | 40         |
| Length( m)                | 4.4        |

## RADIO-FREQUENCY SYSTEM

Both RFQ and DTL share a single RF power source that consists of the signal generator at 325 MHz, amplifier, klystron, high voltage power supply, pulsed modulator, crowbar protection, RF transmission, and control and interlock systems. The RF transmission consists of a power divider with a ratio of 1:2, an isolating attenuator, an isolating phase shifter, and waveguides. The 2.1 MW peak power from the klystron is split accordingly. The isolating attenuator consists of a 4-port circulator, a Y-junction, a high power load and a sliding short. It can be adjustable for amplitudes from 100 to 80% to meet the 0.6 MW power need of the RFQ. The output of the phase shifter can be adjusted for a range of  $45^\circ$ . Figure 6 shows the block diagram of RF transmission system [5].

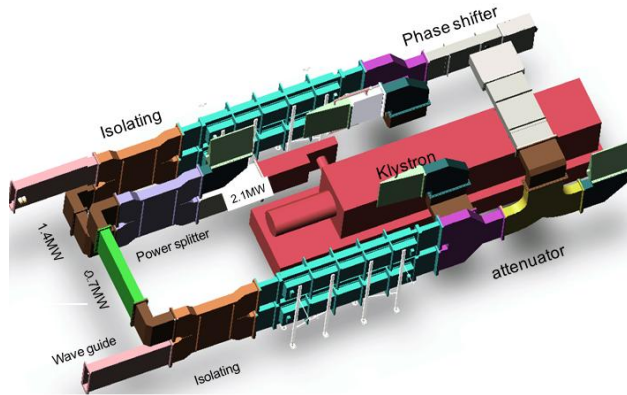


Figure 6: Block diagram of RF transmission subsystem.

## HEBT & TMR

The CPHS high energy beam transport line (HEBT) is designed to deliver a square shaped ( $3.5\text{cm} \times 3.5\text{cm}$ ) on Be-target, 13MeV proton beam at pulse current 50mA with relatively uniform density (10%) using two octupole magnets for nonlinear focusing in both transverse directions. In Fig. 7, we show the picture of the CPHS facilities including the ion source, the LEBT, the RFQ, and the high energy beam transportation, which was installed at Tsinghua university site.

The target station consists of the target, moderator, reflector (TMR) as shown in Fig. 8.

The Be target is 63.5mm in diameter and 1.2mm in thickness. The moderator includes the moderator cell, cryogenic refrigerator, the vacuum vessels for thermal isolation and PT415 to provide the cryogenic environment. The solid methane, 20K, size  $110 \times 110 \times 18$  mm. Reflector is light water, 300K. The target station TMR is under construction.



Figure 7: The picture of the CPHS facilities.

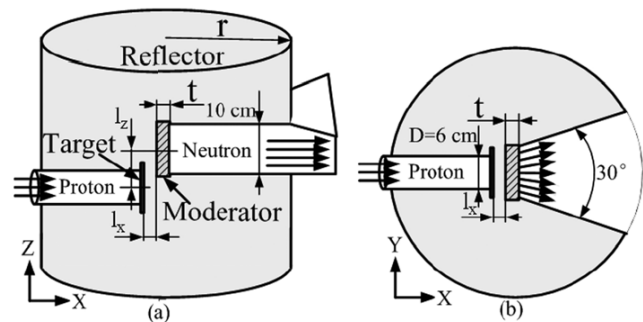


Figure 8: The TMR assembly.

## REFERENCES

- [1] J. Wei, et al., "The Compact Pulsed Hadron Source Construction Status", IPAC'10, Kyoto, Japan, May 2010, MOPE C071, p. 663(2010).
- [2] Feng zhe et al., "Design of the 2.45 GHz ECR Proton Source and LEBT in CPHS" in this proceedings 2010
- [3] Xing Qingzi et al. "development of the 3MEV RFQ for the Compact Pulsed Hadron Source at Tsinghua University" in this proceedings 2010.
- [4] Zheng Shuxin et al., "Research on drift tube linac model cavity for CPHS" in this proceedings 2010.
- [5] Cheng Cheng et al., "The RF System for the Compact Pulse Hadron Source" in this proceedings.

# DEVELOPMENT OF NRA SYSTEM FOR A 1.7 MV TANDEM ACCELERATOR

- HUMAN RESOURCE DEVELOPMENT PROGRAM FOR NUCLEAR ENGINEERING, THE UNIVERSITY OF TOKYO -

Seiji Ito, Hiroyuki Matsuzaki, Akira Morita  
The University of Tokyo

## Abstract

Extremely high sensitivity has been required in the measurement of light elements for the frontier materials science. Ion beam analysis can meet this. We have developed a new NRA system. The system shown successfully its performance by the demonstrative experiment in which fluorine profiles in TiO<sub>2</sub> substrate were clearly obtained using <sup>19</sup>F(p, αγ)<sup>16</sup>O reaction.

This system was applied for the student experiment. The newly developed NRA system has great potential for the frontier research.

## INTRODUCTION

The 1.7MV tandem accelerator (Rutherford Backscattering Spectroscopic Analyzer with Particle Induced X-ray Emission and Ion Implantation Device, RAPID) at the University of Tokyo has been used for various research projects and educational studies since its installation in 1994. Additively, it has been used for the educational purpose recently. Model experiments with ion beam analysis are very helpful for students to understand ion-material interaction which is the foundation of nuclear engineering and materials processing.

Several developments and modifications have also done for new research including, for example, a low level ion irradiation system [1]. In the fall of 2011, we were newly developed a NRA (Nuclear Reaction Analysis) system in order to respond to the recent demand for the sensitive quantification of light elements (H, N, O, F, etc). The performance of new NRA system were demonstrated using <sup>19</sup>F(p, αγ)<sup>16</sup>O reaction. This demonstration was so simple to understand that this model experiment immediately arranged to a student experiment program. The program was used as a part of “Human resource development program for nuclear engineering” proceeded by our department. The new NRA system has great potential for the frontier research for the materials science and functional material process engineering.

## DEVELOPMENT OF NEW NRA SYSTEM

Figure 1 shows the schematic illustration of the 1.7MV tandem accelerator RAPID. RAPID has three beam lines: RBS&ERDA, PIXE and Ion implantation course.

The angle of Ion implantation line is fixed at -7° to the central axis of the accelerator to eliminate neutral particles. NRA detection system was newly developed at the end of the ion implantation line.

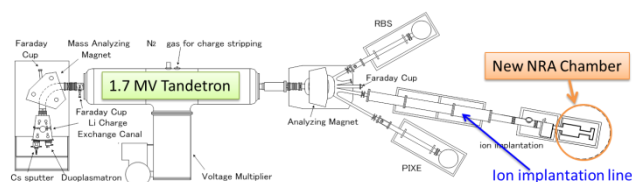


Figure 1: Schematic illustration of the RAPID.

## Outline of New NRA System

Figure 2 shows the layout of new NRA system. The new NRA chamber consists of the main chamber, the sample insertion port and a vacuum pump. The Gamma ray induced by proton beam is detected with a 4 inch bismuth germanate scintillation detector. The BGO detector put in perpendicular to the direction of proton beam travel. The NRA system has several features as follows:

- 1) Chamber design for high counting efficiency.
- 2) Effective electron suppression.
- 3) Effective avoidance against charge-up by using fine copper mesh.

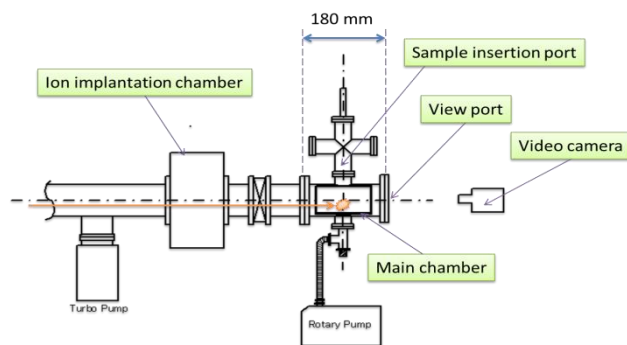


Figure 2: Layout of new NRA system.

## Main Chamber

Figure 3 shows the top view of the main chamber. The special feature is a deeply scooped duct to make the BGO detector being close to the reaction position. Electron suppressor electrode is put in front of the target. The shape of the suppressor is specially designed to suppress secondary electrons effectively. By this design, large effective solid angle for the detector is realized.

\*ito@n.t.u-tokyo.ac.jp

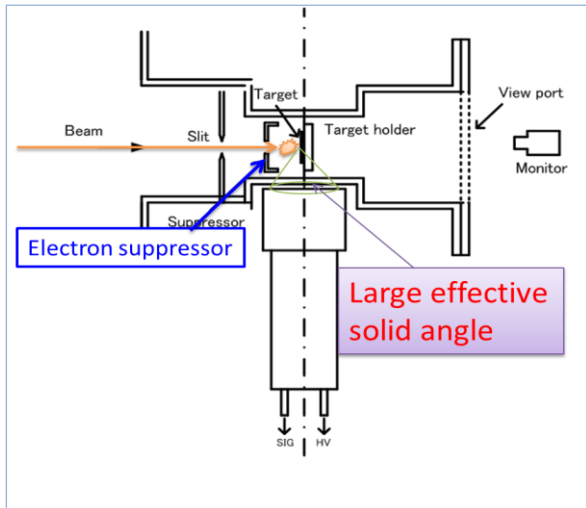


Figure 3: Main chamber.

*Effective Electron Suppression and Monitor*

Target holder is made of metal stainless (SUS304) plate and samples are just put on the plate. This plate can move up and down to select the sample to be analysed.

Figure 4 illustrates the electron suppressor and beam monitor. The electron suppressor electrode is a circular plate with folding edge so that the cross section is L-shape as shown in Figure 4. By this the equi-potential surface becomes surrounding shape by which the secondary electrons will be effectively forced back.

A glass plate is put at the beam monitor position (a hole on the target holder metal plate) to make the beam monitor. The glass is lit by the beam and this light can be observed by a video camera set at the end of the main port. A fine copper mesh (opening 98%) is set in front of the glass to avoid charge-up.

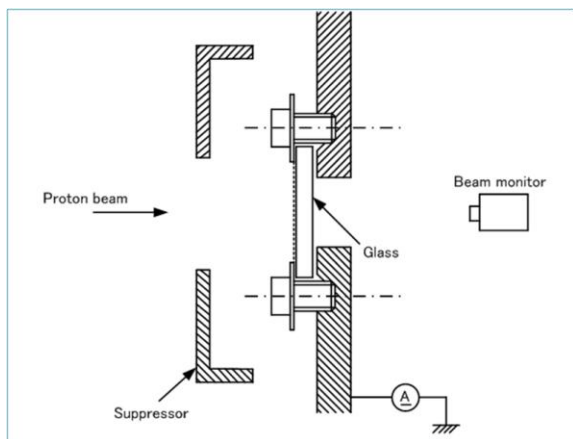


Figure 4: Effective electron suppression and monitor.

*The Effect of the Copper Mesh*

Figure 5 shows comparison of observed ion current profiles with respect to the suppressor voltage:

(A) Beam is at the position of the metal plate  
 (B) Beam is at the beam monitor position (glass with mesh).

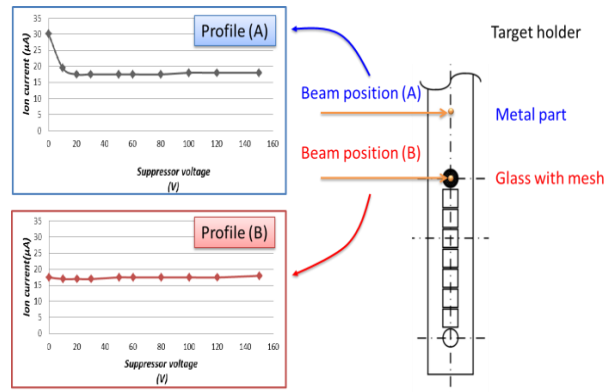


Figure 5: Comparison of observed ion current profiles.

In the profile (B), even at the zero-suppressor voltage, no electron escape was observed. This means that the copper mesh acts not only as charge-up inhibitor but also as an electron suppressor.

**DEMONSTRATION OF NEW SYSTEM**

The NRA experiments were demonstrated using  $^{19}\text{F}(p, \alpha\gamma)^{16}\text{O}$  reaction. The experiment obtains the Fluorine depth profiles of  $\text{TiO}_2$  substrate.

*Target Samples Preparation*

For the demonstration targets were prepared by the ion implantation of Fluorine ion on the  $\text{TiO}_2$  substrates with different dose, i.e.,  $1.0\text{E}16$  (ions/ $\text{cm}^2$ ),  $5.0\text{E}16$  (ions/ $\text{cm}^2$ ) with 524keV and 1024keV energy at room temperature.

Table-1 summarizes the three conditions of target samples preparation A, B and C.

Table 1: Samples Preparation: 3 Conditions

| Sample | Projectile energy (keV) | Total dose (ions/ $\text{cm}^2$ ) |
|--------|-------------------------|-----------------------------------|
| A      | 524                     | $1.0\text{E}16$                   |
| B      | 524                     | $5.0\text{E}16$                   |
| C      | 1024                    | $5.0\text{E}16$                   |

*The  $^{19}\text{F}(p, \alpha\gamma)^{16}\text{O}$  reaction*

We used resonance of  $^{19}\text{F}(p, \alpha\gamma)^{16}\text{O}$  reaction. The resonance energy of projectile proton is 872 and 935 keV (Table 2) [2].

Table 2: Using Nuclear Resonance of Fluorine

| Proton energy (keV) | Reaction                                      | Gamma-ray energy (MeV) | Cross section (mb) |
|---------------------|---|------------------------|--------------------|
| 872                 | $^{19}\text{F}(p, \alpha\gamma)^{16}\text{O}$ | 7.12,6.93,6.13         | 540                |
| 935                 | $^{19}\text{F}(p, \alpha\gamma)^{16}\text{O}$ | 7.12,6.93,6.13         | 180                |

**Results**

Figure 6 shows the results of NRA by using resonance of  $^{19}\text{F}(p, \alpha\gamma)^{16}\text{O}$  reaction. Difference of range due to the injection energy and difference of  $^{19}\text{F}$  ions abundance due to dose are clearly shown. The spread of the spectra are due to the resonance width of the reaction.

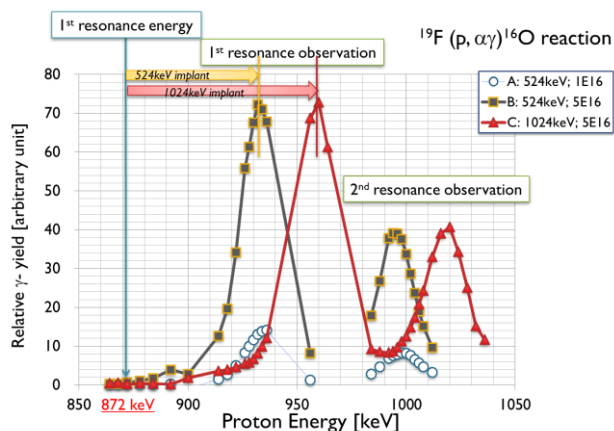


Figure 6: Resonance spectrum of Fluorine

From the observation, positions (depths) of F ion doped were estimated as following (Figure 6, Table 4). The estimations from 1st resonance data and 2nd resonance data are consistent with each other.

The F ions doped with 524keV was estimated to be at 810 – 840 nm depth. The F ions doped with 1024keV was estimated to be around at 1185 nm depth.

Table 3: 1st Resonance (872keV)

|                  | B          | C          |
|------------------|------------|------------|
| Energy           | 524        | 1024       |
| Resonance        | 932        | 959        |
|                  | 60keV      | 87keV      |
| Average Energy   | (932→872)  | (959→872)  |
| Loss             | 74.2keV/μm | 73.6keV/μm |
| Equivalent Depth | 809nm      | 1182nm     |

Table 4: 2nd Resonance (935keV)

|                  | B          | C          |
|------------------|------------|------------|
| Energy           | 524        | 1024       |
| Resonance        | 995        | 1019       |
|                  | 60keV      | 84keV      |
| Average Energy   | (995→935)  | (1019→935) |
| Loss             | 71.3keV/μm | 70.8keV/μm |
| Equivalent Depth | 841nm      | 1182nm     |

**Student Experiment Program**

The demonstrated experimental set up was applied to the student experiment program for the master course of the department of Nuclear Engineering [3].

The results were very simple and helpful to understand the interaction between ions – target or ions – materials, thus very educational.

**SUMMARY**

1. A NRA (Nuclear Reaction Analysis) system was developed at the RAPID accelerator facility, The University of Tokyo to meet sensitive quantification of light elements.
2. The NRA system has several features:
  - 1) Chamber design for high counting efficiency.
  - 2) Effective electron suppression.
  - 3) Effective avoidance against charge-up by using fine copper mesh.
3. We found that the mesh acts not only as charge-up inhibitor but also as an electron suppressor. This indicates a possibility for the sophisticated sample holder without additional electron suppressor electrode.
4. The NRA experiments using  $^{19}\text{F}(p, \alpha\gamma)^{16}\text{O}$  reaction were successfully demonstrated. Since the results were clear, this experimental setup was applied to the student experiment program.
5. The newly developed NRA system has great potential for the frontier research for the materials science and functional material process engineering

**ACKNOWLEDGMENT**

The authors would like to thank Dr. M. Yasumoto, The University of Tokyo for his advises in setting the electronic circuit. We would express our gratitude to Dr. Y. Hirose, The University of Tokyo for his useful suggestion for selecting the target material. We also thank Dr. D. Sekiba, the University of Tsukuba for his in designing the NRA chamber.

**REFERENCES**

- [1] K. Shimada et al., “A Sensitization of Solid State Nuclear Track Detector in Carbon Dioxide for Improved Fast Neutron Dosimeter,” Jpn. J. Health Phys. 46(2), 163(2011).
- [2] J. Bottiger et al., J. Appl. Phys. 47, 1673 (1976).
- [3] H. Matsuzaki, “Measurement of Trace Element in Material by means of nuclear Reaction Analysis”, Text for the Nuclear Engineering Master’s course exercise, Department of Nuclear Engineering and Management School of Engineering, The University of Tokyo.

## NEW DEVELOPMENTS AT THE TANDEM ACCELERATORS LABORATORY AT IFIN-HH

D.G. Ghiță\* , M.S. Dogaru, M.M. Gugiu, S. Dobrescu, C.I. Călinescu, Gh. Căta-Danil,  
M. Enăchescu, P. Ionescu, N. Mărginean, I. O. Mitu, D.V. Moșu, A. Pantelică, D. Pantelică,  
A. Petre, I.V. Popescu, B. Savu, T.B. Sava, C. A. Simion, C. Stan-Sion, M. Stătescu, N.V. Zamfir  
*Horia Hulubei National Institute for R&D in Physics and Nuclear Engineering  
IFIN-HH, Magurele, Romania*

### Abstract

The upgrade of the 9 MV Tandem accelerator at IFIN-HH started in 2006. Remarkable work was done in the last 6 years that can be seen in the improved performance and reliability of the machine. Using original preparation techniques, some new beam species were tested for the first time in our laboratory. This opened the door to new experiments. A major improvement for the laboratory is the installation of 1 MV Tandetron accelerator dedicated to ultra-sensitive accelerator mass spectrometry (AMS) measurements of  $^{14}\text{C}$ ,  $^{10}\text{Be}$ ,  $^{26}\text{Al}$  and  $^{129}\text{I}$ , and 3 MV Tandetron accelerator dedicated to ion beam analysis (IBA). The main directions of the research activity in the laboratory will be shortly presented.

### INTRODUCTION

The Bucharest FN Tandem accelerator was commissioned in 1973. The accelerator was produced by High Voltage Electrostatic Corporation - HVEC USA. The first upgrade of the machine was done in 1983 when a new negative Cs sputtering ion source was installed [1] and the maximum accelerating voltage on the terminal was increased from 7.5 to 9 MV by installing new accelerating tubes with stainless steel elements and inclined field and introducing of  $\text{SF}_6$  into the insulating gas mixture. In 1977 the accelerator column was destroyed and in 1986 it was partially damaged by two major earthquakes. Following these two events a second major upgrade was done, thus the earthquake protection system was installed [2].

Starting with 2006 a major upgrade program is ongoing. The upgrade works from 2006 to 2009, which include the installation of the pelletron charging system, a new sputtering ion source, a dedicated sputter ion source for AMS measurements, installation of titanium, spiraled field accelerator tubes, a lithium charge exchange alpha source, nanosecond pulsing system, new power supplies for the major ion optics elements, and refurbishment of the vacuum system were already reported in Ref. [3].

Nevertheless the upgrade program of our main accelerator continued and other two major experimental facilities are already installed. The upgrade of the electrical system of the main ion optic elements on the tandem accelerator continued with renewal of the power supplies of the beam deflection elements. The old stabilization system of the ac-

celerator functioning since 1973 was also replaced with an in house version, improving the stability of the accelerated beam. The alpha source installed in 2006 was upgraded to a more stable and reliable version. In order to ease the operation of the main power supplies of the bipolar magnets and beam deflectors, automated control system of the power supplies was realized. One important improvement of the accelerator is the installation of a new gas transfer system (made by DILO [4]). Compared with the old system using oil vacuum pumps and compressor, the new system is a state-of-the-art system specially customized to work with our machine. The new gas plant will improve the quality of insulating gas due to its oil free pumps and compressors and will diminish the gas losses at each transfer to an acceptable level. For the safety of the stripping foils and for protecting the accelerating tubes of accidental migration of carbon stripping foils inside them, a fast closing valve [5] was installed on the high energy section after the analyzing magnet. With this occasion, all the beam lines were replaced before and after the analyzing magnet with new beam lines having vacuum treated surfaces, thus improving the vacuum in that area.

One of the most important achievements for the research studies done at the tandem accelerator in this period were the new delivered beams that opened the possibility for new physics experiments in fields of basic and applied research.

Starting with 2010 two new HVE Tandetron accelerators [6] were installed in IFIN-HH with the support of an infrastructure grant [7] funded by the National Authority for Scientific Research [8]. The 1 MV Tandetron accelerator, along with its chemistry laboratory is dedicated for ultra-sensitive accelerator mass spectrometry measurements of C, Be, Al and I elements. The 3 MV machine, presently under commissioning, is dedicated for ion beam analysis techniques. Both machines are aimed to continue the long tradition in the applied physics research, currently being done at the 9 MV tandem accelerator.

### MAIN UPGRADES OF THE 9 MV FN PELLETRON TANDEM ACCELERATOR

#### *Upgrade of the Beam Steering System Power Supplies*

The beam deflection system of the accelerator is an important part in the operating procedure. The beam quality and stability was often affected by the defective operation

\* dghita@tandem.nipne.ro

of the old poorly stabilized power supplies. The operation of the power supplies for the electrostatic deflectors was also not advantageous, pairs of power supplies being connected to the deflecting plates, both being polarized to an identical bias voltage in order to obtain the non-deflected accelerated beam.

The old beam deflection system power supplies of the tandem accelerator were replaced by new high voltage, bipolar output and continuous zero crossing power supplies (made by FuG-Germany [9]). The new devices were extremely stable, having a residual ripple smaller than  $5 \times 10^{-4} pp + 10 mV pp$ . The whole operation procedure for the electrostatic deflectors was also changed. Each pair of plates of an electrostatic deflector requires only one power supply whose output is connected to one of the plates while the second one is grounded. So a much more stable beam was obtained and the machine operation is eased. The power supplies for the double x and the double y deflection system of the LE part of the FN tandem are showed in Figure 1.



Figure 1: Bipolar power supplies block with continuous zero crossing capability for an electrostatic deflection system

### *New Beam Stabilization System*

The stability of the beam was often affected by malfunction of the old and obsolete, but complex beam stabilization system of the FN tandem. The user request of beam time was also often affected. Thus, the work on a new, in-house built system was one of the main goals for our team. The work started with redesigning two preamplifiers for the slit

signal based on modern logarithmic integrated circuits, capable to measure on a wide range of currents (from 100 pA up to 3.5 mA) [10]. The improvement was continued by redesigning the comparator circuit giving the error signal as a result of the variation of the beam on the two image slits of the accelerator. The error signal was fed into the core circuit of the stabilization system, also completely rebuilt using a combination of analog and digital electronic circuits which replaced the electromechanical devices of the old stabilization system. This core circuit is making use of both signals coming from the GVM and slit error circuits, adjusting the voltage on the grid of the corona system vacuum tube and thus stabilizing the high voltage on the terminal. This upgrade improved the stability of the system, reducing the ripple on the terminal by about 20%. Due to its sensitivity the system allowed to decrease the lower limit for stable accelerating voltages from 1.5 MV to 0.8 MV.

### *Upgrade of the Helium Negative Ion Beam Source*

The homemade helium source (a duoplasmatron ion source followed by a lithium vapor charge exchange unit [3]) commissioned in 2006 opened a new range of nuclear physics experiments in our laboratory [11]. The original design proved to obtain good results, but was not able to deliver stable beam for long periods of time, its operation being interrupted very often for cleaning and lithium refill. The design of the lithium oven placed at the ground potential surrounded by high voltage optical elements was not very reliable. Another drawback was that the lithium reservoir was not sealed and the lithium vapours were migrating in the whole source chamber, destroying the insulation of the accelerating elements. In order to solve all the problems, many elements were redesigned. The new layout of the source is presented in Figure 2 a) and the source itself is presented in Figure 2 b). The main modification was in the design of the lithium oven and reservoir. The reservoir was redesigned to be sealed and easy to remove without misaligning the adjacent electrodes. Another improvement consisted in connecting the lithium oven to the HV charge exchange unit and transmitting the low voltage supply through a separating transformer. This design made it more compact and efficient. In order to avoid the contamination of the surrounding accelerating elements with lithium vapors, more efficient condensation elements were designed at the ends of the lithium reservoir. The negative helium source is now very reliable and it can deliver beams for long periods of time with less lithium consumption and higher beam stability.

### *Computer Control System for Power Supplies*

A program to change the old analogic control of the tandem by a computer control was started some years ago, beginning with the computer control of the sputter ion source [3]. This year the computer control of the bipolar magnets

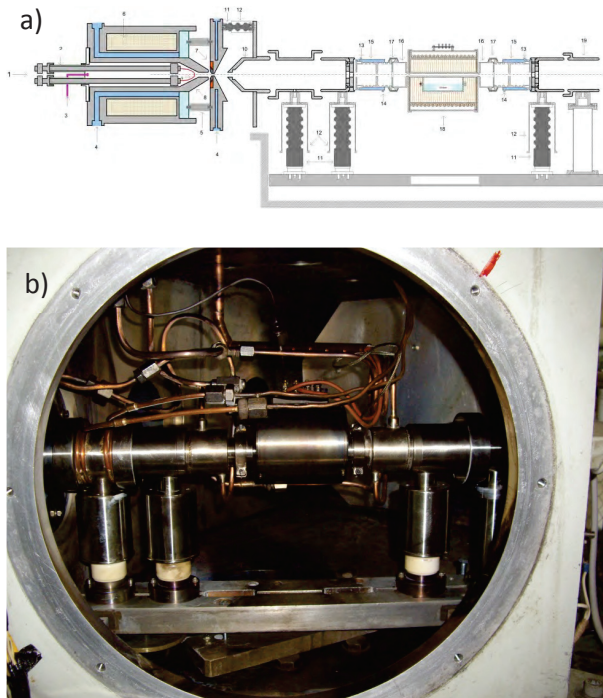


Figure 2: a) The layout of the new design of the helium source, b) The fully functional helium source

(see Figure 3) and the electrostatic and magnetic beam deflectors (see Figure 4) was achieved.

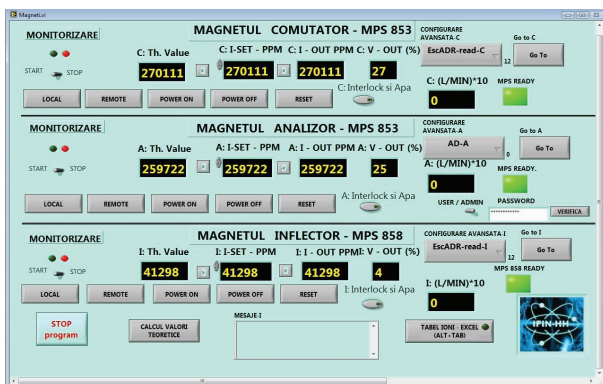


Figure 3: The computer control system for the three bipolar magnets on the accelerator (inflection, analyzing and switching magnet.)

The interesting feature of the control for the magnets is that the operator has to input only the beam specie, the energy and the desired charge state after stripping, and the fields in the magnets will be automatically set to a coarse value. The fine tuning will be done afterwards by the operator.



Figure 4: The computer control system for all the electrostatic and magnetic deflectors on the accelerator.

### New Gas Transfer System

The insulating gas used now in the accelerator tank is a mixture of SF<sub>6</sub> and nitrogen. Two main problems regarding the gas were encountered. First is the problem of gas losses during every transfer to the storage tanks and back to the accelerator tank, and second is the quality of the gas, mainly from the point of view of the moisture, which can damage the nylon links of the pelletron chain, and the oil vapors coming from the pumps and compressors of the old gas system.

As a consequence the complete replacement of the old system by a new one was decided. The gas transfer plant was custom built by DILO [4] in Germany. When designing the system we took into account all the particularities our system has (for example different final pressures for the three storage tanks). A picture of the new installed system can be seen in Figure 5.



Figure 5: The new gas transfer system of the tandem accelerator.

The main advantages of this new system is that it has virtually no gas losses, has very good filtering capacity, being capable to remove moisture and corrosive products resulted from the SF<sub>6</sub> in the moment of sparks in the tank, and it has oil free compressors and vacuum pumps for SF<sub>6</sub> recovery and recirculation. This will ensure much more stable running at high voltage on the terminal.







Figure 10: The hall of the 3 MV Tandatron accelerator

beamlines at the 9 MV tandem accelerator. In order to expand the research in the applied direction and because in this region of Europe this is the only laboratory having the dedicated equipment for this, we invested in this direction.

Besides the development of the accelerator infrastructure there is a big effort in the development of the research infrastructure around these accelerators. Two major breakthroughs were accomplished this year: the commissioning of the mixed detection array consisting of 25 HPGe detectors with anti-Compton shields and the 12 LaBr<sub>3</sub>:Ce fast timing detectors called ROball, which will be used for nuclear structure physics studies at the energies delivered by the 9 MV tandem accelerator [15, 16, 17], coupled with the plunger device dedicated for ps timing measurements.

## ACKNOWLEDGMENT

We would like to thank Dr. Agata Olariu and Dr. Silviu Olariu for initiating and for their work in planning the installation for the two new accelerators. We would also like to thank the National Authority for Scientific Research for the support funding for upgrading of the 9 MV tandem accelerator and for funding the projects for the new infrastructure in the framework of the grant 7PM/1/2008. Many thanks to the technical team of the accelerators, Constantin

Crăciun, Gheorghe Mihon, Gheorghe Ion, Cristian Florea, Cristian Păun, Ionuț Brînzan, Gigi Naghel, Mihai Badea, Stancu Cojocaru, Viorel Bătrâneau, Cristian Popescu, and Laurențiu Povariu, for their highly skilled technical work.

## REFERENCES

- [1] S. Dobrescu and L. Marinescu, AIP Conference Proceedings Vol. 287, Particles and Field Series 53, Editors J. G. Alessi and A. Herscovitch, BNL, pp. 474-483, 1993.
- [2] L. Marinescu, G. Pascovici, V. Zoran, R. Dumitrescu, T. Sireteanu, E. Iordachescu, I. Filimon and A. Winkler, Nucl.Instr. and Meth. A328, 90, 1993.
- [3] S. Dobrescu, et al., Proceedings of 11<sup>th</sup> International Conference on Heavy Ion Accelerator Technology, Venezia, Italy, 2009.
- [4] DILO Armaturen und Anlagen GmbH - Gas handling plants, [http://www.dilo-gmbh.de/cms/front\\_content.php?idcat=7](http://www.dilo-gmbh.de/cms/front_content.php?idcat=7).
- [5] VAT - Fast closing valve, [http://www.vatvalve.com/products/catalog/F/752\\_1\\_V](http://www.vatvalve.com/products/catalog/F/752_1_V).
- [6] High Voltage Engineering - Tandatron Accelerator Systems, [http://www.highvolteng.com/media/Brochures/Tandatron\\_broch.pdf](http://www.highvolteng.com/media/Brochures/Tandatron_broch.pdf).
- [7] 7PM/1/2008, [http://proiecte.nipne.ro/pn2-capacitati\\_mari/index.php](http://proiecte.nipne.ro/pn2-capacitati_mari/index.php).
- [8] National Authority for Scientific Research, <http://www.ancs.ro/>.
- [9] FuG Elektronik GmbH - High voltage power supplies, <http://www.fug-elektronik.de/webdir/2/products.htm>.
- [10] D. V. Moșu et al., A new slit stabilization system for the beam energy at the Bucharest tandem Van de Graaff accelerator, paper submitted to Nuclear Instruments and Methods in Physics Research Section A.
- [11] I. Căta-Danil, et al., Rom. Rep. in Phys., Vol. 60, Issue: 3, Pages: 555-561, 2008.
- [12] C. Michelagnoli, et al., Acta Physica Polonica B Vol. 42, Issue: 3-4, Pages: 825-828, 2011.
- [13] P. J. R. Mason, et al., Phys. Rev. C 85, 064303, 2012.
- [14] A. Olariu, C. Ivan, N. V. Zamfir, Rom. Rep. in Phys., Vol. 63, No. 4, P. 923928, 2011.
- [15] N. Mărginean, et al. Eur. Phys. J., A44, 31-41, 2010.
- [16] Presentation at the European Nuclear Physics Conference, 2012
- [17] C. Mihai, et al., Phys. Rev. C Volume: 83 Issue: 5 Article Number: 054310, 2011.

## TERMINAL VOLTAGE STABILIZATION OF PELLETRON TANDEM ACCELERATOR

Nikolai R. Lobanov<sup>#</sup>, Dimitris Tsifakis, Peter Linardakis, Michael Blacksell, The Department of Nuclear Physics, Research School of Physics and Engineering, The Australian National University, Canberra, Australia

### Abstract

An NEC terminal voltage stabiliser TPS-6.0, based on conventional corona control, has been installed and investigated on the ANU 14UD tandem accelerator. The fluctuations in the charge transport of the electrostatic pelletron generator and their correlation with mechanical oscillations of the chains and terminal voltage ripple have been analysed. Emphasis during commissioning is placed on the components of the two-loop feedback system and on the application of this system to production of high energy-resolution beams. The relationship between transfer functions for the two loops required for optimum operation is discussed. This system produces the beam position at the image slit of the 90° energy-analysing magnet with long-term stability equivalent to a 3.9 kV FWHM fluctuation of the terminal voltage. The concept of novel fast control loop utilizing the high-frequency component from the image slits to control the voltage of the last gap of high-energy acceleration tube is described.

### INTRODUCTION

A variety of nuclear physics experiments require the minimum energy spread of particle beams. High-energy resolution is also required for the need in beam position stability at applications of ion beam analyses. Several methods have been employed to achieve beam energy resolutions of  $\Delta E/E = 10^{-4}$  to  $10^{-5}$  in the electrostatic accelerators. In small machines with a terminal voltage below 5 MV, the stabilization system can be implemented by controlling the up-charging voltage [1]. The modulation of the amplitude of down-charge has a more rapid effect on the terminal voltage than corresponding changes in up-charge. The Daresbury 30 MV tandem has used the laddertron down-charge with the response speed limited to 0.06 s delay [2]. Burger *et al.* refer to the stable periodic pattern of the acceleration voltage fluctuations and have introduced “predictive fluctuation compensation” [3]. A TUNL system has implemented the terminal collector filter circuit for charging system [4]. The potential of the terminal can be controlled by varying the current load [1]. A fast response variation is achieved by modulating the electron beam from a gun at a base of the tube.

Since the weak components of the control loop are the signal delay characterizing the corona transfer function and the response of down-charge or variable load systems, a more direct energy-affecting element with fast response is desirable. The components for the application of the corrective voltages are the ion source, the terminal

or the stripper, the high energy end of the accelerator and the target. Reference [1] describes a terminal ripple reduction system consisting of a capacitive liner along the tank wall facing the terminal, to which a terminal correction voltage derived from a capacitive pick-up or slit current signal is applied. Modulating the terminal stripper is another alternative [5]. The energy of the particles at the terminal is high enough so that a few kV energy modulation does not affect the optics. At a number of laboratories, various techniques such as time of flight, data gating, energy sorting and target potential modulation are being used to improve the energy resolution.

We will describe an energy feedback system yielding high-resolution particle beams, which has been developed for the ANU Heavy Ion Accelerator Facility (HIAF). This system utilizes two principal feedback mechanisms. The standard feedback loop employs a correction signal derived from summing the signal from capacitive pickoff plates (CPO) with a slit difference signal or a generating voltmeter (GVM). This signal is applied to the control grid of a high voltage triode 6BK4 connected to corona points mounted inside the tank. The maximum cut-off control frequency is below 10 Hz because of the transit time for electrons from the corona points to the terminal. Since information about higher frequency beam energy variations is present in the slit difference signal, a correction voltage is generated and applied to the last gap of the high-energy acceleration tube. This new method has the same advantage as modulation of terminal stripper. However it is much simpler since the control element is located at ground potential. The fast correction loop has not been implemented yet and is at R&D stage. In this paper, we will describe elements of both systems, its application for the production of high-resolution particle beams and some measurements of system performance.

### DESCRIPTION OF THE HIAF VOLTAGE CONTROL SYSTEM

The GVM signal is only capable of showing relatively slow voltage variations (<1 Hz) due to the dc filtering of the ac signal generated as the grounded rotating vane alternately covers and uncovers the stator plates connected to the GVM amplifier. The momentum analysed currents intercepted by the control slits at the image position are fed into two matched low-noise logarithmic pre-amplifiers. The slit signals are coupled to the pre-amplifier by short 2 m coaxial cables. The

\*Work supported by Heavy Ion Accelerators Education Investment Fund  
#Nikolai.Lobanov@anu.edu.au

bandwidth of the pre-amplifier depends on the input current and it is approximately 250 Hz at 100 nA or 5 kHz at 1  $\mu$ A. Therefore, the slit current amplifier has a relatively low bandwidth for low slit currents. The dc response is characterized by logarithmic gain in the range of 1 nA to 100  $\mu$ A.

To allow for faster error correction, it has been standard practice to use CPO plates to feed back faster error signals to the TPS. An adjustable crossover frequency determines the frequency above which the CPO error signal takes over from the GVM or slit error signals. All experimental data presented in this work was produced at a crossover frequency set at about 1 Hz.

The conventional corona regulator is used to correct for the large, low-frequency fluctuations in the terminal voltage that are characteristic of the pelletron charging system. The GVM signal is used to maintain the dc terminal voltage in the absence of the slit difference signal. Automatic switching from slit to GVM control is provided when a beam is not present. The CPO provides an ac error signal that may be summed with either the GVM signal or the slit difference signal to reduce low frequency fluctuations in the terminal voltage. The main controller is located in the 14UD control console. The Corona Probe Controller (CPC), CPO and GVM pre-amplifiers are located in the middle of the accelerator tower close-by to the actual devices. The slit difference pre-amplifier is located under the tank next to the slits.

### THE OPEN LOOP FREQUENCY RESPONSE

The measurement of open-loop frequency response and phase shift for 14UD corona regulator was made by exciting the corona triode grid with a signal generator and frequency synthesizer, and observing the resulting signal on a GVM [6]. The reason for using the Frequency Synthesizer was to generate very slow frequencies that the Signal Generator could not maintain with a degree of stability. A chart recorder was used to record the slow response to a step function, as no oscilloscope could be found that had an appropriate time base. The step input measurements were used to measure the 1/e time of the accelerator at different terminal voltages, as shown in figure 1. The step function was kept constant at 1 V for these measurements.

The step function was also used to measure the time difference between changing the triode grid voltage and the resulting response in the terminal voltage, as shown in figure 2. This technique is accurate enough to measure transit time when the terminal potential is positive and the charge transport is caused mainly by negative ions.

A similar delay time has been measured by using phase shift method. This method is based on measurement of the phase shift  $\Phi$  between the GVM output and the sinusoidal signal of frequency  $f$  applied to the regulating triode grid.

The sine wave measurements were used to plot the phase and voltage response to frequency at a terminal

voltage of 14 MV. The transfer function was measured over the frequency range 0 to 10 Hz.

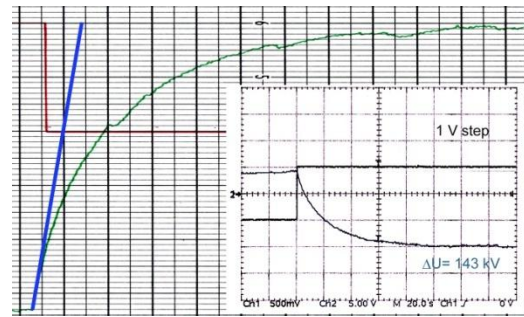


Figure 1: Open-loop response at 8 MV with a 1 V Step Input (red line). The straight blue solid line is the tangent to the GVM signal (green line). Time constant  $\tau_c$  was 10.2 s. The inset shows the same response captured with the oscilloscope.

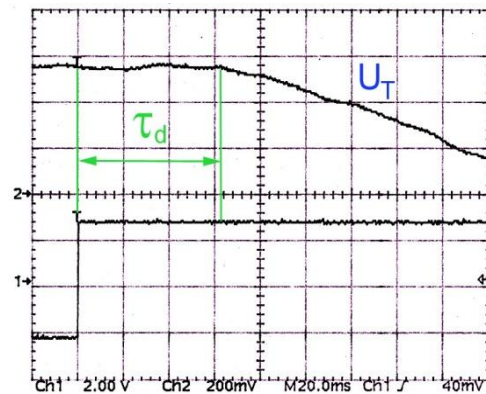


Figure 2: Terminal voltage change with a 1 V Step Input. Measured delay time  $\tau_d=31$  ms.

The last set of step measurements were used to estimate the maximum response time of the accelerator at 14 MV. Figure 3 shows the measured open loop voltage response for 14UD corona regulator.

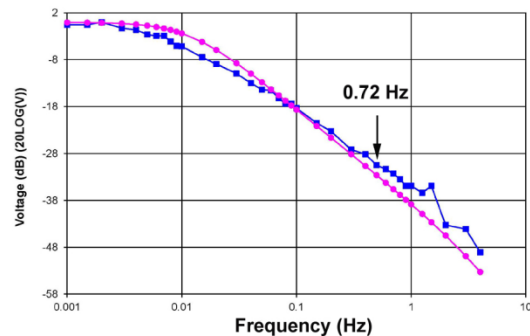


Figure 3: Corona regulator voltage response and curve fitting. Square box is the measured accelerator voltage response; circle is the voltage response calculated from curve fitting equation. 0.72 Hz is the rotation frequency of the chain.

The phase response of the accelerator is shown in figure 4. As shown in figure 2, the 14UD accelerator has a constant 31 ms delay between the triode grid changing and a voltage change appearing on the terminal. The delay depends on the tank SF<sub>6</sub> gas pressure and the position of the corona needles. The closer the needles are to the terminal, the smaller the delay. The measured phase response, figure 4, has the 31 ms delay removed.

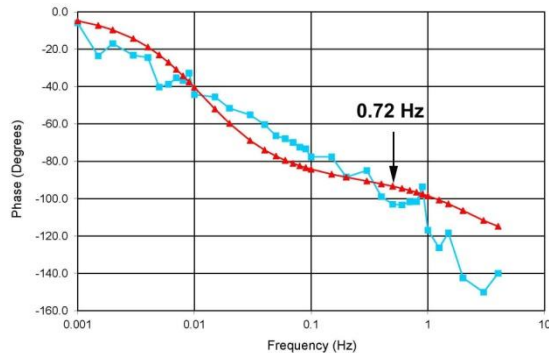


Figure 4: Corona regulator phase response and curve fitting. Square box is the measured accelerator phase response; triangle is the phase response of curve fitting equation. 0.72 Hz is the rotation frequency of the chain.

Using the curve fitting software an equation was found that matched the measured voltage and phase response in the Laplace domain. This program was used to weight the match equally between the phase and voltage. The final Least Squares Error was 4.05353. The equation is shown below:

$$G_p(s) = (1.0 + 0.01s)/(22.6271s^2 + 85.2377s + 1.0) \quad (1)$$

The voltage and phase plots derived from equation (1) fit the measured characteristics of the accelerator adequately, as shown in figures 3 and 4. A black arrow on the Bode plots in figures 3 and 4 marks the frequency 0.72 Hz, which corresponds to the rotation period of the chain. Chains No. 2 and No. 3, installed recently in the tandem, are found to be stimulating the feedback loop into low level oscillation at rotation frequency of the chain. It has been shown subsequently that both chain assemblies have up to 60 degrees torsion twist, causing a mechanical disturbance at each revolution. A stability requirement for a corona regulator is that for all frequencies for which the open loop gain is greater than unity, the accumulated phase shift around the loop must be less than 180° by a phase margin of ~30-40° in practical systems. Evaluation of figure 4 indicates that unity gain for the corona loop is still available at or below 10 Hz at 14 MV terminal voltage, corresponding to given corona points position and ~104 psi pressure of SF<sub>6</sub> gas.

## CONTROL SYSTEM PERFORMANCE

The nature of the error signals can be examined with and without the feedback control loop. Figure 5 contains captured traces of the data logger showing the terminal

fluctuations measured with CPO and the GVM devices. The two CPO probes are mounted on opposite sides of the terminal in order to minimize the effect of terminal vibrations on the CPO<sub>Σ</sub>=CPO<sub>1</sub>+CPO<sub>2</sub> signal.

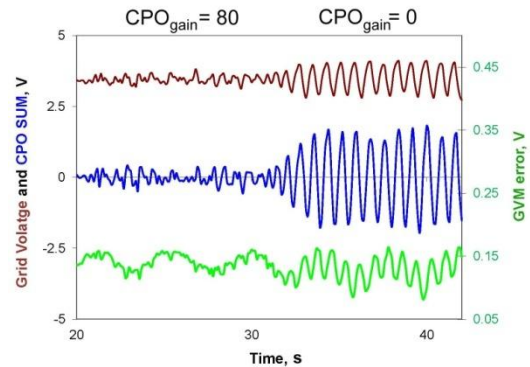


Figure 5: Data logger traces showing grid voltage, CPO<sub>Σ</sub> and GVM error signals without and with CPO feedback.

In figure 5, the CPO gain reduced from optimum to 0 ~32 seconds after starting data logging. The controller crossover frequency was set at 0.9 Hz for all experiments. The logger trace gives the slow variations of the measured signal. The trace on the right was taken with the CPO feedback off, the terminal voltage at 13.5 MV and 125 nA of <sup>12</sup>C<sup>+5</sup> beam on the stop Faraday cup positioned after energy analysing slits. The trace on the left was taken under the same conditions, except that the CPO feedback was on and the gain was adjusted to minimize the slit error signal. In the left trace, the error signal has been greatly diminished. Figure 6 displays the terminal voltage distribution over a period of about 1 hour at 13.5 MV, with both control and CPO gains set to optimum values.

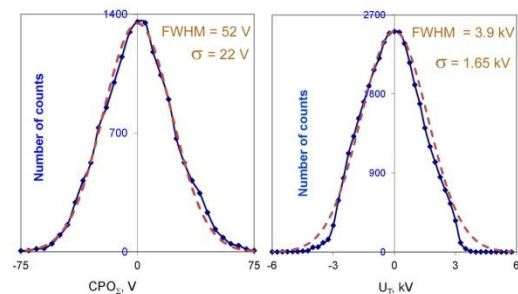


Figure 6: The terminal voltage distribution over a period of about 1 hour. The solid blue line is the output signal from TPS controller. The brown broken line is the normal distribution fit. Both control and CPO gain are set to optimum value. The left image is the CPO<sub>Σ</sub> voltage illustrating quick variation of the terminal voltage. The right image is the GVM error signal. It is assumed that FWHM~2.35σ.

The voltage variation plot was obtained by connecting the calibrated CPO preamp output and GVM error output to a bipolar 12 bit data logger. The CPO has been

calibrated so that a 1 V output is equivalent to a 100 V variation in the terminal potential. The GVM error has been calibrated so that a 1 V output is equivalent to a 100 kV variation in the terminal potential. The GVM-controlled terminal voltage deviation,  $\Delta U$ , as a function of terminal voltage,  $U_T$ , is given by equation [1]  $\Delta U_{[V]} = 133U_T[\text{MV}]$ . One can expect  $\Delta U = 1.8$  kV FWHM at  $U_T = 13.5$  MV. From calibration of the system, one can estimate that the fast terminal voltage ripple with the closed loop control is approximately 52 V FWHM and the slow voltage variation is as high as 3.9 kV FWHM.

The measured performance of the control system is below the expected voltage deviation of 1.8 kV FWHM and it may be caused by cross-talk in the energy-analysing slits. Examination of the slit signals showed that secondary electrons were collected alternately by one slit and then another as the beam shifted across it. This effect displayed a threshold behaviour, producing a nearly square wave output at the slit difference amplifier, as shown in figure 7 on the left bottom oscillogram. The same effect was reported in reference [7], where even as much as 3 kV of suppression voltage was not sufficient to eliminate this behaviour. The image slits at HIAF are not designed with minimization of cross-talk in mind. For instance, the shape of the slit electrodes is cylindrical, which is inferior to sharp edges in terms of avoiding secondary electrons from one slit hitting the other. In addition, the reduction of the cross-talk can be achieved by separation of the slits along the beam axis, fitting slits inside the cage and applying electron suppression voltage.

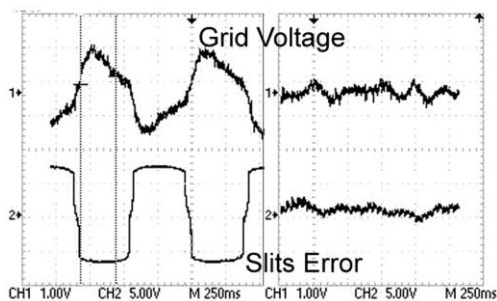


Figure 7: The oscillograms of square wave output at the slit difference amplifier and grid voltage displaying a threshold pattern. The effect is more evident when operating with no CPO control gain as shown on left images. On the right images the same signals are shown with CPO feedback on.

The energy resolution available with this system depends on several factors including the control slit separation and quality of the beam focus at the slit position. The choice of stripper and ion beam are also very important. For the best resolution, it is necessary to use gas stripping as opposed to carbon stripper foils, and light projectile ions to reduce energy straggling of the beam. This system has also been used successfully with bunched and chopped beams.

## ONGOING DEVELOPMENT WORK ON THE FAST CONTROL LOOP

We are continuing to improve on the design of main components in energy stabilization system. R&D on the development of the fast control loop is ongoing. When in slit control, the difference of the two control slit currents is summed with the CPO signal. The detected error signal is converted to a dc level and applied to the voltage control tube (6BK4) grid through the high-pass filter with the cut-off frequency of 10 Hz. The same signal is applied to the CPC triode through the low-pass filter. The fast control loop tube is mounted under the tank at the high-energy end of the accelerator and its anode is electrically connected to the last gap of high-energy (HE) acceleration tube. The cathode of the tube is connected to ground. The conductor enters the 14UD tank through a high pressure, high voltage feed-through. The fast control system amplifier response exhibits corner frequencies near 10 Hz and 1 kHz. The low frequency roll-off is important to avoid competition between the slow corona control system, ranging from dc to approximately 10 Hz, and the fast control loop.

In order to implement the fast control loop, the bandwidth of slit difference amplifier is to be increased up to 1 kHz at 10 nA. This method has a direct effect on the output energy without the phase shift inherent with the corona stabilization system. It is expected that a combination of the power of the corona system at low frequency and the speed of the HE tube modulator at high frequency will prove a very powerful stabilisation system.

Another implementation option of the system is to employ the standard NEC controller TPS7.0 with the capability of driving the liner. However in our case the correction voltage is applied to the acceleration gap rather to the liner electrode.

## CONCLUSIONS

The beam energy spread and overall performance of the tandem accelerator has been investigated. The standard corona stabilization system provides adequate energy resolution and steady beam on target. The performance can be significantly improved with the addition of a fast feedback system. The proposed system can be easily incorporated into existing corona control system. Beam energy spreads in the range 3.9 kV FWHM are routinely produced. Even where high resolution beams are not required, the additional feedback loop is useful in stabilizing accelerated and momentum analysed dc or pulsed beams on targets or at injection point to post-accelerator.

## ACKNOWLEDGEMENT

The authors wish to thank the engineering and technical staff from Electronics Unit RSPE for their help in installation and preliminary tests of the new controller. The authors thank David Weisser for many useful discussions.

**REFERENCES**

- [1] J.A.Ferry, Recent developments in electrostatic accelerator technology at NEC, Nuclear Physics and Methods in Physics Research A328 (1993) 28.
- [2] T.W.Aitken, A laddertron modulation system to correct a repetitive charging pattern, Nuclear Physics and Methods in Physics Research A268 (1988) 422.
- [3] W. Burger, H.Lange, V.Petr, A new method of improving the acceleration voltage stability of Van de Graaff accelerators, Nuclear Physics and Methods in Physics Research A586 (2008) 160.
- [4] C.R.Westerfeldt, E.P.Carter, R.O'Quinn, Modifications to belt and chain charging systems at TUNL, in SNEAP XXXIV, University of Lund, Sweden, 2001, p.141.
- [5] R. Hellborg (Ed.), Electrostatic Accelerators, Springer, Berlin, Heidelberg, 2005.
- [6] W. Trenchuk, M. Blacksell, Design of an electrostatic accelerator control system, Engineering project, FISE, University of Canberra, 1988
- [7] J.E.Cairns, M.W.Greene, J.A.Kuehner, A terminal stabilizer for a tandem accelerator, Nucl.Instrum. and Meth., 114 (1974) 489.

# LINAC EXPERIENCE IN THE FIRST TWO YEARS OF OPERATION @ CNAO (CENTRO NAZIONALE ADROTERAPIA ONCOLOGICA)

S. Vitulli, E. Vacchieri, CNAO Foundation, Pavia, Italy  
 A. Reiter, B. Schlitt, GSI, Darmstadt, Germany

## Abstract

CNAO is the first medical accelerator facility for deep hadrontherapy with protons and carbon ions in Italy. The LINAC injector at CNAO, entirely built by the GSI and Frankfurt University collaboration, is equal to the HIT LINAC working in the hadrontherapy centre of Heidelberg, Germany [3]. It includes a four-rod type RFQ structure accelerating up to 400 keV/u and an IH structure to increase the energy up to 7 MeV/u. Such LINAC works as injector in a 78 m circumference synchrotron where the protons and carbon beams reach respectively 250 MeV/u and 400 MeV/u. The LINAC commissioning was performed during 2009 and from beginning of 2011 it entered into routine and continuous operation (24hrs, 7days). First patient was treated in September 2011. Maintenance periods are foreseen three times per year. Different diagnostic elements are installed along the injection line, like profile grids, faraday cups, current transformers, capacitive pick-ups. The principal parameters are daily monitored, like output energy by means of online not destructive ToF measurements, cavities voltage, cavities RF forward power and beam current transmission. No major faults were observed in the first two years of operation. LINAC beam energy is stable within 0.02 MeV/u on a typical value of 7.17 MeV/u. The relation between LINAC extraction and synchrotron injection is under investigation. This paper summarizes the monitoring issues (i.e. reproducibility of settings and beam parameters as well as long term stability measures) on the CNAO LINAC during daily patient treatments and outlines the measurements performed in the initial commissioning compared within actual status.

CNAO machine is depicted in Fig.1.

Particles originate from one of the two Electron Cyclotron Resonance (ECR) sources, producing either  $C^{4+}$  or  $H^{3+}$  ions, at 8keV/u; they travel along the LEBT line and the LINAC reaching 7MeV/u energy and pass through the Medium Energy Beam Transfer (MEBT) line where a debuncher cavity is placed in order to reduce the beam energy dispersion. Then particles are accelerated in a 25m diameter synchrotron and, finally, are extracted into one of the four extraction lines, delivering either  $C^{6+}$  or proton beam to one of the three treatment rooms.

Extraction energy depends on treatment requirements: the deeper is the tumour to be irradiated, the higher is the required energy. Extraction energy can vary from 120 to 400MeV/u for Carbon ions and from 60 to 250MeV/u for protons. Extraction process is of the order of one second.

Actually beam maximum intensity at patient is  $5 \cdot 10^9$  and  $1 \cdot 10^8$  particles/s per spill, for protons and Carbon ions respectively. It can be reduced up to a factor 10, by inserting pepper-pot filters in the MEBT line and extracting the beam with spills over a longer extraction time.

## THE CNAO MEDICAL EXPERIENCE

From September 2011, 21 patients were treated with protons with an average of 6 patient/day and 35 treatment sessions/patient [1]. Each session is done by two different fields with different irradiation angles for a total of about 10-15 minutes of beam irradiation. The selected cases are principally chordoma (16 patients) and chondrosarcoma (5 patients) tumours in the head-neck (13 patients) or pelvis (8 patients) districts.

For head and neck tumors, solid mask, bite block, infrared-reflecting markers are used for patients fixing into couch. For pelvis tumors, the patient is fixed by means thermoplastic body mask. The dose uniformity is within the requested limit of  $\pm 2.5\%$ .

Today all the 148 foreseen energies are applied for treatments, one room is used with proton beams and with a fixed spot size of 1 cm using a couch for patient positioning.

During next year it will be possible to work all the three rooms, including the vertical line, with variable spot size of proton and carbon ions; in the treatment room both chair and couch for patient positioning will be available.

## THE LINAC INJECTOR

The layout of the CNAO injector includes two ECR ion sources and the LEBT [5]. A particularity of the CNAO

## THE CNAO MACHINE

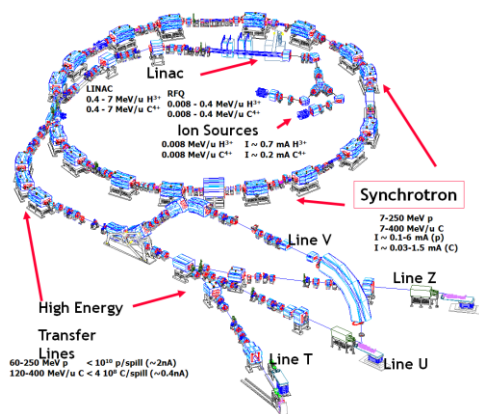


Figure 1: Sketch of the CNAO machine complex.

injection line is to be placed inside the synchrotron resulting a more compact accelerator machine.



Figure 2: RFQ and IH structure in synchrotron room.

A switching dipole magnet merges the two source lines into one. After being bent by a  $75^\circ$ -dipole, the beam enters the RFQ and the IH structure (Fig.2), after the so called intermatching section containing two quadrupoles for focusing and two steerers (horizontal and vertical) for moving the beam (Fig.3).

Also inside the IH-DTL tank there are three magnetic quadrupole triplet lenses for transverse focusing and another triplet behind the tank [4].

Upstream the RFQ, an electrostatic deflector (*Chopper*) is installed. The beam is continuous from the sources to the chopper, while it is pulsed downstream (i.e., 50-100us pulse).

Along the LEBT, three solenoids, four dipoles, eleven quadrupoles and correctors are used to focus, bend and steer the beam.

As concerns beam diagnostics, an AC transformer for non destructive current measurement is placed before the stripper foil chamber [2].

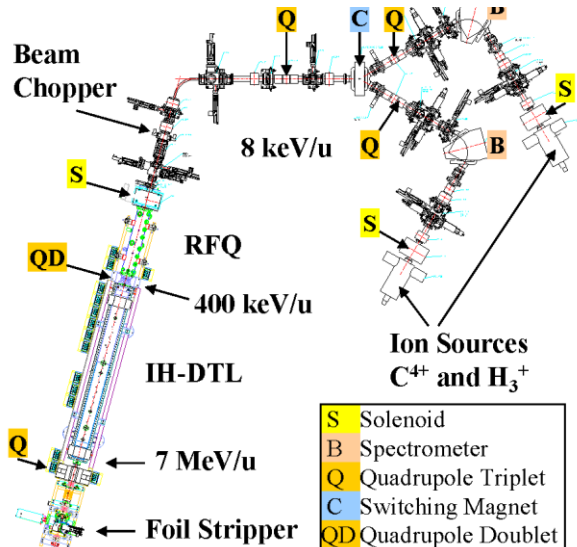


Figure 3: LINAC injector layout. Sketch of magnets and beam diagnostics tanks, from the sources to the stripper tank.

Inside the RFQ and IH structures two tank probes are placed in order to check the RF signal in any time (Fig. 4b).

After the IH structure, along the MEBT line, there are two phase probes @ 3478 mm distance for Time-Of-Light measurements (Fig. 4a), six profile grids for position monitoring and three faraday cups. All the diagnostic devices were delivered by GSI [3,4,9].

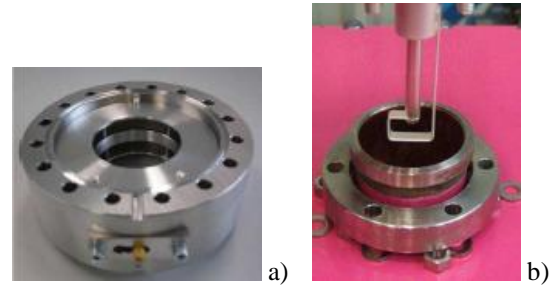


Figure 4: a) Phase probe for beam measurements (installed on the beam line) b) Tank probe for RF measurements (on the top of the corresponding flange in the IH tank).

At the end of the LINAC line, the stripping foil allows scratching the remaining electrons producing a defined charge state (from  $H^{3+}$  to 3 protons; from  $C^{4+}$  to  $C^{6+}$ ). In Table1 the main LINAC Design Parameters are reported.

Table 1: Main LINAC Parameters

| Physical Parameters                  | Values              |
|--------------------------------------|---------------------|
| Beam particle species                | $H^{3+}$ , $C^{4+}$ |
| Operation frequency                  | 216.816 MHz         |
| RFQ injection beam energy            | 8 keV/u             |
| Final LINAC beam energy              | 7 MeV/u             |
| Beam pulse length                    | $\leq 300 \mu s$    |
| Beam repetition rate                 | $\leq 5$ Hz         |
| Stability pulse repetition rate      | 10 Hz               |
| Exit beam energy spread <sup>1</sup> | $\leq \pm 0.4 \%$   |
| Total LINAC length <sup>2</sup>      | 6.95 m              |

<sup>1</sup> straggling effect in the stripper foil not included

<sup>2</sup> including RFQ, IH and Stripper section

## LINAC COMMISSIONING

CNAO LINAC commissioning took place during 2009 as listed in Table 2.  $H_{3+}$  and  $C_{4+}$  ion beams have been used for all beam commissioning phases [6, 7]. The first turn in the synchrotron was achieved in December 2009.

Table 2: Main CNAO LINAC commissioning steps

| Date  | Activity                           |
|---|------------------------------------|
| Jan 09                                      | RFQ installation                   |
| Feb-Mar 09                                  | RFQ RF conditioning                |
| Mar 12 <sup>th</sup> – Apr 3 <sup>rd</sup>  | Beams @ 400 keV/u                  |
| Apr 09                                      | IH installation                    |
| May-Jun 09                                  | IH RF conditioning                 |
| Jun 22 <sup>th</sup> – Jul 15 <sup>th</sup> | Beams 7 MeV/u                      |
| Jul-Nov 09                                  | Completion of the line             |
| Nov-Dic 09                                  | $H^{3+}$ beam @ MEBT end           |
| Dic 09                                      | $H^{3+}$ first turn in synchrotron |

Three different beam diagnostics test benches were used behind LEBT, behind RFQ, and behind the stripper section, respectively, and allowed for beam current, profile, and emittance measurements. Final LINAC test bench contained three phase probes at known distance for accurate Time-of-Flight measurements; a profile grid; two faraday cups and one AC transformer in addition to a mobile emittance device, that is a slit-grid measurement system.

More than 140 measurement series including numerous amplitude, phase, and emittance scans were performed with the IH-DTL. Different LEBT beam energies, RFQ settings, and IH tank RF plunger configurations were investigated.

The LINAC was optimized with respect to high beam transmission, minimum beam emittances and optimized bunch signal amplitudes from the phase probes.

Phase and voltage of RFQ and IH scans were done monitoring the variation of the above mentioned parameters. The RFQ phase is kept fix as reference point.

The current transmission reaches a maximum for determined values of IH phase and voltage as is shown in Fig. 5 and Fig. 6.

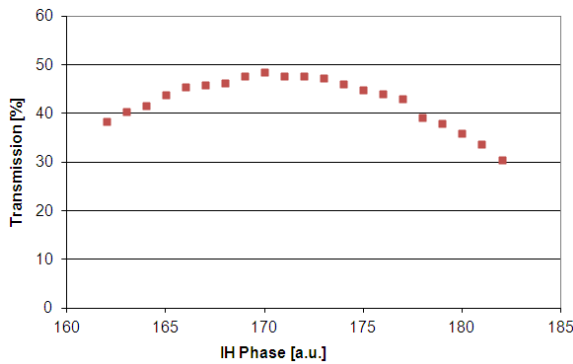


Figure 5:  $C^{4+}$ : IH phase scan as a function of the total LINAC transmission. Settings:  $V_{RFQ} = 5.1V$ ;  $V_{IH} = 5.7V$ .

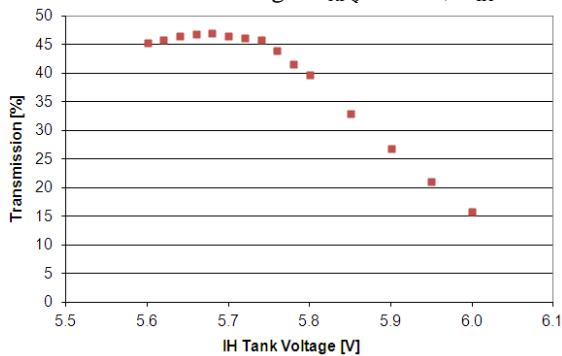


Figure 6:  $C^{4+}$ : IH Voltage scan as a function of the total LINAC transmission. Settings:  $V_{RFQ} = 5.1V$ ;  $\Phi_{IH} = 170$  a.u.

The beam energy can vary within 0.5% by changing RFQ and IH tank voltages or phases (Fig.7 and Fig.8). It means that little adjustments are possible for the future matching within the synchrotron injection. Fig. 7 and Fig. 8 shown the measurements taken by the Time-of-Light

method with the three phase probes installed along the test bench for IH commissioning. They are considered in pairs comparing the calculated energy to improve the measurement accuracy.

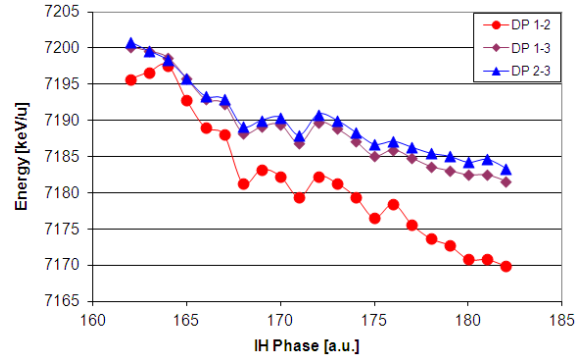


Figure 7:  $C^{4+}$ : IH phase scan as a function of the energy. Settings:  $V_{RFQ} = 5.1V$ ;  $V_{IH} = 5.7V$ . Legend: DP 1-2 = ToF between 1<sup>st</sup> end 2<sup>nd</sup> phps; DP 1-3 = ToF between 1<sup>st</sup> and 3<sup>rd</sup> phps; DP 2-3 = ToF between 2<sup>nd</sup> and 3<sup>rd</sup> phps.

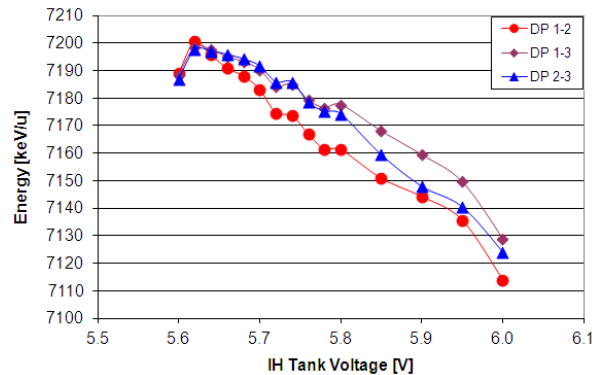


Figure 8:  $C^{4+}$ : RFQ and IH Voltage scan as a function of the energy. Settings:  $V_{RFQ} = 5.1V$ ;  $\Phi_{IH} = 170$  a.u. Legend like Fig. 7.

The experience shows that if the IH voltage increases, the beam energy increases too. On the opposite, if the IH phase increases, the energy decreases.

The final chosen working point corresponds to about 7.2 MeV/u at a RF pulse power of ~910 kW. Table 3 summarizes maximum beam currents achieved behind the stripping foil. Design beam currents were reached and even exceeded.

Table 3: Nominal and measured beam current @ LINAC exit

| Request @ LINAC exit           | Measured    | Nominal     |
|--------------------------------|-------------|-------------|
| current for $C^{6+}$ (7 MeV/u) | 135 $\mu$ A | 120 $\mu$ A |
| current for p (7MeV/u)         | 1.2 mA      | 0.75 mA     |

The measured emittances after RFQ and IH are within the project values (for  $C^{6+}$ : 5.4  $\pi$ -mm-mrad horizontal and 4.2  $\pi$ -mm-mrad vertical plane; for  $H^{3+}$ : 6.8  $\pi$ -mm-mrad horizontal and 6.5  $\pi$ -mm-mrad vertical).

RFQ transmission around 60% has been measured for both  $H^{3+}$  and  $C^{4+}$  beams. The IH transmission, in



The energy outside then LINAC is strongly dependent on different parameters, not only on the IH voltage and phase, but even on the cooling water temperature that must be stable within 0.2°C.

The RF power is not adjusting, but it is a consequence of the set voltage. It can be read on the amplifier cabinet PLC.

### STABILITY LINAC MEASUREMENTS

Periodically energy, current and profile stability measurements for tens hours are foreseen in order to check beam parameters at the LINAC exit.

In terms of energy, a variability of 0.4% is normally acceptable.

In term of current, a variability of 2% does not normally causing troubles for a good injection (Fig. 14).

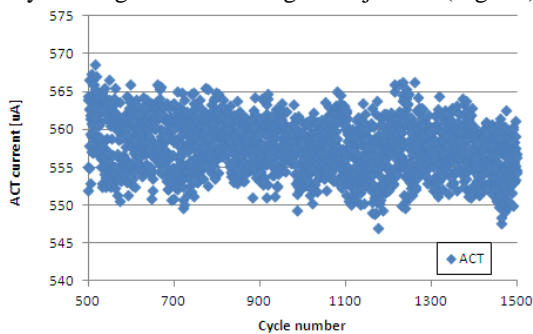


Figure 14: Beam current stability measurements from 00h39 to 10h01 of April 28, 2012.

The beam position along the MEBT line, after the LINAC tank, can be monitored by means of six profile grids (Fig. 15). Such interceptive measurements are done during the night shifts in order to assure the correct beam trajectory.

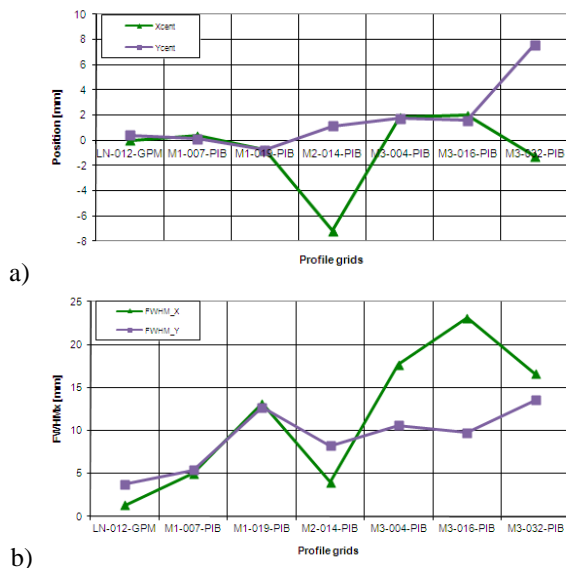


Figure 15: Beam position (a) and width (b) along the MEBT line measured by means of profile grids.

Position stability measurements are planned monthly in order to check the natural beam displacement along the MEBT that normally can reach 0.2mm for the position and 0.4mm for the FWHM.

### BEAM STUDIES IN SYNCHROTRON

Different measurements and trends were studied for understanding a possible involvement of the LINAC behaviour in the occasional instability of the intensity of the accelerated beam after the synchrotron RF cavity trapping [8]. Fig. 16 shows a typical beam spill in the synchrotron DCCT (DC-Current Transformer) that is analysed in order to optimize the injection and acceleration [10].

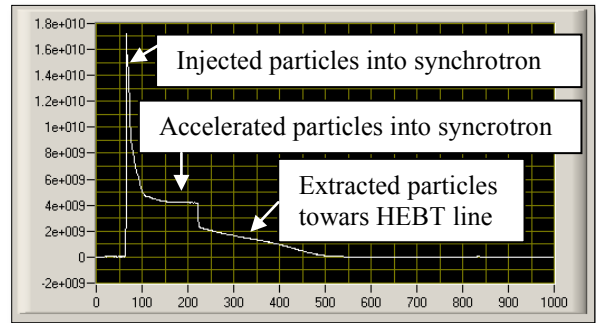


Figure 16: One synchrotron cycle (4.8s duration) as measured by the DC current transformer (acquisition rate: ~5ms/sample). The first peak corresponds to the particles injected in the synchrotron, the next plateau represents the particle accelerated from the RF cavity and the following drop is related to the beam extraction towards the HEBT line (1.3s duration).

The most related element is the debuncher cavity that is placed in the MEBT line as shown in Fig. 17.

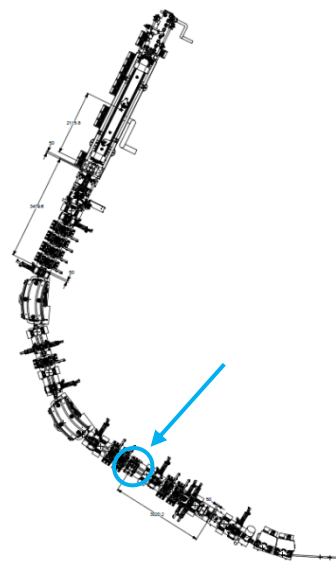


Figure 17: LINAC and MEBT layout showing the debuncher position and the distances between phase and tank probes.

Changing the debuncher phase influences beam energy distribution thus causing different synchrotron injections.

On the other hand, the debuncher voltage variation has not great influence on the energy distributions, as one can deduce from Fig. 18.

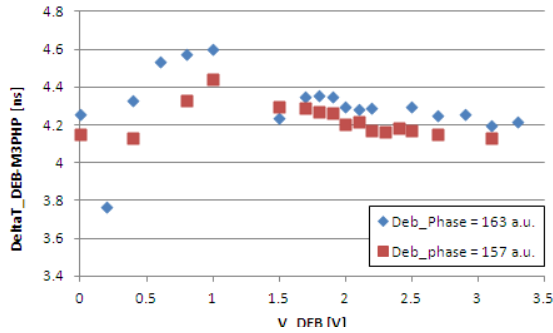


Figure 18: Phase difference between debuncher and MEBT phase probe as a function of the debuncher voltage.

Different scans in phase and voltage were done as a function of the DCCT signal. Fig. 19 shows a study around the typical values of the debuncher phase.

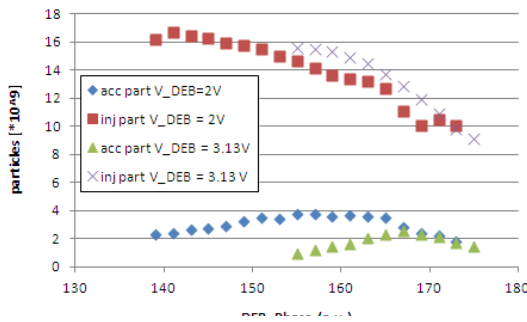


Figure 19: Particles injected and accelerated in the synchrotron as a function of the debuncher phase @ different typical values for the debuncher voltage.

Figure 20 shows the debuncher voltage study: one can deduce that it has not a great influence on the injected and accelerated particle number.

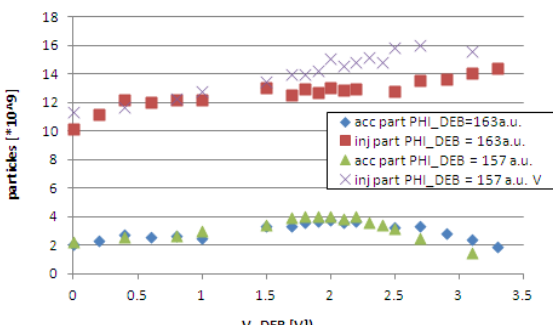


Figure 20: Particles injected and accelerated in the synchrotron as a function of the debuncher voltage @ different typical values for the debuncher phase.

## CARBON MEASUREMENTS

During the afternoon commissioning sessions the carbon beam is in preparation for obtaining the authorization to treat patients before the end of this year.

In term of LINAC injection, carbon beam has similar energy dispersion and even better transmission then proton beam.

## LINAC MAINTENANCE AND UPGRADE

During the last three years, the LINAC and its supply were running in a very reliable way. Only few breakdowns were caused by some hardware faults easily solved by upgrades or using the available spare parts.

For example a Variac transformer of the tetrode tube filament burned twice, much before the waiting usury time; the RFQ anode filter had a short circuit; the capacitor foils broke two time in two week (in both cases an electric discharge made a hole in the foils); some Low Level RF amplifier modules were sent to the producer for repair; some control board cards needed to be replaced in some parts.

In terms of upgrade, all the air filter system inside the RF cabinet was improved to preserve the cabinets from dust diseases; some flow meters were add in synchrotron room, one for each different element to be cooled; all the IGBT transistor cards in the LINAC magnets power supplies were modified mounting more reliable diodes.

The RF tetrode tubes never stop working. Only one was changed in order to verify the spare. IH tubes are around 13400 h working; RFQ tetrode is around 15700h.

Maintenance work is divided into six-monthly and annual activities and includes checks on the ventilation fans, on the flow meters, on the variac transformers, dust cleanness inside the cabinets, check of the electrical wiring, RF reference measurements. Most of these activities reclaim to switch off the machine and can be done only during the maintenance periods that are planned three times in a year.

During patient treatments very rarely breakdowns occur caused by LINAC faults. When it happens, the problem was mainly related to the control system and timing, so that a solution was possible in remote way without loss treatment but only interrupting it for some minutes.

## CONCLUSIONS

LINAC commissioning was done during 2009 finding the working point that corresponds to about 7.2 MeV/u energy at a RF pulse power of ~910 kW.

In the first two years of operation it was stable and reliable. Daily a complete summary of the measured parameters is done to check the correct beam position, energy, current and bunch shape. Same values, like IH e Debuncher voltage and phase, should be adjusted via control system to assure a good matching within the synchrotron that need the LINAC exit energy as initial parameter for an efficient RF cavity trapping and

acceleration. Stability measurements during the night shift have been done to guarantee the oscillation around the set values doesn't exceed the foreseen one. Some studies on the possible involvement of the LINAC parameters in occasional instabilities of the accelerated beam in the synchrotron have been done and shown that, in those cases, a more stable configuration can be reached varying the debuncher phase.

### REFERENCES

- [1] E.Bressi et al, Proc. IPAC2012, THXA02.
- [2] A.Parravicini et al., Proc. HIAT2009, p. 247.
- [3] B. Schlitt, Proc. LINAC2008, p. 720.
- [4] H. Vormann et al., Proc. EPAC2008, p. 1833.
- [5] E. Bressi et al., TU6PFP005.
- [6] P.A. Posocco et al., Proc. HIAT2009, p. 188.
- [7] B. Schlitt et al., Proc. IPAC2010, p. 67.
- [8] L. Falbo et al., Proc. IPAC2011, WEPS006.
- [9] A. Reiter, Proc. EPAC2006, p. 1028.
- [10] C. Priano et al., IPAC2011, WEPS007.

## PHYSICAL DESIGN OF THE SPES FACILITY

M. Comunian, on behalf of SPES design group, INFN,  
Legnaro National Laboratory, Legnaro, Italy

### *Abstract*

SPES (Selective Production of Exotic Species) is the Italian project for a rare isotope beam (RIB) facility based on a cyclotron as primary accelerator and on the existing superconducting linac ALPI as post accelerator. The cyclotron, energy up to 70 MeV and total current of 0.75 mA, shared on two exits, is in construction in the industry. The production of neutron-rich radioactive nuclei, with ISOL technique, employs the proton induced fission on a direct target of UCx; the fission rate expected with a proton beam of 40 MeV and 0.2 mA, is  $10^{13}$  fissions/s. The main goal of physical design of the SPES facility is to provide an accelerator system to perform forefront research in nuclear physics by studying nuclei far from stability, in particular neutron-rich radioactive nuclei with masses in the range of 9–160.

The final RIB energy on the experimental target will be up to 10 MeV/A for  $A = 130$ , with an intensity in the range of  $10^7$ – $10^9$  pps.

### INTRODUCTION

The SPES strategy is to develop a facility for Nuclear Physics research together with a facility for applied Physics based on the same technology and infrastructure.

SPES [1] is designed to provide neutron-rich radioactive nuclear beams (RIB) of final energies in the order of 10 MeV/A for nuclei in the  $A = 9$ -160 mass region. The radioactive ions will be produced with the ISOL technique using the proton induced fission on a Direct Target of UCx [2] and subsequently reaccelerated using the PIAVE-ALPI accelerator complex [3]. A Uranium fission rate of  $10^{13}$  fission/s is foreseen.

A Cyclotron with a maximum current of 0.750 mA having two exit ports will be used as proton driver accelerator with variable energy (30-70 MeV).

Two proton beams can be operated at the same time sharing the total current of 0.750 mA. To reach a fission rate of  $10^{13}$  fission/s a proton beam current of 200  $\mu$ A (40MeV) is needed; the second beam, up to 500  $\mu$ A

70MeV, will be devoted to applications; mainly neutron production for material research and study of new isotopes for medical applications.

The expected rate of fast neutrons is estimated to be  $10^{14}$  n/s at the target output using a Pb target (mean energy 1MeV).

The ISOL technique for radioactive beam production is based on a driver accelerator which induces nuclear reactions inside a thick target. The reaction products are extracted from the target by thermal process, ionized  $1+$ , isotopically selected, ionized  $n+$  and injected into a re-accelerator. In order to produce neutron-rich isotopes it is mandatory to perform fission reactions in Uranium or other actinide targets using protons, deuterons, neutrons or gammas. The SPES choice is to use a proton beam to induce fission on a UCx target (Direct Target).

Fig. 1 shows schematically the SPES main elements located at underground level, a second floor at ground level hosting laboratories and services is not shown.

The driver is the proton cyclotron delivering beam on different targets. Two production ISOL targets are planned to be installed. The production target and the first mass selection element will be housed in a high radiation bunker. Before the High Resolution Mass Spectrometer (HRMS) a cryopanel will be installed to prevent the beam line to be contaminated by radioactive gasses and a RFQ cooler to reduce the input emittance of the HRMS. After passing through the HRMS, the selected isotopes will be stopped inside the Charge Breeder and extracted with increased charge ( $n+$ ). A final mass selector will be installed before reaching the PIAVE-ALPI accelerator, to clean the beam from the contaminations introduced by the Charge Breeder itself.

Two facilities for applied physics are planned: a neutron facility that make use of the proton beam to produce neutrons and an irradiation facility for production and study of radioisotopes for medical use.

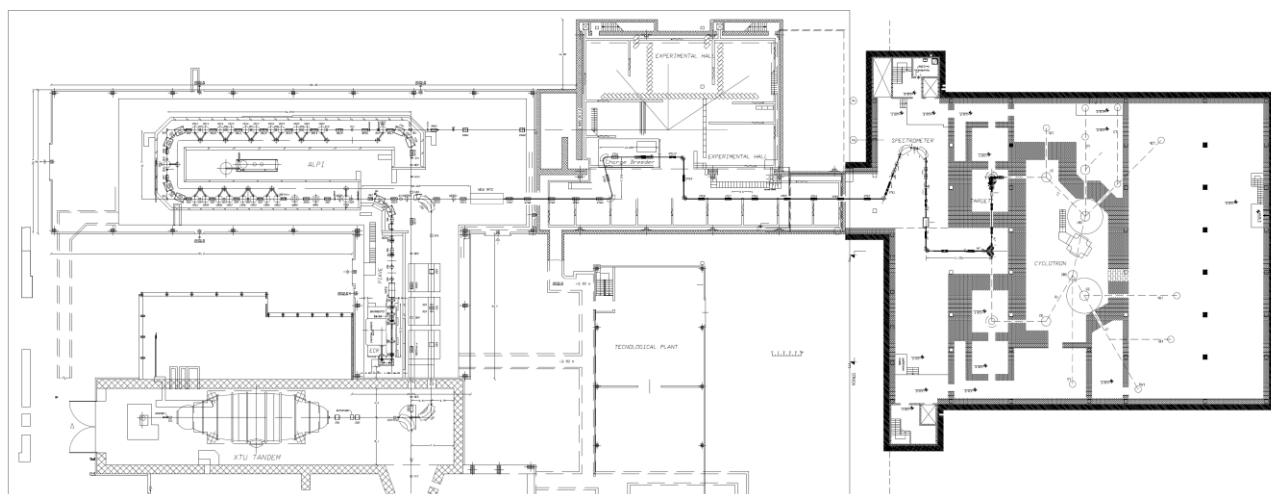


Figure 1: Layout of the SPES and ALPI facility; the dark black part on right is the new Cyclotron area.

### THE CYCLOTRON

Within the SPES project, during the 2010 the tender for supply of the Cyclotron, the transport beam line up to the ISOL target and the ancillary systems, was accomplished out. The INFN assigned the contract to BEST Theratronics Ltd. (Canada). The contract foresees the delivery to LNL and the commissioning of the accelerator and the beam line, within 3 years from the assignment [4]. The BEST cyclotron is a compact four straight sector machine, see figure 2, energized by a pair of room temperature conducting coils. The cyclotron is able to accelerate H beam, provided by an external multi-cusp ion source, up to the energy of 70 MeV. Since the proton extraction is done by the stripping process, the final energy varies within 35-70 MeV. Two independent extraction channels placed at 180° one respect to the other provide the simultaneous extraction of two beams. The maximum beam current deliverable is estimated to be 700  $\mu$ A. The table 1 shows the main parameters of the machine.

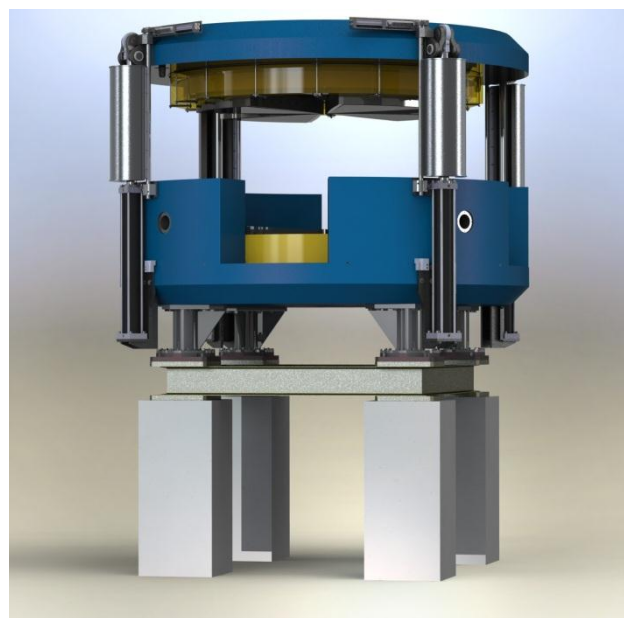


Figure 2: Best Theratronics 70p model.

Table 1: Main Cyclotron parameters

|  |  |
|--|--|
| Main Magnet                            | Bmax field: 1.6 T<br>Coil current: 127 kAT<br>4 sectors, deep valley Hill sector angle: 50°<br>Varying hill gap: 6-4.69 cm |
| RF cavity                              | Frequency: 58 MHz<br>Harmonic: 4 <sup>th</sup><br>Dissipated power: 28 kW Dee voltage: 60-81 kV Dee angle: 36°             |
| External ion source and injection line | Multi-cusp H-, 15-20 mA DC Beam current: 700 $\mu$ A Injection Energy: 40 keV Spiral inflector                             |
| Vacuum                                 | Ion source: $<1 \times 10^{-5}$ torr<br>Main tank: $<1 \times 10^{-7}$ torr  |
| Extraction                             | Simultaneous dual beam<br>2 stripping multi-foil carousels<br>Variable energy 35-70 MeV                                    |

### THE MULTI FOIL DIRECT TARGET

In an ISOL facility, like SPES, the working core is constituted of the production target and the ion source [2]: they have to be carefully designed and optimized in order to obtain the desired high production rate of RIBs. Due to the low pressure of the environment, the power deposited by the proton beam in the target by means of electromagnetic and nuclear interactions can be removed only by thermal radiation towards the surrounding container box. In order to optimize both heat dissipation and fission fragments evaporation, the SPES target consists of seven, 40 mm diameter and 1.3 mm thick, co-axial disks housed in a cylindrical graphite box, see figure 3. In choosing the target material, which should stand the highest possible beam current, it is crucial to optimize the beam-target combination with respect to the highest

production cross section and lowest amount of contaminants. UC<sub>x</sub>, uranium dicarbide dispersed in an excess of graphite, is widely recognized as the reference material for the production of neutron-rich radioactive beams. The preparation of the SPES UC<sub>x</sub> disks is based on the carbon-thermal reduction of UO<sub>2</sub> powders in excess of graphite. The powders are mixed and ground in order to obtain a homogeneous mixture; these powders are uniaxial cold pressed. Finally the heat treatment is performed in a dedicated vacuum furnace. The final bulk density of the disks turns out to be about 3 g/cm<sup>3</sup>, while the U:C atomic ratio is close to 1:4. The calculated in-target fission rate in all the 7 disks approaches 10<sup>13</sup> fps. The distribution of the fission products is shown in Figure 4. The isotope in-target production for some interesting isotopes (Ag, Sn, Cs) reaches values up to 10<sup>11</sup> aps. The <sup>132</sup>Sn isotope, being a double-magic nucleus, is one of the radioactive nuclei of interest and the in-target production yield is here estimated to be 10<sup>10</sup> aps. The output emittance from the target will be in the order of 30 mmrad at 40 kV [5]. An off-line front-end of the thin target is fully operational at LNL, see figure 5.

The beam transport of the radioactive beam is started from the target; see figure 6, with a first rough mass separation made by a Wien filter, after that the beam is transported to the RFQ cooler, figure 7.

The TraceWin simulation [6] is performed at first order, but includes the transfer matrix of the Wien Filter, as custom element. The mass resolving power achieved by the dispersive effect of the Wien Filter and the 90° analyzing dipole is more than 300.

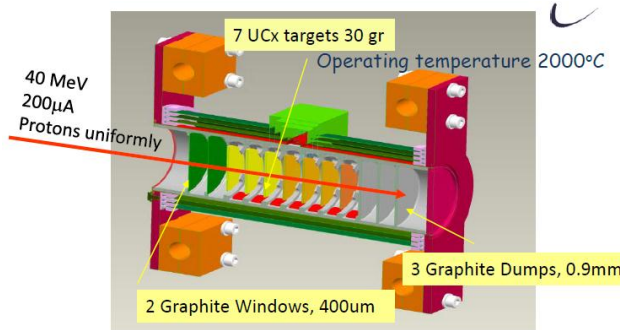


Figure 3: The SPES thin target model.

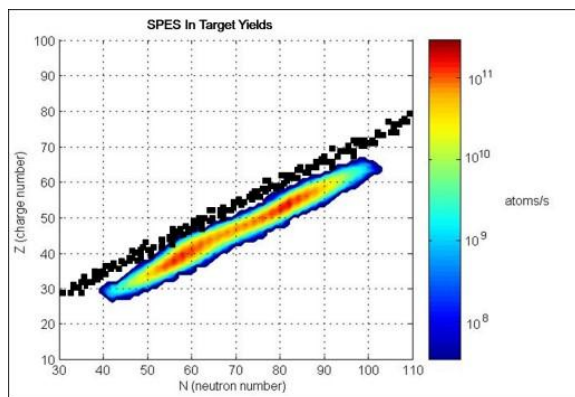


Figure 4: The in-target isotope yields.

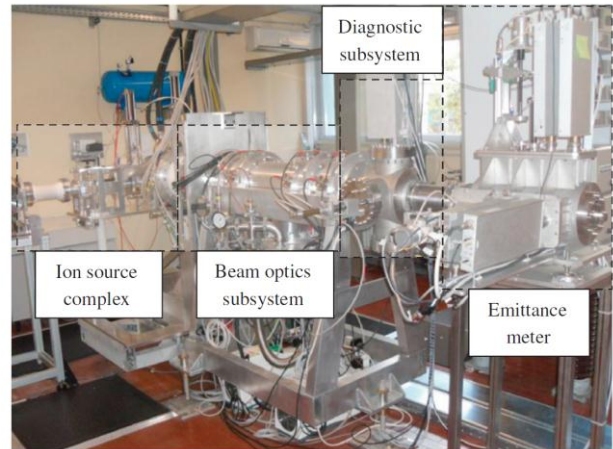


Figure 5: The offline front-end: fully operational at LNL.

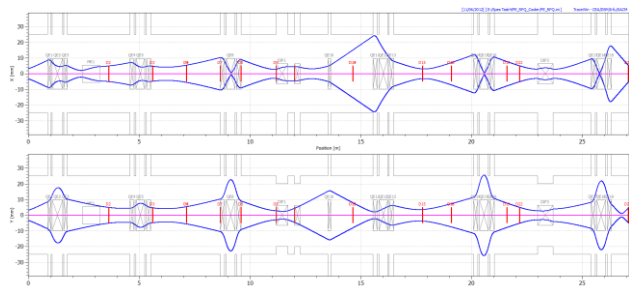


Figure 6: Envelope of the line from the Front-end to the RFQ cooler, from left to right.

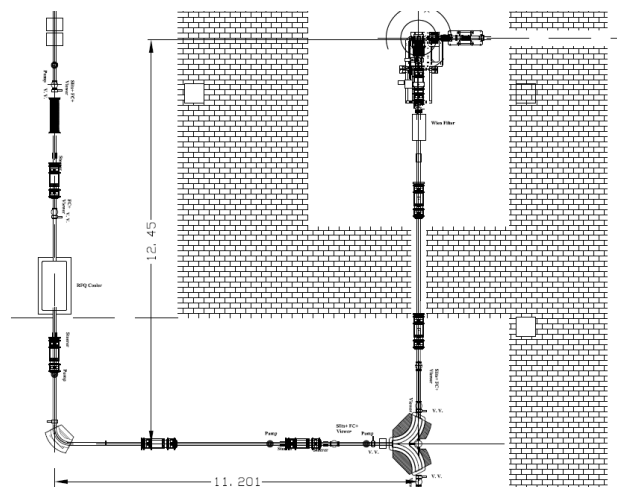


Figure 7: Layout from the Target Front-End to the RFQ-Cooler.

### THE RFQ COOLER

In the framework of the SPES project, the radioactive ion beams transport is under study in order to evaluate the transmission efficiency and the final quality of the delivered beams in terms of mass resolution and longitudinal energy spread. In particular the high resolution mass spectrometer needs a beam emittance of the order of 3π mm mrad and an energy dispersion of about 1 eV to get the minimum resolving power of 20'000. These requirements will be fulfilled with the

radio frequency quadrupole (RFQ) beam cooler device [7].

The gas-filled, RFQ is a device whereby a previously decelerated, low energy ( $E < 100\text{eV}$ ) beam is thermalized via successive collisions with an inert buffer gas. This process allows to decrease, by the energy exchanging with the gas molecules, the radial momentum and the longitudinal energy dispersion of the ions passing through the RFQ.

The preliminary design of the device is carrying on at LNL since 2011, see table 2, and the feasibility study is funded by V committee of INFN in the framework of REGATA experiment, see figure 8.

Table 2: RFQ Cooler main parameters

|                            |                              |
|----------------------------|------------------------------|
| Mass Range                 | 9 – 200 amu                  |
| Tr. Emit. injected beam    | 30 mmmrad (40 keV)           |
| Emittance reduction factor | 10 (max)                     |
| Buffer gas                 | He (293 K)                   |
| Beam intensity             | 50 – 100 nA ( $10^{11}$ pps) |
| Energy spread              | <5 eV                        |
| RF voltage range           | 0.5 – 2.5 kV                 |
| RF frequency range         | 1 – 30 MHz                   |
| RFQ gap radius (R0)        | 4 mm                         |
| RFQ length                 | 700 mm                       |
| Pressure buffer gas (HE)   | 0.1 – 2.5 Pa                 |
| Ione energy                | 100 – 200 eV                 |

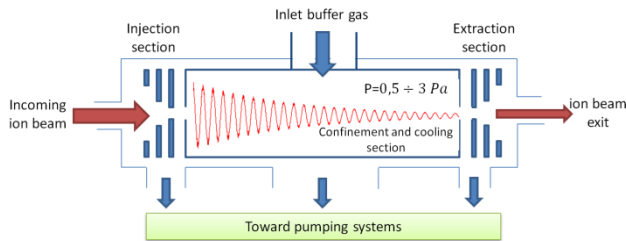


Figure 8: RFQ cooler layout.

## THE HIGH RESOLUTION SPECTROMETER

A crucial task for the experimental use of radioactive beams is not only the beam intensity but also the beam quality. Special efforts have been dedicated to design a mass spectrometer with an effective mass resolution of at least 1/20000. Such design takes advantage of the 260 keV beam energy obtained with the HV platforms. Such high selectivity results in an advantage also for the safety issue, reducing the problems of contaminations along the beam transport areas and in the target location, see figure

The design of the SPES spectrometer is a scaled up version of the separator designed at Argonne. The first order design mass resolution is about 40.000 to reduce the tails of contaminant with higher yields, see figure 10 and table 3.

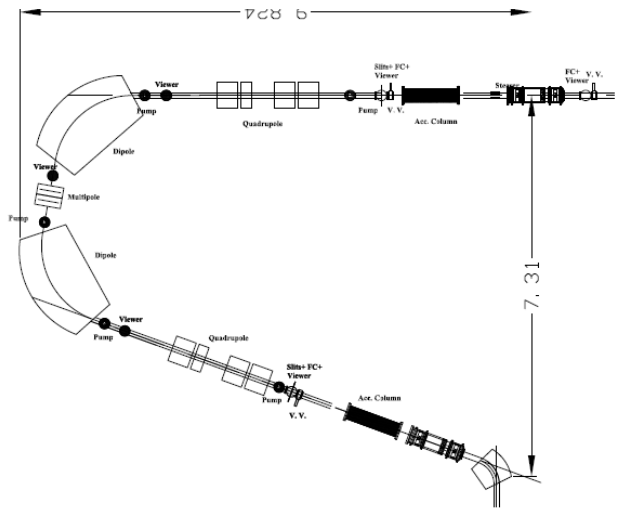


Figure 9: Spectrometer Layout from the RFQ cooler to the transport line to the Charge breeder.

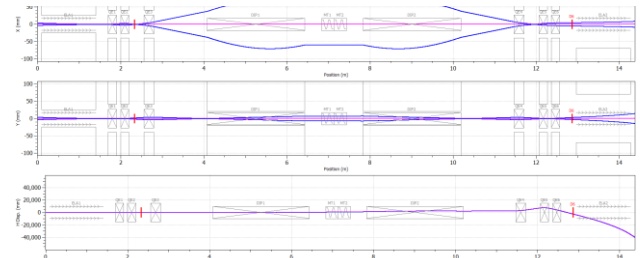


Figure 10: Envelope design of the spectrometer.

Table 3: Spectrometer main parameters

|                               |                |
|-------------------------------|----------------|
| Mass Resolution               | 1/40000        |
| Dipole Bending Angle          | 80 deg         |
| Dipole Bending radius         | 1.5 m          |
| Dipole Edge                   | 28 deg         |
| Dipole max field              | 1.2 T          |
| Energy (1/132)                | 260 keV        |
| Multipole element             | Sextupole      |
| Input tr. Emittance RMS norm. | 0.00171 mmmrad |

## THE TRANSPORT LINE TO THE CHARGE BREEDER

From the High resolution beam spectrometer to the charge breeder is necessary to transport the beam for about 34 meters in a carefully way to avoid beam losses. This periodic line is made by using electrostatic triplets with a period of about 3.6 meters; the total length of the line so may be changed by adding a period or removing a period, table 4 and figure 11.

Table 4: Transport line to the Charge breeder main parameters

|                                    |                   |
|------------------------------------|-------------------|
| Ion                                | 1/132             |
| Electrostatic Triplet lengths (mm) | 200+70+400+70+200 |
| Electrostatic Triplet radius       | 60 mm             |
| Electrostatic max voltage          | 4.03 kV           |
| Dipole Radius                      | 500 mm            |
| Dipole max field                   | 0.67 T            |
| Energy (1/132)                     | 40 kV             |
| Total number of triplets           | 10                |
| Transvers Emittance RMS norm.      | 0.02 mmmrad       |

In figure 12 is reported the layout of the transport line and the maximum envelopes in X and Y.

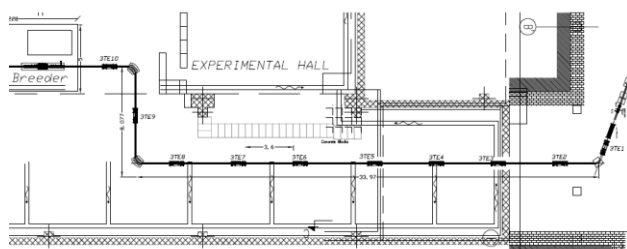


Figure 11: Layout from the Spectrometer to the Charge Breeder in the experimental hall 3 from right to left.

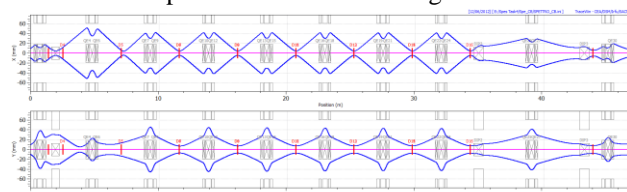


Figure 12: Max Envelope from the Spectrometer to the Charge Breeder from left to right.

## THE CHARGE BREEDER

In 2010 an agreement was signed between the SPES and the SPIRAL2 projects in the framework of the LEA-COLLIGA aiming at sharing know how in the field of radioactive beam production and manipulation, see table 5 and figure 13. The agreement foresees the development of the neutron converter for SPIRAL2 by INFN and the development of an ECR-based charge breeder by LPSC. During 2010 some experimental activities on charge breeding (the so called 1+/n+ method) were performed at LPSC with the Phoenix booster aiming at improving the capture efficiency by means of fine frequency tuning of the microwave injected and checking the plasma characteristics variations measuring the plasma potential.

When a characterized 1+ ion beam is injected into a plasma and then all the ion species are extracted and analyzed, one could expect some information about the characteristics of the plasma itself: its ability to capture 1+ ions and its ability to multi ionize the 1+ ions injected (i.e. plasma temperature and density). The 1+/n+ method developed for radioactive ion beams could be considered as a kind of non perturbative probe because the number of ions injected is exactly known (1+ beam intensity measurement), and extremely low with respect to the initial number of ions present in the plasma, even if some

effects on the plasma were observed during the experiments performed at LPSC, like the partial destruction of the high charge states of oxygen without a corresponding increase of the current of the lowest ones.

Some studies have been performed in a frequency sweep mode: however due to the variation of the net power coupled to the plasma during a sweep and the limited reflected power sustainable by the TWTA that amplify and feed microwave into the plasma chamber, the influence of the fine frequency tuning could not be properly deduced. Further studies are mandatory to verify the usefulness of this technique.

The joined team INFN-LNL/LNS is also involved as deputy coordinator in a European project called EMILIE (Enhanced Multi-Ionization of short-Lived Isotopes at EURISOL) approved in 2011 by the NuPNET [8]. In the framework of this project the INFN team will investigate numerically two important aspects concerning the ECR-based charge breeding: the microwave coupling to plasma chamber of the Phoenix charge breeder installed at LPSC Grenoble and the study of the capture of the 1+ beam by the ECR plasma. The work will lead from one side to a conceptual design of an optimized plasma chamber for the Phoenix charge breeder; on the other side a numerical code (developed at LNS) describing the ECR-plasma dynamics will be adapted to deeply study the capture process in order to understand how to improve it, especially in the case of condensable elements.

Table 5: Charge Breeder main parameters

|                           |                   |
|---------------------------|-------------------|
| Frequency                 | 14.5 GHz          |
| Power Max                 | 1000 W            |
| Magnetic Field Injection  | 1.5 T             |
| Magnetic Field Extraction | 1.0 T             |
| Magnetic Field Radial     | 1.35 T            |
| Efficiency for gas        | 8-10 %            |
| Efficiency for metals     | 3-5 %             |
| Charge breeding time      | From 3 to 15 ms/q |
| Output emittance RMS      | 0.1 mmmrad        |

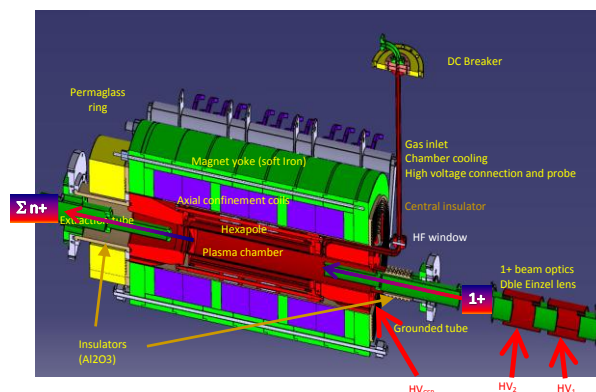


Figure 13: Layout of the Charge Breeder.

A transport line of about 20 meters is necessary to transport the beam from the Charge Breeder to the new RFQ, see table 6; this line is made by using 7 magnetic triplets, with a gradient 3.3 T/m at maximum but with a quite large aperture, this is done for avoid beam losses. This line should also be able to separate ion mass within

1/1000, see figure 14. This beam line also prepares the beam input condition for the new RFQ.

The triplets and doublets used are of the same type of the PIAVE-LEBT magnetics elements.

In figure 15 is reported the layout of the line from the charge breeder to the RFQ and the maximum envelopes in X and Y.

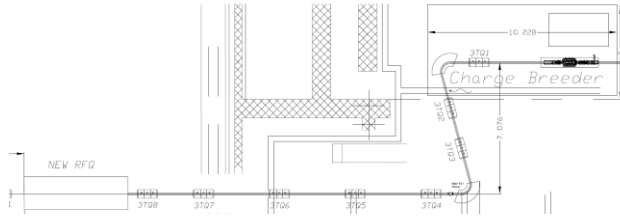


Figure 14: Layout from the Charge Breeder to the new RFQ from right to left.

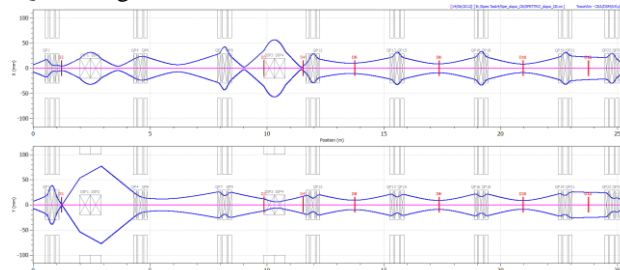


Figure 15: Maximum Envelopes from the Charge Breeder to the injection into the new RFQ from left to right.

Table 6: Transport to the new RFQ main parameters

|                                  |                   |
|----------------------------------|-------------------|
| Ion                              | 132Sn19+          |
| Magnetic Triplet lengths (mm)    | 150+50+200+50+150 |
| Magnetic Triplet radius          | 60 mm             |
| Magnetic max integrated gradient | 0.5 T             |
| Dipole Radius and angle          | 500 mm 105 deg    |
| Dipole max field                 | 0.15 T            |
| Energy (132Sn19+)                | 0.76 MeV          |
| Total number of triplets         | 8                 |
| Transvers Emittance RMS norm.    | 0.1 mmmrad        |

### THE NEW RFQ INJECTOR

The injection to the ALPI Linac is based on the use of a new Radio Frequency Quadrupole, with the adiabatic bunching inside. In this way a high voltage platform can be avoided, and a higher overall transmission could be achieved.

The new RFQ will operate in a CW mode (100% duty factor) at a resonant frequency of 80MHz. This frequency is the same as that of the lowest energy ALPI superconducting structures. The injection energy of ions was set to 5.7 keV/u. This choice is a compromise between the desire to reduce the ion energy to simplify the LEBT and RFQ bunching section design and the need to increase the injection energy to reduce space charge effects. The extraction energy was set to 727 keV/u, higher than the output of PIAVE RFQ, to optimize the beam dynamics of the SRF linac. Table 7 summarizes main RFQ parameters.

Table 7: Principal RFQ parameters

|   |                        |
|---|------------------------|
| Operational mode                        | CW                     |
| Frequency (MHz)                         | 80.                    |
| Injection Energy (keV/u)                | 5.7 ( $\beta=0.0035$ ) |
| Extraction Energy (keV/u)               | 727 ( $\beta=0.0395$ ) |
| Accelerated beam current ( $\mu$ A)     | 100                    |
| Charge states of accelerated ions (Q/A) | 7 – 3                  |
| Internal bunching section               | Yes                    |

The design goals were to minimize the longitudinal and transverse emittances and to optimize the RF losses and transmission of the RFQ structure. The RFQ cells were created using the program CORTO, used for the design of CERN linac3 RFQ, PARMTEQM code package and Toutatis in an iterative cell-by-cell procedure. With this design the RF power consumption is minimized, while a ramped voltage profile allows the RFQ to accelerate the beam more effectively at higher velocities and achieve higher output energy. Figure 16 shows the density plot along the RFQ while Table 8 lists parameters of the RFQ structure. The RFQ transmission is more than 94%, the final RMS normalized longitudinal emittance is 0.05 mmmrad, i.e. 4.4 keVdeg/u, see figure 17.

Table 8: RFQ design parameters

| Parameter (units)                          | Design 1     |
|--|--------------|
| Inter-vane voltage V (kV, $A/q=7$ )        | 63.8 – 120   |
| Vane length L (m)                          | 5.56         |
| RF power (kW, four vanes structure)        | 180          |
| Average radius $R_0$ (mm)                  | 5.03 – 9.574 |
| Vane radius $\rho$ to average radius ratio | 0.8          |
| Modulation factor m                        | 1.0 – 3.16   |
| Total number of cells                      | 293          |
| Synchronous phase (deg.)                   | -90 – -20    |
| Focusing strength B                        | 5.28 – 2.8   |
| Peak field (Kilpatrick units)              | 1.7          |

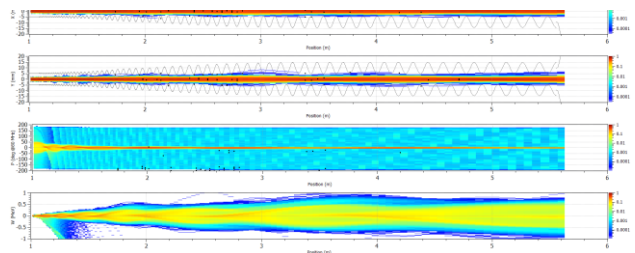


Figure 16: Multiparticles of the new RFQ.

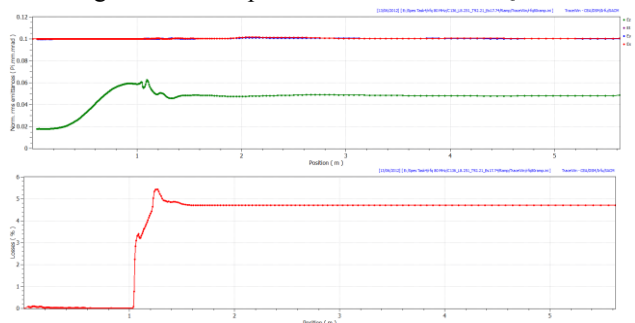


Figure 17: Emittance and losses plot along the new RFQ.

## THE ALPI LINAC UPGRADE

The present configuration of the Legnaro super-conducting accelerator complex (PIAVE injector and ALPI main accelerator) fits the requirements for SPES post acceleration too. Nevertheless an upgrade of its performances both in overall transmission and final energy is needed and a solution which minimizes the impact on the present structures [3].

The super-conducting linac ALPI is injected either by a XTU tandem or by the s-c PIAVE injector. The linac (at the present 64 cavities and a total voltage of 48 MV) is build up in two branches connected by an achromatic and isochronous U-bend (Fig. 1). ALPI period consists in one triplet and 2 cryostats (4 cavities in each cryostat), and a diagnostic box (profile monitor and Faraday cup) in between.

The PIAVE-ALPI complex is able to accelerate beams up to  $A/q = 7$ . Higher  $A/q$  ions suffer from too low injection energy to the medium- $\beta$  cryostats, where the RF defocusing is too strong and the beam gets easily lost onto the cavity beam ports for this purpose a new RFQ injector will be used. In the last years the average cavity accelerating field has been enhanced by more than a factor of two with respect to the original design value [9], see figure 18. The strength of the focusing lenses on the other hand, has remained the same (20 T/m). Therefore, even for  $6 < A/q < 7$  it is hard to design a proper longitudinal beam dynamics such that it will not cause problems on the transverse plane, see figure 19. To fully exploit the available acceleration gradient, some improvements are required in the layout of ALPI.

For SPES, the Radioactive Ion Beam at 727 keV/A will be injected into ALPI by means of the QWRs actual present into PIAVE, see figure 20 and the envelopes in figure 21, by using this layout and with the help of the new RFQ the losses in the ALPI linac are reduced at about 20%: 10% in the first branch of the linac and the other 10% in the high energy branch of the ALPI linac.

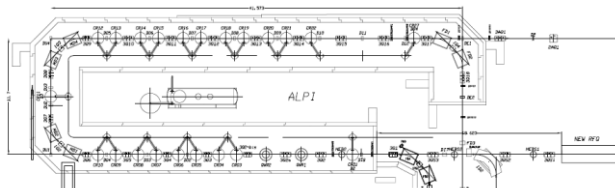


Figure 18: Layout of ALPI with the new RFQ as injector.

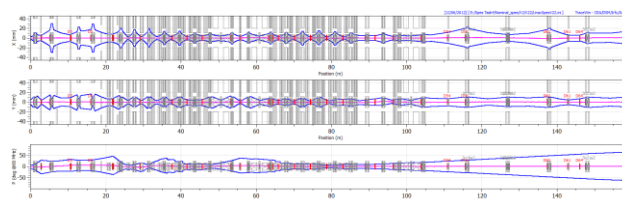


Figure 19: Multiparticles envelopes of the ALPI, with the beam coming out from the new RFQ, from left to right.

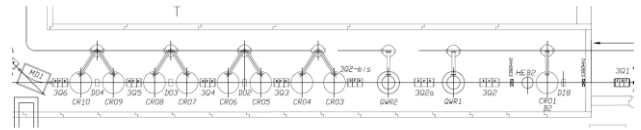


Figure 20: Layout of the new low energy ALPI branch.

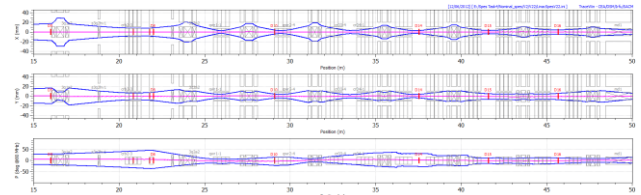


Figure 21: Multiparticles envelope of the new low energy branch, from left to right.

## ACKNOWLEDGMENT

The author wishes to acknowledge the SPES physical design group for the help on preparing this article.

## REFERENCES

- [1] G. Prete et al., "The SPES project: a second generation ISOL facility", *Physics Procedia* 26 (2012) 274 – 283.
- [2] A. Andrighetto et al., "Production of high-intensity RIB at SPES", *Nuclear Physics A* 834 (2010) 754c–757c.
- [3] G. Bisoffi et al., "A Cost-Effective Energy Upgrade Of The Alpi Linac At Infn-Legnaro", these proceedings.
- [4] M. Maggiore et al., "Status Report of the 70 MeV H-Cyclotron", *LNL Ann. Report* 2010.
- [5] J. Montano et al., "Off-line emittance measurements of the SPES ion source at LNL" *NIM A*, 648 (2011) 238-245.
- [6] TraceWin CEA, <http://irfu.cea.fr/Sacm/logiciels/index.php>
- [7] M. Maggiore et al., "Study of the RFQ Beam Cooler for SPES Project", *Proceedings of IPAC2012, New Orleans*.
- [8] P. Delahaye et al., "Prospects for advanced electron cyclotron resonance and electron beam ion source charge breeding methods for EURISOL", *Review Of Scientific Instruments* 83, 02A906 (2012).
- [9] M. Comunian et al., "Beam Dynamics Simulations of the PIAVE-ALPI Linac", *Proceedings of IPAC2011, San Sebastian (E)*, 2034.

**KEK DIGITAL ACCELERATOR AND RECENT BEAM COMMISSIONING RESULT\***

K.Takayama\*, T.Adachi, T.Arai, D. Arakawa, E.Kadokura, T.Kawakubo, T.Kubo, H.Nakanishi, K.Okamura, H.Someya, A.Takagi, and M.Wake, KEK, Tsukuba, Ibaraki Japan  
 Leo Kwee Wah, Graduate University of Advanced Studies, Hayama, Kanagawa Japan  
 LIU Xingguang and T.Yoshimoto, Tokyo Institute of Technology, Nagatsuda, Kanagawa, Japan  
 Y.Barata and S.Harada, Tokyo City University, Todoroki, Tokyo, Japan  
 H.Asao and Y.Okada, NEC Network-Sensor, Futyu, Tokyo, Japan  
 T.Iwashita and K.Okazaki, Nippon Advanced Technology Co. Ltd. (NAT), Tokaimura, Japan

*Abstract*

The early beam commissioning of the KEK digital accelerator, which consists of novel accelerator components such as a permanent magnet x-band ECRIS, an Einzel lens longitudinal chopper, an electrostatic injection kicker, and induction acceleration devices, is reported here. Performance of the Einzel lens longitudinal chopper is described. Results of beam commissioning, such as the beam orbit correction, barrier bucket bunch capture, and induction acceleration are described.

**INTRODUCTION**

The KEK digital accelerator (DA) is a small-scale induction synchrotron (IS) without a high-energy injector [1]. The concept of an IS was experimentally demonstrated in 2006 [2] by utilizing the KEK 12 GeV PS. Instead of an RF cavity, an induction cell is employed as the acceleration device. It is simply a one-to-one transformer, which is energized by a switching power supply generating pulse voltage. Two types of induction cells for acceleration and confinement are employed. It is a crucial point of the IS that voltage timing is controlled by a gate signal of solid-state switching elements based on bunch signals detected at the bunch monitor. This operational performance enables acceleration of ions from extremely low velocities, and is the reason why the DA does not require a high-energy injector. It is understood from these properties that the DA is capable of accelerating any species of ion, regardless of possible charge state.

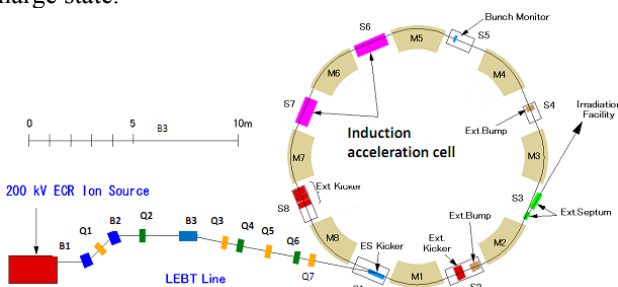


Figure 1: Outline of the KEK Digital Accelerator.

In the KEK DA, schematically shown in Fig. 1, a 5 msec long ion beam is created in the electron cyclotron resonance ion source (ECRIS) and chopped by the newly

\* takayama@post.kek.jp

developed Einzel lens chopper in 5  $\mu$ sec and post-accelerated in the acceleration column attached with the 200 kV high-voltage terminal (HVT), after which it propagates through the low-energy beam transport line (LEBT) to be injected into the ring with the electrostatic injection kicker. The electrostatic kicker voltage is turned off before the injected beam pulse completes a single turn in the DA ring, which is a rapid-cycle synchrotron. The injected beam is captured with a pair of barrier voltage pulses and accelerated with pulse voltages, the pulse length and amplitude of which are controlled in digital. He1+ ions beam commissioning in the KEK-DA is described here.

**MACHINE**

*Permanent Magnet ECRIS [3]*

The ECRIS is embedded on the DC 200 kV high voltage platform. In order to minimize the consumed electric power and avoid troublesome of water cooling on the high voltage platform, the permanent magnet ECRIS being operated in the pulse-mode (10 Hz and 2-5 msec) has been developed. This ECRIS driven by a 9.35 GHz TWT with a maximum output power of 750 W is capable of producing from hydrogen ion to Argon ion, which are extracted at 10-14 kV. The HVT including the Einzel lens chopper and the post-acceleration column is schematically shown in Fig.2.

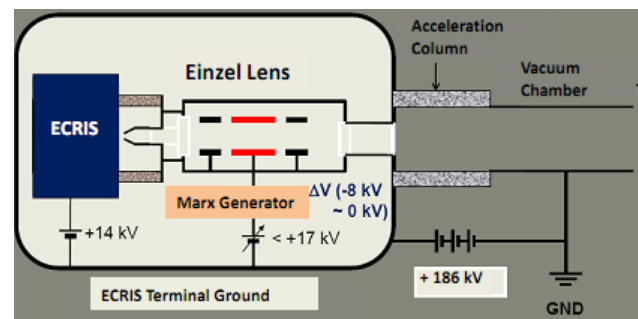


Figure 2: Schematic of the HVT and its contents.

*Einzel Lens Chopper[4]*

As stated in the above introductory part, the revolution time-period of ions in the KEK-DA is around 10  $\mu$ sec. The single-turn injection scheme requires a pulse length

less than 10  $\mu\text{sec}$ . A pulse chopper upstream is necessarily demanded. There are several possible schemes for a chopper. Is it a high energy type or low energy type? Is it a transverse type or longitudinal type? Beam-handling at a low energy stage is apparently preferable, leading to low yields of secondary electrons, small out-gassing, and low energy X-ray emission. Another important factor is its low cost. Careful considerations on a possible space and discharge in the high voltage post acceleration column and quality of chopper voltage have motivated us to develop the Einzel lens chopper, which works as a longitudinal chopper and demands only an additional power supply to control the gate voltage. The chopper head is the Einzel lens middle electrode which is necessary for transverse orbit matching. To realize a fast pulse rising and falling time of the chopped pulse, the solid-state switch driven Marx generator has been developed. A 5  $\mu\text{sec}$ -long pulse of minus 6 kV generated by the Marx generator is superimposed on DC 17 kV of the middle electrode, which prevents ions to propagate downstream except for the gating time-period. The chopped pulse is immediately post-accelerated in the DC acceleration column of 186 kV to enter into the momentum selector or charge-state selector region. Figure 3 shows the 5  $\mu\text{sec}$  pulses chopped at the timing of 0.4 msec from the pulse head respectively, which were measured by a Faraday cup. The rising and falling time are determined by the circuit parameters of the diagnostics circuit system including the stray capacitance of FC. The reconstructed chopped pulse shape is known to be very sharp.

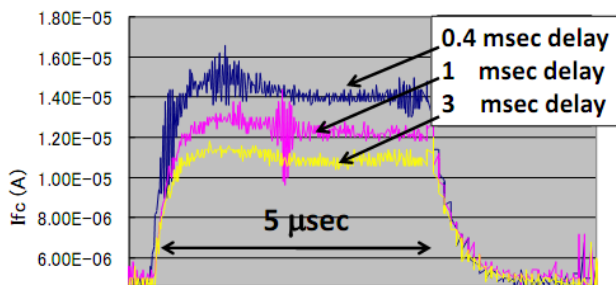


Figure 3: 5  $\mu\text{s}$  chopped pulse profiles, which are chopped at different times from the pulse head of a 5 ms ion pulse.

### Low Energy Beam Transport (LEBT)

The LEBT consists of the momentum selector magnet (or charge state selector), other two bending magnets, 7 focusing quadrupole magnets, a few beam profile monitors, and additional steering magnets, the last four magnets (STH3,4 and STV3,4) of which are used for the purpose of injection error correction.

### Ring Lattice

The lattice consists of eight combined-function (FDF) magnets (M1~M8) symmetrically placed along the beam orbit. Eight straight sections are occupied by the electrostatic injection kicker (S1), extraction kicker (S2,S8), extraction septum magnets (S3), induction

acceleration cells for beam confinement and acceleration (S6, S7), and vertical orbit correction magnets (S4, S5), position monitors (S2, S4, S5, S8), movable screen.monitor (S1), and bunch monitor (S5) Lattice/beam parameters are listed in Table 1.

Table 1: Lattice/beam parameters

|                        |            |                         |
|------------------------|------------|-------------------------|
| Circumference          | $C_0$      | 37.7 m                  |
| Bending radius         | $\rho$     | 3.3 m                   |
| Maximum B              | $B_{max}$  | 0.84 Tesla              |
| Bet. tune in x/y       | $Q_x/Q_y$  | 2.17 - 2.09/2.30 - 2.40 |
| Transition energy      | $\gamma_T$ | 2.25                    |
| Energy (Inj.)/ nucleon | $E_{inj}$  | 200 keV(Q/A)            |
| Rev. frequency         | $f$        | ~80 kHz - 3 MHz         |

### Electrostatic Injection Kicker [5]

From a simple reason that for handling of low velocity ions electrostatic fields are much suitable, the electrostatic injection kicker has been employed. Before the injection, two 80 cm long parallel plates are excited to 20 kV through a pulse forming network line, which is required to counter the injection angle of 11.25 degree. To ensure the field uniformity among two plates, one of which is grounded, three interim electrode panels are inserted. Before the ion pulse completes its first turn, the high voltage is turned off by firing thyatrons, which allow charges on the capacitance including the electrode plates to quickly flow to the ground through the register. Actually the electrostatic kicker voltage was tuned off in a few  $\mu\text{sec}$  with dumped back-and force reflection noises.

## BEAM COMISSIOING

### Beam Orbit

Betatron motions of an injected bunch centroid caused by injection errors were observed by the diagonal electrostatic position monitor in both directions. It turned out that betatron tunes are close to the design values. The injected He1+ ion bunch performed free-circulation in the KEK-DA at the injection fields of  $B_{min}=390$  Gauss and injection optics was optimized by adjusting excitation currents of the steering magnets placed just before the injection point (see Fig.4). The off-set seen in Fig.4, which is left unchanged even after the injection correction is the closed orbit distortion (COD) at the observing position  $s=sM$ .

The KEK-DA is expected to accelerate ions from the quite low energy. Therefore, the magnetic fields of the main magnets at injection are very low as shown in Table 1. At this field level, their remnants fields are relatively large; they should become potential orbit-error sources. Actually we have tried to measure remnant fields at the localized sampling position in the limited area on the pole face. Their magnitudes scatter from 5 Gauss to 10 Gauss [6].

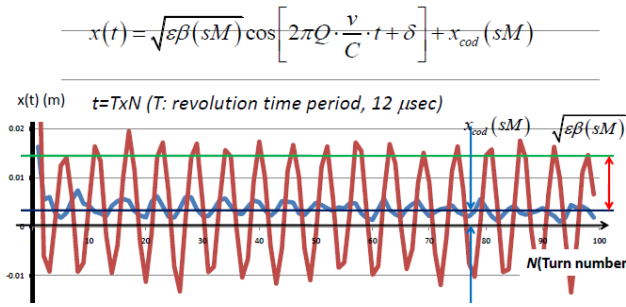


Figure 4: Motion of the beam center: with injection error (brown) and with correction (blue), observed at some position monitor.

The COD, which is a periodic function of  $s$  with the periodicity of  $C$ , has been observed at 5 points along the ring. These data are not enough to recognize its whole profile over the ring. In general, it is known that the COD resulting from random errors is dominated by the harmonic components close to the betatron tune, that is, 2. So, the observed data have been fitted by the 1<sup>st</sup> and 2<sup>nd</sup> harmonics. It is shown in Fig.5. Correction of the fitted COD was tried. For this purpose, 8 figure back-leg coils have been prepared (see Fig. 6). A back-leg coil is wound so as to oppositely encircle the return cores of a pair of every next main magnets. This winding figure is crucial to correct the 2<sup>nd</sup> harmonic component of the COD and to avoid the voltage induced on the power supply for the back-leg coil when the main magnets ramp. The fitted COD was corrected with four independently excited correction currents, which were obtained by mathematically solving the algebraic correction equation. The result is shown in Fig.5. The COD changed its shape as expected at the observing points. Certainly the peak value was substantially reduced, however, the 3<sup>rd</sup> harmonic became visible. At the next step this 3<sup>rd</sup> harmonic component will be corrected.

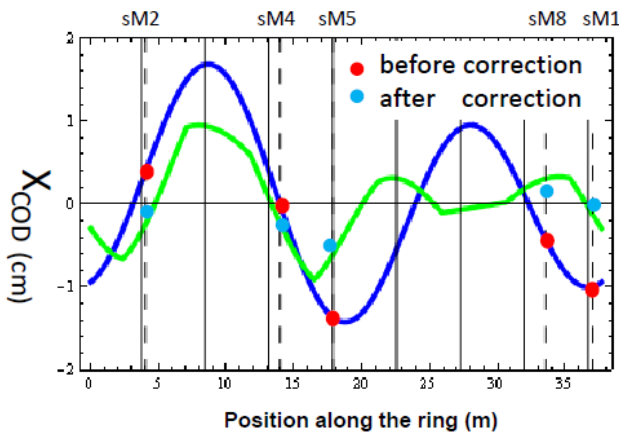


Figure 5: Discretely observed data (red point) of the COD without correction, its 1<sup>st</sup> and 2<sup>nd</sup> harmonics fitted shape (blue line), observed data (sky blue point) with correction, and its fitted shape (green).

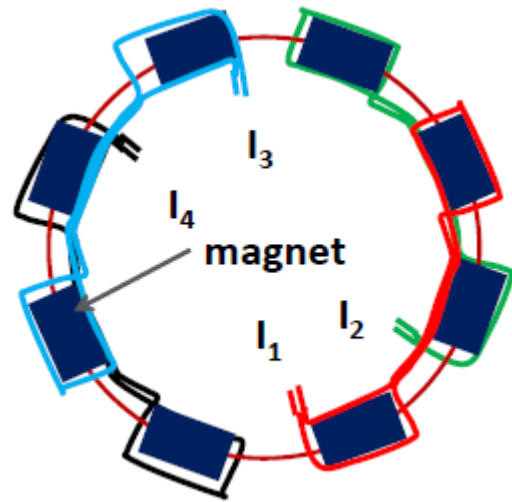


Figure 6: COD correction system with four 8 figure back-leg coils excited by independent power sources.

### Free Circulation in the Ring

The injected bunch circulating in the ring without any longitudinal control has been observed by the bunch monitor (see Fig.7).

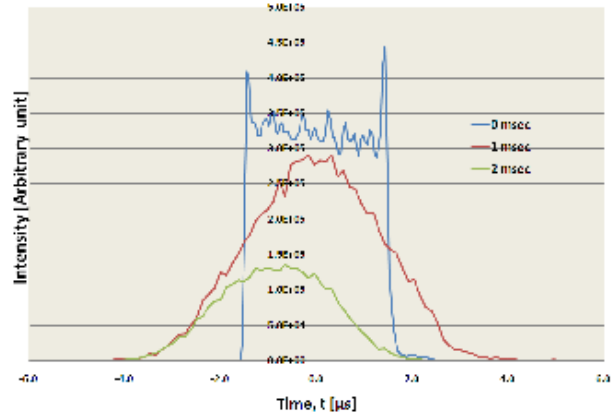


Figure 7: Bunch profiles at the 1<sup>st</sup> turn and 1 msec and 2 msec (measurement).

Mountain views in the time spaces and their projection on the time-turn plane as seen in Figs.8a,b are quite useful for this purpose. Gradual diffusion in the time or on the orbit coordinate indicates a momentum spread of the injected bunch. Meanwhile, something like compression at the early stage of free circulation is visible. This suggests that the injected bunch has a negative momentum spread in the bunch head and a positive momentum spread in addition to an intrinsic momentum spread. It turns out that the seed of this abnormal distribution in the phase space is created as transient effects in the chopper pulse shape and a kind of drift compression takes place during free run in the ring (see Fig.9) [7]. In addition, it has been observed that the speed

of compression depends on the beam intensity [8].

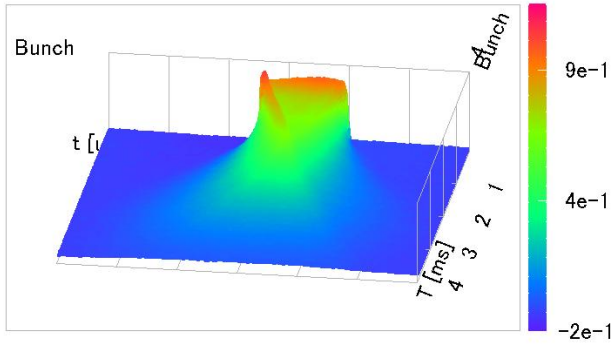


Figure 8a.: Typical mountain view of a bunch profile.

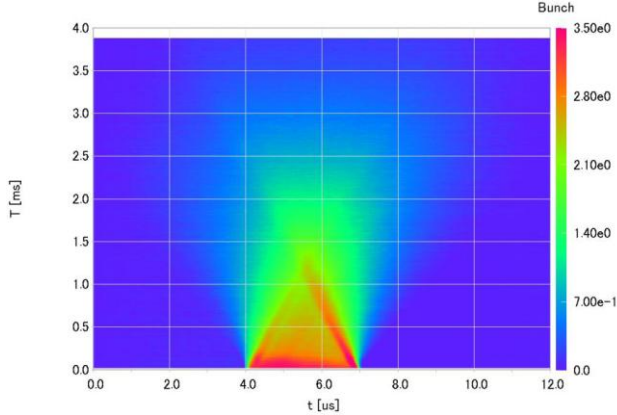


Figure 8b: Projection of the mountain view on the time-turn plane.

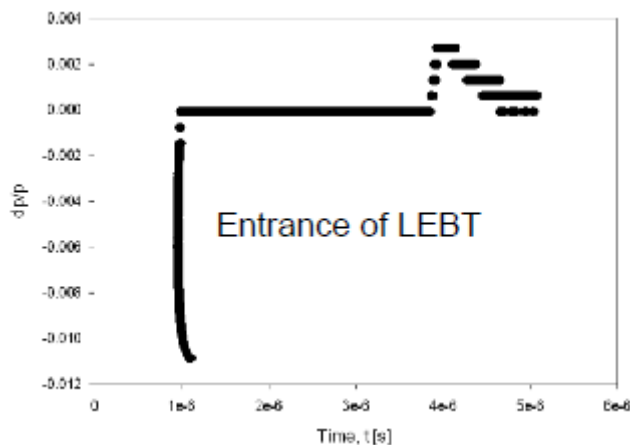


Figure 9: Phase space plot just after the HVT (simulation).

### Barrier Bucket Trapping

At the injection energy, various barrier bucket trapping experiments were conducted. A He1+ bunch was trapped by the barrier voltages that were triggered at the revolution frequency and had a short time duration. Fig.10 shows that a short fraction corresponding this time duration is trapped. Two barrier buckets were generated in one revolution period. As expected, two parts of the injected pulse were captured (See Fig.11). A barrier bucket was created with a sufficiently long width to accommodate the injection pulse. It is shown in Fig. 12 that the captured beam pulse survives through 1 acceleration time period of 50 msec.

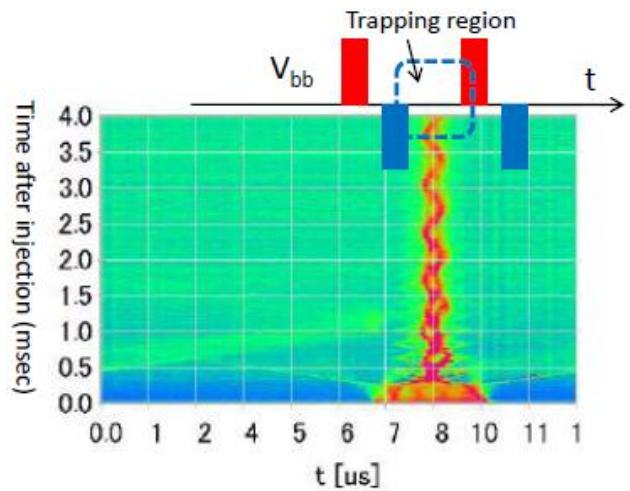


Figure 10: Trapping of a small fraction by the barrier voltages with a short time duration.

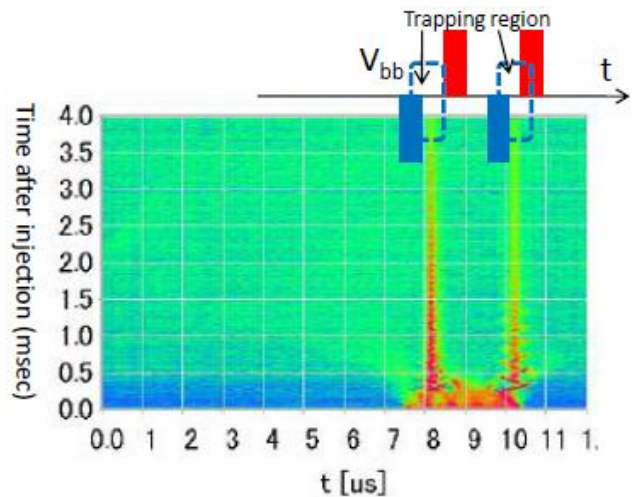


Figure 11: Trapping of two parts of the injected pulse by twin pair of barrier voltage pulses.

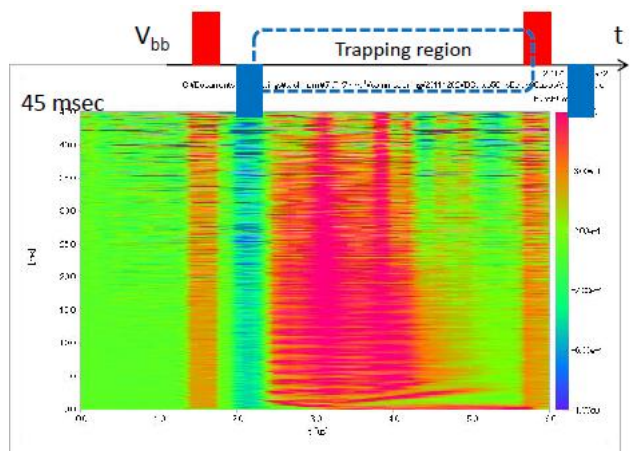


Figure 12: Trapping of a full width of the injected pulse.

### Barrier Bucket Handling (Bunch Squeezing)

Barrier bucket handling of a long bunch, which can't be realized in an RF bucket, has been expected from early

days of induction synchrotron R&D [2]. This was demonstrated by using the present He1+ bunch at the fixed energy. Bunch profiles on the process of bunch squeezing, where the trigger timing for the right barrier voltage pulse is discretely changed by 8 nsec per turn from 0 msec to 7 msec, are shown in Fig. 13. Mountain view of the bunch profile in the same experiment, which delineates typical features of the barrier bucket bunch trapping, is shown in Fig. 14. This experimental result seems to reflect a motion of a bunch injected with an extremely small momentum spread less than 0.025 % and an energy deviation of +0.23 % in the longitudinal phase space. The bunch tail moves forward and a part of the originally bunch head moves backward. Both encounter at 1.5 msec after injection. The latter is reflected by the moving barrier-voltage pulse. The bunch never expands beyond this barrier voltage pulse-edges. Beyond 7 msec, the barrier bucket is fixed. Slightly diffusing of the bunch into the upper region can be attributed to increasing of the momentum spread associated with bunch squeezing.

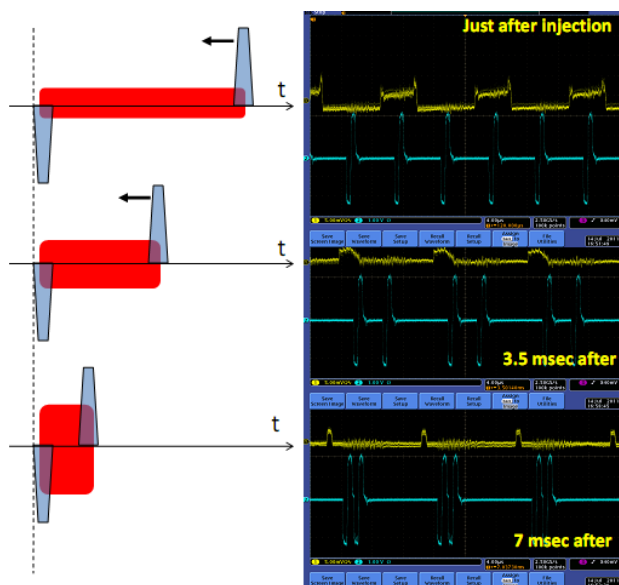


Figure 13: Bunch squeezing experiment (right) and schematic of barrier voltage operation (left).

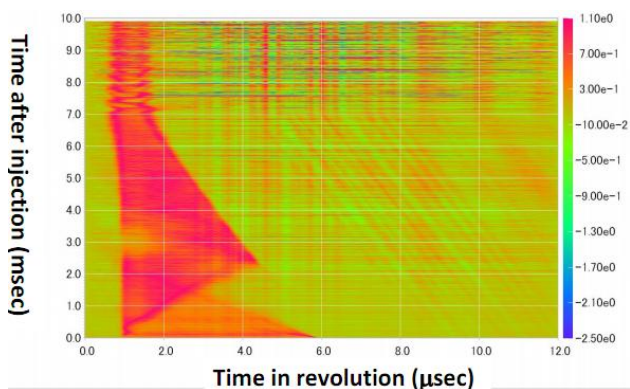


Figure 14: Projection of the mountain views of the bunch profile on the squeezing process.

### Acceleration

At the early stage, the beam orbit was not corrected because all existing monitors didn't work due to primitive reasons, such as poor S/N ratio and circuit short. On the other hand, the acceleration control code for the employed FPGA were under development. Nevertheless, induction acceleration was carried out. The injected beam was accelerated up to 42 msec, reducing its intensity; in other ward, it corresponds to 12 MeV. Preliminary results are shown in Fig. 15.

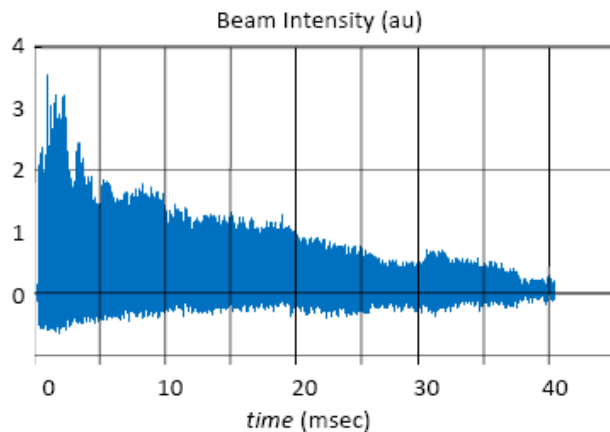


Figure 15: Result of induction acceleration up to 42 msec, corresponding 12 MeV for He1+.

### SUMMARY

We have successfully demonstrated the injection operation of the KEK-DA and barrier bucket beam-handling using He1+ ion beams. The preliminary acceleration has been demonstrated. What we have observed seem to be within our expectation. Hereafter, the induction acceleration under the well managed way will be continued beyond the present stage. From this fall, heavy ion beams will be delivered to users, laboratory experiments for Space Science.

### ACKNOWLEDGMENT

Work supported by a Grant-In-Aid for Scientific Research (A) (KAKENHI No. 23240082)

### REFERENCES

- [1] T. Iwashita *et al.*, "KEK Digital Accelerator", *Phys. Rev. ST-AB* 14, 071301 (2011).
- [2] K. Takayama *et al.*, "Experimental Demonstration of the Induction Synchrotron", *Phys. Rev. Lett.* 98, 054801-4 (2007), "Induction Accelerators", K.Takayama and R.Briggs (Eds.) (Springer, 2010).
- [3] Leo Kwee Wah *et al.*, "Permanent Magnet ECRIS for the KEK Digital Accelerator", *19th Int. Workshop on ECRIS*, August 23-26, Grenoble, France, TUPOT15 (2010).

- [4] T.Adachi, T.Arai, K.W.Leo, K.Takayama, and A.Tokuchi, “A Solid-state Marx Generator driven Einzel Lens Chopper”, *Rev. Sci. Inst.* **82**, 083305 (2011).
- [5] T. Adachi, T. Kawakubo, and T. Yoshii, “Injection and Extraction for the KEK Digital Accelerator”, in Proc. of IPAC’10, p.570-572 (2010).
- [6] K.Takayama, T.Adachi, E.Nakamura, and H.Someya, “Beam Dynamical Issues of The KEK All-Ion Accelerator”, EPAC2008, THPC107.
- [7] K.W.Leo, Dr. Thesis, to be published (2012).
- [8] X.Liu *et al.*, “Longitudinal Beam Motion in the KEK Digital Accelerator: Tracking Simulation and Experimental Results”, in this conference.

# LASER ABLATION OF SOLIDS INTO AN ELECTRON CYCLOTRON RESONANCE ION SOURCES FOR ACCELERATOR MASS SPECTROSCOPY

T. Palchan<sup>1</sup>, R. Pardo<sup>1</sup>, F. Kondev<sup>1</sup>, S. Kondrashev<sup>1</sup>, C. Nair<sup>1</sup>, R. Scott<sup>1</sup>, R. Vondrasek<sup>1</sup>,  
M. Paul<sup>2</sup>, W. Bauder<sup>3</sup>, P. Collon<sup>3</sup>, G. Youinou<sup>4</sup>, M. Salvatores<sup>4,5</sup>, G. Palmotti<sup>4</sup>, J. Berg<sup>4</sup>,  
T. Maddock<sup>4</sup>, and G. Imel<sup>6</sup>

<sup>1</sup> Physics Division, Argonne National Laboratory, 9700 S. Cass Avenue, Argonne, IL 60439 USA

<sup>2</sup> Racah Institute of Physics, Hebrew University, Jerusalem 91904, Israel

<sup>3</sup> Nuclear Structure Laboratory, University of Notre Dame, Notre Dame, IN 46556, USA

<sup>4</sup> Idaho National Laboratory, 2525 Fremont Avenue, Idaho Falls, ID 83415

<sup>5</sup> CEA-Cadarache, 13108 Saint-Paul-lez-Durance, France

<sup>6</sup> Idaho State University, 921 South 8th Avenue, Pocatello, ID 83209

## Abstract

A project using accelerator mass spectrometry (AMS) is underway at the ATLAS facility to measure the atom densities of transmutation products present in samples irradiated in the Advanced Test Reactor at INL. These atom densities will be used to infer effective actinide neutron capture cross-sections ranging from thorium to californium isotopes different neutron energy spectra relevant to advanced fuel cycles. This project will require the measurement of many samples with high precision and accuracy. The AMS technique at ATLAS is based on production of highly-charged positive ions in an ECRIS followed by injection into a linear accelerator. We use a picosecond laser to ablate the actinide material into the ion source. We expect that the laser ablation technique will have higher efficiency and lower chamber contamination than sputtering or oven evaporation thus reducing 'cross talk' between samples. In addition a multi-sample holder/changer is part of the project to allow for a quick change between samples. The results of off-line ablation tests and first results of a beam generated by the laser coupled to the ECR are discussed as well as the overall project schedule.

## INTRODUCTION

Advanced nuclear fuel cycles are currently under evaluation in order to assess their potential to cope with new requirements of radioactive waste minimization, optimization of resource utilization and reduced risk of proliferation. This assessment should account for several key features of the fuel cycle, as of irradiated fuel processing, innovative fuel development and fabrication, waste characterization and disposal. In some cases, the impact of nuclear data and of their associated uncertainties can be crucial in order to assess further exploration. The need for accurate data has been pointed out in recent studies devoted to Generation-IV systems, see e.g. [1]. The very high mass actinides can play a significant role in the feasibility assessment of innovative fuel cycles. As an example, the potential build-up of <sup>252</sup>Cf when recycling all transuranics in a light water reactor, leads to increased neutron emissions that could impact the

fuel fabrication process [2]. As a consequence, the poorly known nuclear data of higher mass transuranics need to be significantly improved.

At present, most evaluated data files provide some information on these isotopes, but up to now, there has been little emphasis on the quality of these data and very little reliable uncertainty estimations have been provided. This situation is due to the difficulty to make both integral and differential cross section measurements for these isotopes.

The MANTRA (Measurements of Actinides Neutrons Transmission Rates with Accelerator mass spectroscopy) project objectives are to obtain valuable integral information about neutron cross sections for actinides that are important for advanced nuclear fuel cycles. The proposed work takes advantage of two experimental facilities: the neutron irradiation capabilities of the Advanced Test Reactor (ATR) at the Idaho National Laboratory and the Accelerator Mass Spectrometry (AMS) capabilities of the Argonne Tandem Linac Accelerator System (ATLAS) at Argonne National Laboratory [3].

In this paper we will concentrate on the requirements of the AMS program and the novel aspects, namely the laser ablation and the multi-sample changer, that are implemented at the ECR ion source to carry out this research project. The requirements placed on the AMS measurements to be performed at ATLAS are quite challenging. These challenges include high-precision isotope ratio measurements, minimization of cross-talk between samples, efficient use of milligram samples, and the processing of an unprecedented number of samples for a facility as complex as ATLAS. Unique element (Z) identification is desirable, but is not expected to be possible except for specific cases.

The measurement configuration for ATLAS uses the ECR-II ion source [4], significantly modified as discussed below, as the source of ions. After acceleration and deceleration (increasing the accelerator m/q resolution but keeping the ion energy within acceptance range of analytical elements) in the ATLAS linac to approximately 1 MeV/u, the actinide ions of interest are counted in the focal plane of the Fragment Mass Analyzer (FMA) [5].

### *Small Sample Size and Cross-Talk*

A major feature of AMS is the ability to analyze small samples. At ATLAS the AMS activities are focused on samples of a few milligrams. For this project, an added complexity is the need to deal with many small samples. The smaller the samples, the less are the radiological problems associated with handling  $\alpha$ -emitting actinides for ATLAS operation. The need to measure many small samples as quickly as possible pushes us to develop efficient sample changing techniques for the ECR source and material delivery techniques which minimize source contamination.

We believe the best approach for this situation is to develop laser ablation for the feeding of sample material into the source. With laser ablation a very small and controllable amount of sample material can be introduced into the source without introduction of extraneous material from the sample holder. Also the angular distribution of ablated material by laser irradiation tends to be strongly peaked around the normal to the surface [6] which is expected to improve the efficiency of capture of ions into the plasma and thereby reduce wall contamination. Finally, the form of the sample material (metal, oxide, etc.) is less critical than with the sputtering or oven technique.

The ECR-II source will also be equipped with a quartz liner. The quartz liner will keep the main body of the source relatively clean of actinides, thus simplifying clean-up. Furthermore, there is some operational evidence that cross talk among samples is reduced. This effect has been observed with other AMS projects at ATLAS. A negative to using a quartz liner is that source performance as measured by charge-state distribution and maximum beam intensity is somewhat reduced. But the beam energy is limited by the bending power of the FMA system and use of high charge state ions is not required. A mass-to-charge ratio of  $\sim 8-9$  will be quite adequate for these measurements.

### **LASER PARAMETERS**

Laser ablation into an ECR source was first developed at ATLAS [7] and used as a plasma diagnostic tool [8] and has since been used by a number of other labs to explore the coupling of laser produced ions into an ECR source. The technique has not been used routinely for ion production and requires development for this application. The controlled release of materials into the plasma by well-focused laser light will eliminate the significant material buildup often seen in the region of the oven throat or beside the sputter cones, two techniques widely used for sample feeding to the ECRIS. This inefficient, indiscriminate injection of material into the source not only reduces the overall sensitivity of the method but is a major source of cross-contamination between samples. Our experience with lasers in the past indicates that the laser ablation approach will be much cleaner, but must be shown to work for this application.

Laser ablation is a term used to describe removal of material by laser action and it is distinguished from evaporation in equilibrium conditions. In order to remove an atom from a solid by means of a laser pulse one should deliver an amount of energy that exceeds the binding energy of that atom. Therefore the absorbed energy density per atom in a laser-heated layer  $E_{\text{abs}}$ , should at least be comparable to the heat of vaporisation in equilibrium;

$$E_{\text{abs}} = 2AF(t_p)/n_a l_s. \quad (1)$$

here  $A$  is the absorption coefficient;  $F$  is the incident laser fluence, the energy per unit surface area during the pulse of duration  $t_p$ ;  $n_a$  is atomic number density and  $l_s$  is the skin depth of the laser in the solid [9]. There are three regimes of laser ablation depending on the laser and target parameters: The thermal ablation, the non-equilibrium semi thermal ablation and the extreme non-equilibrium electrostatic ablation. In the thermal ablation the laser pulse is longer than the major relaxation routes in the irradiated material. Heat conduction and hydrodynamic processes cause the removal of the atoms from the solids. As a consequence the ablation is accompanied by the formation of a large heat-affected zone and throws out molten material [10]. The second regime, non-equilibrium and semi-thermal, is realized when electrons have enough time to transfer the energy to the lattice and the average energy of the ions (temperature) exceeds the binding energy but the distribution function is far from the equilibrium Maxwell distribution. In these conditions, the majority of ions escape the solid before the equilibrium distribution is established. The extreme ablation regime, electrostatic ablation, is completely non-equilibrium and non-thermal. This mode is realized when a short powerful pulse elevates average electron energy during the pulse in excess of the sum of the binding energy of the ions plus the energy necessary for the electron to escape from a solid. The lattice remains cold during the pulse. The energetic electrons escaping from a solid create a huge electrostatic field of charge separation, which pulls the ions out of a solid [11].

In order to avoid a flow of macroparticles molten materials into the ECR ion source, we chose a laser with picoseconds pulse duration. The properties of the laser that we are using in this application are:

- $\lambda = 1064 \text{ nm}$
- 15 ps pulse width
- Repetition rate up to 400 Hz
- Pulse energy: variable, up to 5 mJ per pulse.
- Maximum, power of  $3 \times 10^8 \text{ W}$  per pulse.

### **OFF LINE TEST SET UP AND RESULTS**

For characterization of the laser and to acquire a better understanding of the laser ablated material coupling with the ECR ions source plasma we performed some test in an off line setup. The Experimental set up is shown in Fig 1. A 4000mm focusing lens is placed at the entrance of a vacuum chamber to mimic the distances required at a ECR source. The result of the optical set up is a focal spot

with a diameter of  $450\mu\text{m}$  at the FWHM. The maximum laser intensity at the focal spot is  $2 \times 10^{11} \text{W}/\text{cm}^2$ . An image of the focal spot is presented in Fig 1.

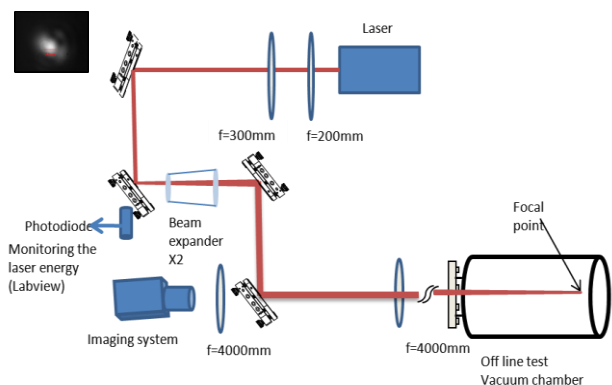


Figure 1: Off line test set up and the laser focal spot image.

The laser induced ablation creates a plasma plume which rapidly expands. Typically the plasma expansion speed is in the order of  $10^6 \text{cm}/\text{sec}$ . During a picosecond ablation the number of ejected species is about  $10^{13}$  atoms/pulse. The ion flux is about 1% [12]. Using a faraday cup located at a distance of 15.8cm from a solid Ta target we extracted the ion velocity by means of time of flight technique. The calculated averaged ion energy is  $40 \pm 10 \text{eV}$ . For Ti the corresponding velocity is  $1.2 \times 10^6 \text{cm}/\text{sec}$ .

A table of examples of ablated material results is included below. In these measurements the laser energy was 1.5-1.6mJ with repetition rate of 400Hz. The resulting laser peak fluence is  $0.7 \text{J}/\text{cm}^2$ . These studies now provide us with the background information needed to better understand the laser/source performance when the laser is coupled to the ECR source.

## INSTALLATION AT THE SOURCE

The installation of the laser at the source is shown in Fig. 2. The laser beam is delivered into the source through the extraction aperture. The ablation target is located at the rear of the ECR chamber near the adage of the plasma.

### Multisample Changer

Due to the relatively large number of samples (up to 50) to be measured in this experiment and the need to rapidly switch between samples to track any changes in accelerator transmission, an entirely new approach to sample handling, one that is fully automated, is required.

A sample changer that can accept 20 samples has been designed and will be mounted on the injection side of the ECR ion source as shown in Fig. 3. Each sample is mounted onto the end of a 2900mm long aluminum rod that travels in UHV compatible plastic holders. The long

longitudinal distance places the mechanism outside of the high magnetic field region of the ECR source. The time to change between samples is less than 1 minute. An absolute encoder is mounted so position information is preserved. In addition, a laser sensor is attached to ensure sample is retracted before rotating. The operation of the multisample changer can be controlled by the accelerator crew or automatically by an experiment program.

Table 1: Ablating rates for different materials

| Sample   | Consumption rate   | Hole depth                               | Image     |
|--|--|--|-----------|
| Fe solid<br>(1 location<br>shooting for<br>39 min)   | 1.3mg/39min<br><br>0.033mg/min   | 1.2mm<br>(for 39 min)                    | <br>0.2mm |
| Fe solid<br>(3 locations<br>13 minutes on<br>each location)                                | 1.4mg/39min<br><br>0.035mg/min<br><br>$3.7 \times 10^{17}$<br>atoms/min  | 1.19mm<br>(for 13 min)<br><br>0.09mm/min | <br>0.5mm |
| Fe oxide<br>powder-<br>MANTRA<br>target<br>(3 locations<br>13 minutes on<br>each location) | 1.3mg/39min<br><br>0.033mg/min<br><br>$1.24 \times 10^{17}$<br>atoms/min | 1.07mm<br>(for 13 min)<br><br>0.08mm/min | <br>0.2mm |
| Al oxide<br>powder-<br>MANTRA<br>target<br>(3 locations<br>10 minutes<br>each)             | 0.1mg/30min<br><br>0.003mg/min<br><br>$1.77 \times 10^{16}$<br>atoms/min | 0.8mm<br>(for 10 min)<br><br>0.08mm/min  | <br>0.5mm |
| Tb +Fe oxide<br>powder<br>MANTRA<br>target<br>(2 locations<br>10 minutes<br>each)          | 0.1mg/20min<br><br>0.005mg/min<br><br>$8.2 \times 10^{15}$<br>atoms/min  | 0.57mm<br>(for 10 min)<br><br>0.05mm/min | <br>0.5mm |
| U metal<br>(3 locations<br>10 minutes<br>each)   | 4mg/30min<br><br>0.13mg/min<br><br>$3.289 \times 10^{17}$<br>atoms/min   |  | <br>0.2mm |
| U oxide<br>(3 locations<br>10 minutes<br>each)   | 0.5mg/30min<br><br>0.016mg/min<br><br>$3.56 \times 10^{16}$<br>atoms/min |  | <br>0.2mm |

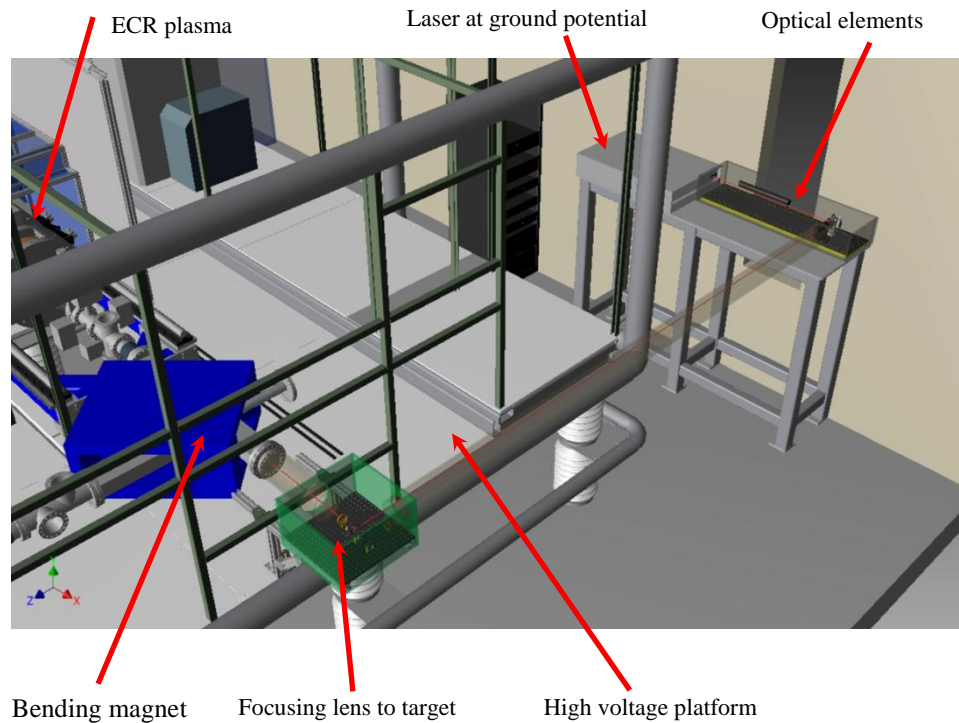


Figure 2: Drawing showing the laser ablation system relative to the ECR source HV platform.

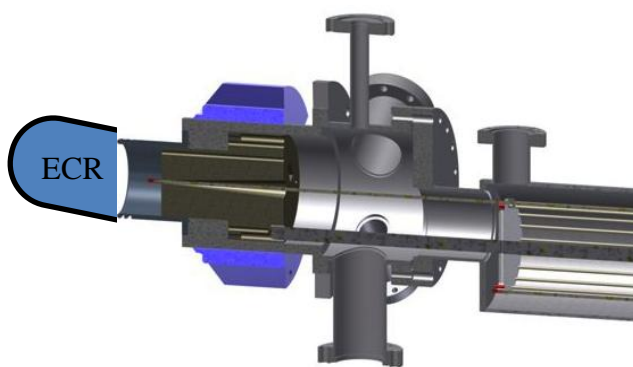


Figure 3: Multisample changer.

### Back Light

In order to monitor the laser beam hitting the target samples, we developed an imaging system. The imaging system is located behind the last mirror that directs the laser beam into the source (see Fig 1). We installed a halogen light at the back of the iron taper, (see Fig 4). This way we can collect the scattered light behind the sample holder when it is in place. Using our imaging system we are able to image the outer edges of the sample holder. During a run when the laser hit the sample we are able to identify where the laser hits the sample.

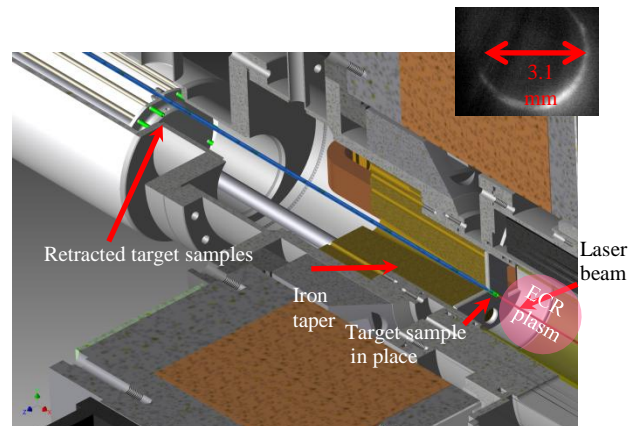


Figure 4: Multisample changer mounted on ECR source showing sample location with the back light.

## TITANIUM SAMPLE AT THE ECR SOURCE

Initial tests of the laser coupled to the ECR source took place with a Ti samples. Fig 5 shows a Ti sample after irradiation. The laser parameters that we used during this test are 25Hz repetition rate and a variable energy of 0.5-1.5mj per pulse. The resulting peak intensity is  $5 \times 10^{10} \text{ w/cm}^2$ . The overall consumption rate was 0.3mg/hour.

*Beam from Ti sample ablated into ECRIS*

By means of laser ablation on a Ti sample we were able to generate a high charge state beam. The charge state distribution is shown in Fig 6. From the charge state distribution it is clearly evident the beam production drops to a very low level of 0.1  $\mu\text{A}$  when the laser is off.

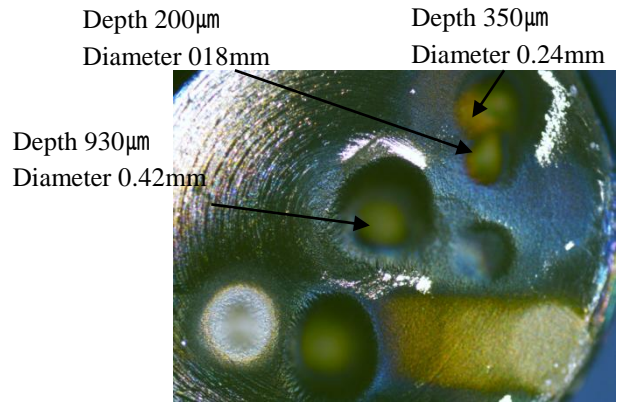


Figure 5: Ti sample after laser irradiations.

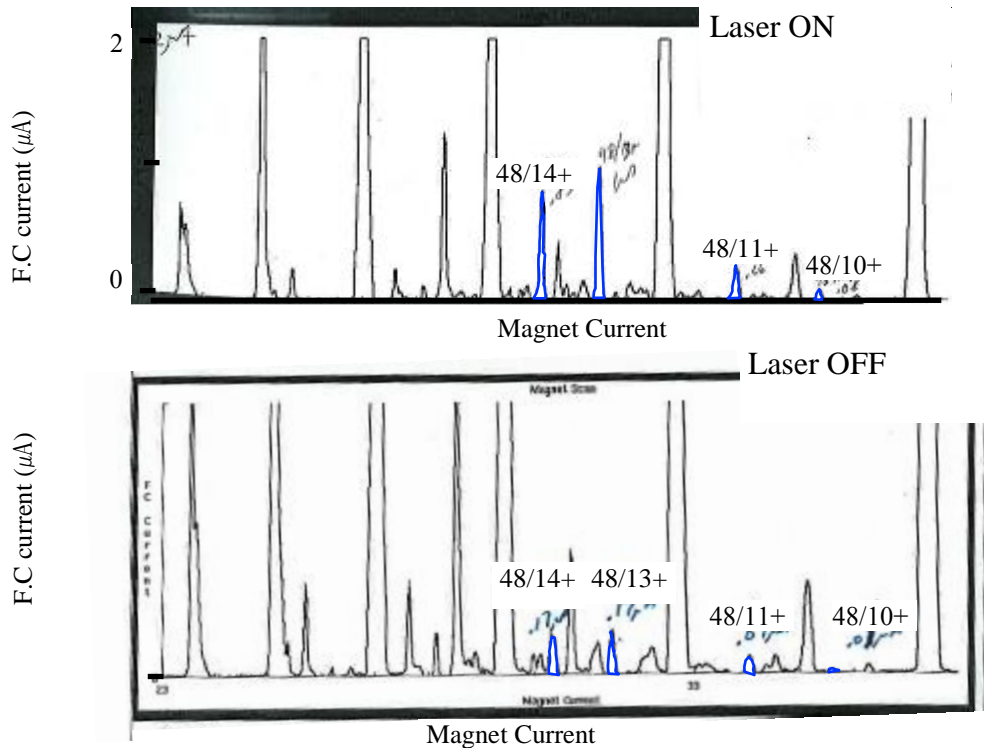


Figure 6: Charge state distribution of Ti beam. The Ti peaks are labeled with mass/charge state in the two figures. The charge-state distribution peaks at 13+. For sputter technique the charge-state distribution peaks at 10+-12+.

*Long-term Beam Output from Ablated Ti Sample*

For long term stability (100minutes) we measured the 48/13+ charge state. The laser energy that we used for those measurements was 1.5mj with 25Hz repetition rate. The focal beam diameter was 0.5mm. Fig 7 shows the faraday cup current trend with the corresponding laser energy.

The generated beam is around 4  $\mu\text{A}$  and stable for the first 10 minutes and then it drops by 80% for the next 20 minutes while on the same time the laser energy is stable. After that the beam stays stable at a lower level of 0.6  $\mu\text{A}$  for more than an hour.

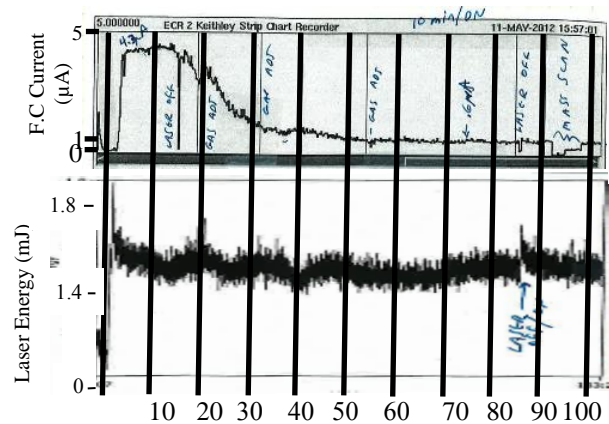


Figure 7: Long term of Ti beam and the corresponding laser energy for 0.5mm diameter in the focal spot.

One of the reasons for this beam current instability current is the drilling rate of the laser in the sample. In order to lower the drilling rate and to gain more stability we changed the laser focal spot on the target to be a bigger. With this new alignment the focal spot was elliptical with major and minor diameter of 0.8mm and 0.6mm respectively.

Fig. 8 shows the long term beam output in the case of the bigger focal spot. The laser energy and repetition rate were the same as in the previous run. Again we measured the 48/13+ charge state. The beam starts with a drop of 37% in the first 2 minutes. After that it stays stable for 20 minutes and then drops 43% in the last 15 minutes. The corresponding laser energy is not stable over the same period of time. We will continue to work to improve the beam stability.

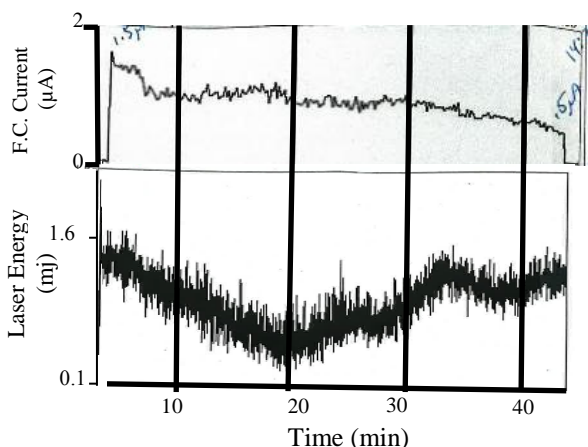


Figure 8: Long term of Ti beam and the corresponding laser energy for the case of elliptical focal spot.

## CONCLUSIONS

We had demonstrated high charge state beams generated at the ECR source from laser ablated material. To improve the stability of the generated ion beam we plan to raster continuously the laser beam on the sample. In addition we plan to investigate the influence of the spatial beam profile, especially a hat top profile, on the production of the ion beam. This work is supported by the U.S. Department of Energy, Office of Nuclear Physics, under contract No. DE-AC02-06CH11357.

## REFERENCES

- [1] M.Salvatores, "Nuclear Data for Advanced Fuel Cycles", Proc. Int. Conf. IEMPT-10, Mito, Japan, 6-10 October 2008.
- [2] G.Youinou, et al., INL/EXT-09-16091, 2009; <http://www.inl.gov/technicalpublications/Documents/4282336.pdf>.
- [3] G.Youinou, et al., "An Integral Reactor Physics Experiment to Infer Actinide Capture Cross-Sections From Thorium To Californium With Accelerator Mass Spectrometry", Eleventh International Conference on Nuclear Data for Science and Technology, Jeju Island, Korea, 2010.
- [4] M. Schlapp, et al., "A new 14GHz electron-cyclotron-resonance ion source for the heavy ion accelerator facility ATLAS" Rev. Sci. Instrum. 69 (1998) 631.
- [5] C.N. Davids, et al., "Startup of the Fragment Mass Analyzer at ATLAS", Nucl. Instrum. and Meth. B 70, 358(1992).
- [6] S. Mao et al., "Initiation of an early-stage plasma during picosecond laser ablation of solids" Appl. Phys. Lett. 77, 2464 (2000).
- [7] R. Harkewicz, et al., Rev. Sci. Inst. 65(4), 1104(1994).
- [8] R C Pardo, et al., Rev. Sci. Inst. 75 (5), 1427(2004).
- [9] E.G.Gamaly, "The physics of ultra-short laser interaction with solids at non-relativistic intensities" Phy. Reports. 508 91 (2011).
- [10] S. Nolte et al., "Ablation of metals by ultrashort laser pulse" J. Opt.Soc. Am. B 14 (10)2716(1997).
- [11] P.T. Mannion, et al., "Langmuir probe investigation of plasma expansion in femto-and picoseconds laser ablation of selected metals" J. of Phy :Conference series 59 753 (2007). Conference on Laser ablation (COLA'05) Banff, Canada 2005.
- [12] W. Marine, et al., "Laser induced plasma formation by picoseconds pulse irradiation" Appl. Surf.Sci. 69 290 (1992).

## EXPERIENCES AND LESSONS LEARNED AT CARIBU WITH AN OPEN 252CF SOURCE

S.I. Baker, J.P. Greene, A. Levand, R.C. Pardo, G. Savard, R.C. Vondrasek, L.W. Weber [ANL, Argonne, USA]

### *Abstract*

The CARIBU (the CALifornium Rare Ion Breeder Upgrade) project at ATLAS is based on the creation of beams of neutron-rich nuclei produced as fission fragments from the 3% fission branch that occurs naturally in the decay of Cf-252. These fission fragments are thermalized in ultra-pure helium gas and turned into a charged beam for use by the ATLAS accelerator or 'stopped' beam experiments. This requires a very thin source, electroplated on a stainless steel or platinum backing so that the fission fragments escape into the helium gas and are efficiently thermalized and collected into an ion beam. The information learned from the successive use of two sources with strengths of 2 mCi and 100 mCi has now prepared us for the installation in mid-summer of a 500 mCi source recently produced by Oak Ridge National Laboratory. This paper will describe the radiological monitoring system and our experience with the two weak "open" sources which have exercised and tested our radiological controls, emissions monitors, and procedures for the CARIBU facility and the source transfer area.

**CONTRIBUTION NOT  
RECEIVED**

## ADVANCED ACCELERATOR TECHNOLOGY ASPECTS FOR HADRONTHERAPY

L. Falbo, CNAO, Pavia, Italy

### Abstract

Nowadays cancer can be considered as one of the wide spread diseases all around the world. About 50% of the patients are successfully cured and in 40% of these cases radiotherapy is the applied treatment modality. Radiation beams are produced by particle accelerators and about 30% of the 17500 particle accelerators running in the world are devoted to radiotherapy.

Classical radiotherapy employs photons and electrons that damage the diseased cells but irradiate also the healthy ones. A better conformation of the dose to the tumour and an increasing sparing of the healthy tissues is obtained using hadrontherapy, a high-precision radiotherapy exploiting the depth-dose deposition characteristics of hadronic particles.

The first hadrontherapy treatments have been performed in particle physics research centers clinically adapted; nowadays there are dedicated facilities designed and built as hadrontherapy clinical centres. The realization of machines for hadrontherapy is more challenging than standard radiotherapy: while many hospitals have a device for classical radiotherapy, hadrontherapy needs a dedicated complex with the needed technology for the hadron acceleration.

This paper will give an overview on the existing hadrontherapy centres presenting the technology that is applied in the hadrontherapy world.

### HADRONTHERAPY RATIONALE

Cancer is one of the major world health problems: about 7 million people are known to die each year because of this disease. Cancer is the hysterical and irregular growth and propagation of a cluster of cells. Radiotherapy technique is based on the principle of using ionizing particles to damage the DNA of the cancer cells in order to first block their ability to regenerate and finally to cause their death.

As soon after their discovery in 1895, X-Rays have been used with medical purposes for the treatment of ill tissues. From these first completely empirical tests, radiotherapy has evolved a lot becoming an important tool in medicine and one of most exploited technique in the fight against cancer: about 40% of cancer patients are cured by radiotherapy, either alone (25%) or in combination with other techniques like surgery or chemotherapy. Nowadays among the 17500 accelerators running in the world, 50% are for medical use and more than 8000 are only for radiotherapy purposes.

Standard radiotherapy uses photons and electrons that deposit the maximum of their energy near the beam entrance and a significant part of energy also after the tumour target. As a consequence not only the tumour cells are damaged but also the healthy ones. Recently several

techniques are employed to confine this problem: computer-aided optimization of the treatment plans (Intensity Modulated Radiation Therapy) allows to reach a better dose conformity irradiating from several directions and using collimators to transversally shaping the tumor. Anyway also considering the recent improvements, the depth dose deposition characteristics of the standard particles represent a great limitation and disadvantage in the radiotherapy field.

Hadrontherapy is the answer to this problem. Indeed it is based on the use of hadrons (the hadrons we are talking about are protons and heavy ions) whose Bragg curve is characterized by a narrow peak that occurs distant from beam entrance: this gives a good dose localization with low dose at the entrance and at the exit of tumour target. This effect is well shown in Fig. 1.

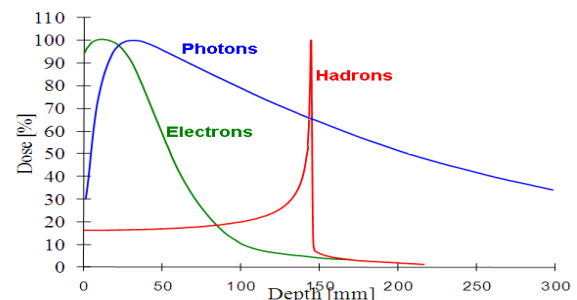


Figure 1: Bragg peaks in the case of photons, electrons and hadrons□

This allows to shape the radiation field not only transversally but also longitudinally using several Bragg peaks at different penetration depths that create the so called SOPB (Spread Out Bragg Peak). In other words hadrontherapy is a high precision kind of radiotherapy. The hadrons mostly exploited are protons and carbon ions. Some figures of merit that allow to understand the advantages of hadrontherapy are the Linear Energy Transfer [1] (LET, whose value along the particle path describes the Bragg curve), the Relative Biological Effectiveness (RBE) [2], i.e. the ratio between the photon and ions doses to produce the same biological effect, the Oxygen Enhancement Ratio (OER) [3], i.e. the dose to produce a biological effect in the absence of oxygen to the dose to produce the same effect in oxygen presence. For Cobalt gamma rays the maximum LET is about 10 keV/μm, for protons it is approximated 100 keV/μm while for heavier ions it may reach 1000 keV/μm presenting a high value in the Bragg peak region and a low one at the beam entrance. The proton RBE is about 1 while ions heavier than helium have a RBE greater than 3 at the Bragg peak and about 1 in the entry channel. The photon OER is about 3 while it decreases when LET is greater than 100 keV/μm approaching to unit at 300

keV/μm. Another aspect to be considered is the multiple scattering: for higher mass the scattering is less relevant giving improvement in the lateral and longitudinal dose distribution. However when increasing the mass there is an increasing of the nuclear fragmentation creating a tailing of the Bragg peak.

Theoretical studies taking into account all these aspects indicate that ions for  $Z > 6$  should not be a good clinical choice. When, during the '80s hadrontherapy had a revival in Europe and Japan, carbon ions were indicated as the best medical choice and often the only solution for radio-resistant tumors. Other species in the range  $1 < Z \leq 6$  could be as or more interesting than carbon ions [4] and clinical experimentations at the existing hadrontherapy facilities could reveal interesting results.

### HADRONTHERAPY FACILITY DESIGN CRITERIA

The considerations reported above are of fundamental importance to define the design of a hadrontherapy centre. Indeed the main points that influence the characteristics of such a facility are the ion species to be accelerated and the technique to shape the radiation field. Three different accelerator types are possible: linear accelerators, cyclotrons, synchrotrons.

The penetration depth ranges between 30 mm and 300 mm. In case of protons and carbon ions, this corresponds to a range of energy respectively of 60 MeV-220 MeV and 120 MeV/u-425 MeV/u. In principle these energy ranges can be obtained with the three accelerators. However linacs are not very practical and feasible for high energies and then we will consider only cyclotrons and synchrotrons that are the main layouts in the hadrontherapy facilities. On the other hand synchrotrons can perform easily the acceleration of both proton and carbon ions. Indeed considering that the limitation is the magnetic rigidity, a synchrotron for carbon ions can accelerate all the species with  $1 \leq Z \leq 6$ ; also Oxygen can be accelerated with such a layout but only up to a penetration range of 190 mm. Even if they are more flexible than cyclotrons, synchrotrons are technologically more complicated and then more costly: for example the synchrotron needs an injection energy of some MeV/u which requires an injector linac. The cyclotron appears to be more compact, especially in the case of a superconducting one. In the case of proton beams acceleration, a cyclotron has a diameter of about 4-5 m while a synchrotron reaches 7-11 m (a synchrotron designed for carbon ions has a diameter of about 20 m).

The maximum energy of carbon ions makes very challenging the realization of a dedicated cyclotron: up to now cyclotrons for 400 MeV/u carbon ions have not been realized yet but a centre has been recently proposed by IBA [5] consisting of a carbon cyclotron and a proton cyclotron. The advantage of more compact accelerators is partially reduced by the overall size of the facility that is occupied mainly by the beam lines and the treatment rooms with the gantries and the technical infrastructures.

The current from the cyclotron is DC while in a synchrotron it is pulsed because of the need to ramp the magnets from the injection value to the extraction value first and then to a maximum value that allows avoiding non repeatability problems when changing energy due to the magnetic hysteresis. As a consequence, generally, currents from cyclotrons are much higher than the one from synchrotrons: in the case of protons cyclotron can deliver about 300 nA instead of some nA from synchrotrons.

There are essentially two techniques to shape beam distribution on the tumor target: passive and active beam delivery. The passive delivery consists essentially in putting before the patient several absorbers able to change beam characteristics. The passive technique consists of: a scatterer to enlarge the beam; a variable degrader and a ridge filter to increase energy spread creating a SOBP; a first collimator to select the central part of the beam; the so called bolus, a device with a "hole" that has the shape of the distal surface of the tumour; a final multileaf collimator that gives the beam the required transverse size. Fig. 2 shows schematically the absorbers used in the passive scanning.

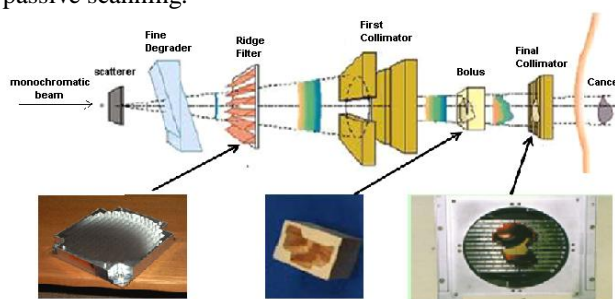


Figure 2: Scheme of a passive scanning.

Some variants to this scheme are the use of a rotating wheel range modulator as variable degrader and the wobbling method. The rotating wheel allows to change the thickness of material the beam passes through: in this way, making rotate the wheel, beams with different energies are obtained resulting in a SOBP. The wobbling method is based on the use of scanning magnets that cause the beam moves on a circle at high frequency before the scatterer so resulting in a flat beam to be adjusted transversally and longitudinally.

There are some evident disadvantages of the passive method. First the bolus and the multileaf collimator are strongly depending on the tumour and then they are specific for each patient. Second, as shown in Fig. 3, the bolus takes into account only the distal surface causing the proximal parts of the tumour are very badly irradiated. Third, the presence of lots of materials between the beam and the patient cause nuclear fragmentation that leads to dose tails after the Bragg peak. In particular in the case of heavy ions, passive scanning has other drawbacks. Indeed heavy ions cause nuclear fragmentation with the target; furthermore since they scatter less than protons thicker scatterers are needed to obtain a large treatment field: thicker scatterers imply larger energy and beam losses

requiring higher energies and currents from the accelerators.

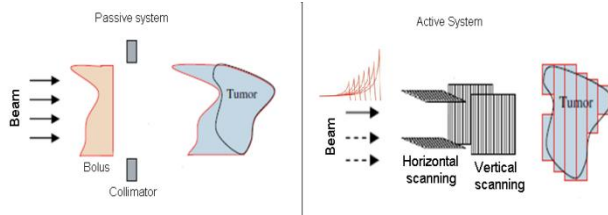


Figure 3: Dose uniformity in the case of passive and active system.

Active scanning was first used in Japan in 1980 [6] and then optimized and regularly used for treatments at PSI [7], GSI [8], HIT and CNAO [9].

In the active scanning method two magnets are used to move the beam in the two orthogonal directions. The tumour is virtually divided in slices in the longitudinal direction and each slices is thought as composed of small volumes called voxels (or spots). Each slice is irradiated fixing the beam energy and irradiating each voxel changing the currents of the scanning magnets. Furthermore for each voxel in a slice it can be taken into account the dose given during the irradiation of the previous slices.

Therefore with active scanning there is no specific hardware for each patient but, above all, the irradiated target is shaped very closely to the tumour target both in the transverse and in the longitudinal planes. The drawback of such beam delivery system is a greater difficulty in operation due to the management of the scanning magnets and of the beam position and also an increased sensitivity of the system to current ripples and changes. To obtain the precision in the dose shaping, the tumour must be known with the same precision that characterizes the active scanning. Problems occur in the cases in which tumour moves because of breathing and heart beating. In this case the passive scanning appears to be the easier solution; anyway considering the superiority of the active method, several studies are in progress worldwide in order to develop methods that allow to use the active scanning also with moving tumours: repainting, gating, beam tracking [10]. Repainting [11] consists in treating multiple (about 10) times the target with a reduced dose: in this way, amplitude, period and initial phase of the organ motion change randomly treatment by treatment and the irradiation uncertainty is statistically reduced. Gating [12] is a technique also used in case of passive scanning. It is based on the irradiation of the tumour only during a precise percentage (about 30%) of the organ motion: in this way a cyclotron treatment increases proportionally while in a synchrotron this disadvantage is mitigated by the cycle times needed to fill the ring. Finally beam tracking [13] is an adjustment of the parameters of the treatment plan in real-time using a 4D organ monitoring signal. A purely active scanning method, i.e. without absorbers, is possible only with a synchrotron because of the need of a variable extraction energy. Indeed the energy from a cyclotron is fixed and

the active scanning is possible only after having changed the beam energy like in the passive methods with a wedge degrader (resulting in a maximum energy variation rate of about 15 MeV/sec).

All these considerations indicate that the best technological layout of a particle accelerator for hadrontherapy is a synchrotron designed for carbon ions equipped with active scanning.

## HADRONTHERAPY IN THE WORLD

The idea of hadrontherapy appeared in 1946 in a paper written by Robert Wilson [14] that proposed the medical use of protons produced by the new high energy accelerators. His idea was realized firstly when 30 patients were treated with protons at the Lawrence Berkely Laboratory (LBL) in 1954. In the next years other treatments have been performed in other research centers worldwide like Uppsala in 1957 and Harvard in 1963. Proton therapy experience followed in new facilities that became operative in Russia (Dubna in 1967, Moscow in 1969 and St. Petersburg in 1975), in Japan (Chiba in 1979, Tsukuba in 1983) and in Switzerland at the PSI center in 1985.

The world's first hospital-based dedicated proton facility started treatments in 1990 after 20 years from the feasibility study at Loma Linda. The LLUMC (Loma Linda University Medical Center) synchrotron has a diameter of 6 m with a 2 MeV injector placed on top of the ring. A beam of  $2 \cdot 10^{10}$  particles per spill is extracted in the range 70-250 MeV with a half-integer resonant extraction scheme. The center is equipped with a fixed beam room with two beam lines (for eye and for head-and-neck treatments), three rotating gantries and a research room with three beam lines. To date over 15000 patients have been treated.

Nowadays 38 hadrontherapy facilities are in operation all around the world: Europe (11 centers distributed in Italy, France, Germany, England, Switzerland, Sweden, Poland, Russia), Asia (8 centers in Japan, 2 in China, 1 in South Korea), America (11 centers in USA and 1 in Canada), South Africa (1 centre). Fig. 4 shows in detail the locations of each facility. Most centers are proton facilities using cyclotron technology with passive beam delivery system. The hadrontherapy synchrotrons are only 14: in Japan HIMAC (Chiba), PATRO (Hyogo), PMRC (Tsukuba), WERC (Fukui), Shizuoka Cancer Center (Shizuoka), GHC (Gunma), STPTC (Koriyama-City), Medipolis Medical Research Institute (Ibusuki); in China, IMP (Lanzhou); in the USA besides LLUMC, M.D. Anderson Cancer Center (Houston); in Russia ITEP (Moscow) and St. Petersburg; in Europe HIT (Heidelberg, Germany) and CNAO (Pavia, Italy).

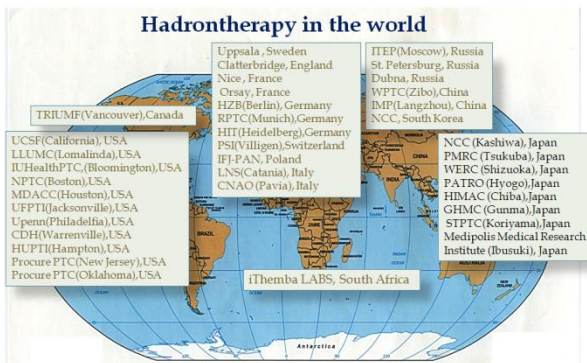


Figure 4: locations of the operative hadrontherapy facilities all around the world.

Other facilities are under construction or will start treatments in the next years in Europe, in Asia, in USA: 12 proton cyclotrons, 2 proton-carbon synchrotrons (Fudan University Shanghai CC in China, MedAustron in Austria), 2 proton synchrotrons (McLaren PTC in USA, PMHPTC in Russia, CMHPTC in Slovak Rep.), 1 carbon synchrotron (HITFIL in China).

Presently carbon ions are produced in Asia at HIMAC, GHC, PATRO and IMP, in Europe at HIT and CNAO. Among these facilities, PATRO [15], HIT [16] and CNAO [17] produce both protons and carbon ions while HIMAC, GHC and IMP are dedicated facilities using only carbon ions. A particular mention is due to HIMAC centre [18] (see Fig. 5): operating since 1994, it is producing the most important clinical results with carbon ions (more than 6600 treated patients). It is equipped with two synchrotrons at the upper and lower floors that are much larger than the others (a 42 m diameter instead of the standard 20-22 m) because they were designed to deliver 800 MeV/u Si ions for clinical experimentation.

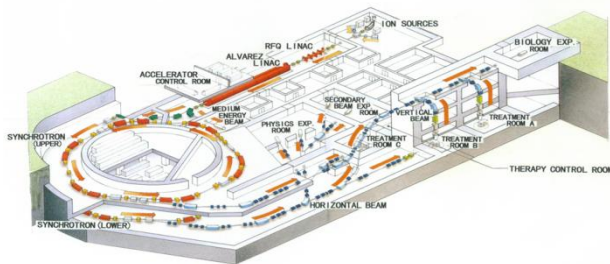


Figure 5: Himac layout.

Up to December 2011, the total number of treated patients with hadrons have been 75571, of which 7881 have been treated with carbon ions [19].

**LAYOUT OF A TYPICAL SYNCHROTRON**

This section will show in detail some aspects of a synchrotron facility able to deliver proton and carbon ions. To give some typical orders of magnitude, datas of CNAO facility, shown in Fig. 6, will be given.

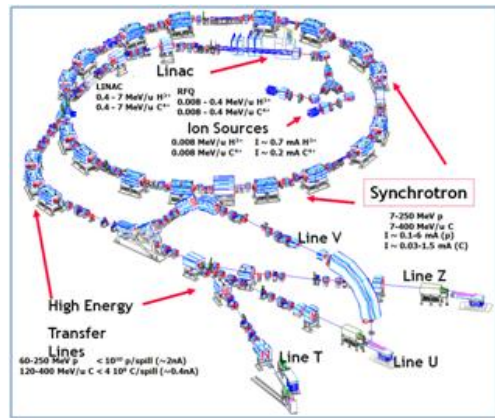


Figure 6: CNAO layout.

The scheme of such a facility is a low energy injector, a ring, several beam lines for the transfer of high energy beams in the treatment rooms. The injector can be placed outside the ring for easier maintenance, or inside the ring to save space. It is made up of two or three sources (depending on the number of species one wants to use with short switching times), a low energy transfer line (LEBT) to select and transport the ions produced by the sources, a linac and the transfer line (MEBT) to transport the preaccelerated beam to the synchrotron. Only few facilities have a PIG source or a EBIS source. PIG is based on the Penning vacuum gauges: a flux of electrons between an anode and a cathode ionizes a gas creating the beam. In the EBIS, ions are trapped inside a dense electron beam and is continuously bombarded by electrons and sequentially ionized. The most used source is the ECR one. It is based on the excitement of the electrons using radiofrequency fields at the electron cyclotron resonance frequency (10 GHz-18 GHz): the plasma electrons are confined by a magnetic trap (the so called minimum B-structure) realized by the superposition of a hexapole and axial structure. ECR source has the advantage to produce high intensity beams for a wide range of charge states.

The 14.5 GHz ECR sources [20] installed at CNAO can produce 250  $\mu\text{A}$  of  $\text{C}^{4+}$  beam with a normalized emittance of  $0.56 \pi \text{ mm mrad}$  and 1000  $\mu\text{A}$  of  $\text{H}^{3+}$  with an emittance of  $0.67 \pi \text{ mm mrad}$  with an energy of 8 keV/u. The RF, can be finely adjusted in frequency, has a power of about 8 W for protons and 180 W for carbon ions and is fed by 400 W TWTA power amplifiers.

The low energy linac is composed by an RFQ (Radio Frequency Quadrupole) and a IH (Interdigital H-type). The source current is DC but it enters in the RFQ pulsed thanks to a electrostatic chopper in the LEBT.

CNAO RFQ [21] is a four-rod type with 70 kV electrode voltage and delivers beams at 400 KeV/u; the IH [21] is a 5.3 MV/m, 3.77 m long, structure and accelerates beams up to 7 MeV/u; both tanks work at 217 MHz. MEBT contains elements to fit the transverse and longitudinal twiss parameters to the ring acceptance, in addition to stripping foils that change the charge status from the one produced by the sources. In CNAO stripping

foils allow to obtain  $C^{6+}$  and  $H^+$ ; quadrupoles match the transverse dimensions while a debuncher tank reduces the beam momentum spread.

In the needed energy range, proton magnetic rigidity varies in the range 1.16-2.31 Tm while the one of carbon ions goes from 3.18 Tm to 6.336 Tm. The use of normal conducting magnets giving at maximum 1.5 T implies that ring length is about 60-80 m (CNAO ring is 77.65 m). The acceleration is usually performed by a single cavity that must be a broadband resonator loaded with standard ferrites or with ferrite-like amorphous alloy (CNAO uses VITROVAC, a Fe-Co alloy). The use of such alloys have several advantages like reducing cavity dimensions and reducing (in some cases eliminating) the current for the cavity polarization [22]. The extraction from the ring is the most important and challenging aspect influencing ring design. Clinical requirements on dose uniformity is  $\pm 2-3\%$ : this requirement with active scanning cannot be fulfilled with a single turn extraction. A single turn extraction means a beam shorter than 1  $\mu\text{sec}$  requiring a passive system. As a consequence a slow extraction in the order of 1 s is mandatory. The slow extraction mechanism is realized by making unstable the particle betatron oscillations: the amplitude of their motion grows steadily until the particle "jumps" into the aperture of an electrostatic septum allowing the extraction. The lattice layout of the ring must be set so that the machine tune at the end of the extraction is near to an unstable value: to extract the beam, a mechanism must force the beam into the unstable region. Essentially three mechanisms are possible to make the beam passing from the stable to the unstable region. These are the amplitude selection, the amplitude-momentum selection, the RF knock out (RFKO). With the amplitude selection, used in the oldest facilities, the quadrupoles settings are changed before the extraction in order to vary the machine tune. In this case the beam that has small momentum spread and great betatron amplitude, acquires progressively the extraction tune.

The beam size, position and energy changes during the extraction because only one amplitude is extracted at a time. In the amplitude-momentum selection, the resonance region is fixed and beam moves towards the resonance. As a consequence momentum spread of the circulating beam is kept large and the extracted beam has fixed position, size and energy. At CNAO, beam is driven into the resonance by a betatron core: it is a toroidal magnet that creates a fem that accelerates the beam towards the instability.

Finally in the case of the RFKO method, the machine tune is fixed and the beam is excited by a transverse RF perturbation. Also in this case size, position and energy are stable. Furthermore with this method a rapid switch off of the dose irradiation is easy to be obtained. Fig. 7 graphically illustrates the three methods using the so called Steinbech diagram in which the resonance is represented in the phase space betatron amplitude-momentum spread.

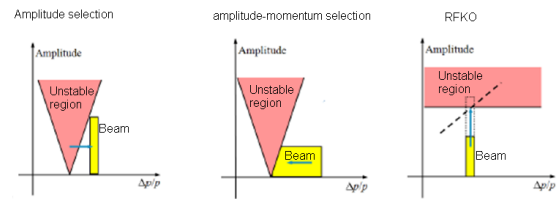


Figure 7: Steinbech diagrams of the three methods to put the beam in resonance.

At LLUMC the unstable tune was chosen to half-integer; nowadays the chosen resonance in all the facilities is obtained by a tune of  $N/3$  and a sextupolar field that feeds the instability (the so called third integer resonance). Another important aspect of the extraction is the intensity quality of the spill. Considering the 2% dose homogeneity and that the time to irradiate a voxel is about 5 msec, beam has to be managed in a time structure of about 100  $\mu\text{sec}$ : this means that the spill intensity spectrum must be controlled up to 10 kHz. This control is not easy with the amplitude selection because it requires a challenging control on the quadrupole ripple; on the contrary by the momentum selection and the RFKO technique spill structure can be well controlled. At CNAO spill ripple is greatly reduced by the use of the empty bucket technique, simply exploiting the RF cavity used for the acceleration; furthermore some improvements can be obtained by a rapid air core quadrupole in feedback on the spill intensity. Finally also the extraction lines are technologically challenging. First the number of lines must be high with rapid switching among the lines in order to maximize the number of patients. Second the beam quality needed at all the energies (stable position, possibility to have round beams with varying dimensions and so on) puts constraints on magnetic lattices and requires precise specifications on power supplies, magnets, control system, beam diagnostics controlling in real time the dose delivered to the patient (the so called nozzle), patient positioning. In particular the extraction lines must be equipped with a system able to guarantee a rapid switch off of the extracted beam (order of 100  $\mu\text{sec}$  considering the requirement on dose uniformity). Indeed a rapid switch off is not possible with a betatron core that is a highly inductive element and then slow; also in the case of the RFKO the time of a switch off is in the order of 1 msec. At CNAO this is obtained by four fast chopper magnets (100  $\mu\text{sec}$ ) (see Fig. 8) installed along the extraction line that create a bump on the beam orbit: if the bump is not performed beam orbit ends on a dump.

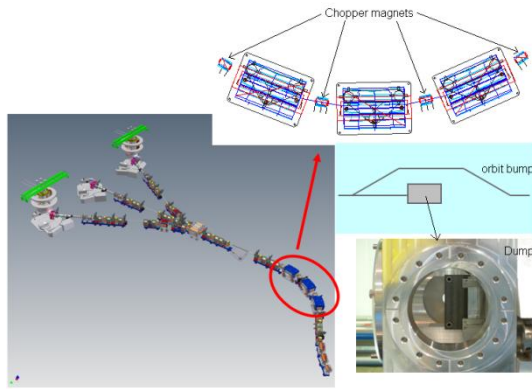


Figure 8: CNAO safety system for a fast beam switch off.

To improve the quality of the treatment, irradiation from different directions is mandatory. This is achieved either displacing the patient, or using several lines in the same room (e.g. horizontal and vertical) or installing rotating beam lines, the so called gantries. Nowadays gantries for protons are present in most facilities; on the contrary a gantry for carbon ions must have a higher weight and size: up to now only the Heidelberg facility is equipped with a carbon ions gantry (weight of 600 tons, diameter of 13 m against the standard dimensions for protons of 100 tons and 10 m) that is under commissioning [23].

## HADRONTHERAPY BUSINESS

Since the construction of the first hospital-based facility most technologic guidelines for the realization of a hadrontherapy centre have been delineated. This allowed some companies to produce projects for the commercialization of ion beam therapy centres with largely standard components. The main companies are IBA, Hitachi, Mitsubishi, Sumitomo, Varian, Still River. Considering the number of built facilities, IBA is the world's most important company. Its centres are based on a 230 MeV normal conducting cyclotron for protons with horizontal beam lines and rotating gantries with passive scanning. Varian, that bought ACCEL in 2007, builds facilities delivering protons in the range 70-250 MeV with an isochronous superconducting cyclotron to 6 treatment rooms. Hitachi has sold 70-250 MeV proton synchrotrons with performances that are similar to the LLUMC. Also Optivus company, that has followed maintenance and improvements of LLUMC, is marketing a proton system very similar to LLUMC.

Still River Systems is offering a miniaturized 250 MeV proton superconducting synchrocyclotron mounted directly on the gantry within the treatment room: installation of the first facility is underway in USA.

Sumitomo has commercialized a 230 MeV proton cyclotron with up to 5 rooms. It is also marketing carbon ions synchrotrons able to deliver  $C^{6+}$  and  $C^{4+}$  to three treatment rooms; even if it has installed injectors to PATRO and GHMC it has not yet sold a complete carbon synchrotron facility.

Mitsubishi markets a 70-250 MeV proton synchrotron for up to 6 treatment rooms; it also has sold two synchrotrons for both 70-250 MeV proton and 70-380 MeV/u carbon ions. The other commercial centre for both protons and carbons has been produced by Siemens. However in Summer 2011 Siemens announced its loss of commercial interest in the hadrontherapy field: as a consequence the nearly finished centre in Kiel will be dismantled selling components to other therapy centres, while the just finished Marburg centre will continue only research activities for about two years before its probable dismantling.

Even if there are a lot of firms, the hadrontherapy field is not limited to firms; the field is still technologically challenging then research centres still contribute to the design and the construction of facilities: e.g. CNAO, that started treatments in September 2011, was born from the PIMMS [24] performed at CERN and built by the help of a strong net of international collaborations with research centres: INFN (Italy), CERN, GSI (Germany), LPSC (France), NIRS (Japan), italian universities (Milan, Pavia, Turin).

Apart the R&D on technological aspects of the actual hadrontherapy facility layouts, lots of ideas are under developments to improve the performance of hadrontherapy centers, mainly in tumour tracking and tumour imaging sectors but also in accelerator technology field (like FFAG, LIBO, DWA and Laser acceleration). FFAG [25] design foresees fixed-field combined-function bending magnets: a strong radial magnetic field gradient in the dipole component allows to keep the beam in a narrow ring like in a synchrotron but without ramping the magnets so having a DC beam with the possibility of fast energy changes.

LIBO (Linac Booster) [26] foresees a proton linac (1.5 m with 27 MV/m) booster from 30 to 250 MeV so it can be used in association with the standard cyclotron for radioisotopes; the application of this idea for carbon is under study.

DWA (dielectric wall-induction linac) [27] idea is based on the use of new dielectrics able to sustain greater voltage gradient (100 MV/m) in order to reach an acceleration of 250 MeV with a 3 m linac.

Finally the acceleration with high power lasers [28] is under study in order to meet the several clinical requirements.

## CONCLUSIONS

Since the birth of the idea, hadrontherapy field has developed a lot with a rapid growth in the last years in terms of treatments and operative facilities all around the world. The centers have passed from the status of research centres to the one of hospital dedicated facilities with firms that commercialize facility models. Carbon facilities are greater and more expensive than proton facilities but the clinical advantages of carbon with respect to protons push to the building of new synchrotrons able to deliver both species. Also R&D

remains an important aspect of this field both in the improvement of the present designs and in the search for new accelerator machine layouts.

[28] P. R. Bolton et al., *Toward laser-driven proton therapy of cancer at PMRC in Japan*, Erice (2010).

## ACKNOWLEDGEMENTS

A special acknowledgement is due to Marco Pullia, Erminia Bressi, Sandro Rossi and Caterina Biscari for the help in finding precious references and for useful discussions.

## REFERENCES

- [1] R. E. Zirkle, *Radiation Biology*, 1, 315-350 (1954).
- [2] International Commission On Radiation Units And Measurements, *The quality factor in radiation protection*, ICRU Report 40 (1986).
- [3] L. H. Gray, *Am. J. Roentgenol.*, 85, 803-815 (1961).
- [4] H. Eickhoff, U. Linz, *Reviews of Accelerator Science and Technology*, 1, 143-161 (2008).
- [5] Y. Jongen, "Design of a K=1600 SC cyclotron for Carbon therapy", *ECPM*, Nice (2006).
- [6] T. Kanai et al., *Med. Phys.*, 7, 365-369 (1980).
- [7] E. Pedroni et al., *Med. Phys.*, 22, 27-53 (1995).
- [8] Th. Haberer et al., *Nucl. Instrum. Methods Phys. Res. A* 330, 296-305 (1993).
- [9] M. Donetti et al., *Dose Delivery at CNAO, PTCOG51*, Seoul (2012).
- [10] N. Saito et al., *Phys. Med. Biol.*, 54(16), 4849 (2009).
- [11] M. H. Phillips et al., *Phys. Med. Biol.* 37, 223-233 (1992).
- [12] H.D. Kubo et al., *Phys. Med. Biol.* 41, 83-91 (1996).
- [13] S.O. Grozinger et al., *Radiat. Oncol.* 3, 34 (2005).
- [14] R. Wilson, *Radiological use of fast protons*, *Radiology* 47,487-491, (1946).
- [15] <http://www.hibmc.shingu.hyogo.jp>.
- [16] Th. Haberer et al., *The Heidelberg Ion Therapy centre, Radiotherapy and Oncology*, Vol. 73, pp. S186-S190, (2004).
- [17] S. Rossi, *Eur. Phys. J. Plus*, (2011) 126:78.
- [18] Y. Hirao et al., *Nucl. Phys.*, A538, 541c, (1992).
- [19] <http://ptcog.web.psi.ch/ptcentres.html>.
- [20] G. Ciavola et al., *Commissioning of the ECR ion sources at CNAO facility, EPAC08*, Genova (2008).
- [21] B. Schlitt et al., *Linac Commissioning at the Italian hadrontherapy centre CNAO IPAC10*, Kyoto (2010).
- [22] L. Falbo et al., *CNAO RF cavity: hardware description, IPAC11*, San Sebastian (2011).
- [23] M. Galonska et al., *Commissioning of carbon beam gantry at HIT accelerator, WAO10*, Daejeon (2010).
- [24] S. Rossi et al., *Proton-Ion Medical Machine Study (PIMMS)*, Part I and II, CERN/PS 1999-010 DI and CERN/PS 2000-007 DR, Geneva (2000).
- [25] M. K. Craddock et al., *FFAG accelerators*, Erice (2009).
- [26] U. Amaldi et al., *Fast-cycling accelerators for hadrontherapy*, *Nucl. Instrum. Methods A* 521,512 (2004).
- [27] G. J. Caporaso, *High Gradients induction Linacs for hadrontherapy*, Erice (2009).

## FOCUSING OF INTENSE HEAVY ION BEAMS WITH PLASMA LENSES

O. Meusel, M. Droba, U. Ratzinger, K. Schulte [IAP, Frankfurt am Main, Germany]

### *Abstract*

Gabor lenses are a special type of plasma lens using a stable confined electron cloud for beam focusing. The electrons provide space charge neutralization of the beam traveling through the lens volume. At the same time a radial symmetric electrostatic self field focuses the beam mass independently. It is possible to control the density and distribution of the confined electrons providing variable focusing strength and moderate emittance growth of the beam. The knowledge of the behavior of the electron column inside this lens type is essential to understand the impact on beam transport. Therefore several diagnostic tools were developed to measure the electron cloud properties with and without ion beam propagation through Gabor lenses. Based on experimental results a new Gabor plasma lens has been designed for focusing heavy ion beams. A comparison of this lens type and a superconducting solenoid is planned at the low energy transport section of the GSI - High Current Test Injector (HOSTI).

**CONTRIBUTION NOT  
RECEIVED**

# **ELECTRON BEAM ION SOURCES, TRAPS, AND STRINGS: VERSATILE DEVICES TO MEET THE HIGH CHARGE STATE ION NEEDS OF MODERN FACILITIES**

E.N. Beebe, J.G. Alessi, A.I. Pikin [BNL, Upton, Long Island, New York, USA]

## *Abstract*

Electron beam ion sources (EBIS) and its variants such as the electron beam ion trap (EBIT) and electron string ion source (ESIS) have been selected to provide highly charged ions for several atomic and nuclear physics facilities. Since the capture and breeding can be short and highly efficient, EBIST devices are increasingly being chosen for trapping and/or reacceleration of radioactive beams. The sources can range from petite to grand, using electron beams from  $\sim 1\text{mA}$  to 10A or more. They often serve accelerators and beam lines in large laboratories but they can be self contained laboratories where experiments are made in situ. We will discuss the basic principles as well as applications of these sources at various facilities around the world. Some emphasis will be placed on the recently commissioned RHIC EBIS source which is now providing beams for both high energy physics at the relativistic heavy ion collider as well as the NASA space radiation laboratory at BNL.

**CONTRIBUTION NOT  
RECEIVED**

## COMMISSIONING OF CARIBU EBIS CHARGE BREEDER SUB-SYSTEMS\*

S. Kondrashev<sup>#</sup>, C. Dickerson, A. Levand, P.N. Ostroumov, R. Vondrasek  
ANL, Argonne, IL 60439, USA  
A. Pikin, BNL, Upton, NY 11973, USA  
G.I. Kuznetsov, M.A. Batazova, BINP, Novosibirsk, 630090, Russia

### Abstract

A high-efficiency charge breeder based on an Electron Beam Ion Source (EBIS) to increase the intensity and improve the purity of accelerated neutron-rich radioactive ion beams is being developed by the ANL Physics Division. The design of the CARIBU EBIS charge breeder is complete and manufacturing of the components and sub-systems is in progress. Two key elements of the breeder - a 6-Tesla superconducting solenoid and a high-perveance electron gun were recently delivered and successfully commissioned. The current status of the ANL EBIS development and commissioning results of different EBIS sub-systems will be presented.

### INTRODUCTION

The Californium Rare Isotope Breeder Upgrade (CARIBU) for the Argonne National Laboratory Argonne Tandem Linac Accelerator System (ATLAS) has been recently commissioned. In its full capacity, the CARIBU facility will use fission fragments from a 1 Curie (Ci)  $^{252}\text{Cf}$  source [1]. The ions are thermalized and collected into a low-energy ion beam by a helium gas catcher, mass selected by an isobar separator, and charge bred to higher charge states for acceleration in ATLAS. To reach energies  $E/A \sim 10$  MeV/u, one should inject ions with a charge-to-mass ratio ( $q/A$ )  $\geq 1/7$  into the ATLAS. In the first stage, the existing Electron Cyclotron Resonance (ECR) ion source is used as a charge breeder [2]. The maximum intensity of radioactive ion beams at the output of the gas catcher for a 1 Curie  $^{252}\text{Cf}$  source will not exceed  $10^7$  ions per second. A charge breeder (CB) based on an Electron Beam Ion Source (EBIS) has significant advantages over the ECR option for ion beam intensities up to about  $10^9$  ions per second, providing higher efficiency, shorter breeding times and significantly better purity of highly charged radioactive ion beams for further acceleration. The EBIS CB project for CARIBU is heavily utilizing state-of-the-art EBIS technology recently developed at Brookhaven National Laboratory [3]. However, the parameters of the electron gun, potential distribution in the ion trap region, electron collector and injection/extraction lines are substantially modified to obtain the highest acceptance and breeding efficiency of low intensity rare isotope beams which is expected to be higher than 20%. Special attention was paid to the vacuum system because the vacuum inside the EBIS trap will define the purity of charge-bred radioactive ion beams.

\*This work was supported by the U.S. Department of Energy, Office of Nuclear Physics, under Contract No. DE-AC02-06CH11357.

<sup>#</sup>kondrashev@anl.gov

### DESIGN OF CARIBU EBIS CHARGE BREEDER

In this section the main features of the CARIBU EBIS design will be highlighted. The main parameters of the CARIBU EBIS CB are presented in Table 1.

Table 1: Main parameters of CARIBU EBIS CB

| Parameter                                 | Low current e-gun            | High current e-gun           |
|---|------------------------------|------------------------------|
| Superconducting solenoid: length/field    | 1 m/6 T                      | 1 m/6 T                      |
| Diameter of IrCe thermionic cathode       | 1.6 mm                       | 4 mm                         |
| Electron beam current                     | 0.2 A                        | 2 A                          |
| Electron beam energy                      | $\sim 2$ keV                 | $\sim 5$ keV                 |
| Electron beam diameter in the trap        | $\sim 230$ $\mu\text{m}$     | $\sim 580$ $\mu\text{m}$     |
| Electron beam current density in the trap | $\sim 480$ A/cm <sup>2</sup> | $\sim 750$ A/cm <sup>2</sup> |
| Ion trap length                           | 0.5 m                        | 0.5 m                        |
| Trap capacity (in elementary charges)     | $\sim 4 \cdot 10^{10}$       | $\sim 2 \cdot 10^{11}$       |

Two e-guns were developed and built for the breeder: a high-current (2 A) and a low-current (0.2 A) e-gun. The low-current e-gun will be used to study the possibility of higher breeding efficiency for shell closures with lower electron beam energies.

Prior to installation into the CARIBU-ATLAS beam line, the breeder will be commissioned off-line and breeding efficiency will be optimized by injecting a pulsed ion beam generated by a surface ionization  $\text{Cs}^+$  ion source. Setup for off-line commissioning of the breeder is presented in Fig. 1.

Scintillator-based pepper-pot emittance meters [7] developed at ANL and Faraday cups will be installed at several locations along the injection and extraction lines to measure emittance and current of injected and extracted ion beams.

Eleven drift tubes are used to transport the electron beam from the EBIS e-gun to the collector entrance. All drift tubes have longitudinal slots to facilitate pumping of the ion trap volume (Figures 2 and 3).

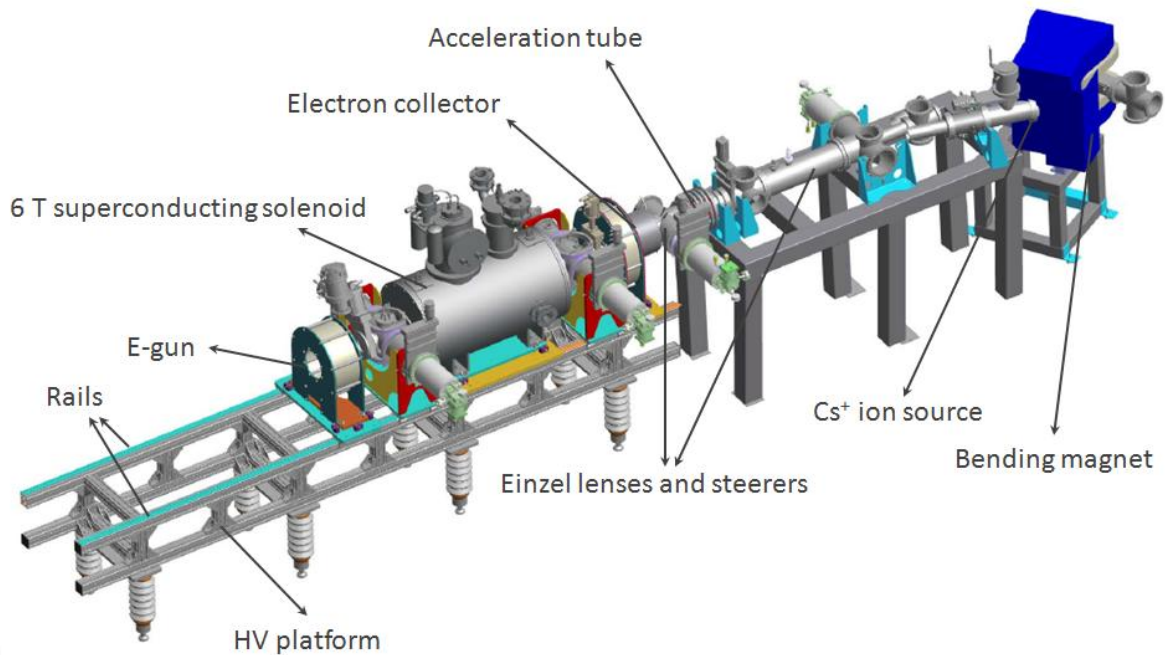


Figure 1: Setup for off-line commissioning of CARIBU EBIS charge breeder.

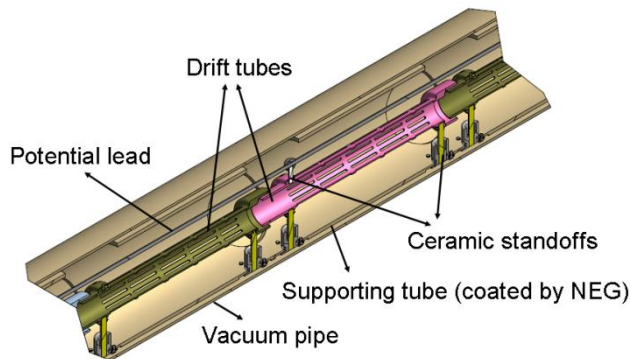


Figure 2: 3D model of drift tube structure.



Figure 3: Photograph of drift tube.

The internal surface of the surrounding (supporting) tube will be coated with non-evaporable getter (NEG) to provide high pumping speed in the trap region.

More details on parameters and design of the CARIBU EBIS CB can be found elsewhere [4, 5, and 6].

### COMMISSIONING OF 6 T SUPERCONDUCTING SOLENOID

An unshielded 6-Tesla superconducting solenoid with a warm bore diameter of 155 mm and a length of 1 m, from Cryomagnetics, Inc., was delivered in October 2011. The photograph of the solenoid installed in the final position on the high voltage (HV) platform for on-site commissioning is presented in Figure 4.



Figure 4: Photograph of 6 T solenoid installed at HV platform.

The warm bore of the solenoid is equipped with x and y translators. In the first step the mechanical axis of warm

bore was aligned with magnetic axis of the solenoid using these translators in real magnetic environment.

The main specified and measured parameters of the solenoid are presented in Table 2.

Table 2: Parameters of the solenoid

| Parameter          | Specification               | Measurements                |
|--------------------|-----------------------------|-----------------------------|
| Central Field      | 6.0 T                       | 6.05 T @ 82.66 A            |
| Maximum Field      | 6.6 T                       | 6.6 T @ 90.17 A             |
| Charge Time to 6 T | 70 min                      | 70 min                      |
| Field Homogeneity  | ± 0.4% over ± 30 cm on axis | ± 0.2% over ± 30 cm on axis |
| Coil Inductance    | 195 H                       | 193 H                       |
| Field Decay Rate   | < 1 ppm/hour                | < 0.01 ppm/hour             |

The simulated and measured axial magnetic field profiles along the solenoid axis are shown in Figure 5 (a, b). A zoomed profile (Figure 5 (b)) shows the flatness of the central field.

As one can see from Table 2 and Figure 5 (a, b) all specified parameters were met. The measured magnetic field homogeneity and field decay rate exceeded the design requirements.

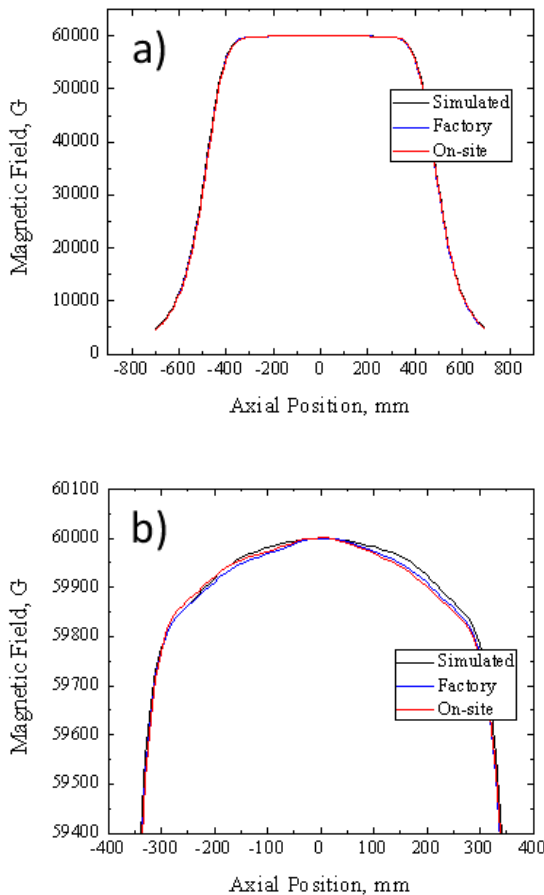


Figure 5 (a, b): Axial magnetic field profiles (Figure 5 (b) is zoomed from Figure (a)).

## COMMISSIONING OF E-GUN

High-current (2 A) and low-current (0.2 A) e-guns have been ordered from BINP (Novosibirsk, Russia) and were delivered in April 2012. The main specified parameters of both e-guns are summarized in Table 3.

Table 3: Main specified parameters of 2 A and 0.2 A e-guns.

| Parameter                             | CARIBU (high current)   | CARIBU (low current)    |
|---------------------------------------|-------------------------|-------------------------|
| Current                               | Up to 2 A               | Up to 0.2 A             |
| Current density at the cathode        | 10–15 A/cm <sup>2</sup> | 10–15 A/cm <sup>2</sup> |
| Magnetic field at the cathode surface | ~ 0.15 T                | ~ 0.15 T                |
| Cathode material                      | IrCe                    | IrCe                    |
| Cathode diameter                      | 4 mm                    | 1.6 mm                  |
| Radius of cathode convex surface      | 6.6 mm                  | 1.8 mm                  |
| Expected cathode lifetime             | ~ 20000 hours           | ~ 20000 hours           |

As mentioned above, a 2 A e-gun is the main option for the new CARIBU EBIS charge breeder and the 0.2 A e-gun will be used to study the possibility of higher breeding efficiency for shell closures with lower electron beam energies.

The engineering model of the e-gun is presented in Fig. 6.

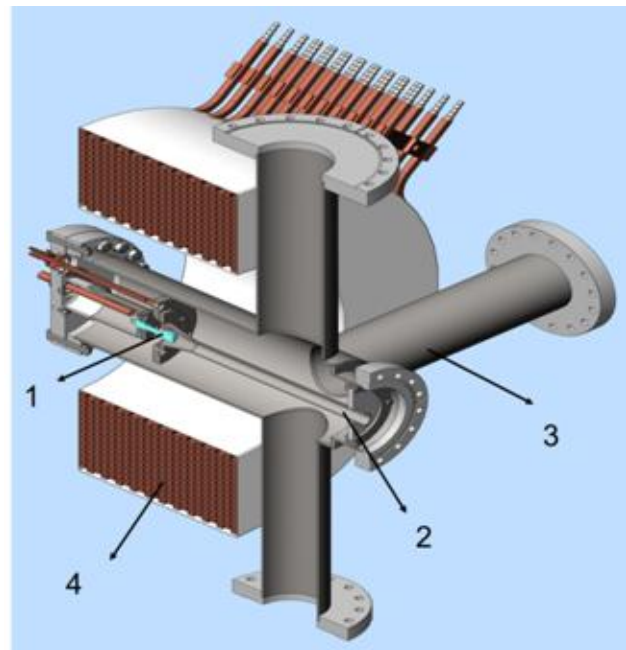


Figure 6: Engineering model of the e-gun (1 – IrCe thermionic cathode, 2 – anode, 3 – vacuum chamber, 4 – magnetic coil).

Both are semi-immersed type e-guns with pure magnetic compression [8]. IrCe thermionic cathodes are used because of their long demonstrated live times [9].

2 A and 0.2 A e-guns are switchable by exchanging the thermionic cathode units only. Pumping of the e-gun vacuum chamber will be provided by turbo and NEG cartridge pumps with total pumping speed for nitrogen of about 1000 l/s.

The photograph of 4 mm IrCe thermionic cathode units mounted for heating tests is presented in Fig. 7.



Figure 7: Photograph of 4 mm IrCe thermionic cathode units mounted for heating tests.

The current-voltage heating curve and the dependence of surface brightness temperature on heating power for 4 mm IrCe thermionic cathode units are reported in Figures 8 and 9.

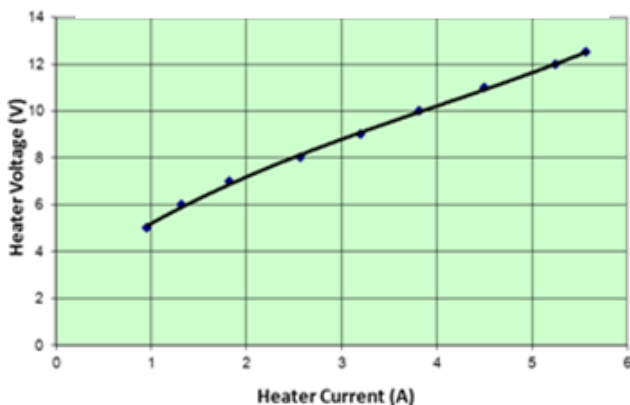


Figure 8: Current-voltage heating curve for 4 mm IrCe thermionic cathode units.

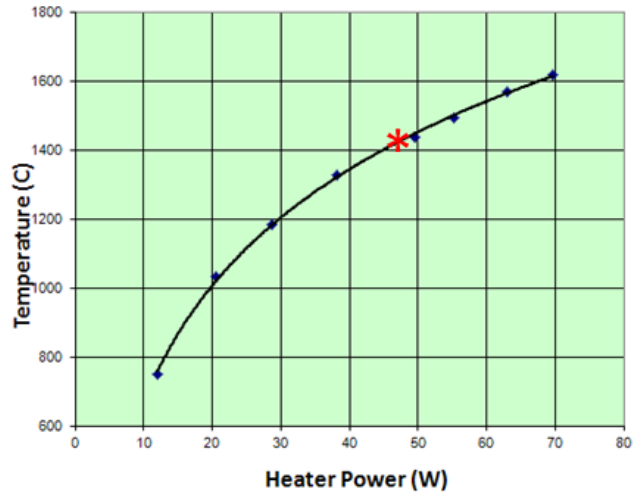


Figure 9: Dependence of surface brightness temperature on heating power for 4 mm IrCe thermionic cathode units.

The red star in Figure 8 indicates CARIBU EBIS charge breeder operational point.

Photograph of the e-gun assembly during factory commissioning is presented in Figure 10.



Figure 10: Photograph of e-gun assembly during factory commissioning.

A pulsed negative voltage with a duration of about 10  $\mu$ s was applied between e-gun cathode and grounded anode. Electron beam current was measured by current transformer. Pulse shapes of the applied voltage and electron beam current are presented in Figure 11.

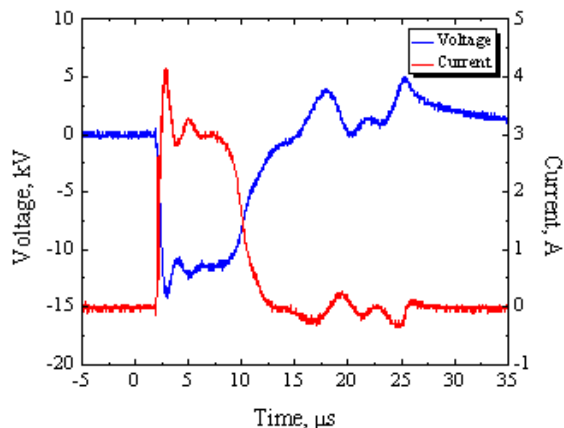


Figure 11: Pulse shapes of applied voltage and electron beam current.

The dependences of electron beam current on applied cathode-anode voltage are reported in Figure 12 for different cathode heating power.

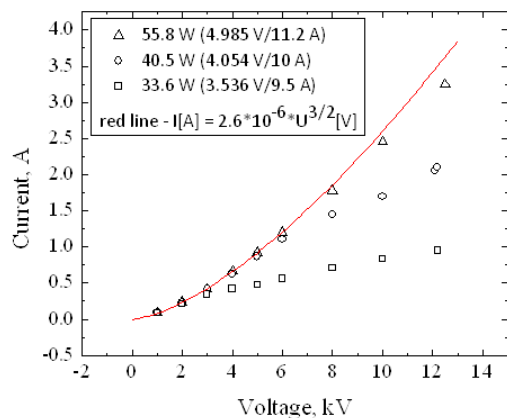


Figure 12: Dependences of electron beam current on applied cathode-anode voltage for different cathode heating power.

As one can see, electron beam current exceeds 3 A for cathode-anode voltage of 12 kV. The perveance of the e-gun was found to be equal to  $2.6 \cdot 10^{-6} \text{ A/V}^{3/2}$ . Experimental data was in good agreement with results of e-gun simulations using SAM code [10].

### SUMMARY

The EBIS charge breeder is an excellent choice for acceleration of CARIBU radioactive ion beams by ATLAS and should provide high efficiency, short breeding times and superior purity of accelerated beams. Design of the CARIBU EBIS charge breeder has been completed. Manufacturing and procurement of different components and sub-systems are currently in progress.

A 6 T superconducting solenoid and a high-perveance e-gun have been recently commissioned and met all specified parameters.

### ACKNOWLEDGMENT

The authors are grateful to S.W.T. MacDonald, D.R. Phillips and A.E. Germain for help with 6 T solenoid cool down.

### REFERENCES

- [1] R. Pardo et al., Nucl. Instr. Meth. B, 261(2007) 965.
- [2] R. Vondrasek et al., Rev. Sci. Instrum., 81 (2010) 02A907.
- [3] A. Pikin et al., JINST, 5 (2010) C09003.
- [4] S. Kondrashev et al., Rev. Sci. Instrum., 83 (2012) 02A902.
- [5] P.N. Ostroumov et al., JINST, 5 (2010) C07004.
- [6] P.N. Ostroumov et al., "Efficiency and Intensity Upgrade of the ATLAS Facility", LINAC'10, Tsukuba, September 2010, MOP045; <http://www.JACoW.org>.
- [7] S. Kondrashev et al., "Emittance Measurements for Stable and Radioactive Ion Beams", LINAC'10, Tsukuba, September 2010, TUP086; <http://www.JACoW.org>
- [8] G.I. Kuznetsov et al., "Formation and Collection of Electron Beams for EBIS", Proceedings of 8-th International Symposium EBIS/T 2000, Upton, New York, November 2000, p. 143.
- [9] G. I. Kuznetsov, Nucl. Inst. Meth. A, 340 (1994), 204.
- [10] B. Fomel et al., "SAM – an interactive code for evaluation of electron guns", Preprint Budker INP96-11, Novosibirsk, 1996.

## DREEBIT EBIS/T FOR APPLICATIONS IN ACCELERATOR PHYSICS

M. Schmidt\*, A. Thorn, DREEBIT GmbH, Dresden, Germany  
G. Zschornack, Technische Universität Dresden, Dresden, Germany

### Abstract

Electron Beam Ion Sources and Traps (EBIS/T) provide light up to heavy ions of low up to high charge states for various applications in accelerator physics such as medical particle therapy and charge breeding. Beside the well-known but quiet costly superconducting EBIS/T type systems compact and permanent magnet-operated EBIS/T from the DREEBIT GmbH are available, favorable for low-budget projects. Moreover, the "flagship" of the DREEBIT ion source family, the superconducting EBIS-SC features operating parameters comparable to the complex and expensive systems in the EBIS/T community.

### HIGHLY CHARGED IONS

#### Properties

Highly charged ions yield interesting properties, in particular for accelerator physics. They feature a very efficient acceleration potential since the kinetic energy gain increases linearly with the charge state for electrostatic accelerator and even quadratically with the charge state for circular accelerators. Furthermore, the potential energy of highly charged ions leads to high power deposition into surfaces connected with higher secondary particle emission at ion solid interactions.

#### Production

However, the production of highly charged ions (HCIs) has led to different technological approaches, such as ion stripping in ion accelerator structures, ECR ion sources, laser ion sources and Electron Beam Ion Sources/Traps (EBIS/T). Beside the mentioned technologies EBIS/T systems have proved as reliable and stable working sources of HCIs of the highest charge states.

### EBIS/T

EBIS/T ionize initially neutrals and low charged ions in magnetically compressed high-dense electron beams up to high and very high charge states. Already small amounts of bare uranium ions have been produced.

Normally, such EBIS/T facilities feature special, sophisticated and complex laboratory installations of the superconducting ion source type.

There are only two suppliers in the world offering commercial EBIS/T systems. One of them is the DREEBIT GmbH Dresden (Germany) marketing a whole family of EBIS/T systems.

The room-temperature Dresden EBIS/T with permanent magnets feature operating parameters which suit most of the user requirements at by far lower initial as well as maintenance costs (see Fig. 1). In addition, in order to satisfy the need for increased ion output, a liquid helium free superconducting EBIS (Dresden EBIS-SC) with closed-cycle refrigerator technology is available complementing the ion source portfolio of the company (see Fig. 2).

### USER-SPECIFIC ION IRRADIATION FACILITY

Based on its ion source knowledge the DREEBIT GmbH has designed and commissioned several customer-specific ion irradiation facilities equipped with Dresden EBIS/T systems (see Fig. 3). The facilities are complemented with the necessary ion optics and ion diagnostics such as Einzel lenses, deflectors, quadrupol beam bender, accel/decel lens systems, Wien filter, Pepper-Pot-Emittance Meter, Retarding-Field Analyzer, Faraday cups. Individual target chamber and target transfer systems. In dependence on the user need different configurations of ion sources and beamline equipment as mentioned above have been accomplished.



Figure 1: Room-Temperature EBIS/T.

### APPLICATIONS

EBIS/T systems have been successfully operated in low energy beamlines so far. In order to extend the application potential investigations on charge breeding as well as in medical particle therapy have been done.

\* mike.schmidt@dreebit.com



Figure 2: EBIS-SC.

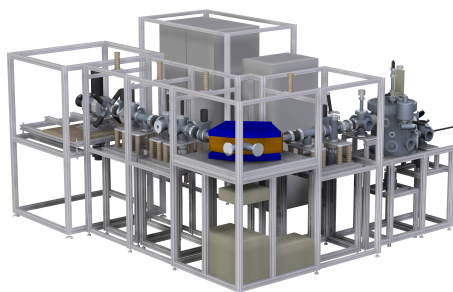


Figure 3: Ion Irradiation Facility L.

### Charge Breeding

Charge breeding via external injection in EBIS/T complements the portfolio of available elements for the production of highly charged ions. In particular the production of short-living radioactive isotopes and their efficient post-acceleration as well as the exact mass determination of them makes efficient charge breeding necessary. [1]. Thereby the species of interest is produced outside the ion source and subsequently injected into the EBIS/T, e.g. as an beam of low charged ions. In the EBIS/T charge breeding converts the low charged ions to highly charged ions. Proving the charge breeding ability and efficiency experiments with gold have been done with a Dresden EBIS-A [2]. A liquid metal alloy ion source was used for producing low charged gold ions extracting them and subsequently injecting them into the EBIS-A for charge-breeding and re-extraction after ionizing (see Fig. 4).

### Medical Particle Therapy

Cancer is the second most common cause of death in the industrial nations. Hence every 3rd person will confront some kind of cancer in its life. About 45 percent of cancer patients can be treated, mainly by surgery and radiation therapy, respectively [3]. Thereby hadron therapy with protons and carbon ions is the second most successful technique in cancer treatment, outmatched only by surgery. Up to now about 71000 patients were treated by particle therapy at 32 particle therapy centers (Europe, USA, Japan,

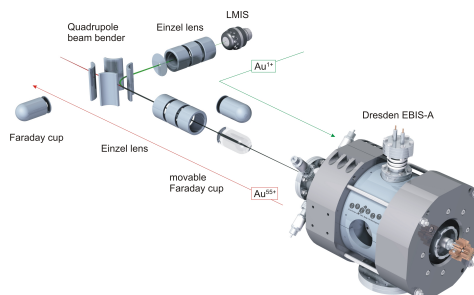


Figure 4: Charge breeding setup with an EBIS-A.

China, South Africa). The trend is increasing.

In contrast to other radiation therapies the ion therapy features a high biological efficiency causing lethal damage in the tumor cells and leaving the healthy tissue intact (BRAGG interaction).

Compared to currently used ion sources (primarily ECR ion sources) in medical particle therapy facilities EBIS/T systems feature significantly better beam quality (emittance). Furthermore the beam purity, a stringent requirement for patient irradiation is much higher since plasma ion sources like ECR work at operating pressures in the order of  $10^6$  mbar (mixing of C, N and O in the plasma) but EBIS/T usually with  $10^{-8}$  mbar and better.

In addition, EBIS/T suit the pulse mode operation regime required by accelerator facilities such as synchrotrons and cyclotrons since they are normally operating in pulsed mode anyway.

Preliminary proof-of-concept experiments with Siemens Medical have been accomplished. As a next step experiments with a Dresden EBIS-SC at the Heidelberg Hadron Therapy Facility HIT are scheduled for 2013.

### ACKNOWLEDGMENT

Work supported by the European Regional Development Fund (ERDF) and the Freistaat Sachsen (project no.100074113 and 100074115) and the German Federal Ministry of Economics and Technology based on a decision of the German Federal Parliament (Central Innovation Program SEM, project no. KF2558701AB0)

### REFERENCES

- [1] A. Thorn, "Ladungsbrüten mit Raumtemperatur - Elektronenstrahlionenquellen" Diss., Dresden, April 2012
- [2] A. Thorn et al, "Liquid Metal Alloy Ion Source based metal ion injection into a Room-Temperature Electron Beam Ion Source" Rev.Sci.Instrum., 83(2):02 A511, February 2012
- [3] S. Peggs, PAC07, June 25'07

## **ELECTRON AND ION BEAM DYNAMICS IN THE CARIBU EBIS CHARGE BREEDER**

C. Dickerson, S.A. Kondrashev, B. Mustapha, P.N. Ostroumov [ANL, Argonne, USA]  
A.I. Pikin [BNL, Upton, Long Island, New York, USA]

### *Abstract*

An Electron Beam Ion Source (EBIS) is being built to charge breed ion beams from the Californium Rare Isotope Breeder Upgrade (CARIBU) for acceleration in the Argonne Tandem Linear Accelerator System (ATLAS) at Argonne National Laboratory (ANL). The overall efficiency of the source and charge breeder system is important since CARIBU will produce many low intensity radioactive ion species. Simulations of the electron and ion beam dynamics have been used to determine the system's expected performance. The details of these simulations and results will be presented.

**CONTRIBUTION NOT  
RECEIVED**

## ECRIS LATEST DEVELOPMENTS

L. Celona, G. Castro, S. Gammino, D. Mascali [INFN/LNS, Catania, Italy]  
G. Ciavola [CNAO Foundation, Milan, Italy]

### *Abstract*

The production of intense beams of highly charged ions (HCI) is one of the most relevant challenge for the future accelerator facilities. Electron Cyclotron Resonance Ion Sources (ECRIS) are nowadays the most powerful devices able to feed accelerators with HCI in a reliable and efficient way. The reliability of frontier solutions for magnets and the increased costs for microwave generators make scaling to larger frequency not viable. Any further improvement of ECRIS output currents and average charge state requires a deep understanding of electron and ion dynamics in the plasma. In the past 20 years different teams have been working in the forefront of ion source developments with both experimental and theoretical activities, proposing different solutions to improve the production rate. The paper will discuss the most recent technological developments in the field, worldwide, together with the modeling issues of non-classical evidences like sensitivity of Electron Energy Distribution Function to the magnetic field detuning, influence of plasma turbulences on electron heating and ion confinement, coupling between electron and ion dynamics and relative impact on the formed ion beam.

**CONTRIBUTION NOT  
RECEIVED**

## PRODUCTION 72 MHZ $\beta=0.077$ SUPERCONDUCTING QUARTER-WAVE CAVITIES FOR ATLAS

M.P. Kelly, Z.A. Conway, S.M. Gerbick, M. Kedzie, R.C. Murphy, B. Mustapha, P.N. Ostroumov, T. Reid [ANL]

### *Abstract*

A total of eight 72 MHz  $\beta=0.077$  superconducting quarter-wave cavities have recently been completed at Argonne National Laboratory. Seven of these will be installed into the ATLAS superconducting heavy-ion linac as part of a beam intensity upgrade, with one remaining for the purposes of continuing to push the performance limits in these structures. Cavities were fabricated using techniques adapted from the worldwide effort to push niobium cavities close to their material limits. Key developments include the use of electropolishing on the complete helium-jacketed cavity. Wire EDM has been used instead of traditional niobium machining in order to minimize performance-limiting defects near the weld seams. Hydrogen degassing at 600°C after electropolishing has also been performed. Initial test results show practical acceleration at 4 Kelvin with cavity voltages,  $V_{acc} > 3$  MV/cavity and at 2 Kelvin with  $B_{peak} > 120$  mT and  $V_{acc} > 5$  MV/cavity.

**CONTRIBUTION NOT  
RECEIVED**

# STATUS OF THE HIE-ISOLDE PROJECT AT CERN

M.A. Fraser, Y. Kadi, A.P. Bernardes, Y. Blumenfeld, E. Bravin, S. Calatroni, R. Catherall, B. Goddard, D. Parchet, E. Siesling, W. Venturini Delsolaro, G. Vandoni, D. Voulot, L.R. Williams

CERN, Geneva, Switzerland

## Abstract

The HIE-ISOLDE project represents a major upgrade of the ISOLDE nuclear facility with a mandate to significantly improve the quality and increase the intensity and energy of radioactive nuclear beams produced at CERN. The project will expand the experimental nuclear physics programme at ISOLDE by focusing on an upgrade of the existing Radioactive ion beam EXperiment (REX) linac with a 40 MV superconducting linac comprising thirty-two niobium-on-copper sputter-coated quarter-wave resonators housed in six cryomodules. The new linac will raise the energy of post-accelerated beams from 3 MeV/u to over 10 MeV/u. The upgrade will be staged to first deliver beam energies of 5.5 MeV/u using two high- $\beta$  cryomodules placed downstream of REX, before the energy variable section of the existing linac is replaced with two low- $\beta$  cryomodules and two additional high- $\beta$  cryomodules are installed to attain over 10 MeV/u with full energy variability above 0.45 MeV/u. An overview of the project including a status summary of the different R&D activities and the schedule will outlined.

## INTRODUCTION

The High Intensity and Energy (HIE) ISOLDE project [1] aims at several important upgrades of the present ISOLDE radioactive beam facility at CERN. The main focus lies in the energy upgrade of the post-accelerated radionuclide beams from 3 MeV/u up to over 10 MeV/u through the addition of superconducting (SC) quarter-wave resonators (QWRs) operating at 101.28 MHz. This will open the possibility of many new types of experiments including transfer reactions throughout the nuclear chart.

The project also includes a design study that aims at improving the target and front-end part of ISOLDE to fully benefit from upgrades of the existing CERN proton injectors, e.g. LINAC4 and upgrade in energy of the PS Booster. This improvement combined with upgrades to the RILIS laser ion source and the radiofrequency quadrupole (RFQ) cooler and buncher (ISCOOL) will lead to an increase of radioactive beam intensities of up to an order of magnitude. The beam emittance will be improved with the implementation of ISCOOL placed after a pre-separator but before a new High-Resolution Separator (HRS). The new HRS, based on the latest magnet technology, will have sufficient mass resolution to permit isobaric separation. IS-

COOL will also permit a tailoring of the time structure of the beam, removing the dependence on the proton beam time structure and diffusion-effusion properties of the target and ion source units. Highly charged ions will be provided for REX and other users through an improved low energy stage of REX-ISOLDE and a possible installation of an upgraded Electron Beam Ion Source (EBIS) charge breeder.

The linac upgrade will be staged in order to deliver higher beam energies to the experiments as soon as possible, with future upgrade stages ensuring a wide range of energy variability and providing an optional  $\sim 100$  ns bunch spacing. The first stage of the upgrade involves the design, construction, installation and commissioning of two cryomodules downstream of REX, the existing post-accelerator. These cryomodules will each house five high- $\beta$  ( $\beta_g = 10.3\%$ ) SC cavities and one SC solenoid. Extra cryomodules will be added to the beam line in a modular fashion until all six cryomodules, including two cryomodules housing six low- $\beta$  ( $\beta_g = 6.3\%$ ) SC cavities and two SC solenoids, are online. The upgrade will be completed with a final stage that will see the linac extended in order to make room to pre-bunch the beam into the existing RFQ accelerator at a sub-harmonic frequency below 101.28 MHz, allowing the bunch spacing to be increased without significant loss in transmission; time-of-flight particle detection will then be viable at the experiments. Also foreseen is a beam chopper to reject the background of populated satellite bunches either side of the main sub-harmonic beam pulses. The staged installation of the linac is shown schematically in Figure 1. The pre-

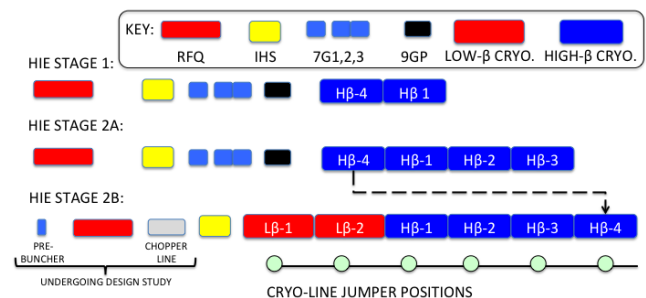


Figure 1: A schematic of the staged installation of the HIE-ISOLDE linac (Existing REX structures: RFQ, IHS: 20-gap IH-structure, 7GX: 7-gap split-ring cavities, 9GP: 9-gap IH-structure).

bunching/chopping scheme is under study and still to be finalised, e.g. chopping could occur before RFQ instead of after.

The beam dynamics studies [2, 3] arrived at a compact lattice, based on cavities operating at a gradient of 6 MV/m,<sup>1</sup> designed both due to the limited space in the experimental hall and to maximise the dynamical acceptance and optical performance of the machine. These considerations influenced the specification of the SC solenoids, alignment system, beam diagnostics system, steering magnets and cryomodules.

The superconducting linac is designed to provide a total accelerating voltage of 39.6 MV with an average synchronous phase  $\phi_s$  of  $-20$  deg, i.e. the minimum voltage required in order to achieve a final energy of at least 10 MeV/u with the heaviest beams that have a mass-to-charge state  $A/q = 4.5$ . The normal conducting 20-gap IH-structure (IHS) limits the  $A/q$  acceptance of the machine to  $2.5 \leq A/q \leq 4.5$ . The energy range accessible with the new SC linac is shown for each stage in Figure 2, including the decelerated beam that opens a range of energy not previously accessible with REX because of the fixed velocity profile of the IHS.

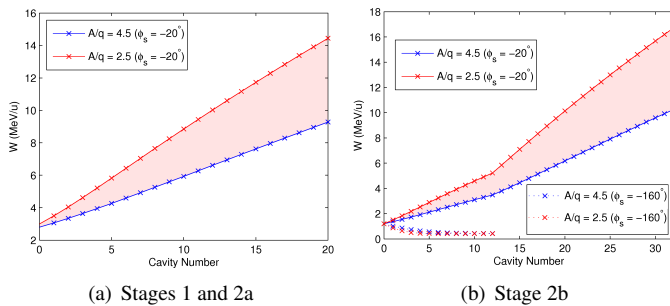


Figure 2: Energy reach of post-accelerated beams for each stage of the upgrade as a function of the  $A/q$  acceptance.

A research and development programme looking at all the different aspects of the SC linac started in 2008 and continued throughout 2011. In particular, the R&D effort has focused on the development of the high- $\beta$  cavity, for which it has been decided to adopt technology based on copper cavities sputter-coated with niobium. The required infrastructure has been determined and the integration of the SC linac and High Energy Beam Transfer (HEBT) lines inside the existing experimental hall has been finalised.

The project has been approved by CERN and its implementation started in January 2010. An overview of the project and its timeline will be given below.

## PHYSICS MOTIVATION

The current REX maximum energy of 3 MeV/u largely restricts the physics program to measurements of collective

<sup>1</sup>Cavity active length definitions: low- $\beta = 195$  mm and high- $\beta = 300$  mm.

degrees of freedom through single-step Coulomb excitation and probing single-particle degrees of freedom of light nuclei through direct nuclear reactions. The provision of exotic beams with energies up to 10 MeV/u will greatly expand the application of these methods to all ISOLDE beams [4]. Complete measurements of low-lying collective structure will be possible and, for particle states, unambiguous physical quantities can be extracted. The versatility of the accelerator, with variable energy down to 0.45 MeV/u, will facilitate measurements of rates of reactions that are the building blocks of nucleosynthesis chains, while the higher energy beams from the new linac will also allow prototype studies of new collective modes using electromagnetic probes and studies of exotic proton-rich and neutron-rich nuclei using fusion and highly-damped binary collisions.

The installation of the TSR storage ring [5] at HIE-ISOLDE has been approved and provides unique opportunities by being located at an ISOL facility. Reaction experiments could benefit from an increased luminosity from being in-ring, through multiple beam passes ( $\sim 1$  MHz), or from extracting electron-cooled beams for ultra-high resolution studies of heavy nuclei and Coulex studies. The TSR could also be used as a beam stretcher to accumulate the pulsed beam delivered by the EBIS and extract it as a d.c. beam over a few seconds, alleviating problems from the high instantaneous rates encountered with pulsed beams.

The 34 letters of intent submitted in 2010 for experiments at HIE-ISOLDE include 284 participants. The demand for the linac upgrade is reflected in 88% of the letters requesting higher beam energies that will be provided by the HIE upgrade.

## INTEGRATION AT ISOLDE

The new HIE-ISOLDE SC linac will require a major increase of equipment to the existing facility's infrastructure. Two new surface buildings will be constructed in order to house the helium compressor station and the helium refrigerator cold box, see Figure 3.



Figure 3: New HIE-ISOLDE buildings.

Ground breaking started at the end of last summer (2011) with the preparation of the site and the construction of

a new secure access point to the experimental hall for personnel and material while HIE-ISOLDE construction work is on-going. Presently, civil engineering works are in progress for the construction of the new buildings adjacent to the existing ISOLDE experimental hall. The construction works should be completed by the third quarter of 2012 after which the installation of the electrical systems and main services will take over. The cryogenic station installation, shown in Figure 4, will start in the second quarter of 2013. The He liquefier will be installed in a separate light construction building as close as possible to the linac in order to minimise the length of the LHe distribution line. This will enable an easier and more stable operation of the cryogenic system. The cryogenic system includes a cryogenic transfer line that will link the cold box to the different interconnecting “jumper” boxes, feeding from the top, the six cryomodules of the new SC linac.

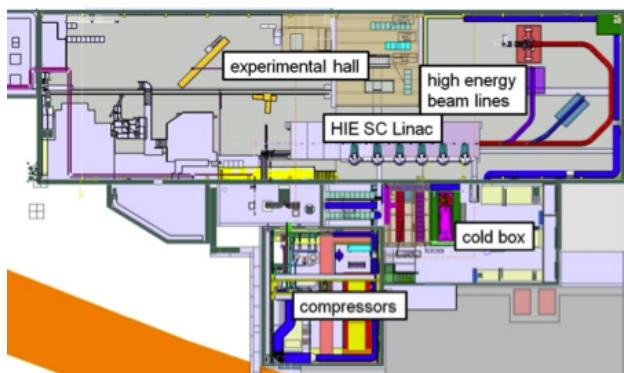


Figure 4: Layout of the HIE-ISOLDE facility.

The shielding tunnel will be installed in its entirety for the full linac along with the cryogenic transfer line, see Figure 5, whereas the linac and high energy beam transfer lines will be installed in stages. A new HEBT, discussed below, will bring the beam into the existing extension of the ISOLDE experimental hall [6].

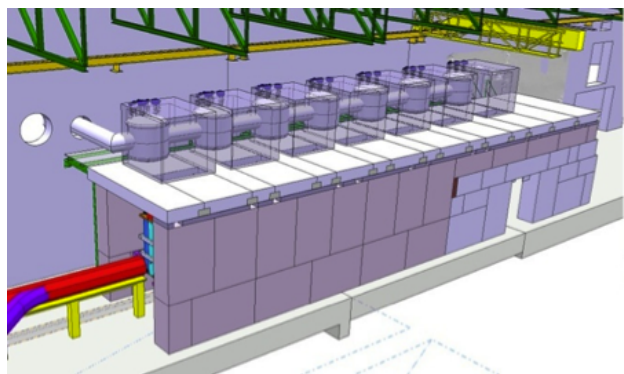


Figure 5: Linac shielding tunnel and cryogenic transfer line.

## CRYOMODULE DESIGN

The cavities will be grouped in common cryomodules with six cavities and two focusing solenoids for the low- $\beta$  cryomodules, and five cavities and one focusing solenoid for the high- $\beta$  cryomodules. Figure 6 shows a 3D model of the high- $\beta$  cryomodule. In order to simplify the mechanical design and assembly, and to minimise the drift length between cavities and the overall length of the machine, a common vacuum was chosen for the beam and cryogenic insulation. The solenoids need to be aligned with a stringent precision of  $\pm 0.15$  mm (i.e.  $\pm 1\sigma$ , where the simulated Gaussian error distribution was truncated at  $\pm 3\sigma$ ) and a system of independent adjustment, useable under vacuum and at operational temperatures, of the solenoid with respect to the cavity string is foreseen. An active position monitoring system based on BCAM CCD cameras [7] is under development. The active components will be cooled to 4.5 K in two stages using gaseous and liquid He. Insulation will be guaranteed by a heat screen at 75 K. A vacuum of  $10^{-8}$  mbar after cryopumping is necessary for optimal operation. To ensure the cleanest vacuum conditions, the vacuum system will be entirely dry, with turbo-molecular pumps backed by dry scrolls. In addition, automatic procedures with staged limitation of conductance, both for slow pump-down in the viscous regime and for venting with dry nitrogen, will be applied. A detailed description of the high- $\beta$  cryomodule design can be found in [8].

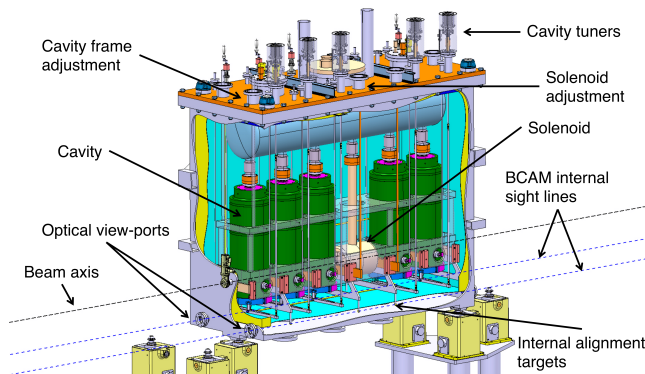


Figure 6: 3D model of the high- $\beta$  cryomodule (beam direction is from right to left).

## CAVITY DEVELOPMENT

The development of the SC cavities started in 2008 and focused on the high- $\beta$  cavity design, which will be installed first. The cavities are based on the niobium sputtered copper technology pioneered at INFN-LNL. They are specified to reach a nominal accelerating field of 6 MV/m on axis over an active length of 300 mm. A  $Q$ -value of  $5 \times 10^8$  is necessary to reach this field with a power dissipation of 10 W. In recent years much effort has been put in the design of a coating facility and the optimisation of the coating process. Since 2011 a single-cavity test-stand has been opera-

tional at CERN [9] working in tandem with the sputtering development to improve the quality factor of the niobium sputtered cavities. The latest tests have shown  $Q$ -values of  $1.5 \times 10^8$  at 6 MV/m; close to the design goal. Further details can be found in [10].

## BEAM DIAGNOSTICS

A beam instrumentation R&D programme is ongoing to provide a solution for the HIE-ISOLDE beam diagnostic system [11]. The space available in the regions between the cryomodules, in which a dipole steering magnet and vacuum valves are also situated, is very constrained, see Figure 7. Dimensioned at 58 mm in the longitudinal direction, the box is extremely compact and is designed to operate in the stray-field of the adjacent steering magnet. More details of the air-cooled steering magnet design specified at 6 T mm can be found in [12].

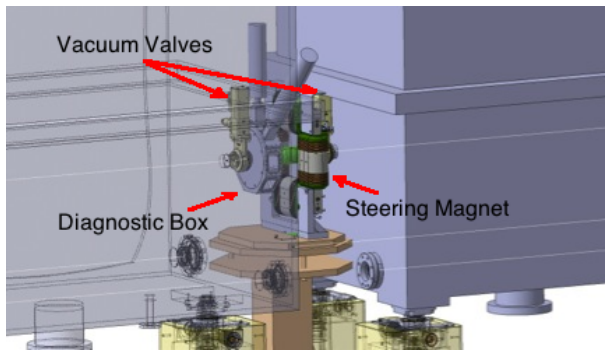


Figure 7: 3D model of the region between cryomodules.

An octagonal solution for the main body of the diagnostic box was chosen to facilitate multiple functionalities in the compact space available for the box, see Figure 8. The same design will be used in the HEBT lines, numbering fifteen units in the first stage of the upgrade. Up to five different devices can be actuated in-and-out of the beam in the transverse plane, with a beam profiling functionality included in two of these five devices as standard: a scanning slit that profiles the beam in front of a Faraday cup. The Faraday cup has been designed with a length of just 20 mm and a sensitivity from 1 – 500 pA. The prototype system will be delivered to CERN by Added Value Solutions (AVS) this summer for testing of the Faraday cup with beam before the Long Shutdown of the CERN accelerator complex commences (December 2012 until April 2014).

A longitudinal beam diagnostics system based on a silicon detector has been developed for the fast, and eventually automated, phasing of the large number of cavities that will accompany the upgrade. The system is capable of providing both relative phase and energy measurements. The proof-of-principle has been tested at REX by phasing the third 7-gap resonator with the system. For more details the reader is referred to [13]. A time-of-flight system for absolute energy measurements is also being considered.

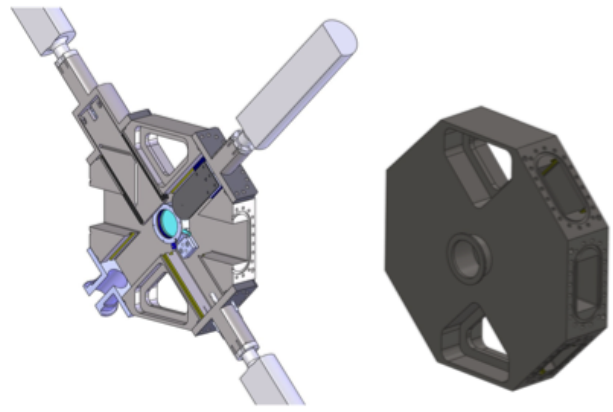
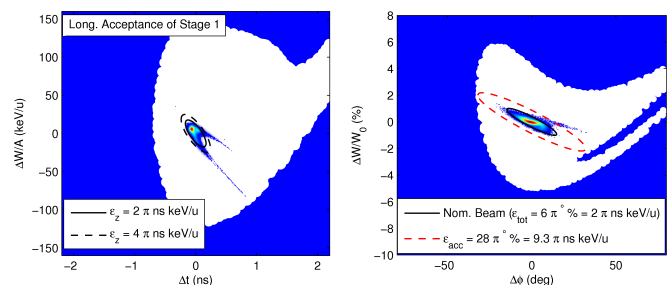


Figure 8: 3D model of the short diagnostic box, courtesy of AVS technology.

## COMMISSIONING AND OPERATION

In preparation for the linac upgrade various recommissioning steps have been undertaken to better understand the optimum working points of the existing accelerating structures, including bead-pull measurements, emittance measurements and end-to-end beam dynamics simulations benchmarked to measurements, described in [3]. The emittance delivered by REX was shown to be compatible with the acceptance of the superconducting linac in both the transverse and longitudinal phase-space planes, see [14] and [15] for the details of the respective measurements. The longitudinal acceptance of the SC linac is compared to the phase-space of the beam delivered by REX in Stages 1 and 2b of the upgrade in Figure 9. The normalised 90% transverse emittance was measured as less than  $0.3 \pi$  mm mrad and the 86% longitudinal emittance was measured as  $1.5 \pi$  ns keV/u.



(a) Stage 1 ( $W_0 = 2.85$  MeV/u). (b) Stage 2b ( $W_0 = 1.2$  MeV/u).

Figure 9: Simulated beam distribution (consistent with measurements) in longitudinal phase-space at entry to the SC linac, compared to the acceptance (shown in white).

To date, transverse emittance measurements using the NTG emittance rig [16] have been limited to those made on high intensity ( $\sim$  nA) pilot beams, which are generated by leaking gas into the EBIS. It is likely that the beam emittance is degraded with respect to the radioactive beam emittance due to the disruptive space-charge effects produced

by the higher beam intensity and resulting compensation of the radial focusing force provided to the trapped ions in the electron beam of the source. For this reason a high sensitivity emittance measurement system using single-particle detectors is being developed to measure the radioactive beam emittance using slits and detectors housed in adjacent diagnostic boxes that were shown previously. An emittance measurement will also be attempted this summer at lower beam intensity ( $\sim 10$  pA) by avoiding the use of slits to sample the phase-space in the emittance rig and instead using the three-gradient method to reconstruct the phase-space distribution by tomography; the beam size at the wire-grid of the emittance rig will be varied as a function of the gradient of an upstream quadrupole.

Due to the short nature of REX experimental runs (typically three to ten days) and the need for frequent energy and beam changes dictated by the physics programme, REX operation requires fast and reliable set-ups and the possibility to switch between beams or change the energy within a few hours. The size and complexity of the machine will increase with the energy upgrade, e.g. the number of cavities will increase from seven in the present linac to thirty-five in the final version of the HIE linac. The cavity phases will also become dependent on  $A/q$  as the full voltage provided by the QWRs can be exploited and the velocity profile changes as a function of  $A/q$  in the SC part of the linac. For this reason an automatic phasing procedure is foreseen using the above mentioned silicon detector either by tracking the relative energy change or, when the 100 ns bunch spacing becomes available, using a time-of-flight method.

Software applications for the control system are being developed in preparation for the commissioning phase, including the possibility of setting machine parameter values directly from beam simulation codes and vice versa. Automated optimisation software is also being investigated to phase the linac quickly and some initial tests have already been done on the existing linac.

## HIGH ENERGY BEAM TRANSFER LINES AND EXPERIMENTAL AREAS

The Miniball segmented germanium array and T-REX experimental setups already operational at REX will be used intensively when the first beams are delivered in 2015. Only the first two high- $\beta$  cryomodules will be installed in the tunnel, downstream of the existing REX linac and an open beam line will also be available for traveling experiments, see Figure 10.

The following year it is foreseen to install a helical-orbit spectrometer that will focus on transfer reactions across the entire nuclear chart, made possible by the upgraded beam energy. The helical-orbit spectrometer will demand a bunch spacing of the order of 100 ns and a scheme to pre-bunch before the RFQ at a sub-harmonic of its natural frequency is foreseen to satisfy this requirement. An active-target experiment for resonant scattering and transfer reactions is also under consideration.

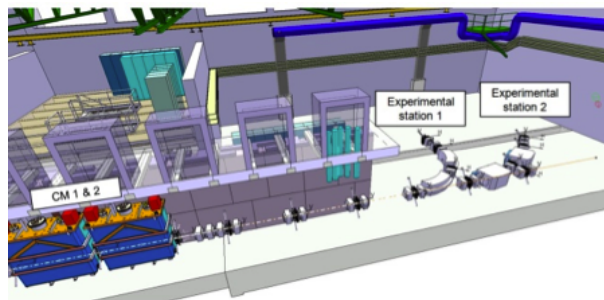


Figure 10: Stage 1 of the HIE upgrade with two high- $\beta$  cryomodules and HEBT lines added to REX.

The HEBT design [6, 11] is highly standardised with only a single type of quadrupole and dipole magnet needing procurement; the exceptions are the 22.5 deg dipoles on the transfer line to the second experimental station that are already procured and being refurbished. Each 90 deg bend is a standardised double-bend achromat consisting of two 45 deg dipoles and a single dispersion suppressing quadrupole. The HEBT is based on a periodic system of doublet cells with a unit length equal to the length of the high- $\beta$  cryomodule. As a result, the installation of the staged upgrade can occur in a modular fashion by the replacement of doublet cells with cryomodules. The HEBT will be extended in a second stage of the installation foreseen during 2017/18 to accommodate a third experimental station. Some space has been reserved behind the third experimental station for the installation of a magnetic spectrometer in the future. The layout of the HEBT is shown in Figure 11. Vacuum in the low  $10^{-7}$  mbar range is obtained

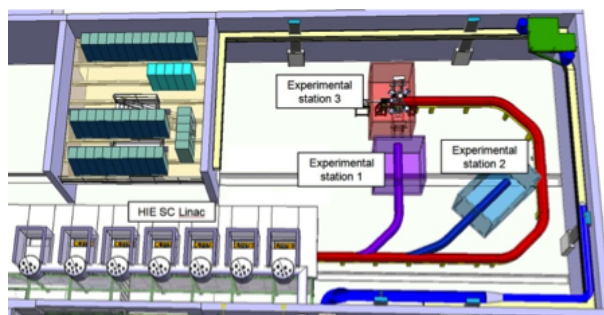


Figure 11: Layout of the HEBT lines in the ISOLDE experimental hall.

by turbomolecular pumps, backed by dry, hermetical multi-roots, connected to the common effluent collector and the air ventilation evacuation. The turbopumps are installed at dedicated ports on the diagnostic boxes, which constitute the major source of length-specific outgassing. Vacuum sectorisation is kept minimal, with the goal of separating in distinct vacuum sectors the different beam lines, as well as to cut the experimental areas from the beam transfer sections.

The extension of the HEBT in the final stage permits

a connection to the TSR storage ring that is expected to become operational at CERN during this period, see Figure 12.

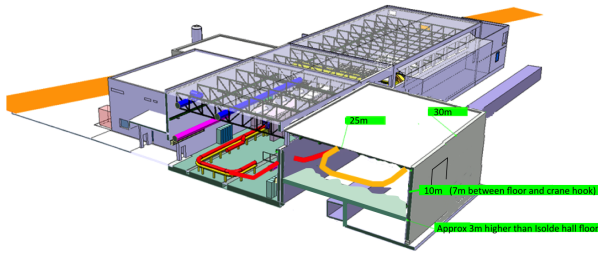


Figure 12: First-floor extension for the TSR behind the experimental hall (shown in orange) connecting to the HEBT via the inclined beam line (shown in red).

## SAFETY ASPECTS

The main hazards that will be introduced by the linac upgrade come from X-rays, neutrons and the cryogenic system. A radiation measurement station has been integrated into the single-cavity test-stand to collect dose rate data specific to the HIE-ISOLDE cavities. These data will be used to confirm the sizing of the tunnel shielding. An access system with key is already used to prevent access during linac operation. When one key is removed from a key box the RF is stopped and the amplifiers cannot be restarted until all keys are back in a key box [17]. A similar system is foreseen for the HIE-ISOLDE tunnel access.

An incident beam of heavy ions at an energy of 10 MeV/u is higher than the Coulomb barrier allowing neutron production. A dose rate of  $0.1 \text{ mSv h}^{-1} \text{ pA}^{-1}$  is expected at 1 m, at an angle of 90 deg from vicinity of the beam loss [18]. During operation and setting-up, a maximum beam intensity of  $\sim \text{ppA}$  is expected in the experimental hall and free access will be possible.

Redundant safety valves will be installed on the He tanks of the cryomodules to mitigate for the cryogenic hazard associated with the 900 litres of LHe inside the six cryomodules. These safety valves will be routed outside the tunnel in order to reduce exposure to an oxygen deficiency hazard during technical access to the tunnel while the cryomodules are cold.

Finally, pumping on radioactive beams implies a risk of radioactive contamination of the vacuum system, demanding an entirely hermetical system, with collection and evacuation of the effluent gases before controlled release to the atmosphere.

## PLANNING AND SCHEDULING

If the carefully planned schedule is respected, the various experiments currently receiving beams from ISOLDE will not suffer from the upgrade works. Civil engineering work

and installation of the main services such as power, ventilation and cooling will take place while the ISOLDE facility is running for the experiments. To guarantee a minimum of perturbation to the operation of the facility, the main services will be connected and the existing services modified only during the CERN Long Shutdown. Civil engineering work inside the experimental hall, such as the construction of the new tunnel, as well as the move of the existing Mini-ball experiment to its new position will also be carried out during this period of shutdown.

Start-up of the low energy (60 keV) part of the ISOLDE facility, excluding the REX post-accelerator, is foreseen for April 2014 as normal. However, at that moment the HIE-ISOLDE linac and HEBT line will still be under construction with the installation of the first two high- $\beta$  cryomodules and the transfer line elements running into the summer of 2014. Beam commissioning at 5.5 MeV/u is planned for the end of the 2014. The remaining two high- $\beta$  cryomodules will be installed in a second stage in 2016, increasing the beam energy to 10 MeV/u, together with an additional bend in the HEBT providing the users with a third experimental station (and making possible the connection of the TSR storage ring). A pre-bunching scheme before the RFQ with chopper and the two low- $\beta$  cryomodules completing the HIE-ISOLDE linac are foreseen for a later stage after 2017.

## OUTLOOK

The main technological options of the linac are now fixed and most components are in their final design or prototyping phase. The HEBT design has been finalised and the components are now in the specification or prototyping phase. The infrastructure installation is under way and should be completed by mid-2013. The cryogenic lines and first phase of the linac and transfer lines installation is planned for 2014. The linac commissioning at 5.5 MeV/u is foreseen for late 2014 and the first physics should take place in early 2015.

## ACKNOWLEDGMENTS

This paper summarises the work of several teams: The ISOLDE Collaboration, the HIE-ISOLDE project team, and numerous groups at CERN within the accelerator and technology sector.

We acknowledge funding from the Swedish Knut and Alice Wallenberg Foundation (KAW 2005-0121) and from the Belgian Big Science program of the FWO (Research Foundation Flanders) and the Research Council K.U. Leuven.

We would also like to acknowledge the receipt of fellowships from the CATHI Marie Curie Initial Training Network (EU-FP7-PEOPLE-2010-ITN Project number 264330) and the COFUND-CERN Marie Curie Fellowship programme.

Support from the Spanish Programme Industry for Science from CDTI is also acknowledged.

## REFERENCES

- [1] M. Lindroos, P.A. Butler, M. Huyse and K. Riisager, "HIE-ISOLDE," *Nucl. Instrum. Meth. B* **266**, pp. 4687-4691 (2008).
- [2] M.A. Fraser, R.M. Jones, M. Pasini, "Beam Dynamics Design Studies of a Superconducting Radioactive Ion Beam Postaccelerator," *Phys. Rev. ST Accel. Beams* **14**, p. 020102 (2011).
- [3] M.A. Fraser, "Beam Dynamics Studies of the ISOLDE Post-Accelerator for the High Intensity and Energy Upgrade," PhD Thesis (University of Manchester), Vol. 13 in EuCARD Series (2012).
- [4] K. Riisager, P. Butler, M. Huyse, and R. Krücken. "HIE-ISOLDE: The scientific opportunities," CERN Report, CERN-2007-008 (2007).
- [5] M. Grieser, Yu. Litvinov, R. Raabe, K. Blaum, Y. Blumenfeld, P. Butler, F. Wenander, *et al.*, "Storage Ring at HIE-ISOLDE," *Eur. Phys. J. ST* **207**, pp. 1-117 (2012).
- [6] D. Voulot, E. Bravin, M.A. Fraser, B. Goddard, Y. Kadi, D. Lanaia, A. Parfenova, A. Sosa, F. Zocca, "HIE-ISOLDE SC linac: operational aspects and commissioning preparation," *Proc. of IPAC'12*, to be published.
- [7] K. Hashemi, BCAM Home Page, Brandeis University, <http://alignment.hep.brandeis.edu/Devices/BCAM/>.
- [8] L. Williams, A. Bouzoud, N. Delruelle, J.-C. Gayde, Y. Leclercq, M. Pasini, J.-P. Tock, G. Vandoni, "Design of the High Beta Cryomodule for the HIE-ISOLDE Upgrade at CERN," *Proc. of IPAC'11*, (MOPC105) (2011).
- [9] O. Capatina, J.-P. Brachet, G. Cuccuru, M. Pasini, T. Renaglia, M. Therasse, B. Vullierme, "Cryostat for Testing HIE-ISOLDE Superconducting RF Cavities," *Proc. of IPAC'11* (MOPC103) (2011).
- [10] M. Therasse, O. Brunner, S. Calatroni, J.K. Chambrillon, B. Delaup, M. Pasini, "HIE-ISOLDE SRF Development Activities at CERN," *Proc. of IPAC'11* (MOPC104) (2011).
- [11] A. Sosa, E. Bravin, M.A. Fraser, J. Galipienzo, Y. Kadi, P. Noguera, D. Voulot, C. Welsch, F. Wenander, F. Zocca, "Beam Instrumentation for the HIE-ISOLDE Linac at CERN," *Proc. of IPAC'12*, to be published.
- [12] J. Bauche, "Compact Inter-cryomodule Combined Corrector Magnets for the HIE-ISOLDE Project at CERN," *Proc. of MT-22* (2011).
- [13] F. Zocca, M.A. Fraser, E. Bravin, M. Pasini, D. Voulot, F. Wenander, *Nucl. Instrum. Meth. A* **672**, pp. 2128 (2012).
- [14] D. Voulot, "REX-linac Emittance Measurements," CERN-BE-Note-2009-012 OP (2009).
- [15] M.A. Fraser, F. Zocca, R.M. Jones, M. Pasini, P.A. Posocco, D. Voulot, and F. Wenander. "Longitudinal Emittance Measurements at REX-ISOLDE," *Nucl. Instrum. and Meth. A* **663**, pp. 1-9 (2012).
- [16] J. Dietrich, I. Mohos, J. Häuser, G. Riehl, F. Wenander, "High Sensitive Beam Emittance Analyzer," *Proc. of EPAC'02*, pp. 1864-1866 (2002).
- [17] D. Voulot, "Safety file - REX-ISOLDE Linac shielding tunnel," CERN-EDMS 1016852, to be published.
- [18] W.F. Ohnesorge, "Heavy ion target area fast neutron dose equivalent rates," *Health Phys.* **39**, pp. 633-636 (1980).

## THE SC CW LINAC DEMONSTRATOR – 1ST TEST OF AN SC CH-CAVITY WITH HEAVY IONS

S. Mickat<sup>1,3</sup>, M. Amberg<sup>3</sup>, K. Aulenbacher<sup>3,4</sup>, W. Barth<sup>1,3</sup>, D. Bänsch<sup>2</sup>, L. Dahl<sup>1</sup>, F. Dziuba<sup>2</sup>,  
V. Gettmann<sup>3</sup>, D. Mäder<sup>2</sup>, H. Podlech<sup>2</sup>, U. Ratzinger<sup>2</sup>, R. Tiede<sup>2</sup>

<sup>1)</sup> GSI Helmholtzzentrum, 64291 Darmstadt, Germany

<sup>2)</sup> IAP, Goethe University, 60438 Frankfurt, Germany

<sup>3)</sup> HIM, Helmholtzinstitut, 55099 Mainz, Germany

<sup>4)</sup> KPH, Johannes Gutenberg-University, 5099 Mainz, Germany

### Abstract

The superconducting (sc) continuous wave (cw) LINAC Demonstrator is a collaboration project between GSI, the Helmholtz Institute Mainz (HIM), and the Institute for Applied Physics (IAP) at the Goethe University Frankfurt. The aim is a full performance test of a 217 MHz sc Crossbar H-mode (CH) cavity, which provides gradients of 5.1 MV/m at a total length of 0.69 m. In addition the Demonstrator comprises two 9.3 Tesla sc solenoids. The configuration of a CH-cavity embedded by two sc solenoids is taken from a conceptual layout of a new sc cw LINAC with nine CH-cavities and seven solenoids. Such an accelerator is highly desired by a broad community of users requesting heavy ion beam energies in the Coulomb barrier range. A successful test of such an sc multigap structure is an important milestone towards the proposed cw-LINAC.

### THE SC CH-CAVITY

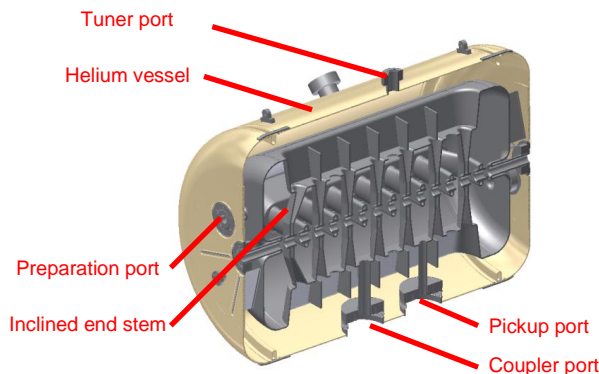


Figure 1: The 217 MHz sc CH-cavity.

The sc CH-cavity is the key component of the Demonstrator project. Four sc CH-cavity types were and are developed at the IAP so far:

- (1) A first prototype of a 360 MHz sc CH-cavity ( $\beta=0.1$ , 19 gaps) was tested at the IAP successfully. In vertical rf-tests maximum gradients of up to 7 MV/m at  $Q_0$ -values between  $10^8$  and  $10^9$  were achieved [1, 2].

- (2) The delivery of a 325 MHz sc CH-cavity ( $\beta=0.16$ , 7 gaps) is imminent [3]. The site acceptance test at RI, Germany is in progress. First rf-tests at room temperature were successful.
- (3) The cavity designed for the cw-LINAC Demonstrator project ( $\beta=0.06$ , 15 gaps) is operated at 217 MHz (fig.1). Its general parameters are listed in table 1.
- (4) The cold part layout of the 17 MeV injector of the MYRRHA (Multi-purpose hybrid research reactor for high-tech applications) project should comprise 176 MHz cavities [4].

### THE SC CW LINAC DEMONSTRATOR

Although the results of the warm and cold rf-tests of the 360 MHz cavity at the IAP were very promising, for a proof-of-principle on the sc CH-cavities tests under real operational conditions must be passed. That is the aim of the Demonstrator project. At the GSI High Charge Injector (HLI) a 217 MHz sc CH-cavity should be operated with heavy ion beam.

The project is financed by HIM mainly and is supported by the Accelerator Research & Development (ARD) program of the Helmholtzgemeinschaft (HGF).

Table 1: General parameters of the sc CH-Cavity designed for the cw-LINAC Demonstrator.

|                       |      |       |
|-----------------------|------|-------|
| $\beta$               |      | 0.059 |
| max A/Q               |      | 6     |
| Frequency             | MHz  | 217   |
| Gap number            |      | 15    |
| Total length          | mm   | 690   |
| Cavity Diameter       | mm   | 409   |
| Gap length            | mm   | 40.8  |
| Aperture              | mm   | 20    |
| Effective gap voltage | kV   | 225   |
| Voltage gain          | MV   | 2.97  |
| Accelerating gradient | MV/m | 5.1   |

The Demonstrator is the first section of the proposed sc cw-LINAC (cp. Future Applications). It is a cryostat housing the cavity, which is embedded by two superconducting solenoids (fig. 2). A study has been worked out which provided a concept to load the cryostat with the solenoids and the cavity as well as to align the three components to the beam axis [5].

The solenoids provide maximum fields of 9.3 T at an effective length of 290 mm and a free beam aperture of 30 mm. The fringe fields have to be reduced from the maximum field to 50 mT at the inner NbTi-surface of the neighbouring cavity. Based on the 9T solenoid design for the ISAC-II cryomodule [6] a coil configuration with two main coils and two bucking coils was assumed to fit the requirements at best (fig. 3). The calculations show that proper gradients can be achieved by using anti-windings. The general parameters of the solenoids are listed in table 2.

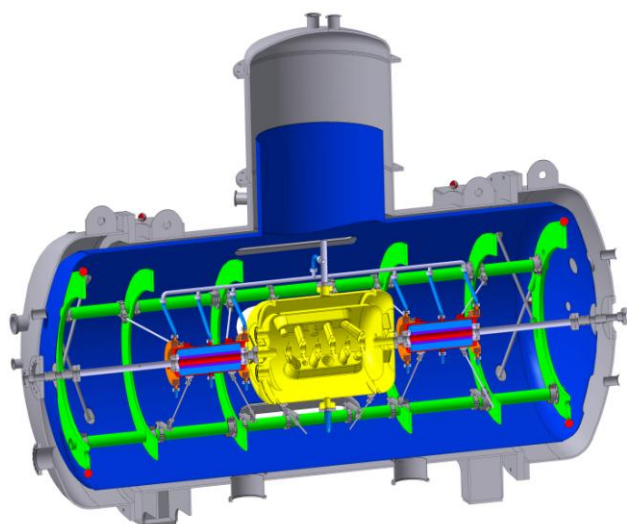


Figure 2: A scheme of the cw-LINAC Demonstrator shows the CH-cavity (yellow) in its centre embedded by two sc solenoids (red-orange). On the top space for a reservoir of liquid helium as well as of liquid nitrogen is reserved.

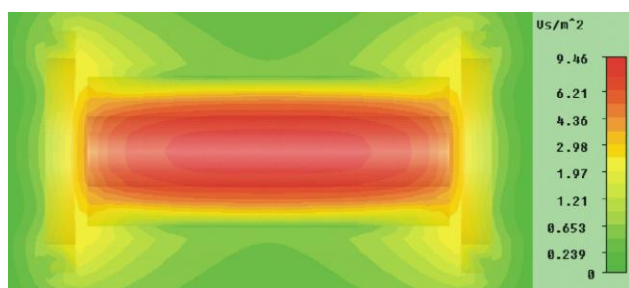


Figure 3: The solenoid field of the chosen coil configuration is calculated. Within the requirements the fringe field is shielded by the compensation coils.

The favoured location to setup the Demonstrator is in straightforward direction of the HLI at GSI (fig. 4). Two

existing experiments at the HLI have to move since the space is needed for the demonstrator test environment including a new radiation protection cave.

The liquid helium (LHe) supply is covered by a 3000 ltr tank. The consumed helium is collected in a 25 m<sup>3</sup> recovery balloon and bottled by a compressor. In operation a consumption of 20 ltr LHe per hour is predicted.

Table 2: General parameters of the sc solenoids designed for the cw-LINAC Demonstrator.

|                   |    |     |
|-------------------|----|-----|
| max. field        | T  | 9.3 |
| B <sup>2</sup> *l | Tm | 24  |
| effective Length  | mm | 280 |
| Beam aperture     | mm | 30  |

For longitudinal matching the beam from the HLI to the demonstrator the existing buncher UN6 BB14 can be used. For transverse focusing an additional magnetic quadrupole doublet is needed. Moreover beam diagnostics like profile grids and an emittance measurement station have to be integrated in the beam line in front of and behind the demonstrator as well as phase probes for time of flight (TOF) measurements. For scheduling of the project see table 3.

## THE SC CW-DEMONSTRATOR SCHEDULING

Table 3: Time Schedule

| cw LINAC Demonstrator Project |   |
|-------------------------------|---|
| 2009                          | Foundation of HIM<br>Funding of the sc cw-LINAC Demonstrator  |
| 2010                          | Tendering of the Demonstrator's components  |
| 2011                          | Delivery of the LHe-supply and the rf-amplifier<br>Ordering of the cavity<br>Beginning of assembling the test facility at GSI HLI |
| 2012                          | Ordering the solenoids and the cryostat   |
| 2013                          | Delivery of the cavity<br>1st rf tests (warm + cold) at IAP   |
| 2014                          | Delivery of the solenoids and the cryostat<br>Commissioning of the Demonstrator at GSI<br>Full performance test at GSI HLI        |

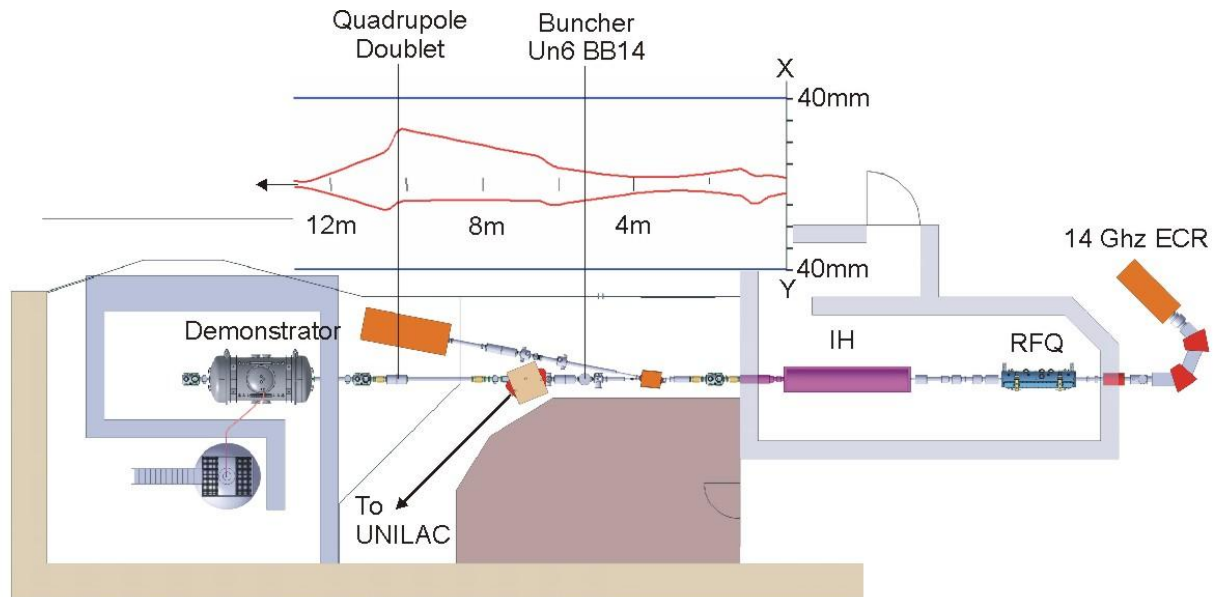


Figure 4: The existing 1.4 AMeV HLI should be used as the injector for the cw-LINAC demonstrator. In longitudinal plane the existing buncher UN6BB, in transverse plane an additional quadrupole doublet should be used to match the beam to the demonstrator.

## FUTURE APPLICATIONS

Successful full performance tests with beam of the sc CH-cavity open a broad field of accelerator applications:

The first 360 MHz prototype was developed within EUROTRANS (European research program for the transmutation of high level nuclear waste in an accelerator driven system). In 2023 MYRRHA as an accelerator driven system (ADS) for transmutation of high level nuclear waste should be commissioned with four 176 MHz sc CH cavities [7].

As a future upgrade option for the GSI universal linear accelerator (UNILAC) an energy booster LINAC with six 325 MHz cavities is discussed [8].

Another application is the sc cw-LINAC, which is highly desired by a broad community of future users. Especially the Super Heavy Elements (SHE) program at GSI and at the Helmholtz Institute Mainz (HIM) benefits highly from such a dedicated accelerator [9].

A conceptual layout of the sc cw-LINAC was worked out [10], which allows the acceleration of highly charged ions with a mass to charge ratio of 6 at 1.4 AMeV from the upgraded HLI including a new source. An sc 28GHz ECR-source is under development at GSI. Nine superconducting CH-cavities operated at 217 MHz accelerate the ions to energies between 3.5 AMeV and 7.3 AMeV, while the energy spread should be kept smaller than  $\pm 3$  AkeV. As beam focusing elements seven superconducting solenoids are applied. The first as well the follow-up proposal for the cw-LINAC was evaluated "excellent" by the HGF in 2011. Strong activities are in progress to receive a funding for the project.

## REFERENCES

- [1] F. Dziuba et al., Development of superconducting crossbar-H-mode cavities for proton and ion accelerators. *Phys. Rev. ST Accel. Beams* 13, 041302 (2010).
- [2] H. Podlech et al., Superconducting CH structure, *Phys. Rev. ST Accel. Beams* 10, 080101 (2007).
- [3] M. Busch et al., Status of the 325 MHz sc CH-cavity at IAP Frankfurt, *Proceedings of IPAC2011 MOPC082*, San Sebastián, Spain, (2011).
- [4] D. Mäder et al., Development of CH-Cavities for the 17 MeV MYRRHA-Injector, *Proceedings of IPAC2011 MOPC082*, San Sebastián, Spain, (2011).
- [5] V. Gettmann et al., The sc cw -LINAC Demonstrator – an R&D project for SRF technology, these proceedings, *SRF2011*, Chicago, USA (2011).
- [6] R.E. Laxdal et al., Magnetic field studies in the ISAC-II cryomodule, *Physica C* 441, p.225–228 (2006).
- [7] <http://myrrha.sckcen.be/en> (2012).
- [8] W. Barth et al., Future Heavy Ion LINACsat GSI, *Proceedings of IPAC2011 WEPS031*, San Sebastián, Spain, (2011).
- [9] S. Mickat et al., The sc cw -LINAC Demonstrator – SRF-technology finds the way into GSI, *Proceedings of SRF2011*, Chicago, USA (2011).
- [10] S. Minaev et al., Superconducting, energy variable heavy ion linac with constant  $\beta$ , multicell cavities of CH-Type, *Phys. Rev. ST Accel. Beams* 12, 120101 (2009).

## COMMISSIONING AND OPERATION OF SUPERCONDUCTING LINAC AT IUAC DELHI

S. Ghosh, A. Rai, B.K. Sahu, P. Patra, A. Pandey, G.K. Chowdhury, D.S. Mathuria, R.N. Dutt, J. Karmakar, S.S.K. Sonti, K.K. Mistri, R. Joshi, A. Sarkar, J. Chacko, A. Chowdhury, S. Kar, S. Babu, M. Kumar, J. Antony, R. Kumar, R. Ahuja, J. Sacharias, P.N. Prakash, T.S. Datta, D. Kanjilal, A. Roy,

Inter University Accelerator Centre (IUAC), Aruna Asaf Ali Marg, New Delhi – 110067, India.

### Abstract

The major part of the superconducting (SC) linac at IUAC has been operational for the past few years and the last accelerating module is in the final stage of completion. At present the superbuncher (SB), the first two linac accelerating modules and the re-buncher (RB) are operational and ion beams in the mass range  $^{12}\text{C}$  to  $^{107}\text{Ag}$  from Pelletron accelerator have been further accelerated and delivered to conduct scheduled physics experiments. A method of random phase focusing to select the accelerating phase of the resonators between  $70^\circ$  and  $110^\circ$  has been successfully tried to reduce the time width of the beam bunch delivered for experiments. Presently, to improve the accelerating fields of the linac resonators in phase locked condition, enhancement of the microphonics damping efficiency with bigger diameter SS-balls, testing of an alternate tuning mechanism based on Piezo Crystal and improvement of the cooling efficiency of the drive coupler are being tried out. The outcomes of all these experiments are being implemented on the resonators of the last cryostat which is under commissioning stage.

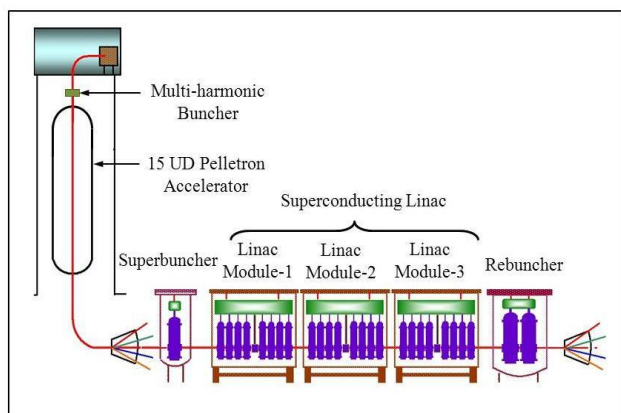


Figure 1: Schematic layout of Pelletron and Linac. The figure is not to scale.

## INTRODUCTION

The Pelletron accelerator of IUAC has been delivering ion beams for experiments since early nineties in the energy range of few tens to few hundreds of MeV [1]. A Superconducting Linear Accelerator (Linac) was chosen to augment the energy of the ions from the existing Pelletron accelerator. The linac was designed to have a

superbuncher cryostat having a single niobium Quarter Wave Resonator (QWR) followed by three accelerating modules, each containing eight QWRs and a rebuncher cryostat housing two QWRs. The complete layout of the Pelletron and linac is given in figure 1. The prototype niobium resonator and the first batch of twelve resonators were built by IUAC in collaboration with Argonne National Laboratory [2]. The remaining resonators for module 2 and 3 are indigenously fabricated using the in-house facilities of electron beam welding, high vacuum annealing furnace and surface preparation laboratory [3]. Eight indigenous resonators were installed in the second module and different beams were accelerated through the first two linac accelerating modules with the help of superbuncher and rebuncher. At present the fabrication work for the remaining resonators to be installed in the last linac module is in the final stage.

### BEAM ACCELERATION THROUGH THE FIRST TWO LINAC MODULES

The beam acceleration in the mass range of  $^{12}\text{C}$  to  $^{107}\text{Ag}$  by the first accelerating module with the help of SB and RB resonators are being carried out since last few years [4,5,6]. Recently, the second accelerating module became operational and during this test, beams were accelerated by the sixteen resonators of module 1 and 2. The accelerating field obtained at  $\sim 6$  watts of power and the phase locked fields at the time of beam acceleration are shown in figures 2 and 3. During linac operation, it was observed that for many resonators, there was a substantial reduction between the phase locked fields and the accelerating fields obtained at 6 watts of input power. A number of steps have been taken to tackle this problem and these are presented in next section.

At the time of operation of the first two linac modules, three beam species from Pelletron accelerator were further accelerated through linac. The final beam was delivered for several months in the beam line of Hybrid Recoil Mass Analyser (HYRA) and National Array of Neutron Detector (NAND) to conduct Nuclear Physics experiment. The beam and their final energies are presented in Table-1.

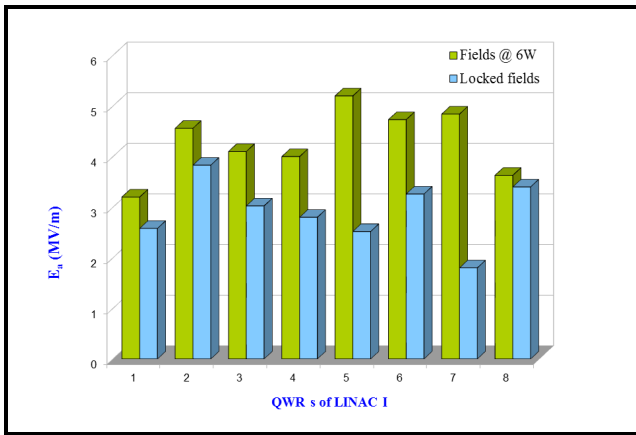


Figure 2: Accelerating field gradients,  $E_a$  at 6 watts of input power and phase locked fields at the time of beam acceleration for the resonators in linac-1.

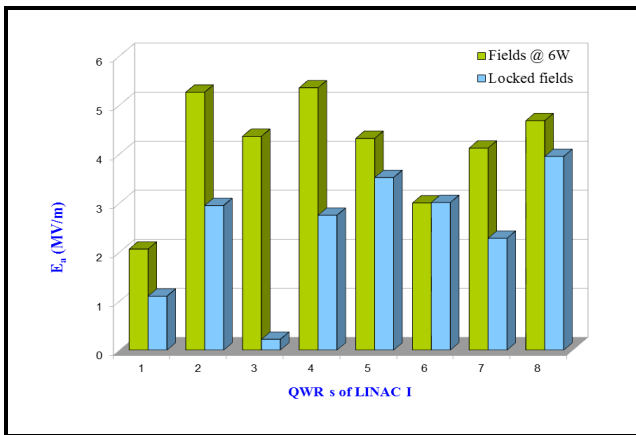


Figure 3: Accelerating field gradients,  $E_a$  at 6 watts of input power and phase locked field at the time of beam acceleration for the resonators in linac-2.

Table 1: Beam Species and Energies Delivered for Experiments

| Beam                            | Energy from Tandem (MeV) | Energy gain LINAC (MeV) | Total energy delivered |
|---------------------------------|--------------------------|-------------------------|------------------------|
| <sup>19</sup> F <sup>7+</sup>   | 100                      | 37                      | 137                    |
| <sup>28</sup> Si <sup>11+</sup> | 130                      | 60                      | 190                    |
| <sup>31</sup> P <sup>11+</sup>  | 130                      | 58                      | 188                    |

### EFFORTS TO MATCH THE PHASE LOCKED FIELDS WITH THE FIELDS OBTAINED AT 6 WATTS OF INPUT POWER

For the resonators installed in linac modules, large amount of RF power is required to bridge the gap between the phase locked fields and the fields obtained at

6 watts of input power. However the power coupler, power cable and the other accessories of the resonator are not well equipped to sustain this high power for prolonged duration. The reason for the requirement of high power is that the resonator picks up vibration from the microphonics present in the ambience of the cryostats. This vibration translates in to RF frequency jitter whose maximum value has been measured to be  $\sim \pm 50$  Hz. If the Q-value of the resonator at the field of  $\sim 4$  MV/m at 6 watts of input power is typically  $\sim 2.0 \times 10^8$ , to accommodate a bandwidth of  $\pm 50$  Hz, the coupling coefficient,  $\beta$  will be equal to 200. The forward power required from the amplifier ( $P_{amp}$ ) is related to  $\beta$  by the following equation:

$$P_{amp} = \frac{(\beta + 1)^2}{4\beta} P_{cavity}$$

where,

$P_{amp}$  = RF forward power required from amplifier

$\beta$  = Coupling coefficient

$P_{cavity}$  = RF power required by the resonator to generate the accelerating field (typically 6 watts).

So the resonator can be locked at the fields obtained at 6 watts of input power but it will be possible only with a supply of huge amount of forward RF power ( $\sim 300$  watts). But since the phase locking of the resonator with  $\sim 300$  watts of power caused several operational problems in the past [4], so it was decided that the resonator would be operated at an accelerating field which could be phase locked with 100 watts of RF power.

The second reason for the lower electric field in phase locked condition with  $\sim 100$  watts of RF power is the large value of stored energy of the resonator ( $0.11\text{J}/(\text{MV}/\text{m})^2$ ) which is intrinsic in nature to the cavity. The relationship between the power required from the amplifier ( $P_{max}$ ), the stored energy ( $U$ ) and the amount of frequency jitter ( $\delta\omega_{shake}$ ) due to the presence of microphonics, is given by:

$$P_{max} = U \cdot \delta\omega_{shake} \text{ ----- (1)}$$

whereas  $U$  is related as

$$U = U_0 E_a^2$$

$U_0$  is the stored energy at 1 MV/m and  $E_a$  is the average accelerating fields.

As the intrinsic stored energy at 1 MV/m is reasonably high, the resonator can not be phase locked at a field greater than  $\sim 3$  MV/m for a total frequency jitter of 100 Hz with a forward power of 100 watts. If the resonator is to be phase locked at 4 and 5 MV/m, the amount of forward power required will be 160 and 250 watts respectively for the same amount of frequency jitter. Therefore to lock the resonators at higher fields, three different approaches are being simultaneously implemented in the linac resonators and they are discussed in the following subsections.

*Improved Vibrational Damping of the Resonator with Bigger Diameter of SS-balls*

Already an innovative vibrational damping mechanism [7] had been adopted and successfully used in all the resonators of module - 1 and 2. However, to extend the success of this mechanism, more extensive experiments are being carried out to improve the efficiency of the damping mechanism.

Table 2: Experimental Results on the Vibrational Damping Mechanism on a Resonator with SS-balls

| Dia of SS balls | Decay time with 0 balls (sec) | Decay time with optimum balls | Optimum no. of balls | Factor of reduction in the vibration |
|-----------------|-------------------------------|-------------------------------|----------------------|--------------------------------------|
| 1               | To be done                    |                               |                      |                                      |
| 2               | 3.70                          | 0.60                          |                      | 06.1                                 |
| 3               | To be done                    |                               |                      |                                      |
| 4               | 3.14                          | 0.40                          | 80                   | 07.8                                 |
| 5               | 3.03                          | 0.51                          | 75                   | 05.9                                 |
| 6               | 2.87                          | 0.30                          | 65                   | 09.6                                 |
| 7               | 3.25                          | 0.39                          | 45                   | 08.3                                 |
| 8               | 2.98                          | 0.26                          | 35                   | 11.4                                 |
| 9               | 3.02                          | 0.27                          | 25                   | 11.2                                 |
| 10              | 2.11                          | 0.29                          | 20                   | 07.3                                 |
| 11              | 2.61                          | 0.28                          | 20                   | 09.3                                 |
| 12              | 2.70                          | 0.26                          | 17                   | 10.5                                 |

During a recent series of single strike experiments conducted on a niobium resonator kept at room temperature, ball diameter starting from 2 mm to 12 mm had been tried along with a mixture of balls of different diameters. The detail of the experiment has been explained elsewhere [7]. The results of the improvement in the decay time of the vibration have been tabulated in Table-2. Final results with mixture of balls of different diameters are not presented as these experiments are presently underway. In the single strike experiment, the resonator, kept at room temperature, is subjected to a vibration by a single strike from a heavy metal disc swinging like a pendulum. Then the frequency excursion of the resonator about its mean value without any SS-balls present inside the bowl shaped structure of the bottom of the central conductor is recorded with the help of Picoscope and computer. Next, SS balls of a particular diameter in groups of 5 are placed inside the central conductor of the resonator [7] and the frequency excursion of the resonator is measured after the single strike. In this way the experiment is carried over for a total number of balls of around 150-200. The experimental results presented in table-2 show that among the different diameter of balls, 8 and 9 mm are the one which have given the best results. Hence, these diameters and optimum number of balls are being used in all the

resonators of module - 2 and 3 in place of 4 mm balls used earlier [7]. However, the performance of the resonators with bigger diameter balls has to be verified at liquid helium temperature during phase locking against the master oscillator. It is expected that with the bigger diameter of SS-balls, there will be more reduction in the total  $\delta\omega_{shake}$  and it will be possible to phase lock the resonators at higher accelerating fields.

*Alternate Tuning Mechanism by Piezo Actuator*

As the Quality factor of niobium resonator is in the range of  $10^9$ , the bandwidth of resonator is around 0.1 Hz. For IUAC QWR, vibration induced fluctuations of the frequency are of the order of few tens to hundred hertz. The frequency fluctuations mentioned here have got two components – one happens in slow time scales (seconds) and the other happens in faster (a few tens to hundreds of  $\mu$ sec) time scale. To tackle the fast frequency drift, power from RF amplifier is fed in over-coupled condition to supply the additional reactive power to the resonator and the whole operation is done electronically (fast tuner). To arrest the slow drift of frequency, a niobium bellow is attached near the high voltage end of the resonator and this is flexed by a few mm with pure helium gas sent from outside of the cryostat. A mass flow control for helium gas is being used to move the niobium bellows. During operation, the tuning scheme operates in a feedback loop to take care of the slow drifts in frequency and thus to reduce the load on the fast tuner. Since this tuning mechanism uses proportional helium gas flow through narrow tubes, the process takes place in the timescale of second. Within this interval of 1 second, all the correction of the loop frequency is being corrected by the fast tuner by supplying more RF power (~100-300 watts). So the average power requirement to maintain the phase lock of the resonator goes up. In addition to this problem, the gas operated tuning system is not so simple and expensive as pure helium gas is being used with partial recovery.

To reduce the average power and to improve the dynamics of control mechanism, an alternate fast tuning mechanism has been tried out successfully [8] and presently being implemented on all the resonators of the last accelerating module of linac. In this scheme, the tuner plate is deflected initially by a mechanical course tuner operated by a stepper motor driven shaft from outside and once the mean frequency is achieved, the control is handed over to the Piezo tuner controller (figure 4). The piezoelectric actuator works in closed loop along with existing resonator control scheme to phase lock the resonator. The response time for the Piezo to correct the frequency deviation is of the order of tens of milli second. So during this short time, the deviation in frequency is very small and the extra power supplied by the amplifier is of negligible amount. Consequently the average power required by the resonator is significantly reduced so the overall power requirement problem gets solved to a major extent.

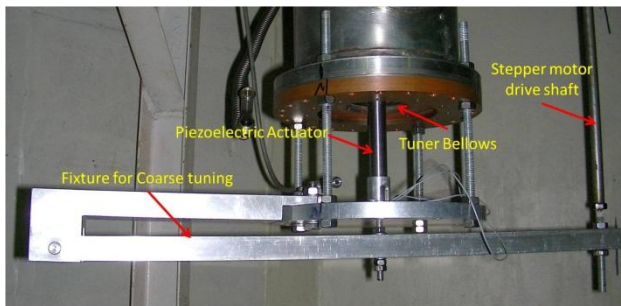


Figure 4: The Piezo-actuators are connected on two resonators of linac-3 prior to loading. The other picture shows the detail of the piezo-actuator and its accessories.

During a recent test of piezo actuator on a resonator in linac module - 3 (figure 4), an excellent and encouraging result was obtained. First, the mechanical shaft of the lever arm of the piezo tuner was adjusted to bring the resonator's frequency approximately 300 Hz above the frequency of the master oscillator as the frequency range of the piezo-actuator was measured to be 600 Hz. The voltage on the piezo actuator was set in such a way that the crystal was at its mid-point of deflection. Forward RF power within the limit of  $\sim 100$  watts was optimized to generate a field of 3.6 MV/m in over-coupled condition. In this condition the resonator was phase locked with piezo actuator as a mechanical tuner along with the electronic tuner. On incorporating of the phase locking of the resonator by the Piezo actuator, the forward power didn't change substantially. Even after intentional induction of mechanical vibration (by mild hammering) into the cryostat housing the resonator, the forward power supplied to the amplifier shot up to 180-200 watts instantly but came down to  $\sim 100$  watts almost immediately. After the success of the piezo actuator as a mechanical tuner on a resonator in linac cryostat-3, it has been decided that all the gas operated slow tuners will be replaced by the piezo actuator in all the resonators in linac module - 2 and 3.

### *The New Cooling Mechanism to Operate the Drive Coupler at Higher Temperatures*

In order to increase the accelerating fields at the time of phase locking, supply of RF power greater than 100 watts may be necessary in future. In the past, when the RF power increases beyond 125 watts or so for continuous operation, a steady increase of the temperature of the drive coupler was observed and that resulted in many operational problems [4]. To eliminate this problem, a separate cooling arrangement was designed to cool the drive coupler. A cold finger was prepared whose one end is kept at LN<sub>2</sub> temperature and the other end is brazed on the brass piece of the drive coupler (figure 5).

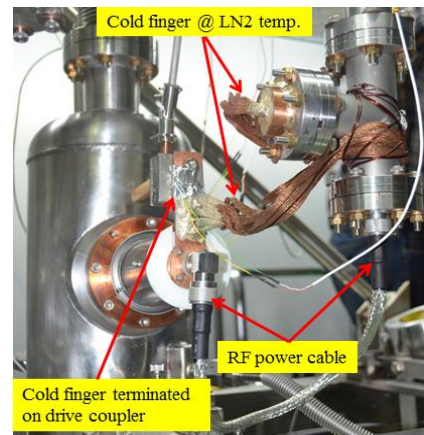


Figure 5: The additional cooling arrangement of the drive coupler at LN<sub>2</sub> temperature.

With this arrangement, the drive coupler has been successfully tested with higher RF power through a high temperature RF cable (275°C). With 270 watts of power delivered to the power coupler, the maximum temperature on the drive coupler was measured to be 317 K. When the cold finger is cooled to LN<sub>2</sub> temperature, a decrease of  $\sim 70$  K was observed within eight hours and after that the temperature remained almost constant. In the next step, the RF power was increased to 400 watts up to the maximum capacity of the RF amplifier. With cold finger kept at LN<sub>2</sub> temperature, the maximum temperature recorded on the drive coupler was 268 K. This temperature is sufficiently low for the long term operation of resonators in linac cryostat. The implementation of the new cold finger is underway on all the resonators of linac-3.

### **IMPROVEMENT IN THE LONGITUDINAL FOCUSING OF THE LINAC BEAM BY RANDOM PHASE FOCUSING OF THE RESONATOR**

In most of the superconducting linear accelerators operational worldwide, heavy ions are accelerated with the ion beam injected at a phase of 70° (or -20°) into each

independently phase locked resonator. Acceleration phase of 70° reduces the acceleration gain by 6% from the case if the beam is accelerated at 90°, but it maintains the narrow time width of the beam bunch within reasonable limits throughout the complete acceleration length of linac. However, if the number of linac resonators are too many (more than 10 or so) and the accelerated beam is delivered at a point which is far off from the exit of linac, then time width of the beam bunch starts to blow up as the beam travels further away from linac. To arrest this problem, a Rebuncher/Debuncher is used approximately halfway between the exit point of the linac and the experimental chamber to squeeze the beam in time or energy. However, the contribution of the rebuncher resonator to bunch the beam in time or energy can be reduced substantially or even eliminated completely by selecting the accelerating phases of a few resonators at 110° instead of 70°.

Table 2: Comparison Between the Reduction of Time Width of Linac Beam Between the Two Cases when all the Resonators were Kept at an acceleration phases of 70 Degree and a Combination of 70 and 110 Degree

| Acceleration Phases of resonators in linac-1 and 2  | Predicted reduction in delta_t (%) from calculation | Experimentally Measured Time width (ns) at scattering chamber | Experimental reduction in delta_t (%) from Expt. |
|---|---|---|--|
| All 70°   | -   | 2.88  | -  |
| Linac-1:<br>70, 70, 110,<br>110, 110,<br>70, 70, 70<br>Linac2:<br>70, 70, 70,<br>70, 70, 70,<br>70, 110 | 38.5  | 1.73  | 40   |

In order to verify this phenomenon which can be called as ‘Random phase focussing’, a simulation code was written to calculate the optimum combination of accelerating phases (between 70 and 110 degree) of the resonators to obtain the minimum time width of the beam bunch at the target location [9]. The simulation was done to inject the beam of 130 MeV <sup>28</sup>Si<sup>11+</sup> from Pelletron into the sixteen resonators in module 1 and 2 kept at the different field levels obtained at the time of beam acceleration. The final energy of the ion beam from Linac would be 186 MeV irrespective of the acceleration phases of the resonators kept at either 70 or 110 degree. The value of time width was calculated first at the experimental chamber ~30 meter down the line from linac

exit when the accelerating phases of all sixteen resonators were kept at 70 degree. Then the same calculation was repeated for the optimum combination of phases of the resonators between 70 and 110 degree to get the minimum value of the time width of the beam bunch. The calculated value of reduction of the time width between the two cases was verified by the experiment and the results are presented in Table-2. Now the calculation on random phase focussing is being extended to include the remaining eight resonators of the last linac cryostat. It is expected that with the combination of phase focussing on all the resonators, the work load on the rebuncher will be reduced substantially, if not eliminated completely.

### USE OF LAST ACCELERATING RESONATOR OF LINAC-1 AS THE REBUNCHER RESONATOR

Table 3: The Measured Time Width of the Linac Beam when the Last Resonator of Module-1 Kept at the Predicted Bunching Field Found by the Simulation Code

| Beam                          | Total energy (Pelletron + Linac) | Bunching field of the last linac resonator | Time width measured at Exp. Chamber (ns) |
|-------------------------------|----------------------------------|--|--|
| <sup>16</sup> O <sup>+8</sup> | 113                              | 0  | 0.84 ns                                  |
|                               |                                  | 0.4  | 0.5 ns                                   |
|                               | 106.8                            | 0.0  | 2.11                                     |
|                               |                                  | 1.7  | 0.8                                      |
|                               | 104.5                            | 0.0  | 2.68                                     |
|                               |                                  | 1.7  | 1.24                                     |
| <sup>19</sup> F <sup>+9</sup> | 124                              | 0.0  | 1.82                                     |
|                               |                                  | 2.08                                       | 0.82                                     |
|                               | 122                              | 0.0  | 1.75                                     |
|                               |                                  | 0.51                                       | 1.09                                     |
|                               | 118.8                            | 0.0  | 2.2                                      |
|                               |                                  | 1.35                                       | 1.47                                     |

The simulation code developed to study the effect of random phase focussing was used to find out whether the last resonator of module-1, could be used as the rebuncher to control the time width of the beam bunch at the experimental chamber. During beam acceleration with only the Superbuncher and linac-1 operational, <sup>16</sup>O<sup>8+</sup> and <sup>19</sup>F<sup>9+</sup> beams with fixed energy from Pelletron were accelerated through linac module - 1. In the absence of the rebuncher, the time width of the beam bunch at the experimental chamber were too large to be used for the experiments. But by applying the calculated bunching

field on the last resonator of module -1, acting as rebuncher, the time width was restricted to a value of 0.5 to 1.5 ns in all the cases [9]. That translates to a time width reduction of 33% to 62% compared to the cases when the last resonator was not used as rebuncher. The theoretically predicted bunching field which was applied on the last resonator of module - 1 and the measured time width of the beam at the experimental chamber is presented in Table-3. During the experiment, the bunching fields of the last linac-1 resonator were intentionally deviated from the calculated optimum values and time width was measured in every occasion at the experimental chamber. But the width measured for the bunching field predicted by the program was found to give minimum values in every cases.

### PRESENT STATUS OF LINAC PROJECT AND FUTURE PLAN

Presently, the Superbuncher, the first two accelerating module and the Rebuncher are fully operational and accelerated beam from Pelletron and linac are being delivered to the experimentalists to conduct scheduled experiments. The last accelerating module, linac-3 is under commissioning stage. Recently four resonators were installed in linac-3 (figure-5) and an off-line test was successfully conducted. Piezo-actuators as frequency tuner were incorporated in two out of four resonators in linac-3 and the existing gas operated tuners were connected in other two resonators. Piezo actuators were successfully tested on the resonator of linac-3. Soon, the remaining four resonators will be installed in linac-3 and Piezo tuners will be installed on all of them. Subsequently, in near future, gas operated tuners will be replaced by Piezo tuners in all the eight resonators of linac-2. After installing the remaining resonators in linac-3, an off-line test is being planned in September '12 and the beam acceleration through the complete linac will be followed immediately.

Figure 5. Four resonators installed in linac-3 prior to the cold test. (Figure 6)

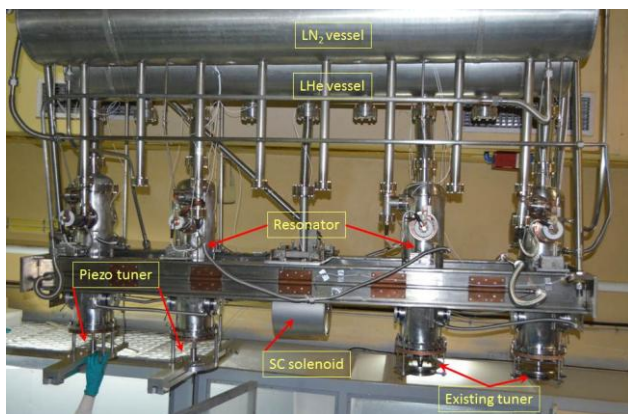


Figure 6: Four resonators installed in linac-3 prior to the cold test.

### CONCLUSION

The superconducting linac project of Inter University Accelerator Centre is on the verge of completion. Since last few years, accelerated beams from Pelletron were further accelerated by the first and second module of linac and the beams have been delivered to conduct scheduled experiments in nuclear physics and materials science. Presently the installation of resonators in the last accelerating module is underway. In a parallel development, efforts are on to improve the locking fields of the linac resonators. To achieve this, three approaches are taken up. First the vibrational damping mechanism with larger diameter of balls and their mixture are being tried out to have further reduction of the frequency window at the time of phase locking of resonator. Secondly, Piezo-based actuator is tried out successfully to decrease the correction time to bring back the frequency of a resonator to its mean value. Thirdly, to avoid any kind of heating related problem in the power coupler, a cooling mechanism has been tested successfully and this system is presently used with the commercially available 100% shielded cable which can withstand up to 275°C. With these modifications the complete superconducting linac system is expected to be fully operational by the autumn of 2012.

### ACKNOWLEDGEMENT

The authors would like to thank members of the Pelletron, beam transport, magnet and RF groups for their help and cooperation.

### REFERENCES

- [1] D. Kanjilal et al, Nucl. Instr. and Meth. A328 (1993), 97-100.
- [2] P.N.Potukuchi, S. Ghosh and K.W. Shepard, Proc. of the 1999 Particle Accelerator Conference, New York, USA, page-952.
- [3] P.N.Potukuchi, Proc. of 14th Int. Conference on RF Superconductivity (SRF2009), p - 542.
- [4] S.Ghosh, et al Physical Review Special Topic – Accelerator and Beams, 12, 040101 (2009).
- [5] A.Rai et al. Proc. of 14th International Conference on RF Superconductivity (SRF2009), p - 244.
- [6] S.Ghosh et al. Proc. of Indian Particle Accelerator Conference (InPAC 2011) at IUAC, New Delhi, Feb. 15-18, 2011 <http://www.iuac.res.in/atmol/MaKaC/confAuthorIndex.py?confId=2>
- [7] S.Ghosh, et al Physical Review Special Topic – Accelerator and Beams, 10, 042002 (2007).
- [8] B.K.Sahu et al. Proc. of International Particle Accelerator Conference (IPAC'10) Kyoto, Japan, p-2920.
- [9] S.Ghosh, Inter University Accelerator Center, New Delhi, India (ghosh64@gmail.com) – Ph.D.Thesis.

# DESIGN STUDIES FOR A NEW HEAVY ION INJECTOR LINAC FOR FAIR

B. Schlitt, G. Clemente, W. Barth, W. Vinzenz, GSI, Darmstadt, Germany

## Abstract

As the GSI UNILAC started operation in 1975, it will be more than 40 years old when the commissioning of the future Facility for Antiproton and Ion Research (FAIR) at GSI will start. To assure reliable operation for FAIR and to provide beams for a variety of experiments, three separate linacs were proposed and are under development: 1.) A dedicated 70 MeV proton linac will serve as injector for the FAIR pbar physics program. 2.) To deliver high-intensity heavy-ion beams for FAIR, the existing post-stripper linac at the UNILAC should be replaced by a new high energy heavy-ion linac with short beam pulses, low pulse repetition rate, and fixed end energy. 3.) A new superconducting cw heavy-ion linac behind the upgraded high charge state injector HLI shall provide ion beams with high duty cycle and adjustable energy in the MeV/u region for the super-heavy element program as well as for further UNILAC experiments. A conceptual design study for the second machine – a new heavy-ion linac injector for FAIR – using 108 MHz IH-type drift tube structures is presented, including a proposal to increase the ion charge states for synchrotron injection as well as a linac beam energy upgrade using 325 MHz CH structures.

## INTRODUCTION

The Facility for Antiproton and Ion Research (FAIR) presently under development at GSI in Darmstadt (Fig. 1) will provide worldwide unique accelerator and experimental facilities allowing for a large variety of forefront research in physics and applied science. The FAIR accelerators will increase the intensity of primary proton and heavy ion beams available for experiments and for the production of secondary beams by up to two orders of

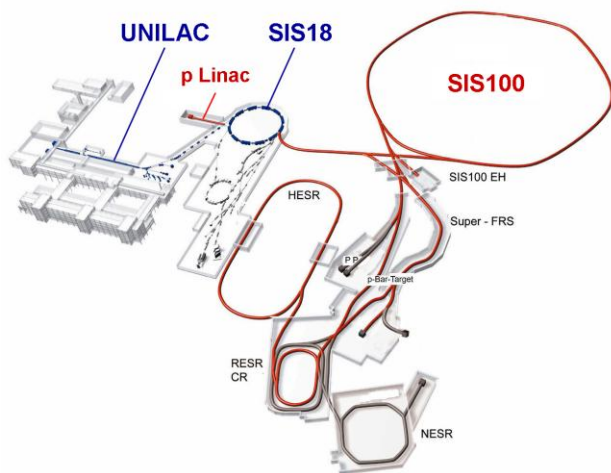


Figure 1: Sketch of the FAIR facility [1]. The existing GSI accelerators (indicated in blue) with the UNILAC heavy-ion linac and the SIS18 synchrotron will serve as injection chain for the new SIS100.

magnitude with respect to the existing GSI facility [1]. Besides the realisation of the challenging FAIR SIS100 synchrotron, various upgrades of the UNILAC linear accelerator (Fig. 2) and of the SIS18 synchrotron play a key role to achieve the FAIR design intensities, since the existing GSI accelerators will serve as injection chain for FAIR [2–7]. As major design parameters, 15 emA  $U^{28+}$  beams at 11.4 MeV/u [2] and 70 mA proton beams at 70 MeV are required for SIS18 injection.

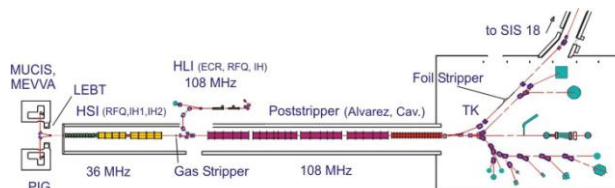


Figure 2: Layout of the present heavy-ion UNILAC accelerator at GSI and low-energy experimental area.

## Present Linac Constraints and Proposals

For high current operation of the UNILAC [2], the 36 MHz High Current Injector (HSI) [8] – comprising a 120 keV/u IH-RFQ and two IH-DTL tanks – accelerates ion beams up to  $U^{4+}$  ( $A/q \leq 59.5$ ) to 1.4 MeV/u (pre-stripper linac). After the gas stripper and the charge separation section, further acceleration to 11.4 MeV/u for synchrotron injection is provided by the 108 MHz post-stripper linac ( $A/q \leq 8.5$ ), consisting of five Alvarez DTL cavities and ten single gap resonators for fine tuning of the linac end energy.

High magnetic rigidity of the ion beams and high beam currents as needed for FAIR injection require very strong electric and magnetic fields for acceleration and focusing along the linac within short beam pulses and at low repetition rate and duty cycle.

On the other hand – contradictory to the requirements for the FAIR injector – experiments using low-energy beams in the MeV/u region behind the UNILAC, like the super-heavy element (SHE) program as well as material research, biophysics, and plasma physics experiments, are demanding ion beams with up to 100 % duty factor, resulting in very high average rf power requirements along the linac. These experiments are currently limited by the maximum duty cycle of the UNILAC of 25 % [9].

Moreover, the focusing magnets along the present post-stripper linac can be operated only in DC mode, which makes the machine inefficient in terms of short pulse operation and represents a major flexibility limitation since the focusing fields cannot be adapted to the varying needs when different ion beams have to be accelerated from pulse to pulse (diverse ion species, magnetic rigidities, and beam currents).

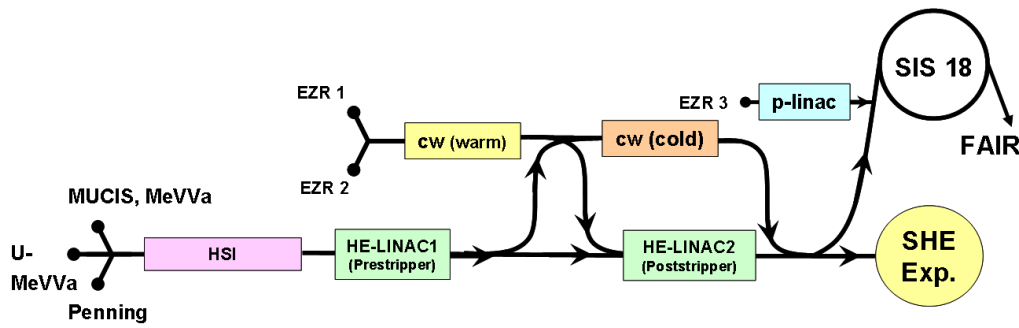


Figure 3: Proposed future GSI linac environment [4].

Finally, as the UNILAC started operation in 1975, most sections of the existing post-stripper linac will be more than 40 years old when the commissioning of FAIR will start. Due to an increased number of failures and problems at the Alvarez DTL, at the single-gap resonators, as well as at the corresponding rf systems during the last years, different proposals are under discussion to replace the post-stripper linac to allow for highly reliable operation of the future FAIR injector linac.

To fulfil the requirements of the various experiments at FAIR and behind the UNILAC, three separate linacs are proposed (Fig. 3) [4]:

1.) A dedicated 70 MeV, 70 mA, 325 MHz proton linac based on room temperature crossbar H-mode (CH) DTL cavities is under development and will serve as injector for the FAIR pbar physics program [10–11].

2.) To deliver high-intensity heavy-ion beams for FAIR, the existing post-stripper linac should be replaced by a new heavy ion high-energy (HE) linac with short beam pulses, low pulse repetition rate, and fixed linac end energy [12].

3.) A new superconducting cw heavy-ion linac [13–14] behind the upgraded high charge state injector HLI [9] should provide ion beams with high duty cycle and adjustable energy in the MeV/u region for the super-heavy element program as well as for further UNILAC experiments.

## ACCELERATION OF INTERMEDIATE CHARGE STATES

No additional stripper is used behind the UNILAC in case of high current operation. For uranium beams,  $U^{28+}$  is selected behind the gas stripper for acceleration along the post-stripper linac and in the synchrotron (FAIR reference ion). Due to the high cross sections for charge exchange processes at collisions with residual gas atoms for intermediate charge states at SIS18 energies [6], significant beam losses are generated in the synchrotron, resulting also in an increasing vacuum pressure caused by ion induced desorption during SIS operation (dynamic vacuum effects), generating over again rapidly rising beam losses. These effects caused severe intensity limitations in the SIS18. Due to a comprehensive upgrade program using dedicated low desorption charge scrapers and NEG coated vacuum chambers as well as further measures [5–7], the particle intensities extracted from

SIS18 could be increased by almost two orders of magnitude during the last years.

Since the reaction cross sections for charge exchange processes are decreasing significantly for highly charged ions, the use of higher uranium charge states for injection and acceleration in the SIS18 was investigated experimentally [6, 15] and by simulations [16]. Higher uranium charge states were produced at the UNILAC by using a foil stripper set-up at 1.4 MeV/u instead of the gas stripper [15]. Highest extracted particle intensities were achieved behind the SIS18 for  $U^{39+}$  beams [6]. In recent experiments, single particle lifetimes of almost 80 s have been measured in the SIS18 at injection energy for  $U^{38+}$ , more than two times higher as measured for  $U^{28+}$  in the same experiment ( $\approx 35$  s) [16]. For higher beam energies during SIS18 acceleration up to the SIS100 injection energy of 200 MeV/u, the lifetime enhancement for the higher charge states is even larger. These results represent a significant improvement as compared to earlier measurements of about 11 s for  $U^{28+}$  in 2010 and 3 s in earlier years [1]. In spite of that, the use of  $U^{38+}$  may be advantageous because of even higher lifetimes.

On the other hand, since the space charge tune shift in the synchrotron

$$\Delta Q_y^{sc} \propto -N \frac{q^2}{A} \frac{1}{\beta^2 \gamma^3}$$

is increasing rapidly for higher charge states  $q$ , the injection of intense  $U^{38+}$  beams into the SIS18 at the

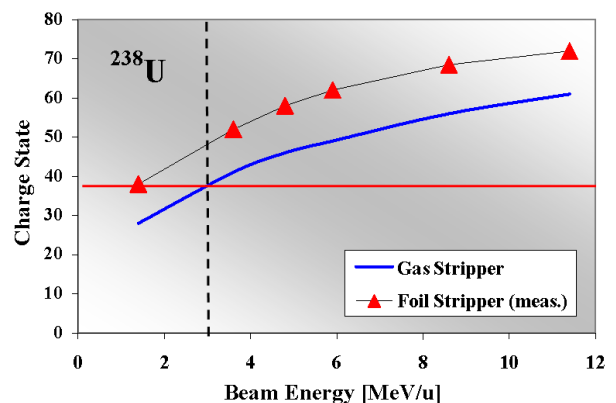


Figure 4: Main uranium charge state after stripping at different stripper materials as function of beam energy.

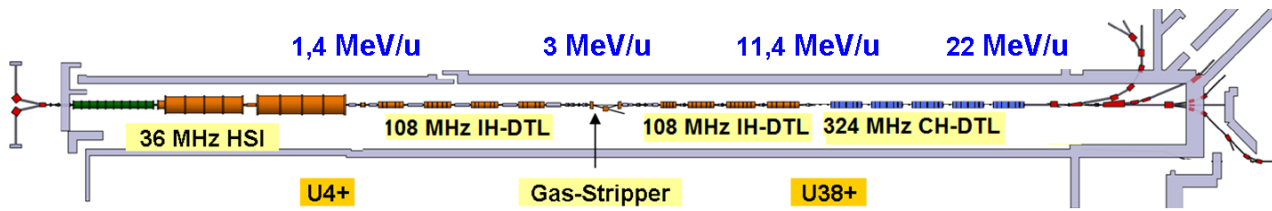


Figure 5: The investigated high-energy (HE) linac concept.

present injection energy of 11.4 MeV/u would cause a significant increase of space charge problems. Hence, the injection energy for  $U^{38+}$  beams has to be increased to about 22 MeV/u for compensation.

To verify these considerations, beam loss simulations were performed using the STRAHLSIM Code [17–18]. Preliminary results confirmed a distinct reduction of beam losses during SIS18 booster operation using  $U^{40+}$  injected into SIS18 at 23 MeV/u as compared to  $U^{28+}$  injected at 11.4 MeV/u [16]. Good agreement between simulations and measurements was achieved for  $U^{28+}$ , whereas verifications are needed for  $U^{38+}$  operation.

### CONCEPTUAL HE LINAC STUDY

Because of the increasing lifetimes for higher charge states, a linac concept using  $U^{38+}$  for synchrotron injection was investigated. Since the gas-stripper provides for a highly reliable operation, it would be preferred for future FAIR operation instead of the foil stripper used for the recent experiments. Hence, the gas stripper must be shifted to higher beam energies to achieve higher charge states with sufficient intensities (Fig. 4).

Finally, a stepwise realisation of a new heavy ion high-energy linac was proposed (Fig. 5, Table 1):

1.) Complete replacement of the existing post-stripper linac: An extension of the present high current injector HSI by four new 108 MHz IH-DTL cavities leads to a pre-stripper end energy of 3 MeV/u and to an uranium charge state around 38+ behind the gas stripper (Fig. 4). The existing gas-stripper and charge separation section could be used again at the new stripper energy but must

Table 1: Main design parameters of the investigated high-energy linac concept (for  $^{238}U$ )

| HE Linac                          | Stage 1      | St. 2        |              |
|-----------------------------------|--------------|--------------|--------------|
| Operation freq.                   | 108.4        | 325.2        | MHz          |
| Linac length                      | 53           | 29           | m            |
|                                   | pre-stripper |              |              |
| Design charge state               | 4+           | 38+          | 38+          |
| Beam energy, in                   | 1.4          | 3.0          | 11.4 MeV/u   |
| Beam energy, out                  | 3.0          | 11.4         | 22 MeV/u     |
| Magn. rigidity, out               | 14.8         | 3.1          | 4.25 Tm      |
| Max. mass / charge                | 59.5         | 6.26         | 6.26         |
| Design ion current                | 20           | 24           | 24 mA        |
| Tot. accel. voltage               | 95           | 53           | 67 MV        |
| No. of rf cavities (Bu = buncher) | 1 Bu<br>4 IH | 1 Bu<br>4 IH | 1 Bu<br>6 CH |
| No. of high-power rf amplifiers   | 5            | 5            | 6+1          |

be dismantled and must be reassembled at the new location. Further acceleration after stripping will be performed by another four 108 MHz post-stripper IH tanks up to beam energies of 11.4 MeV/u.

2.) In a second stage, a 325 MHz linac using crossbar H-mode (CH) drift-tube structures will boost the linac end energy up to 22 MeV/u within the existing UNILAC tunnel.

### Beam Dynamics

The beam dynamics of the entire HE linac is based on the KONUS concept [19], with an external magnetic quadrupole triplet lens behind each cavity. No magnets will be installed inside the cavities – both for the 108 MHz as well as for the 325 MHz sections. Particle tracking simulations were performed for the full 108 MHz linac using the LORASR code [20], starting at the HSI exit with a 20 mA  $U^{4+}$  beam [12]. The input particle distributions for the HE linac (Fig. 6) were derived from the design output particle distribution of the HSI [8]. Immediately behind the 36 MHz HSI structures a

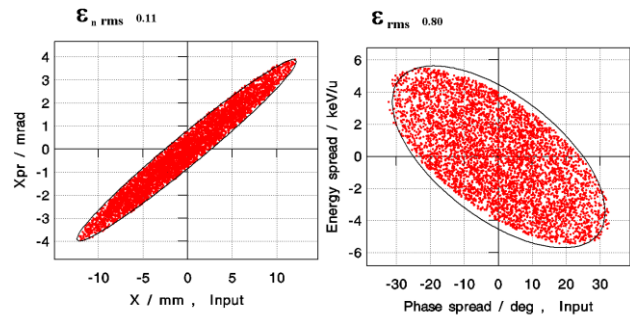


Figure 6:  $U^{4+}$  input particle distribution used for simulations of the new 108 MHz pre-stripper section starting at the HSI exit at 1.4 MeV/u.

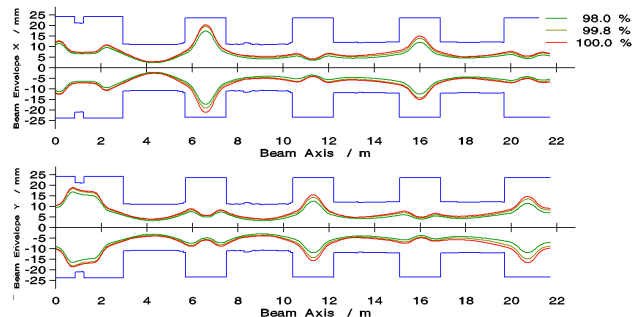


Figure 7: Transverse beam envelopes in the horizontal (top) and in the vertical plane (bottom) along the new 108 MHz pre-stripper section starting at the HSI exit.

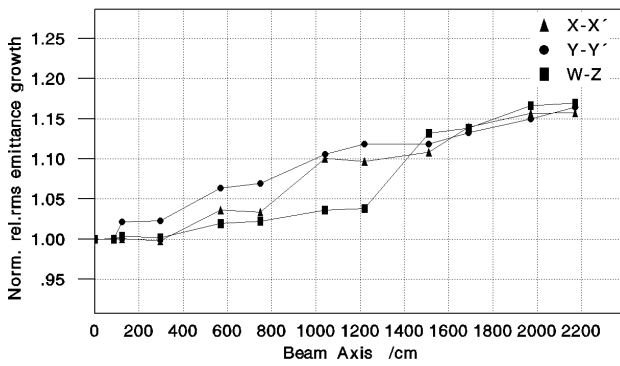


Figure 8: Relative rms emittance growth from HSI exit down to the stripper position for a 20 mA U<sup>4+</sup> beam.

powerful six gaps 108 MHz buncher will compensate the phase jump and will match the beams longitudinally for the acceleration along the 108 MHz IH linac. Transverse beam envelopes presented in Fig. 7 show that the particle dynamics and the design apertures are robust against beam losses. The relative rms emittance growth along the ~22 m long new pre-stripper section is limited to around 16 % in each phase plane as shown in Fig. 8.

*Post-stripper Linac*

Beam dynamics simulations of the new post-stripper linac included investigations of the beam energy best suited for the transition to 325 MHz CH-DTL cavities. Since the ion beams are arranged in a 36 MHz bunch structure generated by the high current injector HSI, only every ninth bucket of the 325 MHz structures can be used for ion acceleration. Hence, very high space charge forces occur due to the large bunch currents corresponding to equivalent macro-pulse currents of >200 emA for a real averaged macro-pulse current of 24 emA. Therefore, 108 MHz IH cavities are used in the investigated design up to the present UNILAC end energy.

**CAVITY DESIGN**

The HE linac study is entirely based on H-mode cavities representing the state of the art for ion acceleration in terms of rf efficiency in the low to medium β range (up to β ≈ 0.2). The very high shunt

Table 2: Main parameters of the 108 MHz IH-DTL cavities of the investigated HE linac concept (for <sup>238</sup>U)

| Cavity               | ΔW (MeV/u) | Eff. Voltage (MV) | Length (m) |
|----------------------|------------|-------------------|------------|
| Pre-Stripper (U4+)   |            |                   |            |
| IH3                  | 0.400      | 25.0              | ≈ 2.9      |
| IH4                  | 0.450      | 26.7              | ≈ 3.1      |
| IH5                  | 0.416      | 26.8              | ≈ 3.1      |
| IH6                  | 0.396      | 23.9              | ≈ 3.0      |
| Post-Stripper (U38+) |            |                   |            |
| IH7                  | 1.800      | 11.5              | ≈ 1.8      |
| IH8                  | 2.370      | 15.9              | ≈ 3.0      |
| IH9                  | 2.200      | 15.3              | ≈ 3.3      |
| IH10                 | 2.200      | 15.0              | ≈ 3.7      |

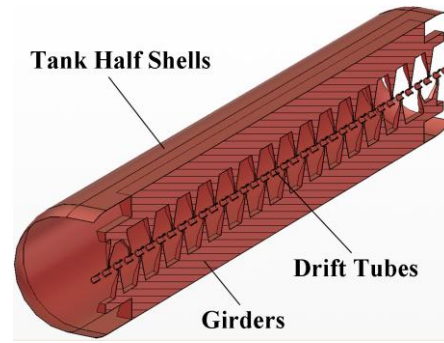


Figure 9: Simulation model of the first 108 MHz IH cavity of the presented HE linac study.

impedances of that kind of cavities allow to cover this energy range within a shorter length when compared to any other solution based on Alvarez DTL [21]. Since no quadrupole magnets need to be installed inside the drift tubes due to the KONUS beam dynamics, the rf power demands will be much lower. At the same time, highest acceleration fields and highest effective voltage gain can be achieved.

Due to the low duty cycle, room-temperature structures are planned for the new linac. Each of the eight 108 MHz IH cavities will have a length between ~3 to ~3.6 meters (Table 2). Preliminary Microwave Studio simulations indicate that the total rf power – including beam loading – will be less than 1.3 MW for each cavity. For example, Figure 9 shows a simulation model of the first IH cavity. Estimated shunt impedances of the pre-stripper structures are compared to different multi-gap structures in Fig. 10, indicating a rf power loss reduction of more than a factor of five as compared to conventional structures. For the second stage of the HE linac, 325 MHz CH-DTL structures will be used, taking significant advantage from the R&D work performed for the FAIR proton linac [11].

**RF CONCEPTS**

To achieve a sufficient reliability of the existing 108 MHz rf amplifiers from the Alvarez DTL for the

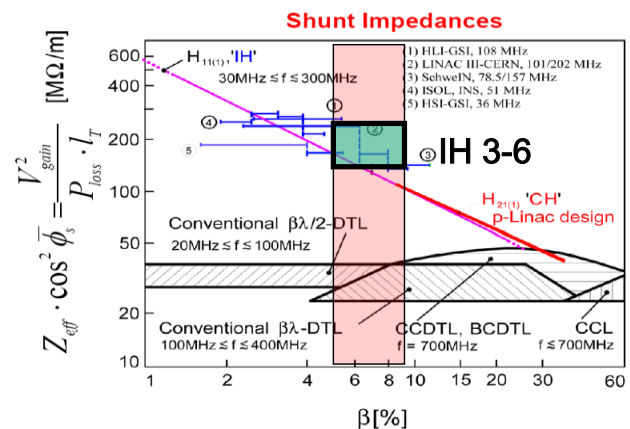


Figure 10: Estimated effective shunt impedances of the new 108 MHz pre-stripper IH cavities as compared to conventional structures and further H-mode cavities.

coming decades, an extensive, very costly, and manpower intensive overhauling would be necessary, including the replacement of many components. Hence, a complete substitution by new 108 MHz, 1.8 MW amplifiers for low duty cycle operation with short pulse length was proposed. A design study for a high-power cavity amplifier has been started recently at THALES based on the TH 558SC tetrode. 120 kW solid state amplifiers are being considered for the drivers and new digital low-level rf systems are planned.

For stage 2 of the presented HE linac study and for possible future linac energy upgrades, respectively, 325 MHz klystron amplifiers similar to those presently under development for the FAIR proton linac are proposed. Since the existing UNILAC rf gallery would be needed completely for the new 108 MHz systems, an extension of the existing building would be necessary for the 325 MHz klystron gallery.

## OUTLOOK

The HE linac concept reported here was proposed to the GSI supervisory board, but no final decision was taken. As an alternative solution, a 108 MHz IH-DTL linac for  $U^{28+}$  as direct replacement of the existing UNILAC post-stripper section is being investigated – but in contrary to the existing machine only for short pulses, low duty cycle, and fixed linac end energy. Ion charge states and beam energy at SIS18 injection would not be increased. On the other hand, the  $U^{28+}$  machine would save significant costs and efforts as compared to the  $U^{38+}$  linac concept. Only about five new IH tanks and five new rf amplifiers would be required, the gas-stripper section need not to be moved to a new position, and no extension of the rf gallery would be necessary.

Design and construction of prototype cavities for a 108 MHz IH structure and for a 325 MHz CH structure for future energy upgrades are planned. An extension of the new high-energy linac up to 100 – 150 MeV/u for direct beam injection into SIS100 maybe subject to future studies as long-term option.

Future activities will also focus on the development of alternative stripper techniques to achieve higher charge states at the present stripper position. Further experiments with foil strippers are ongoing. Beam tests of a plasma stripper set-up developed at the Institute for Applied Physics (IAP) at the Goethe-University in Frankfurt [22] are planned. This would still allow for acceleration of higher charge states for synchrotron injection even with a new post-stripper linac designed for  $U^{28+}$ .

The commissioning start of the FAIR accelerators is planned for 2017 using ion beams delivered by the existing UNILAC. Beam commissioning of the FAIR proton linac is scheduled for 2019. Afterwards, the replacement of the post-stripper section of the UNILAC is planned, while beams for FAIR operation will be provided by the proton linac and possibly by the sc cw heavy-ion linac. First ion beams from a new high energy heavy-ion linac for FAIR are expected for 2022.

## REFERENCES

- [1] O. Boine-Frankenheim, The FAIR accelerators: highlights and challenges, in: Proc. IPAC2010, Kyoto, Japan, p. 2430.
- [2] W. Barth, The injector systems for the FAIR project, in: Proc. LINAC08, Victoria, Canada, 2008, p. 31.
- [3] H. Vormann et al., Advanced UNILAC upgrade for FAIR, in: Proc. LINAC2010, Tsukuba, Japan, 2010, p. 142.
- [4] W. Barth et al., Future heavy ion linacs at GSI, in: Proc. IPAC2011, San Sebastian, Spain, p. 2550.
- [5] L. Dahl et al., Development of the intensity and quality of the heavy ion beams at GSI, these proceedings.
- [6] P. Spiller, L. Bozyk, and P. Puppel, SIS18-intensity record with intermediate charge state heavy ions, in: Proc. IPAC2011, San Sebastian, Spain, p. 2484.
- [7] P. Spiller et al., High intensity intermediate charge state heavy ions in synchrotrons, in: Proc. IPAC2012, New Orleans, USA, THPPP001.
- [8] U. Ratzinger, The new GSI pre-stripper linac for high current heavy ion beams, in: Proc. LINAC96, Geneva, Switzerland, 1996, p. 288.
- [9] L. Dahl et al., UNILAC upgrades for Coulomb barrier energy experiments, Proc. LINAC2010, Tsukuba, Japan, 2010, p. 148.
- [10] G. Clemente, et al., The FAIR proton linac: The first linac based on a room temperature CH-DTL, in: Proc. ICFA ABDW HB2010, Morschach, Switzerland, 2010, p. 115.
- [11] G. Clemente, U. Ratzinger, H. Podlech, L. Groening, R. Brodhage, and W. Barth, Development of room temperature crossbar-H-mode cavities for proton and ion acceleration in the low to medium beta range, Phys. Rev. ST Accel. Beams **14**, 110101 (2011).
- [12] G. Clemente, W. Barth, and B. Schlitt, Conceptual study of a new high energy linac at GSI, in: Proc. IPAC2011, San Sebastian, Spain, p. 2553.
- [13] S. Minaev, U. Ratzinger, H. Podlech, M. Busch, and W. Barth, Superconducting, energy variable heavy ion linac with constant  $\beta$ , multicell cavities of CH-type, Phys. Rev. ST Accel. Beams **12**, 120101 (2009).
- [14] S. Mickat et al., The sc cw linac demonstrator – 1<sup>st</sup> test of a sc CH-cavity with heavy ions, these proceedings.
- [15] W. Barth et al., High current U40+ operation in the GSI-UNILAC, in: Proc. LINAC2010, Tsukuba, Japan, p. 154.
- [16] L. Bozyk, P. Puppel, and P. Spiller, internal communication.
- [17] P. Puppel, P. Spiller, L. Bozyk, and U. Ratzinger, StrahlSim, a computer code for the simulation of charge exchange beam losses and dynamic vacuum in heavy ion synchrotrons, in: Proc. IPAC2010, Kyoto, Japan, p. 594.
- [18] P. Puppel, P. Spiller, and U. Ratzinger, Simulation of the long term beam intensity performance of the NEG-coated SIS18, in: Proc. ICFA ABDW HB2010, Morschach, Switzerland, 2010, p. 91.
- [19] R. Tiede, U. Ratzinger, H. Podlech, C. Zhang, and G. Clemente, KONUS beam dynamics designs using H-mode cavities, in: Proc. Hadron Beams 2008, Nashville, USA, 2008, p. 223.
- [20] R. Tiede, G. Clemente, H. Podlech, U. Ratzinger, A. Sauer, and S. Minaev, LORASR code development, in: Proc. EPAC2006, Edinburgh, Scotland, 2006, p. 2194.
- [21] U. Ratzinger and R. Tiede, Status of the HIIF RF linac study based on H-mode cavities, Nucl. Instr. and Meth. in Phys. Res., Sect. A **415**, 229 (1998).
- [22] C. Teske, Y. Liu, S. Blaess, and J. Jacoby, Physics of Plasmas **19**, 033505 (2012).

## HEAVY ION SUPERCONDUCTING LINACS: STATUS AND UPGRADE PROJECTS

P.N. Ostroumov [ANL, Argonne, USA]

### *Abstract*

We observe that there is an increase in the demand, by the scientific community, for accelerated CW ion beams which can be efficiently provided by SC ion linacs. This demand can be categorized into two areas: existing and new facilities. Existing facilities are being refurbished and upgraded for higher energies and beam intensities. Several new projects are under development or construction worldwide. Recently, development of new SC ion linacs has started in China, Korea and Spain. In this talk I will briefly review both the upgrade and new SC ion linac projects with a primary focus on the advances in heavy-ion linac technologies achieved at ANL in connection with the efficiency and intensity upgrade of ATLAS.

**CONTRIBUTION NOT  
RECEIVED**

## OVERVIEW OF THE RISP SUPERCONDUCTING LINAC

D. Jeon, Y. Chung, H.J. Kim, S.K. Kim [IBS, Daejeon, Republic of Korea]  
E.-S. Kim [KNU, Deagu, Republic of Korea]  
J.-W. Kim [NCC, Korea, Kyonggi, Republic of Korea]  
Y.Y. Lee [BNL, Upton, Long Island, New York, USA]

### *Abstract*

The Rare Isotope Science Project (RISP) got launched December 2011 which consists of In-Flight Fragmentation Facility and ISOL facility, providing unique research opportunities in broad range of sciences. The superconducting driver linac can accelerate up to 200 MeV/u for uranium beam and up to 600 MeV for proton beam. The ISOL post linac which is also a superconducting linac. Design parameters and choices are presented.

**CONTRIBUTION NOT  
RECEIVED**

**STATUS AND UPGRADE PROJECT OF HIRFL**

G.Q. Xiao, Y. He, X. Ma, M.T. Song, J.W. Xia, H.S. Xu, J.C. Yang, Y.J. Yuan, H.W. Zhao, X. Zhou [IMP, Lanzhou]

*Abstract*

Heavy Ion Research Facility at Lanzhou is a heavy ion accelerator complex for nuclear, atomic, and biology application research activities. It is the biggest heavy ion accelerator facility in China, consisting two cyclotrons in series as injector and two cooling storage rings (CSRm and CSRe) as main synclotron and experimental spectrum separately. The species from P to U were accelerated in the machine, And the maximum energy is 1 GeV/u for C. The experimetal teminals are on meterial, biology, canser therapy, SHE, RIB, mass measurement, inner target, and so on. To improve beam intensity and available beam time, a linear injectors SSC-LINAC were proposed in 2009. It consists a 4-rod RFQ and 4 IH-DTL tanks. The RFQ, IH-DTL, and 60 kW solid state amplifier for SSC-LINAC are tested priliminaryly. The operation status and progress of upgrade projects of HIRFL are presented in the paper.

**CONTRIBUTION NOT  
RECEIVED**

# NEW DEVELOPMENTS IN LOW-Z GAS STRIPPER SYSTEM AT RIKEN RADIOACTIVE ISOTOPE BEAM FACTORY (RIBF)

H. Okuno\*, N. Fukunishi, A. Goto, H. Hasebe, H. Imao, O. Kamigaito, M. Kase, H. Kuboki  
RIKEN, Nishina Center for Accelerator-Based Science, Hirosawa, Wako 351-0198, Japan

## Abstract

The RIKEN radioisotope beam factory (RIBF) has been successfully operated for more than five years as the first next-generation exotic beam facility after the extraction of the first beam at the end of 2006. Continual development efforts in these five years have led to improved performance of the accelerators, thereby leading to increase in the intensity of the various heavy-ion beams that have been produced. Furthermore, the operation of a new 28-GHz superconducting electron cyclotron resonance (ECR) ion source and a new injector linac was started from October 2011 to overcome the difficulty in increasing the uranium beam intensity that is currently far below our goal of 1  $\mu\text{A}$  ( $6 \times 10^{12}$  particles/s). However, the most serious problem, which is the design and implementation of a charge stripper for high-power uranium beams, has thus far remained unsolved, despite extensive R&D studies on strippers using large foils mounted on a rotating cylinder and the study of a  $\text{N}_2$  gas stripper. A gas stripper is free from problems related to lifetime issues and uniformity in stripper thickness, although the equilibrium charge state in such a stripper owing to the absence of the density effect. These merits of gas strippers have motivated us to develop a low-Z gas stripper to achieve a higher equilibrium charge state even in gases, by virtue of suppression of the electron capture process in low-Z gas. In this light, we carried out the following R&D programs. The first one included the measurement of the electron-loss and electron-capture cross sections of uranium ions in He gas to extract the equilibrium charge state. The second study obtained measurements of charge distributions and energy spreads using thick layers of windowless He gas targets. The results of these studies were satisfactory, and it was decided to practically construct the proposed machine for He gas stripping. We constructed and installed the new He gas stripper for the operation of an uranium beam in January 2012. Tests using uranium beams are in progress before the the uranium beam series, which is scheduled for the coming autumn 2012.

## INTRODUCTION

### *RI Beam Factory*

The RIKEN Nishina Center for Accelerator-Based Science constructed the Radioisotope Beam Factory (RIBF) [1] with the aim of realizing a next-generation facility that

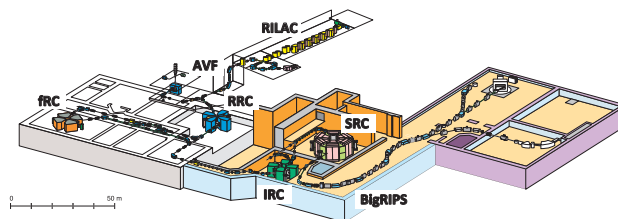


Figure 1: Bird's eye view of RI Beam Factory.

can produce the most intense RI beams in the world at energies of several hundred mega-electronvolts per nucleon over the entire range of atomic masses. The RIBF facility includes an accelerator complex that can accelerate ions over the entire range of masses and deliver 80-kW uranium beams at an energy of 345 MeV/u. Figure 1 shows a bird's eye view of the RIBF. The section on the left indicates the old facility that was completed in 1990. Many experiments have been carried out with light-ion RI beams using the four-sector K540-MeV RIKEN ring cyclotron (RRC) with two injectors, the RIKEN linear accelerator (RILAC), and the AVF cyclotron. The feasibility of conducting such light-ion experiments is enabled by the fact that the RRC can accelerate relatively light ions up to 100 MeV/u, which is the value of the lower limit for RI beam production. In order to expand the mass range for RI beam production up to that of uranium, three ring cyclotrons, the fixed-frequency ring cyclotron (fRC), the intermediate-stage ring cyclotron (IRC), and the superconducting ring cyclotron (SRC) were designed and constructed as energy boosters for the RRC.

The design and construction of the RIBF accelerators was begun in 1997, and the accelerator building was completed at the end of March 2003. In November 2005, an important milestone was reached; the superconducting sector magnets for the SRC were successfully excited at the maximum field level. The first beam was obtained on December 28, 2006 [2]. Many improvements have since been carried out to increase the beam intensity and to commission new beam species to meet the requirements of different experiments. Furthermore, the operation of the new injection system that consists of a 28-GHz superconducting ECR ion source (SC-ECRIS) [3] and a linac (RILAC2) [4] was started in October 2011 to overcome the difficulty in increasing the uranium beam intensity, whose current value is far below our goal of 1  $\mu\text{A}$  ( $6 \times 10^{12}$  particles/s) [5]. The SC-ECRIS was designed to have a large plasma vol-

\* okuno@riken.jp

ume of  $1100 \text{ cm}^3$  and to provide a flat magnetic field distribution in the central region by exciting the corresponding solenoid independently [6]. The RILAC2 is designed to efficiently accelerate ions with a mass-to-charge ratio of 7, thus aiming at the production of heavy ions such as  $^{84}\text{Kr}^{13+}$ ,  $^{136}\text{Xe}^{20+}$ , and  $^{238}\text{U}^{35+}$ , up to an energy of 670 keV/nucleon. It mainly consists of an RFQ linac based on the four-rod structure and three drift-tube linacs (DTLs) based on a quarter-wavelength resonator (QWR).

Table 1 lists the beams accelerated at maximum intensity thus far. These beams have been used in many nuclear experiments including that of the discovery of 45 new isotopes [7], the study of the halo structure and large deformation of extremely neutron-rich Ne isotopes [8, 9] and measurements of the  $\beta$ -decay half-lives of very neutron-rich Kr to Tc isotopes on the boundary of the r-process path, thereby indicating fast r-matter flow [10]. Our goal is to achieve a beam intensity of 1  $\mu\text{A}$  for the entire atomic range. This target intensity has been achieved for He and O. The beam intensity of Ca is 415 pA which is the current world record. The beam intensities of very heavy ions such as Xe and U ion are still relatively small; however, these intensities are increasing due to the operation of the new injector system from October 2011. Further developments in SC-ECRIS are expected to increase the U and Xe beam intensities up to 100 pA in the next few years, which clearly indicates that the problems with respect to the charge strippers for uranium acceleration will be more severe.

Table 1: List of beams accelerated at RIBF accelerator complex along with corresponding maximum beam intensity achieved.

| Ion                    | Energy<br>(MeV/u) | Intensity<br>(pA) | Date     |
|------------------------|-------------------|-------------------|----------|
| polarized $^2\text{H}$ | 250               | 120               | May 2009 |
| $^4\text{He}$          | 320               | 1000              | Oct 2009 |
| $^{14}\text{N}$        | 250               | 80                | May 2009 |
| $^{18}\text{O}$        | 345               | 1000              | Jun 2010 |
| $^{48}\text{Ca}$       | 345               | 415               | May 2012 |
| $^{70}\text{Zn}$       | 345               | 100               | Jul 2012 |
| $^{86}\text{Kr}$       | 345               | 30                | Nov 2007 |
| $^{124}\text{Xe}$      | 345               | 27                | Jun 2012 |
| $^{238}\text{U}$       | 345               | 3.5               | Dec 2012 |

### Charge Strippers for Uranium Acceleration in FAIR, RIBF, and RIBF

Charge strippers in an accelerator complex play an essential role in breeding the required state of a given ion. The charge state  $Q$  is related to the in the equation of motion of the ion as below:

$$\frac{dv}{dt} = \frac{Q}{M}(\mathbf{E} + \mathbf{v} \times \mathbf{B}) \quad (1)$$

Here,  $\mathbf{v}$ ,  $M$ ,  $\mathbf{E}$  and  $\mathbf{B}$  denote the ion velocity, ion mass, electric field and magnetic field, respectively. Therefore  $Q$  is the sensitivity to  $\mathbf{E}$  and  $\mathbf{B}$ , which contribute to beam acceleration, bending, or focusing. The charge state of the ion is a function of projectile energy (Fig. 2) after being passed through a sufficiently thick stripper to reach a state of equilibrium in where electron loss and capture are balanced.

The general requirements of charge strippers are as follows. Firstly, a high charge state is preferred in order to reduce the total accelerating voltage and cost. In this sense solid or liquid strippers are desirable because the density effect in these states can provide approximately 20% higher charge states compared to that for gas. Secondly, the stripping efficiency should be as high as possible although the typical efficiency is around 20%. It is to be noted at this stage that using a large number strippers can decrease the beam intensity to zero. Thirdly, a stripper should possess longevity and operational durability. In particular lifetime-related problems are critical to high-power beam operation because the lifetime of the stripper is anti-proportional to the irradiated beam intensity. Finally the thickness of the stripper should be uniform. Non-uniformity in stripper thickness generates additional energy spread or emittance growth in the longitudinal direction, and this can cause undesirable beam loss in the succeeding accelerators stages.

Table 2 lists the shows specifications of the charge strippers required for the three primary uranium accelerators installed in FAIR, FRIB, and RIBF along with their technical implementation challenges. The accelerator in FAIR accelerates uranium ions up to 1500 MeV/u using synchrotrons. One stripper is installed at the 1.4 MeV/u ion energy stage to increase ion charge from 4+ to 28+ as shown in Fig. 2. The peak power of the pulsed beam is about 1.5 MW at this stripper. The charges are stripped by  $\text{N}_2$  gas introduced by a supersonic gas jet. The acceleration of intermediate charge state ions such as  $\text{U}^{28+}$  ions is very essential to reduce the effect of space charge forces. This reduction allows for higher beam intensities. Furthermore the accelerator at FAIR is free from any problems with respect to charge stripping of ions with energies of around 10 MeV/u; in general, charge stripping is potentially problematic in this energy region. However, the FAIR accelerator faces the technical challenge of dynamic vacuum. Intermediate charge state heavy ions such  $\text{U}^{28+}$  ions are exposed to a high probability of charge exchange due to collisions with residual gas molecules during their acceleration. Since the charge exchange process changes the ions' magnetic rigidity, the involved ions are lost behind dispersive elements, and an energy-dependent gas desorption takes place. The desorbed gas is another source of the charge exchange. The FRIB accelerates uranium ions up to energies of 200 MeV/u using SRF linacs. One stripper is installed at the 16.3 MeV/u ion energy stage to increase charge from 33.5+ to 78+ on average as shown in Fig. 2. Nearly 80% of the input ions can be gathered at the output using the multi-charge acceleration technique [11]. The average beam power at the stripper is about 40 kW. A liquid

Table 2: Charge stripper specifications for uranium acceleration at FAIR, FRIB, and RIBF. The term PW in the table denotes 'plasma window'.

| Item                       | FAIR                                       | FRIB   | RIBF   |
|----------------------------|--|--|--|
| Final energy               | 1.5 GeV/nucleon                            | 200 MeV/u  | 345 MeV/u  |
| Type of accelerator        | Synchrotron                                | SRF linac  | Cyclotron  |
| Number of charge strippers | 1  | 1  | 2  |
| Stripping energy           | 1.4 MeV/u                                  | 16.3 MeV/u   | 11 and 51 MeV/u  |
| Charge state               | 4→28                                       | 33, 34→76-80   | 35→(71/65)→86  |
| Stripping efficiency       | ~14%                                       | ~80%   | ~5%  |
| Beam power at stripper     | 1.5 MW (pulsed)                            | 40 kW  | 7.5 kW   |
| Type of stripper           | N <sub>2</sub> gas<br>(supersonic gas jet) | Liq. Li film (baseline)<br>He gas with PW<br>(alternative) | C-foil → He gas<br>(1st stripper)<br>C-foil (2nd stripper) |
| Technical challenge        | Dynamic vacuum                             | Liq. Li film and PW  | He gas confinement   |

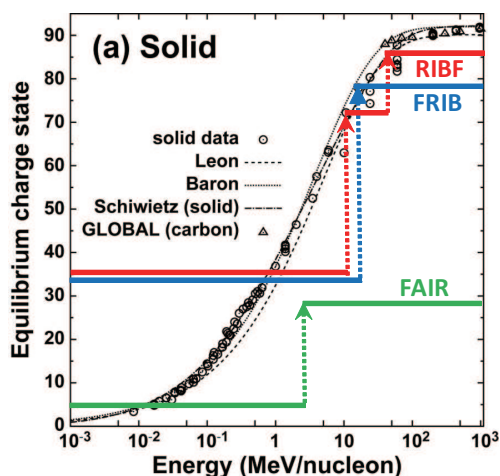


Figure 2: Charge evolutions in uranium acceleration for FAIR, FRIB and RIBF as a function of projectile energy with equilibrium charge state.

lithium film [12] has been adopted as baseline choice of stripper. In order to make liquid lithium film, a rounded lithium jet from a nozzle is impacted on the edge of the deflector. The stability of the film has been successfully demonstrated under actual operating conditions. The alternative stripper available for use is the He gas stripper [13] sandwiched between two plasma windows [14]. The plasma window can reduce conduction by a factor of about 20, thereby leading to improved He gas confinement. The operation of the system has been successfully demonstrated with a window aperture of 2 mm. Scientists at the FRIB facility are attempting to increase beam aperture from 2 mm to more than 6 mm. The RIBF accelerates uranium ions up to 345 MeV/u via the use of cyclotrons. Two charge strippers are installed to increase charge from 35+ to 86+ as shown in Fig. 2. The stripping efficiency is extremely low because of the adoption of the two-step stripping approach. In the rest of the paper, we examine the charge strippers for use in the RIBF.

### CHARGE STRIPPER PROBLEM FOR URANIUM ACCELERATION AT RIBF

Figure 3 shows the RIBF acceleration scheme for uranium beams with the use of two strippers. Uranium beams from the new injector system are accelerated using four cyclotrons, namely, RRC, fRC, IRC, and SRC, up to energies of 345 MeV/u. The first stripper is located behind the RRC, at the ion energy stage of 11 MeV/u, and the second one is located behind the fRC, at the ion energy stage of 51 MeV/u. Carbon foils are used as strippers in both cases. The typical thicknesses of the foils for the first and second strippers are 300 μg/cm<sup>2</sup> and 17 mg/cm<sup>2</sup>, respectively. The problem associated with the first stripper is extremely grave from the viewpoint of our operational experiences. Carbon foils commercially available are currently being used for the first stripper. The carbon foils clearly show radiation damage, and the momentum spread of the beam after it passes through the stripper becomes wider after beam irradiation. Their typical lifetime is about 12 h at intensities of 1-2 eμA. Carbon foils of identical thicknesses are being developed at RIKEN, and the quality of these foils which is approaching that of the commercially available ones [15]. Table 3 lists the requirements of the first stripper with the performances of the carbon foils. As per beam acceleration requirements, firstly, the charge state at this stripper stage should be more than 69+, which is the lowest acceptable charge state with respect to the succeeding cyclotron fRC. Secondly, from our operational experiences, we hope that a stripper's lifetime should be more than one week at a beam intensity of 100 eμA. Thirdly, the level of non-uniformity in the stripper thickness should be less than 10%. The performance of the carbon foils (listed in Table 3), clearly shows that a stripper with a considerably longer lifetime is required for consistent accelerator operation. Therefore, R&D programs focusing on the up-gradation of the first stripper were initiated from 2008.

First, we began conducting irradiation tests on a stripper consisting of a large foil put on a rotating cylinder, which was developed by Ryuto et al. [16], in order to expand the

Table 3: Summary of R&amp;D studies on first charge stripper for uranium acceleration in RIBF

| Item                        | Value                | C-foil            | Rotating C-foil      | N <sub>2</sub> gas | He gas |
|-----------------------------|----------------------|-------------------|----------------------|--------------------|--------|
| Charge                      | ≥69                  | 71                | 71                   | 56                 | 65     |
| Lifetime                    | ≥1 week (at 100 eμA) | 12 h (at 1-2 eμA) | 3-4 days (at 10 eμA) | long               | long   |
| Non-uniformity in thickness | < 10%                | ~30%              | >30%                 | 0                  | 0      |

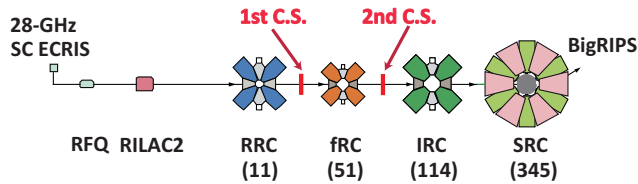


Figure 3: Acceleration scheme for uranium beams using two strippers.

irradiation area, with the objective of realizing long lifetimes. We placed a foil with a diameter of 100 mm on the cylinder, which could be rotated in beam vacuum. The first sample tested in 2008 malfunctioned within a short interval about 15 min. We performed some tests to determine why the rotating foil was prematurely damaged. We found that very slowly (0.05 rpm) rotating carbon nanotube (CNT)-based foils can survive for three or four days at intensities of 10 eμA. Some foil sections were missing after three or four days and the foil required replacement. However, despite the above-mentioned issues, this stripping system was successfully used in the uranium beam series the last year when the RILAC2 became operational as an injector.

Next, we initiated the development of gas strippers. A gas stripper is free from lifetime-related problems although it provides a lower equilibrium charge state than a carbon foil due to absence of the density effect. We did not have data on the equilibrium charge state in N<sub>2</sub> gas, and no empirical formulae are currently available to predict the equilibrium charge state correctly. Therefore, we measured the charge state at 11 MeV/u using a gas target system with a differential pumping system that was formerly used for nuclear experiments [17]. The measured equilibrium charge state in N<sub>2</sub> was 56+, which is far below that in a carbon foil (71+), thereby suggesting that the gas stripper cannot be used for uranium because the acceptable charge state for the fRC is larger than 69+.

Details of the two R&D studies on the charge stripper are summarized in Table 3. The lifetime of the rotating foil is not sufficiently long because we expect an increase in the beam intensity in future beam accelerations. The beam quality after the beam passes through the stripper is quite poor, thereby suggesting that the non-uniformity in the stripper thickness is larger than 30%. In contrast, the lifetime of the gas stripper is sufficiently large, and its uniformity in terms of thickness is good, although the equilibrium charge state is so low that fRC cannot accept the U ions. Therefore, the merits of using a gas stripper moti-

vated us to develop a low-Z gas stripper that may provide higher charge states even in gas.

## R&D STUDIES ON LOW-Z GAS STRIPPER

The equilibrium charge state is determined by the competition between the e-loss and e-capture processes of the ions. The capture cross sections depend strongly on the ion velocity  $V_p$  compared with that of the target electrons. The e-capture phenomenon is particularly highly suppressed because of poor kinematical matching when the ion velocity significantly exceeds that of the 1s electrons,  $V_{1s}$ , where 1s electrons are the fastest-moving target electrons. Such suppression of e-capture is expected in the case of low-Z targets or high ion velocity, because  $V_{1s}$  is approximately equal to  $Z/137$ , thereby resulting in a higher equilibrium charge state for low-Z values or large ion velocities. In fact, a substantial increase in the equilibrium charge state is observed in certain experimental data on the equilibrium charge state or effective charge at intermediate energies in low-Z regions [18, 19, 20].

Table 4 summarizes the reaction conditions under which charge enhancement of the equilibrium charge state in the low-Z region is observed, along with the parameters of  $V_p/V_{1s}$  (the relative projectile velocities with respect to the K-shell electrons) obtained from references [18, 19, 20]. This table also lists the parameters for the reactions for which cross-section measurements were performed in He to obtain the equilibrium charge states. These parameter values show that charge enhancement can be expected in our target reaction [U + He (gas) at 11 MeV/u]. Table 4 further lists the parameters for reactions for which equilibrium charge states were measured in N<sub>2</sub> gas; lower charge states than those obtained with carbon foils were obtained in our previous study, owing to the absence of the density effect [17, 21].

Figure 4 shows the e-loss and e-capture cross sections calculated using the binary encounter model [22] and Schlachter's formula [23] as a function of the charge state for H<sub>2</sub>, He, and N<sub>2</sub>. The two lines for each case intersect at the equilibrium charge state. The figure clearly shows that higher charge states are obtained in gases with Z values lower than that of N<sub>2</sub> gas. There are no data on the equilibrium charge state of uranium in a low-Z gas in this energy region mainly because of the difficulty in confining low-Z gas without using a window. For example, our gas stripper system, mentioned in the previous section, can confine only 0.015 mg/cm<sup>2</sup> of He, which is not sufficient for U ions to reach their equilibrium at 11 MeV/u, while

Table 4: Reactions for which enhancement of equilibrium charge is observed in low-Z target region. The definition of  $V_p/V_{1s}$  is given in the text. The lower part of the table lists the reactions for which equilibrium charge state measurements were carried out in this study and those obtained from references of [17, 21].

| Reaction            | Energy (MeV/u) | $V_p/V_{1s}$ | Ref. |
|---------------------|----------------|--------------|------|
| Ar + H <sub>2</sub> | 1.25           | 7.1          | [18] |
| U + He              | 22             | 14.9         | [19] |
| U + N <sub>2</sub>  | 56             | 6.8          | [20] |
| U + He              | 11             | 10.5         |      |
| U + He              | 14             | 11.9         |      |
| U + He              | 15             | 12.3         |      |
| U + N <sub>2</sub>  | 11             | 3.0          |      |
| U + N <sub>2</sub>  | 14             | 3.4          |      |
| U + N <sub>2</sub>  | 15             | 3.5          |      |

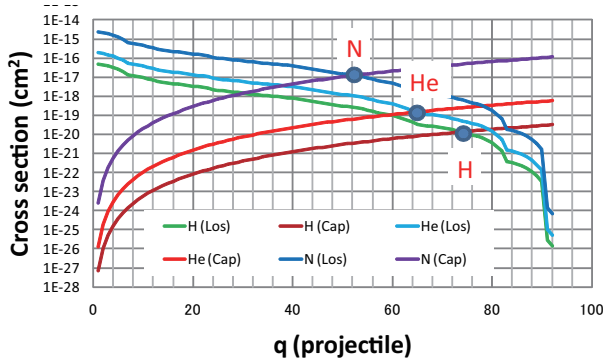


Figure 4: Simple estimation of cross sections for e-loss and e-capture in N<sub>2</sub>, He, and H<sub>2</sub>.

it can confine 1.3 mg/cm<sup>2</sup> of N<sub>2</sub>. Hence, we measured the cross sections of the loss and capture of a 1s electron as a function of the charge state of uranium ions to extract the equilibrium charge from the intersection point of the loss and capture curves.

### Measurements of e-Loss and e-Capture Cross Sections

The experiment to measure the e-loss and e-capture cross sections was conducted at the RIBF using the RILAC and RRC. A schematic of the experimental setup is shown in Fig. 5. Beams of 11 MeV/u <sup>238</sup>U<sup>35+</sup>, 14 MeV/u <sup>238</sup>U<sup>41+</sup>, and 15 MeV/u <sup>238</sup>U<sup>41+</sup> were extracted from the RRC. The incoming ions passed through a carbon foil located in front of a bending magnet, which was used to select the individual projectile charge state,  $Q_i$ . The thickness of the carbon foil was optimized to obtain the maximum intensity of the charge state. Each beam was directed through a windowless, differentially pumped He gas cell. After emerging from the gas cell, the beams passed through a second bending magnet into a Faraday cup (FC) at point F41 in Fig. 5.

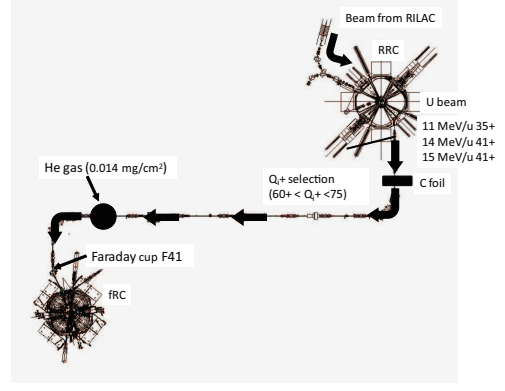


Figure 5: Schematic of experimental setup used for measurement of cross sections of e-loss and e-capture in RIBF beamlines.

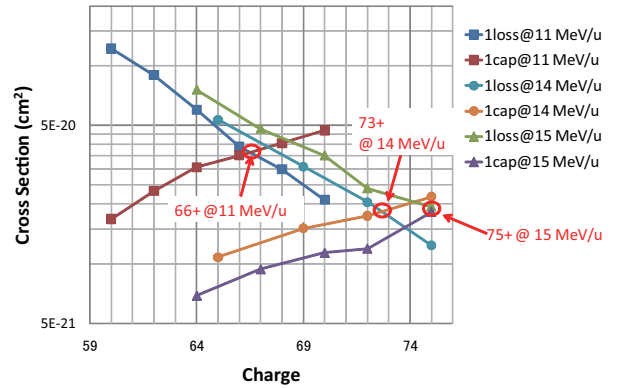


Figure 6: Measured cross sections of e-loss and e-capture as a function of the charge state of uranium ions at 11, 14, and 15 MeV/u in He gas. The cross sections were extracted assuming the thickness of the gas cell to be 13.27  $\mu\text{g}/\text{cm}^2$ .

The FC measured the intensity of the beam current of the charge state for e-loss ( $Q_i + 1$ ), e-capture ( $Q_i - 1$ ), and no reaction ( $Q_i$ ). The pressure of the target He gas was monitored by using a Baratron pressure transducer, and the gas flow was regulated by means of an automated control valve and a flow controller. Further details of the experimental setup can be found given in reference [17]. The cross section of e-loss,  $\sigma_{loss}$ , and that of e-capture,  $\sigma_{capture}$ , were obtained using the following equations:

$$\sigma_{loss} = \frac{1 I(Q_i + 1)}{t \sum I(Q_m)} \quad (2)$$

$$\sigma_{capture} = \frac{1 I(Q_i - 1)}{t \sum I(Q_m)} \quad (3)$$

where  $t$  denotes the gas layer thickness and  $I(Q)$  denotes the beam intensity of ion charge  $Q$  at F41.

The intensity at F41 was normalized by the intensity measured by an FC located upstream of the gas cell in order to cancel the fluctuation in the beam intensity from the RRC. During the measurement, the cell pressure was maintained at a value of 0.56 kPa. At this pressure, the thickness

of the gas layer of the stripper was measured to be  $13.27 \pm 1.81 \mu\text{g}/\text{cm}^2$  using  $\alpha$ -rays from  $^{241}\text{Am}$ .

Figure 6 shows the measured cross section as a function of the charge number of uranium ions at 11, 14, and 15 MeV/u. The absolute values of the cross sections shown in Fig. 6 have a deviation of 13.6%, although the relative values are accurate because the cross sections were extracted assuming the thickness of the gas layer to be the mean of the measurement values obtained as above. The data show that the cross section of the e-capture largely depends on the beam energy, while the e-loss cross section does not depend as much on the beam energy. Because the contribution of multiple electron transfer in He is very small [24], the intersection of the two lines gives a good approximation of the equilibrium charge state. The intersection points show charge state values of 66, 73, and 75 at 11, 14, and 15 MeV/u, respectively. Table 5 lists the equilibrium charge states in He, N<sub>2</sub>, and C. The equilibrium charge state in He is obviously larger than that in N<sub>2</sub> by more than ten and is close to that in C.

Table 5: Equilibrium charge states in He, N<sub>2</sub>, and C at 11, 14, and 15 MeV/u. The data for N<sub>2</sub> and C were taken from references [17, 21].

| Material       | Q <sub>e</sub> @11<br>(MeV/u) | Q <sub>e</sub> @14<br>(MeV/u) | Q <sub>e</sub> @15<br>(MeV/u) |
|----------------|-------------------------------|-------------------------------|-------------------------------|
| He             | 66                            | 73                            | 75                            |
| N <sub>2</sub> | 56                            | 61                            | 62                            |
| C              | 72                            | 76                            | 77                            |

### *Measurements of Charge Distributions and Energy Spread using Thick He Gas Targets*

The measurement results for e-loss and e-capture cross sections show that a low-Z gas stripper can be used to realize a higher charge state of uranium. However, the difficulty in the confinement of low-Z gases still remains due to their tendency to quickly disperse. As mentioned in the previous subsection, the existing gas stripper can confine only  $0.015 \text{ mg}/\text{cm}^2$  (0.7 kPa) of He, while it can confine  $1.3 \text{ mg}/\text{cm}^2$  of N<sub>2</sub>. A simple estimation shows that approximately  $1 \text{ mg}/\text{cm}^2$  of He or H<sub>2</sub> is necessary to achieve a higher charge state, thereby suggesting the necessity of using a new device to solve this problem. At this state, there are two options in terms of constructing a new device. The first one is the use of plasma windows, which has been described in the introduction section of this paper. We began the R&D studies on the use of plasma-window-contained strippers with A. Herschovitch because implementation of plasma window strippers requires special techniques in terms of design and operation. The plasma window was successfully ignited in October 2011 at the RIKEN site. The second option is to use large mechanical booster pumps (MBPs) to confine low-Z gas. Such MBPs are commercially available. Hence, we initiated He

gas confinement at a volume of about  $1 \text{ mg}/\text{cm}^2$  to measure the charge distribution and energy spread [25, 26].

Two gas strippers were prepared in order to measure the stripping performance of He and H<sub>2</sub> with cell lengths of 8 m and 0.5 m as shown in Fig. 7. The cell length was determined by the power of the differential pumping system that was available at that time. Figure 8 summarizes the measured charge evolutions in He gas as functions of the gas layer thickness. The charge is saturated around 65+, and the confinement value of  $0.71 \text{ mg}/\text{cm}^2$  was selected as the optimal operational point. The fraction of 65+ is about 21% at the operational point. The energy spread after the beam was passed through a layer of  $0.7 \text{ mg}/\text{cm}^2$  of He gas was measured to be preliminary around 0.4%. Although the thickness of the He gas layer is completely uniform, the energy spread is not zero due to charge exchange straggling. The energy straggling originates from the charge dependence of the energy loss and the finite width of the charge state distribution in the charge stripper. Further details are available in [27]. For the purpose of comparison, the energy spread after the beam was passed through conventionally used C foils with a thickness of  $300 \mu\text{g}/\text{cm}^2$  was measured to be preliminary around 0.7%.

## COMMISSIONING STATUS OF MACHINE FOR HE GAS STRIPPING

The measured data described in the previous section has enabled the conclusion that the He gas charge stripper can be used for practical operation by increasing the maximum bending power of the fRC to accept U<sup>65+</sup> ions though issues such as heat generation and removal and the use of a He gas recycling system require to be solved. Our choice of the new He gas stripper [28] can confine 7 kPa of He gas over a cell length of 50 cm. The total thickness of the He gas layer is  $0.7 \text{ mg}/\text{cm}^2$ . About  $300 \text{ m}^3/\text{day}$  of He gas can be circulated using 21 pumps. The stripper has a unique recycling system where the outlet of the mechanical booster pump is returned to the gas cell chamber directly. Eight order pressure reduction from 7 kPa to  $10^{-5}$  Pa can be realized in order to connect the gas cell with the beam lines. Beam aperture is more than 10 mm. This system has been installed on the beam line in January, and several offline tests have been completed. Tests with U beams are in progress for a uranium beam series scheduled in the autumn of 2012. Until this time, the following issues need to be continually checked, though no major problems have been encountered thus far. Firstly, the level of impurities such as oil and water have appeared to be kept at minimum because no change in the charge distribution has been observed. Secondly, in the design phase, we were concerned with high-power beams causing "holes" in the gas due to heat generation. However, there has been no sign of this problem from the viewpoint of the charge distribution and energy spread observed thus far. Thirdly, the He gas recycling system has been working satisfactorily, and there has been no He gas loss. In the recycling system, 98% of He

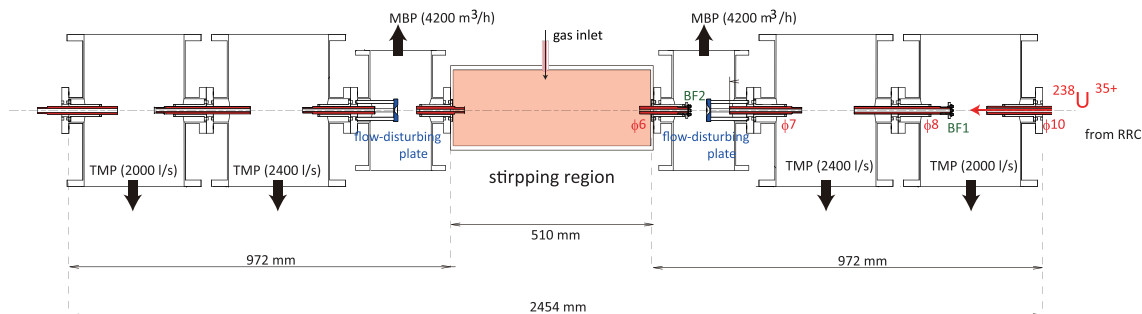


Figure 7: Schematic of 0.5-m gas cell with large differential pumping system for low-Z gas accumulation.

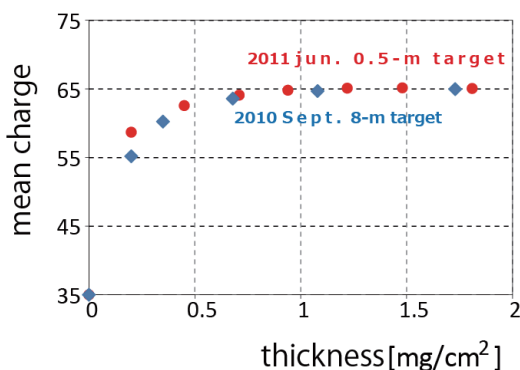


Figure 8: Measured charge evolution in He gas as a function of gas layer thickness.

gas is recycled and 2% is recovered to the He liquefier in the laboratory.

## SUMMARY

The RIBF has been successfully operated from 2007 to 2012 after the extraction of first beam. The new injector system began operation in October 2011 with objective of increasing the produced beam intensity of very heavy ions such as Xe and U ions. The stripper problem remains unresolved. However, we believe that the low-Z gas stripper is an important candidate toward addressing the issue. We carried out the following tests regarding the feasibility of using a low-Z gas stripper. First, the electron capture and loss cross sections were measured. Second, the charge evolution and energy spread were measured using a thick-layered He gas target with the large MBP system. From these two measurements, we decided to construct an actual machine for He gas stripping. We are testing the machine for the next uranium beam series in the coming autumn 2012.

## REFERENCES

[1] Y. Yano, Nucl. Instrum. Methods Phys. Res., Sect. B 261 (2007) 1009.

[2] N. Fukunishi, J. Particle Accelerator Society of Japan 4 (2007) 112.  
 [3] T. Nakagawa, et al., Rev. Sci. Instrum., 81 (2010) 02A320.  
 [4] O. Kamigaito, et al., 3rd Ann. Meeting of PASJ and 31st Linac Meeting in Japan, Sendai, (2006) 502.  
 [5] K. Yamada et al., IPAC'12, New Orleans, May 2012, TUOBA02.  
 [6] G. D. Alton and D. N. Smithe, Rev. Sci. Instrum., 65 (1994) 775  
 [7] T. Ohnishi, et al., J. Phys. Soc. Jpn., 79 (2010) 073201.  
 [8] T. Nakamura, et al., Phys. Rev. Lett., 103 (2009) 262501.  
 [9] P. Doornenbal, et al., Phys. Rev. Lett., 103 (2009) 032501.  
 [10] S. Nishimura, et al., Phys. Rev. Lett., 106 (2011) 052502.  
 [11] P. Ostroumov, et al., Phys. Rev. Lett. 86 (2001) 2798 .  
 [12] Y. Momozaki, et al., JINST 4(2009) 04005.  
 [13] H. Okuno, et al., Phys. Rev. ST Accel. Beams 14 (2011) 033503.  
 [14] A. Hershcovitch, J. Appl. Phys. 78 (1995) 5283.  
 [15] H. Hasebe, et al., Nucl. Instrum. Methods Phys. Res., Sect. A 613 (2010) 453.  
 [16] H. Ryuto, et al., Nucl. Instrum. Methods Phys. Res., Sect. A 569 (2006) 697.  
 [17] H. Kuboki, et al., Phys. Rev. ST Accel. Beams 13 (2010) 093501.  
 [18] T. Mizogawa, et al., RIKEN Accel. Prog. Rep. 22 (1988) 62.  
 [19] R. Bimbot, et al., Nucl. Instrum. Methods Phys. Res., Sect. B 107 (1996) 9.  
 [20] A. Fettouchi, et al., Nucl. Instrum. Methods Phys. Res., Sect. B 245 (2006) 32.  
 [21] H. Kuboki, et al., Phys. Rev. ST Accel. Beams 14 (2011) 053502.  
 [22] M. Gryzinski, Phys. Rev. A 138 (1965) 305; A 38 (1965) 322; A 138 (1965) 336.  
 [23] A. S. Schlachter, et al., Phys. Rev. A 27 (1983) 3372.  
 [24] H.-D. Betz, Appl. At. Coll. Phys. 4 (1983) 1.  
 [25] H. Imao, et al., IPAC11, San Sebastian, Sept. 2011, TUPS088.  
 [26] H. Imao, et al., IPAC12, New Orleans, May. 2012, TH-PPP084.  
 [27] H. Weick, et al., Phys. Rev. Lett. 85 (2000) 2725.  
 [28] H. Imao, et al., to be submitted.

## NEW DESIGN FOR THE SARAF PHASE II LINAC

B. Mustapha, Z.A. Conway, M.P. Kelly, A. Kolomiets, S.V. Kutsaev, P.N. Ostroumov [ANL, Argonne, USA]  
J. Rodnizki [Soreq NRC, Yavne, Israel]

### *Abstract*

We have developed a new design for the 40 MeV/u - 5 mA proton/deuteron SARAF Phase-II Linac. It includes a RFQ, room-temperature bunchers and two types of SC cavities. The new design is based on highly optimized ring-shaped HWR structures operating at 176 MHz, the same frequency as the current SARAF Phase-I linac. We will first present the optimized design of all the components from the RFQ to the SC cavities, then the proposed linac layout, and finally the results of end-to-end beam dynamics simulations including machine errors, realistic corrections and beam loss analysis.

**CONTRIBUTION NOT  
RECEIVED**

# DESIGN STUDY FOR FRONT-END SYSTEM AT RARE ISOTOPE SCIENCE PROJECT

<sup>1,2</sup>Eun-San Kim\*, <sup>1</sup>JungBae Bahng, <sup>1</sup>Ji-Gwang Hwang, <sup>1</sup>Si-Won Jang, <sup>2</sup>Byung-Chul Kim  
<sup>2</sup>Bong-Hyuk Choi, <sup>2</sup>Hye-Jin Kim, <sup>2</sup>Sun-Kee Kim, <sup>2</sup>Dong-O Jeon  
<sup>1</sup>Kyungpook National Univ., Deagu, Korea, <sup>2</sup>IBS, Daejeon, Korea

## Abstract

Heavy ion beams of 400 kW and 70 kW are generated at the RISP by in-flight and ISOL methods, respectively. Front-end system for the in-flight at the RISP consists of two 28 GHz superconducting ECR-IS with 10 keV/u, a LEBT with two 90 degree bends and two bunchers with 40.625 MHz, a RFQ with 81.25 MHz and 300 keV/u, and a MEBT with two re-bunchers. The front-end system design studies have been performed to optimize the beam and accelerator parameters to meet the required design goals. For this, we performed front-end simulations with two-charge state beams and present the design performance and results of the beam dynamics.

## INTRODUCTION

RISP (Rare Isotope Science Project) is designed to accelerate the ions from proton to uranium for 400 kW in-flight system. The accelerator can be segmented into front-end accelerator and superconducting linear accelerator. The front-end includes two ECR ion sources, low energy beam transport (LEBT), radio frequency quadrupole (RFQ) and medium energy beam transport (MEBT). ECR ion source generates various charge states of ions from proton to uranium. LEBT delivers these ion beams to the RFQ efficiently. Bunching at the LEBT is considered by two bunchers. RFQ accelerates the uranium beam up to 300 keV/u. The MEBT matches the beam from the RFQ to the superconducting linac. Fig. 1 shows the layout for the front-end system. We show the design results in the front-end system.

sources are considered for the RISP, as shown in Fig. 1. Superconducting magnets and RF source of 28 GHz are used and the main design parameters from the two R&D groups of KAERI and KBSI are summarized in Table 1[1]. The design of the superconducting magnets is the most important part of the ECR ion source design. The feature of KAERI model is to use five solenoids for adjusting ECR zone efficiently. On the other hand, the step winding technique for sextupole coils is the KBSI's idea to build the ECR ion source compactly.

For the superconducting magnets, 4 K cryogenic system has to be prepared. The ECR ion source needs more than 10 W cooling powers at 4 K during the operation because X-rays from the plasma chamber could be an extra heat load to the cryostat. Reducing the X-rays, therefore, is also a key design factor for the ECR ion source. A tantalum is used as a radiation shielding material. Dual frequency operation improves the overall performance so that considering an extra 18 GHz RF source can be a good choice to achieve high charge states and high current ions. Additionally, a high temperature (2000 °C) oven for solid isotopes and a high voltage platform of 70 kV for heavy ions are necessary.

Table 1: Main parameters of the ECR-IS.

|                        | KAERI   | KBSI           |
|------------------------|---------|----------------|
| Frequency(GHz)         | 28      | 28             |
| RF power (kW)          | 10      | 10             |
| Chamber diameter(mm)   | 150     | 150            |
| Chamber material       | Al      | Al             |
| Mirror length(mm)      | 500     | 500            |
| External voltage(kV)   | 30      | 30             |
| SC wire                | NbTi    | NbTi (OK35,38) |
| Number of solenoid     | 5       | 3              |
| Sextupole winding type | Saddle  | Race track     |
| $B_{inj}(T)$           | 4.2     | 3.6            |
| $B_{ext}(T)$           | 2.2     | 2.1            |
| $B_r(T)$               | 3       | 2.2            |
| $B_{min}(T)$           | 0.3-0.8 | 0.4-0.8        |

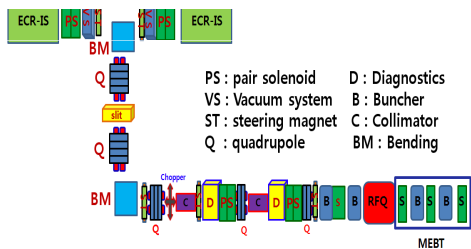


Figure 1: Layout of the front-end system for the drive linac.

## ECR ION SOURCE

The goal of the design of the ECR-IS is to produce various ions with 10 keV/u of the kinetic energy and normalized rms emittance of 0.1  $\pi$ mm-mrad. Two ECR ion

## LEBT

The LEBT consists of two 90 degree bends and quadrupoles for achromatic optics, solenoids for beam matching with ECR-IS and RFQ, two bunchers, steering magnets, collimation systems and diagnostics. Fig. 2 shows designed optics and beam envelopes for the LEBT beam line that is optimized by TRANSPORT code. The

\* eskim1@knu.ac.kr

dc beam from the ECR-IS is bunched before injection into the RFQ. To get a short bunch length with high bunching efficiency, two bunchers with the 40.625 MHz are applied. To perform the beam simulations, IMPACT-Z code is utilized for 6-dimension tracking that includes the effect of space-charge force[2,3,4,5]. A normalized rms emittance of  $0.1 \pi$  mm-mrad and intrinsic energy spread of 0.05% are considered. 20,000 macro-particles are initially generated in 4-dimensional longitudinal distributions with uniform longitudinal distributions in phase spaces and are tracked in the simulations.

Fig. 3 shows the (top) initial horizontal, vertical and longitudinal beam distributions for two-charge state beam of  $^{238}\text{U}^{33+}$  (blue) and  $^{238}\text{U}^{34+}$  (red) with  $400 \text{ e}\mu\text{A}$  in the LEBT. Fig. 3 also shows the beam distributions (middle) before and (bottom) after first buncher in the LEBT. Fig. 4 shows the beam distributions (top) before and (bottom) after second buncher in the LEBT. Two-charge state beam due to first buncher with 40.625 MHz is bunched as well as longitudinally separated from each other due to velocity difference. Second buncher in 40.625 MHz is used to provide each of two-charge state beams with the same velocity at the entrance of RFQ. A distance between first buncher and second buncher is given by 1.18 m, which corresponds to the two-charge state beam of  $^{238}\text{U}^{33+}$  and  $^{238}\text{U}^{34+}$ . Fig. 5 shows the longitudinal beam distribution at the entrance of RFQ.

The cores of the two-charge state beams well overlap and tail particles increases the beam emittance. The simulation shows that the designed LEBT under the effect of space-charge force provides good beam matching and bunching for the two-charge state beam. Adequate transverse and longitudinal emittances are also obtained by the entrance of RFQ. It is shown that the space-charge effect for the uranium beam of the  $400 \text{ e}\mu\text{A}$  is small in the LEBT.

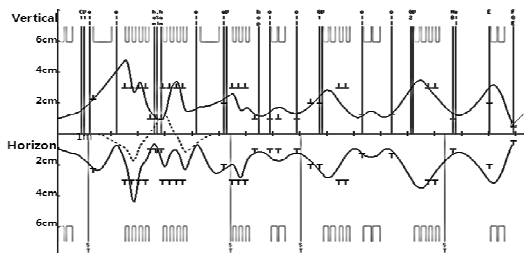


Figure 2: Designed optics and envelopes for LEBT.

### RFQ

The RFQ is designed to accelerate the beam of  $12 \text{ p}\mu\text{A}$  two-charge state ( $^{238}\text{U}^{33+}$  and  $^{238}\text{U}^{34+}$ ) beams from 10 keV/u to 300 keV/u. PARMTEQ is used to get the RFQ design parameters[6]. Table 2 shows the main input parameters of RFQ. Charge state of 33.5 for the simulations of U beam in PARMTEQ is used for multi-charge state beam of

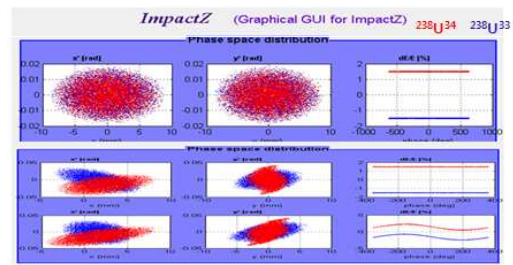


Figure 3: (top) Initial beam distributions, beam distributions (middle) before and (bottom) after first buncher in the LEBT .

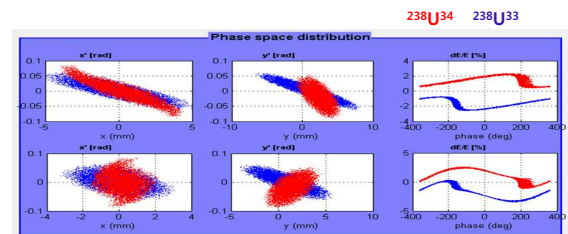


Figure 4: Beam distributions (top) before and (bottom) after the second buncher in the LEBT.

the uranium.

Fig. 6 shows the behavior of the physical quantities of the RFQ as a function of length. The vane voltage is fixed to be 70 kV. The focusing strength(B) is adopted as a constant of 5.08 along the RFQ. The accelerating efficiency is fixed to be 0.55 in order to reduce length of the RFQ. The synchronous phase becomes to -30 degrees at the end of gentle buncher from -90 degrees at the entrance of the RFQ. The modulation factor increases from 1 to about 2 and the average radius is 5.32 mm. The total length of RFQ is 3977.87 mm and number of cell is 220. The maximum peak surface electric field E that occurs at cell 218 is 17.7659 MV/m and the value E corresponds to  $1.69 E_k$ , where  $E_k$  is the Kilpatrick criterion. 10,000 particles are

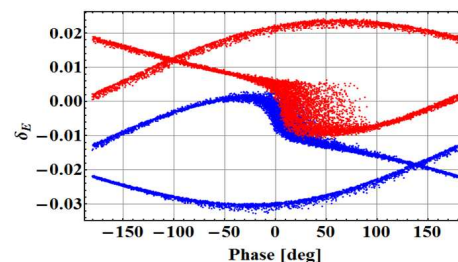


Figure 5: Longitudinal beam distribution at the entrance of RFQ.

generated by the beam current of  $12 \text{ p}\mu\text{A}$ .

Table 2: Main parameters of the RFQ.

|                            |   |
|----------------------------|---|
| Reference particle         | $^{238}\text{U}^{33+}$ and $^{238}\text{U}^{34+}$ |
| RF frequency               | 81.25 MHz   |
| Input charge state         | 33.5  |
| Input energy               | 10 keV/u  |
| Output energy              | 300 keV/u   |
| Beam current               | 12 $\text{p}\mu\text{A}$                          |
| Input normalized emittance | $0.1 \pi \text{ mm-mrad rms}$                     |
| Vane voltage               | 70 kV   |
| Total length               | 4 m   |

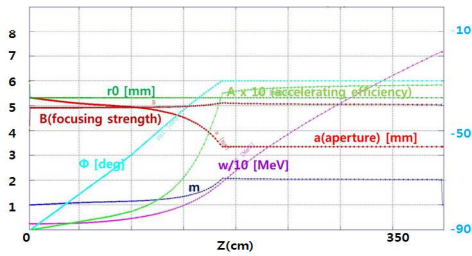


Figure 6: Evolution of synchrotron phase, modulation factor, focusing strength, aperture, kinetic energy and acceleration efficiency along RFQ.

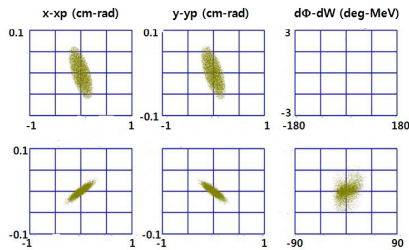


Figure 7: Beam distributions at the entrance (top) and exit (bottom) of the RFQ.

Fig. 7 shows the (top) input and (bottom) output particle distributions in the transverse and longitudinal phase spaces. We used 4D water bag model for input transverse particles and 2D uniform model for longitudinal particles. Their Twiss parameters are  $\alpha_{x,y} = 0.7445$  and  $\beta_{x,y} = 4.7536 \text{ cm/radian}$ . Fig. 8 shows the particle distributions in the transverse (horizontal, vertical) envelopes, phase deviation and kinetic energy deviation as a function of cell number. Transmission rate in the RFQ shows 90.8%. The normalized rms transverse emittance of output beam are  $\epsilon_x = 0.12 \pi \text{ mm-mrad}$  and  $\epsilon_y = 0.12 \pi \text{ mm-mrad}$ , respectively. Then the longitudinal emittance is 6.6 MeV-deg.

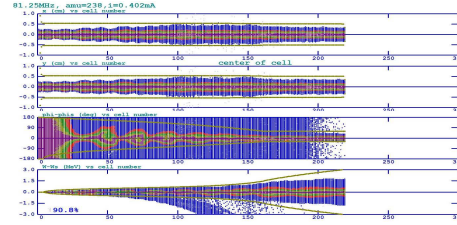


Figure 8: Beam envelopes, phase deviation and kinetic energy deviation along RFQ.

Each single charge state of +33 and +34 with  $12 \text{ p}\mu\text{A}$  was also tracked by the same RFQ design.

TRACK code is also used for the simulations of the two-charge state beam. Field informations from PARI and PARMTEQM are used. In the TRACK code, the aperture radius is fixed to be 5.32 mm. Twiss parameters and emittance of input beam are the same as the PARMTEQ program. 10000 particles are used and beam current is  $12 \text{ p}\mu\text{A}$ . Fig. 9 shows the results of TRACK code for the two-charge state beam ( $^{238}\text{U}^{33+}$  in blue and  $^{238}\text{U}^{34+}$  in green). The beam transmission rate is 93% and the normalized rms transverse emittance of output beam are  $\epsilon_x = 0.103 \pi \text{ mm-mrad}$  and  $\epsilon_y = 0.103 \pi \text{ mm-mrad}$  in horizontal and vertical direction, respectively, and longitudinal emittance is 1.3 keV/u ns.

When the two-charge state beam from the LEBT is tracked by TRACK code in the RFQ, the beam transmission rate is 80% and normalized rms transverse emittances of output beam are  $\epsilon_x = 0.14 \pi \text{ mm-mrad}$  and  $\epsilon_y = 0.14 \pi \text{ mm-mrad}$  in the horizontal and vertical directions, respectively, and longitudinal emittance is 1.08 keV/u ns.

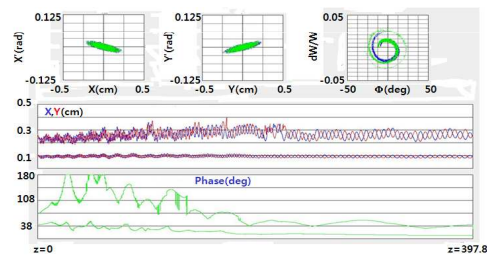


Figure 9: Beam distributions at the exit of RFQ by TRACK code.

### MEBT

The Medium Energy Beam Transport (MEBT) system, which is installed between the RFQ linac and superconducting linac, requires to match the optical parameter in transverse plane and also remove the unaccelerated ion beams from the RFQ linac. The optics design of the MEBT

system is performed by using TRACE3D code and particle tracking is performed by using IMPACT-Z code. The optics function is matched to the betatron function at the entrance of the superconducting linac. MEBT is studied to find the better way to compensate the growth of transverse emittance due to the effect of the space-charge. The MEBT system also provides the enough space for beam diagnostic devices such as beam profile monitor, beam position monitor and wire scanner. The transverse beam size can be controlled by the knobs which are installed in the up-stream of beam diagnostic devices to measure the beam information in MEBT system.

Five room temperature quadrupole magnets are used to minimize the transverse emittance growth of two-charge state beams and provide the transverse focusing to achieve the small beam size and focusing gradient at the entrance of the superconducting linac. Two rebunchers are also used to provide flexible longitudinal matching from the exit of the RFQ to the entrance of the superconducting linac. TRACE3D code to design the MEBT is used. To estimate the space charge effect in MEBT system, we performed the calculation by using IMPACT-Z code. The results on the beam distributions and beam envelopes are shown by Fig. 10. The quadrupole magnets have a field of less than 0.5 T at the pole-tip. The room temperature rebuncher has 81.25 MHz and  $\beta_{opt} = 0.025 \lambda/4$ . The total length of the MEBT is about 3.7 meters.

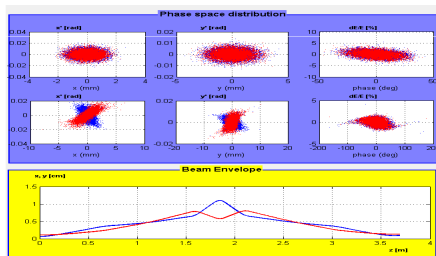


Figure 10: (top) Initial and (middle) final phase space beam distributions, and (bottom) beam envelopes in the MEBT by IMPACT code.

## FRONT-END SIMULATIONS

Fig. 11 shows the beam distributions in transverse and longitudinal phase planes at the (top) entrance of MEBT and at the (bottom) exit of MEBT when the front-end beam simulations from the LEBT to MEBT are performed. When the two-charge state beam from the LEBT is tracked to the MEBT, the beam transmission rate is 79% and normalized rms transverse emittances of output beam are  $\epsilon_x = 0.2 \pi$  mm-mrad and  $\epsilon_y = 0.14 \pi$  mm-mrad in the horizontal and vertical directions, respectively, and longitudinal emittance is 9.3 MeV-degree.

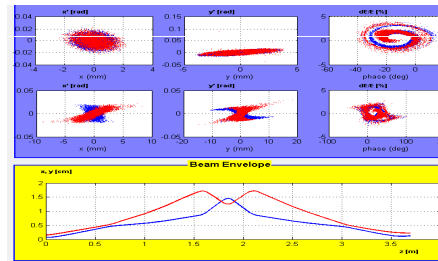


Figure 11: Phase space beam distributions at the (top) entrance and at the (bottom) exit of the MEBT by the front-end simulations.

## SUMMARY

First front-end beam simulations at RISP are performed to optimize the front-end system. The results show that the performance results exist within scope of the requirements by RISP.

The beam from the ECR-IS will be used for the front-end simulations and performance on multi-harmonic buncher in the LEBT will be examined as the future works. In addition to front-end system for the driver linac, front-end system that includes charge breeder, LEBT, RFQ and MEBT for the re-accelerator will be also studied.

## REFERENCES

- [1] B. Oh et al., RISP Heavy-ion workshop, May, Daejeon, Korea (2012).
- [2] J. Qiang et al., J. Comput. Phys. 163 p. 434 (2000).
- [3] X. Wu et al., PAC'07, Albuquerque, June 2007, TUPAS053, p. 1769.
- [4] R.W. Garnett et al., PAC'05, Knoxville, June 2005, p. 4218.
- [5] T.P. Wangler et al., PAC'07, Albuquerque, June 2007, TH-PAS051, p. 3606.
- [6] Q. Zhao et al., PAC'07, Albuquerque, June 2007, TUPAS054, p. 1772.

# DEVELOPMENT OF THE INTENSITY AND QUALITY OF THE HEAVY ION BEAMS AT GSI

L. Dahl, W. Barth, M. C. Bellachioma, L. Groening, O. Kester, M. Kirk, D. Ondreka, N. Pyka, P. Spiller, J. Stadlmann, H. Vormann, S. Yaramishev, GSI, Darmstadt, Germany  
 L. Bozyk, Y. El-Hajek, C. Xiao, IAP, Frankfurt, Germany

## Abstract

For injection into the future FAIR SIS100 synchrotron the GSI linear accelerator UNILAC and synchrotron SIS18 have to provide  $1.5 \cdot 10^{11}$  p/spill for the reference  $U^{28+}$  beam. The MEVVA ion source extracts 37 emA of  $U^{4+}$  beam. For improved transmission in the front end accelerator the RFQ vanes were revised and exchanged. A new ion source terminal with direct beam injection into the RFQ is calculated and partly realized for loss free beam transport to the RFQ. To improve the quality of the space charge dominated beam in the DFFD periodic focussing Alvarez section a transversal 4<sup>th</sup> order resonance was investigated by simulations and experimentally. The multi turn beam injection into the SIS18 requires emittances below  $\beta\gamma\epsilon_x/\beta\gamma\epsilon_y = 0.8/2.5 \mu\text{m}$ . This suggests introducing a new concept for emittance transfer by solenoidal stripping. A set-up for experimental proof of principle will be installed at the foil stripper. The SIS18 has been equipped with NEG-coated chambers for all magnets and the injection septum. Newly installed ion catchers improve especially the dynamic vacuum pressure. The effect on progress in beam quality development and intensity will be reported.

## INTRODUCTION

For the reference ion  $U^{28+}$  the UNILAC has to inject  $2 \cdot 10^{11}$  particles per  $60 \mu\text{s}$  into the SIS18. This again injects four batches of  $1.5 \cdot 10^{11}$  particles each into the future FAIR SIS100 synchrotron [1] with a repetition rate of 2.7 Hz to fill it finally with  $6 \cdot 10^{11}$  particles for acceleration up to 2.7 GeV/u for radioactive beam production. Alternatively SIS100 accelerates intense proton beams up to 30 GeV for pbar-production.



Fig. 1: The existing GSI accelerators UNILAC and SIS18 and the future accelerator facility FAIR.

This booster operation of the SIS18 [2] is the most challenging case concerning beam intensity, repetition rate, and dynamic vacuum challenges. Heavy ion beams of energies up to 30 GeV/u will be provided by the FAIR synchrotron SIS300, using higher charge states and a slower cycling rate. SIS300 can also serve as a stretcher for the production of radioactive beams, which will be injected, cooled, and stored in a system of rings with internal targets and in-ring experiments (Fig. 1).

GSI uses heavy ion sources of e.g. MUCIS or MEVVA type which generate for a whole string of low charged ions beams of sufficient intensity. As the UNILAC was originally not designed for space charge dominated beams different measures are necessary to reduce beam losses and improve beam quality.

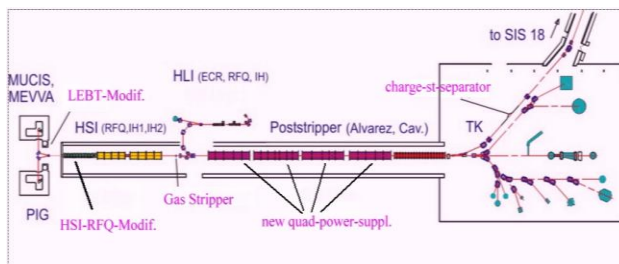


Fig. 2: Schematic overview of the UNILAC, experimental area, transfer channel to SIS, and locations of upgrades.

The scheme of the UNILAC is presented in Fig. 2. The prestripper accelerator HSI (high current injector) comprises a 36 MHz RFQ and two IH-type drift tube DTLs for final energy of 1.4 MeV/u, suited for ions with mass to charge ratios up to 65. A gas stripper increases the charge states, e.g.  $U^{4+}$  delivered by the MEVVA source is stripped to  $U^{28+}$ . Five 108 MHz Alvarez DTLs accelerate the ions up to 11.4 MeV/u. Finally a chain of ten single gap resonators allows exact adjusting of any energy between 3.6 and 12.4 MeV/u. A second injector HLI (high charge state injector) with an ECR source injects directly into the post stripper section. Finally, up to three different ion species can be accelerated interchangeably to different energies. Different experiments in any mixture on basis of a 50 Hz pulse-to-pulse switching mode can be accomplished. The transfer channel to SIS18 includes a foil stripper for another charge state increase and is also suitable for 4 Hz pulse-to-pulse operation of beams from different ion species passing through different stripping foils.

The SIS18 rigidity is 18 Tm with warm magnets of 1.8 T maximum field strength. The present ramp power is limited to 4 T/s. This allows a repetition rate of  $\sim 1$  Hz only. The ring includes 12 double dipole magnets with

magnetic quadrupole triplet or doublet focussing in each of the 12 sections. Two rf-cavities with a frequency range of 800 kHz up to 5.6 MHz apply 32 kV acceleration voltage each. Depending on the mass to charge ratio the beam extraction energy is for example 220 MeV/u for  $U^{28+}$ , 1 GeV/u for  $U^{73+}$ , and up to 2 GeV/u for lighter heavy ions. A scheme of the SIS18 is given in Fig. 3.

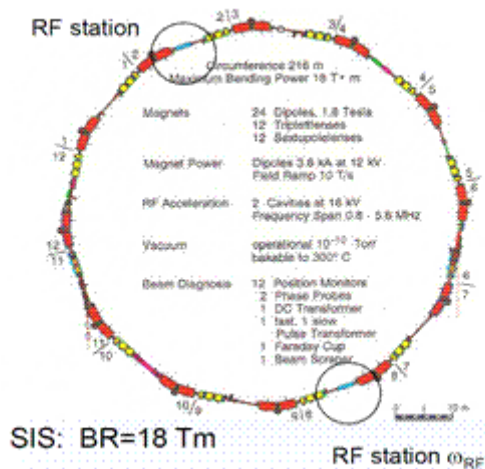


Fig. 3: The SIS18 synchrotron.

## BEAM DEVELOPMENT AT THE UNILAC

### New Design for the RFQ Vanes

In 2009 the 36 MHz RFQ accelerator was upgraded by exchange of the mini vanes [3]. The new vanes should provide for higher transverse acceptance and phase advance and finally improved beam transmission. This implies a new input radial matcher design and improved beam dynamics for gentle bunching to get rapid and uniform separatrix filling.

Table 1: Main RFQ parameters

|                                       | New Design   | Old Design (bef. Upgr. '09) |
|---------------------------------------|--------------|-----------------------------|
| Inter vane voltage, kV ( $U^{4+}$ )   | 155          | 125                         |
| Average Aperture Radius, mm           | 6.0          | 5.245 - 7.745               |
| Electrode Width, mm                   | 8.4          | 9.0 - 10.8                  |
| Maximum field, kV/cm                  | 312.0        | 318.5                       |
| Modulation                            | 1.012 - 1.93 | 1.012 - 2.09                |
| Synch. Phase, degree                  | -900 - -280  | -900 - -340                 |
| Aperture, mm                          | 4.10         | 3.81                        |
| Min. transverse phase advance, degree | 31.8         | 25.8                        |
| Norm. transverse acceptance, mm mrad  | 0.856        | 0.73                        |
| Output energy, keV/u                  | 120          | 118.5                       |
| Number of cells with modulation       | 394          | 343                         |
| Length of electrodes, mm              | 9217.4       | 9217.4                      |

Beam dynamics calculations were carried out with the codes DYNAMION and PARMTEQ-M and predicted 18 emA of  $U^{4+}$  beam at the RFQ exit (see Table 1). This value meets the FAIR requirements.

Due to the enlarged normalized acceptance of  $0.86 \mu\text{m}$  and the maximum rf voltage of 155 kV the  $U^{4+}$  beam

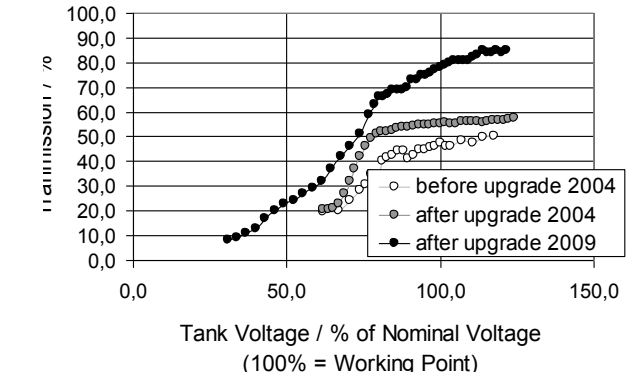


Fig. 4: Measured RFQ beam transmission of an  $Ar^{+}$  beam of 10 emA intensity depending on rf voltage before and after exchange of the vanes.

Fig. 4 shows the increase of beam transmission up to 90%. Concerning space charge forces the 10 emA  $Ar^{+}$  beam is equivalent to a 15 emA  $U^{4+}$  beam.

### New Ion Source Terminal and Compact LEBT

The existing LEBT includes a  $77.5^\circ$  mass spectrometer which causes filamentation of the transverse emittances and therefore an emittance growth of  $\sim 50\%$ . For this reason a new ion source terminal with straight LEBT has been calculated and planned (see Fig.5) [4].

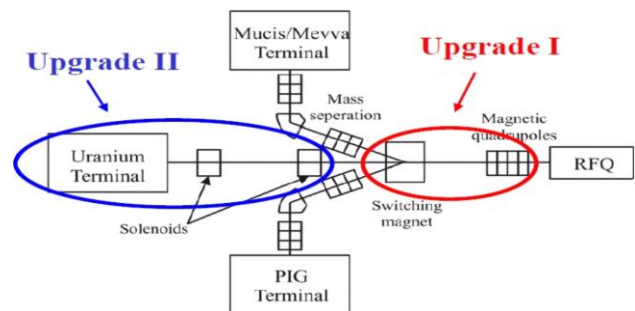


Fig. 5: New third ion source terminal and compact LEBT.

The red indicated area is already bought and partly installed. For the blue indicated area the first sc solenoid is in house and used for a high current ion source test bench. The aperture will be completely enlarged and all beam diagnostics are exchanged by aperture suited devices.

The ion sources deliver 37 emA of  $U^{4+}$  beam and 18 emA of a  $U^{3+}$ . The compact LEBT transports the entire  $U^{4+}$  fraction to the RFQ entrance. Calculations with the codes PARMILA-Transport and DYNAMION demonstrate that a part of the  $U^{3+}$  fraction of the beam will be lost in front of the RFQ, another one in the RFQ

tank. Finally only 1.6 emA reach the RFQ exit but 20.3 emA of  $U^{4+}$  beam is accelerated in the RFQ (Table 2).

Table 2:  $U^{4+}$  front end beam intensities for the existing and the future compact LEBT

|               | MeVv-ion source output           | Entrance RFQ                     | Exit RFQ                            |
|---------------|----------------------------------|----------------------------------|-------------------------------------|
| Existing LEBT | 37 mA $U^{4+}$ analyzed          | 16.0 mA                          | 14.0 mA                             |
| Compact LEBT  | 37 mA $U^{4+}$<br>18 mA $U^{3+}$ | 37 mA $U^{4+}$<br>18 mA $U^{3+}$ | 20.3 mA $U^{4+}$<br>1.6 mA $U^{3+}$ |

This injection scheme provides the necessary front end beam intensity to satisfy the requirements for FAIR.

#### 4th Order Space Charge Driven Resonances

Assumed is a periodically breathing beam envelope with phase advance  $\sigma_{env}$  and envelope with radial symmetry. The single particles experience constant external focusing with  $\sigma_0$  from magnets and electric field of breathing beam size. From this derives the resonance condition:  $\sigma_{env} = 360^\circ \rightarrow \sigma = 90^\circ$ . This means: 4th order space charge driven resonance occurs at  $\sigma = 90^\circ$ , i.e.  $\sigma_0 \geq 90^\circ$ , envelope oscillates 4 times faster than single particle.

The UNILAC Alvarez DTL quadrupoles follow the DFFD periodic focusing. For this reason the Alvarez section including 180 quadrupoles is well suited for a 4th order resonance experiment [5, 6, 7].

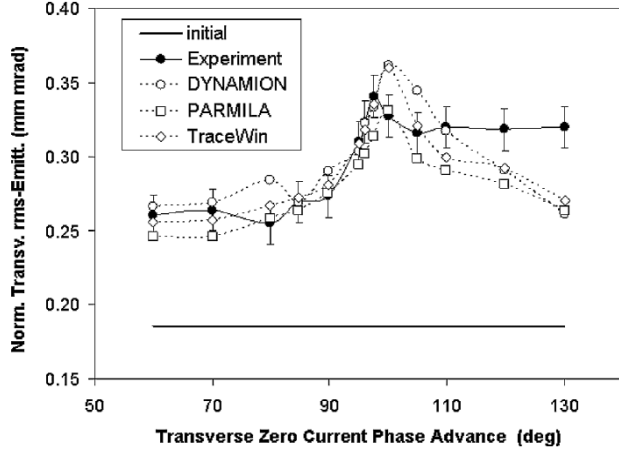


Fig. 6: A strong emittance growth in the Alvarez DTL calculated and measured.

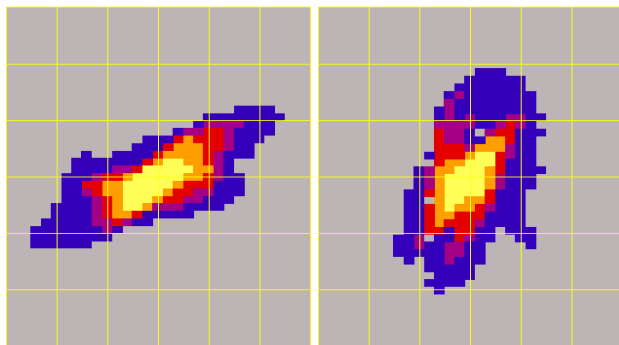


Fig. 7: Measured emittances behind the Alvarez DTL

An  $Ar^{10+}$  beam of 7 emA was used to allow for high phase advance settings of the quadrupoles. This beam is equivalent to a 15 emA beam of  $U^{28+}$ , corresponding to the FAIR requirements. The results of different simulation codes and experimental data are shown in Fig. 6. A significant emittance growth occurs at  $\sigma_0 = 100^\circ$ . Considering tune depression  $\sigma \approx 90^\circ = 360^\circ / 4$ .

In the measurements four wings were observed in the transverse emittances at  $\sigma_0 = 100^\circ$  in good agreement with three simulation codes (see Figure 7). For linacs so far resonances considered to be of no concern for operation. But there is evidence for enveloped matched operation of the UNILAC DTL.

#### Beam Quality Development

Table 3 shows the requirements of beam intensity and quality for injection into SIS18 and the measured maximum intensity.

Table 3:  $U^{28+}$  beam requirements on the UNILAC

| required ions/60μs            | Transverse emittances [μm]                                     | measured ions/60μs             |
|-------------------------------|--|--------------------------------|
| $2.0 \cdot 10^{11}$<br>15 emA | $\beta\gamma\epsilon_x = 0.8$<br>$\beta\gamma\epsilon_y = 2.5$ | $0.8 \cdot 10^{11}$<br>5.7 emA |

With the  $U^{28+}$  beam intensity the UNILAC currently reaches ~ 40% of the desired value. A big step towards 15 emA is expected with the operation of the new ion source terminal and compact LEBT. Particularly a progress in beam brilliance by optimizing the extraction and pre-acceleration cascade geometry is expected with the commissioning of this new accelerator part.

A further challenge is to adapt the horizontal and vertical emittances to the values derived from SIS18 multi turn injection scheme, see Table 3. Fig. 8 demonstrates the present discrepancies in terms of brilliances.

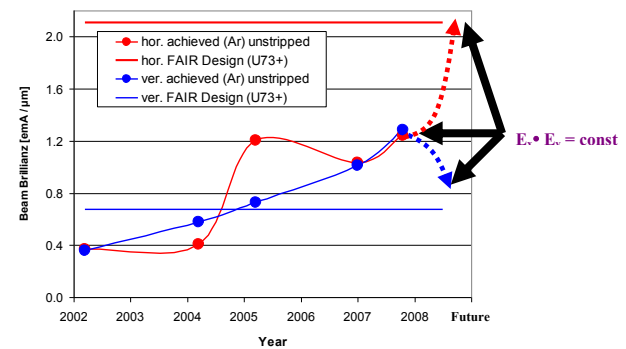


Fig. 8: Measured and required beam brilliances at Alvarez DTL exit.

To overcome this problem, an emittance transfer method was developed and an experimental proof of principal is foreseen [8]. This method requires a non-symplectic beam transformation creating x-y-coupling and skewed quadrupoles. The non-symplectic element will be given by a Helmholtz coil around the foil stripper chamber and a change of the magnetic rigidity by ionization in the midplane. The beam is correlated at the exit of the solenoid field. The skewed quadrupoles retract

the correlation. A scheme of the experiment for proof of principle is given in Fig. 9. First experiments are foreseen to start in autumn 2013.

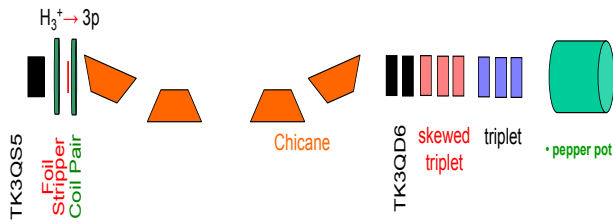


Fig. 9: Beam line configuration at the foil stripper section for an emittance transfer experiment.

Beam simulations with the PARMILA-Transport code were carried out with the result of complete beam transmission, a reduction of  $\epsilon_x$  of 41%, a growth of  $\epsilon_y$  of 142% and a growth of the  $\epsilon_{4d}$  of 42%. The emittance growth is due to foil scattering and unavoidable [9].

If these results will be confirmed by the beam experiments, the UNILAC beam quality would fit the SIS18 requests.

## BEAM DEVELOPMENT AT THE SIS18

### Ionization Beam Loss and Dynamic Vacuum

The most challenging task of the SIS18 synchrotron is the acceleration of ions with intermediate charge states in booster operation to fill the FAIR SIS100 with four batches of  $1.5 \cdot 10^{11}$   $U^{28+}$  particles each.

Ionization beam loss with a desorption factor  $\eta \sim 10,000$  causes local pressure bumps and is by far the dominating loss process. It begins significantly earlier as space charge and current depending effects. This was observed from static residual gas pressure measurements and by means of current measurements on a charge catcher system one section downstream. Fig. 10 shows significant pressure bumps driven by the beam losses. Due to that, the main goal was the generation of the static vacuum pressure  $p_0 < 5 \cdot 10^{-12}$  mbar by an average pumping speed increased by a factor of 100 and the stabilization of the dynamic pressure  $p(t) < 1 \cdot 10^{-9}$  [10].

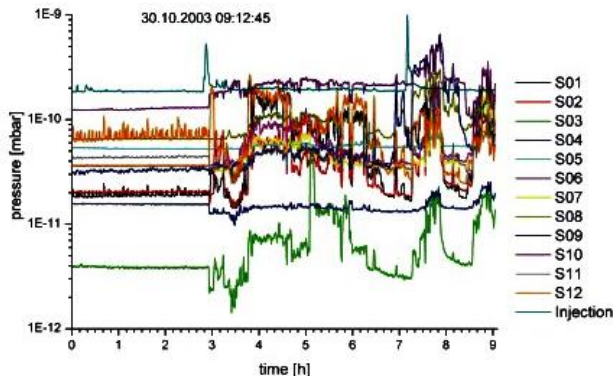


Fig. 10: Vacuum pressure in the 12 SIS18 sections during high current operation.

To improve the vacuum, GSI established a NEG (non evaporable getter) coating facility [11]. 24 dipole magnet

chambers, 16 quadrupole chambers and 13 straight pipes were replaced between 2006 and 2009 by NEG coated chambers, which corresponds to 65% of the SIS18 circumference. Additionally, to overcome the dynamic vacuum instability 10 collimation systems equipped with thin film coated (see Fig. 11) absorbers were designed and commissioned. At the same time an upgrade of the bake-out system for a temperature of 300°C was completed.



Fig. 11: NEG coated scraper chamber with Au coated Cu ion catcher blocks. Diagnostics: extractor ion gauge and current measurement of charge exchanged ions.

The reduction of the initial beam loss has an outstanding importance for the dynamic vacuum and FAIR booster operation. Initial beam loss originates initial pressure bumps, which dominate the dynamic vacuum situation and ionization beam loss in the machine cycle. Therefore, the reduction and control of the beam loss at multi turn injection was a major issue of the development program. Various experiments have been carried out to study the beam injection process. From these experiences a new injection system has been derived with the following characteristics:

- Increased acceptance
- Injection of  $U^{28+}$  at 11.4 MeV/u
- Protection of septum electrodes
- (1.5 MW beam peak power)
- No HV break downs
- Reduced ionization beam loss
- Introduction of NEG panels
- Aim for reduced gas production.

Fig 12 demonstrates the implications of the vacuum improvement on the increase of life time for intermediate charged heavy ions of a factor of 10 with NEG coated vacuum chambers and even a factor of 40 considering the new injection chamber. Under these improved conditions a new intensity record was reached with only  $3.0 \cdot 10^{10}$   $U^{27+}$  particles injected by the UNILAC due to device failures and  $2.1 \cdot 10^{10}$   $U^{27+}$  particles extracted at the SIS18 (see Fig. 13) [12].

Another record of highest average intensity was reached in 2012. A Nitrogen beam with continually more

than  $10^{11}$  ions per cycle has been generated with an energy of 2 GeV/u. Due to fast ramping with 4 T/s and a short extraction time of 0.5 s, an average beam intensity of  $3.0 \cdot 10^{10}$  ions/s has been extracted.

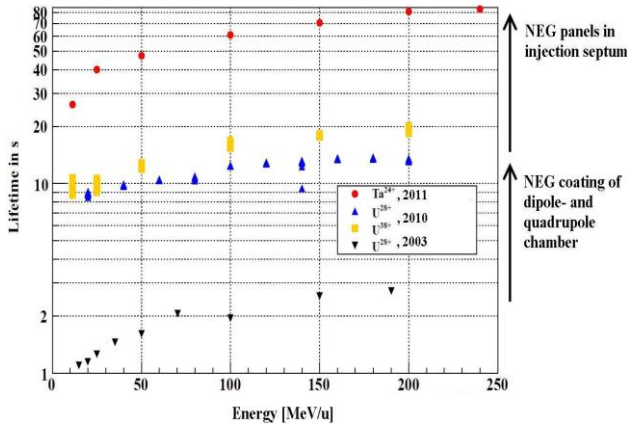


Fig. 12: Beam life time of intermediate charged heavy ion beams in the SIS18 for three developing stages.

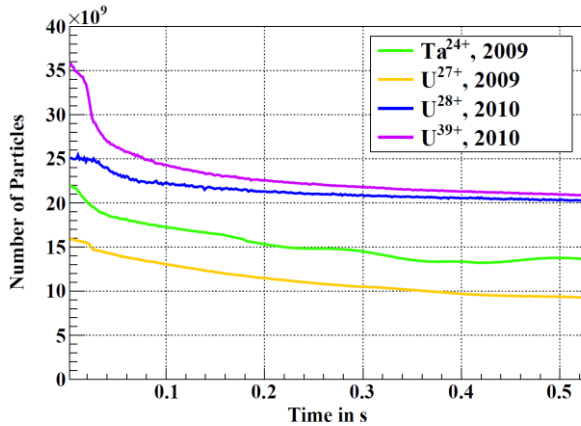


Fig. 13: Development of beam intensity at SIS18.

### SIS18 UPGRADES IN PROGRESS

#### Faster SIS18 Ramping Cycles

Since 2011 GSI is connected with the 110 kV power grid. In 2013 high performance power supplies for all dipole and quadrupole magnets will be introduced. Thus, the ramping rates listed in Table 4 can be realized and a repetition rate of the SIS18 cycles  $f_{rep} = 2.7$  Hz eases additionally the booster operation by fast crossing of the still remaining rise of the dynamic vacuum by ionization effects.

Table 4: SIS18/100/300 field ramping rates

|              | Pulse Power | Field Rate |
|--------------|-------------|------------|
| SIS18 (now)  | + 5 MW      | 1.3 T/s    |
| SIS18 (2013) | + 42 MW     | 10 T/s     |
| SIS100       | ± 26 MW     | 4 T/s      |
| SIS300       | ± 23 MW     | 1 T/s      |

#### New h=2 Acceleration Cavity

A new h=2 accelerator cavity [13, 14, 15] is under construction as complementary cavity to the both existing cavities for h=4 operation. These provide 32 kV acceleration voltage and a frequency range of 800 kHz to 5.6 MHz. The new cavity will provide 50 kV by three modules each driven with two tetrode tubes of 300 kW anode dissipation power working in push-pull-operation able to operate independently from each other. According to h=2 operation the frequency range is 400 kHz to 2.7 MHz. Since the cavities are filled with lossy MA-ring-cores, which are iron based Finemet FT3M ring cores from Hitachi, the cavities show a broadband behaviour and thus no cavity tuning during the acceleration ramp will be necessary. Due to limited installation space in the SIS18 ring, the cavities are based on nano-crystalline novel magnetic alloy materials (MA-materials). The Q-value is 0.5. A comparable ferrite driven system would have a length of 7 m. The overall consumption is 1.6 MW. The cavity is cooled by oil, suppressing parasitic modes and avoiding corrosion. A parameter overview is given in table 5.

Table 5: Broadband cavity with power unit

|  |  |
|--|--|
| Duty cycle   | 100%   |
| Frequency range with the hardest requirements                          | 0,429 MHz - 1,6 MHz (full range 0,4 - 2,7 MHz) |
| Overall voltage  | 16.7 kV  |
| Number of gaps   | 2  |
| Number of ring cores per unit  | 16   |
| Shunt impedance Rp per half gap (one stack of 4 ring cores) at 429 kHz | 440 Ω  |
| Parallel inductance Lp per half gap at 429 kHz                         | 308 μH   |
| Parallel capacitance Cp per half gap                                   | 50 pF  |
| RF dissipation power per unit  | 80 kW  |
| RF dissipation power per ring core                                     | 5 kW   |

The advantages of the h=2 cavities are the following:

- Sufficient rf voltage for fast ramping with low charge state heavy ions:
  - U<sup>73+</sup> acceleration with 4 T/s ( $2 \cdot 10^{10}$  ions)
  - U<sup>28+</sup> acceleration with 10 T/s ( $2 \cdot 10^{11}$  ions)
- Bucket area for loss free acceleration and 30% safety
- Flat bunch profile for lower inc. tune shift
- Two harmonic acceleration:
  - h=4 (existing cavity) and h=2 (new cavity)
- Compatible with SIS100 RF-cycle
- 50 kV – high power requirements – additional space provided in tunnel.

Commissioning of the first module is planned for 2013.

## CONCLUSION AND OUTLOOK

With the sequence of upgrade measures at the UNILAC a maximum beam intensity of ~ 40% of the desired values was reached already in 2007. Unfortunately this intensity was not reproducible afterwards due to successive different hardware failures. Particularly the Alvarez DTL, which is in operation since 40 years, had different prolonged break downs. Therefore the SIS18 performance could not be proofed with the maximum beam intensity of the UNILAC afterwards. This means, the intensity records of the UNILAC and SIS18 do not correspond to each other and the SIS18 output intensity is to be seen under these temporary restrictions. Scaling linearly the SIS18 record with the best reached UNILAC intensity of  $8.0 \cdot 10^{10}$  U<sup>28+</sup> particles/60  $\mu$ s, the SIS18 output intensity would be  $5.6 \cdot 10^{10}$  particles. Consequently both machines perform presently about 40% of the FAIR requirements.

Presently the UNILAC as well as the SIS18 have reached full performance. In July and September 2013 machine experiments are planned to confirm or even to overshoot the intensity records in combined operation.

The missing intensity factor for FAIR of roughly 2.5 can be gained by the planned straight LEBT and new ion source terminal. The SIS18 performance will be increased by the introduction of the powerful h=2 cavities and the 2.7 Hz cycle frequency. These residual measures are realizable easily before FAIR commissioning will start.

## REFERENCES

- [1] FAIR Baseline Technical Report, Vol. 2, GSI Darmstadt, Germany (2006)
- [2] P. Spiller et al., High Intensity Intermediate Charge State Heavy Ions in Synchrotrons, Proceedings of IPAC2012 New Orleans, LA, USA (2012)
- [3] H. Vormann et al., Advanced Unilac Upgrade for FAIR, Proceedings of LINAC2010 Tsukuba, Japan (2010)
- [4] L. Dahl, et al., A New LEBT and RFQ Input Radial Matcher for the UNILAC Front-End, Proceedings of LINAC2006 Knoxville, USA (TN) (2006)
- [5] D. Jeon et al., Prediction of 4<sup>th</sup> Order Transverse Resonances, PRST-AB 12 054204, (2009)
- [6] L. Groening et al., Experiment on 4<sup>th</sup> Order Transverse Resonances, PRL 102, 234801 (2009)
- [7] L. Groening et al., Parametric Resonance, PRL 103, 224801 (2009)
- [8] L. Groening, Transverse Emittance Transfer, PRST-AB 14, 069201 (2009)
- [9] C. Xiao, Transverse Emittance Transfer, Internal Report IAP-DYNA-190412, Goethe University Frankfurt, Institute of Applied Physics, Frankfurt, Germany (2012)
- [10] P. Puppel, et al., Simulation of the Long Term Beam Intensity Performance of the NEG-Coated SIS18, Proceedings of ICFA HB Morschach, Switzerland (2010)
- [11] M. C. Bellachioma, NEG Coating Facility, Proceedings of IPAC2012 New Orleans, LA, USA (2012)
- [12] P. Spiller et al., SIS18-Intensity Record with Intermediate Charge State Heavy Ions, Proceedings of IPAC2011 San Sebastián, Spain (2011)
- [13] P. Hülsmann, et al., Development of a New Broadband Accelerating System for the SIS18 Upgrade at GSI, Proceedings of IPAC2010 Kyoto, Japan (2010)
- [14] K.-P. Ningel et al., "Dual Harmonic Operation at SIS18", Proceedings of IPAC2010 Kyoto, Japan (2010)
- [15] H. Klingbeil, "A Fast DSP-Based Phase Detector for Closed-Loop RF Control in Synchrotrons", IEEE Trans. Instr. Meas., Vol. 54, No. 3, pp. 1209-1213, June 2005

# THE HITRAP DECELERATOR AND BEAM INSTRUMENTATION

F. Herfurth\*, Z. Andjelkovic, N.P.M. Brantjes, W. Barth, G. Clemente, L. Dahl, S. Fedotova, P. Gerhard, M. Kaiser, O. Kester, H.-J. Kluge, C. Kozhuharov, M. Maier, D. Neidherr, W. Quint, A. Reiter, T. Stoehlker, G. Vorobjev, S. Yaramyshev  
 GSI Helmholtz Centre for Heavy Ion Research, Darmstadt, Germany  
 U. Ratzinger, A. Schempp  
 Institute for Applied Physics, Goethe University, Frankfurt am Main, Germany

## Abstract

A linear decelerator is being commissioned for heavy, highly-charged ions (HCI) at GSI in Darmstadt/Germany. HCI with only one or few electrons are interesting systems for many different experiments as for instance precision tests of the theory of quantum electrodynamics (QED). In order to transform heavy HCI produced at 400 MeV/u to stored and cooled HCI at low energy the linear decelerator facility HITRAP has been setup behind the experimental storage ring (ESR). The ions are decelerated in the ESR from 400 to 4 MeV/u, cooled and extracted. The ions are then matched to an interdigital H-type structure (IH) using a double drift buncher, decelerated from 4 to 0.5 MeV/u in the IH, and then down to 6 keV/u in a 4-rod radio frequency quadrupole (RFQ). To detect and analyze the weak and sparse ion bunches a new type of energy analyzing detector has been developed along with improvements of other standard beam instrumentation. One million highly charged ions have been decelerated with the IH from 400 MeV/u to about 0.5 MeV/u per cycle. The RFQ has shown in off-line tests to decelerate ions, however, the measured longitudinal acceptance does not fit the properties of the ion beam decelerated in the IH. This requires a refined design, which is underway.

## INTRODUCTION

Heavy, highly-charged ions, as for instance  $U^{91+}$  or even the bare  $U^{92+}$ , are well suited for cutting edge experiments in atomic, nuclear and solid state physics [1]. They are simple but come along with a very strong electric field due to the heavy nucleus and hence the large amount of positive charge enclosed in the small nuclear volume. This suits perfectly well to test quantum electrodynamics (QED) theory at the strong-field limit. Quantities that can be calculated with high precision and which are at the same time sensitive to the investigated QED effects are the g-factor of the bound electron, the electron binding energies of the innermost electrons or the hyperfine splitting of the electronic levels. To be decisive, those measurements require the same high precision as the calculations. For this, the ions have to be stored and cooled in a well defined environment at very low energy. This is possible in a Penning trap by electron and resistive cooling to about 4K [2]. The

observation of the stored particles will then allow for mass measurements at the ppt level, corresponding to a determination of the electron binding energies with eV precision. Similarly, the bound-state g-factor can be determined with a precision that even tests our knowledge of fundamental constants like the mass of the electron. Laser excitation of the transition energies between hyperfine levels will become feasible several hundred times more precise than presently [3].

Heavy, highly-charged ions are very instable systems when in close contact with electrons since a huge potential energy is concentrated in a very small volume. When those HCI at very low energy come close to neutral matter relaxation processes happen very fast and give snapshot-like insight into the dynamics and correlation of the electrons in the neutral collision partner. If energy and position are well defined the exchange of multiple charges can be studied by a complete analysis of the kinematics of all involved particles. For that, highly-charged ions are accumulated in a Penning trap and cooled. After ejection a well defined ion beam will be targeted to a cold sample of neutral atoms and the products will be investigated by a reaction microscope [4]. Two different target types will be applied for HITRAP experiments: a pulsed gas target [5] and a magneto optical trap [6].

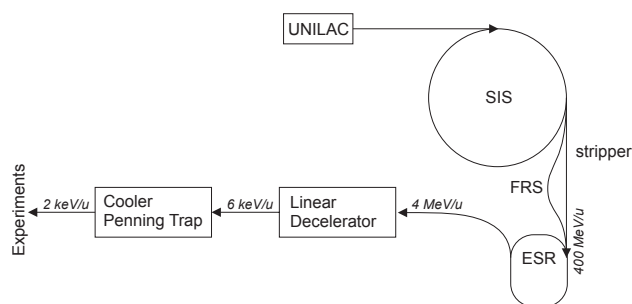


Figure 1: The HITRAP facility at the GSI accelerator complex. UNILAC stands for Universal Linear Accelerator, SIS is the heavy ion synchrotron and ESR is the Experimental Storage Ring. The beam from the SIS can be sent directly into the ESR or fragmented by nuclear reactions and then analyzed and separated in the Fragment Separator (FRS).

\* F.Herfurth@gsi.de

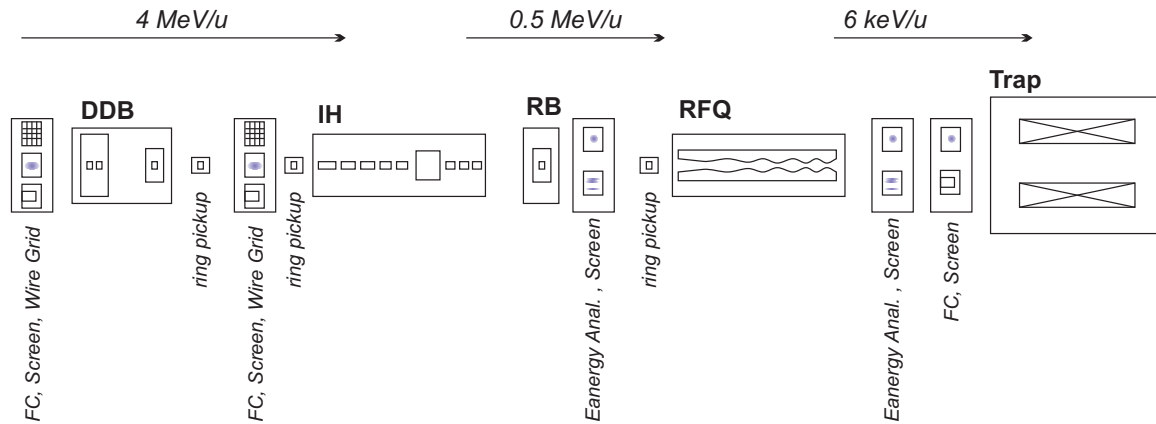


Figure 2: The functional units of the HITRAP linear decelerator: the double drift buncher (DDB), the interdigital H-type structure (IH), a spiral re-buncher (RB), the four-rod radio frequency quadrupole structure (RFQ) and the cooler Penning trap (Trap). Additionally indicated are the major diagnostic units. For description see text.

When the large potential energy is concentrated and released on a small surface spot of solid matter, self-ordering has been observed. This phenomenon needs further investigation to clarify the role of impact energy and potential energy. This can be accomplished only if the impact energy, i.e. the kinetic energy of the particle, is well below the potential energy of a few 100 keV [7].

All those experiments require that kinetic energy and spatial position of the highly-charged ions can be well controlled. This is in contradiction to the most efficient production process that employs stripping of electrons at high energies by sending relativistic highly-charged ions with still many electrons through matter. The solution is a decelerator and storage facility for highly-charged ions produced by stripping all electrons of the ions from a 400 MeV/u beam - the HITRAP facility.

## THE HITRAP FACILITY

HITRAP is setup at the accelerator facility of the GSI Helmholtz Centre for Heavy Ion Research in Darmstadt/Germany (fig. 1). The universal linear accelerator UNILAC is used to deliver intermediate charged ions with 11 MeV/u to the heavy ion synchrotron SIS. After acceleration to 400 MeV/u the ions are sent through a thin foil such that all electrons are stripped of the nucleus. The experimental storage ring ESR is then used to cool the ion beam produced that way and decelerate it to 4 MeV/u in two steps. After initial stochastic cooling the beam is decelerated to 30 MeV/u and then cooled with electrons. The next deceleration step from 30 MeV/u to 4 MeV/u is followed by another electron cooling period before the coasting beam is bunched in 1  $\mu$ s bunches and ejected towards the HITRAP linear decelerator facility.

The linear decelerator (fig. 2) consist of a double drift buncher at 108 and 216 MHz for preparation of the beam to the longitudinal acceptance of the first decelerating structure, the interdigital H-type structure (IH). There, the ions

are decelerated from 4 MeV/u down to 500 keV/u. An intermediate rebuncher will ensure maximum efficiency when the beam is injected into the second decelerating structure, a four-rod radio frequency quadrupole decelerator (RFQ). Both decelerating structures run at 108 MHz and require a power of 200 and 80 kW, respectively. In the RFQ the ion beam is decelerated from 500 keV/u to 6 keV/u and then dynamically captured in a Penning trap for final cooling.

## BEAM INSTRUMENTATION

In fig. 2 the main instrumentation to detect the ion beam along the linear decelerator is indicated. To tune the beam transport from the ESR through the beam line into the IH structure, two kind of position sensitive detectors and standard Faraday cups are used. They are typically grouped in a common diagnostic chamber. Additionally, to monitor the functioning of the double drift buncher (DDB), ring shaped, capacitive pick-ups are installed. They also deliver additional energy information by time-of-flight measurements if there is sufficient beam intensity of at least 1  $\mu$ A. An overview of those diagnostic installations can be found in [8].

During commissioning it turned out that it is not sufficient to detect the beam intensity and position alone. It is indispensable to have an energy dispersive detector behind the decelerating structures since the beam behind the IH and RFQ is a mixture of decelerated and non decelerated components. Therefore, after attempts with a large magnetic dipole and a diamond detector, a one-shot energy sensitive detector has been developed [9, 10].

The functional principle is shown in fig. 3. When the beam enters from the left, it is first made sure with at least one, and after the IH with two slit systems that it is narrow enough for the required resolution. The slits are typically 0.1 mm wide. The beam is then deflected in a magnetic dipole field of  $B = 0.5$  T (for the RFQ it is only 0.1 T) with

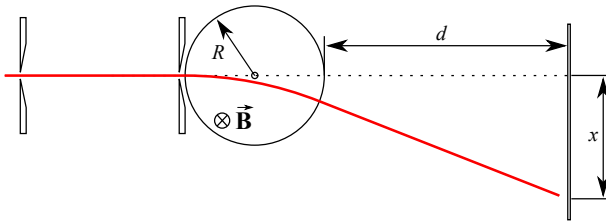


Figure 3: Principle setup of the energy analyzing detector installed behind the IH and the RFQ. The beam enters from the left through one or two slits before it is deflected in a permanent magnet and finally hits a screen with a deviation  $x$ . The complete setup is retractable remote controlled from the beam line.

an effective radius  $R \approx 30 \text{ mm}$ . At a distance  $d \approx 100 \text{ mm}$  an MCP detector in combination with a phosphorous screen is used to read the deviation  $x$ .

The first slit is only available at the setup after the IH and makes sure that geometrical beam deviations from axis do not dominate the measurement of the deviation  $x$  and hence the beam energy. The slit, as well as all other components of the system can be retracted from the beam line.

For the very low energy after the RFQ of about  $6 \text{ keV/nucleon}$  we used an electrostatic  $180^\circ$  analyzer with spherical electrodes developed at the University of Frankfurt. With this device it is possible to measure also the energy spread of the decelerated beam.

Special instrumentation has also been developed to determine the emittance of the incoming, i.e.  $4 \text{ MeV/nucleon}$  beam, and the decelerated beam after the IH, i.e. at about  $500 \text{ keV/nucleon}$  [11]. Requirements were a compact device that can handle low intensities of only  $1 \mu\text{A}$  peak current for  $3 \mu\text{s}$  once a minute.

## STATUS OF COMMISSIONING

Funding for the construction of HITRAP has started in 2005 and commissioning of first components started 2007. About two commissioning beam times have been granted per year with an average duration of 6 days. An overview of those beam times and the achieved or planned steps is displayed in table 1.

Presently, the deceleration to  $500 \text{ keV/u}$  has been shown and is working efficiently [14]. The major breakthrough was the successful installation of an energy sensitive detector, which gives shot by shot the complete energy spectrum of the ions after the IH structure [10]. However, the optimization of the combination of two bunchers (combined in the double drift buncher) and the IH is still difficult and not completely understood. The large parameter space given by three RF amplitudes and two phases requires the investigation of many different settings. This takes a lot of time and is virtually impossible due to the low repetition rate of at most one shot every 30 seconds. Two improvements have been implemented: the energy of the particles enter-

ing the ESR was limited to  $30 \text{ MeV/u}$  for commissioning of the linear decelerator which saves one deceleration step and hence time; the longitudinal analysis of the bunches created by the double drift buncher has been enhanced by a dedicated analysis procedure [15] (see also above).

The focus of recent beam times was on the detailed investigation of the IH structure output. Supported by detailed simulations [16] the deceleration efficiency was increased and reached about 50%, very close to the theoretical limit.

In the most recent beam time the third buncher, the rebuncher between the IH and RFQ structures, was taken into operation. With a measured loaded Q-value of about 5000 and an effective impedance of  $29 \text{ M}\Omega/\text{m}$  it yields a designed gap voltage of  $100 \text{ kV}$  for  $A/q = 3$ . For the  $^{50}\text{Ti}^{22+}$  ions used in the recent beam time this corresponds to about  $80 \text{ kV}$  gap voltage and hence a maximal theoretical energy change of about  $35 \text{ keV/nucleon}$ .

The action of the rebuncher was tested by measuring the beam on the energy sensitive detector after the buncher and changing the phase relative to the master oscillator driving the IH radio frequency and the radio frequency of the rebuncher. The result is shown in fig. 4. The maximal position change of about  $0.8 \text{ mm}$  corresponds to about  $50 \text{ keV/nucleon}$  energy variation which is pretty close to the expected value.

Two more conclusions can be drawn from fig. 4. The relative energy shift can be measured to a precision of less than  $1 \text{ keV}$ , which means that the energy measurement is dominated by systematic uncertainties. The full-width-half-maximum of the peak on the detector corresponds to  $45 \text{ keV/nucleon}$ . This is a convolution of the geometrical spread due to the imaging, the slit sizes and camera issues with the actual energy spread of the ion beam. This has not yet been disentangled, but first rough estimated show that at least half of that spread is due to real energy spread.

All efforts to decelerate the beam further with the RFQ structure failed so far. The most probable reason is a slight mismatch of the IH output energy distribution and the energy range accepted by the RFQ. This was found in recently updated simulations of the RFQ structure using the code DYNAMION [17] accompanied by a detailed 3D measurements of the electrodes. To verify those findings and work towards a solution the RFQ was installed at a Pelletron accelerator at the Max-Planck Institute for Nuclear Physics in Heidelberg/Germany.

### RFQ off line tests

The RFQ was installed at the Pelletron accelerator in Heidelberg and tested with  $\text{H}_2^+$  ions with total kinetic energy around  $1 \text{ MeV}$ . This corresponds to the necessary energy of about  $500 \text{ keV/nucleon}$ . About  $500 \text{ nA}$  were available at the entrance of the RFQ.

It has been shown that the HITRAP RFQ can decelerate ions from  $517 \text{ keV/nucleon}$  to  $6.7 \text{ keV/nucleon}$ . The energy spectrum measured behind the RFQ with an electrostatic energy analyzer is shown in fig. 5. The measured energy

Table 1: Overview of conducted commissioning beam times.

| Date    | Ion                     | Comment   |
|---------|-------------------------|---|
| 5-2007  | $^{64}\text{Ni}^{28+}$  | Vacuum separation ESR/HITRAP installed - acceptance test          |
| 8-2007  | $^{20}\text{Ne}^{10+}$  | Double Drift Buncher test using diamond detector in front of IH   |
| 8-2008  | $^{197}\text{Au}^{79+}$ | Bunches transported through IH, analyzed on diamond det. [12]     |
| 10-2008 | $^{64}\text{Ni}^{28+}$  | First decelerated particles at 500 keV/u with energy spectrometer |
| 2-2009  | $^{58}\text{Ni}^{28+}$  | First run after IH retuning. 4 MeV/u transport-mode test          |
| 6-2009  | $^{132}\text{Xe}^{54+}$ | Beam measured with pepper-pot emittance meter [11, 13, 9]         |
| 3-2010  | $^{86}\text{Kr}^{33+}$  | Improved IH energy analyzer [10]                                  |
| 4-2010  | $^{86}\text{Kr}^{35+}$  | Beam to RFQ, energy analysis sensitive only to 6 keV/u [14]       |
| 11-2010 | $^{86}\text{Kr}^{35+}$  | RFQ Energy analyzer also to 500 keV/u sensitive                   |
| 5-2011  | $^{54}\text{Cr}^{24+}$  | IH Energy measurements  |
| 6-2011  | $^{14}\text{N}^{7+}$    | IH Energy measurements, RFQ parameters scanned                    |
| 9-2011  | $^{136}\text{Xe}^{50+}$ | IH and DDB combined optimisation, ESR energy scan                 |
| 5-2012  | $^{50}\text{Ti}^{22+}$  | IH and DDB combined optimisation, RB test, RFQ scan               |

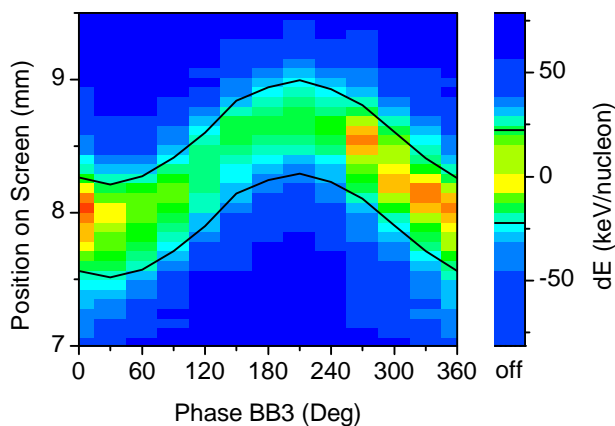


Figure 4: Results of the commissioning of the spiral rebuncher between IH and RFQ. Shown are position on the screen, corresponding energy shift, and intensity (in arbitrary units) of the beam on the energy analyzing detector versus the phase of the radio frequency driving the buncher cavity. A power of 1.1 kW was used for all phases. The lines are the FWHM limits of a gaussian fit of the beam profile at each phase.

spread of about 6% is somewhat lower than expected without the intertank debuncher installed at the end of the RFQ but not used for the presented measurement. This is probably due to the very low energy spread of the incoming beam from the Pelletron. The energy of the beam itself is more than 10% higher than the design value, which complicates the injection into the cooler Penning trap especially for ions with mass to charge ratio close to three.

With the available flexibility and control of the beam at the test facility it was also possible to map in detail the acceptance of the RFQ concerning the energy of the incoming ions. For deceleration to the designed energy and the

optimal RF setting the accepted energy ranges from about 512 to about 522 keV/nucleon FWHM. The range is hence as expected but in comparison to the observed spread for the ion beam coming from the IH (compare fig. 4 and its explanation) to narrow.

The major result from the off-line test is that the central value of the accepted energy is not the designed and required 500 keV/nucleon but about 17 keV/nucleon to high. This has been anticipated in refined calculations before the off-line test and could be verified by those.

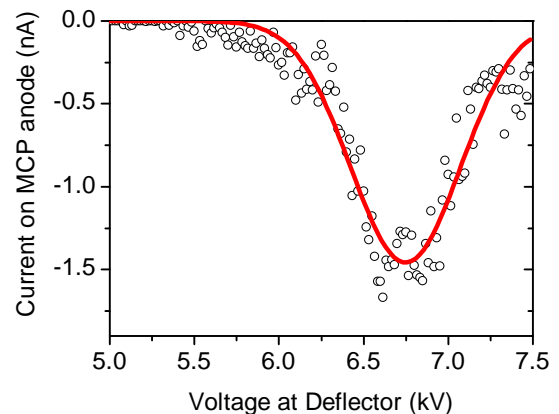


Figure 5: Energy spectrum of decelerated beam as measured behind the RFQ during off-line tests. The voltage at the deflector is equivalent to the ions energy per nucleon. The line is a gaussian fit to the data that yields a central energy of 6.75 keV/nucleon and a FWHM of 0.76 keV/nucleon.

### Cooler Penning trap and EBIT

The cooler Penning trap is tested offline with deuterium ions from a cross beam ion source. An electron source has

been installed already to provide the electrons for the electron cooling scheme [18]. It is based on UV-light-released electrons from a GaAs surface and is fully compatible with the required ultra-high vacuum. Electrons have been captured already in the cooler Penning trap and the ion capture process is being tested in the moment.

In order to test the low energy beam lines that connect to the experiments as well as the trap operation, a compact, room temperature electron beam ion trap (EBIT) of the Dresden type has been installed. It's beam has been used to commission the vertical beam line between the trap and the experimental platform. It has also been used for charge breeding and can to provide ions for experiments when they are not available as gaseous elements [19].

## SUMMARY AND OUTLOOK

The HITRAP facility has been conceived to the decelerate and cool beams of heavy, highly charged ions produced at 400 MeV/nucleon at the GSI accelerator complex in Darmstadt, Germany. It's setup has been started in 2006 and commissioning is still ongoing. The cooling, deceleration and extraction of heavy, highly charged ion beams in the experimental storage ring (ESR) is meanwhile a routine operation. Up to ten million ions can be extracted from the ESR at 4 MeV/nucleon and sent to HITRAP.

The HITRAP linear decelerator has three major components, a double drift buncher (DDB), an IH and an RFQ structure. Commissioning of the DDB and the IH has reached reproducible operation conditions. Ions are decelerated to 500 keV/nucleon and investigations towards higher stability of operation and higher efficiency are ongoing. Major efforts went into the characterization of the energy spectrum of the decelerated ion beam, which showed a larger energy spread than anticipated. In the section between the IH and the RFQ a rebuncher is installed to re-focus the transversal phase space. The rebuncher has been commissioned recently and shows the expected behavior.

The last step of deceleration, the RFQ, has been commissioned off-line. It has been shown that the structure decelerates ions from about 500 keV/nucleon to about 6 keV/nucleon but does not reach the exact design specifications. This made it impossible to achieve deceleration in the dedicated on-line commissioning runs.

For final deceleration the existing RFQ resonator will be equipped with new electrodes. After detailed simulations of the present electrodes explain most of the experimentally observed features, calculations for a new set of electrodes have been started with the aim to have a new set of electrodes available end of this year. Furthermore, a completely new and different structure based on the IH concept is discussed. Major parameters to be optimized are the energy acceptance, the transversal acceptance and the energy spread of the decelerated ion beam.

## REFERENCES

- [1] H.-J. Kluge et al., *HITRAP: A Facility at GSI for Highly Charged Ions*, Adv. Quant. Chem. **53** (2008) 83.
- [2] G. Maero et al., *Numerical investigations on resistive cooling of trapped highly charged ions*, Applied Physics B: Lasers and Optics (2011) 1.
- [3] M. Vogel, W. Quint, and W. Nörtershäuser, *Trapped Ion Oscillation Frequencies as Sensors for Spectroscopy*, Sensors **10** (2010) 2169.
- [4] J. Ullrich et al., *Recoil-ion momentum spectroscopy*, Journal of Physics B: Atomic, Molecular and Optical Physics **30** (1997) 2917.
- [5] D. Tiedemann et al., *The Gas Jet Target for Experiments at HITRAP*, Tech. Report PNI-AP-12, GSI SCIENTIFIC REPORT, 2011.
- [6] S. Götz et al., *A novel ultra cold atom target for collision experiments with heavy ion beams*, Tech. Report PNI-AP-25, GSI SCIENTIFIC REPORT, 2011.
- [7] A. S. El-Said et al., *Creation of Nanohillocks on CaF<sub>2</sub> Surfaces by Single Slow Highly Charged Ions*, Phys. Rev. Lett. **100** (2008), 237601.
- [8] M. Witthaus et al., *Beam Diagnostics for the HITRAP Decelerator*, DITANET-Workshop "Low Current, Low Energy Beam Diagnostic", 23.- 25. Nov. 2009 (<http://www-bd.gsi.de/ditanet/>), 2009.
- [9] F. Herfurth et al., *HITRAP — Heavy, Highly-Charged Ions and Antiprotons at Rest*, Act. Phys. Pol. B **41** (2010) 457.
- [10] G. Vorobjev et al., *Diagnostic Scheme for the HITRAP Decelerator*, 10th European Workshop on Beam Diagnostics and Instrumentation for Particle Accelerators, 2011, p. 311.
- [11] J. Pfister et al., *Commissioning of the HITRAP decelerator using a single-shot pepper-pot emittance meter*, Proceedings of the XIV Linear Accelerator Conference, 2008, p. 564.
- [12] L. Dahl et al., *The HITRAP Decelerator Project at GSI - Status and Commissioning Report*, Proceedings of the XIV Linear Accelerator Conference - LINAC08, 2008, p. 102.
- [13] F. Herfurth et al., *The HITRAP Decelerator Linac at GSI*, Proceedings of PAC09, Vancouver, BC, Canada, 2009, p. 1961.
- [14] F. Herfurth et al., *HITRAP - A Decelerator for Heavy, Highly-charged Ions*, Proceedings of Linear Accelerator Conference LINAC2010, Tsukuba, Japan, 2010, p. 151.
- [15] A. Reiter, C.M. Kleffner, and B. Schlitt, *Improved Signal Treatment for Capacitive Linac Pick-Ups*, 10th European Workshop on Beam Diagnostics and Instrumentation for Particle Accelerators, 2011, p. 128.
- [16] G. Clemente, private comm., 2011.
- [17] S. Yaramishev et al., *Development of the versatile multi-particle code DYNAMION*, Nucl. Instr. and Meth. A **558** (2005), 90.
- [18] Claude Krantz, *Intense Electron Beams from GaAs Photocathodes as a Tool for Molecular and Atomic Physics*, Ph.D. thesis, Ruprecht Karls Universität, Heidelberg, Germany, 2009.
- [19] G. Vorobjev et al., *Demonstration of charge breeding in a compact room temperature electron beam ion trap*, Review of Scientific Instruments **83** (2012), 053302.





— F —

Facco, A. MOB01, P016, TUA02  
 Falbo, L. WEA01  
 Fedotova, S. THB05  
 Fraser, M.A. WEC02  
 Fukunishi, N. THB01

— G —

Galatà, A. P009, TUA02  
 Gammino, S. WEB05  
 Ganni, V. MOB01  
 Gerbick, S.M. WEC01  
 Gerhard, P. THB05  
 Gettmann, V. WEC03  
 Ghita, D.G. TUB02  
 Ghosh, S. WEC04  
 Gibson, P.E. MOB01  
 Glasmacher, T. MOB01  
 Goddard, B. WEC02  
 Greene, J.P. TUC04  
 Groening, L. THB04  
 Guan, X. TUA03  
 Gugiu, M.M. TUB02

— H —

Harada, S. P013, TUC02  
 Harle, L.L. MOB01  
 Hasebe, H. THB01  
 He, Y. THA03  
 Herfurth, F. THB05  
 Holland, K. MOB01  
 Hwang, J.G. THB03

— I —

Imao, H. THB01  
 Imel, G. TUC03  
 Ionescu, P. TUB02  
 Ito, S. TUB01  
 Iwashita, T. P013, TUC02

— J —

Jang, S.W. THB03  
 Jardin, P. P002  
 Jeon, D. THA02, THB03  
 Johnson, M.J. MOB01, P016  
 Jones, S. MOB01  
 Joshi, R. WEC04

— K —

Kadi, Y. WEC02  
 Kadokura, E. TUC02  
 Kaiser, M. THB05  
 Kamalou, O. P002  
 Kamigaito, O. MOB05, THB01

Kanjilal, D. TUA01, WEC04  
 Kar, S. WEC04  
 Karande, J.N. P005, P006  
 Karmakar, J. WEC04  
 Kase, M. THB01  
 Kawakubo, T. TUC02  
 Kazarinov, N.Yu. P003  
 Kedzie, M. WEC01  
 Kelly, M.P. WEC01, THB02  
 Kester, O.K. THB04, THB05  
 Kim, B. THB03  
 Kim, D.G. MOB02  
 Kim, E.-S. THA02, THB03  
 Kim, H. THB03  
 Kim, H.J. THA02  
 Kim, J.S. P017  
 Kim, J.-W. MOB02, THA02  
 Kim, M. MOB02  
 Kim, S.K. MOB02, THA02, THB03  
 Kirk, M.M. THB04  
 Kluge, H.J. THB05  
 Kolomiets, A. THB02  
 Kondev, F.G. TUC03  
 Kondrashev, S.A. TUC03, WEB02, WEB04  
 Konrad, M. P004  
 Kozhuharov, C. THB05  
 Kubo, T. TUC02  
 Kuboki, H. THB01  
 Kumar, M. WEC04  
 Kumar, R. WEC04  
 Kunz, P. MOA01  
 Kutsaev, S.V. THB02  
 Kuznetsov, G.I. WEB02

— L —

Labrecque, F.S. MOA01  
 Lascar, D. MOC04  
 Lassen, J. MOA01  
 Laune, J. MOB03  
 Lee, Y.Y. THA02  
 Leitner, D. MOB01  
 Leitner, M. MOB01  
 Leo, K.W. TUC02  
 Levand, A. MOC04, TUC04, WEB02  
 Li, J. P014  
 Linardakis, P. TUB03  
 Lister, K. MOC04  
 Liu, X. P013, TUC02  
 Lobanov, N.R. TUB03  
 Lutton, F. MOB03

— M —

Ma, X. THA03  
 Machicoane, G. MOB01  
 Maddock, T. TUC03  
 Mäder, D. WEC03

Maggiore, M.M. **P009**  
 Maier, M.T. **THB05**  
 Manikonda, S.L. **MOB03, MOB04**  
 Marchetto, M. **MOC01**  
 Marginean, N.M. **TUB02**  
 Marti, F. **MOB01**  
 Mascali, D. **WEB05**  
 Mathuria, D.S. **WEC04**  
 Matsuzaki, H. **TUB01**  
 Maunoury, L. **P002**  
 Meusel, O. **WEA02**  
 Mickat, S. **WEC03, WEC03**  
 Miller, S.J. **P016**  
 Minarello, A. **P009**  
 Mistri, K.K. **WEC04**  
 Mitu, I.O. **TUB02**  
 Mjøs, A. **MOA01**  
 Modanese, P. **TUA02**  
 Morita, A. **TUB01**  
 Morris, D. **MOB01**  
 Morton, A.C. **MOC03**  
 Mosu, D.V. **TUB02**  
 Murphy, R.C. **WEC01**  
 Mustapha, B. **WEB04, WEC01, THB02**

— N —

Nair, C. **TUC03**  
 Nakanishi, H. **TUC02**  
 Nanal, V. **P005, P006**  
 Neidherr, D. **THB05**  
 Nolen, J.A. **MOB03, MOB04, MOB01**  
 Nonn, P.N. **P004**  
 Nozar, M. **MOA01**

— O —

Okada, Y. **TUC02**  
 Okamura, K. **TUC02**  
 Okamura, M. **P018**  
 Okazaki, K. **TUC02**  
 Okuno, H. **THB01**  
 Ondreka, D. **THB04**  
 Osswald, F.R. **P003**  
 Ostroumov, P.N. **WEB02, WEB04, WEC01, THA01, THB02**  
 Ozelis, J.P. **MOB01**

— P —

Palchan, T. **TUC03**  
 Palit, R. **P006**  
 Palmieri, A. **P010**  
 Palmieri, V. **P010**  
 Palmotti, G. **TUC03**  
 Pandey, A. **WEC04**  
 Pantelica, A. **TUB02**  
 Pantelica, D. **TUB02**

Parchet, D. **WEC02**  
 Pardo, R.C. **MOB04, MOC04, TUC04, TUC03**  
 Patra, P. **WEC04**  
 Paul, M. **TUC03**  
 Payet, J. **MOB03**  
 Peaucelle, C. **P003**  
 Peng, S. **MOB01**  
 Pengo, R. **TUA02**  
 Peterson, D. **MOC04**  
 Petit, E. **MOC02**  
 Petre, A. **TUB02**  
 Phillips, D.R. **MOC04**  
 Pikin, A.I. **P017, P018, WEB01, WEB02, WEB04**  
 Pillay, R.G. **P005, P006**  
 Pisent, A. **TUA02**  
 Podlech, H. **WEC03**  
 Popescu, I. **TUB02**  
 Popielarski, J. **MOB01**  
 Popielarski, L. **MOB01**  
 Porcellato, A.M. **P009, P010, TUA02**  
 Pose, M.S. **P006**  
 Powale, S.M. **P006**  
 Pozdeyev, E. **MOB01**  
 Prakash, P.N. **WEC04**  
 Pyka, N. **THB04**

— Q —

Quint, W. **THB05**

— R —

Rai, A. **WEC04**  
 Raparia, D. **P018**  
 Ratzinger, U. **WEA02, WEC03, THB05**  
 Rehm, E. **MOB04**  
 Reid, T. **WEC01**  
 Reiter, A. **TUB04, THB05**  
 Ritter, J. **P018**  
 Rodnizki, J. **THB02**  
 Roy, A. **WEC04**  
 Rozario, C. **P006**  
 Russo, T. **MOB01**

— S —

Sacharias, J. **WEC04**  
 Sahu, B.K. **WEC04**  
 Saito, K. **MOB01**  
 Salvatores, M. **TUC03**  
 Sarkar, A. **WEC04**  
 Sarkar, S.K. **P006**  
 Sasa, K. **P012**  
 Sava, T.B. **TUB02**  
 Savajols, H. **MOB03**  
 Savard, G. **MOB04, MOC04, TUC04**



## *Institutes List*

### **ANL**

Argonne, USA

- Alcorta, M.
- Back, B.
- Baker, S.I.
- Bertone, P.
- Caldwell, S.
- Clark, J.A.
- Conway, Z.A.
- Davids, C.N.
- Dickerson, C.
- Gerbick, S.M.
- Greene, J.P.
- Kedzie, M.
- Kelly, M.P.
- Kolomiets, A.
- Kondev, F.G.
- Kondrashev, S.A.
- Kutsaev, S.V.
- Lascar, D.
- Levand, A.
- Lister, K.
- Manikonda, S.L.
- Murphy, R.C.
- Mustapha, B.
- Nair, C.
- Nolen, J.A.
- Ostroumov, P.N.
- Palchan, T.
- Pardo, R.C.
- Peterson, D.
- Phillips, D.R.
- Rehm, E.
- Reid, T.
- Savard, G.
- Schelt, J.V.
- Scott, R.H.
- Seweryniak, D.
- Sternberg, M.G.
- Sun, T.
- Vondrasek, R.C.
- Weber, L.W.
- Zabransky, B.

### **BARC**

Mumbai, India

- Singh, S.

### **BINP SB RAS**

Novosibirsk, Russia

- Batazova, M.A.
- Kuznetsov, G.I.

### **BNL**

Upton, Long Island, New York, USA

- Alessi, J.G.
- Beebe, E.N.

- Lee, Y.Y.
- Okamura, M.
- Pikin, A.I.
- Raparia, D.
- Ritter, J.
- Snydstrup, L.

### **CEA Cadarache**

Saint Paul Lez Durance, France

- Salvatores, M.

### **CEA/DSM/IRFU**

France

- Authier, M.
- Drouart, A.
- Payet, J.

### **CEA/IRFU**

Gif-sur-Yvette, France

- Delferrière, O.

### **CERN**

Geneva, Switzerland

- Bernardes, A.P.
- Blumenfeld, Y.
- Bravin, E.
- Calatroni, S.
- Catherall, R.
- Fraser, M.A.
- Goddard, B.
- Kadi, Y.
- Parchet, D.
- Siesling, E.
- Vandoni, G.
- Venturini Delsolaro, W.
- Voulot, D.
- Williams, L.R.

### **CNAO Foundation**

Milan, Italy

- Ciavola, G.
- Falbo, L.
- Vacchieri, E.
- Vitulli, S.

### **Department of Energy Sciences, Tokyo Institute of Technology**

Yokohama, Japan

- Liu, X.

### **DREEBIT GmbH**

Dresden, Germany

- Schmidt, M.
- Thorn, A.

**Far-Tech, Inc.**

San Diego, California, USA

- Evstati, E.G.
- Kim, J.S.
- Zhao, L.

**FIAS**

Frankfurt am Main, Germany

- Bozyk, L.H.J.
- El-Hayek, Y.

**FRIB**

East Lansing, Michigan, USA

- Binkowski, J.
- Facco, A.
- Johnson, M.J.
- Miller, S.J.
- Xu, Y.
- Bernard, E.C.
- Bultman, N.K.
- Casagrande, F.
- Chouhan, S.
- Compton, C.
- Davidson, K.D.
- Facco, A.
- Gibson, P.E.
- Glasmacher, T.
- Harle, L.L.
- Holland, K.
- Johnson, M.J.
- Jones, S.
- Leitner, D.
- Leitner, M.
- Machicoane, G.
- Marti, F.
- Morris, D.
- Nolen, J.A.
- Ozelis, J.P.
- Peng, S.
- Popielarski, J.
- Popielarski, L.
- Pozdeyev, E.
- Russo, T.
- Saito, K.
- Webber, R.C.
- Wei, J.
- Weisend, J.
- Williams, M.
- Yamazaki, Y.
- Zeller, A.
- Zhang, Y.
- Zhao, Q.

**GANIL**

Caen, France

- Bajeat, O.
- Chautard, F.
- Delahaye, P.
- Dubois, M.

- Jardin, P.
- Kamalou, O.
- Lutton, F.
- Maunoury, L.
- Petit, E.
- Savajols, H.
- S n cal, G.
- Souli, M.
- Stodel, M.-H.

**GSI**

Darmstadt, Germany

- Andjelkovic, Z.
- Barth, W.A.
- Bellachioma, M.C.
- Brantjes, K.
- Clemente, G.
- Dahl, L.A.
- Fedotova, S.
- Gerhard, P.
- Groening, L.
- Herfurth, F.
- Kaiser, M.
- Kester, O.K.
- Kirk, M.M.
- Kluge, H.J.
- Kozhuharov, C.
- Maier, M.T.
- Mickat, S.
- Neidherr, D.
- Ondreka, D.
- Pyka, N.
- Quint, W.
- Reiter, A.
- Schlitt, B.
- Schreiber, G.
- Spiller, P.J.
- Stadlmann, J.
- St hlker, T.
- Vinzenz, W.
- Vormann, H.
- Vorobjev, G.
- Yaramyshev, S.G.

**HIM**

Mainz, Germany

- Amberg, M.
- Aulenbacher, K.
- Barth, W.A.
- Gettmann, V.
- Mickat, S.

**Horia Hulubei National Institute for Physics and Nuclear Engineering**

Bucharest, Romania

- Cata-Danil, Gh.
- Dogaru, M.S.
- Enachescu, M.
- Gugiu, M.M.

- Ionescu, P.
- Mosu, D.V.
- Pantelica, A.
- Pantelica, D.
- Petre, A.
- Popescu, I.
- Simion, C.A.
- Stan-Sion, C.
- Statescu, M.
- Zamfir, N.V.

#### IAP

Frankfurt am Main, Germany

- Bänisch, D.
- Droba, M.
- Dziuba, F.D.
- Meusel, O.
- Mäder, D.
- Podlech, H.
- Ratzinger, U.
- Schempp, A.
- Schulte, K.
- Tiede, R.
- Xiao, C.

#### IBS

Daejeon, Republic of Korea

- Choi, B.
- Chung, Y.
- Jeon, D.
- Kim, B.
- Kim, D.G.
- Kim, H.J.
- Kim, H.
- Kim, M.
- Kim, S.K.
- Song, J.
- Yun, C.C.

#### IFIN

Magurele- Bucuresti, Romania

- Calinescu, I.C.
- Dobrescu, S.
- Ghita, D.G.
- Marginean, N.M.
- Mitu, I.O.
- Sava, T.B.
- Savu, B.

#### IMP

Lanzhou, People's Republic of China

- Chai, W.P.
- He, Y.
- Li, J.
- Ma, X.
- Shi, J.
- Song, M.T.
- Xia, J.W.

- Xiao, G.Q.
- Xu, H.S.
- Yang, J.C.
- Yuan, Y.J.
- Zhao, H.W.
- Zhou, X.

#### IN2P3 IPNL

Villeurbanne, France

- Peaucelle, C.

#### INFN/LNL

Legnaro (PD), Italy

- Bisoffi, G.
- Chiurlotto, F.
- Comunian, M.
- Dainelli, A.
- De Lazzari, M.
- Facco, A.
- Galatà, A.
- Maggiore, M.M.
- Minarello, A.
- Modanese, P.
- Palmieri, A.
- Palmieri, V.
- Pengo, R.
- Pisent, A.
- Porcellato, A.M.
- Stark, S.
- Stivanello, F.

#### INFN/LNS

Catania, Italy

- Castro, G.
- Celona, L.
- Gammino, S.
- Mascali, D.

#### INL

Idaho Falls, Idaho, USA

- Berg, J.F.
- Maddock, T.
- Palmotti, G.
- Youinou, G.

#### IPHC

Strasbourg Cedex 2, France

- Boutin, D.
- Osswald, F.R.

#### IPN

Orsay, France

- Laune, J.

#### ISU

Pocatello, Idaho, USA

- Imel, G.

**ITEP**

- Moscow, Russia
- Chalykh, B.B.

**IUAC**

- New Delhi, India
- Ahuja, R.
  - Antony, J.
  - Babu, S.
  - Chacko, J.
  - Choudhury, A.
  - Chowdhury, G.K.
  - Datta, T.S.
  - Dutt, R.N.
  - Ghosh, S.
  - Joshi, R.
  - Kanjilal, D.
  - Kar, S.
  - Karmakar, J.
  - Kumar, M.
  - Kumar, R.
  - Mathuria, D.S.
  - Mistri, K.K.
  - Pandey, A.
  - Patra, P.
  - Prakash, P.N.
  - Rai, A.
  - Roy, A.
  - Sacharias, J.
  - Sahu, B.K.
  - Sarkar, A.
  - Sonti, S.S.

**JINR**

- Dubna, Moscow Region, Russia
- Kazarinov, N.Yu.

**JLAB**

- Newport News, Virginia, USA
- Arenius, D.
  - Ganni, V.

**KEK**

- Ibaraki, Japan
- Adachi, T.
  - Arai, T.
  - Arakara, D.A.
  - Iwashita, T.
  - Kadokura, E.
  - Kawakubo, T.
  - Kubo, T.
  - Nakanishi, H.
  - Okamura, K.
  - Someya, H.
  - Takagi, A.
  - Takayama, K.
  - Wake, M.

**KNU**

- Daegu, Republic of Korea
- Kim, E.-S.

**Kyungpook National University**

- Daegu, Republic of Korea
- Bahng, J.
  - Hwang, J.G.
  - Jang, S.W.

**LBNL**

- Berkeley, California, USA
- Wan, W.

**LEHIPA Project, Physics Group**

- Mumbai, India
- Singh, P.
  - Singh, S.

**LPSC**

- Grenoble, France
- Thuillier, T.

**NCC, Korea**

- Kyonggi, Republic of Korea
- Kim, J.-W.

**NETS**

- Fuchu-shi, Japan
- Asao, H.
  - Okada, Y.

**Nippon Advanced Technology Co. Ltd.**

- Ibaraki-prefecture, Japan
- Iwashita, T.
  - Okazaki, K.

**Northern Illinois University**

- DeKalb, Illinois, USA
- Erdelyi, B.

**Research School of Physics and Engineering, Australian National University**

- Canberra, Australia
- Blacksell, M.C.
  - Linardakis, P.
  - Lobanov, N.R.
  - Tsifakis, D.

**RIKEN Nishina Center**

- Wako, Japan
- Fukunishi, N.
  - Hasebe, H.

- Imao, H.
- Kamigaito, O.
- Kase, M.
- Kuboki, H.
- Okuno, H.

**Sokendai**

Ibaraki, Japan

- Adachi, T.
- Leo, K.W.

**Soreq NRC**

Yavne, Israel

- Rodnizki, J.

**Technische Universität Dresden, Institut für Angewandte Physik**

Dresden, Germany

- Zschornack, G.

**The Hebrew University of Jerusalem, The Racah Institute of Physics**

Jerusalem, Israel

- Paul, M.

**The University of Tokyo**

Tokyo, Japan

- Ito, S.
- Matsuzaki, H.
- Morita, A.

**TIFR**

Mumbai, India

- Deshpande, R.D.
- Dhumal, P.
- Karande, J.N.
- Nanal, V.
- Palit, R.
- Pillay, R.G.
- Pose, M.S.
- Powale, S.M.
- Rozario, C.
- Sarkar, S.K.
- Sawant, M.E.
- Shinde, A.A.
- Sinha, S.R.
- Takke, A.N.

**TIT**

Yokohama, Japan

- Liu, X.
- Takayama, K.
- Yoshimoto, T.

**Tokyo City University**

Tokyo, Japan

- Barata, Y.
- Harada, S.

**TRIUMF, Canada's National Laboratory for Particle and Nuclear Physics**

Vancouver, Canada

- Ames, F.
- Bernier, N.
- Bricault, P.G.
- Dombsky, M.
- Kunz, P.
- Labrecque, F.S.
- Lassen, J.
- Marchetto, M.
- Mjøs, A.
- Morton, A.C.
- Nozar, M.
- Wong, J.

**TU Darmstadt**

Darmstadt, Germany

- Bonnes, U.
- Burandt, C.
- Eichhorn, R.
- Konrad, M.
- Nonn, P.N.

**TUB**

Beijing, People's Republic of China

- Guan, X.

**University of Notre Dame**

Indiana, USA

- Bauder, W.
- Collon, P.

**UTTAC**

Tsukuba, Ibaraki, Japan

- Sasa, K.

*Participants List*

|                       |  |                        |   |
|-----------------------|--|------------------------|---|
| Anger, Pascal         | CEA-GANIL  | Mickat, Sascha         | GSI Helmholtzzentrum für<br>Schwerionenforschung GmbH               |
| Baker, Sam            | Argonne National Laboratory                          | Miller, Samuel         | FRIB/Michigan State<br>University                                   |
| Beebe, Edward         | Brookhaven National<br>Laboratory                    | Morton, Colin          | TRIUMF  |
| Bisoffi, Giovanni     | INFN   | Mustapha, Brahim       | Argonne National Laboratory   |
| Bonnes, Uwe           | TU Darmstadt   | Newlin, Anna           | Argonne National Laboratory   |
| Bricault, Pierre      | TRIUMF   | Nolen, Jerry           | Argonne National Laboratory   |
| Celona, Luigi         | INFN-LNS   | Okuno, Hiroki          | RIKEN   |
| Chautard, Frederic    | GANIL / CNRS   | Okuno, Kozue           | RIKEN   |
| Comunian, Michele     | INFN LNL   | Osswald, Francis       | CNRS  |
| Dahl, Ludwig          | GSI Helmholtzzentrum                                 | Ostroumov, Peter       | Argonne National Laboratory   |
| Dickerson, Clayton    | Argonne National Laboratory                          | Palchan, Tala          | Argonne National Laboratory   |
| Falbo, Luciano        | CNAO   | Palit, Rudrajyoti      | Tata Institute of Fundamental<br>Research                           |
| Fraser, Matthew       | CERN   | Pardo, Lucinda         | Argonne National Laboratory   |
| Ghita, Dan Gabriel    | IFIN-HH  | Pardo, Richard         | Argonne National Laboratory   |
| Ghosh, Subhendu       | Inter University Accelerator<br>Center               | Peters, Christopher    | Argonne National Laboratory   |
| Guan, Xialing         | Qinghua University                                   | Petit, Eric            | CEA/GANIL   |
| He, Yuan              | IMP  | Pikin, Alexander       | Brookhaven National<br>Laboratory                                   |
| Hendricks, Matthew    | Argonne National Laboratory                          | Porcellato, Anna Maria | INFN-LNL  |
| Herfurth, Frank       | GSI Helmholtzcenter for<br>Heavy Ion Research        | Power, Maria           | Argonne National Laboratory   |
| Ito, Seiji            | The University of Tokyo                              | Repnaw, Roland         | Max-Planck-Institute for<br>Nuclear Physics                         |
| Jeon, Dong-O          | RISP/IBS   | Rifuggiato, Danilo     | INFN-LNS  |
| Jin, Tao              | IMP  | Roosa, Michael         | Thomson Broadcast   |
| Kamigaito, Osamu      | RIKEN  | Ruelas, Marcos         | RadiaBeam Technologies,<br>LLC.                                     |
| Kanjilal, Dinakar     | Inter University Accelerator<br>Center               | Sasa, Kimikazu         | University of Tsukuba   |
| Kelly, Michael        | Argonne National Laboratory                          | Schlitt, Bernhard      | GSI Helmholtzzentrum fuer<br>Schwerionenforschung                   |
| Kim, Jin-Soo          | FAR-TECH, Inc.                                       | Scott, Robert          | Argonne National Laboratory   |
| Kim, Jong-Won         | National Cancer Center                               | Shi, Aimin             | Modern Physics Institute of<br>Chinese Academy of Sciences          |
| Kondrashev, Sergey    | Argonne National Laboratory                          | Shi, Jian              | Institute of Modern Physics   |
| Kunderova, Helena     | GSI Helmholtzzentrum                                 | Stark, Sergey          | INFN-LNL  |
| Laxdal, Robert        | TRIUMF   | Takayama, Ken          | High Energy Accelerator<br>Research Organization                    |
| Lighthall, Holly      | Argonne National Laboratory                          | Vitulli, Silvia        | Fondazione CNAO   |
| Liu, Jian             | Geely group  | Vondrasek, Richard     | Argonne National Laboratory   |
| Liu, Xingguang        | Tokyo Institute of Technology                        | Yin, Da-yu             | Institute of Modern<br>Physics(IMP), Chinese<br>Academy of Sciences |
| Lobanov, Nikolay      | The Australian National<br>University                | Zinkann, Gary          | Argonne National Laboratory   |
| Luo, Yong             | Argonne National Laboratory                          |                        |   |
| Maggiro, Mario        | INFN-LNL   |                        |   |
| Manikonda, Shashikant | Argonne National<br>Laboratory                       |                        |   |
| Marchetto, Marco      | TRIUMF   |                        |   |
| Meusel, Oliver        | Institut for Applied Physik,<br>University Frankfurt |                        |   |